

**Smart pH and Thermosensitive Injectable Hydrogels:  
Chitosan – Hydroxyapatite – Heparin Based  
Functionalised Biomaterials for Bone Regeneration**

by

**Fatma Zehra Kocak**

Engineering Department, Lancaster University  
United Kingdom

A thesis submitted to Lancaster University for the Degree of  
Doctor of Philosophy in Materials Science

March, 2021

## ABSTRACT

Hard and soft tissue repair and regeneration require multiple surgical interventions, as very often-repeated clinical procedures are required. In addition, insufficient vascularisation remains as the main challenge for bone repair and regeneration. Therefore, bone regeneration via minimal invasive biomaterials promoting angiogenesis by bioactive agents are very much considered at present. Hereof, among new generation biomaterials, *in-situ* forming stimuli responsive injectable hydrogels have been of interest both in clinical and non-clinical communities. In this study, novel pH and thermosensitive *in-situ* formed injectable hydrogel compositions were developed by a heparin (Hep) functionalised chitosan (CS) polymer matrix integrated with a non-sintered hydroxyapatite (HA) system neutralised with sodium bicarbonate (NaHCO<sub>3</sub>). Due to designed bioactive features, CS/HA/Hep hydrogels are desired to ensure strong chemical anchorage and biological bridging by promoting vascular network formation at bone tissue defects due to the potential binding capacity of Hep for endogenous angiogenic growth factors and proteins. The production and optimisation of hydrogel compositions and their modification for pre-sterile synthesis technique with glycerol additive for enhancing mechanical properties meanwhile were investigated. The versatile properties of hydrogels were investigated for many aspects, such as injectability, gelation, rheology, mechanical properties, degradability, bioactivity, biocompatibility and angiogenesis.

Hydrogel compositions showed facile injectability allowing suitable manual injection by 21 gauge (G) minimum needle thickness, and fast gelation at average body temperature (37 °C). In modified hydrogels, slight pH increment at solutions above 6.4 provided interpenetrating cross-linked morphology starting gelation in 2-3 minutes with enhanced elasticity, and mechanical strength. Hydrogels showed great bioactivity confirmed in Simulated Body Fluid (SBF) by forming mineralised carbonated apatite layer. The gradual hydrogel degradation was confirmed over 6-weeks up to 60% and 70% in PBS and Lysozyme-PBS media respectively. All developed hydrogels were cytocompatible and ensured proliferation of osteoblast-like cells. Optimal CS/HA/Hep hydrogel compositions showed excellent pro-angiogenic capacity in *ex-ovo* chick embryo's CAM model. Novel tuneable injectable pH and thermosensitive hydrogels (CS/HA/Hep) have tremendous clinical potential for minimal invasive surgery for bone repair and regeneration and targeted drug delivery applications.

## DECLARATION

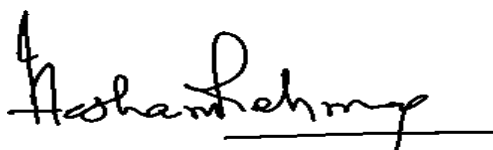
I declare that this thesis has not been submitted in support of an application for another degree at this or any other university. It is the result of my own work and includes nothing that is the outcome of work done in collaboration except where specifically indicated. Acknowledgement is made in the text of assistance received and all major sources of information are properly referenced. Many of the ideas in this thesis were the product of discussion with my supervisor.



Signed .....

Date ..... 29/09/2020.....

Student: Fatma Zehra Kocak



Signed .....

Date ..... 26/09/2020.....

Supervisor: Prof. Ihtesham Ur Rehman

## ACKNOWLEDGEMENTS

First and foremost, all praises and thanks to Almighty Allah (S.W.T) for countless blessings. I would like to express my gratitude to all who have supported me in this challenging but life changing journey that started at The University of Sheffield. I am overwhelmed in all gratefulness to express my appreciations to my main supervisor Prof. Ihtesham Ur Rehman. He has provided invaluable support and guidance to me throughout this project. Without his guidance, I would be lost in this very challenging and interdisciplinary field. His enthusiasm in biomaterials field and encouragements to our group inspired me so much, which triggered my interests in gaining new knowledge and experience in this field. I would like to extend my gratitude to my second supervisor Dr. Muhammad Yar, Associate Professor at IRCCBM COMSATS University Islamabad Lahore Campus for his precious support and encouragements from the beginning of this Ph.D. project. I am also thankful to Dr. Timothy Douglas for all his feedback during his co-supervision at Lancaster University. I would like to thank to all my colleagues, especially my seniors Nihad, Adibah and Daniela; and Hafsa, Yasser, Fahad, Michael and Zhiyi. I also thank to MSc students who worked with me; Karim A. Shahid (2017-2018) and Benjamin Carrera-Knowles (2019-2020), who has been recently awarded the ‘Armourers and Brasiers’ Company’ medal for the best final year project in Materials Science.

I am very grateful to all staff and colleagues training me on various instruments and techniques. I am thankful especially to Dr. Chris Holland, who trained me to do rheology studies, Nihad Al-Furaiji to perform HA synthesis, Daniela Lazaro to conduct Spectroscopy, Ahtasham Raza and Hafsa Akhtar in carrying out Cell cultures, Sarah Shafaat and Naside Mangir in CAM assay studies, Valeria Najera to do Histology, Nathan Halcovitch in doing XRD, Jessica Fisher in TGA&DSC, Sara Baldock performed SEM, and Timothy Forber, who let me borrow his design of syringe rig for injectability tests. I owe special thanks to ‘Extrasul (Sao Paulo, Brazil)’ for their kind gift of sodium bovine heparin, and the Sheffield University Learned Society, and Lancaster University departmental funds awarded me to participate at conferences in Japan and Pakistan. I am very grateful to the ‘Turkish Ministry of National Education’ for fully funding my studies and making this Ph.D. possible. I would like to thank to my supervisor Prof. Dr. Necmettin Tarakcioglu in Turkey for advising me to apply for this scholarship opportunity. I owe special thanks to my uncle M. Akif Ozdas who has

encouraged and motivated me during my Ph.D. and all my family who always support me not only during my challenging times but throughout my life.

Note: This Ph.D. study has been carried out by the support of the government of 'The Republic of Turkey'.

## DEDICATION

Dedicated to the One, Almighty Allah (S.W.T.),

All patients who undertake bone treatments,

especially to my uncle M. Akif Ozdas who has motivated me

throughout my Ph.D.,

all Ceramic Engineers in the World,

and

My Family

## PUBLICATIONS AND PRESENTATIONS

### **Published Article:**

Kocak, F. Z., Talari A. C. S., Yar, M., Rehman I. U. (2020) 'In - Situ Forming pH and Thermosensitive Injectable Hydrogels to Stimulate Angiogenesis: Potential Candidates for Fast Bone Regeneration Applications', International Journal of Molecular Sciences, 21(5), pp. 1–26, <https://doi.org/10.3390/ijms21051633>.

### **Research Presentations:**

#### ***Oral Presentations:***

1. 7<sup>th</sup> International Symposium on Biomedical Materials (ISBM): Science and Technology Innovation and Knowledge Economy, '*Minimally Invasive Thermosensitive Hydrogels to Promote Angiogenesis for Bone Regeneration and Drug Delivery*', Lahore, Pakistan (11-12 December 2019).
2. PGR departmental conference, '*Smart Thermoresponsive Injectable Hydrogels for Sufficiently Vascularized Bone Regeneration*' Lancaster University, UK (3-4 Jul 2019)
3. British Council, Biomaterials UK-Russia Symposium, '*Thermosensitive Chitosan Based Pro-Angiogenic and Bioactive Hydrogels for Bone Regeneration*', Lancaster University, UK, (11-12 February 2019)

#### ***Poster Presentations:***

1. British Council Researcher Links UK-Russia Workshop: Patient-tailored biomaterials for tissue regeneration, combating microbial contamination and drug delivery, '*Thermosetting, Injectable Bioactive Hydrogels for Bone Bioengineering*', Lancaster, UK, (2-4 October 2019)

2. Bioengineering and Health Materials Symposium, '*In-situ Forming, Injectable Bioactive Hydrogels for Bone Regeneration*', Lancaster, UK, (15 October 2019)
3. 224<sup>th</sup> Infrared & Raman Discussion Group (IRDG) Meeting, '*Characterisation of Bioactive and Biodegradable Thermosetting Injectable Hydrogels for Bone Bioengineering*', Lancaster, UK, (19 September 2019)
4. 5<sup>th</sup> World Congress of the Tissue Engineering and Regenerative Medicine (TERMIS), '*Pro-angiogenic Thermosensitive Injectable Hydrogels for Bone Regeneration*', Kyoto, Japan, (5 September, 2018)
5. Engineering Researcher Symposium-2018, '*pH/Thermosensitive Injectable Hydrogels for Bone Regeneration*', University of Sheffield, UK, (26 June 2018)

**Prize:**

Learned Society Funding award (450£) in The University of Sheffield for attendance of *5<sup>th</sup> World Congress of the Tissue Engineering and Regenerative Medicine (TERMIS)*, Japan 4-7 Sep 2018.

**Project Mentoring:**

1. Shahid, K. A., 2018, '*An Introduction to Chitosan-Based Hydrogels for Dental Pulp Regeneration*', The University of Sheffield, UK.
2. Carrera-Knowles, B. 2020, '*The Evaluation of Thermosensitive Chitosan-Based Injectable Hydrogels for Bone Regeneration*', Lancaster University, UK.

## PREFACE

This thesis is formed in six different chapters. The opening chapter of the thesis starts with the Literature Review (See Chapter 1) and end with a final ‘Summary, Conclusions and Future Works’ Chapter (See Chapter 6). The remaining chapters are inner structured individually with titles of ‘Introduction, Materials and Methods, Results and Discussion, and Summary and Conclusions’.

Chapter 1 involves a detailed fundamental knowledge of the subject area, e.g. bone structure, bone failures and diseases. Then, a comprehensive literature review is included related to bone repair and regeneration techniques, types of biomaterials used in bone tissue engineering and different regenerative approaches, particularly minimal invasive injectable hydrogels, as well as desired biomaterial properties including bioactivity, osteoconductivity and vascularisation were dealt with in details. Furthermore, the main characterisation techniques which are commonly used to analyse the chemical, physical and biological properties of injectable materials are elaborated in detail. Following this literature review, in the last section of this chapter the project aims, and objectives are identified comprehensively.

In Chapter 2, Hydroxyapatite (HA) synthesis by sol-gel technique, physical and chemical characterisation of HA and its comparison with commercial HA are described. The effect of synthesis parameters e.g., initial pH and heat treatment parameters on HA properties including particle size, shape and formation of different phases and their attribution to crystallinity are investigated. The investigated chemical and physical properties of HA by various characterisation techniques are elaborated including chemical analyses: functional group analyses by FTIR-ATR and Raman spectroscopy; chemical phase and crystallinity evaluation by X-Ray Diffraction (XRD); and elemental analysis by Energy Dispersive X-Ray Spectroscopy (EDS), Morphological analyses by Scanning Electron Microscopy (SEM); and BET (Brunauer, Emmett and Teller), and thermal analyses by Simultaneous Thermal Gravimetric Analyses & Differential Scanning Calorimetry (TGA&DSC). The pure HA with small carbonate content and biphasic HA ( $\beta$ -TCP) were obtained with at varying pH conditions. A HA

composition (HA-5D) obtained with small carbonate content in non-sintered form was chosen as optimal because of its rough surface features with high surface area which is expected to enhance bioresorbability and bioactivity. This HA (HA-5D) compound was employed in synthesis of modified hydrogel.

Chapter 3 deals with synthesis and optimisation of pH and thermo-sensitive injectable hydrogels (CS/HA/Hep) by using a sol-gel method, and their main characterisations. In this chapter, synthesis and characterisation of initial hydrogels and their modification denoted as modified hydrogels are discussed. Modified hydrogels were produced with total sterile preparation technique that involve additionally heat sterilisation of pre-synthesised HA powders (HA5-D) and CS dispersions with the glycerol additive as heat protective agent and for enhancing mechanical properties. The various characterisations techniques used to investigate properties of injectable solutions and hydrogels including physical, chemical and mechanical analyses for initial and modified hydrogel formulations, comparatively. These involve physical characterisations by injectability analyses (qualitative and quantitative), gelation and viscoelastic behaviour analyses by rheology, and morphology analyses by SEM; thermal analyses by TGA/DSC; chemical analyses by FTIR-ATR and FT-Raman spectroscopy, and XRD analyses; and mechanical characterisations by compressive strength tests. The results gained from the synthesis works and characterisations are evaluated in ‘Results’ section and discussed in the light of literature in ‘Discussion’ section. The summary of the overall chapter and remaining challenges are outlined in ‘Summary and Conclusions’ section. Further characterisations of injectable hydrogel compositions are dealt with in the following two chapters.

Chapter 4 involves biochemical characterisations of mainly modified hydrogels including bioactivity tests performed by Simulated Body Fluid (SBF), liquid absorption (swelling) capacity, *in-vitro* degradation tests performed comparatively in the presence or absence of an enzyme (Lysozyme) in Phosphate Buffer Saline (PBS) media. These tests include other associated analyses, such as, pH and weight measurements, chemical analyses by FTIR-ATR and EDS, and morphological characterisations by SEM. In addition, drug release studies of Hep and local Hep determination by a colorimetric Toluidine Blue assay are dealt with in Chapter 4.

In the following Chapter of the thesis (See Chapter 5), biocompatibility and angiogenesis assessments of hydrogels are dealt with. Cell culture studies performed with initial hydrogels include *in-vitro* cell cytocompatibility tests by cell attachment and proliferation tests with osteoblast-like cell (MG-63) are discussed. In addition, cell differentiation experiments including Calcium and Collagen deposition analyses by Alizarin-Red and Sirius-Red assays results are assessed. The evaluation of angiogenesis for initial and modified hydrogels via the *ex-ovo* CAM assay, and quantification of angiogenesis via vascular index method and qualitative assessment of angiogenesis by histology studies are included.

Following this chapter, an overall ‘Summary, Conclusions and Future Works’ is described in Chapter 6, outlining all major results explicitly and future studies including non-conclusive experimental studies which were hindered due to COVID-19 pandemic and additional beneficial works related to the aims and objectives of this project. Finally, an Appendix section is given to cover some additional experimental studies performed but which were required as a learning process but are not directly related to the project or partially completed. Some additional images and the Abstract of a published article are also included in this section of the thesis. Subsequently, all references used and cited in this thesis are listed in bibliography.

# TABLE OF CONTENTS

<b><u>ABSTRACT</u></b>	<b><u>II</u></b>
<b><u>DECLARATION</u></b>	<b><u>III</u></b>
<b><u>ACKNOWLEDGEMENTS</u></b>	<b><u>IV</u></b>
<b><u>DEDICATION</u></b>	<b><u>V</u></b>
<b><u>PUBLICATIONS AND PRESENTATIONS</u></b>	<b><u>VI</u></b>
<b><u>PREFACE</u></b>	<b><u>VIII</u></b>
<b><u>TABLE OF CONTENTS</u></b>	<b><u>XI</u></b>
<b><u>LIST OF TABLES</u></b>	<b><u>XVI</u></b>
<b><u>LIST OF FIGURES</u></b>	<b><u>XVII</u></b>
<b><u>LIST OF ABBREVIATIONS</u></b>	<b><u>XXXI</u></b>
<b><u>LIST OF SYMBOLS</u></b>	<b><u>XXXIII</u></b>
<b><u>1 LITERATURE REVIEW</u></b>	<b><u>1</u></b>
<b><u>1.1 INTRODUCTION</u></b>	<b><u>1</u></b>
<b><u>1.2 BONE</u></b>	<b><u>2</u></b>
1.2.1    BONE STRUCTURE AND PROPERTIES	<u>2</u>
1.2.1.1    Chemical Structure of Bone	<u>2</u>
1.2.1.2    Classification and Architecture of Bone	<u>4</u>
1.2.1.3    Mechanical Properties of Bone	<u>6</u>
<b><u>1.3 BONE REMODELLING AND GROWTH</u></b>	<b><u>6</u></b>
1.3.1    BONE FRACTURE HEALING AND ROLE OF BLOOD VESSELS	<u>8</u>
<b><u>1.4 BONE HEALTH AND FRACTURES</u></b>	<b><u>10</u></b>
1.4.1    THE ROLE OF HORMONES IN BONE HEALTH	<u>10</u>
1.4.2    COMMON BONE DISEASES	<u>11</u>
1.4.2.1    Paget's disease	<u>11</u>
1.4.2.2    Rickets and Osteomalacia	<u>12</u>
<b><u>1.5 BONE REPAIR AND REGENERATION</u></b>	<b><u>12</u></b>
1.5.1    TRANSPLANTATION TECHNIQUES	<u>12</u>
1.5.2    BONE TISSUE ENGINEERING	<u>12</u>
<b><u>1.6 BIOMATERIALS</u></b>	<b><u>13</u></b>
1.6.1    REQUIRED PROPERTIES OF BIOMATERIALS FOR BONE REPAIR AND REGENERATION	<u>13</u>
1.6.1.1    Biocompatibility	<u>13</u>
1.6.1.2    Bioactivity	<u>14</u>
1.6.1.3    Osteoinduction, Osteoconduction and Osteointegration	<u>16</u>

1.6.1.4	Biodegradability	17
1.6.1.5	Architecture and Porosity	17
1.6.2	CLASSIFICATION OF BIOMATERIALS USED FOR BONE REPAIR AND REGENERATION	18
1.6.2.1	Metals	18
1.6.2.2	Ceramics	19
1.6.2.3	Polymers	29
<b>1.7</b>	<b>ADVANCED REGENERATIVE MEDICINE TECHNIQUES</b>	<b>35</b>
1.7.1	DRUG DELIVERY SYSTEMS	35
1.7.2	GROWTH FACTORS	36
1.7.3	ANGIOGENESIS, GROWTH FACTORS AND HEPARIN	38
<b>1.8</b>	<b>INJECTABLE BIOMATERIALS FOR MINIMAL INVASIVE SURGERY</b>	<b>41</b>
1.8.1	HYDROGELS	41
1.8.1.1	Classification of Hydrogels	42
1.8.2	<i>IN-SITU</i> FORMED INJECTABLE HYDROGELS	43
<b>1.9</b>	<b>PH AND THERMO-SENSITIVE INJECTABLE CHITOSAN/HYDROXYAPATITE/HEPARIN HYDROGELS</b>	<b>48</b>
1.9.1	PH AND THERMOSENSITIVE CHITOSAN HYDROGELS	48
1.9.2	CHITOSAN- HYDROXYAPATITE HYDROGELS	50
1.9.3	HEPARIN INCORPORATED CHITOSAN HYDROGELS	51
1.9.4	STERILIZATION OF THERMOSENSITIVE CHITOSAN SOLUTIONS	51
<b>1.10</b>	<b>MAIN CHARACTERISATION TECHNIQUES USED FOR THERMOSENSITIVE INJECTABLE HYDROGELS</b>	<b>56</b>
1.10.1	PHYSICAL ANALYSES	56
1.10.1.1	Injectability and Syringability	56
1.10.1.2	Sol-gel Transition and Rheology	58
1.10.1.3	Gel Morphology	59
1.10.1.4	Thermal Analysis by TGA/DSC	63
1.10.1.5	Surface Area Measurement - Brunauer-Emmett-Teller (BET)	64
1.10.1.6	Swelling (Liquid Absorption Capacity)	64
1.10.2	CHEMICAL ANALYSES	65
1.10.2.1	FTIR Spectroscopy	65
1.10.2.2	Raman Spectroscopy	67
1.10.3	BIOLOGICAL ANALYSES	71
1.10.3.1	Evaluation of Biodegradation	71
1.10.3.2	Evaluation of Biocompatibility	73
1.10.3.3	Evaluation of Angiogenesis	77
<b>1.11</b>	<b>SUMMARY</b>	<b>81</b>
<b>1.12</b>	<b>AIMS AND OBJECTIVES</b>	<b>84</b>
1.12.1	AIMS	84
1.12.2	OBJECTIVES	84
1.12.3	HYPOTHESIS	87
<b>2</b>	<b>HYDROXYAPATITE SYNTHESIS AND CHARACTERISATION</b>	<b>88</b>
<b>2.1</b>	<b>INTRODUCTION</b>	<b>88</b>
<b>2.2</b>	<b>MATERIALS AND METHODS</b>	<b>88</b>
2.2.1	MATERIALS	88
2.2.2	SOL-GEL SYNTHESIS OF HYDROXYAPATITE	89
2.2.3	CHARACTERISATION OF HYDROXYAPATITE POWDERS	93
2.2.3.1	Raman Spectroscopy	93
2.2.3.2	FTIR-Photoacoustic (PAS) Spectroscopy	93
2.2.3.3	X-Ray Diffraction (XRD)	94

2.2.3.4 Energy Dispersive X-Ray Spectroscopy (EDS)	94
2.2.3.5 Scanning Electron Microscopy (SEM)	95
2.2.3.6 Surface Area Measurements by Brunauer-Emmett-Teller (BET)	95
2.2.3.7 Simultaneous Thermal Gravimetric Analyses & Differential Scanning Calorimetry (TGA & DSC)	95
<b>2.3 RESULTS</b>	<b>95</b>
2.3.1 SYNTHESIS OF HA AND REACTION YIELDS	95
2.3.2 RAMAN SPECTROSCOPY	96
2.3.3 FTIR- PAS SPECTROSCOPY	101
2.3.4 X-RAY DIFFRACTION (XRD)	106
2.3.5 THERMAL GRAVIMETRIC ANALYSES & DIFFERENTIAL SCANNING CALORIMETRY (TGA & DSC)	110
2.3.6 ENERGY DISPERSIVE X-RAY SPECTROSCOPY (EDS)	112
2.3.7 SCANNING ELECTRON MICROSCOPY (SEM)	114
2.3.8 BET (BRUNAUER, EMMETT AND TELLER)	120
<b>2.4 DISCUSSION</b>	<b>121</b>
<b>2.5 SUMMARY AND CONCLUSIONS</b>	<b>126</b>

---

<b>3 CHITOSAN/HYDROXYAPATITE/HEPARIN BASED PH AND THERMOSENSITIVE INJECTABLE HYDROGELS</b>	<b>128</b>
--	------------

<b>3.1 INTRODUCTION</b>	<b>128</b>
<b>3.2 MATERIALS AND METHODS</b>	<b>130</b>
<b>3.3 SOL-GEL SYNTHESIS OF PH AND THERMOSENSITIVE INJECTABLE (CS/HA/HEP) HYDROGELS</b>	<b>130</b>
<b>3.4 CHARACTERISATION OF INJECTABLE HYDROGELS</b>	<b>134</b>
3.4.1 INJECTABILITY	134
3.4.1.1 Qualitative Injectability Analyses	135
3.4.1.2 Quantitative Injectability Analyses	135
3.4.2 TEST TUBE INVERT METHOD FOR INCIPIENT GELATION TIME	137
3.4.3 RHEOLOGY MEASUREMENTS	137
3.4.4 MORPHOLOGICAL ANALYSES BY SCANNING ELECTRON MICROSCOPY (SEM)	138
3.4.5 THERMAL ANALYSES BY SIMULTANEOUS TGA & DSC	139
3.4.6 MECHANICAL ANALYSES BY COMPRESSION TESTS	139
3.4.7 FOURIER TRANSFORM INFRARED-ATTENUATED TOTAL REFLECTANCE (FTIR-ATR) SPECTROSCOPY	140
3.4.8 FOURIER TRANSFORM-RAMAN (FT-RAMAN) SPECTROSCOPY	141
3.4.9 X-RAY DIFFRACTION (XRD) ANALYSES	141
<b>3.5 RESULTS</b>	<b>142</b>
3.5.1 SYNTHESIS OF INJECTABLE HYDROGEL SOLUTIONS	142
3.5.2 SOLUTION PH, HOMOGENEITY, STABILITY AND GELATION FEATURES	145
3.5.3 SOL-GEL TRANSITION AND GELATION FEATURES	147
3.5.4 INJECTABILITY MEASUREMENTS	152
3.5.4.1 Qualitative Injectability Analyses	152
3.5.4.2 Quantitative Injectability Analyses	154
3.5.5 RHEOLOGY ANALYSES	159
3.5.6 MORPHOLOGICAL ANALYSES BY SEM	163
3.5.7 MECHANICAL ANALYSES BY COMPRESSION TESTS	172
3.5.8 CHEMICAL ANALYSES	174
3.5.8.1 FT-IR-(ATR) Analyses	175
3.5.8.2 FT-Raman Analyses	185

3.5.8.3 XRD Analyses	190
3.5.9 THERMAL ANALYSES BY TGA & DSC	191
<b>3.6 DISCUSSION</b>	<b>194</b>
<b>3.7 SUMMARY AND CONCLUSIONS</b>	<b>202</b>

<b>4 BIOACTIVITY, BIODEGRADATION AND DRUG RELEASE STUDIES FOR SYNTHESIZED HYDROGELS</b>	<b>204</b>
---	------------

<b>4.1 INTRODUCTION</b>	<b>204</b>
<b>4.2 MATERIALS AND METHODS</b>	<b>205</b>
<b>4.3 SWELLING (LIQUID ABSORPTION) TESTS</b>	<b>205</b>
4.3.1 PREPARATION OF TEST SAMPLES AND PHOSPHATE BUFFER SALINE (PBS) MEDIA	205
4.3.2 pH ANALYSES	206
4.3.3 WEIGHT ANALYSES	206
<b>4.4 IN-VITRO DEGRADATION TESTS</b>	<b>206</b>
4.4.1 PREPARATION OF TEST SAMPLES AND DEGRADATION MEDIA	207
4.4.2 pH ANALYSES	208
4.4.3 WEIGHT ANALYSES	208
4.4.4 MORPHOLOGICAL ANALYSES BY SEM	208
4.4.5 CHEMICAL ANALYSES BY FTIR-ATR	209
<b>4.5 BIOACTIVITY TESTS BY SIMULATED BODY FLUID (SBF)</b>	<b>209</b>
4.5.1 PREPARATION OF TEST SAMPLES AND SBF MEDIA	209
4.5.2 pH ANALYSES	210
4.5.3 WEIGHT ANALYSES	210
4.5.4 CHEMICAL ANALYSES BY FTIR-ATR	211
4.5.5 MORPHOLOGICAL ANALYSES BY SEM	211
4.5.6 ELEMENTAL ANALYSES BY EDS	211
<b>4.6 DRUG (HEP) DELIVERY ANALYSES BY TOLUIDINE BLUE (TB) ASSAY</b>	<b>211</b>
4.6.1 TOLUIDINE BLUE (TB) SOLUTION PREPARATION	212
4.6.2 LOCAL HEP DETERMINATION	212
4.6.3 DRUG (HEP) RELEASE STUDIES	212
<b>4.7 STATISTICAL ANALYSES</b>	<b>214</b>
<b>4.8 RESULTS</b>	<b>214</b>
4.8.1 SWELLING ANALYSES BY WEIGHT AND pH CHANGE	214
4.8.2 <i>IN-VITRO</i> DEGRADATION ANALYSES	216
4.8.2.1 Weight and pH Analyses During Degradation	216
4.8.2.2 Morphological Analyses by SEM	220
4.8.2.3 Chemical Analyses by ATR	223
4.8.3 BIOACTIVITY ANALYSES BY SBF	226
4.8.3.1 Weight and pH Tests	226
4.8.3.2 Morphological Analyses by SEM	229
4.8.3.3 Elemental Analyses by EDS	233
4.8.3.4 Chemical Functional Group Analyses by ATR	236
4.8.4 HEPARIN DETERMINATION AND DRUG (HEPARIN) RELEASE STUDIES	238
4.8.4.1 Local Heparin Determination by Toluidine Blue (TB) Assay	238
4.8.4.2 Heparin Release Studies	243
<b>4.9 DISCUSSION</b>	<b>247</b>
<b>4.10 SUMMARY AND CONCLUSIONS</b>	<b>251</b>

---

**5 BIOMATERIALS AND BIOPROCESSING OF SYNTHESIZED HYDROGELS** **252**

---

<b>5.1 INTRODUCTION</b>	<b>252</b>
<b>5.2 MATERIALS AND METHODS</b>	<b>252</b>
5.2.1 MATERIALS	252
<b>5.3 CELL CULTURE STUDIES</b>	<b>253</b>
5.3.1 ALAMAR BLUE (RESAZURIN) ASSAY	255
5.3.2 PREPARATION OF RESAZURIN SOLUTION	255
5.3.3 ALAMAR BLUE ASSAY	255
5.3.4 CELL ATTACHMENT OBSERVATION BY OPTICAL MICROSCOPY	256
5.3.5 EXTRACELLULAR MATRIX PRODUCTION ASSAYS	256
5.3.5.1 Calcium Deposition Analyses by Alizarin Red Assay	256
5.3.5.2 Collagen Deposition Analyses by Sirius Red Assay	257
<b>5.4 ANGIOGENESIS EVALUATION BY EX-OVO CHICK CHORIOALLANTOIC MEMBRANE (CAM) ASSAY</b>	<b>258</b>
5.4.1 QUANTIFICATION OF ANGIOGENESIS BY VASCULAR INDEX METHOD	261
5.4.2 HISTOLOGY	261
<b>5.5 STATISTICAL ANALYSIS</b>	<b>262</b>
<b>5.6 RESULTS</b>	<b>262</b>
5.6.1 CELL VIABILITY AND PROLIFERATION	262
5.6.2 CELL ATTACHMENT/MORPHOLOGY OBSERVATION BY OPTICAL MICROSCOPY	265
5.6.3 CALCIUM AND COLLAGEN DEPOSITION DURING CELL CULTURE	268
5.6.3.1 Calcium Deposition Evaluation via Alizarin Red Assay	268
5.6.3.2 The Collagen Deposition Evaluation by Sirius Red Assay	272
5.6.4 THE ANGIOGENESIS STUDIES BY CAM ASSAY	273
5.6.4.1 Histology Analyses of Hydrogels Tested in CAM Assay	281
<b>5.7 DISCUSSION</b>	<b>285</b>
<b>5.8 SUMMARY AND CONCLUSIONS</b>	<b>287</b>

---

**6 SUMMARY, CONCLUSIONS AND FUTURE WORKS** **288**

---

<b>6.1 SUMMARY</b>	<b>288</b>
<b>6.2 CONCLUSIONS</b>	<b>289</b>
<b>6.3 FUTURE WORKS</b>	<b>295</b>

---

**APPENDIXES** **297**

---

---

**REFERENCES** **303**

---

## LIST OF TABLES

<b>Table 1. 1</b> Mechanical and mineralogical properties of bone samples from different species. Table was adapted with kind permission from Springer Nature (Rogers & Ziopoulos, 1999). ....	6
<b>Table 2. 1</b> HA samples fabricated by using different synthesis or heat treatment parameters, including commercial HA products as comparison with or without treatments, and their denotations .....	92
<b>Table 2. 2</b> Atom percentages, Ca/P ratios and their means counted from weight % of elements obtained from EDS analyses of five different points.....	114
<b>Table 3. 1</b> The composition of different injectable hydrogel formulations * .....	133
<b>Table 3. 2</b> The pH values measured in all steps of synthesis of initial hydrogels including pH of reagent solutions and their mixtures, final solution after neutralization, and after gelation, which were given with measured temperature during pH measurements. (pH values of stock acetic acid (0.5 M) and NaHCO <sub>3</sub> (0.48 M) solutions were 2.24 and 8.50, respectively while pH of Deionised water (Dw) was 6.58. The pH values of Hep solutions in Dw for SI, SII and SIII compositions were measured as 6.58, 6.56 and 6.61, respectively.) .....	145
<b>Table 3. 3</b> The pH values of solutions at 4 °C and 20 °C for modified injectable hydrogel formulations in different compositions .....	146
<b>Table 3. 4</b> The incipient gelation time of initial hydrogel compositions was determined by the test tube inversion method at 37 °C immediately after the synthesis of the liquids at 4 °C. ....	148
<b>Table 3. 5</b> The incipient gelation time for all modified hydrogel compositions was measured by test tube inversion method at 37 °C immediately after synthesis of liquids at 4 °C. ....	149
<b>Table 3. 6</b> Qualitative injectability assessment by rating the flow of different hydrogel compositions through manual injection via a range of needle sizes (1). ....	152
<b>Table 3. 7</b> The quantitative injectability results by measurements of forces in different stages of injection for diverse non-modified initials hydrogel solution compositions: CI, CII and SI obtained in the same day of synthesis (Day 0). Experiments were performed using both a needleless and 19 G needle-coupled syringe. The results were expressed as mean ± standard deviations (SD) (n=6) (SD for experimental replicates). ....	156
<b>Table 3. 8</b> The quantitative injectability force measurements during injection of non-modified initial hydrogel solutions: CI, CII and SI obtained after 3 days of synthesis (Day 3). Experiments were performed by both a needleless and 21 G needle coupled syringe. The results were expressed as mean ± SD (n=6) (SD for experimental replicates). ....	157
<b>Table 3. 9</b> The quantitative injectability results of Modified sterile hydrogel solutions for the compositions of CI, CII, S0 and SI. Experiments were performed using both a needleless and a 19 G needle coupled syringe. The results obtained on the synthesis day (Day 0) of the solutions, and 1 day after synthesis (Day 1) are represented as D0 and D1 respectively. The results were expressed as a mean ± SD (n=6) (SD for experimental replicates). ....	159
<b>Table 3. 10</b> The peak assignments of chemical functional groups from ATR spectra of hydrogels. ....	179

## LIST OF FIGURES

**Figure 1. 1** Hierarchical structure of human bone densely packed compact bone and porous spongy bone structures in macro scale; parallel collagen fibrils and hydroxyapatite among them circular lamellar structure surrounding blood vessels and nerves in Haversian channels. figure was reproduced with kind permission: © 2015 by Springer Nature Publishing group (Wegst et al., 2015). ..... 3

**Figure 1. 2** The demonstration of a bone horizontal section involving cortical and trabecular bone including osteons composed of a central channel hosting blood vessels, nerves, and lymphatic vessels (branch through the perforating channels) and surrounding mineralised concentric lamellas. Interstitial lamellae locating between osteons and circumferential lamellae laying under periosteum that has periosteal artery and veins. This used figure licensed under ©CC BY 4.0 by Rice University “Anatomy and physiology textbook, 6.3. Bone structure”. ..... 5

**Figure 1. 3** The schematic diagram of bone fracture healing which involve three main stages namely (i) inflammation (ii) repair and (iii) remodelling stages. This figure was adapted from (Anatomy & Physiology (Biga et al., n.d.) licensed under ©CC BY 4.0 <https://open.oregonstate>. ..... 9

**Figure 1. 4** Crystal lattice structure illustration of A-type and B-type CHA (Different coloured atoms represents following elements; O: red, Ca1: light blue, Ca2: dark blue, P: yellow, OH: pink, C: green) used with kind permission © 2011 Biomedical Materials (Marković et al., 2011) by IOP Publishing Group. ..... 24

**Figure 1. 5** Molecular structure of chitosan taken from the study by (Shahzad et al., 2015) ..... 32

**Figure 1. 6** Growth factor release mechanisms mimicking the ECM-growth factors interactions. **A.** Increasing the affinity of biomaterial matrix for growth factors **B.** Engineering the signalling microenvironment of growth factors **C.** Engineering growth factors to interact with biomaterial matrices **D.** Engineering growth factors to bind biomaterial/endogenous matrices. (This figure was reused after obtaining permission for the study by Martino et al., (2015) from Elsevier publishing group). ..... 38

**Figure 2. 1** HA synthesis reaction set-up: A white HA solution formed during the reaction which took place by constant stirring of reagents in a round-bottom three-necked reactor placed in a silicone oil bath at 85 °C on a hot plate. A glass condenser which has water flow in the outer layer providing refluxing ethanol, which was equipped on top neck of the reactor and a dropping funnel for feeding reagent solution at a side neck, and a thermometer. ..... 89

**Figure 2. 2** The production steps of raw hydroxyapatite powders; **a.** wet, neutral HA precipitate obtained after 4 h of reaction, filtration, and washing steps, **b.** HA powder dried at 80 °C for 48 h and calcinated at 200 °C for 24 h in a furnace, **c.** the appearance of dried HA pieces, **d.** fine HA powders acquired after crushing with a mortar and pestle **e.** final HA powders obtained after sieving under 150 µm and steam autoclaved at 132 °C. ..... 91

**Figure 2. 3** The effect of drying methods on chemical properties of HA: Raman spectrum of HA-4 sample obtained via pre pH adjustment of reagents prior to reaction (equal to HA-2): HA-4 (FD) represents a freeze dried sample (freezing at -30 °C 15 h

and drying at -20 °C for 33 h), while HA-4 (OD) is the same sample dried in oven at 200 °C for 48 h.....	96
<b>Figure 2. 4</b> A comparative Raman spectrum of heat-treated (at 950 °C, 6 h) HA-2 sample and commercial raw HA (P218 R), respectively denoted as HA-2 S-950 and P218R S-950. The vertical blue grade-lines represent the corresponding Raman shift for HA-2 sample spectra.....	97
<b>Figure 2. 5</b> The effects of a pH pre-adjustment process applied prior to HA synthesis reaction. The spectra in blue colour represents an HA-2 sample, acquired with pre-adjustment of pH precursor solutions to 10.5 prior to the reaction. However, HA-1 was not exposed to this additional process: pH was maintained at 10 only during the reaction which was the common process for all HA samples.....	98
<b>Figure 2. 6</b> A contrastive Raman spectrum of heat-treated (at 950 °C, 6 h) samples: HA-2 was obtained via pre adjustment of reagent pH at 10.5 prior to the sol-gel synthesis reaction whereas HA-1 was not exposed to pH pre-adjustment. The pink and blue grade lines represent the wavenumbers corresponding to HA-1 and HA-2 sample spectra respectively.....	100
<b>Figure 2. 7</b> The effects of different sintering temperatures on HA chemical properties. Raman spectrums of a HA-4 sample which is a reproduction of HA-2 dried at 200 °C for 48 h, and sintered at different temperatures including 950 °C, 1100 °C and 1300 °C for 6 h (heating rate: 10 °C/min).....	101
<b>Figure 2. 8</b> FTIR-PAS spectrographs of dried (80 °C- 48 h) HA samples: HA-2 which was obtained by extra pH pre-adjustment (10.5) of reagents prior to the synthesis reaction while HA-1 was not exposed to this process.....	102
<b>Figure 2. 9</b> FTIR-PAS spectrums of <b>a.</b> HA-1 sample dried at 80 °C, 48 h and <b>b.</b> sintered HA-1 sample at 950 °C, 6 h.....	103
<b>Figure 2. 10</b> FTIR-PAS spectral analyses of HA-2 sample sintered at different temperatures: 950 °C, 1100 °C and 1300 °C for 6 h.....	105
<b>Figure 2. 11</b> X-Ray diffraction patterns of dried forms of HA-1 and HA-2 samples obtained through the sol gel method. HA-2 was acquired with additional pre-pH adjustment while HA-1 was not treated with this process.....	106
<b>Figure 2. 12</b> The phase matching of XRD patterns of the HA-2 dried sample (at 80 °C for 48 h) and the HA ICDD standard (PDF card no: 01-073-84-19).....	107
<b>Figure 2. 13</b> The phase matching of XRD patterns of HA-2 S950 (sintered at 950 °C for 6 h) and HA ICDD® standard (PDF card no: 04-016-16-47).....	107
<b>Figure 2. 14</b> The comparison of XRD patterns for HA-2 samples which were treated in different temperatures including; 950, 1100 and 1300 950 °C for 6 h. ....	108
<b>Figure 2. 15</b> The comparison of XRD patterns for HA-1 and HA-2 samples which were sintered at 950 °C for 6h entitled as HA-1 S950 and HA-2 S950, respectively. The stars represent the formation of new peaks in the HA structure, attributed to $\beta$ -TCP phase. ....	109
<b>Figure 2. 16</b> The comparison of XRD patterns for HA-1 samples which were treated in different temperatures including 950, 1100 and 1300 950 °C for 6 h. ....	109
<b>Figure 2. 17</b> The comparison of XRD patterns for HA-1 samples which were treated in different temperatures including 950, 1100 and 1300 950 °C for 6 h. ....	110
<b>Figure 2. 18</b> TGA & DSC graphs demonstrating % of weight and heat flow changes (W/g) versus temperature, as well as the 1 <sup>st</sup> derivative of weight (wt%/ $^{\circ}$ C) for the HA-1 sample, which was produced without pH pre adjustment of reagents, and dried at 80 °C for 48 h.....	111

**Figure 2. 19** TGA & DSC graph demonstrating % weight and heat flow changes (W/g) with temperature, as well as 1<sup>st</sup> derivative of weight (wt%/<sup>o</sup>C) for HA-2 sample which produced with extra pH pre adjustment of reagents, and dried at 80 °C for 48 h..... 112

**Figure 2. 20** EDS elemental analysis of HA-5 sample (Dried at 200 °C for 24 h and autoclave sterilised at 132 °C) **a.** SEM image of a bulk specimen region of a hydroxyapatite sample, and the four EDS spectral points (Spectrum 9-12) at left and one spectra point (Spectrum-13) at right **b.** EDS elemental analyses spectra indicating weight percentages of detected elements in the HA structure (Spectrum 9-13)..... 113

**Figure 2. 21** SEM microstructure images of freeze-dried HA-4 sample with increasing magnifications. Scale bars at image **a.** to **f.** represent 250, 20, 10, 5, 2, and 1  $\mu$ m, respectively. .... 115

**Figure 2. 22** SEM microstructure images of HA-4 sample dried in an oven at 200 °C for 24 h with increasing magnification. Scale bars at image **a.** to **d.**, represent 20, 5, 2 and 1  $\mu$ m, respectively. .... 116

**Figure 2. 23** SEM microstructure images of an HA-4 sample dried at 200 °C for 24 h and sintered at 950 °C for 6 h, with increasing magnification. Scale bars from **a.** to **d.**, represent 10, 2, 1 and 0.5  $\mu$ m, respectively. .... 117

**Figure 2. 24** SEM microstructure images of the HA-4 sample dried at 200 °C for 24 h and sintered at 1300 °C for 6 h, with increasing magnification. Scale bars from **a.** to **d.**, represent 250, 50, 10 and 5  $\mu$ m, respectively. (The small crystals indicated by yellow arrows in image-d were attributed to  $\alpha$ -TCP phase crystals)..... 118

**Figure 2. 25** SEM microstructure images of a HA-1 sample dried at 80 °C for 48 h and sintered at 950 °C for 6 h, with increasing magnification. Scale bars from **a.** to **d.**, represent 50, 5, 2 and 1  $\mu$ m, respectively. .... 119

**Figure 2. 26** SEM morphology images of HA-5 D dried HA with small carbonate content (80 °C for 48 h, and 200 °C for 24 h) after autoclave sterilisation (132 °C for 20 min) presented in increasing magnifications. Scale bars from **a.** to **d.**, represent 20, 3, 2, and 1  $\mu$ m, respectively. .... 120

**Figure 2. 27**  $N_2$  adsorption isotherms of HA-3 S950 sample: **a.** adsorbed volume per gram versus relative pressure, and **b.** pore volume versus pore size ..... 121

**Figure 3. 1** Experimental set up for synthesis of pH and temperature sensitive hydrogels: the reaction flask is placed in an ice bath at 4°C, controlled by a thermometer and with a quick-fit dropping funnel for dropwise addition to the solution. .... 132

**Figure 3. 2** The illustration of synthesis steps of pH and thermosensitive CS based composite hydrogels (CS/HA/Hep) with the network structures of mixtures and the ionic crosslink mechanism stimulated by the given ionic reaction and temperature (37 °C) (This figure was reused after modification from our earlier published paper (Kocak et al., 2020) licensed under CC BY 4.0. .... 134

**Figure 3. 3** The images of different sized BD needles used in qualitative injectability assessments shown at left image and the corresponding sizes of needles given at right across..... 135

**Figure 3. 4** The injectability test measurements set up carried out by using by using a UTM instrument (Instron® 3345, Norwood, MA, USA) in compression mode. The injection forces were measured during displacement of the syringe plunger at a certain speed until all 5 mL of hydrogel solution, in a 10 mL syringe fixed into a syringe ring, was expelled . .... 136

**Figure 3. 5** A rotational TA-AR 2000 Rheometer (TA Instruments®, Newcastle, DE, USA) instrument during rheology analysis of a hydrogel specimen, performed by using a cone geometry ( $\varnothing = 40$  mm, 2°) which is covered by a metal chamber. .... 137

**Figure 3. 6** An image taken prior to compression testing of a modified hydrogel specimen placed onto a lower compression plate in an Instron® UTM instrument (Instron® 3345, Norwood, MA, USA). ..... 140

**Figure 3. 7** The images of liquid hydrogels obtained after gradual neutralisation by NaHCO<sub>3</sub> **a.** CI: sole CS solution (with initial concentration of 5 % (w/v)) having transparent yellow colour **b.** whiter and slightly opaque composite solution CII: CS/HA(10:1). ..... 143

**Figure 3. 8** The composite SI (CS.0.1HA.0.005Hep) solution obtained via powder mixing method of Hep (0.12 mg/mL) into a CS/HA solution causing large precipitates after the neutralisation process which results in a heterogeneous solution..... 143

**Figure 3. 9** The homogenous neutral solution of SI (CS.0.1HA.0.005Hep), achieved by dropwise and gradual addition of Hep in water solution form, is acquired without any precipitates in **a.** a glass petri-dish and **b.** a tilted plastic container in which the solution exhibits easy flow. ..... 144

**Figure 3. 10** Photographs of sterile hydrogel solutions (2 mL) taken into test tubes upon neutralisation: **a.** CI: sole CS and **b.** composite SI (CS.0.1HA.0.005Hep) solution. 145

**Figure 3. 11** Demonstration of sol-gel transition using the test tube invert method. Liquid composite hydrogel solution (SI, non-modified) in a test tube which flows easily when the tube is reversed (left), and gelation started from the surface of the solution in 7 min after placing the tube in an oil bath at 37 °C (right). ..... 148

**Figure 3. 12** A diagram of the sol-gel transition in a modified composite hydrogel (SI: CS.0.1HA.0.005Hep) obtained from a solution having a final pH above 6.4. Incipient gelation occurred at 3 min in a test tube placed in an oil bath at 37 °C is shown at left. The photographs of stable and elastic hydrogels acquired after further incubation at 37 °C for 24 h and 48 h are shown at the **Top** and **Bottom** images at the right side of the diagram. A hydrogels showing flexible behaviour when pressed on by a spatula, is demonstrated at the top right corner for a 24 h sample..... 149

**Figure 3. 13** Demonstration of the effect of last solution pH on the physical strength and stability of modified hydrogels including CI (CS) and SI (CS.0.1HA.0.0005Hep) solutions. These specimens were obtained with a lower and higher final solution pH of 6.21 and 6.43; and 6.25 and 6.46, respectively, upon their incubation at 37 °C for 24 h. The weaker hydrogels obtained below pH 6.4 are shown at the left side of the image (only top surfaces) while the more stable hydrogels obtained from solutions having pH above 6.4 are seen at the images in the middle and right side showing their top and bottom surfaces respectively..... 151

**Figure 3. 14** The photographs of physically and mechanically stable modified hydrogels taken from different angles for hydrogels with different compositions: CI (CS), CII (CS.0.1HA) and S0 (CS.0.1HA.0.0015Hep) synthesised with the last pH of 6.40-6.45 in final solution and acquired upon 48 h of incubation at 37 °C. ..... 151

**Figure 3. 15** Photographs captured from the videos taken during from injectability tests. The steady or drop flow features of a sterile modified composite hydrogel formulation (SI) was tested immediately after synthesis, through a range of needles with increasing Gauge sizes. ..... 153

**Figure 3. 16** Quantitative injectability test results of non-modified initial hydrogel solutions with different compositions including CI, CII and SI on the same day of their synthesis (Day 0). The force measurements during injection through a 10 mL syringe **a.** without a needle (needleless) and **b.** coupled with a 19 G needle. ..... 155

**Figure 3. 17** Injectability of non-modified initial hydrogel solutions with different compositions including CI, CII and SI, 3-days after their synthesis. The force

measurements during injection through a 10 mL syringe <b>a.</b> without a needle (needleless) and <b>b.</b> coupled with a 21 G needle.....	156
<b>Figure 3. 18</b> Injectability of Modified sterile hydrogel solutions with different compositions including CI, CII, S0 and SI at Day 0 and Day 1 of the synthesis represented as D0 (at left) and D1 (at right). The force measurements versus time obtained during injection through a 10 mL syringe for D0 and D1 were given for the cases of needleless ( <b>a.</b> and <b>c.</b> ), and 19 G needle ( <b>b.</b> and <b>d.</b> ).....	158
<b>Figure 3. 19</b> The viscous ( $G''$ ) and elastic modulus ( $G'$ ) changes for the sole CS solution (6% w/v initial concentration neutralised by $\text{NaHCO}_3$ ) during the temperature sweeps by heating step (1) from 15 to 60 °C, with sol-gel transition starting at 35.9 °C and cooling step (2) where temperature was lowered back to 15 °C.....	160
<b>Figure 3. 20</b> Temperature dependent elastic and viscous modulus changes during oscillation tests carried out at a 1 Hz constant frequency and with heating from 15 to 37 °C at the speed of 1 °C/min for all initial liquid hydrogel formulations: <b>a.</b> CI (CS) <b>b.</b> CII (CS.0.1HA) <b>c.</b> SI (CS-0.1HA.0.005Hep) <b>d.</b> SII (CS.0.1HA.0.015Hep) <b>e.</b> SIII (CS.0.1HA.0.025Hep).....	161
<b>Figure 3. 21</b> The elastic and viscous modulus changes for the CII (CS.0.1HA) liquid hydrogel formulation during a temperature sweep by heating (1) from 15 to 37 °C followed by a time sweep involving holding the temperature at 37 °C and then cooling the temperature back to 15 °C: <b>a.</b> whole test including temperature and time sweeps <b>b.</b> a time sweep only while holding the temperature at 37 °C.....	162
<b>Figure 3. 22</b> SEM microstructure images of freeze-dried hydrogels at different magnifications: ( <b>a-c.</b> ) CI (CS): sole CS hydrogel obtained after neutralisation by $\text{NaHCO}_3$ given, and ( <b>d-f.</b> ) CII (CS.0.1HA) hydrogel with HA particles deposited on a CS matrix. Yellow arrows and green squares respectively identify HA crystals and sodium salt crystals, originating possibly from the used neutralizing agent. (Scale bars correspond to <b>a.</b> 100 $\mu\text{m}$ , <b>d.</b> 20 $\mu\text{m}$ , <b>b and e.</b> 10 $\mu\text{m}$ , <b>c and f.</b> 5 $\mu\text{m}$ .).....	164
<b>Figure 3. 23</b> SEM micrographs of freeze-dried hydrogels taken after 8 months of storage given at different magnifications ( <b>a-d.</b> ) CI (CS): from sole CS, and ( <b>e-h.</b> ) CII (CS.0.1HA) yellow arrows indicate HA particles. (Scale bars correspond to: ( <b>a</b> and <b>e.</b> ) 100 $\mu\text{m}$ , ( <b>b, c, f</b> and <b>g.</b> ) 10 $\mu\text{m}$ , ( <b>d</b> and <b>h.</b> ) 1 $\mu\text{m}$ .).....	165
<b>Figure 3. 24</b> SEM images of freeze-dried composite hydrogel, SIII (CS.0.1HA.0.025Hep) which has the max Hep concentration (0.60 mg/mL). Yellow arrows show HA particles, while salt crystals deposited due to $\text{NaHCO}_3$ salt are demonstrated in a green square. (Scale bars correspond to: <b>a.</b> 100 $\mu\text{m}$ , <b>b.</b> 10 $\mu\text{m}$ , <b>c-d.</b> 5 $\mu\text{m}$ , <b>e.</b> 6 $\mu\text{m}$ <b>f.</b> 3 $\mu\text{m}$ .).....	166
<b>Figure 3. 25</b> SEM images of freeze-dried composite hydrogel SI (CS.0.1HA.0.005Hep) with 0.12 mg/mL Hep, taken at different magnifications. Yellow arrows show HA particles while the green square demonstrates the bubbles formed on the surface of the hydrogel due to $\text{CO}_2$ release during gel formation. (Scale bars correspond to <b>a.</b> 100 $\mu\text{m}$ , <b>b.</b> 10 $\mu\text{m}$ , <b>c.</b> 5 $\mu\text{m}$ , <b>d-e.</b> 20 $\mu\text{m}$ <b>f.</b> 10 $\mu\text{m}$ .).....	167
<b>Figure 3. 26</b> SEM images of modified hydrogel, CI obtained from sole CS after neutralization by $\text{NaHCO}_3$ to a pH slightly higher than 6.4. Images were taken from <b>a.</b> bottom <b>b.</b> top and <b>c.</b> cross-section and ( <b>d-f.</b> ) the magnified versions of square areas in image c. All images have a 100 $\mu\text{m}$ scale bar except <b>f.</b> with a 1 $\mu\text{m}$ scale bar.....	168
<b>Figure 3. 27</b> SEM images of modified hydrogel composite CII (CS.0.1HA) having a pH above 6.4. The cross-section images were taken at different magnifications. Yellow arrows and square show porous HA crystals covering on polymer matrix. (Scale bars correspond to <b>a.</b> 100 $\mu\text{m}$ , <b>b-d.</b> 10 $\mu\text{m}$ , <b>e-f.</b> 1 $\mu\text{m}$ .).....	169

<b>Figure 3. 28</b> SEM images of modified composite hydrogel, SI (0.12 mg/mL of Hep) (CS.0.1HA.0.005Hep) obtained with a pH above 6.4 in final solution. The cross-section images were taken at different magnifications. Yellow arrows and square show spherical HA crystals seemingly coated by Hep. (Scale bars correspond to: (a-b). 100 $\mu$ m, c. 10 $\mu$ m, (d-f). 1 $\mu$ m.).....	170
<b>Figure 3. 29</b> SEM micrographs of a sole CS hydrogel obtained with a pH between 6.2-6.4 in final solution after gelation and freeze drying, at different magnifications. (Scale bars correspond to: (a-b). 100 $\mu$ m, c. 10 $\mu$ m, d. 1 $\mu$ m.) .....	171
<b>Figure 3. 30</b> The compression test steps applied on a composite modified hydrogel specimen, S0 (CS.0.1HA.0.0015Hep) a. top and b. bottom images of sample, and c. sample placed between compression plates d. the loading cell is lowered until it has just a contact with the sample and for e. and f., the sample's appearance after an applied compression of up to 75% strain.....	172
<b>Figure 3. 31</b> The compression stress-strain curves performed up to a 40% strain in modified hydrogel samples. These hydrogels were obtained at pH ranges of 6.2-6.4 in final solution in different compositions: a. CI (CS) b. CII (CS.0.1HA) and c. SI (CS.0.1HA.0.005Hep). Black dotted curves belong to three replicates of the same experiment whereas red curves indicate the mean values of these repetitions.....	173
<b>Figure 3. 32</b> The compression stress-strain curves performed up to a 75% strain in the samples. These modified hydrogels were obtained at a pH slightly above 6.4 in final solution in different compositions: a. CI (CS) b. CII (CS.0.1HA), c. S0 (CS.0.1HA.0.0015Hep), and d. SI (CS.0.1HA.0.0050Hep) (Black dotted curves belong to three replicates of the same experiment whereas red curves indicate the mean values of these repetitions), and e. the comparison of the means of all sample groups.....	174
<b>Figure 3. 33</b> The comparative ATR spectrums of reagent powders used in synthesis of composite hydrogels including a. CS, b. Hep c. HA, d. NaHCO <sub>3</sub> and e. initial composite hydrogel specimen SI (CS.0.1HA.0.005Hep).....	176
<b>Figure 3. 34</b> The overlay of ATR spectrums for all initial hydrogels with different compositions including CI: CS, CII: CS.0.1HA, SI: CS.0.1HA.0.005Hep, SII: CS.0.1HA.0.015Hep, and SIII: CS.0.1HA.0.025Hep are presented with a. peak numbers and b. peak assignments of chemical functional groups.....	178
<b>Figure 3. 35</b> The comparative ATR spectra for autoclaved and non-autoclaved CS powders.....	181
<b>Figure 3. 36</b> The comparison of ATR spectra for commercial HA (P218 R) powder used in the synthesis of initial hydrogels versus the own synthesis HA5-D powder which was utilised in the synthesis of modified hydrogels. ....	181
<b>Figure 3. 37</b> The comparative ATR spectra of initial and modified forms of hydrogel composition SI: CS.0.1HA.0.005Hep.....	183
<b>Figure 3. 38</b> The comparison of ATR spectrums of modified hydrogels obtained in different compositions (CI: CS, CII: CS.0.1HA, and SI: CS.0.1HA.0.005Hep) analysed from a. top b. and bottom surface.....	184
<b>Figure 3. 39</b> The demonstration of the FT-Raman square area mapping analyses of an initial hydrogel sample SI (CS.0.1HA.0.005Hep). a. during data collection: the sample at top left with a red framed square area covering the analyses points, and the collected spectra are given at the bottom, and a heat map at the left bottom corner showing the analyses regions. b. after data collection is complete: the sample at right corner, heat map at left corner and the average spectra is given at the bottom. ....	186
<b>Figure 3. 40</b> The comparison of FT-Raman spectra of reagent powders, which were used in the synthesis of hydrogels a. Hep, b. CS, c. NaHCO <sub>3</sub> and d. the commercial HA (P218 R). ....	186

**Figure 3. 41** The comparison of FT-Raman spectra of initial hydrogels obtained in different compositions: **a.** without Hep including CI: CS and CII: CS.0.1HA, and **b.** compositions with different Hep concentrations: SI: CS.0.1HA.0.005Hep (0.12 mg/mL), SII: CS.0.1HA.0.015Hep (0.36 mg/mL), and SIII: CS.0.1HA.0.025Hep (0.60 mg/mL) and **c.** the overlay spectrums of all hydrogel compositions..... 188

**Figure 3. 42** The comparison of XRD patterns of commercial reagent powders which were used in the synthesis of hydrogels including Hep, CS, NaHCO<sub>3</sub> and HA (P218 R) and a freeze-dried composite initial hydrogel sample SII: CS.0.1HA.0.015Hep. (The right -Y axis shows the intensity of only the NaHCO<sub>3</sub> XRD pattern, due to its excess intensities. The intensity of all other samples are indicated by the left Y axis)..... 190

**Figure 3. 43** TGA/DSC curves obtained from thermal analyses of reagent powders between 25-700 °C including **a.** CS and **b.** Hep..... 192

**Figure 3. 44** TGA/DSC curves obtained from thermal analyses of reagent powders between 25-700 °C including **a.** HA and **b.** NaHCO<sub>3</sub>. ..... 193

**Figure 4. 1** The swelling analyses results of different modified hydrogel compositions: CI (CS), CII (CS.0.1HA) and SI (CS.0.1HA.0.005Hep) with standard error bars (n=3) **a.** % liquid absorption ratio, and **b.** pH change in supernatant PBS media in which hydrogels were incubated at different time points of swelling tests up to 72 hours.. 215

**Figure 4. 2** The comparative in-vitro degradation weight analyses plotted as the percentage of dry weight remaining ratios of the modified hydrogels: CI (CS), CII (CS.0.1HA) and SI (CS.0.1HA.0.005Hep) in different time intervals up to 42 days, during incubation in PBS and Lysozyme (5 mg/mL) in PBS solution with standard deviation (n=4). Statistical analyses performed by 2-way ANOVA; Tukey multiple comparison tests were performed with  $\alpha$ : 0.05. The adjusted p-values above show differences of the degradation profile of the CI sample in PBS media (purple line) while below p-values belong to comparison of the SI sample in Lysozyme + PBS media (bright green line). The p-value connected with a vertical line demonstrates the significant difference between the CI sample in PBS and Lysozyme + PBS media at day 14..... 217

**Figure 4. 3** The pH alteration of supernatant media taken at different time intervals of up to 42 days in the in-vitro degradation tests of modified hydrogels in **a.** PBS and **b.** Lysozyme (5 mg/mL) solution in PBS. The involved hydrogel specimens are CI (CS), CII (CS.0.1HA) and SI (CS.0.1HA.0.005Hep)..... 218

**Figure 4. 4** The appearance of modified hydrogels during *in-vitro* degradation tests: the same specimens were photographed in each time intervals up to 42 days which were incubated in PBS and lysozyme (5 mg/mL) media are given in the left and right column, respectively. Test specimens, labelled at the top of the columns belong to CI (CS), CII (CS.0.1HA) and SI (CS.0.1HA.0.005Hep) specimens. ..... 219

**Figure 4. 5** The appearance of a modified hydrogel, CI (CS) becoming a hard, brown thin film after 42 days of incubation in Lysozyme (5 mg/mL) media in PBS during *in-vitro* degradation test. (The image of the sample with a ruler on a tissue at left and on a white paper at right). ..... 220

**Figure 4. 6** The SEM micrographs of modified hydrogel CI (CS) during degradation in PBS and in Lysozyme (5mg/mL Lysozyme in PBS) media. The images at the three columns from left to right show top, cross-section and bottom sites while the vertical labels given at left represent the following: D0: hydrogels before incubation in media **(a-c)**; D14 PBS : after 14 day incubation in PBS **(d-f)**; D14 Lysozyme: after 14 day incubation in Lysozyme **(g-i)**, D42 Lysozyme: after 42 day incubation in Lysozyme

media (j-l). (The scale bars at the images are respectively (a-d, f-g and i-j). 100 $\mu$ m, (e and l). 10 $\mu$ m, and (h and k). 100 $\mu$ m.).....	221
<b>Figure 4. 7</b> The SEM micrographs of modified composite hydrogel SI (CS.0.1HA.0.005Hep) during degradation in both PBS and Lysozyme (5mg/mL Lysozyme in PBS) media. The images in the three columns from left to right show top, cross-section and bottom sites while the vertical labels given at left represent the following: D14 PBS : 14-days of degradation sample in PBS (a-c); D28 PBS : 28-days of degradation sample in PBS (d-f); D42 PBS: 42-days of degradation sample in PBS (g-i), D42 Lysozyme: 42-days of degradation sample in Lysozyme media (j-l). (The scale bars at the images are respectively (a and f-g). 10 $\mu$ m, (b-e, h and j-k). 100 $\mu$ m), 10 $\mu$ m, (i and l). 1 $\mu$ m.).....	222
<b>Figure 4. 8</b> The HA crystals present in SEM micrographs of modified composite hydrogels during degradation tests in PBS <b>a</b> . CII (CS.0.1HA) after 14 days of incubation (10 $\mu$ m scale bar); and <b>b</b> . SI (CS.0.1HA.0.005Hep) after 28 days of incubation (1 $\mu$ m scale bar). .....	223
<b>Figure 4. 9</b> The comparative ATR spectra of degradation samples, CI (CS) modified hydrogels at different time intervals over 42 days of incubation in <b>a</b> . PBS and <b>b</b> . Lysozyme in PBS solution (5mg/mL). .....	224
<b>Figure 4. 10</b> The comparative ATR spectra of degradation samples, CII (CS.0.1HA) modified hydrogels at different time intervals over 42 days of incubation in <b>a</b> . PBS and <b>b</b> . Lysozyme solution in PBS (5mg/mL). .....	225
<b>Figure 4. 11</b> The comparative ATR spectra of degradation samples, SI (CS.0.1HA.0.005Hep) modified hydrogels in different time intervals over 42 days of incubation in <b>a</b> . PBS and <b>b</b> . Lysozyme solution in PBS (5mg/mL). .....	226
<b>Figure 4. 12</b> The bioactivity test results performed by incubation of modified hydrogels (CI (CS), CII (CS.0.1HA) and SI (CS.0.1HA.0.005Hep)) in SBF media in different intervals up to 21 days to investigate biominerilization by <b>a</b> . the comparison of % of the dry weight ratio of hydrogels and <b>b</b> . the pH changes in different time intervals of the bioactivity tests. Results were expressed as a mean $\pm$ SD (N=3). Statistical analyses were performed by 2-way ANOVA; Tukey multiple comparison tests were performed with $\alpha$ : 0.05. Weight increase percentage values between time intervals for the same sample group were demonstrated with loosely dashed lines, and the statistical difference between samples were shown with solid line with adjusted p values.....	227
<b>Figure 4. 13</b> The physical indication of biominerilisation during bioactivity studies of modified hydrogels incubated in SBF media up to 21 days. The images of Day-7 and Day-21 samples are shown at left and right column, respectively. From top to below image labels 'Day-0 hydrogel' indicates the specimens before incubation in SBF, 'Day-7 wet hydrogels' represents the samples incubated 7 days in SBF and imaged after washing, and 'Day-7 (freeze-dried)' demonstrates the samples freeze-dried after washing. The test specimens are labelled on top of the columns belong to CI (CS), CII (CS.0.1HA) and SI (CS.0.1HA.0.005Hep). .....	228
<b>Figure 4. 14</b> The SEM micrographs of modified hydrogel CI (CS) during bioactivity studies in SBF. The left and right column belong to the samples exposed to 7-days and 21-days of incubation in SBF media, respectively. The images <b>a</b> and <b>d</b> belong to top surface of samples while <b>b</b> , <b>c</b> , <b>e</b> , and <b>f</b> are cross-section images. (The scale bars at the images are as follows: (a-b and e). 100 $\mu$ m, (c-d and f). 10 $\mu$ m).....	230
<b>Figure 4. 15</b> The SEM micrographs of the top surfaces of modified composite hydrogel CII (CS.0.1HA) samples after incubation in SBF media for 7 days and 21 days at left and right column, respectively. (The scale bars at the images are (a and e). 100 $\mu$ m, (b and f). 10 $\mu$ m, and (c-d. and g-h). 1 $\mu$ m).....	231

**Figure 4. 16** SEM micrographs of a modified composite hydrogel SI (CS.0.1HA.0.005Hep) in SBF. Starting at left, the first and second column pairs belong to the sample after 7 and 14 days incubation in SBF media, respectively. The images **a-d** and **e-f** are top and cross-section images, respectively for 7-day samples while **g-h** and **i-l** images are top and cross-section images, respectively for 14-day samples. (The scale bars at the images are as following: **(a, e, g and j-k)**. 100  $\mu$ m, **(b-d and h)**. 1  $\mu$ m, **(f, i and l)**. 10  $\mu$ m)..... 232

**Figure 4. 17** The EDS analyses determining elemental composition of modified hydrogel CI (CS) after 7 days incubation in SBF media and freeze-drying **a**. SEM micrographs from top surfaces of the specimen **b**. elemental composition, **c**. the colour mapping of elements distributed on the sample and **d**. colour distribution density for each individual element on the specimen region. .... 233

**Figure 4. 18** The EDS analyses determining elemental composition of modified composite hydrogel CII (CS.0.1HA) after 7 days incubation in SBF media and freeze-drying **a**. SEM micrographs from top surfaces of the specimen **b**. elemental composition, **c**. the colour mapping of elements distributed on sample and **d**. colour distribution density for each individual element on specimen region. .... 234

**Figure 4. 19** The EDS analyses determining elemental composition of modified composite hydrogel SI (CS.0.1HA.0.005Hep) after 7 days incubation in SBF media and freeze-drying **a**. SEM micrographs from top surfaces of the specimen **b**. elemental composition, **c**. the colour mapping of elements distributed on sample and **d**. colour distribution density for each individual element on specimen region. .... 235

**Figure 4. 20** The comparative ATR spectra of bioactivity test specimens of modified CI (CS) hydrogels (top surfaces) in different experiment intervals up to 21 days. .... 236

**Figure 4. 21** The comparative ATR spectra of modified hydrogels (top surfaces) **a**. before incubation in SBF (Day-0) including CI(CS), and the comparative spectra of **b**. CII (CS.0.1HA) and **c**. (CS.0.1HA.0.005Hep) after incubation in SBF for different periods (7, 14, and 21-days)..... 237

**Figure 4. 22** The photographs of Toluidine Blue (TB) stained hydrogels (30 min) for local determination of Hep via purple colour formation in TB/Hep complexes. The images belong to the composite modified hydrogels having a pH of 6.4-6.5 in solution, including the CII (CS.0.1HA) control sample without Hep and the S0 (CS.0.1HA.0.0015Hep) sample containing the minimum Hep concentration (33  $\mu$ g/mL). CII and S0 hydrogels **a**. before TB staining and **b**. after TB staining, **c**. S0 hydrogel specimens in two different plastic petri dishes from their top surfaces, and **d**. the comparison of top and bottom surfaces of an S0 hydrogel specimen..... 239

**Figure 4. 23** The optical microscope images of Toluidine Blue (TB) stained hydrogels (30 min) for local determination of Hep, indicating a TB/Hep complex by purple colour: The comparison is of **(a-d)**. CII (CS.0.1HA) control sample without Hep and **(e-p)**. S0 (CS.0.1HA.0.0015Hep) with 33  $\mu$ g/mL Hep. These composite modified hydrogel specimens were prepared with a pH range of 6.2-6.4 in solution. The purple to pink colours indicates Hep locations distributed on the samples. The yellow particles at the bottom surfaces belong to HA particles. (Scale bars correspond to the following: **(e-f)**. 0.4 mm, **(c, g, k, o)**. 0.05 mm, **(d, n and p)**. 0.1 mm and other images **(a-b, h-j, l-m)**. 0.2 mm)..... 240

**Figure 4. 24** The photographs of a Toluidine Blue (TB) stained composite modified hydrogel, SI (CS.0.1HA.0.005Hep) with 120  $\mu$ g/mL Hep, which was obtained with a pH 6.4-6.5 (stable hydrogel) indicating the presence of Hep with dense purple colour. The appearance of SI sample from different angles given as **a**. top, **b**. bottom, **c**. top to lateral, and **d**. lateral images..... 241

**Figure 4. 25** Toluidine blue stained freeze-dried initial hydrogels to indicate local Hep after 2-years of storage to investigate their stability **a-b**. CII (CS.0.1HA) as control, **c**. SI (CS.0.1HA.0.005Hep)-120  $\mu$ g/mL Hep **d-f**. SII (CS.0.1HA.0.015Hep)-360  $\mu$ g/mL Hep and **g-h**. SIII (CS.0.1HA.0.025Hep)-600  $\mu$ g/mL Hep (Scale bars : **(a and d-h)**. 0.2 mm and **(b-c)**. 0.05 mm) ..... 242

**Figure 4. 26** Heparin (Hep) standard solutions prepared in gradually increasing concentrations from 0 to 140  $\mu$ L in vials and made complex with toluidine blue (TB) by using hexane (Hex) while the ratio of TB: Hep: Hex was 1.5:1:1.5 **a**. the TB/Hep complex formed after vigorous shaken on the top of the tubes on purple colour, **b**. after extraction of some of the unreacted TB solution and the solutions were settled, and **c**. the extracted unreacted TB solutions which were used in absorbance measurements to obtain a standard curve for different concentrations of Hep ..... 244

**Figure 4. 27** Absorbance measurement for Hep standard solutions in D.H<sub>2</sub>O to obtain a standard curve for different concentrations of Hep: **a**. The colour difference at unreacted liquid extracts were placed as 100  $\mu$ L aliquots with 8 replicates into columns at increasing concentrations, and **b**. Hep standard curve obtained with absorbance measurements of specimens at 630 nm wavelength of the light. The linear region from 0 to 60  $\mu$ g/mL Hep concentrations (shown by green rectangular frame) by dark-blue straight line used as standard curve having the line equation and R<sup>2</sup> value on top while nonlinear portion of rest of the curve is given in yellow colour. ..... 245

**Figure 4. 28** The drug (Hep) release study performed with the D.H<sub>2</sub>O immersion media of hydrogels incubated at 37 °C, in different time periods of 4 hours (Day 0), Day 1, 3 and 7. **a**. the change of the absorbance values of TB extract solutions were performed by using Hep release media for modified hydrogel specimens obtained with a pH 6.2-6.3 in solution, including CII (CS.0.1HA) as a control and S0 (CS.0.1HA.0.0015Hep) with 33  $\mu$ g/mL Hep **b**. the cumulative Hep release of Hep from S0 (CS.0.1HA.0.0015Hep) calculated from the standard curve. ..... 246

**Figure 4. 29** The drug (Hep) release profile in SBF performed by using the supernatant media taken during bioactivity studies at different time interval over 21 days. The absorbance measurements are of the sole TB solution and the TB extract solutions of modified hydrogel samples after complexation with hexane including CII (CS.0.1HA) both used as controls and SI (CS.0.1HA.0.005Hep) with 120  $\mu$ g/mL Hep. (The decrease of absorbance indicates an increase of Hep concentration). ..... 247

**Figure 5. 1** Demonstration of an *ex-ovo* CAM assay steps for in-situ forming injectable thermosensitive hydrogels (CS/HA/Hep): 1. the incubation of fertilized hen eggs in day-0 (D0), 2. cracking at day-3 (D3), 3. the solution injection into CAM tissue and in-situ gelation at average body temperature (37.5 °C) at day-7 (D7), 4. the imaging of micro-vessel formations at day-10 (D10) and day-14 (D14) which is also the sacrificing day of embryos (5), 6. quantifying blood vessels from CAM images via the vascular index method and 7. histological assessment of CAM-tissue sections. (This diagram was reused from our published paper (Kocak et al., 2020) licensed under CC BY 4.0.). 260

**Figure 5. 2** The cell viability and proliferation analyses by fluorescent measurements up to 4-weeks of cultures in three individual experiments: **a**. freeze-dried hydrogels (solid foam) seeded with 20,000 cells/sample grown in 1 mL media in 24 well-plate, **b**. freeze-dried hydrogels (solid foam) seeded with 2,000 cells/ sample grown in 2 mL of media in 12 well-plate, **c**. oven-dried hydrogels (obtained in gel form at 37 °C) seeded with 50,000 cells per hydrogel which were grown in 1 mL media in 24 well-plate (Hydrogel specimens used in experiments shown in graphs **a.** and **b.** are CI(CS), CII(CS/HA), SI(CS.HA.0.005Hep) and SIII(CS.HA.0.005Hep), and CI, CII and SI

samples in the experiment are shown in plot **c**. (The experiments were performed with 4 sample replicates and results are expressed as the mean $\pm$ SD)..... 263

**Figure 5. 3** The cell morphological images by optical microscopy: 28-days of cell culture study performed via seeding 20,000 cell per sample on freeze-dried hydrogels at different intervals: at day-16 (**a**, **b**, and **c** for CI (CS), CII (CS.0.1HA), SI (CS.0.1HA.0.005Hep) samples, respectively); and day-28 ( **d**, **e** and **f** for CI, CII, SI, respectively). (Scale bars are 0.2 mm)..... 265

**Figure 5. 4** The appearance of freeze-dried hydrogel samples incubated in media without cells for 28-days **a-b.**, and **c-d** show CI (CS) and CII (CS.0.1HA) samples, respectively and **e-f** SIII (CS.0.1HA.0.025Hep) samples. (Scale bars: **(a-d)**. 0.2 mm, and **(e-f)**. 0.05 mm) ..... 266

**Figure 5. 5** Cellular morphology images by optical microscopy during cell culture studies. The images belong to CI, sole CS sample in hydrogel form obtained upon incubation at 37 °C and seeded by 50,000 cell per specimen. The images **a-d** show sample surfaces with attached cells in transparent CS hydrogels at Day-28 of culture after cell fixation. The other images taken at **e-f**. Day 15 and **g-h** Day 21 show the cell attachments on the circular sample edges or adjacent to the samples. (Scale bars: **a**. 0.4 mm, **(b, e, and g)**. 0.2 mm, **(c-d and h)**. 0.1 mm and **f**. 0.05 mm) ..... 267

**Figure 5. 6** Cellular morphology images by optical microscopy in cell culture studies performed with samples in hydrogel form obtained upon incubation at 37 °C: 28 days of cell culture study performed via seeding of 50,000 cells per hydrogel specimen of the CII (CS/HA) sample at different intervals: **a-b.** Day-10, **c-d.** Day-15 and **e-h.** Day-21 (The darker areas at the corners of images belong to samples and the brighter areas with attached adjacent cells are in the wells of the well-plate). (Scale bars: **(a and g)**. 0.1 mm, **(b and h)**. 0.05 mm, **(c-d and f)**. 0.2 mm and **e**. 0.4 mm) ..... 267

**Figure 5. 7** Cellular morphology images during the cell culture study by optical microscopy for the hydrogel form of the SI (CS.HA.0.005Hep) sample seeded by 50,000 cells/hydrogel and imaged at different intervals: **a-e.** Day-15, **f-h.** Day-21 (The image **e** belongs to the sole SI sample incubated in media without cells while other images belong to the cell seeded samples in the wells of a well-plate). (Scale bars: **a**. 0.4 mm, **(b-f)**. 0.2 mm, **(g-h)**. 0.05 mm) ..... 268

**Figure 5. 8** The results of Alizarin Red (AR) assay for calcium deposition in hydrogel specimens: CI (CS), CII (CS/HA), SI (CS.HA.0.005Hep) which were tested after 28-days of cell culture (50,000/hydrogel) **a.** The AR standard curve obtained with plotting absorbance measurements of AR solutions in different concentrations (0, 5, 10, 25, 50, 100 and 250  $\mu$ g/mL in perchloric acid (5%(w/v)) and **b.** AR concentrations in samples obtained via correlating the absorbance measurements of AR destained solutions (sample immersion media containing AR dye released from samples after staining) with the standard curve equation, which indicates calcium deposition capacities. ..... 269

**Figure 5. 9** The images during AR staining for calcium measurements of hydrogel specimens (obtained upon gelation at 37 °C): CI (CS), CII (CS/HA), SI (CS.HA.0.005Hep) without cells as control and the same hydrogel groups seeded with cells (50,000 cells per hydrogel) fixed after 28-days of cell culture. The above image was taken after samples were stained by AR and washed to remove unbounded AR stains whereas the image below shows samples destained by perchloric acid which provided dissolution of bound AR in samples to a liquid phase. The swelling occurred in hydrogels due to acidic media. ..... 270

**Figure 5. 10** The images of swollen hydrogels after destaining and waiting in acid for long time showing a high amount of swelling leading to weakening and dissolution of these hydrogels in acidic low pH (Test specimens: CI (CS), CII (CS/HA),

SI(CS.HA.0.005Hep)). Therefore, these samples could not be used for further SR analyses for collagen determination.....	270
<b>Figure 5. 11</b> The correlated AR concentrations in freeze-dried SI (CS.HA.0.005Hep) hydrogels with increasing cell concentrations (40,000-85,000) as an indication of calcium deposition, which were tested after 28-days of culture and cell fixation.....	271
<b>Figure 5. 12</b> The images during AR staining for calcium measurements with a composite hydrogel SI (CS.HA.0.005Hep) in freeze-died form. The SI sample without cells is shown as a control. Increasing cell concentrations (40,000-100,000) were tested by AR assay after 28-days of culture and cell fixation in a 48 well-plate. The AR stained and the samples destained by perchloric acid leading to swelling of the hydrogels are at the top and bottom halves of the image, respectively.....	271
<b>Figure 5. 13</b> The results of the Sirius Red (SR) assay for collagen deposition in freeze-dried hydrogel, of the composite SI specimen (CS/HA.0.005Hep) with increasing cell concentrations (40,000-100,000) tested after 28-days of cell culture, and cell fixation. <b>a.</b> The SR standard curve obtained by plotting absorbance measurements of SR solutions with different concentrations (0, 1, 2.5, 5, 10, 25, 50, and 100 $\mu$ g/mL in picric acid (1 % (w/v))) <b>b.</b> The correlated SR concentrations in freeze-dried hydrogels as an indication of calcium deposition and the concentrated SR solution as a control.....	272
<b>Figure 5. 14</b> The images during SR staining for collagen deposition assay with a composite hydrogel SI (CS.HA.0.005Hep) in freeze-died form. SI sample without cells shown as control and with increasing cell concentrations (40,000-100,000) were stained by SR assay after 28-days of culture and cell fixation. The SR staining, washing and destaining step of samples by a basic 0.2M (NaOH:MeOH) solution leading to shrinkage of hydrogels (the bottom image) are demonstrated.....	273
<b>Figure 5. 15</b> The vascular index counted from CAM images taken at Day-14 of chick embryos' incubation (which is also the sacrificing day) for each sample group as the Mean $\pm$ SD for 6 specimens with tested initial hydrogels: CII (CS.HA) without Hep, SI (CS.HA.0.005Hep) (0.12 $\mu$ g/mL Hep in hydrogel solution), and SIII (CS.HA.0.025Hep) (0.60 $\mu$ g/mL Hep) .....	274
<b>Figure 5. 16</b> The comparative CAM images taken at Day-14 (the sacrificing day of chick embryos) with tested initial hydrogels: two representative sample images from <b>a.</b> CII (CS.HA) and <b>b.</b> SI (CS.HA.0.005Hep) sample groups. The three images in rows from left to right show, respectively: direct imaging of CAM, after white cream injection underneath the CAM as a contrast for red blood vessels, and the processed versions of the middle images by North-east shadow in ImageJ Software (All scale bars are 2 mm).....	275
<b>Figure 5. 17</b> The comparative CAM images taken at Day 14 (the sacrificing day of chick embryos) with tested initial hydrogels: two representative sample images from <b>a.</b> SII (CS.HA.0.015Hep) and <b>b.</b> SIII (CS.HA.0.025Hep) sample groups. The three images at rows from left to right show, respectively: direct imaging of CAM, after white cream injection underneath the CAM as a contrast for red blood vessels, and the processed versions of the middle images by North-east shadow in ImageJ Software (All scale bars are 2 mm).....	276
<b>Figure 5. 18</b> The vascular index counted from CAM images taken at Day-14 as the Mean $\pm$ SD from 7-11 specimens for each tested modified hydrogel group: CI (CS) and CII (CS.HA) without Hep; and S0 (CS.HA.0.0015Hep) (0.03 $\mu$ g/mL Hep) and SI (CS.HA.0.005Hep) (0.12 $\mu$ g/mL Hep) as well as Filter Paper (F.p.). The adjusted p-values counted by one-way ANOVA method are CI&S0(*): 0.0298, F.p.&CII(*):0.0287, F.p.&S0 (**): 0.0026, S0&SI(ns):0.2902.....	277

**Figure 5. 19** The CAM images taken at Day-14 of filter paper (F.p.) implants ( $\varnothing$ : 5.5 mm) applied in Day-7 after being wet by PBS, which was used as negative control in comparison to hydrogels. The images of two representative samples are given in two rows including direct imaging of CAM (at left) and after white cream injection underneath the CAM as contrast to blood vessels (at right), (All scale bars are 2 mm). ..... 278

**Figure 5. 20** The comparative CAM images taken at Day-14 (the sacrificing day of chick embryos) with tested modified hydrogels: two representative sample images from **a.** CI (CS) and **b.** CII (CS.HA) sample groups. The three images at rows from left to right showing, respectively: direct imaging of CAM, after white cream injection underneath the CAM as a contrast for red blood vessels, and the processed versions of the middle images by North-east shadow in ImageJ Software (All scale bars are 2 mm). ..... 279

**Figure 5. 21** The comparative CAM images taken at Day-14 (the sacrificing day of chick embryos) with tested modified hydrogels: two representative sample images from **a.** SI (CS.HA.0.005Hep) and **b.** S0 (CS.HA.0.0015Hep) sample groups. The three images at rows from left to right show, respectively: direct imaging of CAM, after white cream injection underneath the CAM as a contrast for red blood vessels, and the processed versions of the middle images by North-east shadow in ImageJ Software (All scale bars are 2 mm). ..... 280

**Figure 5. 22** The histology images of Hydrogel- CAM tissue sections (horizontal) after H&E staining, obtained via optical microscope imaging. The images belong to one initial hydrogel specimen CII (CS.0.1HA). (Scale bars: **(a- b)**. 0.4 mm; **(c-d)**. 0.2 mm, **(e-f)**. 0.1 mm, respectively. Green stars indicate blood cells while yellow and black arrows show the blood vessels, and hydrogel samples, respectively). ..... 281

**Figure 5. 23** The histology image of CAM sample sectioned in vertical direction after H&E staining for an initial hydrogel specimen CII (CS.0.1HA). (Scale bars: **a.** 0.2 mm and **b.** 0.1 mm) ..... 282

**Figure 5. 24** The histology image of the composite initial hydrogel specimen, SI (CS.HA.0.005Hep)-(0.12 mg/mL Hep) retrieved from CAM. (Scale bars: **(a-b and d)**. 0.2 mm and **c.** 0.1 mm, respectively. The green stars indicate blood cells while yellow and black arrows show the blood vessels, and hydrogel samples, respectively). ..... 283

**Figure 5. 25** The histology image of the composite initial hydrogel specimen, SIII (CS.HA.0.025Hep)-(0.60 mg/mL Hep) retrieved from CAM. (Scale bars: **(a-b)**. 0.4 mm and **(c-d)**. 0.2 mm. The green stars indicate blood cells while yellow and black arrows show the blood vessels, and hydrogel samples, respectively). ..... 284

**Figure 5. 26** The histology images of the composite initial hydrogel specimen, SIII (CS.HA.0.025Hep)-(0.60  $\mu$ g/mL Hep) retrieved from CAM, given with 0.2 mm scale bars (the green stars indicate blood cells while yellow and black arrows show the blood vessels, and hydrogel samples, respectively). ..... 284

**Figure A. 1** Comparison of chemical structure of bovine and porcine originated sodium Heparin ..... 297

**Figure A. 2** ATR spectra of Hydrogels obtained with porcine Hep for different hydrogel compositions CI (CS) and CII (CS.0.1HA) (at above), and samples with Hep at different concentrations: SI (CS.0.1HA.0.005Hep)-0.12 mg/mL, SII (CS.0.1HA.0.015Hep)-0.36 mg/mL and SI (CS.0.1HA.0.025Hep)-0.60 mg/mL(at below graph). ..... 298

**Figure A. 3** FT-Raman spectra of hydrogels obtained with porcine Hep for different hydrogel compositions including CI (CS) and CII (CS.0.1HA) and samples with Hep at

different concentrations: SI (CS.0.1HA.0.005Hep)-0.12 mg/mL, SII (CS.0.1HA.0.015Hep)-0.36 mg/mL and SI (CS.0.1HA.0.025Hep)-0.60 mg/mL ..... 298

**Figure B. 1** FTIR-ATR chemical analyses **a.** CMC and **b.** composite hydrogel with 0.6 mg/mL Hep, HA/CS:0.3 with or without CMC..... 299

**Figure C. 1** SEM image of top surface of a modified composite hydrogel specimen looking like a face..... 300

**Figure C. 2** Histology images of CAM tissues having blood vessels at different shapes with composite hydrogel sample **a.** SI, **b.** SIII ..... 300

**Figure C. 3** A chick embryo image during its development day of 10 during CAM assay, which formed a good vascular network (after injection of thermosensitive solution on CAM and *in-situ* formed hydrogel upon incubation at 37.5 °C, at day 7).  
..... 301

## LIST OF ABBREVIATIONS

3D:	3-Dimensional
ALP:	Alkaline Phosphatase
AR:	Alizarin Red
ATR:	Attenuated Total Reflectance
A-W:	Apatite-Wollastonite
bFGF:	Basic Fibroblast Growth Factor
BE:	Backscattered Electrons
BMP:	Bone Morphogenetic Protein
BSA:	Bovine Serum Albumin
BSC:	Biological Safety Cabinet
CAM:	Chorioallantoic Membrane
CMC:	Carboxymethyl Cellulose
CPD:	Critical Point Drying
CHA:	Carbonated HA
CS:	Chitosan
DDA:	Degree of deacetylation
DGF:	Dynamic Glide Force
DMEM:	Dulbecco's Modified Eagles' Medium
DMSO:	Dimethyl Sulphoxide
DRIFT:	Diffuse Reflectance-sampling
DSC:	Differential Scanning Calorimetry
DTA:	Differential Thermal Analysis
ECM:	Extracellular matrix
EDS:	Energy Dispersive X-ray
ELP:	Elastin like Polypeptides
ELISA:	Enzyme-Linked Immunosorbent Assay
ES:	Embryonic Stem Cells
FCS:	Fetal Calf Serum
FESEM:	Field Emission Scanning Electron Microscopy
FGF:	Fibroblast Growth Factor
FTIR:	Fourier Transform Infrared (IR) spectroscopy
GelMA:	Gelatine modified with methacrylate group
β-GP:	β-glycerophosphate disodium
HA:	Hydroxyapatite
HAMA:	Methacrylated Hyaluronic Acid
HB-EGF:	Heparin-Binding Epidermal Growth Factor
Hep:	Heparin
H&E:	Hematoxylin-Eosin
HMDS:	Hexamethyldisilizane
HPSGs:	Heparan Sulphate Proteoglycans
HPF:	High Pressure Freezing
HRSEM:	High Resolution Imaging Scanning Electron Microscopy

HUVECs:	Human Umbilical Vein Endothelial Cells
KGM:	Konjac glucomannan
IGF:	Initial Glide Force
LCST:	Lower Critical Solution Temperature
MeOH:	Methanol
MSCs:	Mesenchymal Stem Cells
Mw:	Molecular Weight
MTT:	3-(4,5-Dimethylthiazolyl-2)-2,5-diphenyltetrazolium bromide
pK <sub>a</sub> :	Degree of acidity
pK <sub>b</sub> :	Degree of basicity
pH:	Potentiometric hydrogen ion concentration
PAS:	Photo-Acoustic-sampling
PAMPS:	Poly (2-acrylamido-2-Methylpropanesulfonic acid)
PBS:	Phosphate Buffer Saline
PCL:	Polycaprolactone
PDGF:	Platelet-Derived Growth Factors
PDMAAm:	Poly (N,N0-dimethylacrylamide)
PES:	Polyethersulfone
PEGDA:	Poly (ethylene glycol) diacrylate
PMMA:	Polymethyl Methacrylate
PNIPAAm:	Poly (N-isopropylacrylamide)
PTH	Parathyroid Hormone
PVA:	Poly-vinyl Alcohol
SAXS:	X-ray scattering
SBF:	Simulated Body Fluid
SD:	Standard Deviation
SE:	Secondary Electrons
SEM:	Scanning Electron Microscopy
SGF:	Simulated Gastric Fluid
SR:	Sirius Red
TB:	Toluidine Blue
TCP:	Tricalcium Phosphate
TEM:	Transmission Electron Microscopy
TEOF:	Triethyl Orthoformate
TGA:	Thermal Gravimetric Analysis
TGF $\beta$	Transforming Growth Factor Beta
TPP:	Tripolyphosphate
UCST:	Upper Critical Solution Temperature
UTM:	Universal Test Machine
UV:	Ultraviolet
VEGF:	Vascular Endothelial Growth Factor
XRD:	X-Ray Diffraction

## LIST OF SYMBOLS

%:	Percentage
$\emptyset$ :	Diameter
$^{\circ}\text{C}$ :	Celsius Degree
$\text{F}_{\text{max}}$ :	Force (maximum)
cm:	centimetre
h:	Hours
K:	Kelvin
kDa:	Kilodalton
kPa:	Kilopascal
kN:	Kilonewton
G:	Gauge
GPa:	Gigapascal
G':	Elastic Modulus
G'':	Viscous Modulus
mm:	Millimetres
mL:	Millilitres
nm:	Nanometre
$\mu\text{m}$ :	Micrometre
$\mu\text{L}$ :	Microliter
MPa:	Megapascal
N:	Newton
Pa:	Pascal
$\partial$ :	Tangent (angle)
v:	Frequency

# 1 LITERATURE REVIEW

## 1.1 Introduction

Bone is a tissue that forms the skeleton of animal and human bodies which have substantial roles in preserving tissues and organs, providing motion, and generation and hosting of blood and minerals. Bone tissues damage in daily life due to injuries, diseases or innate abnormalities. Current bone repair and regeneration methods mainly rely on grafting techniques, such as autografts, allografts, xenografts. Despite the vital benefits of these methods, they involve some restrictions, such as donor supply, immune reactions and surgical drawbacks. Alternative regenerative therapies by 3D tissue engineered implantable scaffolds also comprise undesired severe surgical outcomes, such as tissue damage, blood loss, pain and trauma leading patient discomfort, long healing time, high cost etc. (He et al., 2013). In this regard, *in-situ* forming injectable hydrogels offer regenerative treatments to targeted tissues by minimally invasive methods. Liquid regenerative solutions can be injected at targeted tissue defects on which crosslinked hydrogels were formed *in-situ* by the effect of a stimuli, such as temperature, light and pH. Injectable thermosensitive liquids can form physically crosslinked hydrogels *in-situ* by moulding complex shaped voids due to the natural body temperature. The pH and thermosensitive injectable hydrogels are excellent tools for site specific drug delivery of desired therapeutic agents (e.g. medicines, cells, growth factors, and genes) which also allow their *in-situ* encapsulation upon fast gelation in body. Furthermore, extracellular matrix (ECM) mimetic structure of hydrogels increase cytocompatibility and reduce immune reactions (Klouda, 2015; Naahidi et al., 2017; Nguyen & Lee, 2010; Radivojša Matanović et al., 2015).

Bone treatments often fail due to insufficient vascularisation during healing phase. The regeneration of critical bone fractures strongly relies on swift invasion of vascular network to the defect site via branching from the existing vessels, termed as ‘angiogenesis’(Grosso et al., 2017; Risau, 1997). Therefore, there is a significant need

for functional biomaterials not only providing ionic binding between bone defects but also ensuring biological bridging by promoting angiogenesis. The aim of this study was to develop proangiogenic, biodegradable and bioactive, pH and thermosensitive injectable hydrogels for minimal invasive and vascularised bone regeneration. In this study, novel hybrid injectable hydrogels are developed from biodegradable CS polymer matrix integrated with inorganic HA mineral and a highly anionic glycosaminoglycan Hep which are aimed to be proangiogenic and bioactive biomaterials stimulating bone regeneration.

## 1.2 Bone

Bone is a skeletal tissue of the body providing constructional support having versatile functions, including; conserving organs, ensuring motions along with muscles, carrying mineral sources and participating in generation of blood cells (Dorozhkin, 2016).

### 1.2.1 Bone Structure and Properties

#### 1.2.1.1 Chemical Structure of Bone

Bone is a composite material consisting of organic and inorganic compounds. Bone has a wonderful hierarchical architecture consist of various substructures from macro to nano sizes. In the molecular level of this hierarchy, bone is composed of proteins, mainly collagen, biological apatite and water (Dorozhkin, 2016) (Figure 1.1). The most essential organic component of bone is Type-I collagen (amounting to 95%) and other proteins and proteoglycans. Inorganic matrix of bone composed of a calcium phosphate compound, hydroxyapatite with diverse ionic substitutions, and this mineral formed by cells are aligned among fibrillar collagens (Katsimbri, 2017; Liu et al., 2016; Marks & Odgren, 2002).

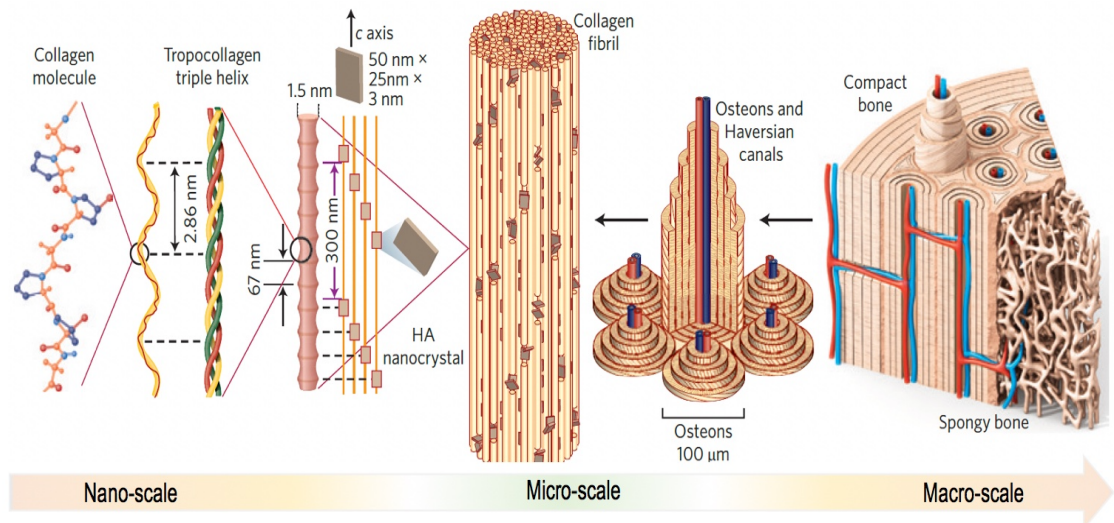


**Figure 1.1** Hierarchical structure of human bone densely packed compact bone and porous spongy bone structures in macro scale; parallel collagen fibrils and hydroxyapatite among them circular lamellar structure surrounding blood vessels and nerves in Haversian channels. figure was reproduced with kind permission: © 2015 by Springer Nature Publishing group (Wegst et al., 2015).

Three types of main bone cells are located in bone and involve to bone remodelling process which are osteoblasts, osteoclasts and osteocytes (Katsimbri, 2017).

Osteoblasts are known as bone forming cells which is a type of mesenchymal stem cells and capable of differentiation to other cells; osteoblasts, chondrocytes, and adipocytes etc. Osteoblasts generate Type-I collagen which is the main bone organic compound. In addition, osteoblast-based matrix cavities in young bones (osteoid) include phosphate which forms hydroxyapatite mineral when it contacts to calcium in body fluid.

Osteoclasts are the cells which provide bone resorption. Osteoclasts are generated particularly in the inflammatory regions by differentiating from dendritic cells. Osteoblasts are also differentiated into osteocytes which are initially embedded into newly formed bones and it takes its last shape after bone mineralisation and located in bone lacunae.

Osteocytes with branched shaped form 95% of all bone cells, and they provide communication between lacunae and canaliculi by signalling. Osteocytes discern the bone fractures and react with motional and metabolism signals to launch the bone regeneration process (Katsimbri, 2017).

### 1.2.1.2 Classification and Architecture of Bone

Bones are classified as compact and spongy bones, and their portions range according to the function of the bones in specific parts of the body. When the osteons are tightly packed the bone is referred to as compact or cortical bone. On the other hand, bone which is characteristically less dense and weaker in strength in the microporous structure is named as cancellous, spongy or trabecular bone (Currey, 2012; Olszta et al., 2007).

#### 1.2.1.2.1 Cortical Bone

Cortical bones provide mechanical support in skeleton. Compact bones construct the outside of bones while spongy bones build interior sites of bones depending on bone types. Cortical bones particularly locate at crusts of bones beneath the periosteum (the exterior fibrous film covering bones), long bones shafts, and spine. The horizontally sectioned compact bone with its components are illustrated in Figure 1.2. Cortical bone is comprised from osteons, interstitial tissue, lacunae and cement lines. Osteons, are also known as Haversian system, consist of concentric mineralized lamellas which surround the Haversian (central) channel hosting blood vessels, nerves ( $\sim 50 \mu\text{m}$ ) and lymphatic vessels. Interstitial tissues are separated from osteons by the cement lines (Wang et al. 2010, p.16-18; Marks and Odgren, 2002).

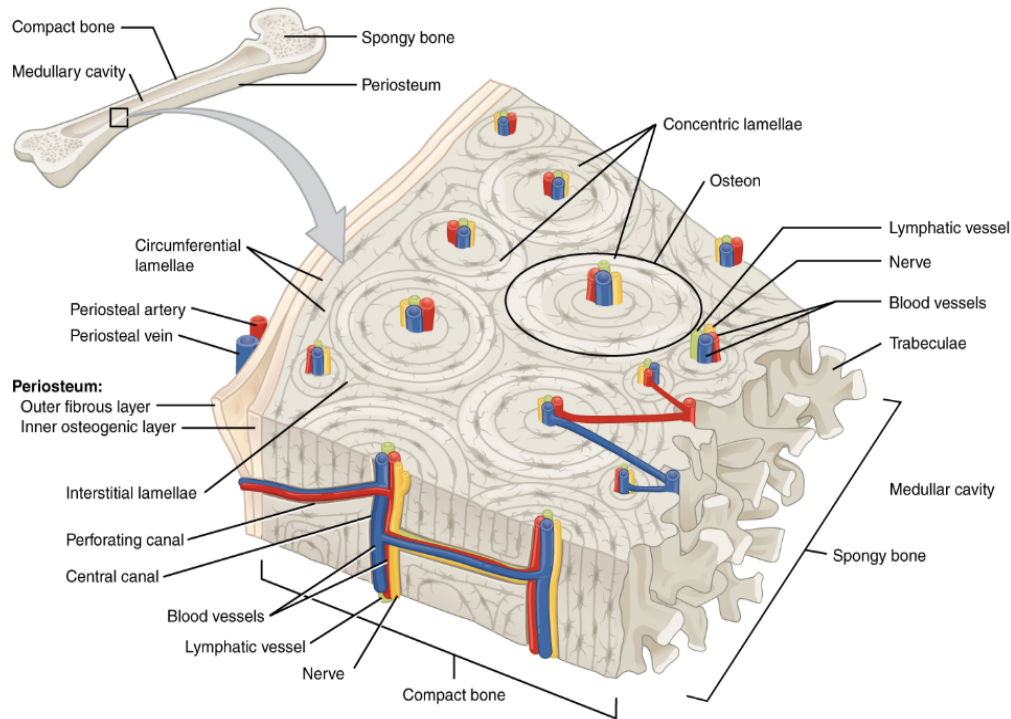


**Figure 1. 2** The demonstration of a bone horizontal section involving cortical and trabecular bone including osteons composed of a central channel hosting blood vessels, nerves, and lymphatic vessels (branch through the perforating channels) and surrounding mineralised concentric lamellae. Interstitial lamellae located between osteons and circumferential lamellae laying under periosteum that has periosteal artery and veins. This used figure licensed under ©CC BY 4.0 by Rice University “Anatomy and physiology textbook, 6.3. Bone structure”.

Cortical bone has the porosity of 5-10% which is provided by Haversian channel and connective canals between them known as Volkmann’s (perforating) canal which blood vessels and nerves branch through. There are also Lacunae; spaces which contain osteocytes that generate small channels called canaliculi, and temporary resorption channels formed by osteoclasts (bone eating cells) during the first step of bone remodelling (Wang et al. 2010, p.16-18).

#### 1.2.1.2.2 Trabecular Bone

Cancellous or spongy bone is found in the short bones, as with vertebral bones and medullar channels at the tips of long bones and it has a role in metabolism. Cancellous bone has a trabecula structure comprising from interconnected layers and rods at the thickness around 200  $\mu\text{m}$ . Trabecular bone has high pores ratio accounting for 75-90%, and these pores are stuffed with medulla (Wang et al. 2010, p.16-18).

### 1.2.1.3 Mechanical Properties of Bone

Bone, despite its high stiffness, due to its elasticity, can undergo various stresses, such as, compression, strain, bending and shear forces. The resistance of the bone against these stresses is affected by multiple factors, e.g. manner, orientation and intensity of loading in addition to bone type and age. For instance, as reported strength of bone samples ranges between 79 to 151 MPa longwise, whereas 51 to 56 MPa in crosswise. The anticipated values of elastic modulus of bones vary from 17 to 20 GPa longitudinally, which change between 6-13 GPa transversally. It is considered that having lower elastic modulus in transversal direction is stemmed from the isotropic nature, which includes parallel orientation of osteons (Wang et al. 2010 p.43, 83; Dorozhkin 2015). Another factor impacting on mechanical aspects is the degree of mineralization. To exemplify, as the calcium ratio of bone surges, elastic modulus raises and failure strength declines. In Table 1.1, contrastive mechanical and mineralogical properties of bone samples of different species were presented (Rogers & Ziopoulos, 1999).

**Table 1.1** Mechanical and mineralogical properties of bone samples from different species. Table was adapted with kind permission from Springer Nature (Rogers & Ziopoulos, 1999).

Species	Young's modulus (GPa)	Bending Strength (MPa)	Vickers Hardness (VHN)	Approximate Mineral Fraction % (wt/wet wt)
<b>Human femur</b>	16-18	200-220	40-60	55
<b>Bovine femur</b>	18-22	220-240	50-70	65
<b>Whale tympanic bulla</b>	26-32	45-55	150-170	83
<b>M. rostrum</b>	40-42	50-60	200-220	96

### 1.3 Bone Remodelling and Growth

Bone remodelling is a lifelong renewal process of bone to ensure its biomechanical function and mineral balance. In addition, bone remodelling is also necessary for repair of bone defects. During bone remodelling, new bones are generated while the old bones are exposed to resorption at the same rate. Otherwise, bone diseases occur due to the generation of bone deficiency (osteoporosis) or outgrowth (osteopetrosis). The new

bone generation and extension of bones take place more in early age of human beings rather than bone remodelling which is more common in adults (Katsimbri, 2017).

Bone generation include primary and secondary osteogenesis (ossification). Primary bone formation takes place in epiphyseal cartilage zones which consist of 'ground substance', and weak and tiny collagen fibril clusters. Due to fast mineralization, a randomly arranged 'woven' bone microstructure occurs whereby collagen cannot be arranged in a lamellar structure, and its connection with hydroxyapatite spheres is weak (Olszta et al., 2007). Secondary bone formation occurs via realignment of woven bones. It entails arrangement of hydroxyapatite sheets in the collagen fibrils which are ordered as parallel-lamellar fibre layers encircling the blood vessels and nerves to construct osteons in the human Haversian canal (Currey, 2012; Olszta et al., 2007).

Bone remodelling takes place in five steps; activation, resorption, reversal, formation and termination. In the activation step, bone remodelling begins with the signal detection by bone arising from hormones and mechanical alterations. Then, in the second step, osteoclasts are activated after withdrawal of the osteocyte cells and the removal of the endosteal membrane by enzymes. Bone resorption occurs via the polarization of osteoclasts once they link to the bone matrix leading to actin ring formation. Osteoclasts differentiate into a large osteoclast population; they adhere to bone tissues, secrete enzymes and hydrogen ions, decreasing pH to disintegrate bone mineral and organic phases (Katsimbri, 2017).

The Howship's lacunae channels forms and the resorption process is completed with the death of osteoclasts. Bone resorption takes 2-4 weeks. The remaining bone cells; monocytes, osteocytes and pre-osteoblasts with the help of signalling factors are the basis for new bone formation. . New bones (osteoids) are produced by osteoblast cells to fill the holes formed by osteoclasts until they become passive bone lining cells. Eventually, following osteoid generation, about a month later, they are exposed to mineralisation as hydroxyapatite with some ions e.g. carbonate and magnesium. The knowledge of natural bone remodelling has also contributed to development of tissue engineering strategies to repair and regeneration of bone tissues by employing biomarkers and active agents (Katsimbri, 2017).

### 1.3.1 Bone Fracture Healing and Role of Blood Vessels

Blood vessels have significant role to ensure metabolic activity of organisms by providing oxygen, nutrients and minerals, and carrying the metabolism products. Blood vessels in bone marrow is also a zone for blood generating hemopoietic stem cells and other bone cells (Hankenson et al., 2011).

Bone fracture healing strongly depends on the resorption of destroyed tissue debris and sufficient vascular bridge formation. The most challenging circumstances for repair are the insufficient blood supply to the defect sites due to the blood vessel deficiency (Hankenson et al., 2011; Stegen et al., 2015). As reported, a blood vessel should present in each 100-200  $\mu\text{m}$  distance to be able to maintain both metabolic activity and reconstruction of tissues (Bienert, 2018; R. K. Jain et al., 2005).

Blood vessel formation is related to two different terms; vascularisation and angiogenesis. During vasculogenesis, mesodermal cells known as angioblasts differentiate into endothelial cells resulting in the generation of vascular plexus which give rise to the formation of primary blood vessels. Following this, formation of further endothelial cells leads to the occurrence of new blood vessels through sprouting or splitting from primitive vessels. This process is referred to as angiogenesis (Risau, 1997).

Bone fracture repairs follow three main overlapping stages including (i) inflammation, (ii) repair and (iii) remodelling (see Figure 1.3). In the inflammation stage, an injury site is occupied by blood which is encapsulated by soft tissue, and hematomas form. Then, inflammatory cells (such as macrophages, monocytes, granulocytes, and lymphocytes), while secreting growth factors and cytokines, invade and penetrate hematoma towards fracture pieces and lead to further fibrous thrombus formation. Blood vessel ingrowth through clots leads to granulation tissue development. In addition, mesenchymal stem cells, derived from bone marrow, periosteum and soft tissue, are employed and subsequently differentiate into osteoblasts (Schindeler et al., 2008; Zhao, 2010).

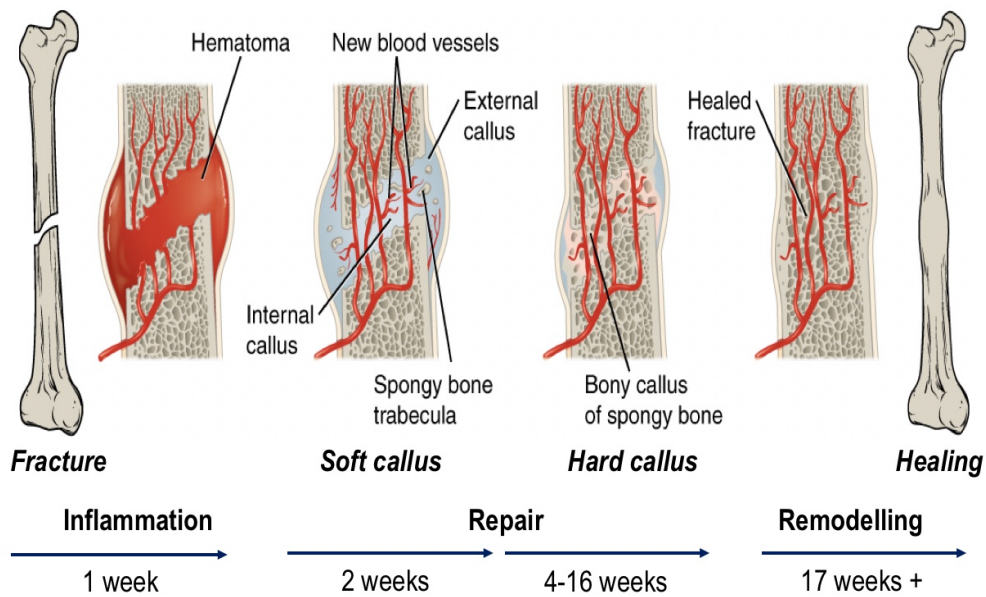


**Figure 1. 3** The schematic diagram of bone fracture healing which involve three main stages namely (i) inflammation (ii) repair and (iii) remodelling stages. This figure was adapted from (Anatomy & Physiology (Biga et al., n.d.) licensed under ©CC BY 4.0 <https://open.oregonstate.edu/aandp/chapter/6-5-fractures-bone-repair/>)

During the bone repair stage, via chondrocyte and fibroblast activity, a fibrous and granulation tissue designated as soft callus, forms a mineralised fibrocartilage zone that eventually fixes the defective site. The unstable soft callus is then resorbed. Meanwhile, revascularization progresses to form hard callus which has a mineralised but non-uniform structure. Microvascular transformation into soft callus is stimulated by angiogenic growth factors, e.g. VEGF, FGF and TGF. At mechanically stronger sites or at the borders of pre-mineralised zones, primary bone can be produced through intermembranous ossification. However, most cases also involve endochondral osteogenesis. Vascularisation has significant importance in woven bone development, providing oxygen supply that ensures osteoblast differentiation from osteoprogenitor cells which construct mineralised ECM with proteins (Schindeler et al., 2008).

The repair stage is followed by remodelling; it involves rearrangement of disorganised woven bone to lamellar (secondary) bone, which ultimately transforms into a compact structure. As discussed previously in Section 1.3, remodelling involves breaking down of old bone components, draining of degradation products through the vascular network and the synthesis of osteoid as units of young bones which are subsequently mineralised while microvasularity is ensured (Schindeler et al., 2008).

## 1.4 Bone Health and Fractures

Bone may damage due to numerous factors, such as injuries, infection, trauma, tumour or genetic diseases etc. (Chen et al. 2015). Minor damages in a human body can be reconstructed and healed by the body itself. However, the repair of major injuries remains a challenge which researchers have been trying to address with different approaches.

Prior to dealing with bone diseases, the factors affecting bone health need to be addressed. There are numerous factors that have an impact on bone health. The genetic and environmental parameters, such as nourishment and physical motion play a significant role in bone healthiness. For instance, congenital bone disorders can be caused by the wrong signalling of genes, and insufficient nourishment might lead to decrease in bone minerals and strength of bones (US Department of Health and Human Services, 2004 p.16).

### 1.4.1 The Role of Hormones in Bone Health

One of the important factors that has an impact on bone functions is hormones. There are three essential hormones that modulate calcium including parathyroid hormone (PTH), calcitriol and calcitonin. The PTH helps bone resorption and regeneration as well as calcium balancing; calcitriol, a derivative of vitamin D, ensures gastral absorption of calcium and phosphorous; and calcitonin balances the amount of calcium in blood and prevent bone fraction.

Among the sex hormones, oestrogen contributes to the extension of bones in childhood and early puberty, reaching its highest level at the end of puberty at which cessation of bone growth starts. In addition, oestrogen impacts on osteoclasts and osteoblasts to prevent bone fractions and to provide for regeneration of bones. Its deficiency causes bone deprivations during menopause. The hormone testosterone, which also comprises oestrogen by transformation in adipocytes, has an effect on the growth of muscles, inducing stress on the bones triggering bone formation or vice versa.

Growth hormone, thyroid hormones (Triiodothyronine, thyroxine and Calcitonin ), cortisol, insulin and leptin also affect bone. Growth hormone which is secreted by the pituitary gland triggers the growth of bones at puberty, and its deficiency impairs bone formation following resorption in the elderly. Thyroid hormones stimulate energy supply to the cells as well as bone resorption and regeneration. In addition, cortisol, produced by the adrenal gland is a hormone that modulates the metabolism and ability of organism to defeat deformation forces (US Department of Health and Human Services, 2004 p.26-29).

#### 1.4.2 Common Bone Diseases

Bone tissue become more sensitive to breakdown in the absence of a balanced bone resorption and regeneration process; leading to the alteration of bone weight, hardness and structure. Osteoporosis, osteopetrosis, osteogenesis imperfecta and bone tumours are among common bone diseases. However, common bone diseases relevant to this project including Paget's disease, rickets and osteomalacia are discussed below.

##### 1.4.2.1 Paget's disease

Paget's disease is the second most frequent bone disease after osteoporosis. This is an disease that can lead to bone fragility, deformation and pain as well as the risk of osteoarthritis at connected joints. This disease results from intense osteoclast activity leading to rapid bone resorption and over formation of disorganized new bones. In addition, it may result in the generation of excess vascularized tissue in the bone marrow space and compressive force exposure to nerve tissues. Paget's disease which is commonly associated with environmental conditions rather than genetic, may also be caused by viral infections. Significant amounts of alkaline phosphatase production, curved legs and joint defects are the primary indicators of this disease. Bisphosphonates can be utilized to treat this disease (US Department of Health and Human Services, 2004, p.55).

#### 1.4.2.2 Rickets and Osteomalacia

The malformation of bones such as curved legs due to the slow mineralisation of bones leading to deformations during bone development in children are called rickets. On the other hand, osteomalacia is the same version of this disease in adults, leading to fractures at load-bearing bones such as the hips, pelvis and feet. Both diseases generally occur due to external factors such as vitamin D deficiency. Cases based on genetic factors are very rare (US Department of Health and Human Services, 2004, p.54).

### 1.5 Bone Repair and Regeneration

#### 1.5.1 Transplantation Techniques

Traditional grafting methods have been utilized for bone repair and regeneration, such as autografts, allografts, and xenografts. However, a number of challenges can be encountered in the application of these methods. For instance problems with donor supply, disease transformation, tissue incompatibility and adverse immune reactions (He et al., 2013). Due to these limitations, some successful artificial implants and prostheses have been developed together with operational enhancements. These include; orthopaedic vehicles ensuring long usage time with pain mitigation, heart valves and heart-pacers. However, they also have led to some issues with the lack of viability and self-repair capacity of implants in comparison with that of native tissue and their incongruence with biological tissue (Hench and Jones, 2005 p.88-89).

The drawbacks of the aforementioned treatments eventually give rise to development of regenerative medicine strategies that trigger cell activity, and the natural regeneration and recovery of tissues (Hench and Jones, 2005 p.88-89).

#### 1.5.2 Bone Tissue Engineering

In bone tissue engineering, scaffolds are used as a model on which cell communications and generation of extra cellular matrix occur (Karageorgiou & Kaplan, 2005). These 3D scaffolds might be harvested with certain cells, growth factors or cytokines to

promote self-repair of tissues (Swetha et al., 2010). Cells can be cultured in vitro by seeding isolated cells provided by a certain tissue biopsy belonging to the patient. These cultured cells are assembled into the scaffolds which are comparable with ECMs (Lee & Mooney, 2001). In addition, it is possible to insert scaffolds straight into the defected areas in the body. This is referred to as *in-vivo* regeneration (O'Brien, 2011). Having injectable and implantable forms, scaffolds are also useful for drug delivery and transmission of bioactive agents (Edgar et al., 2016).

## 1.6 Biomaterials

Historically, biomaterials are divided into three groups:, the first generation which consists of bioinert materials that minimise immune reactions, second generation bioactive and degradable materials enabling interaction with tissues and the triggering of regeneration and third generation biomaterials targeting desired cell and gene activities via atomic alterations in materials (Hench & Polak, 2002).

### 1.6.1 Required Properties of Biomaterials for Bone Repair and Regeneration

Numerous parameters should be considered for manufacturing an ideal scaffold for a certain function, region and patient due to the mechanical, biological, and structural properties of complicated bones, as well as personal factors such as age, diet and mobility etc. (Karageorgiou & Kaplan, 2005). Hench and Jones (2005, p.202) have pointed out that the explicit requirement of scaffolds is their biomimetic construction modelled on natural tissues.

#### 1.6.1.1 Biocompatibility

The recent definition of biocompatibility has been reported by Zhang & Williams, (2019) as following:

*“The ability of a material to perform with an appropriate host response in a specific application”.*

In addition, biocompatibility as a term specific to scaffolds has been defined by Williams, (2008) as following:

*“The biocompatibility of a scaffold or a matrix for a tissue engineering product refers to the ability to perform as a substrate that will support the appropriate cellular activity including the facilitation of molecular and mechanical signalling systems, in order to optimize tissue regeneration, without eliciting any undesirable local or systemic responses in the eventual host”.*

It is crucial that an ideal scaffold should be biocompatible. That is, being in harmony with a body chemically, biologically, physically and mechanically. In biological aspects, they need to provide adhesion, migration and proliferation of cells without immunogenic and cytotoxic effects (Edgar et al., 2016; O’Brien, 2011; Scholz et al., 2011).

#### 1.6.1.2 Bioactivity

The scope of bioactivity first described by Hench *et al.*, (1971):

*“A bioactive material is one that elicits a specific biological response at the interface of the material which results in the formation of a bond between the tissues and the material”.*

In addition, in the classification of biomaterials according to their bonding properties with native tissues, bioactive materials are characterized between inert and resorbable materials as follows (Cao & Hench, 1996):

- i.** almost inert materials that provide only a morphological bonding
- ii.** porous materials enabling tissue ingrowth through the pores which is a biological bonding
- iii.** bioactive materials that involve bioactive bonding at the tissue-matter interface
- iv.** bioresorbable materials that can degrade in time and be replaced with regenerated host tissue

Bioactivity in relation with bone refers to the ability of a biomaterial to have anchorage with the native bone tissue at the interface. The term ‘bioactivity’ for biomaterials used in bone tissue repair or regeneration has also been defined as the deposition of a mineralized hydroxyl carbonated apatite layer on the surface of the biomaterial *in vitro* in simulated body fluid or *in-vivo* body fluid tissue without isolation by a fibrous tissue (Kokubo, 1991; LeGeros & Ben-nissan, 2014).

The bioactivity index ( $I_B$ ) has been defined by Hench, (1988) as a constant that has reciprocal proportion with the required time for bonding covering 50% of an interfacial area  $t_{0.5bb}$  ( $I_B = 100/t_{0.5bb}$ ). The amount of bioactivity alters according to various factors, such as type of material, and the anchorage dimensions, type and strength. (Cao & Hench, 1996).

A range of biomaterials, including and particularly bioceramics, possess bioactivity. Examples are bioglasses e.g. Bioglass®, A-W glass ceramics or Ceravital®, calcium phosphates including hydroxyapatite, and composites of bioactive materials including coatings (Cao & Hench, 1996). Although bioactive bone tissue engineering materials show carbonated hydroxyl apatite layer formation on the surface, according to their biochemical interactions, bioactive materials are divided into two groups, osteoprotective and osteoconductive. Osteoconductive materials facilitate a biocompatible interface where the region is only exposed to extracellular response, promoting bone formation on its porous surface. However, osteoprotective materials promote both an extracellular and intracellular response. Here osteoprogenitor cells lead to a swift osteoid and mineralised bone production without fibrous tissue formation. This course of action is named osteoproduction or osteostimulation (Cao & Hench, 1996; LeGeros & Ben-nissan, 2014, p. 54; Nicholson, 2020, pp. 61–62). The bioactive materials showing both osteoprotective and osteoconductive features are designated Class A while materials having only osteoconductivity are categorised as Class B materials. 45S5 Bioglass® and synthetic hydroxyapatite are examples of Class A and Class B materials, respectively. Class A materials provide bonding not only with bone but also with soft tissues (Cao & Hench, 1996).

The chemical modification of hydroxyapatite, involving ionic substitutions to mimic biological apatite in hydroxyapatite crystal lattice, and morphological modifications lead to better resorbability and bioactivity. For instance, carbonate substituted in hydroxyapatite has showed major impacts *in-vivo* on enhancing osteointegration, bioresorbability and biocompatibility (Landi et al., 2003); silicon contributes to production of collagen (type 1), differentiation of osteoblasts leading to osteogenesis; strontium has an effect on stimulating osteoblast formation while preventing osteoclast generation and the expression of angiogenic and vascular endothelial growth factors (VEGF) (Lin & Chang, 2015; Lin et al., 2013).

#### 1.6.1.3 Osteoinduction, Osteoconduction and Osteointegration

Osteoinduction is a process of generation pre-osteoblast cells from the premature cells (undifferentiated and pluripotent cells) that are required for bone regeneration. Osteoinduction has a major role in bone fracture repair. Osteoinduction can be provided by using a stimuli that enables conversion of undifferentiated cells to osteogenic cells. For example, using demineralised bone or bone morphogenetic proteins as a stimulus (BMP) (Urist, 1965; Urist et al., 1979). Osteoinductive materials are described as materials which promote differentiation of progenitor cells to osteoblasts leading to formation of new bone (Nicholson, 2020, p. 62).

Osteoconduction describes the capacity for bone growth through the porous pathways inside tissue engineered scaffolds. Osteointegration is designated as the strong bonding between biomaterial and bone tissue. In addition, osteointegration is also attributed to the generation of bone like tissue at the vicinity of the biomaterial and an absence of fibrous layer development at the place where biomaterial and tissue contact takes place. Some definitions of osteointegration also cover the biomechanical attachment of biomaterial to natural tissue, which involve sufficient strength of the material against mechanical forces (Albrektsson & Johansson, 2001).

#### 1.6.1.4 Biodegradability

Biodegradability is one of the significant parameters in tissue engineering since scaffolds provide temporary support and have to substitute with natural ECM generated by cells over time in the body (Babensee et al., 1998). However, degradation products should have no immunological or inflammatory effects, and leave the body with no deleterious effect on other organs (O'Brien, 2011). The rate of biodegradation depends on the function of the biomaterial, for instance, for long-period purposes, gradual degradation is preferable while fast degradation is suitable once regeneration of tissues are required (Edgar et al., 2016). As reported by Hutmacher (2000) biodegradable scaffolds should maintain their physical characteristics for up to a minimum of 6 months; covering 4 months of cell-culture process and 2 months upon implantation into the body. Following this, it is expected that they need to start degradation and be excreted from the body with no adverse effects within the required period of time.

#### 1.6.1.5 Architecture and Porosity

Constructive properties of scaffolds that can be controlled through fabrication processes are also very important. These structural properties involve porosity, pore size, range of pores, surface morphology and geometry (2D or 3D) (Edgar et al., 2016; Karageorgiou & Kaplan, 2005; O'Brien, 2011). These scaffolds should have enough porosity to promote tissue growth through the pores. Furthermore, they have to ensure conveying of nutriments, oxygen, growth factors and wastages (Holzwarth & Ma, 2011).

According to a report by Hulbert et al. (1970) in bone tissue engineering, the lowest pore size of scaffolds should be 75 to 100  $\mu\text{m}$  to maintain cell activities and diffusion. However, other later studies have shown that (Götz et al., 2004; Karageorgiou & Kaplan, 2005) the suggested particle size should be at least 300  $\mu\text{m}$  since larger pores result in more vascular structure promoting osteogenesis, generation of young bones. Moreover, scaffolds with small pore sizes are exposed to chondrogenesis ahead of ossification, indicating eligibility for anaerobic tissue regenerations such as cartilage. However, wide pore sized scaffolds give rise to straightforward ossification (Karageorgiou & Kaplan, 2005). In relation to the mechanical necessities of scaffolds,

their properties should be comparable with the natural bone tissues in which they will be implanted (O'Brien, 2011).

For bone regeneration applications, as well as porosity, permeability of the materials is also crucial. The permeability can be associated with the interconnectivity between the pores that provide transfer of the liquids through the scaffold for sufficient angiogenesis, osteoinductivity and osteoconductivity (Forrest, 2005; Shalaby & Salz, 2007). It was reported that permeability of scaffolds can be enhanced by the presence of the micropores accompanying macropores (Hing et al., 2003, 2005). This study comparing HA scaffolds having 10% and 20% microporosity in total pore volume (the pores range from macro ( $>50\text{ }\mu\text{m}$ ) to micro scale ( $<20\text{ }\mu\text{m}$ )) has shown that significantly increased and rapid bone ingrowth was achieved with the higher microporosity that increases nutrient diffusion and angiogenesis leading to enhanced bioactivity and osteointegration. Angiogenesis will be covered in detail in Section 1.7.3.

### 1.6.2 Classification of Biomaterials Used for Bone Repair and Regeneration

In terms of the biomaterial classes; metals, ceramics, polymers and their composites are utilized in bone tissue engineering (Stevens et al., 2008).

#### 1.6.2.1 Metals

Among the biomaterials, metals are convenient for load-bearing bone implants due to their high durability, malleability and abrasion strength (Ba'rtolo & Bidanda, 2008). Some instances of metal alloys that have been harnessed in orthopaedic field are aluminium, stainless steel, cobalt chromium alloys, and titanium alloys. Even though metal alloys ensure to increase biocompatibility and toughness, and decrease in mass, metals may have some issues in rooting from their fracturing, stress shielding, chemical abrasions which may cause inflammation, inhibit bone generation and increase tissue deprivation. Furthermore, metals which are bioinert and deprived of tissue interactions can only be harnessed as long-lasting implants rather than for bone regeneration (Ba'rtolo & Bidanda, 2008; Stevens et al., 2008).

### 1.6.2.2 Ceramics

Bioceramics can be bioinert, bioactive, bioresorbable and/or porous materials accordingly with their binding types with host tissues (Hench, 1991). The utilisations of bioceramics cover healing and rebuilding skeletal destructions and damage from diseases. These include; hip, knee, dental and joint implants, as well as periodontal and orthopaedic treatments. Compact bioinert materials such as alumina and zirconia provide an anchorage with tissues physically from the surface by filling the injured bone parts. This is referred to as morphological fixation. However, in porous bioinert compounds mechanical bonding with tissues occur (biological fixation). These involve porous multi-crystal alumina and metal coating with HA. As for bioresorbable ceramics e.g. tricalcium phosphate, such compositions are compact ceramics which may be either porous or solid. They are exposed to a gradual, eventual dissolution and substitution by host tissues.

Regarding bioactive ceramics, glasses and glass-ceramics, these enable a chemical binding with tissues because of their active surface structures. This attachment is called bioactive fixation. Despite their compact and solid nature, their attachment occurs because of their surface modification and the generation of a carbonated hydroxyapatite (CHA) sheet. Since the composition of this layer is identical to bone mineral in terms of chemistry and construction, they can form strong anchorage with tissues. Moreover, this layer which binds at the interface with natural tissues, can have a protective role against mechanical loads (Hench, 1991).

#### 1.6.2.2.1 Bioglass and Glass Ceramics

Certain bioactive glasses do possess good bioactivity and cell attachment that encourage bone growth. In comparison with ordinary glass formulations, bioactive glasses contain less than 60% silicon oxide and more alkali oxides with a higher proportion of CaO to P<sub>2</sub>O<sub>5</sub> (Hench, 1991). The first bioactive glass with the tradename of Bioglass® was developed by Professor Larry Hench in 1969 and was named as 45S5 (45% of SiO<sub>2</sub> and the proportion of Ca/P is equal to 5). This composition has found different clinical

applications, such as in periodontics, middle ear operations, and orthopaedics (denoted as NovaBone®) (Juhasz & Best, 2012).

Glass-ceramics are crystallised from glass phase and they differ from bioactive glasses with their low percentage of alkali oxides. One of the glass ceramics, apatite-wollastonite (A-W) (Cerabone®) have better mechanical characteristics than bioglass with regard to toughness, strength and Young's modulus. This makes them applicable for load bearing applications, such as iliac crests, spine and bone filler (Juhasz & Best, 2012).

#### 1.6.2.2.2 Calcium Phosphates

Calcium phosphates consist of anhydrous or hydrated CaO and P<sub>2</sub>O<sub>5</sub> compounds. Calcium orthophosphates are significant to life in terms of their ample amount in the earth and being part of creatures such as in bones, teeth, and antlers. They can be found in a variety of chemical forms including; acidic (compounds with H<sub>2</sub>PO<sub>4</sub><sup>-</sup> or HPO<sub>4</sub><sup>2-</sup>), hydrate (CaHPO<sub>4</sub>.2H<sub>2</sub>O) and hydroxide (Ca<sub>10</sub>(PO<sub>4</sub>)<sub>6</sub>(OH)<sub>2</sub>). Because of their structural stability, all calcium orthophosphates have quite low water solubility and do not dissolve in bases. However, they are soluble in acidic mediums. In nature, they are found as transparent crystals and are white in powder form (Dorozhkin, 2016).

Among the calcium phosphates except hydroxyapatite, two polymorphs of tricalcium phosphates (TCP) are well known for biomedical utilisations; namely  $\alpha$ -TCP and  $\beta$ -TCP having the chemical formula of Ca<sub>3</sub>(PO<sub>4</sub>)<sub>2</sub> (Dorozhkin, 2016; Sheikh et al., 2017; Tamimi et al., 2006).  $\alpha$ -TCP, the high temperature form of  $\beta$ -TCP (>1125), is more soluble than  $\beta$ -TCP. Although it is more reactive than  $\beta$ -TCP, fast resorption of  $\alpha$ -TCP restricts its utilisations. It has been reported that  $\beta$ -TCP is utilised in bone grafts, dental materials and self-setting Ca(PO<sub>4</sub>)<sub>2</sub> compositions. However,  $\alpha$ -TCP is generally utilized as biphasic, together with HA or the silica stabilised form in the compositions of bone scaffolds requiring bioresorbability and porosity, (Dorozhkin, 2016).

### 1.6.2.2.3 Hydroxyapatite (HA)

Hydroxyapatite or hydroxylapatite is an assortment of apatite minerals and its stoichiometric formula is  $\text{Ca}_{10}(\text{PO}_4)_6(\text{OH})_2$  (Ca to P ratio of 1.67) (Okada & Furuzono, 2012). Hydroxyapatite has two distinct crystal structures including hexagonal and monoclinic. Whereas hexagonal structure has the following lattice parameters;  $a=b=9.432 \text{ \AA}$ ,  $c=6.881 \text{ \AA}$  and  $\gamma=120^\circ$ , in monoclinic structure;  $a= 9.421 \text{ \AA}$ ,  $b=2a$ ,  $c=6.881 \text{ \AA}$ , and  $\gamma=120^\circ$ . Differentiation between two crystal system results from the positions of hydroxyl ions in the molecular structure (Liu et al., 2013).

It is a well-established fact that hydroxyapatite has significant impact on bone regeneration owing to its unique controllable bioactive properties (Liu et al., 2013). Incrementation in bioactivity enhances cell adhesion and osteoconductivity and provides proliferation and alkaline phosphate secretion of osteoblasts, which contributes to early healing of bones (Arun Kumar et al., 2015) and biocompatibility (Zakaria et al., 2013). Therefore, HA has a wide range of applications as a biomaterial, including; bone fillers (Higashi et al., 1986), glass ionomer cements (Najeeb et al., 2016), implant coatings (Darr et al., 2004), in addition to being a delivery agent for drugs and growth factors (Matsumoto et al., 2004) (Okada & Furuzono, 2012).

### 1.6.2.2.4 The Impacts of Structural Features on HA Properties

There are a number of factors determining final properties of HA and their successful utilization for different biomedical applications. These factors inevitably involve morphology, crystallinity, shape, size, particle distribution, which might be controlled by synthesis methods and synthesis conditions.

#### *Crystallinity*

The harnessing of crystalline or amorphous HA strongly depend on its application. Crystalline stoichiometric HA with favourable shapes are preferred for mechanical strengthening while more amorphous, ionically substituted HA with small particle size

(nano HA), is more suitable in terms of resorbability of biomaterial (Lin & Chang, 2015).

### ***Crystal Size and Distribution***

Size is one of the most crucial factors affecting HA behaviour for related applications. For instance, the use of nano-sized HA powder would be the perfect choice to achieve mechanically strengthened final material with good sintering due to large surface area (Lin, Kaili et al., 2012). In addition, nano HA give rise to enhancements at bioactive and resorbable features in comparison to micro sizes. Moreover, it is reported that nano sized HA stimulates better cellular performance e.g. cell adhesion, proliferation, differentiation which might be associated with their rough surfaces with a wider area. Furthermore, hybrid micro/nano sized HA crystals give the best biological results when compared with sole micro or nano-sized counterparts due to enhanced surface energy that enable binding with targeted proteins and help provide stem cell differentiation for fast bone reconstruction (Lin & Chang, 2015; Xia et al., 2013).

### ***Crystal Shape***

Crystal shape is also a significant factor affecting final biomaterial features such as strength, resorbability and biocompatibility. The rod and wire shaped one dimensional, and two-dimensional sheet shaped crystallized HA particles enhance material toughness, while 3D porous clusters can be harnessed when drug loading and delivery applications are required (Lin & Chang, 2015; Sadat-Shojaei et al., 2013).

To summarize, the final biomaterial features of HA for specific applications are correlated with its compositional and structural features that can be adjusted by synthesis parameters. The size uniformity of particles is important especially for drug loading applications. Surface topology of HA, for instance, micro-nano hybrid particle structures, can lead to enhance osteoinductivity of biomaterials. Bioresorption of HA needs to be monitored by controlling structural features of HA, e.g. the crystallinity, size and shape of the crystals. This can be achieved by choosing suitable synthesis methods and parameters of HA.

#### 1.6.2.2.5 Biomimetic Ionic Substitutions of HA

It is reported that hydroxyapatite in hard tissues of vertebrates differs from stoichiometric because biological apatite contains different substitute ions in trace amounts. These substitutions include many ions: i.e.  $\text{SiO}_4^{4-}$ ,  $\text{CO}_3^{2-}$ ,  $\text{Zn}^{2+}$ ,  $\text{Mg}^{2+}$ ,  $\text{Na}^+$ ,  $\text{K}^+$ ,  $\text{F}^-$  and  $\text{Cl}^-$  (Chaudhry et al. 2012; Okada & Furuzono 2012; Bang et al. 2014). These substitutions strongly affect physical, chemical and biological characteristics of hydroxyapatite, such as crystallinity, thermal behaviour, solubility, cell activity and osteointegration. (Juhasz & Best, 2012).

#### *Carbonate*

In human bone, among other substitutions, the biggest ionic concentration belongs to carbonate (up to 8 wt%). Carbonate in the lattice structure of HA cause distortions that increase HA solubility. This contributes to enhancement of bioresorption of HA and better connection properties with tissue at the biomaterial surface (Chaudhry et al. 2012).

It has been reported by several researchers that carbonated hydroxyapatite (CHA) has several crucial contributions to bone tissue engineering. Lee et al. (2008) report that the carbonate substitution of HA causes more amorphous structures and weak linkages that increase solubility and bioactivity of stable HA. Therefore, it leads to the release of more calcium and phosphate ions, triggering the generation of young bones. Furthermore, in comparison with HA, CHA has a higher amount of resorption by osteoblasts (Bang et al., 2014). Overall, CHA has had great attention due to the effects of  $\text{CO}_3^{2-}$  anion on various tissues, such as in the case of dental applications.

There are three distinct variations of carbonate substitutions depending on the lattice location of the carbonate in apatite. If carbonate ions substitute with hydroxyl ions, it refers to A-type, whereas it is called B-type when it replaces with phosphate ions. Additionally, an AB type occurs a simultaneous substitution of A and B types in bone structure (Lee et al. 2008; Bang et al. 2014). An illustrative image of A- and B-type  $\text{CO}_3^{2-}$  substituted HA lattice structure is given at Figure 1.4 (Marković et al., 2011). In

human bone, carbonate anions position in the space of  $\text{PO}_4^{3-}$  ions in crystal lattices that are B-type. In addition, Lee et al. (2008) have stated that B type CHA has more coherence with bone cells in terms of surface energy, thus, it promotes adherence of cells and occurrence of collagenous matrixes.

As mentioned in the literature, the type of carbonated HA depends on synthesis methods which are used. In sintered hydroxyapatites, generally A-type substitution is common. On the other hand, B-type carbonate substituted apatite can be obtained in low temperature synthesis methods although the substitution amount might be less than the desired biological concentrations (Vallet-Regí & Gonzalez-Calbet, 2004). It is common that A-type is produced in a solid-phase reaction requiring high temperature or pressure, while B-type is synthesised via wet methods such as precipitation, hydrothermal and sol-gel methods (Lee et al., 2008).

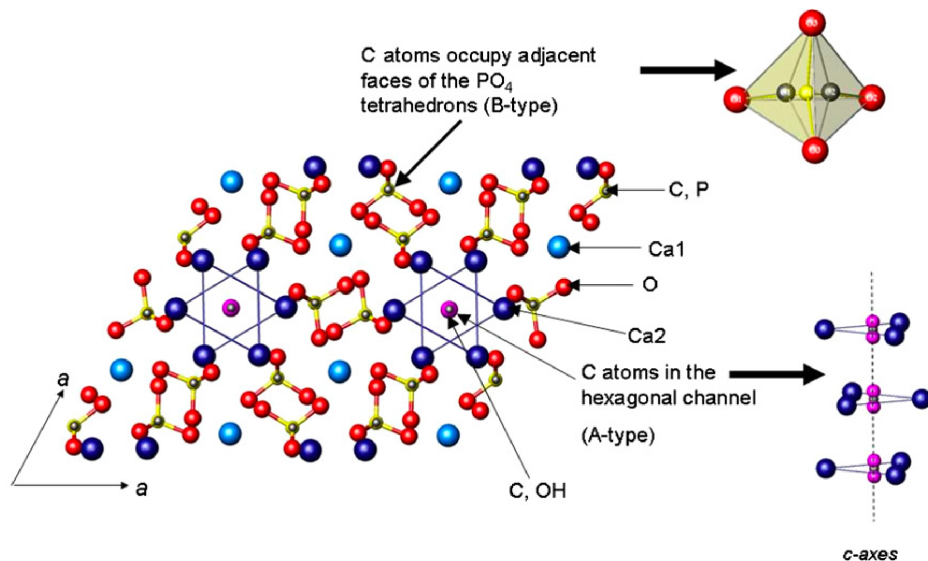


**Figure 1.4** Crystal lattice structure illustration of A-type and B-type CHA (Different coloured atoms represents following elements; O: red, Ca1: light blue, Ca2: dark blue, P: yellow, OH: pink, C: green) used with kind permission © 2011 Biomedical Materials (Marković et al., 2011) by IOP Publishing Group.

### Silicate

Pietak et al. (2007) have reported that silicon has significant effects on growing and improvement of musculoskeletal systems. It has been known that it promotes cartilage production and function of extra cellular matrix. Substitutions of silicon have good impacts on biominerallisation, differentiation and proliferation which result in

improving the osteoclastic resorption process. In addition, through the substitution of  $\text{SiO}_4^{4-}$  and  $\text{PO}_4^{3-}$  ions, silicate can form a more electronegative surface, raising solubility that promotes mineralisation. Furthermore, high amounts of silicon can bind the ECM contents of connective tissues, such as hyaluronic acid, chondroitin sulphate and heparan sulphate. Thus, it can act as a crosslinking agent that controls flexibility and construction of connective tissues, bone and cartilage (Pietak et al., 2007; Schwarz, 1973).

Bang et al., (2014) has compared the properties of CHA and silicon-substituted carbonated hydroxyapatite (Si-CHA). In a structure of Si-CHA,  $\text{CO}_3^{2-}$  and  $\text{SiO}_4^{4-}$  ions competed to replace  $\text{PO}_4^{3-}$  leading to production of the favourable AB type carbonated apatite. Because of co-substitution of silicate and carbonate ions, the particle size of Si-CHA was smaller than CHA, which increased the dissolution of HA. Therefore, Si-CHA provides sustained and increased distribution of  $\text{Ca}^{2+}$  in comparison to CHA.

### ***Magnesium***

Magnesium (Mg) is an element that has an important role in bone health in spite of its low amounts (approximately 0.5-1.5% in bone and teeth). Magnesium has an influence on the metabolism of bone components. It has a role in calcium circulation by its collaborative effect on hormones that adjust calcium consumption. Insufficient magnesium reduces osteoblast and osteoclast function, impairs construction of bone and leads to bone brittleness. Therefore, magnesium substitution in HA in trace amounts is preferred in bone biomaterials. Magnesium cation surges the nucleation of HA particles while preventing crystallisation. The exchange of calcium and magnesium ions in the lattice structure of HA lead to increased deformations enabling enhancement of amorphous structure and bioresorption of HA. Magnesium is also used with other substitutions in HA, especially carbonate groups (Landi et al., 2006; Laurencin et al., 2011; Percival, 1999).

## *Fluoride*

As it has been reported by Jha *et al.*, (1997), fluoride in blood plasma and saliva is a required element for bone health. The approximately 95 % of enamel is comprised from apatite involving trace amount of fluoride (0.04-0.07 wt %). The favourable concentrations of fluoride is able to protect tooth from decays. This might be due to the fact that the substitute form, fluorapatite, is more stable against acids than normal hydroxyapatite.  $F^-$  anion (fluoride ion) substitutes  $OH^-$  ions in an HA lattice irreversibly and increases crystallinity and stability of HA (Jha *et al.*, 1997). Moreover, the biomineralisation process is accelerated by the presence of fluoride accompanied with calcium and phosphate compounds. The amount of fluoride in different bones is variable. For instance, the amount of fluoride in spongy bone is greater than in that of cortical bone. The insufficiency of fluoride can cause developmental issues. On the other hand, overconsumption of fluoride might also cause diseases such as acromegaly and lead to toxicity (Ringe, 2004; Weatherell, 1966). It has been reported that the optimal levels of fluoride (0.8-1.1 M) in HA coatings can induce biocompatibility, cell differentiation with alkaline phosphate activity and osteocalcin level (Wang *et al.*, 2007).

## *Citrate*

Citrate is found in most vertebrates including fish, birds and mammals, and approximately 80 percent of citrate in the whole body is found in bone. Citrate forms 5.5% of the organic matrix of bone. It is found anchored with apatite crystals making them more stable nanocrystals due to citrate's hampering effect on crystal growth and its triggering the nucleation process. There are some studies regarding beneficiary effects of the citrate compound on biocompatibility and on the role of calcium citrate in triggering the early stage of healing in bones. However, it should be noted that citrate locates at the interfaces of apatite layers rather than being a substitution in the apatite lattice due its big size. (Hu *et al.*, 2010; Schneiders *et al.*, 2007; Zhang *et al.*, 2012).

#### 1.6.2.2.6 Hydroxyapatite Synthesis Methods

Due to high consumption rate of HA in various applications, there are efforts to provide continuous production of HA in addition to batch processes. One of the major requirements of these synthesis methods is reproducibility. The HA synthesis techniques can be classified into two fundamental groups: solid-state synthesis and wet synthesis. Solid-state synthesis methods have a number of limitations. Ionic interactions and chemical reaction speeds in dry synthesis methods are very low despite their benefits for industrial batch production. However, the major concern is the fact that dry synthesis methods do not comply with the *in-vivo* hydroxyapatite formation that occurs upon contact with body fluids. On the other hand, wet synthesis methods are performed with a biomimetic reaction performed at low temperatures by using a solvent. Wet synthesis methods are more beneficial and are the preferred techniques in HA synthesis since they allow monitoring of morphological features of particles. The main drawbacks of wet synthesis are the decrease in crystallinity, second phase formation which might occur due to low temperature processes and extraneous trace elements due to solvent involvement (Sadat-Shojai et al., 2013). In the present work, only wet synthesis techniques which are more suitable for biomedical applications were discussed. These include the hydrothermal, chemical precipitation and sol-gel methods.

#### ***Hydrothermal Method***

In the hydrothermal method, the reaction is carried out in hot pressurised water both in stationary and mobile (flowing) states. When the mixture of precursors is heated, the pressure surges automatically. In traditional batch hydrothermal methods, organic surfactants are involved, HA synthesis occurs at the temperatures of 60-150 °C in approximately 24 h. This method has some drawbacks due to; the long reaction time, involving organic chemicals which can have adverse effects for biological applications, and difficulties in monitoring. Therefore, continuous hydrothermal synthesis is attractive owing to its small sized particle yield (less than 500 nm) in addition to its easy control (Zakaria et al. 2013; Chaudhry et al. 2006). Recently, Chaudhry et al. (2006) have improved on one stage of a novel rapid hydrothermal flow synthesis, decreasing reaction time enormously, from 18 h to several seconds. This reaction occurred at 24

MPa and below 400 °C. This method involved mixing of pumped reactant solutions in a connected ‘Tee’ junction followed by flow of the mixture into overheated water in a flow-meter reactor, leading to a fast aging process. After cooling and filtration at the experimental setup, HA precipitates were obtained. It has been reported that pure, crystalline nano-sized HA samples with ionic substitutions, such as, silicate and carbonate were successfully synthesised with this continuous hydrothermal method (Chaudhry et al., 2013).

### ***Chemical Precipitation Method***

In this method, either aqueous solutions of precursors are mixed or a hydrolysis process of calcium phosphate occurs (Zakaria et al. 2013). Precipitation includes nucleation which consists of casually dispersed particles in the solution; generating clusters, followed by crystal growth. The nucleation rate strongly depends on the supersaturation, which means dissolution of more solids than required for the balanced state of a solution. As the supersaturation increases, nucleation speed surges, which leads to formation of thin particles both in the solution and final HA (Norton et al., 2006). After precipitation of HA, byproducts are separated from the liquid phase. Chemical precipitation methods have several drawbacks because of the heterogeneous distribution of crystals with minor crystallinity and a low calcium ratio. However, having been highly affected by the temperature and the speed of the reaction, wet chemical methods can give a small sized pure product with high yield at low temperatures. (Zakaria et al. (2013).

### ***Sol-gel Method***

The sol-gel method has been extensively reported in literature and it appears to be the method most suited to the requirements of this project. This method offers several advantages over other methods requiring high temperature or pressure, such as in solid state reactions (Boyer et al., 1997), as well as in supercritical fluid and hydrothermal methods (Norton et al., 2006). The first advantages of the sol-gel method is the fact that it mixes reagents at the molecular level, leading to homogeneous particles that provide good control over the size and shape of resulting particles. In the sol-gel process, a

suspension of 1 to 100 nm sized particles in a solvent, referred to ‘sol’, transform into a porous and solid gel. Sol-gel synthesis can be performed in the following main ways; (a). gelation of a colloidal solution, (b). hydrolysis and polycondensation reactions when alkoxides or nitrates are involved, followed by either hypercritical drying or (c). drying at room temperature after aging (Norton et al., 2006).

Sol-gel synthesis results in homogeneous and pure products at relatively low temperatures and pressures; and at lower calcination and sintering temperatures (under 1000 °C) (Kuriakose et al. 2004; Zakaria et al. 2013; Sadat-Shojaei et al. 2013). In addition, it is possible to obtain stoichiometric pure nano-sized crystalline structures by utilizing ethanol instead of alkaline oxides at alkaline pH, also at respectively low temperatures (85 °C) (Kuriakose et al., 2004). Furthermore, Fathi et al. (2008) has reported that sol gel synthesised HA has a relatively higher bioresorption ratio resembling that of biological apatite. One drawback in the sol-gel method is that it is time intensive requiring a long time for obtaining the product.

### 1.6.2.3 Polymers

Biodegradable polymers can be divided into two groups: natural and synthetic polymers. In this thesis, only natural polymers and their properties will be addressed. Natural polymers consist of proteins; e.g. collagen, silk, fibrin gels and soy, polysaccharides; such as chitin and chitosan, alginate, hyaluronic acid and starch as well as biofibres, including lignocellulose. Having super arranged network structures, natural polymers sometimes include ligands which provide an extracellular structure able to connect cell receptors. Natural polymers can also lead to the extension of cells. They can also simultaneously induce an immunologic response (Swetha et al., 2010).

#### 1.6.2.3.1 Collagen

Being the major connective tissue protein in animals, collagen comprises one quarter of all proteins in vertebrate bodies (Stenzel et al., 1974). Collagen is utilised in tissue engineering applications due to excellent biocompatibility, biodegradation, and good inflammatory responses. Collagen has substantial contributions to osteogenic activity

and bone formation. Furthermore, it has a strong binding capacity for proteoglycans and glycosaminoglycans, which increases mechanical characteristics of newly formed tissues (Jazayeri et al., 2016).

#### 1.6.2.3.2 Gelatine

Gelatine consist of peptides and proteins, and it is obtained from collagen after its semi hydrolysis. The water miscible gelatine can be obtained via its modification with methacrylic anhydride leading to brittle hydrogel due to strong hydrogen bonds in its structure. Therefore, some solvents are used to modify it in terms of elasticity. Gelatine modified with methacrylate group (GelMA) forming UV crosslinked hydrogel is utilized for functional vascular network formation, and as a drug delivery tool for angiogenic and vascular growth factors. The protein binding capacity of gelatine results from its capability to form polycomplexes with proteins due to its charged nature that can be either positive or negative (Chen et al., 2012; Tabata & Ikada, 1998).

#### 1.6.2.3.3 Cellulose

Nature is the richest source of cellulose and can be produced by plants and bacteria. Cellulose includes inter and intra hydrogen linkages that give it strength, by forming insoluble fibrous structures (Mischnick & Momcilovic, 2010). It has a wide range of applications as a biomaterial including the healing of periodontal injury, in monitored tissue reformation and in the use of hydrogels for bone regenerations (Fricain et al., 2002; Jazayeri et al., 2016). A derivative of cellulose, carboxymethyl cellulose, has combined with chitosan to form injectable biocompatible thermosensitive hydrogels and has been reported useful in the application of cartilage generation (Chen & Fan, 2008).

#### 1.6.2.3.4 Alginate

Alginate is a common natural anionic polysaccharide which is acquired from algae and terra-bacteria. Being consumed as food, alginate has many nutrients e.g. vitamins, iodine, sterols and salts. Chemically, alginate is a linear copolymer consisting of

mannuronic and guluronic acid linkages. Due to its gelation, swelling, thickening and stabilising capacities, alginate is utilised in a wide range of applications, e.g. paper, textile and packaging. In addition, alginates have potential utility in biomedical applications including drug and cell delivery, dentistry and wound healing. Alginates have ability to form gels with mild sol-gel reaction with the additive of multivalent cations, especially calcium, without temperature effect. In wound recovery, alginate provides a moisturized surrounding and mitigate infections due to bacteria.

Alginate gels allow the delivery of various active agents (e.g. medicine, proteins and cells) into the body in a sustainable way by ingestion or injection. However, alginate gels are exposed to dissolution due to the diffusion of calcium ions into the physiological environment which reduces the availability of gels in the body for a time. Also excess calcium ions may lead to haemostasis, and due to the weak adhesion property of alginate, its chemical modification with peptides may be required in some regenerative medical applications (Lee & Mooney, 2012).

#### 1.6.2.3.5 Silk

Taken from silk-worm specie, *Bombyx mori*, silk has better mechanical strength and toughness than most polymers due to involvement of crystallized structures ( $\beta$  sheets). The tensile strength and elastic modulus of a single fibroin are 610-690 MPa, and 15-17 GPa, respectively. Moreover, silk has great biocompatibility, tuneable degradability, minor response of inflammation and immunogenicity. Silk has been clinically used as suture biomaterial (Rockwood et al., 2011). 3D printed silk fibroin and hydroxyapatite composite scaffolds for bone fracture repair showed enhanced cell proliferation and differentiation with increasing silk ratio in silk-HA composites (Huang et al., 2019).

#### 1.6.2.3.6 Chitin and Chitosan

The second most frequent polymer in the planet is chitin. Chitosan has the chemical formula of  $(C_6H_{11}O_4N)_n$  and it is obtained from chitin as the end product of deacetylation reaction (Nikpour et al., 2011). The main source of chitin is crustaceans shells including shrimp, crab, lobster, and oyster, many other sources are also available,

such as insects, seaweeds, fungi and yeasts (Synowiecki & Al-Khateeb 2003; Prabaharan 2012, p.13). CS is obtained after several chemical and heat treatments of chitin including; deproteinisation, demineralisation, decolouration and deacetylation (Jayakumar et al. 2012, p.31). Being biodegradable and biocompatible polysaccharide, chitosan have long linear chains including irregular arrangements of  $\beta$  (1-4)-linked-D-glucosamine (deacetylated) and N-acetyl-D-glucosamine (acetylated) units (Kim 2014, p.3 ) (Figure 1.5).

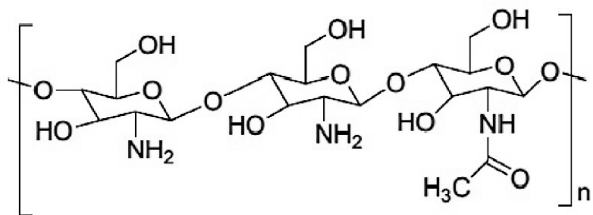


**Figure 1. 5** Molecular structure of chitosan taken from the study by (Shahzad et al., 2015)

By the elimination of acetyl groups (CH<sub>3</sub>-CO), chitosan can be dissolved in diluted acids, and amine (NH) units become free, leading to its cationic structure (Kim, 2014, p. 3).

The insufficient solubility properties of CS leads to drawbacks for biomedical applications, such as, drug delivery; leading quick water adsorption and fast drug delivery (Jayakumar et al. 2012, p.32). Therefore, in recent years, researches have been trying to overcome this by improving solubility by chemically modifying chitin and producing chitosan derivatives.

### ***Modifications of Chitosan***

Through the modification process it is aimed to improve chitosan features biochemically, physiochemically and biologically, especially solubility (Yar et al., 2017). Amine and hydroxyl groups in the structure of chitosan enables its modifications chemically. Chitosan modifications, especially organic solvent soluble ones, can be used with other organic soluble synthetic polymers, making possible controlled degradation time for different applications (Shahzad et al., 2016).

These modified chitin derivatives have a wide range of applications owing to their unique properties such as polyelectrolyte and reactive features, good adsorption ability, biodegradability, gel forming capacity, antibacterial properties and tumour resistance (Synowiecki & Al-Khateeb, 2003). To give some examples, they are widely used in bone regeneration (Zhang et al., 2008), drug delivery and tissue engineering (Liu et al., 2014), wound dressing (Shahzad et al., 2015), anti-tumor materials (Zheng et al., 2015) and dental applications, such as anti-inflammatory root canal dressing materials for periapical lesions (Jayakumar et al. 2012, p.37).

There are a variety of synthetic methods used to obtain different chitosan derivatives. Some examples are: quaternization, deoxycholic acid derivation, galactosylation, polyethylenimine (PEI) grafting and thiolation (Jayakumar et al. 2012, p.43). One of these modification methods obtaining chitosan in the form of carboxylate salts i.e. formate, acetate, lactate, malate, citrate, glyoxylate, pyruvate, glycolate, poly (ethylene glycol) and ascorbate due to the high positive charge of CS (Kim, 2014, p. 7). Thiolated chitosan, in particular, is a type of modification promoting the properties of chitosan in terms of muco-adhesion and drug release, as well as *in-situ* gelation properties owing to the generation of disulphide linkages (Jayakumar et al. 2012, p.45-46).

One method in chitosan modification is the Mannich reaction enabling the modification of different amino groups on chitosan. The Mannich reaction is advantageous in terms of affordability and it leads to occurrence of iminium ions providing substantial reactivity against different nucleophiles. Thus, since chitosan includes amino sides, it is possible to modify them via the Mannich reaction (Yar et al. (2017). In addition, it has also been reported that Mannich base like dibasic chitosan derivatives were used for heparin binding hydrogels promoting angiogenic activity (Yar, Gigliobianco, et al., 2016).

Recently, Yar et al. (2017) has reported a method for chemical chitosan modification with a Mannich reaction. They synthesised chitosan derivatives by using 2-chloroaniline with formaldehyde. A chitosan and aniline reaction resulted in a novel chemical group ( $-\text{NH}-\text{CH}_2-\text{NH}-$ ) approved by FTIR analysis. They synthesised hydrogel films composed of chitosan and polyvinyl alcohol (PVA) both with and

without heparin loading for wound healing applications by means of improving vascularisation. Heparin loaded hydrogel films have shown greater angiogenic efficiency compared to specimens without heparin. Synthesized hydrogels also ensured good cell attachments.

### ***The Effects of Molecular Weight and Degree of Deacetylation of Chitosan***

Chitosan has diverse polymorphs with distinct molecular weight (Mw) and degree of deacetylation (DDA). Because of treatments during deacetylation processes, mean Mw and DDA of chitosan are measured. The DDA express the ration of primary amines as a percent. Chitosan with the Mw from 10 to 1000 kDa and 66-95 % DDA are available commercially (Jayakumar et al. 2012, p.32).

In comparison with lower Mw (500-800 kDa), high Mw chitosan (~1400 kDa) has more mucoadhesive features due to its more viscous structure. In addition, higher DDA, the proportion of chitosan in solutions, lower temperature and lower pH results in more viscosity (Jayakumar et al. 2012, p.31-32). Due to the different properties of diverse Mw and DDA, there are various papers in the literature dealing with their effects (Jelvehgari et al. 2010; Jayakumar et al. 2012; Gupta and Jabrail, 2008).

It has been discussed by Gupta and Jabrail, (2008) that drug release characteristic of chitosan is affected by its rheological features. Rheological features of chitosan are altered by: Mw, DDA, arrangements of acetyl groups in chitosan, and pH. In addition, the degree of crosslinking is affected by DDA, but not by Mw. In this respect, monitoring the DDA of chitosan is important since high crosslinking provides a hydrophobic network structure and low swelling. In addition, DDA has an impact on the biodegradation, immunological, physical and chemical features of chitosan.

It has been reported that in drug delivery applications, optimum loading and sustainable release properties have been achieved via high Mw and high DDA, whereas low-Mw and low-DDA microspheres had burst release (Gupta and Jabrail, 2008). In addition, Jelvehgari et al. (2010) has reported, regarding drug delivery, that high Mw of chitosan

provided higher zeta potential providing electrostatically stable, good dispersed nanoparticles in colloids.

It has been reported that antibacterial activity of chitosan decreases in neutral pH at molecular weights bigger than 29.2 kDa, while it increases along with Mw in acidic pH. Chang et al. (2015) explains that the pH effects depend on changes in water solubility and the zeta potential properties of chitosan. It was also reported that immune response properties of chitosan are more immediate with low Mw CS (12 weeks), while it took 24 weeks for high Mw chitosan (Jayakumar et al. 2012, p.127). In terms of gelation properties, Chenite et al. (2000) has states that high DDA decreases gelation temperature and that the effect of Mw in gelation was insignificant.

In the light of reported literature to date, DDA and Mw are two important parameters affecting polymer properties in terms of drug release, mucoadhesiveness, viscosity, gelation and antibacterial properties (Jayakumar et al. 2012, p.31-32; Jelvehgari et al. 2010; Chang et al. 2015). Therefore, it is indicated to select a chitosan with DDA and Mw levels appropriate to the application. In this respect, chitosan with high DDA may be useful, due to gelation, for drug delivery applications. In contrast to low Mw chitosan, high Mw provides supreme drug delivery but shows slow immune response and lower antibacterial properties. Therefore, in this project, the selection of Medium Mw with high DDA is indicated in order to balance thermosensitive gelation features and biological response for drug delivery and bone regeneration applications.

## 1.7 Advanced Regenerative Medicine Techniques

### 1.7.1 Drug Delivery Systems

As expressed, by Jain (2008, p.1.), a drug delivery system is a controlled mechanism or tool for delivery of bioactive agents into a certain region of the body for treatment. Biomaterial carriers enable the release of diverse cells and growth factors to stimulate bone generation. In terms of cell therapies, adult stem cells such as mesenchymal stem cells (MSCs), and embryonic stem cells (ES) have been utilised. Growth factors have a capability of affecting cell activities by conveying signals by binding to cell receptors.

Growth factors that are employed in bone regeneration include: osteogenic, angiogenic, inflammatory and systemic factors. These growth factors can be used singly or in combination (Vo et al., 2012).

Hydrogels are quite attractive tools for the encapsulation of therapeutic agents, and their sustainable delivery can be monitored by their crosslink mechanisms. Stimuli responsive hydrogels such as pH responsive hydrogels, have gelation above or below a critical pH and can facilitate site specific delivery through a certain route. Drug release through pH responsive hydrogel systems can occur via diffusion, swelling and monitoring mechanisms chemically. The diffusion based drug delivery model is associated with the Fick's diffusion law. The diffusion coefficient of hydrogels depends on the porosity and pore size of hydrogels. Drug delivery is monitored by swelling once drug release is above the swelling rate. In this case the drug is desorbed upon absorption of water (Lin & Metters, 2006; Rizwan et al., 2017).

The amount of hydrophobic parts resisting the absorption leads to shape and volume change that determines the speed of drug delivery. Furthermore, delivery is associated with the bonding strength of the hydrogel due to crosslinking and composition. The forces by media lead to flexion of the polymer bonds that cause swelling and while drug release is taking place. The large molecules entrapped into hydrogels, whose delivery is not possible with diffusion mechanisms, are delivered by the degradation of polymers via hydrolytic or enzymatic reactions involving the breakdown of polymer backbone (Lin & Metters, 2006; Rizwan et al., 2017).

### 1.7.2 Growth Factors

Although growth factors have been employed in animal studies, their applications in humans are restricted by cost and reliability concerns. The main problem in drug delivery systems is the rapid delivery of growth factors; thus it is necessary to develop effective delivery systems. Delivery of growth factors from an optimal carrier, occurs in a programmed time and dosage, into a desired location and the carrier contributing to ECM formation and vascularisation. It was reported that, ECM mimicking delivery systems have improved monitoring of growth factor signalling. There are some growth

factors, such as, BMP-2, VEGF-A and platelet-derived growth factors PDGF-BB, are able to bind heparan sulfate proteoglycans within the ECM, thus they are termed ‘heparin-binding growth factors’. Delivery of growth factors bound to ECM can be controlled by the strength of these bonds and by protease activity (Martino et al., 2015).

Several growth factor delivery approaches in a natural ECM mimicking environment, are summarised and illustrated in Figure 1.6. Heparin and heparin sulfate like components can bond covalently or be co-delivered into matrix, to control growth factor release (Figure 1.6.A). Engineering the signalling microenvironment method involve forming molecular complexes between ECM components and growth factor receptors (Figure 1.6.B). In addition, the engineering growth factors method, provides the attraction between growth factors and a biomaterial matrix, by modifying growth factors (Figure 1.6-C). Finally, Figure 1.6.D shows engineered growth factors enable connection to ECM binding biomaterials, such as, collagen and fibrin (Martino et al., 2015).

It should be noted that caution is required in using external growth factors alone or within a scaffold, since they might induce severe side effects. For instance, BMP usage in clinic was reported to cause toxicity, malformation of bones, immune reactions and carcinogenesis, leading to recent restrictions in its clinical applications (Carragee et al., 2011; Hustedt & Blizzard, 2014).

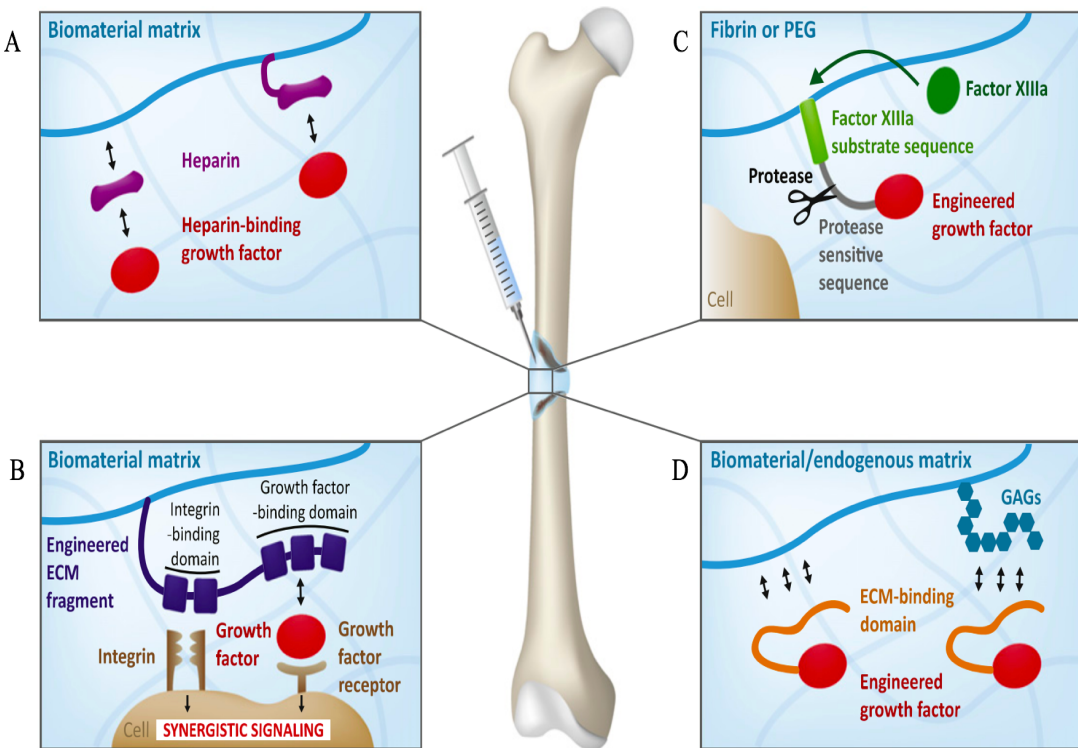


**Figure 1.6** Growth factor release mechanisms mimicking the ECM-growth factors interactions. **A.** Increasing the affinity of biomaterial matrix for growth factors **B.** Engineering the signalling microenvironment of growth factors **C.** Engineering growth factors to interact with biomaterial matrices **D.** Engineering growth factors to bind biomaterial/endogenous matrices. (This figure was reused after obtaining permission for the study by Martino *et al.*, (2015) from Elsevier publishing group).

### 1.7.3 Angiogenesis, Growth Factors and Heparin

During vasculogenesis endothelial cells known as angioblasts differentiate into mesoderm and result in generation of vascular plexus which gives rise to the formation of primary blood vessels. The generation of new blood vessels through sprouting or splitting from primitive vessels via endothelial cell activities, is referred to angiogenesis (Risau, 1997). As it has been stated that angiogenesis is necessary not only for bone formation and but also during healing, this shows the importance in osteogenesis (Forrest, 2005).

When tissue engineered biomaterials are implanted into large-scaled bone defects, the tissue healing, strongly rely on keeping cells alive by swift branching of present blood vessels occupying the defect site. In case of deficient blood supply, cells cannot survive

since their metabolic activities are impaired because of insufficient nourishment, oxygen, and insufficient transfer of metabolic by-products. The sufficiently grown microvascular structure also maintains the regulation of the various cells that participate in the remodelling and reconstruction of tissue, including hematopoietic stem cells, osteoprogenitor and immune cells (Grosso et al., 2017).

Vascular endothelial growth factor (VEGF), which is an endothelial cell related mitogen that takes a critical role in regulating angiogenesis, which is associated with its ability to provide transfer and proliferation of endothelial and progenitor cells. The VEGF is expressed by the hypertrophic chondrocyte region in the epiphyseal growth region, and it has role on modulating remodelling of cartilage. In addition, VEGF has a role in generation of endochondral bone by monitoring apoptosis of chondrocytes and employing chondroclast activates leading the resorption of cartilage tissue that is then replaced by bone. The occupation of blood vessels through the metaphysis bone region concurrently occur with; mineralisation of ECM, death of chondrocytes, resorption of ECM and generation of bone. In addition, VEGF is generated by osteoblasts and regulates the osteogenic growth factors. As reported, the absence of VEGF that postpones bone formation from the callus, shows the impact of VEGF on osteogenesis as well. An impairment of a natural blood vessel network in the epiphyseal growth region, due to inactivation of VEGF, has been reported (Gerber et al., 1999; Raftery et al., 2017). Therefore, VEGF has been investigated to promote angiogenesis by combining it with biomaterials.

Along with VEGF, a number of growth factors have been investigated as to stimulating angiogenesis, comprising basic fibroblast growth factor (bFGF), and transforming growth factor beta (TGF $\beta$ ) (Fujita et al., 2004; Oliviero et al., 2012). However, growth factor delivery involves many challenges, such as their instability due to their high solubility that reduce their performance and activation time. This becomes more challenging upon fractures in tough conditions. To combat their instability, the approach to utilise a high level of growth factors also leads to toxic effects and malformation of bones. In addition, regional inflammatory reactions, adverse effects on nerves and risk of malignant tissue formations have been reported (Carragee et al., 2011; Raftery et al., 2017).

Due to the instability issues of growth factors, they are usually harnessed by their immobilisation in a scaffold matrix, thus providing for their controlled delivery. One approach is to bind these growth factors with heparin and heparan sulphate proteoglycans (HPSGs) that, due to their highly anionic nature, have great binding capacity with proteins involving growth factors (Tae et al. 2007). Heparin and HPSGs are proficient at binding pro-angiogenic receptors with the majority of angiogenic growth factors, comprising VEGF, bFGF, and TGF $\beta$  (Chiodelli et al., 2015; Oliviero et al., 2012).

Heparin (Hep), consisting of glucosamines and residuals of uronic acid, is an anionic and sulphated polysaccharide. Heparin, is important because of its high anticoagulant capacity due to its anti-thrombin III binding property via a penta-saccharide and array. Oliviero et al. (2012) has pointed out that this physical binding efficiency of heparin can monitor the cells thanks to its molecular orientation, which results in angiogenesis. The binding heparin with pro-angiogenic factors provides proliferation, generation of protease and migration of endothelial cells, as well as leading cells in blood vessel formation (Oliviero et al., 2012; Yar et al., 2017).

As Chiodelli et al. (2015) reported that heparin or HPSG has a regulatory role in angiogenesis. This is determined by their linkages, especially sulfate bonds, with angiogenic growth factors, proangiogenic recipients, antiangiogenic agents and angiogenic effectors. There is a huge number of molecules that monitor angiogenic activity because of their linkages with heparin and HSPGs. Angiogenic or antiangiogenic effects are based on the molecular properties of protein and the interactions of heparin and HSPGs with cells or ECM.

In a recent research (Shahzadi et al., 2016), heparin has incorporated in composite hydrogels in order to evaluate its potential to induce angiogenesis. It has been investigated via chick Chorioallantoic Membrane (CAM) assay to evaluate the potential attachment of physiologically available angiogenic growth factors to pro-angiogenic receptors by using heparin bonded chemically crosslinked chitosan poly-vinyl alcohol (PVA) hydrogels. Triethyl-orthoformate (TEOF) crosslinked and heparin bonded hydrogels led to more blood vessel generation when compared with heparin-free control

samples (Shahzadi et al., 2016). In addition, direct mixing of heparin in chitosan-PVA-poycaprolactone (PCL) hydrogels in the absence of any growth factors has been investigated for angiogenesis on chick embryo's CAM tissues. It was found that heparin bonded chitosan-PVA-PCL hydrogels led to significantly more angiogenesis than the sole collagen control gels (Yar, Gigliobianco, et al., 2016).

Therefore, the functionalisation of scaffolds or hydrogels with heparin for its potential physiological binding activity can provide advantages by avoiding utilisation of angiogenic growth factors and their non-foreseeable adverse effects, such as instability and the risk of malformed or carcinogenic tissue formation. Thus, in this study, heparin functionalised injectable hydrogel compositions that are based on hydroxyapatite dispersed chitosan matrixed thermosensitive hydrogels are investigated for angiogenesis by utilization of the *in-vivo* CAM assay model.

## 1.8 Injectable Biomaterials for Minimal Invasive Surgery

There are several challenges in conventional cell-scaffolds techniques requiring invasive surgery that may lead to casualty of bones, devastation of vicinal tissues and traumas. There are also difficulties in their production and in cell seeding to inner cavities. Thus, *in-situ* forming gels have attracted attention since these can be applied to the body via minimally invasive endoscopic and transdermal surgical methods (Amini & Nair, 2012; He et al., 2013).

### 1.8.1 Hydrogels

Hydrogels are polymer based crosslinked porous structures which resemble native ECM in terms of their high water content, due to their water absorption and swelling capacity, and their elasticity (Amini & Nair, 2012; Klouda, 2015). Due to the constructional analogy between body constituents and hydrogels, they are quite beneficial for tissue engineering and drug delivery applications (Lee & Mooney, 2001).

### 1.8.1.1 Classification of Hydrogels

A number of elements can that be considered to categorize hydrogels, depend on crosslinking mechanism, biodegradability, synthesis methods, physical features, ionic charge etc. In the literature, diverse categorisations of hydrogels are present (Rizwan et al., 2017; Ullah et al., 2015). In terms of crosslinking mechanisms, hydrogels are divided into two groups: chemically and physically crosslinked hydrogels. The physical hydrogels occur due to the crosslinking based physical interactions, such as hydrogen bonding, crystallisation, and hydrophobic interactions. On the other hand, the chemical crosslinked hydrogel formation occurs via chemical polymerisation reactions leading to covalent bonds between molecules. The physical hydrogels are reversible while chemical hydrogels have irreversible, persistent bonds (Ullah et al., 2015).

Chemical crosslinking involves the chemical reactions of reactive functional groups of materials. The small molecules as crosslinker, or a different polymer reacting with a base polymer, can provide crosslinked-polymer network-structures. Although the chemical crosslinking can provide mechanically strengthened hydrogel structures, biocompatibility issues arise from crosslinker leftovers that require strict decontamination of acquired hydrogels. Furthermore, the excess crosslinker linkages can limit drug delivery processes. For instance, chitosan crosslinking with glutaraldehyde can cause toxicity, the utilisation of genipin was found more biocompatible in comparison to glutaraldehyde. However, undesired drug-genipin interactions might occur (Bhattarai et al., 2010; Chen et al., 2004).

To avoid using crosslinkers, different polymers can be crosslinked by increasing their reactivity via modification reactions such as Shift base and Michael addition reactions. However, these methods require a very tedious processing and purification processes, and the possible toxicity of crosslinked final products should be also considered. (Bhattarai et al., 2010). Although the material toxicity in chemically crosslinked hydrogels is a big concern, there are *in-situ* formed injectable hydrogel types that can reduce the toxicity. Examples are photo-crosslinked and enzymatically crosslinked hydrogels since they form in the mild body environment. In this thesis, two types of *in-situ* formed, chemically crosslinked hydrogels will be identified. Being the subject of

this thesis, these physically formed injectable pH and/or thermosensitive hydrogels will be discussed in more detail in the following sections.

#### 1.8.1.1.1 Stimuli Responsive Hydrogels

Hydrogels having responses in the presence of a certain surrounding stimuli, known as smart hydrogels, have the ability to alter their structural integrity, strength, and swelling capacity in association with a particular stimulus (Ullah et al., 2015). According to stimuli types, hydrogels are divided into three main groups by Rizwan *et al.*, (2017): physical (light, temperature, electrical and magnetic fields etc.), chemical (e.g. pH, ionic elements, chemical agents) and biological stimuli (such as, enzymes, antigen, and DNA).

#### 1.8.2 *In-situ* Formed Injectable Hydrogels

Prepared liquid hydrogel formulations are injected into tissue defects, and form gel *in-situ* by filling and moulding injured sites with complex architecture. *In-situ* formation of injectable hydrogels via a stimuli make them superior in terms of their applicability without, or by minimal surgical intervention (Amini & Nair, 2012). Furthermore, since their gelation occurs in moderate conditions in the body, they promote encapsulation of cells, proteins and peptides. In addition, hydrogels may be assigned as an artificial extra cellular matrix in cartilage. They promote reconstruction of durable and complicated bone systems as a delivery vehicle for cells and growth factors. Hydrogels are quite transitable, particularly for filling complex craniofacial bone defects and enabling repair via sustainable delivery of specifically targeted regenerative agents, such as growth factors and cells (He et al., 2013).

Among *in-situ* formed injectable hydrogels, chemically crosslinked UV or enzyme stimulated hydrogels and physically crosslinked pH and thermosensitive hydrogels are discussed in the following sections.

#### 1.8.2.1.1 Light Sensitive Hydrogels

Photon reactive chemical groups can be used to modify materials that provide crosslinking upon exposure to UV light. This is very practical and cost available chemical crosslinking mechanism. UV crosslinked methacrylated gelatine (GelMA) with methacrylated hyaluronic acid (HAMA) hydrogels for wound healing (Eke et al., 2017) along with photo-crosslinked GelMA and poly(ethylene glycol)diacrylate (PEGDA) for bone healing applications (Wang et al., 2018) have been reported. The chitosan-pluronic hydrogels were photo-crosslinked at 37 °C by functionalisation of precursors with photo-responsive acrylate groups, and were integrated with plasmid DNA for local gene transfer investigation (Lee et al., 2009). Although functional, the main drawback of photo-crosslinking is that the extended time of exposure to irradiation may threaten the living adjacent tissues and organisms (Bhattarai et al., 2010).

#### 1.8.2.1.2 Enzyme-crosslinked Hydrogels

Having an *in-situ* crosslinking mechanism, the enzyme initiated crosslinked hydrogels occur at respectively mild conditions out of chemically crosslinked hydrogels. Different enzymes including tyrosinase, transferase, lysyl oxidase and horseradish peroxidase can be utilized as catalysts for crosslinking. Enzymes can have a role in increasing the mechanical strength of the polymers as well as in integration. However the reported instability and short activation time of enzymes lead some limitations in application of enzymatically produced hydrogels (Moreira Teixeira et al., 2012).

The crosslinking of gelatine and chitosan by tyrosinase enzyme that oxidize tyrosine in protein and form o-quinone reactive groups were explored for increasing gel mechanical strength. This was inspired by the sclerotization process (shell hardening) in insects including the polymer polysaccharide entanglement mechanism (Chen et al., 2002). In another study, elastic and stable dextran and tyramine hydrogels were obtained by using horseradish peroxidase enzyme with hydrogen peroxide. The crosslinked hydrogels were provided by binding them with either the urethane or diglycolic group involving esters. The second group, anchored by ester group, has showed quick degradation, 4-10 days, whereas the urethane group hydrogels led to

much more stable hydrogels losing just nearly one quarter of their weight in 5 months (Jin et al., 2007).

#### 1.8.2.1.3 pH Sensitive Hydrogels

pH sensitivity is a factor providing the acquisition of reversible sol-gel hydrogels. The pH dependent ionic interactions leading to proton loss or gain, provides phase alterations in polymers (Liu et al., 2016). As reported by Ullah *et al.*, (2015) in pH responsive hydrogels, swelling occurs due to the abrupt alteration of the electrostatic net charge at the ionised pendant sites that leads to electrostatic repulsion and associated sudden volume change, due to the osmotic swelling potency.

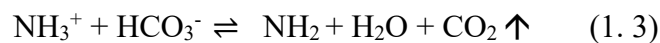
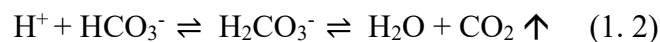
pH sensitive hydrogels having anionic pendent groups e.g. carboxylic and sulphated groups are termed anionic hydrogels whereas cationic pendent groups (for instance, amine) involved hydrogels are designated as cationic hydrogels. Anionic hydrogels (such as carboxymethyl chitosan) swell when pH is raised above  $pK_a$  and are feasible for drug delivery at high pH levels (e.g. intestine possess pH 7.4). On the other hand, cationic hydrogels (such as chitosan) swell in low pH under the  $pK_b$  once ionisation occurs, and are beneficial for drug delivery in acidic pH, such as in the stomach (Rizwan et al., 2017; Ullah et al., 2015).

The delivery of pH sensitive formulations is affected by the conditions of the targeted delivery route in the body, such as acidity and presence of enzyme activities. The gastrointestinal route for drug delivery is the most common way involving a wide pH range in different regions: in saliva between 5 and 6; stomach: 1-3; small intestine 6.6.-7.5; and colon: 6.4-7 (Bhattarai et al., 2010).

Being the subject of this study, chitosan-based solutions require pH neutralisation in order to be used in the body since chitosan is soluble in only acid media. Chitosan based hydrogels neutralised by weak base  $NaHCO_3$  or  $Na_2CO_3$  is based on the reactions of either bicarbonate or carbonate anion with hydrogen cation, leading to the release of carbon dioxide that causes the increase in pH leading to gelation (Liu et al., 2016).

In this study, sodium bicarbonate ( $\text{NaHCO}_3$ ) salt which is a weak base has been used as a neutralising agent due to its cost effectiveness compared to other salts, e.g. betaglycerol phosphate. It also enables slower neutralisation in comparison to strong bases, such as  $\text{NaOH}$ . Having a gradual ionic reaction between chitosan and  $\text{NaHCO}_3$  ensures a slow release of carbon dioxide during the reaction (Equation 1.1-1.3) (Liu et al., 2011). Thus, performing neutralisation reactions in sealed flasks at low temperature also protects the solutions from sudden gelation resulting in heterogeneity. Therefore, in this project, experiments were performed by using a dropping funnel fitted flask placed in an ice bath.

Protonation and deprotonation of amine groups in chitosan with the action of  $\text{HCO}_3^-$  in  $\text{NaHCO}_3$  and  $\text{H}^+$  ions in the acidic environment provide an ionic crosslinking of chitosan with neutral  $\text{NH}_2$  linkages. The reaction product, carbon dioxide, is non-toxic and can easily be metabolically released from the body (Liu et al., 2011)



Therefore, keeping solutions closed at all time and storing them in low temperatures extends solution stability to facilitate injection. Upon injection into a body, hydrogels are constituted *in-situ*, in consideration of the two driving forces, pH and temperature (due to hydrophobic interactions).

#### 1.8.2.1.4 Thermosensitive (Sol-gel) Hydrogels

Thermo-responsive hydrogels have a unique *in-situ* phase transition in the body that makes them quite a useful tool for injectable pharmaceuticals and therapeutic agents by *in-situ* encapsulation (due to quick gelation). Since they are natural, and no-crosslinker is used for their formation, this makes them biocompatible and very beneficial for tissue engineering and drug delivery applications. Their mechanical properties can be strengthened by producing composite materials such as with inorganic compounds or

making them polycomplex by adding oppositely charged natural compounds such as heparin. Accordingly, heparin was involved in the chitosan-based composite hydrogels produced in this project. Also polyol additives were utilised to contributed to mechanical enhancement by avoiding any other toxic crosslinker or synthetic material.

Thermosensitive polymer hydrogels undergo a phase alteration owing to the presence of similar amounts of hydrophobic and hydrophilic groups in their networks (Radivojša Matanović et al., 2015). As Klouda (2015) has reported that these thermosensitive hydrogels can be produced by sol gel process via either heating or cooling methods. Mostly, thermally responsive hydrogels are soluble below a certain temperature, (known as lower critical solution temperature (LCST)) whereas they form insoluble gels above this temperature in a body. On the other hand, some others can become gels via cooling under the upper critical solution temperature (UCST) (Klouda, 2015; Radivojša Matanović et al., 2015).

In drug delivery applications, a drug is loaded into thermosensitive polymer formulations at room temperature and administrated to the body via injection. Upon injection, hydrogel shrinks and forms a protective layer, and the dimension of pores decreases, providing for encapsulation of drugs and their sustainable delivery. One very common thermosensitive polymer employed in biomedical application is Poly(N-isopropylacrylamide) (PNIPAAm) which has an LCST at the vicinity of physiological temperature (Kondiah et al., 2016). Recently, thermosensitive elastic PNIPAAm hydrogels were integrated with cardiac stem cells for heart regeneration in static and heart mimic dynamic stretching culture conditions to stimulate cardiac differentiation (Li et al., 2016). The hyaluronic acid/PNIPAAm injectable porous hydrogels synthesised by the thermo-radical copolymerisation technique, formed hydrogels at nearly 30 °C. Adipose derived stem cell encapsulated hydrogels were found to be non-cytotoxic and were found beneficial for drug delivery and tissue engineering applications (Tan et al., 2009).

Pluronic® and Tetronic® thermosensitive hydrogels which are amphiphilic copolymers that generate micelles in water, were approved by the FDA and EP and are commercially available (Fernandez-Tarrio et al., 2008; Ullah et al., 2015). Pluronics are

polyethylene oxide based triblock copolymers and are known for their bioadhesion, stability and thermosensitive gel forming capacity at almost 30 °C, and are commonly used for injectable pharmaceutical delivery (Shriky et al., 2020). Another example of thermosensitive hydrogels are elastin-like polymers which mimic animal elastin and are composed of polypeptides. This polymer type is soluble in water containing media below a certain temperature (~10 °C) while it forms self-assembled hydrogel networks above the critical temperature (~30 °C). The elastin like hydrogels are used in biosensors, drug delivery and biomaterials applications (Bessa et al., 2010).

## 1.9 pH and Thermo-sensitive Injectable Chitosan/Hydroxyapatite/Heparin Hydrogels

### 1.9.1 pH and Thermosensitive Chitosan Hydrogels

In this project, a natural polysaccharide chitosan (CS) was employed as a pH and thermosensitive injectable hydrogel matrix. CS was used due to its unique features, involving biocompatibility, biodegradability, antibacterial properties and in-situ gelation at the region of normal body temperature. Chitosan based neutralised solutions are found as liquid at room temperature and upon injection they can form naturally, physically crosslinked hydrogels at body temperature. Thus, the toxicity that results from utilisation of any crosslinker or synthetic materials can be avoided. Therefore, as previously discussed, chitosan has been utilised for numerous applications in drug delivery and tissue engineering applications.

Chitosan hydrogels include strong and weak water bonds, and thus can swell and dehydrate in certain surrounding circumstances (Kim, 2014, p. 27). Thermoresponsive chitosan hydrogels neutralised by a polyol,  $\beta$ -glycerophosphate disodium ( $\beta$ -GP) has been first reported by Chenite et al. (2000). Chitosan has been kept as liquid above the critical pH 6.2 where chitosan is stable by the neutralization with  $\beta$ -GP up to pH 7.15, while crosslinked hydrogels formed upon elevating temperature close to 37 °C. Thus, thermoreversible, pH-dependent gel formation occurred in the absence of any crosslinking and chemical modifying agents. At lower pH values between 6.8-6.9, the gelation point surged to 45 °C, which was considered to be more due to electrostatic repulsion and less to hydrogen bonding at lower pH. Cytotoxicity assays showed a cell

viability above 80%. The sol-gel transition in this CS- $\beta$ -GP system occurs due to the fact that  $\beta$ -GP increases intra-hydrogen binding of chitosan because of a decrease in repulsive forces via basicity of salt as well as surging ammonium and phosphate group attractions. Moreover, hydrophobic interactions in chitosan can be improved by glycerol-water interactions since it gives rise to gel formation as temperature increases (Chenite et al., 2000).

In addition, Hoemann et al. (2005), utilised chitosan- $\beta$ -GP hydrogels in the presence of a crosslinker, hydroxyethyl cellulose, for cartilage healing. They have used highly cationic chitosan with high DDA, including 84% and 90% with final pH at approximately 6.8. When sterile chitosan solution was injected into rabbits for both chondral and osteochondral defects, *in-situ* gelation occurred within 5-10 minutes. Chitosan hydrogels have showed great adhesion in healing adult articular cartilage. *In-vitro* and *in-vivo* tests showed that chitosan- $\beta$ -GP hydrogels had good histological, biological and mechanical properties. They achieved more than 90% cell viability of chondrocytes in chitosan matrix during an all *in-vitro* cultured period. The chitosan- $\beta$ -GP hydrogels have been already used in clinic for cartilage replacement with a commercial product (BTS-CarGel<sup>®</sup>) (Méthot et al., 2016; Shive et al., 2006, 2015).

Some researchers have investigated alternative neutralising agents to  $\beta$ -GP, such as magnesium glycerol phosphate (Lisková et al., 2015) and calcium glycerol phosphate (Kami et al., 2017) Recently, other neutralizing agents were harnessed including easily available weak base di-sodium carbonate ( $\text{Na}_2\text{CO}_3$ ) (Li et al., 2014), and sodium bicarbonate ( $\text{NaHCO}_3$ ) (Rogina et al., 2017).

The use of sodium bicarbonate to neutralize thermosensitive chitosan hydrogel system was first reported by Liu et al. (2011). Physically crosslinked gel formations with this system occur gradually from the surface to bulk, driven by hydrogen bonds,  $\text{CO}_2$  evaporation, and hydrophobic forces due to NH bonds becoming neutral. Sodium bicarbonate has also been investigated for its mechanical strengthening and gelation properties. Furthermore, the addition of sodium bicarbonate led to better cell cytocompatibility than hydrogels with sole  $\beta$ -GP (Deng et al., 2017).

### 1.9.2 Chitosan- Hydroxyapatite Hydrogels

The combination of CS with HA has utmost importance for bone regeneration applications, since it provides a bioactive composite with excellent bioactivity and biocompatibility, enormously contributing to osteointegration, cell adhesion, osteoconductivity and proliferation. However, use of monolithic hydroxyapatite or calcium sulphate in bone filling applications leads to shrinkage and brittleness. Therefore, it is sensible to use polymer/ceramic systems. Taking into account these properties, chitosan and hydroxyapatite hydrogels have been well investigated by researchers (Yar, Farooq, et al. 2016; Shahzad et al. 2015; Arun Kumar et al. 2015).

Shahzad et al. (2015) have produced antibacterial wound dressing hydrogel from CS, HA and PVA. These hydrogels have shown high antibacterial capacity, great interconnected porous structure, high swelling capacity and sustainable drug release in addition to enabling cell growth. In another study performed by (Yar, et al. 2016), anti-inflammatory hydrogels have been improved based use of CS, HA and PVA, ensuring drug (meloxicam) delivery for periodontal treatments. In addition to swelling and sustainable drug release, these hydrogels were cytocompatible and improved cell proliferation with anti-inflammatory properties.

In another study, reported by Liu et al. (2014), thermosensitive hydrogels were produced from the combination of water soluble thiolated CS (chitosan-4-thiobutylamide or CS-TBA) and HA neutralised by  $\beta$ -GP at 37 °C. In these hydrogels, nano-sized HA particles were dispersed homogeneously, and produced better mechanical properties and the sustainable release of bovine serum albumin (BSA), compared to the hydrogels with unmodified CS. These gel compositions had suitable biodegradation rates after 28 days for unmodified and modified CS amounting to ~49 %wt and ~52 % wt, respectively.

In addition, CS/HA thermosensitive hydrogels with gentamicin were harnessed to increase porosity of bone cement polymethyl methacrylate (PMMA). This led to enhancement of eventual features of composite with better mineralization and cell viability (Sa et al., 2015). Recently, chitosan/hydroxyapatite hydrogels neutralised by

sodium bicarbonate has been also investigated by *in-situ* synthesis of hydroxyapatite that contributes to increment in pH (2017). This hydrogel system enabled good cell viability and proliferation in encapsulated cells (Rogina et al., 2017).

### 1.9.3 Heparin Incorporated Chitosan Hydrogels

Regarding chitosan (CS) and heparin (Hep) composite hydrogels, in one study, UV stimulated CS matrixed hydrogels in which Hep was used to bind growth factors was investigated. The composition of hydrogels was formed from CS with azide groups (light reactive) and lactose (Az-CS-LA) crosslinked with UV light (Hattori et al., 2013; Ishihara et al., 2003). The results showed that heparin could be bound electrostatically in the CS hydrogel structure with sustainable release of various growth factors achieved simultaneously. The *in-vivo* studies with mice showed that the addition of Hep to the FGF-1 or FGF-2 provided their sustainable release via degradation of CS, and this stimulated substantial vascularisation as well as surging haemoglobin in tissue (Ishihara et al. 2003).

### 1.9.4 Sterilization of Thermosensitive Chitosan Solutions

It is necessary to identify a suitable sterilization method for thermosensitive solutions, comprising biodegradable polymers including chitosan, to avoid major alterations in the physiochemical and gelation properties of polymers. Sterilization is necessary for elimination of pathogens, e.g. bacteria, fungi and viruses, in biomaterials. Among the main sterilization techniques in clinic, heat sterilisation,  $\gamma$ -irradiation, ethylene oxide and plasma are well accepted. However, these techniques have limitations in the case of degradable polymers, which are more susceptible to degradation and morphological deterioration. Therefore, some aseptic techniques and other alternative methods have been recently employed for sterilisation, e.g. iodine, peracetic acid, supercritical CO<sub>2</sub>, UV, freeze-drying and filtering. The efficiency of these methods differ based on assortment and type of pathogens. (Dai et al., 2016).

Among these techniques, heat, ethylene oxide and plasma have the highest inactivation ability against all pathogens including prions, myobacteria, vegetative bacteria,

enveloped and non-enveloped viruses, bacteria spores and fungi. Gamma and electron beam sterilization with high efficiency has the same ability except for prions. Peracetic acid has also high deactivation capacity for microorganisms except myobacteria (Dai et al., 2016).

Among the methods mentioned medium inactivation capacity, iodine is effective to deactivate all pathogens except myobacteria. Although ethanol has ability for myobacteria deactivation, it is not efficient for deactivation of bacteria spores, non-enveloped viruses and prions. As for UV at medium efficiency, it has the ability to inactivate only vegetative bacteria and enveloped viruses among all previously mentioned pathogens (Dai et al., 2016).

Respectively new sterilisation techniques, including supercritical carbon dioxide, antibiotics and freeze-drying, take place in the low deactivation category. While supercritical carbon dioxide is efficient to kill vegetative bacteria, bacteria spores, non-enveloped and enveloped viruses, antibiotics and freeze drying methods only have the ability to inactivate vegetative bacteria (Dai et al., 2016).

As reported, gamma irradiation of thermosensitive chitosan-polyol systems causes occurrence of agglomerates in suspension, substantial polymer degradation, discoloration and significant decrease in viscosity compromising thermogelling properties (Jarry et al., 2002). Galante *et al.*, (2016) has reported the protective effects of sugar additives, e.g. mannitol and glucose, on chitosan nano particle suspension, by decreasing agglomerate formation and zeta potential during sterilisation via gamma irradiation. However, Jarry *et al.*, (2002) has reported that gamma irradiation has led to a large viscosity decrease in spite of polyol additives having been used before exposure to the sterilisation at -80 °C.

Although ethylene oxide treatment has a high efficiency of and relatively low process temperature, it has the risks of chemical toxicity and ignition (Marreco et al., 2004). Another recent method approved for sterilization of medical tools (ISO 14937) is ozone treatment, providing sterilization via oxidation and destruction of living organisms in materials. As Galante et al. 2016, has reported, ozonisation did not cause any physical

change in chitosan hydrogel nanoparticles but it has shown a slight toxicity which can be prevented by utilizing sugar components. These sugar additives caused formation of new chemical bonds but did not affect cytotoxicity.

Ultraviolet irradiation has recently been used for sterilization of biodegradable materials. UV is generally preferred for sterilization of surfaces and transparent materials. UV leads to impulse of photons leading to the destruction of the DNA of pathogens. The impact of UV varies depends on the microorganism types, exposure time and the wavelength of the UV(Dai et al., 2016).

Ethanol which is a disinfectant rather than a sterilisation agent. A 60-80% concentration of ethanol ensures protein denaturation and break down of lipids in pathogens. However, some virus types and bacterial spores cannot be eliminated by ethanol. Therefore, it might be used only in surface sterilisation (Dai et al., 2016; Galante et al., 2016). In addition, it has been reported that 70% ethanol sterilisation led to more than 30% reduction in tensile strength as well as morphological deterioration in sole chitosan membranes. However, glycerol as an additive before sterilisation, prevented these impairments (Galante *et al.*, 2016).

The utilisation of freeze-drying for sterilization of biodegradable materials has also been reported. During lyophilisation, low temperature ensures denaturation of proteins and enzymes, and water removal leads to the destruction and deactivation of pathogen membranes. Lyophilisation can be used as a sterilization technique with the accompaniment of other techniques (Dai et al., 2016).

Finally, recently improved non-thermal plasma technique may be suitable for thermosensitive liquid formulations due to eliminating thermal, chemical, radiation and pressure effects. The plasma technique uses the dielectric barrier discharge principle at normal room conditions. It provides antimicrobial features in sterilized solutions over a long period of time. It is quite efficient to destroy multi-drug resistant bacteria, fungus, spores and prions in an affordable way and in short time such as 3 minutes (Albala et al., 2015).

For thermosensitive materials sterilization, instead of using a terminal sterilization method, alternatively, each component can be sterilised individually prior to synthesis of final formulations under sterile conditions. This strategy has been recently standardized by the FDA (US Food and Drug Administration) for injectable formulations. This technique protects liquid phase features but requires strict cleanroom synthesis methods along with current good manufacturing practice (cGMP), and standards (e.g. ISO 14644 and 14698) against airborne contamination. This technique includes many requirements including large set up facilities, education, permissions and has high costs (US Food and Drug Administration, 2004; Albala *et al.*, 2015). Prior to synthesis of thermosensitive solutions, reagent solutions, except for polymer solutions with high viscosity, can be filter sterilized with 0.2  $\mu$  or smaller filter membranes (Munarin *et al.*, 2013; U.S. Department of Health and Human Services Food and Drug Administration Center, 2004).

Among sterilization techniques, heat treatments including steam and dry autoclaving are the most efficient methods to discard living organisms from the materials. Their simplicity, affordability and non-toxicity are the reasons for this preference. However, high process temperatures reaching up to 160 °C during autoclaving process lead to deterioration of the chemical and mechanical properties of materials. It has been reported that steam autoclaving of biodegradable materials having low glass transition temperature, causes a major decrease in molecular weight, and in mechanical and rheological properties (Dai *et al.*, 2016; Jarry *et al.*, 2002).

Jarry *et al.* (2002) investigated the impact of steam and dry autoclaving on chitosan solutions for thermosensitive hydrogel formulations. In the case of dry autoclaving of chitosan, polymer bonds exposed to cleavage and cross-linkage resulted in less solubility and high increase in viscosity after autoclaving, indicating unsuitability for injectable formulations. On the other hand, steam autoclaving also leads to a significant molecular weight lost in the first 10 minutes, during which, the highest decline of up to 30% occurred. There was as well, a 3 to 5-fold loss of viscosity. However, after steam autoclaving, gelation properties were still preserved, and 10 min was found sufficient in terms of sterility. To mitigate adverse effects of steam autoclaving, the effects of diverse sugars in chitosan solutions such as glucose, glycerol, mannitol, sorbitol and

polyethylene glycol have been investigated. It has been seen that with polyol additives prior to autoclaving, chitosan solutions were able to minimize the decrease of molecular weight and compressive strength. Polyol additives also improved temperature-sensitive gelation behaviour. The stabilizing effects of polyols on polymers is considered due to their impact on alterations in water structure and the hydrophobic interactions that protect polymers from degradation. Although there was minor increase in viscosity after sugar additives in comparison to the control, there was still a high decrease in viscosity of between 20 and 50 % that occurred after autoclaving (Jarry et al., 2001, 2002).

Overall, there is no perfect method available for sterilization of thermosensitive injectable solutions; particularly those, such as chitosan, that consist of biodegradable polymers. Most current sterilisation techniques can cause alterations in structural and morphological properties as well as in the temperature dependent gelation features of polymers. Non-thermal plasma techniques can be a preference for sterilisation of injectable formulations depending on the availability such systems. Individual sterilisation of each component before the application of thermosensitive solutions might be the best choice by providing aseptic synthesis conditions. This may possibly be followed by an additional terminal sterilisation by UV or lyophilization. Reactant solutions might be sterilised by using filter sterilisation while high viscosity involved polymer suspensions can be sterilised by using an autoclave, due to its safety. However, heat induced viscosity deterioration can be prevented or mitigated by autoclaving CS in the form of water dispersions along with sugar additives, e.g. glycerol, glucose, and mannitol, as reported by Yen and Sou, (1998) for thermosensitive and stable chitosan hydrogel solutions.

In this study, the pre-sterilisation of reagents ensured in modified sterile hydrogel formulations. Chitosan dispersion in water-glycerol media, and hydroxyapatite powders were autoclaved individually while all the remaining liquid reagent solutions, including sodium bicarbonate and heparin solutions, were filter sterilised. Prior to biological studies, the terminal UV treatment has been applied to avoid airborne contamination during storage.

## 1.10 Main Characterisation Techniques Used for Thermosensitive Injectable Hydrogels

### 1.10.1 Physical Analyses

#### 1.10.1.1 Injectability and Syringability

Both injectability and syringability strongly depend on viscosity, rheology and the density of the formulations that are subject to injection. In addition, the injection apparatus and needle geometry, (shape, size, bore diameter etc.) play important roles during injection (Zhang et al., 2018). The needle gauge sizes required for injections during orthopaedic and dental applications are in the range of 10–16 G and 16–25 G, respectively (Burguera et al., 2007).

The term syringability, refers to the flow capability of a pharmaceutical solution through a needle, into a container. It covers the following factors; solution drawing capacity into the syringe, needle blocking and bubbling in solution, and dosage adjustment. Injectability consists of the required force for injection, as well as flow uniformity or blockage parameters which cover the injection period (Cilurzo et al., 2011).

Cilurzo *et al.*, (2011) has reported a qualitative injectability test, which was performed by trained observers on both air and a human tissue model, referred to as a panel test, is based on scoring the injection capacity of a solution from 1 to 4. In addition, quantitative analyses were performed based on the force measurements during this injection. However, many researchers perform injectability tests by injecting the solution into open air in the absence of a tissue model for injection (Alves et al., 2008; Moreira et al., 2018; Zhang et al., 2018). Also, some researchers use the term ‘syringability’ when analysis is based on the weighing of solutions expelled from a syringe using consistent force and time. However, injectability tests involved measuring the force required for the displacement of a syringe plunger while a solution flows through a needle. The Equation 1.4 gives the formula for syringability (Moreira et al., 2018).

$$\text{Syringability (\%)} = \frac{\text{weight of expelled solution from syringe}}{\text{weight of solution before injection}} * 100 \quad (1.4)$$

Both tests can be carried out by using a texture analyser or a universal testing machine in compression mode. A syringe filled with a certain volume of the solution is fixed downwards into a syringe rig. In injectability tests, the machine loading cell is lowered at a certain speed close to the manual injection speed (1 mm/s) and frequency. The required forces against displacement of the syringe plunger is measured and plotted via software. From these experiments, three different forces can be determined after data analyses: initial glide force (IGF): the loading force to initiate movement of syringe plunger; dynamic glide force (DGF): the force to sustain syringe movement; and the maximum force during injection ( $F_{\max}$ ) (Cilurzo et al., 2011; Moreira et al., 2018).

Furthermore, Zhang et al., (2018), has also counted the ‘total work’ parameter which refers to the required work for whole injection process. This is measured by counting the area below the curve in a force vs displacement graph. Total work is expressed by the given formula at Equation 1.5 where WT, D, and F symbolise: total work, distance, and force, respectively.

$$\text{WT} = \int_{D(F=0)}^{D_{\max}} F * dD \quad (1.5)$$

The correlation between needle size, syringe volume, and solution viscosity factors and injectability have also been investigated. It has been found that when the solution concentration increases, the total work of injection surges more disproportionately when the inner diameter of the needle reduced. The total work is increased with an increase of syringe volume, but disproportionate increase occurs when the needle diameter is reduced. In addition, during the solution injections, various non-Newtonian flow features were encountered. Injectability performance is strongly depend on material features, such as particle size and distribution, zeta potential, viscosity etc. Solution concentration affects the rheological and injection performance enormously, hence such formulations need to be investigated more methodically while assessing the functionality of these products before commercialization (Zhang et al., 2018).

In this study, injectability performance of liquid hydrogels were assessed by both qualitative and quantitative methods. These, in repeated experiments, involved manual flow rating for a range of needle thicknesses, and quantitative force-displacement measurements performed by UTM in compression mode in which IGF, DGF and  $F_{max}$  forces were counted for each set of hydrogel groups (See Chapter 3).

#### 1.10.1.2 Sol-gel Transition and Rheology

##### 1.10.1.2.1 Turbidity via Light Scattering

Sol gel transition of solutions might be determined by using different methods. One method involves the measurement of turbidity via light scattering. This method is based on the increase in scattered light due to the heterogeneity of the solution showing sol-gel transitions that can be detected as optical density values by using a microplate reader in visible light. The average of multiple measurements of sol specimens in well plates that are incubated at 37 °C are obtained in different time intervals to signify gelation (Matsumoto et al., 2006).

##### 1.10.1.2.2 Test Tube Invert Method

This method is very simple semi-quantitative measurement of the gelation speed of thermosensitive solutions. This involves placing a 1 or 2 mL of a thermosensitive solution into a glass test tube with a cap and leaving it in a water bath at 37 °C for gelation. The tube is inverted once every minute. This is repeated until the flow of the solution against gravity stops. This flow ending point is considered the indicator of initiation of gelation, and the time recorded as the incipient gelation time of the solution (Li et al., 2014; Wu et al., 2016). Due to its simplicity and being a very efficient technique, this technique is used to determine the incipient gelation time of liquid hydrogels in this study (See Chapter 3).

### 1.10.1.2.3 Rheology Measurements

Rheological dynamic mechanical analyses entail inducing an oscillatory stress (or strain) onto the material and the measurement of the remaining strain (or stress) on the material at certain frequencies and temperatures. The oscillatory measurements give a storage (elastic) and loss (viscous) modulus, and the modulus obtained from their combination is expressed as complex modulus which represents the resistance of material against deformation. The correlation between the elastic ( $G'$ ) and viscous ( $G''$ ) modulus and phase angle ( $\delta$ ) is expressed in Equation 1.6. where  $\delta$  signify the angle of the curves of these moduli versus time or frequency. In the viscoelastic region,  $\delta$  is between 0 (for elastic solids) and  $90^\circ$  (for Newtonian fluids). When the phase angle equal to  $45^\circ$  ( $\tan \delta: 1$  (max)), it means that the storage and elastic moduli become equal. This point is called the gelation point. After this point, the elastic properties of the material dominate its viscous features (Rafipoor et al., 2014).

$$\tan \delta = \frac{G''}{G'} \quad (1.6)$$

Rheology measurements are found to be very beneficial and are utilised in this study to determine sol-gel transition times, temperature of liquid hydrogels and viscoelastic change in hydrogel over time at body temperature (See Chapter 3).

### 1.10.1.3 Gel Morphology

#### 1.10.1.3.1 Scanning Electron Microscopy (SEM)

SEM works by electron beam irradiation on a solid sample and the interpretation of the signal formation from a raster scan of the electron beam gathered by a detector (Luo, 2016). The electrons are scattered in elastic and inelastic ways due to interactions with atoms of the material. Secondary electrons (SE) form due to emittance of the valence electrons of the atom in an inelastic manner while backscattered electrons (BE) occur due to elastic scattering of the electrons (Michio & Feiyu, 2016).

Most energy that is produced by SE is taken into the sample except for a small portion that is close to the material surface and can be transmitted out of the sample allowing for imaging of the topological features of a material. In contrast, BE have high energy that cause surplus electron dispersal, allowing for bulk compositional analysis. SEM does not require thin transparent sample preparation and allows for thick sample analysis, but the sample material should be water free, and a metal coating is required if material is not conductive (Luo, 2016; Michio & Feiyu, 2016). SEM coupled with energy dispersive X-ray (EDS) can provide elemental analysis in addition to the morphology of the materials.

In this project, SEM analyses were performed to study morphological structural features of freeze-dried hydrogels. Mineralisation of hydrogels incubated in SBF were studied with elemental analyses by EDS.

#### 1.10.1.3.2 Transmission Electron Microscopy (TEM)

TEM is a high-resolution imaging technique that gives chemical and structural details of materials. In TEM, materials can be imaged at the angstrom level via electron beam activity and involving as well, sample electrons. Following electron penetration, the image exposed is magnified via objective and projector lenses, and final images are obtained in 2D form. TEM involve analysis of very thin samples under a hundred nm, to provide penetration of electrons through the samples. Therefore, there are various sample preparation techniques prior to TEM imaging that include, ion milling, polishing, sectioning etc. For imaging of light delicate biological samples, low dose imaging techniques can be utilized (Luo, 2016).

Both SEM and TEM imaging techniques require dehydration of wet samples such as hydrogels and biological samples, thus there are diverse sample preparation techniques that are discussed below.

### 1.10.1.3.3 Preparation of Hydrogels for SEM and TEM

Prior to imaging with SEM or TEM, hydrogels require to be totally dehydrated as they have abundant water in their structures. There are different processes for dehydration of hydrogels in the literature involving, freeze drying, vacuum drying, critical point drying and cryo specimen preparation techniques etc. (Hawkins *et al.*, 2007; Zhang & Peppas, 2002).

Freeze-drying involves the treatment of materials at low temperatures below their freezing point. After material is frozen, the lyophilisation process takes place that involves the gradual sublimation of water found as ice crystals in the material, in a vacuum. The freeze drying method is one of the practical methods used to dry swollen hydrogels since it enables conservation of fundamental structural properties of materials such as porosity (Lin, Meyers and Olevsky, 2012; Luo, 2016). For better protection of morphology, hydrogels can be exposed to instantaneous freezing in liquid nitrogen or ethane (-196 C°), and the fractured hydrogels are subsequently lyophilised at -80 C° under vacuum before SEM or FESEM imaging (Matzelle *et al.*, 2002; Zheng, Zhang and Cheng, 2016).

Cryo preparation is considered a convenient method particularly for hydrogels or the fixation of organisms, such as cell, protein, yeast etc. before their imaging. These cryo techniques involve the sudden freezing and immobilization of these active agents, and thus prevent the ice crystal formation that can destroy morphological structure. Although some antifreeze sugar compounds such as glycerol and sucrose have also been employed for preserving structure from ice formation, they were found insufficient for the desired fixation of biological organisms. Cryo imaging systems such as cryo-TEM, and high resolution imaging scanning electron microscopy HRSEM integrated with high pressure freezing (HPF) systems allow cryopreservation in large scale and imaging at nanoscale reaching up to 200,000 magnifications with topographical information (Apkarian *et al.*, 1999, 2003).

A typical process for a thermosensitive hydrogel imaging with cryo techniques includes heating (>32 °C) of small amount of hydrogel solution (5-10 µl) on gold plaque for

hydrogel formation and introduction of hydrogels into either HPF or by plunging into liquid ethane for freezing (-183 °C). Then frozen hydrogels are fractured in the cryo stage by using a pre-cooled blade. Subsequently specimens are rinsed with liquid nitrogen and etched in vacuum and at low temperature. Subsequently, samples are coated with chromium and imaged by in-lens field emission SEM at -115 °C under vacuum (Apkarian *et al.*, 2003).

In the critical point drying (CPD) method, after immersion in a graded alcohol series, hydrogels are treated with liquid carbon dioxide at low temperature and high-pressure in a critical drying machine. This is followed by the increase of temperature up to a critical point which is about 31 °C; this provides the evaporation of carbon dioxide that previously substituted with ethanol. Then, samples can be coated by gold prior to SEM imaging. The CPD method is advantageous since it can eliminate surface tension that is a detriment to the materials as it inhibits the contact between liquid and gas phases (Hawkins *et al.*, 2007; Zhang & Peppas, 2002).

In order to eliminate complex tool and equipment necessities that CPD methods and other cryo-imaging techniques require, Hawkins *et al.*, (2007) have developed a chemical CPD technique which is based on utilizing highly effective hexamethyl disilizane (HMDS) prior to TEM imaging of hydrogels. As a summary, hydrogels placed on a TEM grid were exposed to instant freezing by immersion into liquid nitrogen while being shaken for 30 seconds. The frozen hydrogels were then plunged sequentially into absolute methanol and HMDS, again while being shaken for some seconds. Following these steps, hydrogels were placed into fume cupboards to provide evaporation of the HMDS content. This process made hydrogels ready for the TEM analyses. Similarly HMDS has been used to replace the CPD process for preparation of samples for electron microscopy imaging of, for example, sinusoidal endothelial cells (Braet *et al.*, 1997), and micro animal specimens, such as gastrotricha (Hochberg & Litvaitis, 2000) and tardigrades (Shively & Miller, 2009).

The protective impacts of HMDS on wet sample specimens results from its diminishing effect at the surface tension and protein binding capacity that prevents destruction of samples by eliminating meniscus formation during air contact (of wet samples).

Furthermore, it facilitates rapid drying in minutes, which is very promising compared to other techniques (Braet et al., 1997).

In this study, hydrogels were freeze-dried prior to SEM imaging due to its easy availability and its protection of the main morphological structure of porous hydrogels. To observe cell attachment on the surface of hydrogels, it would be useful to choose a protocol that involve drying via HMDS utilization due to its simple processing that does not require complex tools and equipment and is suitable for the dehydration of biological specimens, resulting in quality imaging with the available SEM. However, these experiments could not be performed due to the COVID 19 lock down period.

#### 1.10.1.4 Thermal Analysis by TGA/DSC

Thermal analyses of materials involve thermal gravimetric analysis (TGA), differential thermal analysis (DTA) and differential scanning calorimetry (DSC). In TGA, samples are heated in a specific atmosphere such as argon, nitrogen or air, and the weight changes in specimens are measured. TGA provide detection of temperature dependent changes in material including dehydration, calcination, and disintegration. DTA analyses are carried out by the simultaneous heating of both an inert sample and the specimen. Their comparison gives specific reaction temperatures, such as oxidation, melting, and different phase formations (King, 2002). Regarding DSC, it measures the energy changes in samples, such as heat capacity and enthalpy at increasing temperatures that are measured by calorimetry. DSC provides extensive information about materials, e.g. glass transition temperature, crystallisation and melting point. DSC is also performed by heating both the specimen and a reference inert sample (Schick, 2009). In this project, simultaneous TGA/DSC measurements were performed for thermal analysis of hydroxyapatite particles in high temperatures up to 1500 °C (See Chapter 2). In addition, the reagents used in the hydrogel synthesis including CS, HA, Hep and NaHCO<sub>3</sub> were analysed by using the TGA/DSC technique, heating specimens up to 700 °C (See Chapter 3).

#### 1.10.1.5 Surface Area Measurement - Brunauer-Emmett-Teller (BET)

BET method consists of outgassing a small amount of sample in vacuum environment. Then, the surface of the specimen is saturated by single-layer N<sub>2</sub>, and the consumed N<sub>2</sub> amount is calculated as representative of the surface area of the specimen (King, 2002). In this project, this technique was utilized to measure the surface area of produced hydroxyapatite particles (See Chapter 2).

#### 1.10.1.6 Swelling (Liquid Absorption Capacity)

Swelling or liquid absorption capacity is a very important parameter in regard to hydrogels. Their swelling behaviour have direct effects on drug loading and delivery applications. For instance, chitosan based cationic hydrogels swell in low pH under the pK<sub>b</sub> once ionisation occurs, and thus are beneficial for drug delivery in acidic pH e.g. in the stomach (Rizwan et al., 2017; Ullah et al., 2015).

As reported by Ullah *et al.*, (2015), in pH responsive hydrogels, swelling occurs due to the abrupt alteration of degree of ionization leading to electrostatic repulsion causing a change in volume due to osmotic swelling. The swelling ratio of the hydrogels depends on two main factors (i). polymer features: e.g. such as ionisation degree, pK<sub>a</sub> and pK<sub>b</sub>, the rate of crosslinking, concentration, the rate of hydrophobic and hydrophilic groups, electrostatic charge, and (ii). properties of absorption medium: pH, ionic strength neutralising agent and its valence (Gupta et al., 2002; Ullah et al., 2015).

In this study, swelling capacity of hydrogels were tested by immersing hydrogels in Phosphate Buffer Saline (PBS) media up to 72 h. In different intervals. Weight measurements of hydrogels were performed after washing and removal of surface water. In addition, the pH of the media has been recorded at regular time points (See Chapter 4).

## 1.10.2 Chemical Analyses

Spectroscopic techniques are routinely used for the chemical structural characterisation of materials. Spectroscopy exploits the electromagnetic radiation engaged with atoms inside the materials. This then leads to energy acquisition and loss, and alterations of atom energy states due to vibration, rotation, and electron motion in atoms. The classifying of the harvested energies and motions enables the characterisation of materials. Utilizing the absorption and scattering modes of light, vibrational spectroscopy techniques are non-invasive and used particularly to study material chemistry in a range of specific applications from the pharmaceutical industry to clinical research (Rehman, Movasaghi and Rehman, 2012, p.1-3; Swarbrick, 2014). The differentiation of healthy and tumorous tissues and diagnosis of various cancer types by using *in-vivo* non-invasive Raman or IR spectroscopy techniques have been extensively reported (Huang et al., 2003; Shafer-Peltier et al., 2002; Stone et al., 2002).

### 1.10.2.1 FTIR Spectroscopy

Electromagnetic radiation of light in the infrared region that is associated with light absorption is referred to as infrared (IR) spectroscopy. IR light hitting a sample can cause an excitation of the molecules towards an upper vibrational stage that give rise to absorption of the light in specific wavelengths. The atomic bonding and interactions contribute to identification of molecules using the absorption spectrum in a specific wavelength as a fingerprint. IR spectroscopy investigates the alteration at dipole moment of the molecules due to the oscillation of molecules that occur in all organic compounds and particularly materials having covalent bond characteristics. FTIR and Raman spectroscopy are generally used as supplementary techniques for each other in completing chemical characterisations (Baker *et al.*, 2008; Rehman, Movasaghi and Rehman, 2012 p.8-10). The main drawbacks of the FTIR technique, are the requirements of sample preparation and its non-suitability for aqueous sample analyses. The FTIR analysis in direct transmission in the mid-infrared region is challenged with opaque and thick materials. Therefore, it obligates complex sample preparations that may also cause some changes to the materials. Therefore, other techniques such

as diffuse reflectance (DRIFT) and attenuated total reflectance (ATR) can be suitable for such materials.

#### 1.10.2.1.1 FTIR-Attenuated Total Reflectance (ATR)

ATR is a sampling technique that is used in conjunction with FTIR. A sample is analysed in close contact with a crystal (ZnSe, Diamond, Germanium etc.) surface that possess a higher refractive index than that of the specimen. The total reflection of IR light through the crystal leads to generation of a special wave that reach through the sample; a small amount of energy is absorbed by the sample and the attenuation of the ephemeral wave occurs. The energy is transmitted back, and the light that is reflected from the other side of the crystal forms the spectrum collected by a detector (Baker, Hughes and Hollywood, 2016, p.2-12).

In this work, the ATR technique was used for chemical characterisations due to its simplicity and ability to identify chemical functional groups that were envisaged to be present in the bulk and surface of the material. Mostly, it is a surface technique and functional groups that are orientating on the surface are easily analysed. ATR was used to analyse HA samples, normal dried hydrogels (See Chapter 3) and freeze-dried hydrogels after being treated in SBF for bioactivity tests, or in PBS or Lysozyme/PBS solutions for degradation studies (See Chapter 4).

#### 1.10.2.1.2 FTIR-Photo-Acoustic Sampling (PAS)

Due to the high optical density of solid materials, analysing chemical properties of opaque materials in the mid-infrared region requires special sample preparation including chemical treatment which can interfere with analysed specimens. Also, difficult and time-consuming size reductions may be required. On the other hand, in the FTIR-PAS technique, the IR beam is absorbed by the specimen and it is converted to heat which conveys towards the surface of the sample and generates a gas that leads to PAS signal formation. The gas formed due to a thermal dilation affecting a fine layer of the surface; providing sufficient optical density for the measurement of the absorbance spectrum. Therefore, this FTIR-PAS technique is a very suitable method for

the characterisation of solid samples in the mid-IR region with minimal or no sample preparation requirement (Rehman & Bonfield, 1997). Therefore, in this study, the FTIR-PAS technique has been employed to identify chemical composition of hydroxyapatites that were either synthesised in our laboratories or commercially acquired. (See Chapter 2).

#### 1.10.2.2 Raman Spectroscopy

Raman spectroscopy utilizes the scattering of the light provided by a laser to detect polarisation of the molecules upon photon exposure and molecular vibrations. The lasers employed in Raman spectroscopy involve the visible, near infrared and near ultraviolet regions of light. Once the light impacts on the interatomic bonds and electrons in the molecules, molecules can be excited by a photon to another energy level, it obtains a diverse oscillatory state that upon relaxation disperses a photon. After scattering a molecule, if the photon preserves its energy with unaltered frequency it is referred as *elastic* (Rayleigh) *scattering* whereas the situation that the photon has gained or lost the energy upon interaction with molecule, is defined as *inelastic* (Raman) *scattering* (Rehman, Movasaghi and Rehman, 2012a, p.4-6).

Raman scattering exposure occurs in very small segment of light in comparison with elastic scattering. When a photon reaches an upper energy level, the frequency of the dispersed photon is shifted to a lower frequency to balance energy. This energy shift is termed *Stokes shift or red-shift*; in the opposite situation where incident photon loses energy is known as *anti-Stokes shift or blue-shift*. These Raman shifts that result from frequency differences between initial and emitted light, cause changes in wavelength ( $\text{cm}^{-1}$ ) that can identify the molecules (Mahadevan-Jansen and Richards-Kortum, 1997; Rehman, Movasaghi and Rehman, 2012a, p.4-6). There are two main vibrational modes of molecules: *stretching* and *bending*, and are based on the changes in length and angle of the molecular bonds, respectively. There are in total, six vibrational modes involving sub-types of stretching (*symmetric and asymmetric*); and bending (*scissoring, twisting, wagging, and rocking*) (Rehman, Movasaghi and Rehman, 2012a, p.4-6).

Both Raman and Infrared spectroscopy techniques are non-invasive complementary techniques for chemical characterisation. Raman has advantages over FTIR due to minimal or no sample preparation requirement, allowance of liquid sample analysis and having a wider wavelength from 4000 to 50  $\text{cm}^{-1}$ . FTIR is more suitable for organic material analysis while Raman is suitable for almost all samples. Raman has higher resolution, lateral: 1-2  $\mu\text{m}$  and confocal: 2.5  $\mu\text{m}$ , than FTIR which has 10-20  $\mu\text{m}$  laterally. The main disadvantages of Raman spectroscopy, to be discussed later, involves the problems of fluorescence and glass peak interference (Rehman, Movasaghi and Rehman, 2012a, p.12). In this study, dispersive Raman was used to characterise chemical groups in HA samples as a complementary technique to FTIR (See Chapter 2).

#### 1.10.2.2.1 Confocal Raman

The confocal micro-spectroscopy technique of Raman is a quite useful technique for three-dimensional imaging of biological specimens, e.g. cells and tissues in multiple directions and amplitudes (Baker, Hughes and Hollywood, 2016, p.2-12). Confocal Raman imaging provide extensive applications in the biomedical field including cancer diagnosis, differentiation between healthy and malignant cells (Shafer-Peltier et al., 2002; Terentis et al., 2013), and tracking drug delivery systems developed against biofilm formation (Takahashi et al., 2017), the compositional analysis of compact human bone at osteonal and interstitial sites (Nyman et al., 2011).

#### 1.10.2.2.2 FT-Raman

In Raman, the main challenges are the interference or noise of laser induced fluorescence and of glass peaks from substrates in the spectra (Rehman, Movasaghi and Rehman, 2012 p.8-10). The problem of high fluorescence in some samples can be prevented by harnessing the FT-Raman technique. In the utilisation of lasers in the visible light spectrum, fluorescence can be an issue. In the FT-Raman technique, by using a near-infrared laser (Nd:YVO<sub>4</sub>), the fluorescent effect on natural samples can be avoided. Thus, FT-Raman technique is able to eliminate the deproteination process of biological tissues that is a common method used in other techniques to avoid

fluorescence; but that leads to chemical alteration of tissue. The non-invasive analysis with only a small amount of specimen, and minimal sample preparation requirements make FT-Raman a useful technique, especially for the characterisation of fluorescent samples (Smith & Rehman, 1994).

In this study, the FT-Raman technique was used to characterise hydrogel samples to avoid fluorescence as this was not possible with the dispersive Raman technique due to the intense fluorescence problems faced particularly, in chitosan hydrogels (See Chapter 3).

#### 1.10.2.2.3 X-Ray Diffraction (XRD)

Being a non-destructive technique, X-ray diffraction provides efficient study of the chemical, structural, physical, and crystallographic properties of materials including phase and component analysis, crystallinity, thickness, density, porosity, atomic texture etc. X-rays which are a radiation source having electromagnetic waves in the angstrom level (0.01-1 nm), diffract the electrons of the material depending upon electron arrangements (Luger, 2014). X-ray diffraction may require sample preparation. For example, powder specimens might need grinding and pressing to obtain fine smooth surface features. The crystallinity and particle size alterations due to heat processes on the materials can be differentiated by diffraction patterns with different peak shapes and intensities. For instance, the annealing process binds the granules enhancing crystallinity. The nano sized particles with less crystal planes lead to widening of peak area by lowering peak intensities whereas bulk substances give sharp peaks with high intensities (Sharma et al., 2012). XRD is a powerful tool to evaluate crystalline material structures, especially polymorphs at molecular grade. In this respect, powder X-ray diffraction is utilised for stability analysis of pharmaceuticals (Thakral et al., 2018).

Recently, Zeller-Plumhoff *et al.*, (2019) have reported the investigation of bone generation at the interface of several biodegradable or non-biodegradable implants with quantitative analysis, by using two dimensional XRD and X-ray scattering (SAXS) techniques. These analyses can give information of bone ultrastructure involving its apatite layer formation, thickness and texture. In addition, the quantification of each

component in multiphase materials, such as ionic substitutions in hydroxyapatite crystal lattices can be carried out by the by using Rietveld refinement analysis based on phase density comparison from XRD patterns (Kannan et al., 2008; McCusker et al., 1999).

In this study, XRD analysis has been carried out for raw and sintered hydroxyapatites as supplementary chemical analysis to FTIR and Raman techniques. XRD analysis helped to identify different phases in biphasic hydroxyapatites, and carbonate substitutions in some compositions (See Chapter 2). In addition, a hydrogel sample and reagents including CS, HA,  $\text{NaHCO}_3$  and Hep were also analysed by using the XRD technique (See Chapter 3).

#### 1.10.2.2.4 Evaluation of Bioactivity by Simulated Body Fluid (SBF) Test

Bioactivity evaluation in the SBF is based on a chemical reaction between the biomaterial surface and a liquid, facilitating formation of a hydroxy carbonate apatite layer (Ohtsuki et al., 2009). SBF, first developed by Kokubo (1991), is an ionic solution that mimics the composition of blood plasma. This composition has slight concentration changes some of the ions for better representation of the blood plasma, and to obtain a stable reproducible solution (Kokubo & Takadama, 2006). In the preparation of SBF, the main procedure involves dissolution of various salts in ion-exchanged distilled water and pH adjustment to obtain a final pH of 7.4 at 37 °C.

After certain incubation intervals, samples of SBF immersion medium is taken for different quantitative or qualitative analyses including chemical and morphological analyses. The dissolved calcium ion concentration released into SBF media can be detected quantitatively by using atomic absorption spectrometer technique (Fathi et al., 2008), or using elemental calcium and phosphorous detection kits, and analysis of liquid specimens via a spectrometer (Borkowski et al., 2016).

Another quantitative technique is the weight gain and/or loss analyses during the incubation intervals in SBF indicating mineralisation or degradation. On the other, carbonated apatite layer formation on the surface and their crystal structures can be investigated by using SEM technique coupled with the EDS for performing proportional

elemental analysis to detect Ca, O, P and C percentage in the compositions. In addition, chemical analyses of mineralised samples can be performed by using FTIR, Raman and XRD techniques (Borkowski et al., 2016; Kokubo, 1990).

In this study, bioactivity tests were performed via SBF tests over 3-weeks. The associated analyses that were carried out, in different intervals, covered weight gain/decrease analyses, pH measurements of the media, morphological analyses by SEM, chemical analyses by FTIR-ATR and EDS (See Chapter 4).

### 1.10.3 Biological Analyses

#### 1.10.3.1 Evaluation of Biodegradation

Degradation mechanisms of polymers involve mechanical, thermal, photo and chemical degradation. The biodegradation of polymers commonly occurs via chemical pathway based on hydrolysis, either in the presence or absence of an enzyme as a catalyst. During hydrolysis, a polymer is exposed to swelling. Then, due to water invasion leading to destruction in the network, polymer cleavage occurs by forming oligomers and monomers. The released polymer components during degradation cause formation of cracks and porosity, effect the surrounding pH and lead to reduction in the polymer mass. The speed of hydrolysis depends on chemical bonding, molecular weight, pH, and crystallinity. These parameters can also be used to measure the degree of degradation. In addition, in natural based polymers, enzymes accelerate the speed of biodegrading hydrolysis reactions (Göpferich, 1996).

Polymers are degradable in different enzyme media according to their types. For instance, elastin like polypeptides (ELP) are degradable in the presence of trypsin, elastase, or collagenase (Li et al., 2012; Ong et al., 2006). In addition, enzyme-crosslinked hyaluronic acid based hydrogels are suspected to be degradable by hyaluronidase enzymes (Lee et al., 2009) and fibrin gels are degradable via activated plasmin (Li et al., 2012).

Ong *et al.*, (2006) has reported a quantification of trypsin enzyme stimulated degradation of elastin like polypeptides (ELP) by immuno-labelling of proteins involving utilisation of special tagging that involves a genetical approach. This allowed tracking/detection of enzymatically degraded ELP residues in both *in-vitro* and *in-vivo* degradation tests, by using a quantitative ELISA analyses that involve specific protocols including optical density measurements.

In a study, degradation of thermosensitive and chemically crosslinked poly (organophosphazenes) hydrogels was investigated *in-vivo* in mice. The degradation was analysed by using the FE-SEM imaging technique and fluoresceinamine tagging for the thiol groups of crosslinked polymers which were photographed by a camera (Potta *et al.*, 2009).

Degradation mechanisms of chitosan involves hydrolytic, enzymatic and oxidative degradation. Hydrolysis reactions, which are relatively slow and less effective, provide degradation of glycosidic linkages in chitosan. Hydrolytic degradation might be suitable for water-soluble chitosan derivatives, low molecular weight chitosan or polyelectrolyte complexes with weak bonding (Jennings, 2017).

Chitosan degradation by enzymatic reactions involve recruitment of lysozyme, chitinase  $\beta$ -or glucosidase enzymes in the body. Lysozyme is found in different parts of the body, e.g. serum at ranging quantities between 1-14  $\mu\text{g}/\text{ml}$ . However, in tissue defect sites, lysozyme is secreted by macrophages and neutrophils. Degradation of chitosan by lysozyme includes the breakage of glycosidic linkages, reduction in molecular weight and dissolution. Chitosan fragments after cleavage include saccharide and glucosamine side-products, which are either utilised with proteoglycans or removed from the body as metabolic by-products. Another enzyme that has a role in chitosan degradation is chitosanase or chitinase, which is particular to chitin. The human body is poor in these enzymes and are found as chitotriosidase and acid mammalian chitinase. In addition, intestinal depolymerisation of chitosan also occur due to  $\beta$ -glucosidase enzymes secreted by bacteria (Jennings, 2017).

Oxidative degradation based on free-radical formation by macrophages, which is not very common, leads to breakdown of polymers, crosslinking, decrease of molecular weight and the opening of rings. This might be caused by irradiation by UV and gamma light. Alternatively, local oxidative degradation might occur between the biomaterial and tissue surface which is raised from the formation of hydrogen peroxide and superoxide secreted by phagocytic cells (Jennings, 2017).

It is a common approach to use lysozyme for *in-vitro* degradation studies of biomaterials including hydrogels. For *in-vitro* degradation studies, the samples are weighted and immersed in a certain volume of lysozyme media prepared in PBS, and incubated at 37 °C (Aleem et al., 2017; Jin et al., 2009; Qasim et al., 2017). Qasim *et al.*, (2017) has reported for both *in-vitro* and *in-vivo* degradation studies for chitosan-hydroxyapatite porous scaffolds. The measurements of *in-vitro* degradation of samples, incubated in lysozyme media was evaluated chemically by the FTIR-PAS technique, and the analysis of liquid degradation media by pH analyses and UV-vis spectroscopy. Degradation of samples were evaluated morphologically by using the SEM technique. On the other hand, *in-vivo* degradation was determined by histological examination of degradation and morphometric analysis of histology slides via an optical microscope.

In this study, *in-vitro* biodegradation tests were performed over a 6-week period that involved using both PBS and Lysozyme added PBS solution as immersion media for comparison. At different intervals, degradation was analysed by weight measurements of hydrogels, pH measurements of the media, morphological analyses by SEM, and chemical analyses by FTIR-ATR (See Chapter 4).

#### 1.10.3.2 Evaluation of Biocompatibility

Biocompatibility investigation includes *in-vitro* analyses covering various types of cell culture studies, e.g. cell cytotoxicity, proliferation, adhesion and differentiation, and in *in-vivo* animal studies. For studying bone formation *in-vitro* with cells, osteoblasts, osteosarcoma, and mesenchymal stem cells or human osteoblasts from peripheral blood can be recruited. The osteosarcoma cells (e.g. MG-63, SaOS-2, and TE85) are commonly used as they are practically immortal and grow fast (Dillon et al., 2012).

### 1.10.3.2.1 Cell Cytotoxicity and Proliferation Assays

To quantify cell cytotoxicity and proliferation, cell counting can be performed manually in different intervals. Some dyes which reacts with the cell components can be harnessed as indicators of viability. The two most common dyes involved are 3-(4,5-Dimethylthiazolyl-2)-2,5-diphenyltetrazolium bromide (MTT) and Resazurin (Alamar blue).

#### *MTT Assay*

MTT plasma is a water-soluble dye that can go through cell membranes and is exposed to reduction by healthy cells, due to the action of dehydrogenase compounds. During the reduction reaction, formation of formazan occurs, leading to a colour change to purple. The amount of dissolved formazan is detected by optical density (OD) measurements that represents the quantity of live cells by a microplate reader in the visible range (Burton, 2005).

#### *Alamar Blue (Resazurin)*

Likewise, MTT, Alamar Blue dye is also used to measure cell viability and proliferation with similar principles. Resazurin which is a non-fluorescent dye, is reduced by enzymes, by cell metabolic activity, to fluorescent pink coloured resorufin. In contrast to MTT, resazurin is advantageous in terms of enabling reutilisation of cells in proceeding experiments due to its non-toxicity. This provides cost and time efficiency, particularly when primary cells are in question. Resazurin is added into cell media in the proportion of one to ten, and cell metabolic activity can be measured by using a fluorescent reader or a colorimeter (Brien et al., 2000).

In this project, due the benefits of Alamar Blue assays in terms of cytocompatibility that allows reuse of cells during all culture periods, it has been used for analysis of cell attachment, cytotoxicity and in proliferation assays (See Chapter 5).

### 1.10.3.2.2 Cell Adhesion and Morphology Imaging by SEM

Cell morphology analysis of cultured cells after they proliferate can be performed by SEM. As described, in the SEM characterisation technique, wet cells and tissues are required to be fixed in place and totally dehydrated prior to electron microscopy imaging. As an example of the preparation process reported by Braet et al., (1997) cells are fixed by using glutaraldehyde (2%) and preferentially with post fixative osmium (1%). Then, this is followed by the dehydration process with sequential ethanol treatments (70%, 80%, 90%, 100%, 100%, 100%) at 10 min intervals. Then, samples are dried via HMDS chemicals for three minutes, and then dried a desiccator for about 25 min. By increasing the HMDS immersion time to 5 minutes, samples can simply be dried in a fume cupboard for evaporation of HMDS for 30 min. Dried samples are then imaged upon gold coating by using SEM (Braet et al., 1997; Shively & Miller, 2009).

For morphological analyses of cells and their adhesion onto hydrogels, SEM is a very efficient and available technique. However, hydrogels include abundant water content in their structure that requires a full dehydration process prior to imaging. Given the complexity of most drying processes for hydrogels or tissues, HMDS as chemical drying agent offers a very simple technique with efficient outcomes that can be employed in this study for sample preparation for SEM. However, these could not be performed due to a covid 19 lockdown period.

### 1.10.3.2.3 Cell Differentiation Analyses

Osteoblast cells either root from mesenchymal progenitor cells during intramembranous ossification, or they differentiate through osteochondral progenitor cells in endochondral ossification. The differentiation of osteoblasts are affected by diverse stimuli including physical, mechanical and biological signalling factors (Rutkovskiy et al., 2016). The whole differentiation process takes a whole month. ALP secretion, collagen type transformation and ECM production are provided by downregulation of DNA which occurs in the first week of differentiation. Then, formation of osteocalcin, osteonectin, osteopontin and sialoprotein biomarkers occur, and the differentiation process is finalised with the apatite layer deposition starting after two weeks.

Differentiation can be tested via detection of different biomarkers such as ECM components (proteins such as fibronectin, vitronectin, osteopontin, laminin, osteonectin), alkaline phosphatase (ALP), collagen, and calcium phosphate. The determination of these markers can be done by performing different assays, such as mineralisation by Alizarin-Red assay; collagen detection by Sirius-Red assay, or ECM protein formation by ELISA (Hanna et al., 2018).

### ***Alkaline Phosphatase (ALP) Assay***

Alkaline phosphatase enzyme is one of the osteogenic biomarkers that facilitate the hydrolysis process of phosphomonoesters (such as inorganic pyrophosphate,  $\beta$ -glycerol phosphate, and ATP) to inorganic phosphates and alcohol during mineralisation. ALP stimulates mineralisation by breaking down inorganic pyrophosphate that is responsible for inhibiting hydroxyapatite formation (Balcerzak et al., 2003; Orriss et al., 2007). The ALP enzyme activities of cells can be determined by using a commercial kit with the basis of transformation of p-nitrophenyl phosphate substrate into yellow chromogen p-nitrophenol with the ALP. In different time points of a cell culture ALP activities can be determined by absorbance measurements of ALP treated cell media via a microplate reader at 405 nm (Cui et al., 2010; Orriss et al., 2007).

### ***Alizarin Red Assay for Calcium Deposition Analysis***

Alizarin Red-S (ARS) dye has an ability to form a chelate by binding to  $\text{Ca}^{2+}$  ions. By harnessing this feature, ARS is utilised in staining of tissues involving bone and cartilage, and for calcium detection in joint liquid. In addition, formation of mineralised extracellular matrix in cell-seeded biomaterials can be effectively determined by this staining technique. By utilisation of ARS and Von Koska staining techniques, it is possible to determine mineralised components locally via phase contrast imaging of stained tissues or organisms. Due to the limitations of this technique, colorimetric measurement of calcium can be carried out. (Gregory et al., 2004; Puchtler et al., 1969; Tetteh, 2016). The ARS assay basically involves dissolution of 1% (w/v) of ARS stain in de-ionised water following pH adjustment ( $\sim 1$ ) by using NaOH. After some culture period, cells fixed in scaffolds are treated with ARS solution and incubated on a shaker.

For quantitative analyses, images of samples involving non-cell involving control sample are taken (Tetteh, 2016).

In this study, the ARS assay was carried out to detect the deposition of ECM compounds, and calcium in cell seeded hydrogels. After staining by ARS, samples were immersed in perchloric acid, and absorbance measurements of the immersion media were conducted by using a microplate reader at 405 nm wavelength of the light (See Chapter 5).

### ***Sirius Red Assay for Collagen Deposition Analysis***

Sirius Red (SR) or Direct Red (DR) is a highly anionic dye that has an ability to anchor some amino acids (e.g. lysine and hydroxyproline) and guanidine molecules from collagen, via sulphonic acid linkages. The dark red colour is generated upon molecular binding by a dye that expands through collagen fibres that can provide detection of collagen via fluorescent measurement. The treatment of cell seeded scaffolds with SR solution prepared in saturated picric acid (1mg/mL) in dynamic rotation mode, and following washing steps, enables the elution liquid to be measured via an absorbance spectrophotometer for quantification. In addition, treated dried samples can be imaged via an optical microscope (Qasim, 2015).

In this study, SR assay has been performed for determination of collagen formation in cell seeded hydrogels. This involved absorbance measurements of the destaining solution which in immersion media, contains the released stains from samples (See Chapter 5).

#### **1.10.3.3 Evaluation of Angiogenesis**

There are various *in-vitro* or *in-vivo* techniques to investigate angiogenesis, and pro-angiogenic and anti-angiogenic response from materials. Among these methods, some techniques currently utilised involve *in-vivo* Matrigel assay and chick Chorioallantoic Membrane (CAM) assay; *in-vitro* cellular tube formation and aorta ring assay, and

respectively, new chick aortic arch and Matrigel sponge assays. Some of these techniques will be explained in this section.

#### 1.10.3.3.1 Aortic Ring Assay

This method includes the harvesting of animal aorta from rat or mouse, slicing them as rings and culturing them in a media. The culture explants can be encapsulated in plasma clots which are then cultured in an appropriate serum media, or they may be directly embedded in Matrigel, a commercially available hydrogel matrix, along with the angiogenic factors or test materials. During culture periods of up to two weeks, the expansion of endothelial cells as well as other cells can be controlled and detected via fluorescent labelling or electron microscopy imaging techniques. Since this technique involves cells other than the endothelial cells, that are in their original state and are not passaged or proliferated, it is more imitative of the *in-vivo* system. However, the drawback of this assay is that the aorta model includes a bigger vascular structure in comparison to the microvasculature that occurs during angiogenesis (Auerbach et al., 2003; Nicosia, 2009).

#### 1.10.3.3.2 Chick Aortic Arch Assay

The Chick Aortic Arch method originates from the idea of the aortic ring assay with some alteration. This method is advantageous since it enables the use of developing chick embryos rather than sacrificing mature test animals. Also the culture time of aorta rings is as short as 1 to 3 days in serum-free media. In this technique the aortic arches of chick embryos in their 12-14<sup>th</sup> development day are extracted and cut into slices following their culturing in Matrigel with the desired test agents, so as to stimulate or mitigate angiogenesis. This method provides observation of flourishing endothelial cells and microvasculature by using fluorescein labelling or staining techniques for quantification (Auerbach et al., 2003).

#### 1.10.3.3.3 Corneal Angiogenesis Assay

One of the *in-vivo* techniques used to study angiogenesis is performed on non-vascular corneas of test animals including mice and rats. The lack of native vascularity provides easy and more accurate evaluation of the effects of agents to angiogenesis. Test material is placed in an opened hollow, and with the implementation of stain or labelling agents, a vascular network may be identified for the performance of quantitative measurement of blood vessels, vessel area, and expansion of vessels with time; or for histogram and pixel analyses of fluorescent labelled images. This technique has limitations in terms of allowing limited area for implantation, possessing inflammation risk and requirement of practical experience (Auerbach et al., 2003).

#### 1.10.3.3.4 Chick Chorioallantoic Membrane (CAM) Assay

The chorioallantoic membrane (CAM) is a tissue surrounding the chick embryo's surface. It hosts blood vessel and capillaries and provides gas circulation. The CAM assay technique is respectively a very practical and preferred *in-vivo* technique to study angiogenesis, anti-angiogenesis and biocompatibility of tissue engineered materials (Mangir et al., 2019; Ribatti et al., 1996). The utilisation of chick embryos as an *in-vivo* animal model to study angiogenesis have numerous advantages over other animal models which comprise ethical restrictions, high costs, tedious processing and time, as well as invasive tests on animals. The CAM assay is carried out by using either *in-ovo* or the subsequently developed *ex-ovo* technique. In *in-ovo* experiments, fertilised chick embryos are incubated in a humidified incubator at 37 °C. After the incubation period between day 7 and day 9, a square window from the top of the eggshells are cut out and one or two test materials are implanted onto the chorioallantoic membrane of the embryos. The embryos, after adhering to the shells, are returned to the incubator. Then, in desired times of up to 14 days, the formation of microvascularity is imaged by using a microscope (Auerbach et al., 2003; Shahzadi et al., 2016).

Due to some limitations of *in-ovo* techniques, an *ex-ovo (shell-less)* CAM assay technique was developed. It provides an easy real time imaging and visualisation of whole CAM tissue during the development of the embryo at every stage (Mangir et al.,

2019). In this technique, briefly, fertilised chick embryos which are incubated in a rotating humidified egg incubator at 37.5 °C are taken out of their shells with a specific cracking technique in sterile conditions after 3 days of incubation. Upon an explicit pre-vascular network development of the embryo, such as at day 7, sterile test materials are implanted on the shiny CAM border. At following days, the CAM area hosting implant is imaged to investigate formation of new blood vessels by using a portable microscope. At day 14, embryos are sacrificed and the retrieved implant can be used for further histological analyses.

The quantification of the blood vessels can be carried out by using different techniques that involve manual, semi quantitative or quantitative techniques. One of the most common techniques to quantify blood vessels is the vascular index method as described by Barnhill and Ryan, (1983) which was utilised in this study. Briefly, using ImageJ software, on a CAM image, an imaginary circle is drawn surrounding the sample with a 1 mm margin. The blood vessels between the sample border and the circle, except for primary vessels, are counted. Then, using a Neuron-J plug-in at image-J provides tracking of the vessels and one can monitor this tracking. This technique can be considered as semi quantitative since it allows measurement of vessel length and density (Eke et al., 2017).

However, due to the tedious and time consuming manual and semi quantitative tasks, recently, automatic quantification approaches have been developed for branching network structures, e.g. neurons and blood vessels (Meijering, 2010). For morphometric analyses of branched structures, specific software has been used such as Neuron-J tracking integrated with Java originated XL-Calculations. These classify the branching neurons as either primary, secondary or tertiary (Popko et al., 2009). Additionally, splitting colour channels via Adobe Photoshop™ filtering and skeletonization by Image-J and the quantification of branching points by AngiTool® software (Mangir et al., 2019) or MATLAB® provides for counting vessel diameter length as well as branch out spots and tortuosity (Talavera-Adame et al., 2008).

The automatic quantification techniques could be advantageous in terms of providing better classification as well as easier and more comprehensive measurements. However,

these techniques require specific software with a standardized method to yet to be developed that is based on some mathematical models.

In this study, *ex-ovo* CAM assay has been performed due to its aforementioned benefits, such as minimal invasiveness compared to other animal models, easy availability, low cost and providing excellent visualisation and imaging of blood vessel network formation at every stage of chick embryo development. Thermosensitive solution drops applied on CAM formed *in-situ* gel upon incubation at 37.5 °C. For quantification of vessels, a semi quantitative technique has been used, including vessel tracking with Neuron-J plug-in using Image-J software and the manual counting of blood vessels as described by (Barnhill & Ryan, 1983). More details on this technique are explained in Chapter 5.

#### 1.10.3.3.5 Histological Analyses of CAM Tissues

Histology is very useful to differentiate individual units of tissue by using specific stains and imaging them using an optical microscope. For instance, Hematoxylin-Eosin (H&E) staining, has been used for more than a century to provide staining of cell nuclei to blue using Hematoxylin, and the connective tissues and cytoplasm stained pink using Eosin (Gurcan et al., 2009). The counting of vascularity at CAM tissues from randomly chosen histology sections have also been reported (Ribatti et al., 1996).

In this study, CAM tissues attached to hydrogels were stained by H&E staining for observation of tissue-hydrogel interactions and inflammatory reactions as well as blood vessel, cell and connective tissue morphologies (See Chapter 5).

### 1.11 Summary

Hard and soft tissue repair and regeneration require multiple surgical interventions, as very often, repeated clinical procedures are required. Surgery related treatments including transplantation methods and scaffold implants involve significant concerns including; injuries and infections in harvested tissue sites, illness transfer, painful, long healing times, and high cost etc. To tackle these challenges, minimal invasive tissue

engineering materials, such as *in-situ* formed hybrid injectable hydrogels possessing proangiogenic response through their functionalisation with active agents can be exploited.

The pH and thermosensitive hybrid homogenous formulations in liquid form. Upon injection into targeted tissue defects, crosslinked hydrogels form due to the stimulus of natural body temperature. These solutions can be mixed *ex-situ* with therapeutic agents, such as cells, growth factors and medicines, and provide their *in-situ* encapsulation, upon fast gelation, sustainable delivery. These formulations could be very efficient for filling complex shaped voids while in liquid form and subsequently setting as hydrogel, filling bone tissue defects. This is especially applicable to treatment of non-weight bearing craniofacial bones.

Bone tissues have unique self-recovery capability at modest damage. However, repairing major bone defects can be quite challenging. The regeneration of critical bone fractures strongly depends upon the swift development of a vascular network in the defective site, via branching from existing vessels (angiogenesis) (Risau, 1997; Grossi *et al.*, 2017). Current bone treatments often fail due to the lack of sufficient angiogenesis. Therefore, there is a significant need for developing functionalised tissue engineered materials providing delivery of active agents that stimulate the angiogenesis required for eventual bone regeneration.

The various growth factors that have been explored to induce angiogenesis in tissue engineering, comprise VEGF, bFGF and TGF $\beta$  (Fujita *et al.*, 2004; Oliviero *et al.*, 2012). However, growth factor delivery involves many challenges, such as instability, due to their high solubility, that reduce their performance and activation time. This becomes more challenging in ruined fracture conditions. Their high concentrations also lead to toxicity and malformation of bones. In addition, regional inflammatory reactions, adverse effects on nerves and risk of malignant tissue formations have also been reported in the literature (Carragee *et al.*, 2011; Raftery *et al.*, 2017).

To overcome instability issues, growth factors are mostly harnessed in an immobilised form into scaffolds. In this regard, heparin (Hep) and heparan sulfate proteoglycans

(HPSGs) are commonly used as growth factor binding agents since they have good binding capacity for proteins involving angiogenic growth factors, due to their highly anionic nature (Tae et al. 2007). Heparin and HPSGs are proficient to bind pro-angiogenic receptors with the majority of angiogenic growth factors, comprising VEGF, bFGF, and TGF $\beta$ . The regulatory role of heparin or HPSG on angiogenesis is especially determined by anionic sulfate bonds. As it has been pointed out, the physical binding efficiency of heparin can monitor the cells thanks to its molecular orientation that may promote angiogenesis. The binding of heparin with pro-angiogenic factors provides proliferation, generation of protease and migration of endothelial cells, as well as leading cells to blood vessel formation (Chiodeli et al., 2015; Oliviero et al., 2012)..

By considering the aforementioned effects of heparin, the potential proangiogenic capacity of heparin for binding physiologically available angiogenic growth factors to pro-angiogenic receptors, that might lead to angiogenesis have been investigated. Heparin bonded triethyl orthoformate (TEOF) and crosslinked chitosan poly-vinyl alcohol (PVA) hydrogels designed for wound healing, led to more blood vessel generation as compared to heparin-free control samples in the Chick Chorioallantoic Membrane (CAM) assay model (Shahzadi et al., 2016). In addition, also using the CAM assay, heparin bonded chitosan-PVA-PCL hydrogels for wound healing application led to significantly more angiogenesis than sole collagen control gels (Yar, Gigliobianco, et al., 2016).

In addition, block copolymer Konjac glucomannan (KGM) and Hep chemically crosslinked by tyramine by copolymerisation were investigated as injectable hydrogels for their angiogenesis potential via macrophage activation, leading to endogenous growth factor attachment and stimulation of blood vessel formation and maturation (Feng et al., 2017). In addition, Sun *et al.*, (2011) has investigated deproteinated bone matrixes coated by CS and Hep scaffolds for bone regeneration. Hep functionalised scaffolds have led to blood perfusion and micro vessel formation starting at 3 days after implantation in rabbits, and tissue infiltration into scaffolds occurred.

In this study, *in-situ* formed, physically crosslinked pH and thermosensitive hydrogels, composed of counter charged polycomplexes of natural polysaccharides, integrated

with inorganic bone mineral, carbonated HA was chosen to be investigated as a minimally invasive vascular bone regenerative biomaterial. Novel Hep functionalised injectable hydrogel compositions (CS/HA/Hep), produced via a polymer blending method was tried and investigated for different aspects including; angiogenesis by utilisation of the *in-vivo* CAM assay model, bioactivity, degradation, biocompatibility etc.

## 1.12 Aims and Objectives

### 1.12.1 Aims

1. To synthesise and characterise novel in-situ formed pH and thermosensitive injectable hydrogels composed of CS, HA and Hep (CS/HA/Hep) which are designed to be; biocompatible, bioactive, pro-angiogenic and biodegradable temporary supports that stimulate bone angiogenesis and osteogenesis for non-load bearing applications
2. To develop minimally invasive biomimetic hybrid hydrogels functionalised for bioactive features, not only for facilitating interfacial bonding with natural bones but also for stimulating vascular network bridging via porous hydrogels that enhance angiogenesis and eventual bone regeneration

### 1.12.2 Objectives

1. Sol-gel synthesis of composite hydrogels (CS/HA/Hep) will be optimised to obtain homogeneous liquid formulations obtained after pH neutralisation with  $\text{NaHCO}_3$ , which can allow facile manual injections at room temperature, and initiate formation of physically crosslinked hydrogels at average body temperature ( $37^\circ\text{C}$ ) in several minutes.

Hep inclusion via the polymer blending method, making polycomplex hydrogels with counter charged CS, will be optimised to sustain solution homogeneity for its stability, sustainable release and activity.

- 2.** HA synthesis at different conditions will be optimised to adjust its crystal size, shape and heat treatment properties to enhance its bioresorption for better bioactivity performance. HA powders will be characterised, in terms of chemical aspects, by FTIR and Raman spectroscopy, XRD, and elemental analyses by EDS; thermal analyses by TGA/DSC; surface area and particle size measurements by BET; and morphological analyses by SEM technique. Optimal HA powders will be chosen and used in modified hydrogel compositions.
- 3.** The hydrogels will be modified for pre-sterile synthesis of injectable formulations; which includes heat sterilisation of CS dispersions with a polyol (glycerol) additive and utilisation of pre-synthesised carbonated non-sintered HA (HA-5D). The involvement of glycerol aims to improve mechanical properties and hydrogel elasticity.
- 4.** Diverse characterisation techniques of initial and modified hydrogels in their injectable liquid and crosslinked hydrogel forms will be conducted in terms of their physical, chemical, mechanical and biological performance.
- 5.** Injectability will be assessed by qualitative manual injection ratings from a broad range of needles (18-25 gauge) and quantitative analyses by force-displacement measurements during injection at manual injection rates, performed by using a Universal Test Machine (UTM) in compression mode.
- 6.** The gelation features, including sol-gel transition and incipient gelation time will be tested by the test tube inversion method. Rheology measurements will also evaluate viscoelastic behaviours of hydrogels.

7. The chemical and structural analyses of hydrogels will be undertaken by FTIR-ATR and FT-Raman spectroscopy techniques; elemental analyses by EDS and crystallinity and phase analyses by XRD techniques.
8. The mechanical analyses of hydrogels will be conducted by compressive strength measurements by UTM
9. Bioactivity will be evaluated in terms of the capacity of a carbonated apatite mineral layer formation on hydrogels in Simulated Body Fluid (SBF). The associated analyses will be carried out at different intervals of up to 3 weeks comprising weight and pH measurements, chemical analyses by ATR/ EDS and morphological analyses via SEM.
10. Swelling properties of hydrogels in PBS media will be investigated by weight and pH analyses for a period of 72 hours. *In-vitro* degradation properties in the presence and absence of an enzyme (lysozyme) in PBS media will be assessed at different intervals of up to 6 weeks. The weight and pH measurements, chemical analyses by ATR, and morphological analyses via SEM will be conducted.
11. The Hep drug release study will be performed by using a colorimetric Toluidine Blue (TB) assay making a chemical complex with Hep, and light absorption measurements of noncomplexed TB. The local Hep presence will also be determined by TB staining of hydrogels and imaged by optical microscopy.
12. Among *in-vitro* biological tests, cell culture studies covering cell attachment, cytotoxicity, and proliferation analyses will be performed by employing MG-63 osteosarcoma cells with the Alamar blue assay protocol. In addition, ECM deposition on hydrogels will be analysed by Alizarin Red and Sirius-Red assays for calcium and collagen deposition, respectively.
13. *In-vivo* biological characterisation of hydrogels in terms of angiogenesis will be carried out by using an *ex-ovo* chick Chorioallantoic Membrane (CAM) assay

in which thermosensitive liquid hydrogels will be applied on CAM tissue forming *in-situ* crosslinked hydrogels upon incubation at 37.5 °C. The associated histology analyses will be performed for qualitative assessment of angiogenesis with hydrogel tissue specimens retrieved from CAM imaged after sectioning and staining by H&E. The optimal Hep concentrations will be determined accordingly by these angiogenesis studies.

### 1.12.3 Hypothesis

It has been hypothesised that Hep functionalised CS/HA hydrogels (CS/HA/Hep) promote angiogenesis due to the highly anionic nature of Hep that facilitates binding endogenous growth factors. As it has been reported, the Hep molecule has the ability to anchor the majority of angiogenic growth factors with pro-angiogenic receptors. This results in the proliferation, generation of protease and transfer of endothelial cells (Chioldelli et al., 2015; Oliviero et al., 2012). The functionalisation of hydrogels with heparin for its potential physiological binding activity can provide advantages by avoiding utilisation of any external angiogenic growth factors and their non-foreseeable adverse effects. To our knowledge, Hep functionalised injectable CS/HA hydrogel systems that promote angiogenesis in bone regeneration have not been investigated to date. Thus, in this study, novel injectable thermosensitive CS/HA/Hep hydrogels with different compositions are investigated in terms of their contribution to micro-vascularity through *in-vivo* chick embryo's CAM assay model, as well as many other aspects such as injectability, gelation, rheological and mechanical properties, biodegradation, bioactivity etc.

## 2 HYDROXYAPATITE SYNTHESIS AND CHARACTERISATION

### 2.1 Introduction

This chapter describes the synthetic procedures optimized for the preparation of hydroxyapatite (HA) powders by using a sol-gel technique and their characterisations. The effect of initial pH on HA formation has been investigated: an additional pH pre-adjustment (10.5) of reagent solutions prior to the reaction provided acquisition of pure HA with small carbonate substitution; whereas the absence of the pH pre-adjustment (initial pH 8) gave rise to the formation of biphasic HA with  $\beta$ -TCP at high temperatures ( $\geq 950$  °C). The effects of different sintering temperatures (950, 1100 and 1300 °C) on HA particle morphology, size and formation of different phases, were also investigated. All HA powders were characterised by using a range of techniques, including particle size, morphology, chemical and thermal analyses.

### 2.2 Materials and Methods

#### 2.2.1 Materials

The following reagents were used for hydroxyapatite synthesis: calcium nitrate tetrahydrate ( $\text{Ca}(\text{NO}_3)_2 \cdot 4\text{H}_2\text{O}$ ) (Acros Organics, Belgium); di-ammonium hydrogen phosphate ( $(\text{NH}_4)_2\text{HPO}_4$ ) (VWR-Prolabo Chemicals, Germany); ammonium hydroxide ( $\text{NH}_4\text{OH}$ ) of 35% (Thermo Fisher Scientific, UK); and ethanol ( $\geq 99.8\%$ , AnalaR NORMAPUR®, VWR-Prolabo Chemicals, France). The commercial reactor grade ‘R’ non-sintered (P218R) and sinter ‘S’ grade (1300 °C) (P220S) HA were supplied by (Plasma Biotal, CAPTAL®, Buxton, UK) and analysed for comparison. For HA synthesis, de-ionised ultrapure (Type-I) water (Veolia Water Technologies, PURELAB® Chorus, 18.2 MΩ.cm, Wycombe, UK) was used.

## 2.2.2 Sol-gel Synthesis of Hydroxyapatite

Hydroxyapatite powders were synthesised by using a sol-gel technique which was adapted from the protocol reported by Kuriakose et al. (2004). The Sol-gel reaction took place in a three-necked, 2 L round-bottom glass flask placed into an oil bath (silicone oil) which was adjusted to and maintained, at 85 °C for the whole reaction. To prevent evaporation of volatile ethanol, a glass condenser fitted on the top neck of the reactor ensured the refluxing of ethanol. An image of the reactor system during HA synthesis is shown in Figure 2.1.

Calcium nitrate tetrahydrate ( $\text{Ca}(\text{NO}_3)_2 \cdot 4\text{H}_2\text{O}$ ) and di-ammonium hydrogen phosphate ( $(\text{NH}_4)_2\text{HPO}_4$ ) were used as Ca and  $\text{PO}_4$  precursors, respectively. The pH of the solution was adjusted by ammonium hydroxide ( $\text{NH}_4\text{OH}$ ) during the reactions. The reactant solutions were prepared at a stoichiometric ratio of 0.5 M  $\text{Ca}^{2+}$  and 0.3 M  $\text{PO}_4^{3-}$  ions (equal to 1.667). For this, 0.5 M Ca precursor solution was prepared by dissolving the respective amount of  $\text{Ca}(\text{NO}_3)_2 \cdot 4\text{H}_2\text{O}$  in 500 mL of ethanol, while  $(\text{NH}_4)_2\text{HPO}_4$  was dissolved in 500 mL de-ionised water to make a 0.3 M solution.



**Figure 2. 1** HA synthesis reaction set-up: A white HA solution formed during the reaction which took place by constant stirring of reagents in a round-bottom three-necked reactor placed in a silicone oil bath at 85 °C on a hot plate. A glass condenser which has water flow in the outer layer providing refluxing ethanol, which was equipped on top neck of the reactor and a dropping funnel for feeding reagent solution at a side neck, and a thermometer.

After their dissolution, the pH of both Ca and PO<sub>4</sub> precursor solutions were adjusted to 10.5 prior to the reaction. This step was not applied to one sample, referred to as HA-1, so as to investigate the effects of pH pre-adjustment. Afterwards, an (NH<sub>4</sub>)<sub>2</sub>HPO<sub>4</sub> solution was added into the calcium nitrate solution dropwise by maintaining constant stirring. Once the addition of (NH<sub>4</sub>)<sub>2</sub>HPO<sub>4</sub> was completed, the pH of the solution was measured and adjusted to 10. Following the first pH adjustment, this process was repeated every hour during the whole reaction to maintain the pH at 10. After 4 hours of reaction, stirring was stopped and the solution was filtrated by using grade-1 filter papers with 11 µm retention (Whatman<sup>TM</sup>, 125 mm Ø, Buckinghamshire, UK).

After filtration, HA precipitates were washed with deionised water, and this was repeated 4-5 times until a neutral pH (8) was achieved. After washing steps, neutral white HA precipitate was collected in a glass dish. The process steps for acquisition of fine hydroxyapatite powders from wet HA precipitate are presented at Figure 2.2. Thereafter, the drying process of HA samples was carried out at 80 °C for 48 h and further calcinated at 200 °C for 24 h in a furnace (Carbolite® Gero, ELF 11/14B, Hope, Derbyshire, UK). The dried HA powders were then grinded using mortar and pestle.

For the synthesis of sterile hydrogel formulations, dried carbonated HA (denoted as HA-5 D in Table 2.1) was utilised after autoclave sterilisation. Sterilization was carried out by using an automatic autoclave operating at 132 °C and 2 bar in 20 min including heating and ventilation times (5 min each) (LMS, Jencons Scientific Ltd., Leighton Buzzard, Bedfordshire, UK).

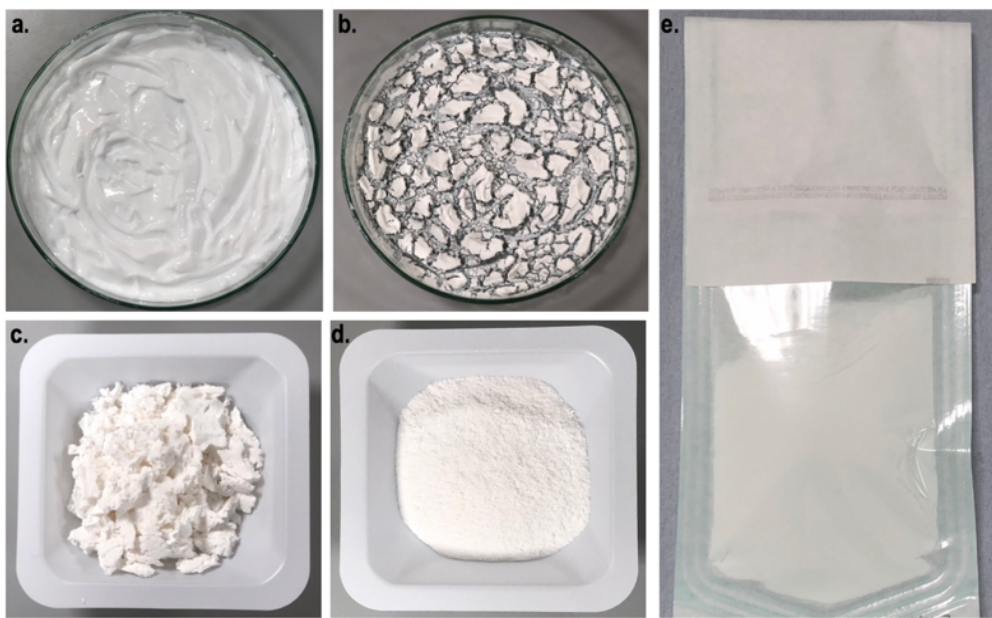


**Figure 2. 2** The production steps of raw hydroxyapatite powders; **a.** wet, neutral HA precipitate obtained after 4 h of reaction, filtration, and washing steps, **b.** HA powder dried at 80 °C for 48 h and calcinated at 200 °C for 24 h in a furnace, **c.** the appearance of dried HA pieces, **d.** fine HA powders acquired after crushing with a mortar and pestle **e.** final HA powders obtained after sieving under 150 µm and steam autoclaved at 132 °C.

According to different synthesis and heat treatment parameters, the produced HA samples and their commercial counterparts used with or without any treatments are summarised in Table 2.1.

The prepared dried HA powders were also further sintered to evaluate the structural and chemical changes as well as stability, of HA products in different temperatures. Sintering treatments were performed at 950 °C, 1100 °C and 1300 °C at a heating rate of 10 °C/min for 6 h in a furnace (Carbolite® Gero, ELF 11/14B, Hope, Derbyshire, UK). Commercial non-sintered HA (P218R) was also sintered at the same conditions of 950 °C and 1100 °C. The sinter grade P220S (1300 °C) was used directly for comparison.

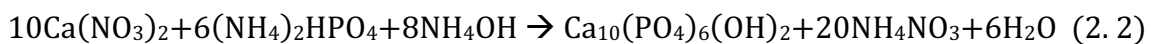
**Table 2. 1** HA samples fabricated by using different synthesis or heat treatment parameters, including commercial HA products as comparison with or without treatments, and their denotations

	HA Samples & Denotation	Process Parameters
Samples	HA-1	pH adjustment only during the reaction: maintaining a constant pH 10
	HA-2	pH pre-adjustment of Ca and PO <sub>4</sub> precursor solutions (10.5) followed by pH adjustment during the whole reaction (10)
	HA-3	The repeat of HA-2
	HA-4	The repeat of HA-2
	HA-5	The repeat of HA-2
Dried samples	HA-1 D	HA-1 dried at 40 °C for 48 h and 80 °C for 48 h
	HA-2 D	HA-2 dried at 40 °C for 48 h and 80 °C for 48 h
	HA-3 D	HA-3 dried at 40 °C for 48 h and 80 °C for 48 h
	HA-4 D	HA-4 dried at 40 °C for 48 h and 200 °C for 48 h
	HA-4 FD	HA-4 freeze-dried by freezing at -30 °C for 15 h and drying at -20 °C for 33 h (total 48 h)
	HA-5 D *	HA-5 dried at 80 °C for 48 h and 200 °C for 24 h, sieved <150 µm and Autoclave sterilised (132 °C, 20 min)
Commercial HA	P218 R	Commercial HA-reactor 'R' grade non-sintered (Plasma Biotal, CAPTAL®, Buxton, UK)
	P220 S	Commercial HA-sinter 'S' grade (at 1300 °C) (Plasma Biotal, CAPTAL®, Buxton, UK)
Sintered samples	HA-1 S 950; HA-1 S 1100; HA-1 S 1300	HA-1 D sintered at 950 °C for 6 h; 1100 °C for 6 h; 1300 °C for 6 h;
	HA-2 S 950; HA-2 S 1100; HA-2 S 1300	HA-2 D sintered at 950 °C for 6 h; 1100 °C for 6 h; 1300 °C for 6 h;
	HA-3 S 950; HA-3 S 1100; HA-3 S 1300	HA-3 D sintered at 950 °C for 6 h; 1100 °C for 6 h; 1300 °C for 6 h;
	HA-4 S 950; HA-4 S 1100; HA-4 S 1300	HA-4 D sintered at 950 °C for 6 h; 1100 °C for 6 h; 1300 °C for 6 h;
	P218R S950; P218R S1100	P218R sintered at 950 °C for 6 h; 1100 °C for 6 h;

\* HA-5 D was used for synthesis of sterile injectable hydrogel formulations

The reaction yields of HA products were calculated based on the ratio of dry mass of HA powders (40 °C for 48 h) and the theoretical mass was counted by the stoichiometric molar ratio of the reagents (Equation 2.1) using the HA synthesis reaction equation (Equation 2.2).

$$\% \text{Yield} = \frac{\text{Experimental mass}}{\text{Theoretical mass}} \times 100 \quad (2.1)$$



### 2.2.3 Characterisation of Hydroxyapatite Powders

In this section, the methods used to analyse properties of prepared raw and sintered hydroxyapatite powders in terms of their chemical, morphological and thermal features are described. The chemical analyses techniques utilised are explained in the following sequence; FTIR-Photoacoustic (PAS) and Raman spectroscopy techniques, XRD, and EDS. Furthermore, morphological analyses carried out by the SEM and BET techniques and the TGA-DSC technique to assess thermal properties of hydroxyapatite samples are elucidated.

#### 2.2.3.1 Raman Spectroscopy

Raman characterisations were performed by a non-invasive dispersive micro-Raman instrument (Thermo Nicolet dxr<sup>TM</sup>, Thermo Fisher Scientific Inc, Madison, WI, USA) for analyses of HA powders equipped with a 532 nm laser. Spectral data was collected by using a 10 mW laser power with 10 sec exposures for 30 scan times. 128 scans were carried out over the spectral range of 4000–400 cm<sup>-1</sup> by using a 25 µm pinhole spectrograph aperture and a x10 magnification objective lens. Prior to experiments, the system was fully calibrated by using a polystyrene standard. HA powders for analyses were mounted as a thin layer in the middle of a glass slide. Thermo Nicolet OMNIC<sup>TM</sup> (Version 9.5.9, Thermo Fisher Scientific Inc, Madison, WI, USA) software was used to obtain data. Spectral data were plotted by using GraphPad Prism (Version 7.0, San Diego, CA, USA) software.

#### 2.2.3.2 FTIR-Photoacoustic (PAS) Spectroscopy

FTIR analyses were performed via a Thermo Nicolet<sup>TM</sup> iS50 FTIR spectrophotometer (Thermo Fisher Scientific Inc, Madison, WI, USA) in conjunction with a photoacoustic (PAS) sampling accessory. HA powders were filled into metal sample holders ( $\varnothing=10$  mm, x 2.5 mm depth) and the sample surface was flattened to level it with the top of the holder. The analyses were carried out in helium media, and carbon background was collected prior to sample collections carried out every two hours. Spectral data was

acquired in the mid-infrared region (4000-400  $\text{cm}^{-1}$ ), at 8  $\text{cm}^{-1}$  resolution, 200 spectrograph apertures accumulating 256 scans.

The spectral data were tabulated using Thermo Nicolet OMNIC<sup>TM</sup> (Version 9.5.9, Thermo Fisher Scientific Inc, Madison, WI, USA) software. Multiple spectra were plotted as PAS intensity versus wavenumbers by using GraphPad Prism (Version 7.0, San Diego, CA, USA) software.

#### 2.2.3.3 X-Ray Diffraction (XRD)

HA powders were characterised by an X-ray diffractometer (Bruker D2 Phaser, Dublin, Ireland UK) equipped with a LNEXEYE detector. Finely ground smooth HA powders were mounted on the background sample silicon wafer substrate PMMA holder ( $\varnothing=25$  mm, x 1 mm depth). Experiments were carried out by using Cu-K radiation ( $\alpha_1=1.5406$  and  $\alpha_2=1.54439$ ). Standard 2.5° soller slit apertures with 1 mm divergence slits and a Ni radiation filter (2.5 mm) were used with a 3 mm of magnetically held air scatter screen. The XRD patterns were acquired over an angle range of  $2\theta=5-80^\circ$  with 0.02° step size using DIFFRAC.SUITE<sup>TM</sup> Software. Sample rotation was set at 15 rpm and lower and upper discriminators were adjusted to 0.11 and 0.25, respectively.

For analyses of XRD data ICDD<sup>®</sup> and ICSD Fiz Karlsruhe GmbH databases were utilised for acquisition of high-quality ranked standards for comparison. The PDF<sup>®</sup>-4<sup>+</sup> software was utilised for data analyses, and some XRD pattern graphs were plotted in GraphPad Prism (Version 7.0, San Diego, CA, USA) software.

#### 2.2.3.4 Energy Dispersive X-Ray Spectroscopy (EDS)

A Schottky Field Emission Scanning Electron Microscope (FESEM) (JEOL JSM-7800F, Tokyo, JAPAN) equipped with an X-ray Energy Dispersive Spectrometer (EDS) with large area (50  $\text{mm}^2$ ) was used for HA analysis. A Silicon Drift Detector (SDD) (Oxford Instruments, UK) was used for elemental analyses of HA powders by EDS.

#### 2.2.3.5 Scanning Electron Microscopy (SEM)

Microstructure analyses of HA were performed by using a Field Emission Scanning Electron Microscope (FE-SEM) instrument (FEI Inspect<sup>TM</sup> F50, Hillsboro, Oregon, USA) after carbon coating of samples. Some samples were analysed after coating with gold (5 nm) and micrographs were acquired using a Schottky FE-SEM (JEOL JSM-7800F, Tokyo, Japan) instrument.

#### 2.2.3.6 Surface Area Measurements by Brunauer-Emmett-Teller (BET)

For surface area measurements of HA powders, BET instrument (3 Flex Micromeritics<sup>®</sup> Instrument Corporation, Norcross, GA 30093 USA) was recruited. The approximately 100 mg of HA sample was analysed in a glass tube by using nitrogen as adsorptive gas at 77 K after degassing overnight at 200 °C.

#### 2.2.3.7 Simultaneous Thermal Gravimetric Analyses & Differential Scanning Calorimetry (TGA & DSC)

The analyses of HA powders were carried out in a simultaneous TGA/ DSC instrument (TA instruments, STD Q600 V20.9 Build 20, New Castle, DE, USA). The temperature was increased from room temperature to 1300 °C at the rate of 5.00 °C/min in air flow of 100.0 mL/min. The data was acquired and analysed by plotting percentage of weight loss, heat flow (W/g) and the 1<sup>st</sup> derivative of the weight loss versus temperature in TA Advantage<sup>TM</sup> (TA Instruments, Thermal Advantage Q Series<sup>®</sup>, Universal V4.5A, New Castle, DE, USA) software.

### 2.3 Results

#### 2.3.1 Synthesis of HA and Reaction Yields

The HA production reaction yields were calculated for the dried forms of two different samples HA-1 and HA-2 (obtained with pH pre-adjustment of reagents). Their chemical

characterisations, to be addressed in detail in following sections, indicated that both samples involved carbonate contents in their dried forms that mostly receded from HA structure in sintering above 950 °C. HA-1 forming biphasic  $\beta$ -TCP phase upon sintering at 950 °C was obtained with a yield of 78 % whereas HA-2 sample preserving pure HA phase at 1100 °C was obtained with a product yield reaching 86 %, counted by their dry mass.

### 2.3.2 Raman Spectroscopy

Raman spectrums of HA-4 samples which were freeze dried HA-4 (FD) and oven dried HA-4 (OD) are compared in Figure 2.3. In comparison to HA-4 (FD), HA-4(OD) had more intense peaks throughout the spectra, indicating a more crystalline structure due to heat treatment. The hydroxyl stretching peaks of HA were assigned at 3571 and 3572  $\text{cm}^{-1}$  for HA-4 (FD) and HA-4 (OD), respectively. As Rehman & Bonfield (1997) state that phosphate bonds are found in four vibrational modes in both Raman and infrared, including;  $\nu_1$ ,  $\nu_2$ ,  $\nu_3$  and  $\nu_4$ . The sharpest intense Raman active  $\nu_1$  phosphate symmetric stretching groups located at 962  $\text{cm}^{-1}$  in oven-dried HA-4 had double the intensity to that of HA-4 (FD) designated at 961  $\text{cm}^{-1}$ (Khan et al., 2013).

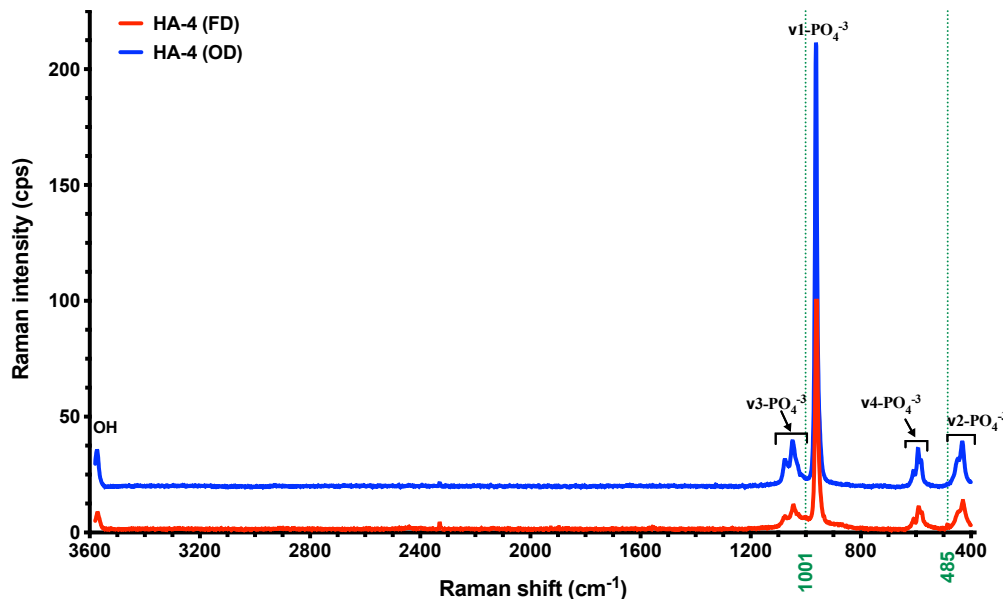


**Figure 2.3** The effect of drying methods on chemical properties of HA: Raman spectrum of HA-4 sample obtained via pre pH adjustment of reagents prior to reaction (equal to HA-2): HA-4 (FD) represents a freeze dried sample (freezing at -30 °C 15 h and drying at -20 °C for 33 h), while HA-4 (OD) is the same sample dried in oven at 200 °C for 48 h.

The  $\nu_3$  (1000-1100  $\text{cm}^{-1}$ ) and  $\nu_2$  (400-500  $\text{cm}^{-1}$ )  $\text{PO}_4^{3-}$  regions were broader in HA-4 (FD) with additional weak peaks at 1001  $\text{cm}^{-1}$  and 485  $\text{cm}^{-1}$ . The sharpest  $\nu_3$  phosphate bond for HA-4 (FD) and HA-4 (OD) were seen at 1045 and 1047  $\text{cm}^{-1}$  respectively, and at an overlapping  $\nu_3$   $\text{PO}_4^{3-}$  vibration assigned at 1075  $\text{cm}^{-1}$  for both. The peaks located at 429  $\text{cm}^{-1}$  and 431  $\text{cm}^{-1}$  for HA-4 (FD) and HA-4 (OD), respectively were attributed to  $\nu_2$  phosphate groups. Also, an overlapping very weak shoulder peak was detected at 446  $\text{cm}^{-1}$ . The  $\nu_4$  asymmetric bending mode of  $\text{PO}_4^{3-}$  bonds were designated at 581, 591 and 607  $\text{cm}^{-1}$  in HA-4 (OD), whereas the corresponding asymmetric phosphate ( $\nu_4$ ) peaks at the spectra of HA-4 (FD) sample were seen at 580, 590 and 608  $\text{cm}^{-1}$  (Antonakos et al., 2007).

The comparative Raman spectrums of HA-2 samples and commercial raw HA (P218 R) after heat treatment at 950  $^{\circ}\text{C}$  for 6 h, which were denoted as HA-2 S-950 and P218R S-950 respectively, are shown in Figure 2.4. The intensities of surface-active functional hydroxyl groups overlapping at 3573  $\text{cm}^{-1}$  and P-O  $\nu_1$  bonds at 962  $\text{cm}^{-1}$  and 963  $\text{cm}^{-1}$  for HA-2 S-950 and P218R S-950 respectively, were much higher in HA-2 S-950, indicating more crystallinity (Khan et al. 2013).

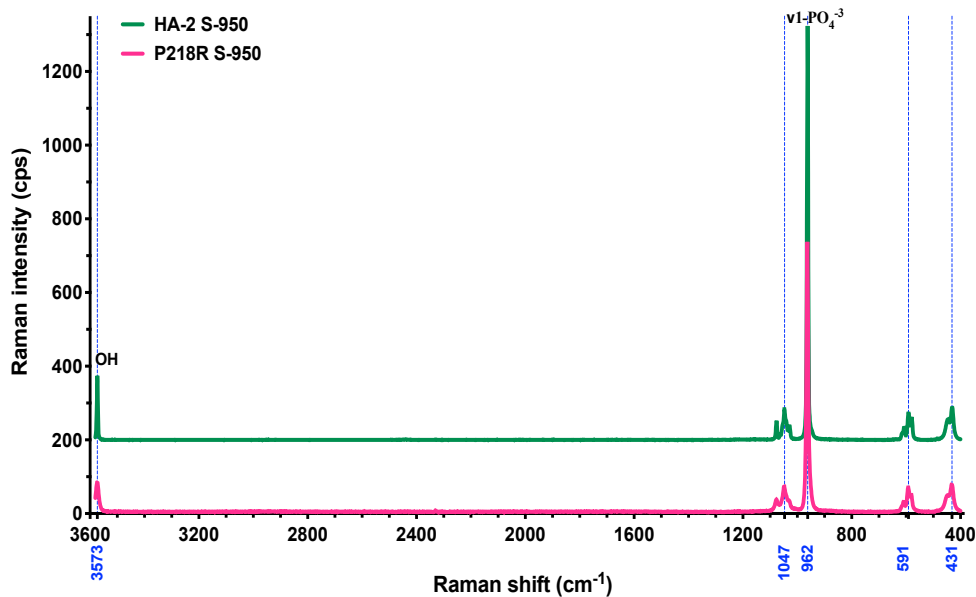


**Figure 2. 4** A comparative Raman spectrum of heat-treated (at 950  $^{\circ}\text{C}$ , 6 h) HA-2 sample and commercial raw HA (P218 R), respectively denoted as HA-2 S-950 and P218R S-950. The vertical blue grade-lines represent the corresponding Raman shift for HA-2 sample spectra.

The most explicit peaks in phosphate  $\nu_3$  mode took place at  $1076\text{ cm}^{-1}$  and  $1047\text{ cm}^{-1}$  in the HA-2 S-950 spectrum, whereas the commercial HA counterpart showed the corresponding peaks at  $1077\text{ cm}^{-1}$  and  $1049\text{ cm}^{-1}$ . The region from  $650$  to  $400\text{ cm}^{-1}$  involved a series of  $\nu_2$  and  $\nu_4$  frequencies due to O-P-O bending vibrations. In this region,  $\nu_4$  and  $\nu_2$  bonds were detected at  $591\text{ cm}^{-1}$  and  $431\text{ cm}^{-1}$  respectively in HA-2 S-950, whereas corresponding vibrations were assigned at  $592$  and  $432\text{ cm}^{-1}$  for P218R S-950 (Elliott, 1994 p.171; Khan *et al.*, 2013).

The chemical and structural effects of an extra pH pre-adjustment (10.5) process applied to reagent solutions prior to HA synthesis reaction were investigated by Raman and FTIR spectroscopy techniques. Except for HA-1, all HA samples including HA-2 were treated with a pre-pH adjustment of 10.5. in addition to a consistent pH adjustment of 10 during the whole reaction. The comparative Raman spectra of dried HA-1 and HA-2 samples denoted as HA-1 D and HA-2 D, respectively are shown in Figure 2.5.

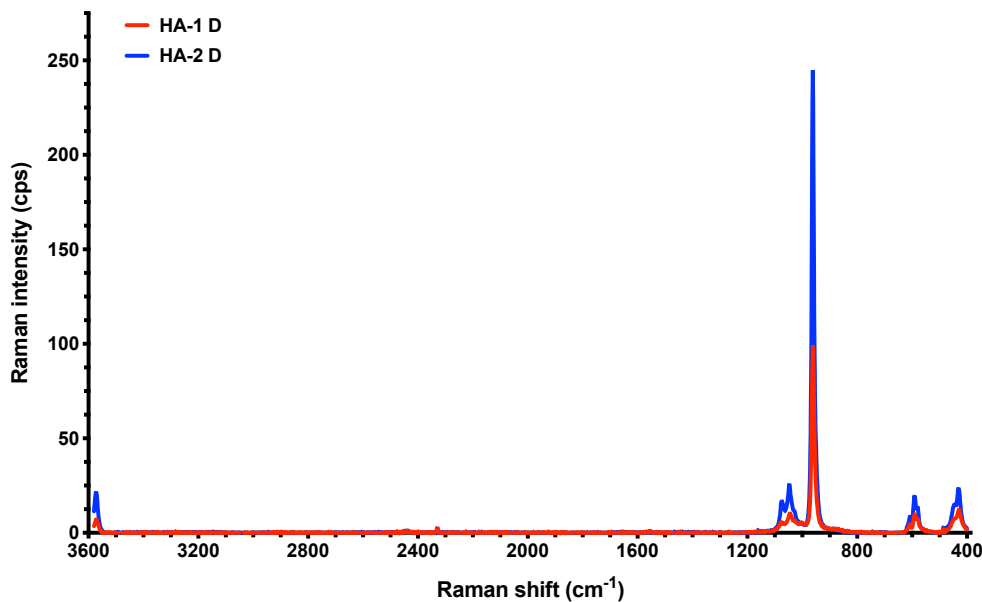


**Figure 2.5** The effects of a pH pre-adjustment process applied prior to HA synthesis reaction. The spectra in blue colour represents an HA-2 sample, acquired with pre-adjustment of pH precursor solutions to 10.5 prior to the reaction. However, HA-1 was not exposed to this additional process: pH was maintained at 10 only during the reaction which was the common process for all HA samples.

The peaks in HA-2 D sample spectra had higher intensity than those of HA-1 D throughout the whole spectral region; especially  $\nu_1\text{ PO}_4^{3-}$  peaks ascribed at  $962\text{ cm}^{-1}$  in HA-2 D was significantly higher than corresponding HA-1 D peak at  $961\text{ cm}^{-1}$ . This

signified that HA-2 D prepared with pH pre-adjustment led to more crystalline structure in comparison to that of HA-1 D. Additionally, hydroxyl peaks were positioned at 3571 and 3572  $\text{cm}^{-1}$  in HA-1 D and HA-2 D, respectively (Khan et al., 2013).

The differences at peak intensities between HA-1 D and HA-2 D spectra were higher in  $\nu_3$  phosphate region compared to  $\nu_2$  and  $\nu_4$  vibrational regions. In HA-2 D spectra, the sharpest  $\nu_3 \text{PO}_4^{3-}$  peak positioned at 1047  $\text{cm}^{-1}$  with an accompanying shoulder at 1075  $\text{cm}^{-1}$ , and HA-1 D possessed the reciprocal Raman shifts at 1075 and 1045  $\text{cm}^{-1}$  as well as a weak peak at 1001  $\text{cm}^{-1}$  that might be assigned for  $\nu_3 \text{PO}_4^{3-}$  bonds or  $\text{HPO}_4^{3-}$  impurities (Antonakos et al., 2007; Khan et al., 2013). The sharpest  $\nu_4$  phosphate groups in HA-2 spectrum were detected at 591  $\text{cm}^{-1}$  with two accompanying shoulders at 607  $\text{cm}^{-1}$  and 580  $\text{cm}^{-1}$ , while HA-1 D possessed corresponding  $\nu_4 \text{PO}_4^{3-}$  bonds assigned at 579, 590 and 608  $\text{cm}^{-1}$ . The strongest  $\nu_2 \text{PO}_4^{3-}$  bond was seen at 429 and 431  $\text{cm}^{-1}$  for HA-1 D and HA-2 D samples respectively, and a weak shoulder overlapped at 446,  $\text{cm}^{-1}$  for both samples. In this  $\nu_2$  P-O region. Also a discrete weak peak emerged at 485  $\text{cm}^{-1}$  and 484  $\text{cm}^{-1}$  in HA-1 D and HA-2 D spectra respectively (Khan et al., 2013; Marković et al., 2011).

Sintering (at 950 °C for 6 h) caused significant changes in the chemical phases of HA-1 in comparison to HA-2 (Figure 2.6). Both HA-1 and HA-2 samples possessed an overlapping  $\text{OH}^-$  stretching vibration at 3573  $\text{cm}^{-1}$ , whereas the peak intensity in the HA-1 sample was lower. The symmetric stretching of  $\nu_1 \text{P=O}$  bonds were located at 962  $\text{cm}^{-1}$  as a single peak in HA-2. However, this  $\nu_1$  phosphate region was broader for the HA-1 sample, where the main peak at 962  $\text{cm}^{-1}$  was accompanied by a slightly visible ridge, a long shoulder at 970  $\text{cm}^{-1}$  and a more explicit sharp shorter shoulder at 948  $\text{cm}^{-1}$  which were attributed to the characteristic, less crystalline  $\beta$ -TCP phase formation in HA (Khan et al. 2013; Cuscó et al. 1998).

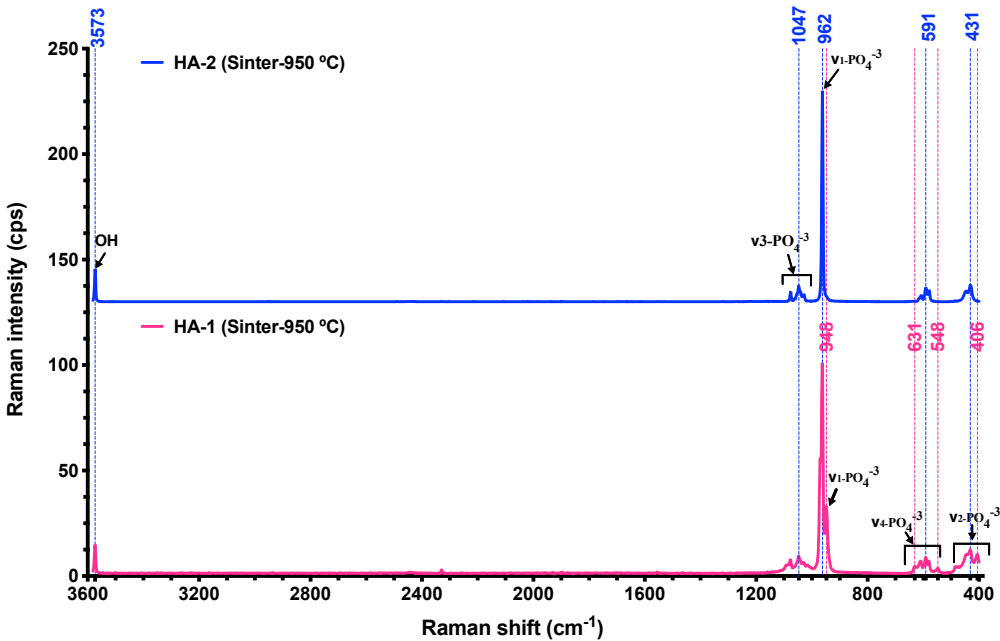


**Figure 2. 6** A contrastive Raman spectrum of heat-treated (at 950 °C, 6 h) samples: HA-2 was obtained via pre adjustment of reagent pH at 10.5 prior to the sol-gel synthesis reaction whereas HA-1 was not exposed to pH pre-adjustment. The pink and blue grade lines represent the wavenumbers corresponding to HA-1 and HA-2 sample spectra respectively.

As reported,  $\beta$ -TCP peaks involving O-P-O bending of  $v_2$  and  $v_4$  vibrational modes assigned over the range 530-645 ( $v_4$ ) and 370-505  $\text{cm}^{-1}$  ( $v_2$ ), were distributed in broader Raman shift regions for phosphate bonds in comparison to HA (Cuscó et al., 1998). The additional phosphate peaks in the HA-1 sample, in comparison to HA-2, were located for  $v_4$  at 548, 631  $\text{cm}^{-1}$ ,  $v_2$  at 406 and 477  $\text{cm}^{-1}$  and  $v_3$  at 1015  $\text{cm}^{-1}$ , presenting as a small peak accompanying a small broad shoulder at 1091  $\text{cm}^{-1}$  (Khan et al. 2013; Cuscó et al. 1998). The presence of  $\beta$ -TCP phase in the HA-1 sample was further confirmed by XRD analyses.

The effects of different sintering temperatures on HA chemical properties were investigated via Raman spectroscopy for the HA-4 sample is shown in Figure 2.7. Temperature increase from 950 °C to 1100 °C led to higher peak intensities of hydroxyl stretching at 3572  $\text{cm}^{-1}$  and symmetric stretching of phosphate peaks overlapping at 961  $\text{cm}^{-1}$ , indicated increasing crystallinity. All HA samples including HA-4 prepared with pH pre-adjustment (of 10.5), except HA-1, were stable up to 1100 °C. As aforementioned, the HA-1 sample formed  $\beta$ -TCP phase upon heat treatment at 950 °C.

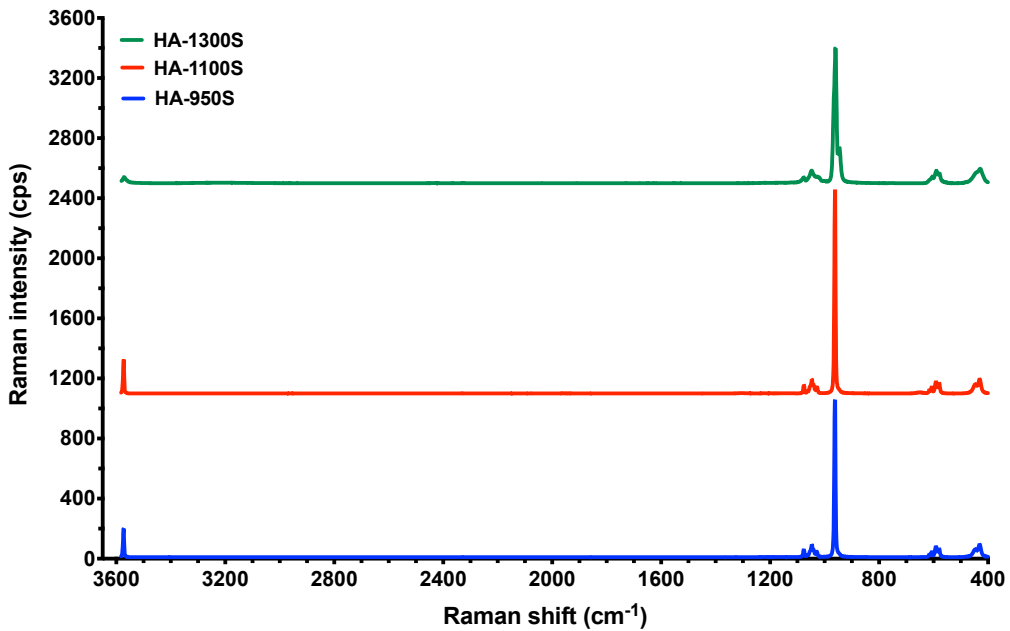


**Figure 2.7** The effects of different sintering temperatures on HA chemical properties. Raman spectrums of a HA-4 sample which is a reproduction of HA-2 dried at 200 °C for 48 h, and sintered at different temperatures including 950 °C, 1100 °C and 1300 °C for 6 h (heating rate: 10 °C/min).

HA-4 sintered at 1300 °C denoted as HA-1300S, have led to decrease of Raman intensities in all spectral regions. In addition, the  $\nu_1$  phosphate peak shifted to 959  $\text{cm}^{-1}$  by forming a shoulder at 946  $\text{cm}^{-1}$ . This was attributed to the characteristic  $\beta$ -TCP peak converting into  $\alpha$ -TCP phase above 1120 °C as has been reported (Bigi et al., 1997; Kwon et al., 2003). The most intense  $\nu_3$  phosphate bonds were expressed at 1047  $\text{cm}^{-1}$  with the sharpest shoulder at 1077  $\text{cm}^{-1}$  and a weak broad shoulder at 1028  $\text{cm}^{-1}$ , possibly raised from HA or  $\beta$ -TCP, and an individual very weak peak at 1005  $\text{cm}^{-1}$ , attributed to the  $\beta$ -TCP phase. The  $\nu_2$  O-P-O bending was located at 579, 589 and 605  $\text{cm}^{-1}$  whereas  $\nu_2$   $\text{PO}_4^{3-}$  bonds were seen at 429  $\text{cm}^{-1}$  (Khan et al., 2013; Marković et al., 2011)

### 2.3.3 FTIR- PAS Spectroscopy

FTIR-PAS spectra of the dried HA samples, HA-1 and HA-2 are shown in Figure 2.8. Hydroxyl stretching bonds were seen at 3569  $\text{cm}^{-1}$  in HA-1 and a more intense peak at 3570  $\text{cm}^{-1}$  in HA-2. The broad region at 2800-3600  $\text{cm}^{-1}$  was attributed to water adsorption. In addition, the peaks at 629  $\text{cm}^{-1}$  and 631  $\text{cm}^{-1}$  for HA-1 and HA-2, respectively were attributed to the  $\text{OH}^-$  libration mode. (Lafon et al., 2008; Marković et al., 2011). P-O  $\nu_1$  stretching at 962  $\text{cm}^{-1}$  overlapped in both samples but this peak was

more intense in the HA-2 sample. In HA-1, there was a single sharp peak at  $1031\text{ cm}^{-1}$  determined as  $\nu_3$  phosphate groups, whereas this region in HA-2 was divided into two sites at  $1032\text{ cm}^{-1}$  and  $1091\text{ cm}^{-1}$  in a broader shape. Peaks over the region of  $500\text{-}700\text{ cm}^{-1}$  were seen for  $\nu_4$ -phosphate bonds. The HA-1 sample exhibited two sharper well defined peaks for  $\nu_4$  phosphate groups at  $564\text{ cm}^{-1}$  and  $602\text{ cm}^{-1}$  while those of HA-2 were found at  $565\text{ cm}^{-1}$  and  $603\text{ cm}^{-1}$ . (Berzina-Cimdina & Borodajenko, 2012; Rehman & Bonfield, 1997).

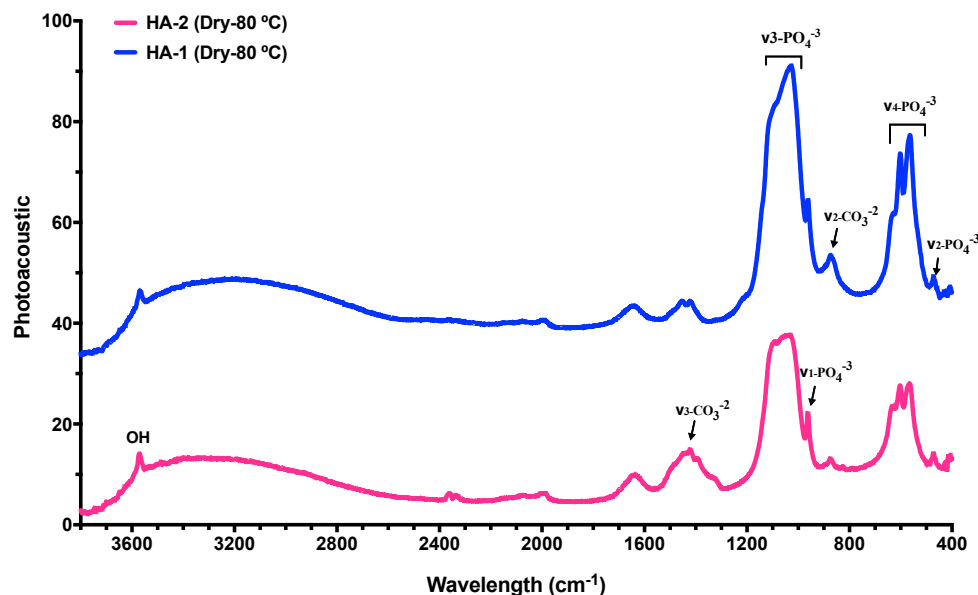


**Figure 2.8** FTIR-PAS spectrographs of dried ( $80\text{ }^{\circ}\text{C}$ - 48 h) HA samples: HA-2 which was obtained by extra pH pre-adjustment (10.5) of reagents prior to the synthesis reaction while HA-1 was not exposed to this process.

As reported in the literature, FTIR active carbonate bonds involve  $\nu_2$ ,  $\nu_3$  and  $\nu_4$  vibrations while Raman detects  $\nu_1$  and  $\nu_4$  vibrational modes. These vibrations can be either A-type replacing with  $\text{OH}^-$  group or B-type substitutions taking the place of  $\text{PO}_4^{3-}$  bonds. HA-1 had a stronger B-type  $\nu_2$  stretching of carbonate bonds assigned at the  $874\text{ cm}^{-1}$  in comparison to that of HA-2 detected at  $873\text{ cm}^{-1}$ . In addition, the peaks at  $1422\text{ cm}^{-1}$  and  $1421\text{ cm}^{-1}$  for HA-1 and HA-2, respectively, referred to  $\nu_3$  stretching of B-type carbonate while an additional A-type carbonate ( $\nu_3$ ) bond appeared at  $1453\text{ cm}^{-1}$  in HA-1 (Marković et al., 2011). The weak peak at  $1394\text{ cm}^{-1}$  in HA-2 was attributed to the remaining nitrate from the reagents (Lafon et al., 2008; Sutter et al., 2005). Peaks at  $1645\text{ cm}^{-1}$  and  $1646\text{ cm}^{-1}$  in HA-1 and HA-2 spectra respectively, were attributed to water absorption peaks in bending mode (Lafon et al., 2008; Marković et al., 2011).

The comparative FTIR-PAS spectrum of dried (80 °C) and sintered (950 °C) HA-1 sample is shown in Figure 2.9. Sintering at 950 °C led to formation of a very intense OH<sup>-</sup> stretching group at 3572 cm<sup>-1</sup> whereas dried HA-1 had a shorter peak at 3570 cm<sup>-1</sup> as a shoulder to H<sub>2</sub>O adsorption over a broad range 2800-3600 cm<sup>-1</sup>. The broad small peak at 1645 cm<sup>-1</sup> was also attributed to water adsorption in the dry sample. (Marković et al., 2011; Rehman & Bonfield, 1997). The dried HA-1 sample showed B-type carbonate v<sub>2</sub> vibrations at 874 cm<sup>-1</sup> and v<sub>3</sub> carbonate bonds at 1453 cm<sup>-1</sup> (A-type) and 1422 cm<sup>-1</sup> (B-type). Sintering at 950 °C caused removal of carbonate bonds (Marković et al., 2011). In HA-1 sinter form, the peaks at the region of 1950-2200 cm<sup>-1</sup> might be attributed to absorbed carbonate peaks, or overtones and harmonic bonds of v<sub>1</sub> and v<sub>3</sub> phosphate groups (Berzina-Cimdina & Borodajenko, 2012; Koutsopoulos, 2002; Ooi et al., 2007).

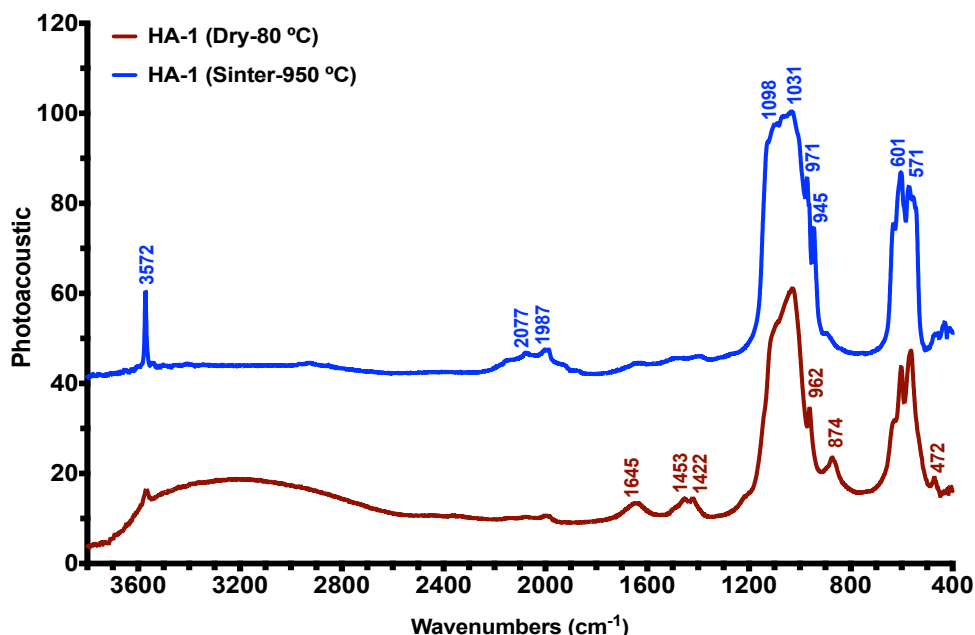


**Figure 2. 9** FTIR-PAS spectra of **a.** HA-1 sample dried at 80 °C, 48 h and **b.** sintered HA-1 sample at 950 °C, 6 h.

A phosphate v<sub>1</sub> band is seen at 962 cm<sup>-1</sup> in dried HA-1 while the sintered sample formed two shoulders at 945 cm<sup>-1</sup> and 971 cm<sup>-1</sup> which were attributed to the characteristic  $\beta$ -TCP phase as reported in the literature (Berzina-Cimdina & Borodajenko, 2012). These results corresponded with Raman data. There was one intense peak assigned for phosphate v<sub>3</sub> vibration at 1028 cm<sup>-1</sup> in dried HA-1 whereas three distinct sites on a broader v<sub>3</sub> region were detected at 1031, 1062, and 1098 cm<sup>-1</sup> in sintered HA-1. Dried

HA-1 had  $\nu_4$  phosphate bonds ascribed at 564 and 602  $\text{cm}^{-1}$  while those of sintered HA-1 shifted to 571 and 601  $\text{cm}^{-1}$  as the intensities of these peaks reversed. Also, a very small peak was detected at 556  $\text{cm}^{-1}$ . The most defined phosphate  $\nu_2$  vibration was detected at 472  $\text{cm}^{-1}$  in dried HA-1 while those peaks in sintered form were shifted to the right with a broader region with its highest intensity at 431  $\text{cm}^{-1}$  (Marković et al., 2011; Rehman & Bonfield, 1997).

The comparative effect of different sintering temperatures on chemical functional bonds in the HA-2 sample, analysed via FTIR-PAS analyses, is presented in Figure 2.10. The increasing sintering temperature between 950  $^{\circ}\text{C}$  and 1300  $^{\circ}\text{C}$  caused gradual decrease at the intensities of hydroxyl peaks at 3572  $\text{cm}^{-1}$ . It has been reported that increasing temperature up to 1000  $^{\circ}\text{C}$  led to increase at the  $\text{OH}^-$  peak intensity, due to more crystalline structure whereas higher temperatures caused partial break down of HA (Ooi et al., 2007). Similarly, very sharp phosphate  $\nu_1$  peaks overlapping at 963  $\text{cm}^{-1}$  gradually lost intensity with increasing temperature.

Interestingly, in the case of 1100  $^{\circ}\text{C}$ -sintered HA, the hydroxyl peak was accompanied with a shoulder at 3543  $\text{cm}^{-1}$  wavelength, ascribed to apatite special  $\text{OH}^-$  stretching vibration as well as a  $\text{OH}^-$  libration peak assigned at 630  $\text{cm}^{-1}$  (Lafon et al., 2008). This HA sample (sintered at 1100  $^{\circ}\text{C}$ ) possessed an additional peak at 711  $\text{cm}^{-1}$  that was designated to weak B-type  $\nu_4$   $\text{CO}_3$ , reported to be found in biological apatite. The  $\nu_3$ - $\text{CO}_3$  bonds located at 1410 and 1474  $\text{cm}^{-1}$  for 950  $^{\circ}\text{C}$  sintered HA became smaller with increasing temperatures. In addition, it had a peak at 893  $\text{cm}^{-1}$  attributed to carbonate stretching in  $\nu_2$  vibrational mode (Antonakos et al., 2007; Marković et al., 2011).

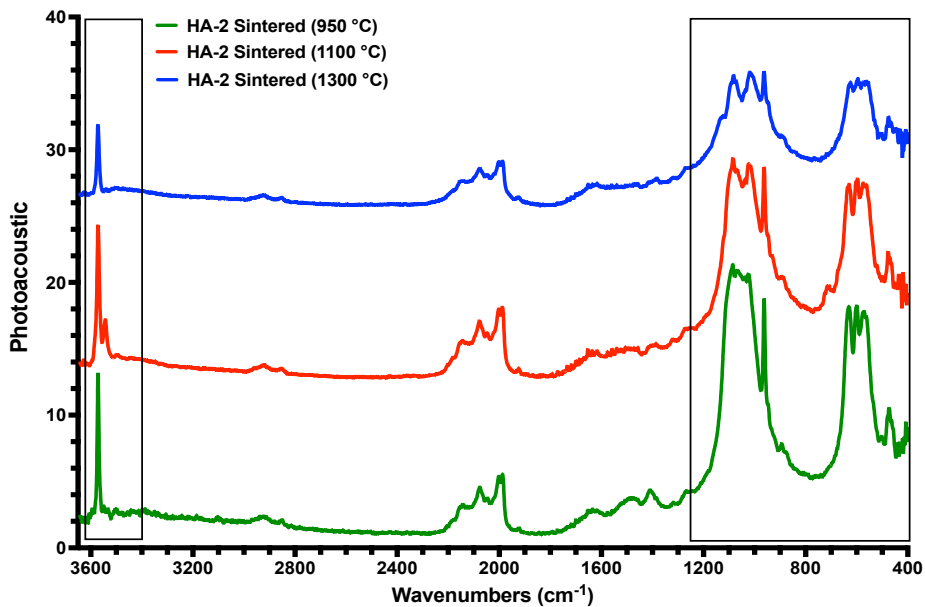


**Figure 2. 10** FTIR-PAS spectral analyses of HA-2 sample sintered at different temperatures: 950 °C, 1100 °C and 1300 °C for 6 h.

The intense and broad peak region at 1000-1100  $\text{cm}^{-1}$  splits into multiple weaker peaks with its summit designated for phosphate  $\nu_3$  bonds manifested at 1024, 1070 and 1086  $\text{cm}^{-1}$  for 950 °C sintered HA. It has been noted that there are superposing B-type  $\nu_1 \text{CO}_3^{2-}$  bonds locating at 1070  $\text{cm}^{-1}$  as reported by (Antonakos et al., 2007; Penel et al., 1998). The temperature increase led to two more explicit peaks at 1023 and 1085  $\text{cm}^{-1}$  for 1100 °C sintered HA and at 1019 and 1082  $\text{cm}^{-1}$ . For HA treated at 1300 °C, those peaks intensities reduced to the same level as the sharp  $\nu_1$  phosphate peak. In contrast,  $\nu_4$  phosphate regions exhibited the opposite trend, showing more intense explicit peaks, located at 571 and 599  $\text{cm}^{-1}$  for 950 °C sintered HA. In this case, peak intensities decreased and shifted to the right upon increasing temperature. For 1100 °C sintered HA at the same region, multiple but weaker phases were detected at 596, 575 and 562  $\text{cm}^{-1}$ ; becoming respectively weaker for the 1300 °C sample. The peak adjacent to the  $\nu_4$  phosphate peaks at 631  $\text{cm}^{-1}$  was assigned to the hydroxyl group. In addition, an explicit sharp peak at 473  $\text{cm}^{-1}$  was assigned to  $\nu_2$  phosphate bonds for 950 °C sintered HA, located at 476  $\text{cm}^{-1}$ , showing gradual decrease of intensity in samples treated with higher sintering temperatures (Lafon et al., 2008).

### 2.3.4 X-Ray Diffraction (XRD)

X-Ray diffraction analyses of HA specimens were utilised to identify phase and crystallinity changes stemming from different synthesis parameters or heat treatments. HA samples were compared with high quality ranked standards acquired from the ICDD® and ICSD Fiz databases. In addition, both the commercial HA P218R (non-sintered) and its sintered forms, at 950 °C and 1100 °C for 6h, denoted as P218R S950, and P218R S1100 respectively, and P220S (1300 °C sinter grade) referred as P220S 1300 were utilised for comparison. The multiple X-Ray diffraction patterns were also plotted in GraphPad Prism (Version 7.0, San Diego, CA, USA) software.

The diffraction patterns of the dried forms of HA-1 and HA-2 almost exactly matched with each other, although HA-2 had higher peak intensities over the whole diffraction pattern, indicating its more crystalline nature (Figure 2.11.). The comparison of HA-2 dried sample with standard hydroxyapatite from ICDD® data base (PDF card no: 01-073-84-19) is shown in Figure 2.12. The main HA peaks were superimposed with HA standard positioned at the following 2θ angles and corresponding planes: 26°(002); 32-34° (211), (112), (300), (202); 40° (310); and 46-55° (222), (213), and (411) (Chaudhry et al., 2006; Choi et al., 2006).

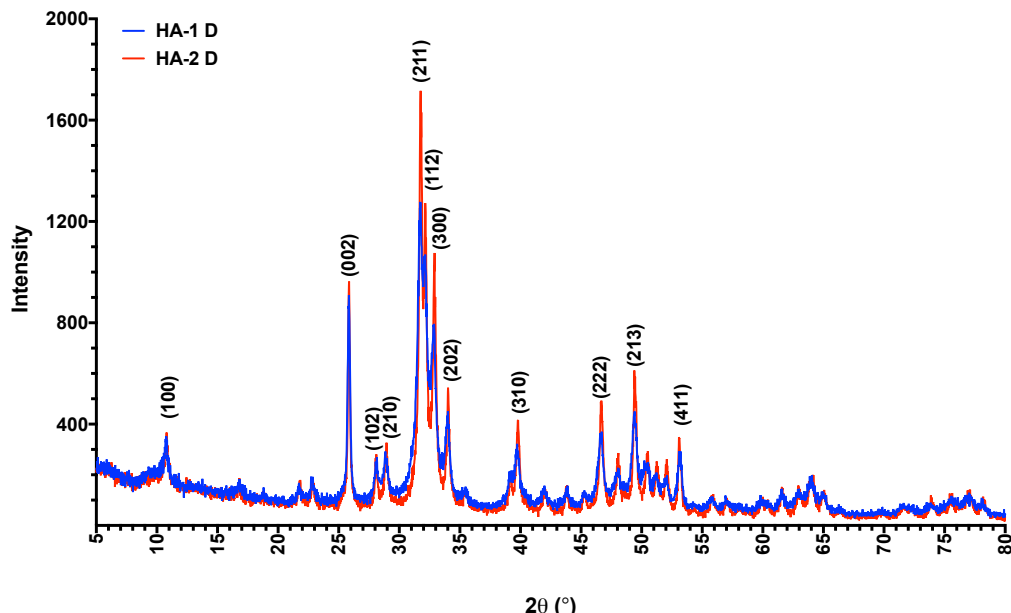


**Figure 2. 11** X-Ray diffraction patterns of dried forms of HA-1 and HA-2 samples obtained through the sol gel method. HA-2 was acquired with additional pre-pH adjustment while HA-1 was not treated with this process.

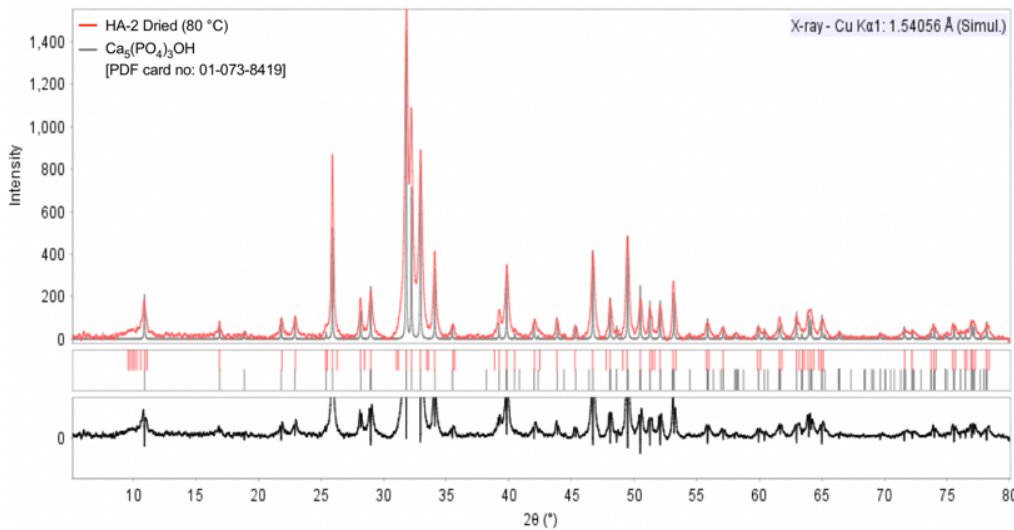


**Figure 2. 12** The phase matching of XRD patterns of the HA-2 dried sample (at 80 °C for 48 h) and the HA ICDD standard (PDF card no: 01-073-84-19)

At the 2θ angle region of 32-34°, three shoulder peaks rose adjacent to the main HA peak at 31.76°. However, the standard HA had discrete peaks in the same region. This was considered to be due to difference at calcination temperature since the peaks in the XRD pattern of the sintered HA sample (HA-2 S950) better matched with the standard HA (PDF card no: 04-016-1647) (Figure 2.13).

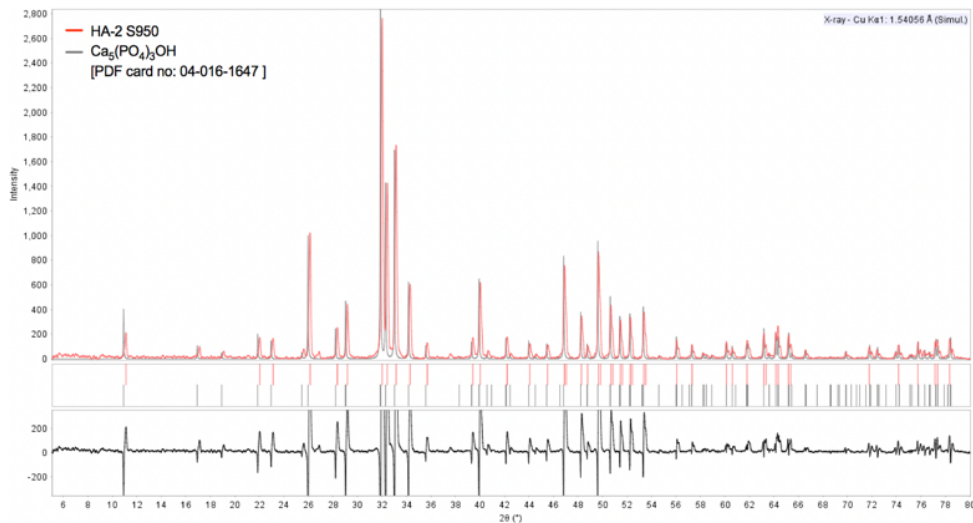


**Figure 2. 13** The phase matching of XRD patterns of HA-2 S950 (sintered at 950 °C for 6 h) and HA ICDD® standard (PDF card no: 04-016-16-47)

In addition, the HA-2 sample preserved the main single pure HA phase after sintering at 1100 °C (Figure 2.14). However, its diffraction pattern has descended up to quarter of the levels of the peak intensities for HA-2 treated at 950 °C. Further crystallinity decrease was observed in HA-2 S1300.

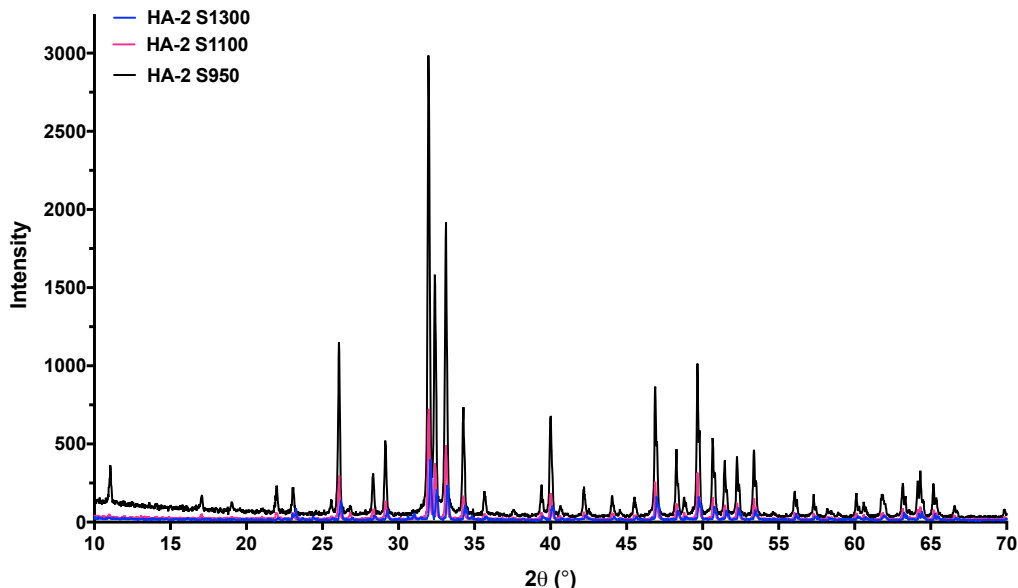


**Figure 2. 14** The comparison of XRD patterns for HA-2 samples which were treated in different temperatures including; 950, 1100 and 1300 950 °C for 6 h.

In the HA-1 sample, the pure HA phase was not stable upon sintering at 950 °C and the formation of tricalcium phosphate biphasic TCP- $\beta$   $\text{Ca}_3(\text{PO}_4)_2$  phase was detected. It has been reported in the literature that  $\beta$ -TCP phase can occur above 700 °C (Figure 2.5.13) (Kwon et al., 2003). The peak differences between pure HA (HA-2 S950) and biphasic HA-1 S950 are comparatively highlighted in Figure 2.15. New peaks detected confirmed  $\beta$ -TCP characteristic peaks (ICSD Fiz, code#97500) at 20 angles of 13.60°, 16.94°, 20.19°, 27.75°, and with the main  $\beta$ -TCP peak appearing at 30.99°.

The  $\beta$ -TCP phase peaks being small individual peaks or shoulders were intermediately into HA by broadening the characteristic region of HA peaks located between 35-40°. In this region, the intensities of the main HA peaks decreased while intervening  $\beta$ -TCP phases extended the area. A sharper peak with a shoulder was observed at the 34.32° angle. The less intense multiple small peaks root from  $\beta$ -TCP phase raised in a broad region between 20 angle of 35-60° in contrast to that of the HA2 S950 sample.

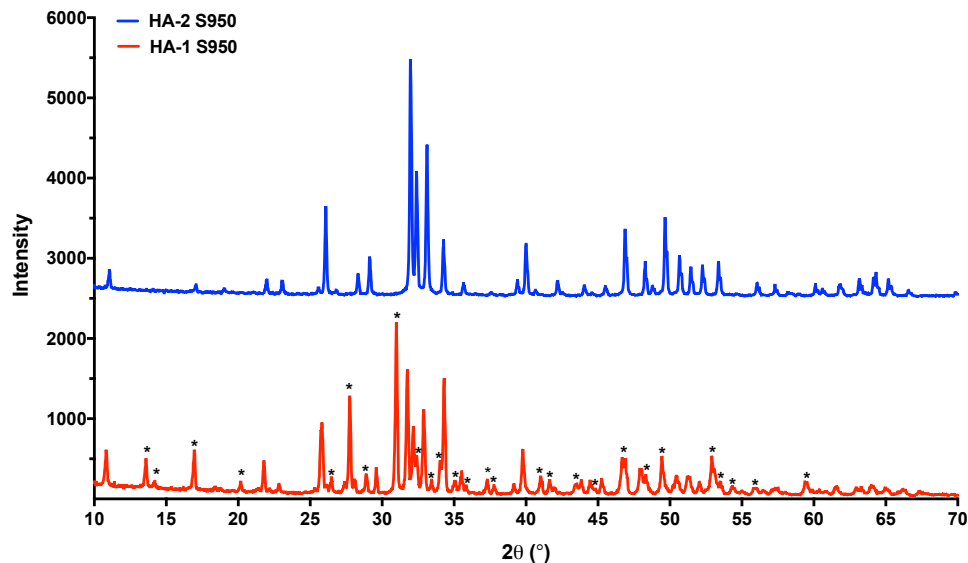


**Figure 2. 15** The comparison of XRD patterns for HA-1 and HA-2 samples which were sintered at 950 °C for 6h entitled as HA-1 S950 and HA-2 S950, respectively. The stars represent the formation of new peaks in the HA structure, attributed to  $\beta$ -TCP phase.

In the diffraction pattern of the HA-1 sample sintered at 1100 °C (HA-1 S1100), the peak positions remained the same as that of HA-1 S950, except for a slight increase at the peak intensities in the  $2\theta$  region of 31-35° and a slight decrease of other peak intensities. This indicated that biphasic HA with  $\beta$ -TCP phase was stable at 1100 °C (Figure 2.16.).

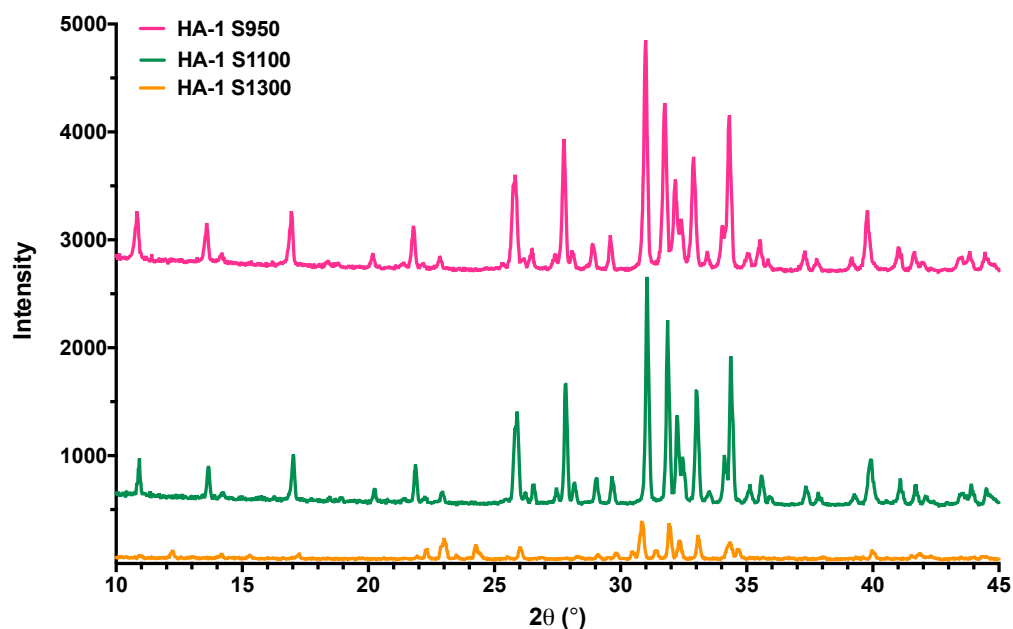


**Figure 2. 16** The comparison of XRD patterns for HA-1 samples which were treated in different temperatures including 950, 1100 and 1300 950 °C for 6 h.

However, the diffraction pattern for HA-1 S1300 was substantially altered, with marked decrease at the peak intensities, with some peaks disappearing, and some new peaks formed. The peak differences between HA-1 S1300 and HA-2 S1300 can be seen in Figure 2.17. The intensities of characteristic HA peaks in HA-2 S1300 at the  $2\theta$  angle of  $32.11^\circ$  and  $32.51^\circ$  were higher than at the intensities of corresponding peaks of the HA-1 S1300 sample, which has additional peaks that may stem from TCP phases.

In comparison to the XRD pattern of HA-2 S1300, multiple new peaks were detected in HA-1 S1300 located in the  $2\theta$  regions of  $10-17^\circ$ ,  $22-25^\circ$ ,  $30-32^\circ$ ,  $41-43^\circ$ . These peaks can be attributed to the presence of less crystalline  $\alpha$ -TCP phase transformed from  $\beta$ -TCP above  $1100^\circ\text{C}$  (Bigi et al., 1997; Kwon et al., 2003). The peaks in HA-1 S1300 at  $2\theta$  angles of  $30.44^\circ$  and  $30.85^\circ$  were attributed to a characteristic  $\alpha$ -TCP phase with a slight shift from the standard (ICSD Fiz, code #923) observed at  $30.34^\circ$  and  $30.70^\circ$ .

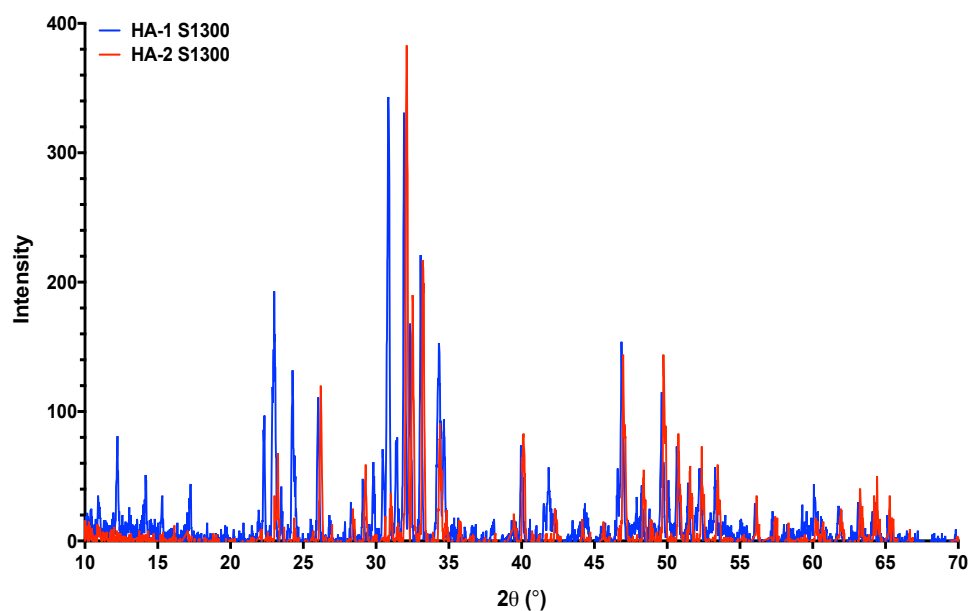


**Figure 2. 17** The comparison of XRD patterns for HA-1 samples which were treated in different temperatures including 950, 1100 and 1300  $950^\circ\text{C}$  for 6 h.

### 2.3.5 Thermal Gravimetric Analyses & Differential Scanning Calorimetry (TGA & DSC)

Thermal properties of HA powders were analysed between  $25^\circ\text{C}$  and  $1300^\circ\text{C}$  by using a simultaneous thermal analysis (STA) technique. The TGA & DSC graphs of the two main samples, HA-1 and HA-2, are shown in Figure 2.18 and Figure 2.19 respectively.

In HA samples, the initial weight loss occurring below 50 °C and continuing onwards up to about 175 °C was considered as due to the removal of adsorbed water. The second step in weight loss occurring between 200 °C and 400 °C was attributed to dehydration of lattice water (Chaudhry et al., 2006; Pazarlioglu & Salman, 2017).

The weight loss in HA-1 sample between 400 °C and 700 °C was attributed to carbonate decomposition (Figure 2.18.) (Chaudhry et al., 2006; Lafon et al., 2003). A total 6.52 % of weight loss occurred up to 750 °C. There was a sudden decrease in weight between 750-780 °C, spiking up at 764 °C at the 1<sup>st</sup> derivative curve which was attributed to the β-TCP phase formation in HA that was also detected by chemical analyses for HA-1 samples sintered at 950 °C and above (Kwon et al., 2003). The weight loss percentage for the regions of 400-700 °C and 750-780 °C were counted for carbonate and β-TCP phase, and were 0.84% and 0.4 %, respectively. The endothermic DSC peak at 1162 °C was associated with β-α TCP phase transition. There was an unexpected weight gain amounting to approximately 1.2 % between 780-1300 °C this might have occurred due to buoyancy effects that stem from gas density changes in temperature, and rapid purge of air (Mansfield et al., 2010).

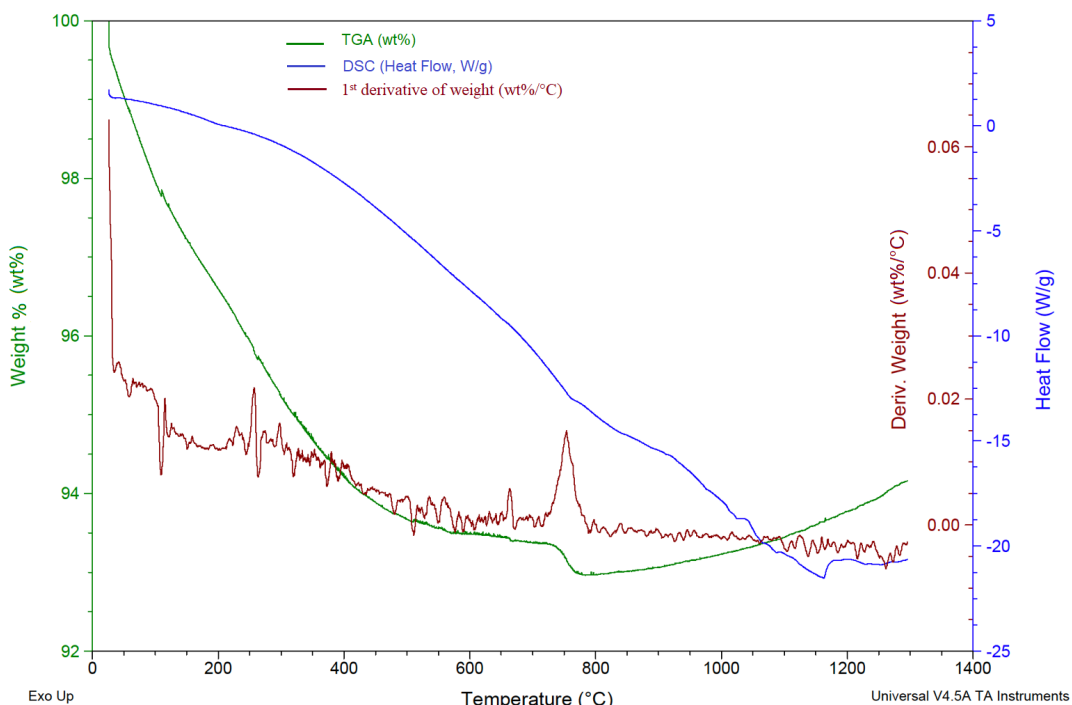


**Figure 2. 18** TGA & DSC graphs demonstrating % of weight and heat flow changes (W/g) versus temperature, as well as the 1<sup>st</sup> derivative of weight (wt%/<sup>o</sup>C) for the HA-1 sample, which was produced without pH pre adjustment of reagents, and dried at 80 °C for 48 h.

At the region of 400-900 °C, in the 1<sup>st</sup> derivative weight loss curve of HA-2 (Figure 2.19) rapid changes were detected at 400 °C, 581 °C, 673 °C and 902 °C, and were attributed to carbonate removal. The maximum temperature for carbonate decomposition, reaching above 900 °C, might be associated with dissipation of A-type carbonate (Lafon et al., 2003). The weight loss between 400-900 °C was counted for carbonate amount and was at 1.55 wt%. In the rest of the analysis, a gradual weigh loss was shown, with an eventual peak raised at 1235 °C that indicated the decomposition of HA. In the HA-2 sample, a total of 7.3% of weight loss occurred during heat treatment between 25 °C and 1300 °C.

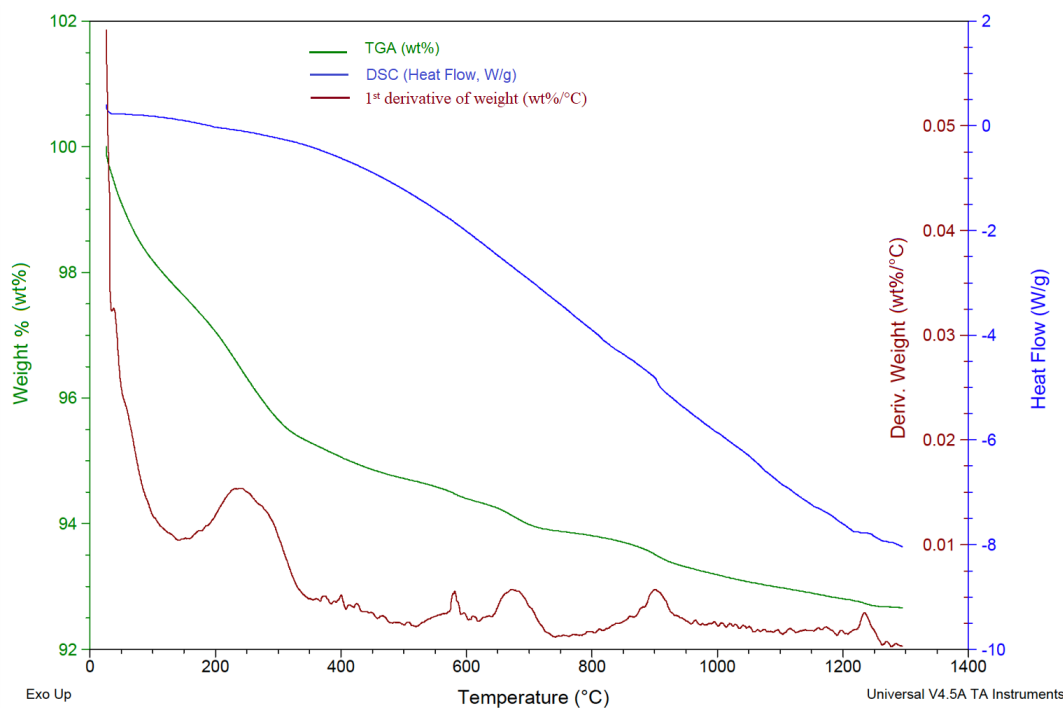


**Figure 2. 19** TGA & DSC graph demonstrating % weight and heat flow changes (W/g) with temperature, as well as 1<sup>st</sup> derivative of weight (wt%/ $^{\circ}$ C) for HA-2 sample which produced with extra pH pre adjustment of reagents, and dried at 80 °C for 48 h.

### 2.3.6 Energy Dispersive X-Ray Spectroscopy (EDS)

This elemental analysis was performed on an autoclave sterilised HA-5 specimen that was chosen for use in injectable hydrogel formulations. The EDS spectra were collected from five different points in the bulk regions of HA powder in an SEM image (Figure 2.20).

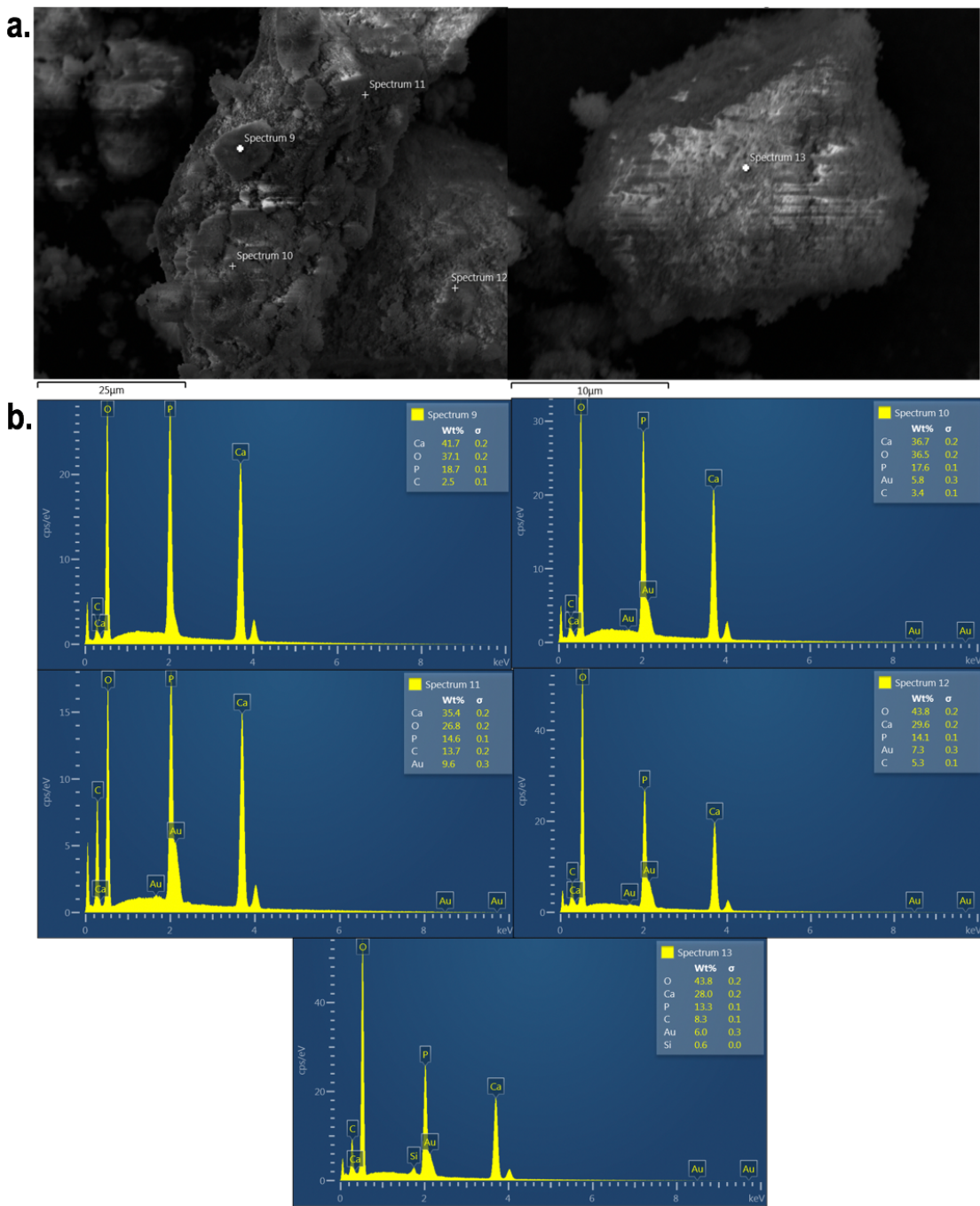


**Figure 2. 20** EDS elemental analysis of HA-5 sample (Dried at 200 °C for 24 h and autoclave sterilised at 132 °C) **a.** SEM image of a bulk specimen region of a hydroxyapatite sample, and the four EDS spectral points (Spectrum 9-12) at left and one spectra point (Spectrum-13) at right **b.** EDS elemental analyses spectra indicating weight percentages of detected elements in the HA structure (Spectrum 9-13).

The Ca/P ratio in the HA sample was counted via the atomic percentage of each elements acquired from five different EDS spectra (Spectra 9-13) including the spectra shown in Figure 2.20, with their mean values summarised at Table 2.2. The Ca/P ratios,

obtained from four different point locations between 1.61 and 1.72, are close to that of stoichiometric value (1.67), except at Spectrum point 11, having a slightly higher ratio (1.87). This high value in the ratio of Ca/P (1.87) might stem from the carbonate substitution in the dried HA form, confirmed by FTIR-(PAS) (Landi et al., 2006). In this location (Spectrum 11), the higher C content, amounted to 13.7 wt % while the atomic percentage of P and O elements were lower, this might indicate occurrence of B-type  $\text{CO}_3^{2-}$  substituting with  $\text{PO}_4^{3-}$ . In other locations, atomic percentages of carbon present were between 2.5 % and 8.3 wt%, resembling that of biological apatite (2.3-8 wt% of carbonate) (Gibson & Bonfield, 2002). From the mean atomic percentage values of elements, the Ca/P ratio of 1.69 was closer to that of stoichiometric HA (1.67).

**Table 2. 2** Atom percentages, Ca/P ratios and their means counted from weight % of elements obtained from EDS analyses of five different points.

Element	Atom % for each EDS spectrum					
	<i>Spectrum 9</i>	<i>Spectrum 10</i>	<i>Spectrum 11</i>	<i>Spectrum 12</i>	<i>Spectrum 13</i>	<i>Mean</i>
<b><i>Ca</i></b>	24.94	22.46	20.94	16.75	15.16	20.05
<b><i>O</i></b>	55.59	55.95	39.71	62.09	59.40	54.55
<b><i>P</i></b>	14.47	13.93	11.17	10.32	9.32	11.84
<b><i>C</i></b>	4.99	6.94	27.04	10.01	14.99	12.79
<b><i>Au</i></b>	0.00	0.72	1.14	0.83	0.66	0.67
<b><i>Si</i></b>	0.00	0.00	0.00	0.00	0.46	0.09
<b><i>Sum</i></b>	100.00	100.00	100.00	100.00	100.00	100.00
<b>Ca/P ratio</b>	<b>1.72</b>	<b>1.61</b>	<b>1.87</b>	<b>1.62</b>	<b>1.63</b>	<b>1.69</b>

### 2.3.7 Scanning Electron Microscopy (SEM)

The morphological analyses of HA samples obtained with different experimental parameters, including drying methods (freeze-drying or oven drying), additional pH pre-adjustment of reagents and sintering at high temperatures (950 °C, 1100 °C and 1300 °C) were investigated by SEM.

The SEM images of the freeze-dried and oven dried samples in different magnifications are shown in Figure 2.21 and Figure 2.22, respectively. Both samples had a spherical agglomerated morphology. At higher magnifications, interconnected porous needle-like crystal morphology of small spheres are seen in the freeze-dried HA sample. The oven dried HA sample shows a more spherical morphology with smoother and bigger agglomerate layers of particles in comparison to the freeze-dried samples.

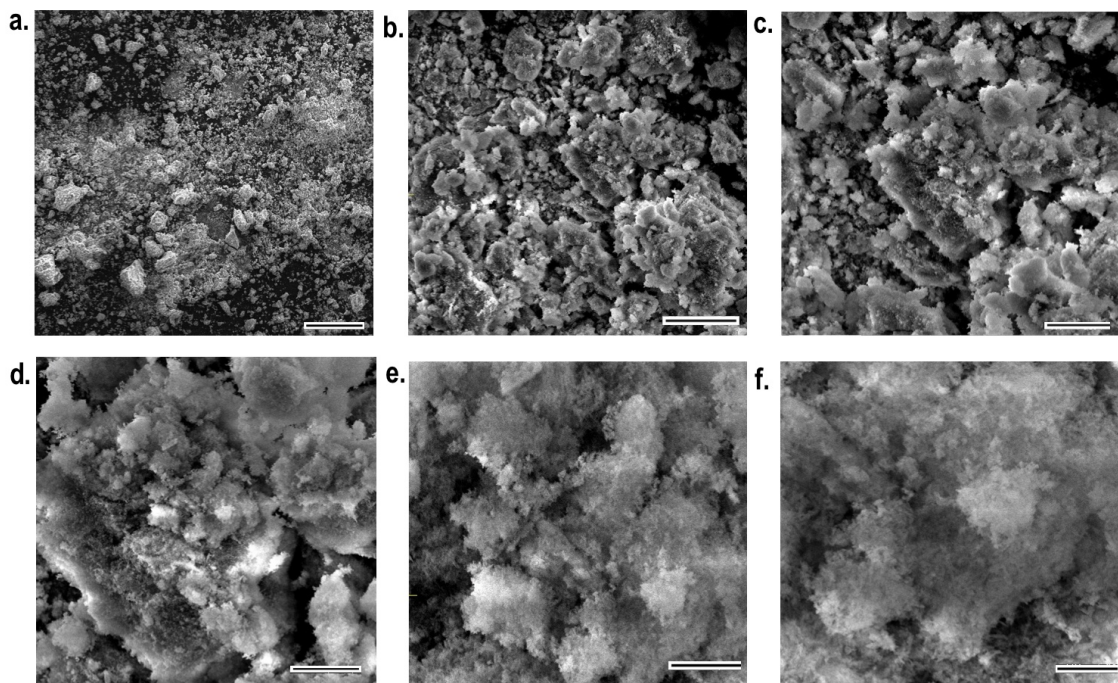


**Figure 2. 21** SEM microstructure images of freeze-dried HA-4 sample with increasing magnifications. Scale bars at image **a.** to **f.** represent 250, 20, 10, 5, 2, and 1  $\mu\text{m}$ , respectively.

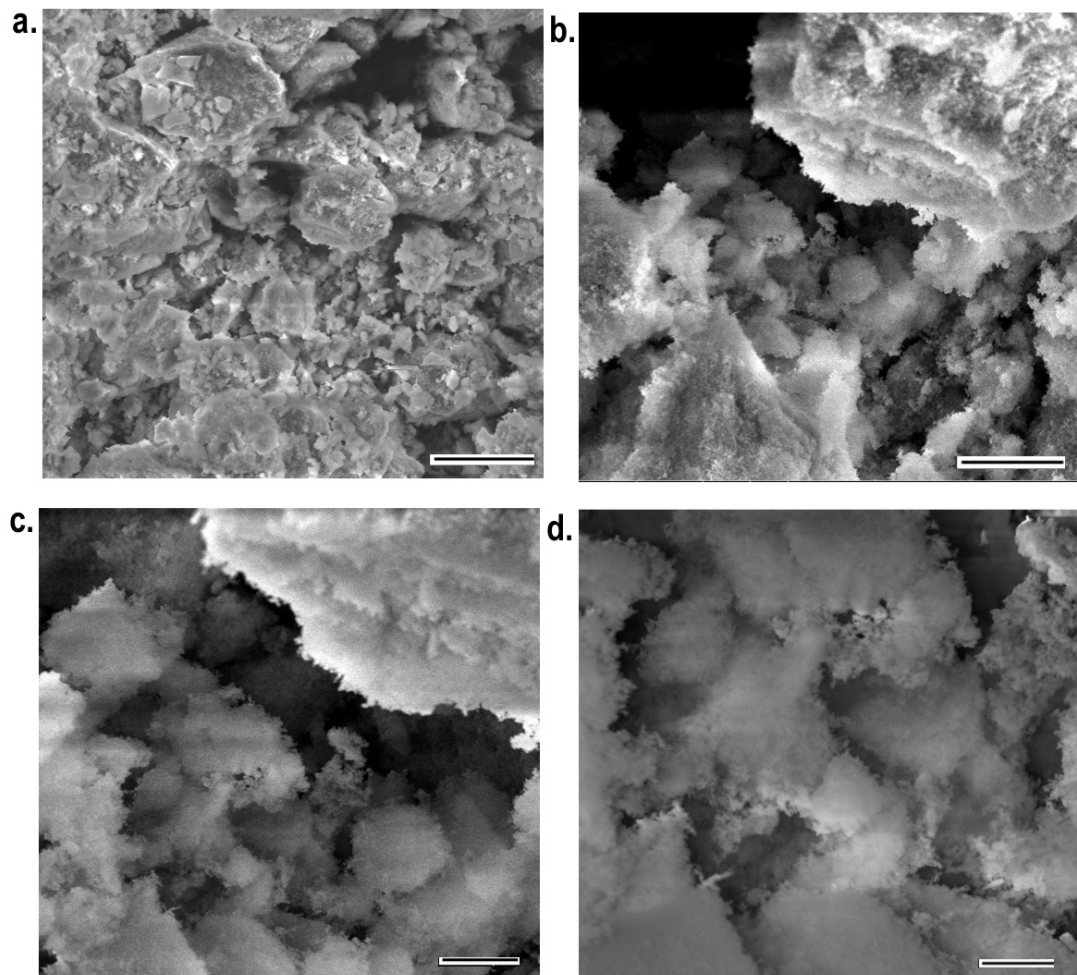


**Figure 2. 22** SEM microstructure images of HA-4 sample dried in an oven at 200 °C for 24 h with increasing magnification. Scale bars at image **a.** to **d.**, represent 20, 5, 2 and 1  $\mu\text{m}$ , respectively.

The sintering of an HA-4 sample at 950 °C for 6 h led to the formation of round crystals having porosity with interconnectivity (Figure 2.23). Those small particles that dispersed at a nanometre scale can be seen in Figure 2.23.d.

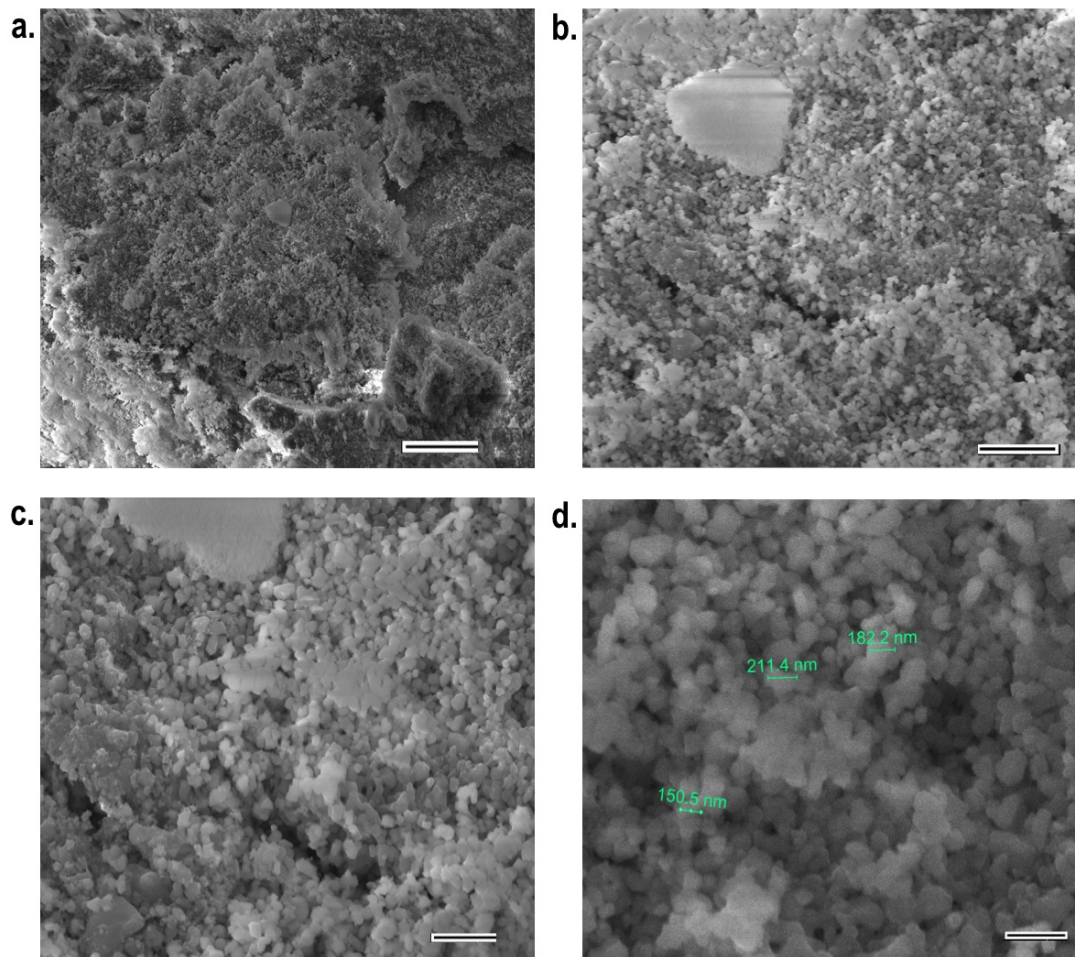


**Figure 2.23** SEM microstructure images of an HA-4 sample dried at 200 °C for 24 h and sintered at 950 °C for 6 h, with increasing magnification. Scale bars from **a.** to **d.**, represent 10, 2, 1 and 0.5  $\mu$ m, respectively.

After sintering at 1300 °C for 6 h, the particles were melted and connected to each other, reducing the particle boundaries, making a compact structure with bigger particles. The smaller particles were also present on the surface of compact HA structures which were attributed to  $\alpha$ -TCP phase crystals which are stable between 1140 and 1470 °C (Khan et al., 2013). This was confirmed by Raman analyses of 1300 °C-sintered samples (Figure 2.24).

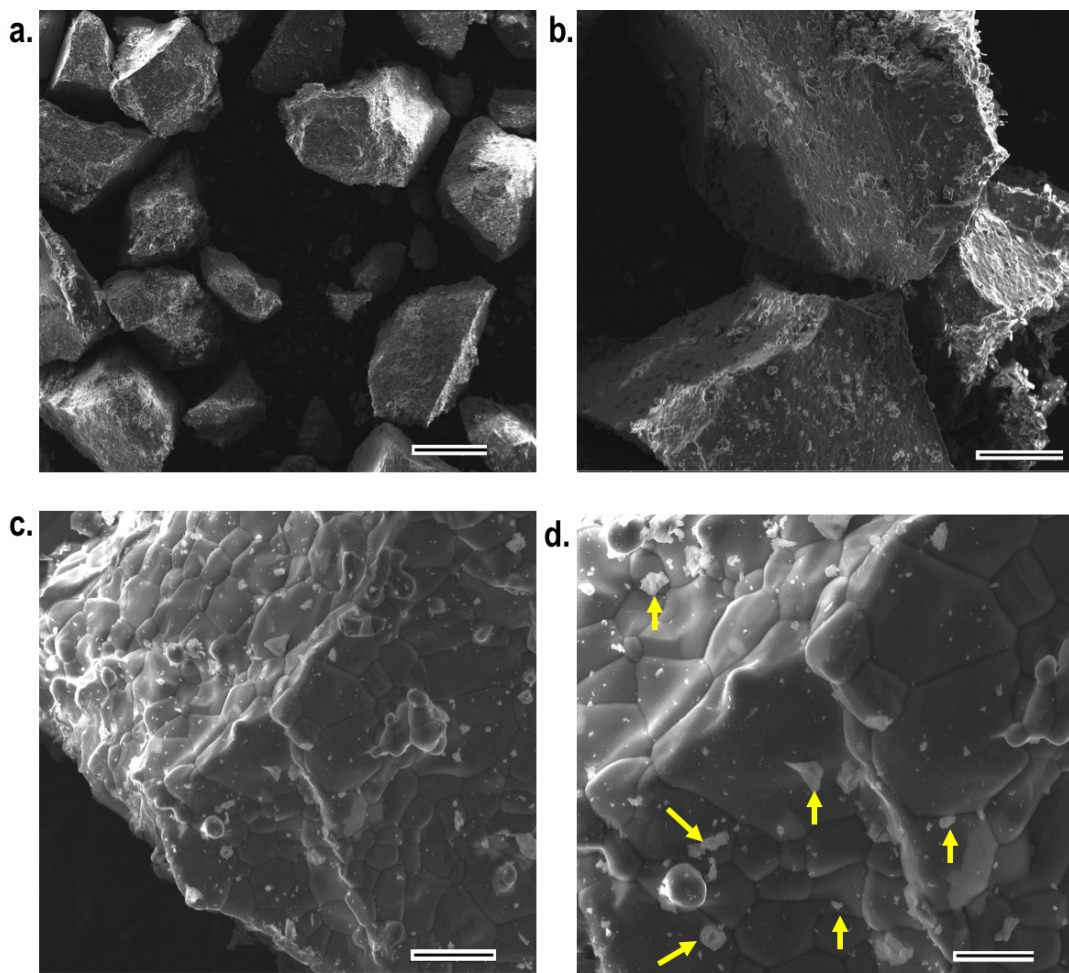


**Figure 2.24** SEM microstructure images of the HA-4 sample dried at 200 °C for 24 h and sintered at 1300 °C for 6 h, with increasing magnification. Scale bars from **a.** to **d.**, represent 250, 50, 10 and 5  $\mu\text{m}$ , respectively. (The small crystals indicated by yellow arrows in image-d were attributed to  $\alpha$ -TCP phase crystals).

The HA-1 sample, which was prepared with reagents with a lower initial pH of 8, differed from other samples in morphology. The HA-1 sample sintered at 950 °C exhibited an amorphous dispersion of very small crystals (Figure 2.25.a.), and at higher magnifications, long rod-like particles with porous and interconnected structure and their agglomerates can be seen (Figure 2.25.(b-d)).

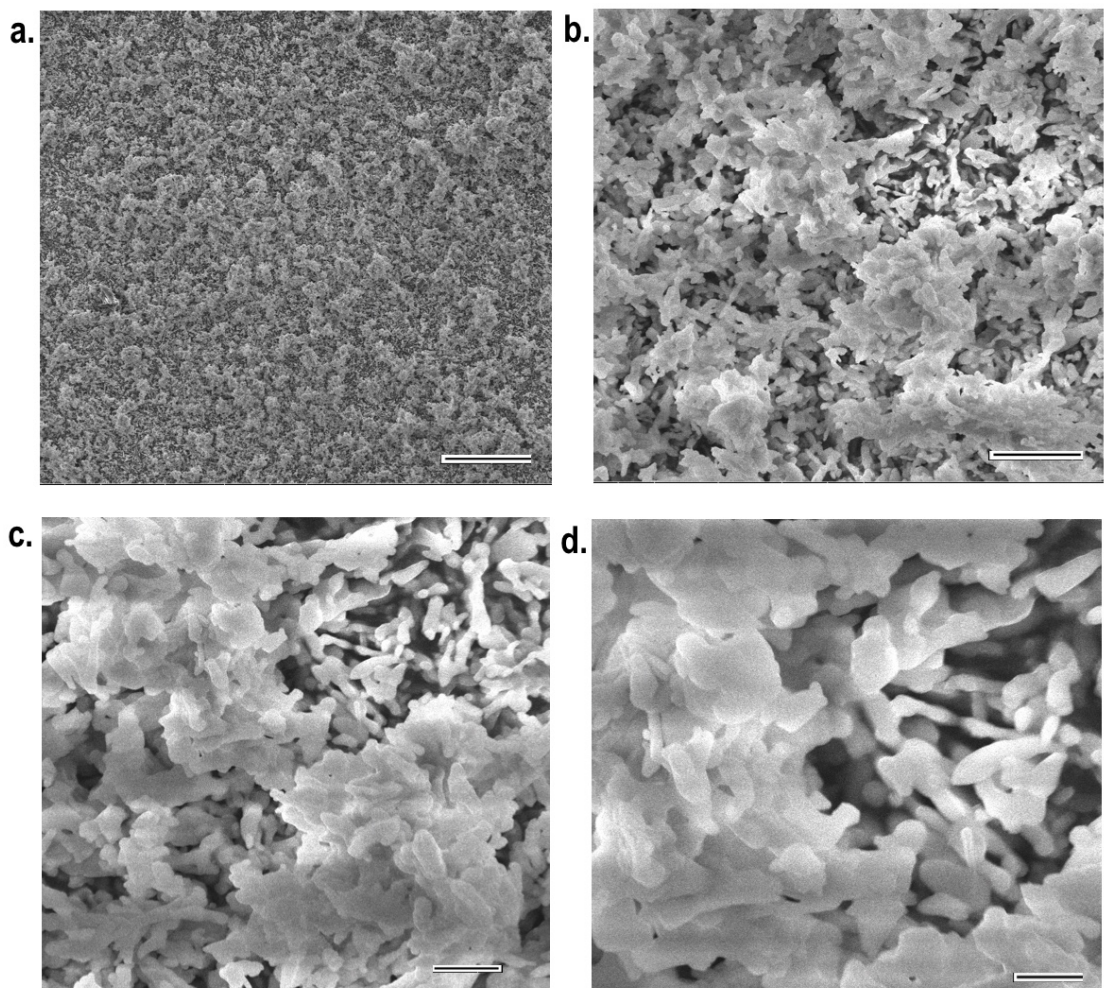


**Figure 2.25** SEM microstructure images of a HA-1 sample dried at 80 °C for 48 h and sintered at 950 °C for 6 h, with increasing magnification. Scale bars from **a.** to **d.**, represent 50, 5, 2 and 1  $\mu\text{m}$ , respectively.

The morphology of the HA-5 D dried HA (80 °C for 48 h, and 200 °C for 24 h) and autoclave sterilised (132 °C for 15 min) sample, selected for injectable formulations, is shown in Figure 2.26. The HA-5 sample showed a nano-sized rough spherical agglomerated morphology possessing nano channels between parallel planes as well as micropores between agglomerates.

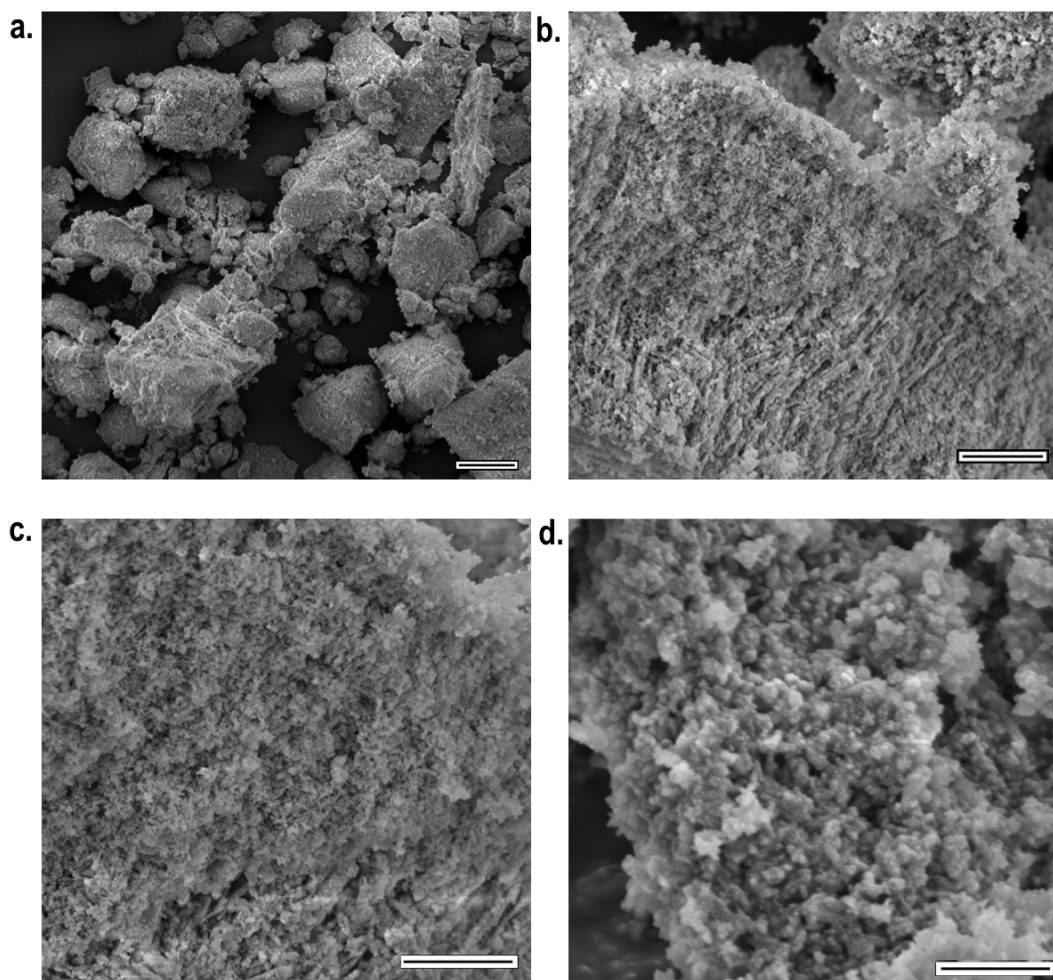


**Figure 2.26** SEM morphology images of HA-5 D dried HA with small carbonate content (80 °C for 48 h, and 200 °C for 24 h) after autoclave sterilisation (132 °C for 20 min) presented in increasing magnifications. Scale bars from **a.** to **d.**, represent 20, 3, 2, and 1  $\mu\text{m}$ , respectively.

### 2.3.8 BET (Brunauer, Emmett and Teller)

The surface area measurement by BET was performed on the HA-3 S950 sample which was sintered at 950 °C. For the HA-3 S950 sample, BET specific surface area, sample density and average pore radius were measured at 52.81  $\text{m}^2/\text{g}$ , 1.262  $\text{g}/\text{cm}^3$  and 1.68 nm, respectively. The  $\text{N}_2$  adsorption isotherms and pore volume versus pore size plots are shown in Figure 2.27.

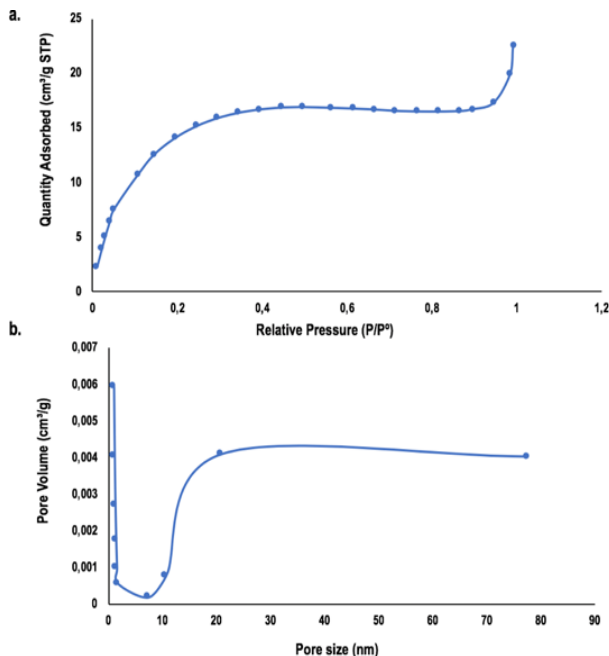


**Figure 2.27** N<sub>2</sub> adsorption isotherms of HA-3 S950 sample: a. adsorbed volume per gram versus relative pressure, and b. pore volume versus pore size

## 2.4 Discussion

HA has undoubtedly, a significant place in bone regeneration among bioceramics due to its unique bioactivity providing chemical bonding with natural tissues (Liu et al., 2013). As reported, increments in bioactivity stimulate cellular activities, osteoconductivity and alkaline phosphate secretion of osteoblasts, which contributes to early healing of bones (Arun Kumar et al., 2015). However, high stability of the crystalline structure of HA retards or hinders its dissolution, which then decreases its efficiency. Bioactivity and the osteoinductive capacity of HA can be improved by enhancing its bioresorption *in-vivo*, which can be developed by involving ionic substitutions in HA lattice structures. In this regard, as reported, carbonate substitution in HA significantly enhances *in-vivo* osteointegration, bioresorbability and biocompatibility (Landi et al., 2003).

Mostly, the sintered form of HA is preferred in tissue engineering applications to increase its mechanical performance. However, in terms of biological properties, recent studies show that non-sintered HA provides quicker bioresorption and better regeneration of the alveolar maxilla bones of pigs (De Carvalho et al., 2019), as well as better osteointegration, tissue infiltration, bioresorption and mineralisation leading

to the faster regeneration of rabbit femur condyles (Dau et al., 2020). These results were associated with the porous and interconnected rough microstructure of non-sintered HA leading to better biomaterial-tissue interaction, bioresorption and regeneration.

Thus, controlling microstructural properties, such as particle size, shape, porosity and phase purity have significant impacts on the performance of the final HA product. These factors are affected by different parameters, e.g. the synthesis conditions, such as solid or wet state synthesis, the reaction temperature, pH, mixing and reaction speed, solvent effect, and heat treatments (Sadat-Shojaei et al., 2013). Depending on these factors, the final HA properties show variations. Therefore, in light of the literature, in this study, the synthesis of HA particles was optimized to acquire nano-porous non-sintered HA crystals, having a small amount of carbonate substitution, with rough, porous and interconnected particle morphology by using a straightforward and cost available method.

In this study, sol-gel synthesis of HA was carried out at a constant 85 °C in the ethanol/water (1:1) solvent media. The effect of two different initial pHs (8 and 10.5), drying types (freeze drying and normal oven drying) and different sintering temperatures (950, 1100 and 1300 °C), on the morphology, chemical structure and the phase purity of HA were investigated. The nano HA powders were produced with an initial pH of 10.5 (for reagent solutions) and dried at (200 °C). This non-sintered HA was obtained with small carbonate substitutions, which occur due to dissolved CO<sub>2</sub> in air without using any external chemical. These optimal conditions have led to promising, thermally more stable, and roughly spherical and porous HA crystals with high surface area (HA-5 D) in dried form that is expected to enhance bioresorption and bioactivity for bone regeneration when involved in injectable hydrogel formulations.

HA produced with the sol-gel technique has also been reported to lead to better bioactivity, leading to efficient carbonated apatite layer formation ensuring better bonding with tissues (Li & De Groot, 1994; Sadat-Shojaei et al., 2013). As has been discussed, the utilisation of ethanol as a solvent for HA synthesis provides a straightforward and cost effective method as compared to the other complex sol-gel

synthesis protocols (Herradi et al., 2018; Kuriakose et al., 2004). Some researchers have used absolute ethanol to dissolve both calcium and phosphate precursors. However, in this work, calcium nitrate was dissolved in ethanol while a diammonium hydrogen phosphate precursor was dissolved in de-ionised water since this reagent could not be dissolved in ethanol. Herradi *et al.*, (2017), has reported a similar reagent-solvent system but with using room temperature synthesis and an additional aging process. However, the thermal stability of this HA was lower since it accumulates  $\beta$ -TCP phase at 750 °C even when the initial pH of reagent solutions was at 10. In the present sol-gel method, the aging process has not been used. After 4 hrs of reaction at 85 °C, homogeneous sol was immediately filtrated, and all side products were removed. Neutral HA crystals were obtained by adjusting pH to about 8 via multiple washing steps. The stoichiometric HA powders obtained were thermally stable up to 1100 °C while a  $\alpha$ -TCP phase was present at 1300 °C sintered HA as confirmed by Raman. Wang *et al.*, (2010), has compared the effects of different solvents such as absolute ethanol, ethanol solution of 50% in water and water. They found that the increasing ethanol ratio in a solvent led to increasing particle size and more aggregation. This was associated with a more alkaline media leading to supersaturation. In the present system, nano sized HA powders with high surface area were obtained with some aggregation.

Chemical analyses by FTIR-PAS, Raman, XRD and EDS have provided substantial information about HA specimens. The effects of different synthesis conditions and heat treatments on HA chemical features as well as cues about structural and functional properties of HA were elaborated in detail. The phase transition points were determined by the simultaneous thermal gravimetric analysis method. The morphological properties were defined by employing SEM and BET techniques.

The pH pre-adjustment had an enormous impact on the final chemical, morphological and thermal properties of HA. The XRD and EDS analyses showed that pure HA phase have a Ca/P ratio of 1.69, which was close to stoichiometric HA with some carbonate substitutions confirmed by FTIR-PAS. The phase purity of HA was achieved by providing the initial pH pre-adjustment (10.5) of precursor solutions before the synthesis reaction where the pH was maintained at 10. The pure HA phase conserved its purity up to 1100 °C and the  $\alpha$ -TCP phase was present at 1300 °C sintered HA. On

the other hand, the exceptional biphasic HA-1 sample which was prepared without pH pre-adjustment (initial pH of precursor solutions were 8) possessed biphasic HA with less crystalline  $\beta$ -TCP at 950 °C and 1100 °C, and an  $\alpha$ -TCP phase seen at 1300 °C. Dardouri, Borges and Omrani, (2017) have reported the occurrence of different phases, such as dicalcium phosphate and calcium hydrogen phosphate at low pH values (8-9.5), while higher initial pH (>10) values increased the HA phase purity. However, they reported that the formation of  $\beta$ -TCP and CaO phases at 1050 °C and  $\alpha$  TCP phase at 1300 °C for the HA samples produced even with an initial pH above 10 (Dardouri et al., 2017).

The initial pH (8 versus 10.5) also influenced morphology of samples. HA-1 S950 sample (initial pH 8) possessed a rod-like morphology although other samples prepared at higher initial pH (10.5) had needle-like crystals forming a spherical morphology. This has been associated with hydroxyl ions and rich alkaline solutions. Higher pH led to more nucleation process rather than crystal growth towards the c-axis. This resulted in an isotropic spherical crystal morphology. Similarly, a direct impact of the initial pH on crystallisation and final HA morphology has been reported in the literature (Dardouri et al., 2017).

The freeze-drying process has advantages since it protects particles from contraction; contrary to other drying processes including higher heat treatments (Wang et al., 2010). It can also reduce the agglomeration of primitive particles. The more uniform and thinner particle sizes could be obtained via freeze-drying processes providing high density and compact HA upon sintering at high temperatures (Hattori et al., 1987; Lu et al., 1998). Raman spectroscopy analyses of freeze-dried HA samples synthesised in this work possessed less intensity of peaks indicating a less crystalline structure than that of oven-dried samples which involve more intense surface active  $\text{OH}^-$  groups. Sphere-shaped crystal agglomerates composed of needle-like crystals were obtained. However, similar morphology and small particles were obtained in oven-dried HA. Since there was not much additional contribution; the freeze-drying method was not used in further studies due to long process time and energy consumption.

FTIR spectroscopy indicated evidence of carbonate substitutions in all dried HA samples. The B-type  $\nu_2 \text{CO}_3^{2-}$  vibrations were dominant in HA-1 (initial pH 8) whereas

the stronger carbonate peaks were observed at the  $v_3\text{CO}_3^{-2}$  region for the HA-2 (initial pH 10.5) sample. The carbonate substitution was considered beneficial since carbonate substitution in HA enhances the bioresorption of HA by decreasing crystallinity and crystal size and thus ensures better anchorage with native tissue leading to regeneration of bone tissues (Chaudhry et al., 2013; Ito et al., 1997; Khan et al., 2013). The sintering at a high temperature of 950 °C and above caused a decrease in the PAS intensities of carbonate peaks. Although high temperature treated HA provides tissue response, and osteoconductivity, it cannot be replaced by host tissue due to its stability. On the other hand,  $\beta$ -TCP resorbed quicker than speed of new bone formation which is undesired as it causes generation of fibrous tissue. Lee et al., (2008) have compared commercial HA (Neobone®),  $\beta$ -TCP (Cerasorb®) and carbonated apatite (CAp) (Cystrans®) products in terms of their osteogenic performance.  $\beta$ -TCP was quickly resorbed in physiological pH while CAp was stable, but it resorbed at pH 5.3 which resembles that of Howship's lacunae. These three compounds were tested on dog mandible bone, and out of all, CAp stimulated regeneration of new bones at the highest scale in 4 weeks while it was gradually resorbing, and had very good anchorage with native bone without fibrous tissue formation. The desired bioresorption behaviour may be related to the smallest particle size and largest surface area that characterize CAp among all compounds (Lee et al., 2008).

De Carvalho et al., (2019) has reported detrimental effects of sintering HA at high temperature (1200 °C) leading to less bone regeneration and biomaterial/tissue interaction when demineralised bovine HA was utilised. On the other hand, non-sintered and lower temperature sintered (820 °C) HA preserved rough surface features, showing better biointegration with tissue and better regeneration of the alveolar maxilla bones of pigs. The highest proportion of bone regeneration and biointegration of HA with tissues was achieved by using non-sintered HA, which was significantly higher than that of sintered HA at 1200 °C.

In addition, recently, the comparative effects of sintered versus non-sintered silicate substituted commercial HA for regeneration of rabbit femur condyle bones were investigated histologically. The amount of newly regenerated bone and bioresorption of silicate substituted HA were found to be significantly higher than those of its sintered counterparts. The bioresorption of composite material from HA and poloxamer led to

further bioresorption as well as soft tissue formation. The beneficiary effect of non-sintered HA is related to hybrid porosity, including nano and micro pores facilitating cell activities, tissue infiltration and terminal mineralised tissue formation (Dau et al., 2020). As aforementioned, the carbonated non-sintered HA with smaller size, greater surface area and lower crystallinity, paves the way to faster bioresorption, better osteoconductivity and enhanced osteoinductivity. Therefore, a carbonated non-sintered HA-5 specimen was chosen for injectable hydrogel formulations. This HA-5 sample, prepared with pre-pH adjustment and a normal oven drying process (80 °C for 48 h and 200 °C for 24 h) was utilised in hydrogels after heat sterilisation (132 °C, 2 bar). It was made up of small spherical crystals forming long parallel planes in spherical or rectangular agglomerates with a range of particle sizes.

In bioactivity studies in SBF, hydrogels containing HA-5 stimulate the formation of active carbonated apatite layers. This was confirmed and is described in detail in Chapter 5. The small carbonate content, which occurs naturally during the reaction, due to dissolved CO<sub>2</sub> in air without using additional chemicals, seem beneficial to stimulate bioresorption of HA. Also, the presence of surface-active hydroxyl groups was presumed to provide covalent bonding with the matrix polymer in hydrogels. Furthermore, the biomimetic sol-gel synthesis leading to nano-sized and high product yield (86%) in non-sintered HA powders, can also reduce the energy and cost in comparison to other synthesis conditions, e.g. high temperature treatments and freeze-drying.

## 2.5 Summary and Conclusions

The chemical and structural properties of different prepared HA samples were elaborated on by detailed complementary analyses, using Raman and FTIR spectroscopy. In addition, XRD analyses have shown that crystallinity and different phases occurred due to the heat treatments. The Ca/P ratio in HA was determined by EDS analyses, while SEM analyses provided the morphological information of the HA powders.

The nano-sized HA powders with high surface area (52.81 m<sup>2</sup>/g for HA-3 S950) were obtained by using a sol-gel technique. Initial pH played a very significant role in particle

shape, crystallinity and phase purity of the HA particles. Two main types of HA specimen were acquired with different initial pH conditions and with small amounts of carbonate substitution in their dried forms. The less crystalline HA-1 sample with initial pH of 8 acquired with 78 % yield in its dried form possessed  $\beta$ -TCP and  $\alpha$ -TCP phases when sintered at 950 and 1300 °C. This was confirmed by XRD, Raman and FTIR-PAS techniques. The phase transition points were present at 764 °C and 1162 °C and determined by TGA&DSC analyses, respectively for  $\beta$ -TCP and  $\alpha$ -TCP phase occurrence. The biphasic HA exhibited more amorphous and rod like morphology and was different from the pure HA counterpart.

On the other hand, the HA-2 sample prepared with an additional pH (10.5) pre-adjustment of the solution, prior to the reaction, in which pH was maintained at 10, provided acquisition of pure HA with a Ca/P ratio of 1.69 which was close to stoichiometric HA with a high product yield of 86 %. FTIR-PAS analyses showed formation of A and B type carbonate substitutions in HA which account for 1.55 % wt determined from TGA&DSC. In addition, EDS analyses showed that carbon contents were in the range of 2.5-14 %wt. at different HA particle locations. Carbonate substitution is a desired property of HA for biomedical applications since carbonate ions enhance bioresorption and tissue-biomaterial interactions and the final regeneration process (Chaudhry et al., 2013; Ito et al., 1997; Khan et al., 2013). HA was thermally stable at 1100 °C while  $\alpha$ -TCP phase was present in 1300 °C-sintered HA, leading to a significant decrease in crystallinity. In both the freeze-dried and oven dried forms, needle-like particles forming spherical agglomerates were seen in the SEM analyses. Upon sintering of oven-dried HA, spherical nano particles with micro-porosity were obtained at 950 °C, whereas the integration of the grain boundaries of the crystals led to a compact structure of HA at 1300 °C.

In conclusion, in this study non-sintered and carbonated HA (initial pH 10.5) were chosen to be used for the development of injectable modified hydrogel formulations; due to its purity, nano-sized particles with high surface area, and its hybrid nano and micro porosity. In the light of the literature, the chosen HA features (HA-5 D) to be utilised in injectable hydrogel formulations were presumed to facilitate better bioresorption and cellular activities and hence, can lead to better binding properties with tissues and to better stimulate bone regeneration.

### 3 CHITOSAN/HYDROXYAPATITE/HEPARIN BASED pH AND THERMOSENSITIVE INJECTABLE HYDROGELS

#### 3.1 Introduction

This chapter describes novel *in-situ* formed injectable pH and thermosensitive liquid hydrogels. These hydrogels were neutralised by  $\text{NaHCO}_3$  at 4 °C, which formed ionically crosslinked hydrogels (CS/HA/Hep) at body temperature. It is believed that upon injection *in-situ* at targeted bone defects, they will support vascularized bone regeneration and act as drug delivery tool. The first set of hydrogels, denoted as ‘initial hydrogels’, were synthesised by using an aseptic technique without the CS sterilisation step, and commercial non-sintered HA was involved in their synthesis. The physical and chemical characterisations of initial hydrogels are covered in this chapter and the investigated biological characteristics, including biocompatibility and angiogenesis, are dealt in Chapter 5. A second set of experiments covered the modification of the initial hydrogels, referred to as ‘modified hydrogels’. The modified hydrogels were produced to ensure a totally sterile synthesis technique involving CS pre-sterilisation to facilitate sterile formulations. Meanwhile it was also aimed to enhance the mechanical strength of initial hydrogels. CS sterilisation was ensured by autoclaving of chitosan-water dispersion by the addition of glycerol to protect CS from heat and improve elasticity of the hydrogels. In addition, pre-synthesised HA-5 powder (details are elaborated in Chapter 2) was selected and utilised after autoclaving in modified hydrogels owing to its non-sintered form containing some carbonate substitutions that possess large surface area due to its rough porous spherical morphology. This was expected to significantly improve its bioresorption leading to the desired final bioactive features. The main physical and chemical characterisations of modified hydrogels are described in this chapter. Further characterisations of modified hydrogels including swelling, biodegradation, bioactivity and Hep release studies are shown in the following chapter (See Chapter 4), while angiogenesis studies are given in Chapter 5.

Most of the characteristics of initial and modified hydrogels are discussed in this chapter. These include pH measurements, solution storage stability, and gelation capacity tests via determination of incipient gelation time (at 37 °C) by the test-tube inversion method. Rheology measurements were used for sol-gel transition temperature and viscoelastic behaviour analyses. Injectability tests by qualitative and quantitative measurements, morphology analyses by SEM, mechanical characterisations by compression tests, thermal analyses by TGA/DSC were also performed. The chemical characterisations of hydrogels were carried out through FTIR-ATR and FT-Raman spectroscopy, and XRD analyses.

The homogeneous liquid formulations were obtained with facile injectability and a thermosensitive gelation capacity that initiates within a few minutes and settles with time at average human body temperature, 37 °C. Modification of the hydrogels that allowed for further pH neutralisation of up to 6.5 while maintaining the homogeneity of injectable solutions, showed faster gelation, starting within 2-3 min, resulting in increased physiological pH ranges. Hydrogel modification by a glycerol additive in sterile technique has improved elasticity of hydrogels and mechanical properties. Furthermore, the final pH of the solutions in modified formulations, greatly affected the rate of crosslinking, as well as the morphological and mechanical properties of the hydrogels. SEM analyses of higher pH specimens showed a flat bone like hierarchical morphology containing macropores separated by dense interlocking micropore walls; whereas a less crosslinked more homogeneous microporous structure was obtained using lower pH hydrogels (6.2-6.4 in solution). The hydrogels obtained with higher pH solutions (6.4-6.5) had significantly higher mean for Young's modulus and compression strength accounting for 1.51 MPa and 310 kPa at 75 % strain, respectively for a composite S0 sample (CS/HA/Hep). The injectability of both initial and modified hydrogel solutions showed similar trends with the maximum injection force by 19 G needle measuring around 15 kPa. However, after 24 h of storage, modified liquid hydrogels were more viscous, reducing their injectability while they maintained a constant flow from a needleless syringe. In this instance, adhesive solution properties were observed as well.

### 3.2 Materials and Methods

The materials used were: chitosan (medium molecular weight (CS) (100–300 kDa, Deacetylation degree:  $\geq 90\%$ )), glacial acetic acid (Aca), glycerol (99%) (from: ACROS Organics™, Thermo Fisher Scientific, Geel, Belgium), sodium bi-carbonate ( $\text{NaHCO}_3$ ) (purchased from: Fluka®, Sigma Aldrich, USA), and sodium bovine heparin (Injectable grade, 156 IU/mg) (gifted by Extrasul (Ext. An. Veg. LTDA, Sao Paulo, Brazil)), and medical grade commercial non-sintered hydroxyapatite used in synthesis of initial injectable hydrogel formulations (HA) (CAPTAL® ‘R’, Batch No: P218R) (supplied by (Plasma Biotal, Buxton, UK)). The non-sintered carbonated HA powders (HA-5 D) were synthesised as described in Chapter 2 and utilised for synthesis of modified injectable hydrogels. De-ionised ultrapure (Type-I) water (Veolia Water Technologies, PURELAB® Chorus, 18.2  $\text{M}\Omega\text{.cm}$ , Wycombe, UK) was also used for all synthesis works.

### 3.3 Sol-gel Synthesis of pH and Thermosensitive Injectable (CS/HA/Hep) Hydrogels

A sol-gel synthesis technique was applied to manufacture the thermosensitive injectable formulations, which includes both the acquisition of a homogeneous solution at 4 °C and the formation of ionically crosslinked hydrogels at 37 °C stimulated by both pH and temperature. Sodium bicarbonate ( $\text{NaHCO}_3$ ) a salt which is a weak base, was used as a neutralising agent, and mild reaction conditions were provided by cold reagent solution mixing which took place in an ice bath at 4 °C.

All reactions were carried out in sterile conditions. Hydrogels were prepared in a sterile fume hood by using a pre-sterile synthesis technique. All glassware and tools used in the synthesis were sterilised by using an automatic steam autoclave (LMS, Jencons Scientific Ltd., Leighton Buzzard, Bedfordshire, UK). Prior to the synthesis reactions, all reagent solutions including sodium bicarbonate, acetic acid and injectable grade sodium bovine heparin solutions were filter sterilised by using 0.22  $\mu\text{m}$  polyethersulfone (PES) membrane filter. The pH of each reagent solutions and their mixtures were measured by using a pH-meter (Mettler-Toledo GmbH, Analytical, FiveEasy Plus™, Greifensee, Switzerland).

A totally sterile synthesis technique was implemented to produce modified sterile solutions. Prior to synthesis of modified hydrogels, CS was sterilised by using steam autoclaving in water dispersion form with a glycerol additive as a heat protective agent. Glycerol as a polyol was harnessed since it is reported that polyols are capable of enhancing gel elasticity and reducing CS degradation and viscosity loss in the solution due to heat (Jarry et al., 2002; Yen & Sou, 1998). In addition, in the sterile modified formulations, pre-synthesised carbonated HA (HA-5 D) was used. Hydroxyapatite powder (HA-5 D) was prepared as explained in Section 2.1.2, and was also utilised after steam autoclaving.

Firstly, non-modified, initial hydrogels were synthesised. Initial experiments covered the investigation of the optimal CS concentration for facile injectability and gelation properties of neutralised hydrogel solutions. The details of synthesis and the characterisations of these initial liquids and crosslinked hydrogels are given in following text. Briefly, at first, different initial concentrations of CS solutions (4, 5, 6, 7 and 8%(w/v)) were prepared and the final hydrogel solutions were obtained upon neutralisation of CS solutions by NaHCO<sub>3</sub>. These sole CS formulations were initially tested in their liquid and hydrogel forms. These characterisations include qualitative injectability assessment by comparing flow capacity of liquid hydrogels through a 19 G needle, rheology analyses to test main viscoelastic and gelation behaviours and assessment of gelation features including the test tube inversion method to determine incipient gelation time. Among different initial concentrations, 5%(w/v) CS solution which accounts for ~ 2.4 %(w/v) CS in the final neutral solution led to preferable viscosity, injectability and gelation features, thus it was chosen as an optimal concentration. The subsequent synthesis of composite hydrogels was carried out using this concentration.

Initial hydrogel formulations were prepared as was reported earlier in this project (Kocak et al., 2020). In detail, the homogeneous CS solution of 5 %(w/v) was prepared by dissolving 1 g of CS in 20 mL of 0.5 M acetic acid with constant stirring for 3 hours. For modified injectable hydrogel formulations, preparation of the CS solution has differed slightly due to an additional CS sterilisation step. For this, 1 g of CS was dispersed into 10% (w/v) of glycerol-water solution for 15 min. Then, the CS dispersion with the glycerol additive was sterilised by using the automatic steam autoclave

operating at 132 °C and 2 bars for 20 min that included the times for ventilation and for reaching the autoclaving temperature (5 min each). After sterilisation, the CS dispersion was cooled down to room temperature. Then, the CS solution was obtained by the addition of glacial acetic acid to make a 0.5 M acetic acid solution by constantly stirring for 3 h.

For both synthesis methods, following its acquisition, the CS solution was chilled in a fridge at 4 °C for 15 min prior to pH neutralisation. Then, 0.48 M of stock sodium bicarbonate ( $\text{NaHCO}_3$ ) solution kept refrigerated at 4 °C, was added dropwise into the cold CS solution in a flask placed into an ice bath at 4 °C while constant stirring was maintained. For solution stability, mild ionic reaction conditions were provided by using a dropping funnel to add reagent solution fitted into the reaction flask. This was done to prevent air coming into contact with the solution to minimise the speed of carbon dioxide release which can trigger gelation via a pH dependent ionic crosslinking reaction. The reaction set up is shown in Figure 3.1.

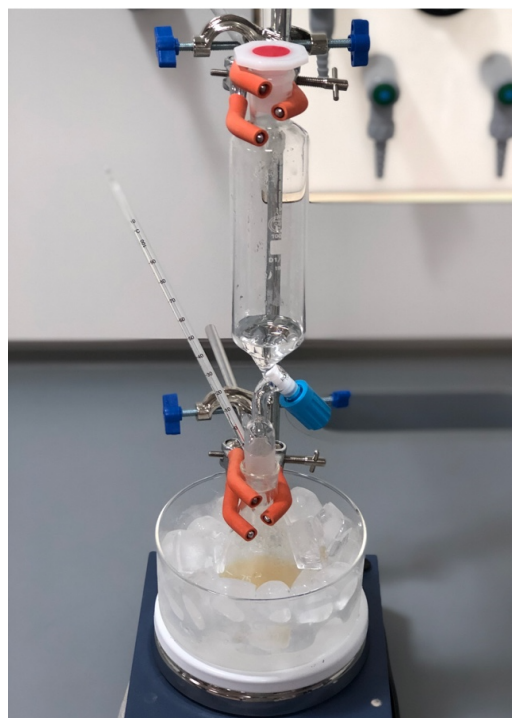


**Figure 3. 1** Experimental set up for synthesis of pH and temperature sensitive hydrogels: the reaction flask is placed in an ice bath at 4°C, controlled by a thermometer and with a quick-fit dropping funnel for dropwise addition to the solution.

For initial hydrogel formulations, CS/HA compositions were prepared by using non-sintered commercial HA powders (P218R, Plasma Biotal, CAPTAL®, Buxton, UK) whereas pre-synthesised HA (HA-5D) was utilised in the modified hydrogels. For both

methods, a CS solution of 5% w/v was prepared as aforementioned. Then, related HA powder was mixed into the CS solution while ensuring that the weight ratio of HA/CS was 1/10. The HA powders were thoroughly dispersed into the CS solution overnight by constant stirring, to obtain a homogenous mixture. Then, the solution pH was neutralised by dropwise addition of cold NaHCO<sub>3</sub> solution (0.48 M) in an ice bath at 4 °C.

The composite CS/HA/Hep hydrogels of the initial formulations were produced with three different Hep concentrations, 0.12, 0.36 and 0.60 mg/mL Hep in final solution for SI, SII and SIII samples respectively. However, in modified hydrogels, only the lowest Hep concentration (0.12 mg/mL) and another lower concentration (0.03 mg/mL) were used, which were denoted as the SI and S0 samples respectively. The compositions of the different hydrogels are summarised in Table 3.1. The sterile Hep solutions were freshly prepared by dissolving the respective amount of injectable grade sodium bovine Hep in 5 mL of de-ionized water. The Hep solution was added dropwise into the CS/HA mixture with maintained constant stirring. Subsequently, the pH of CS/HA/Hep solution was adjusted by the dropwise addition of NaHCO<sub>3</sub> solution as described earlier. For the control samples prepared in the absence of Hep, instead of a Hep solution an equal volume of de-ionized water was added to obtain similar viscosity and concentrations in the compositions. In Figure 3.2, the synthesis steps of injectable composite hydrogels (CS/HA/Hep), the network structure of reagent mixtures and the mechanism of pH dependent ionic crosslinking and gelation which was further stimulated by body temperature, are illustrated. To maintain homogeneity after synthesis and during storage, the final pH of solutions was adjusted by NaHCO<sub>3</sub> to 6.2-6.3 and 6.3-6.5 for initial and modified hydrogels respectively.

**Table 3. 1** The composition of different injectable hydrogel formulations \*

Sample Names	Sample Codes	Chemical compositions			
		(w/w, %)			mg/mL
		CS	HA	Hep	
CI	CS	100.00	0.00	0.00	0.00
CII	CS-0.1HA	90.91	9.09	0.00	0.00
S0	CS-0.1HA-0.0015Hep	90.81	9.08	0.11	0.03
SI	CS-0.1HA-0.005 Hep	90.50	9.05	0.45	0.12
SII	CS-0.1HA-0.015 Hep	89.69	8.97	1.35	0.36
SIII	CS-0.1HA-0.025 Hep	88.89	8.89	2.22	0.60

\* Initial formulations include all compositions (CI, CII, SI, SII and SIII) except S0 which has the lowest concentration of Hep. In modified hydrogels, however, only S0, SI, CI and CII compositions were used.

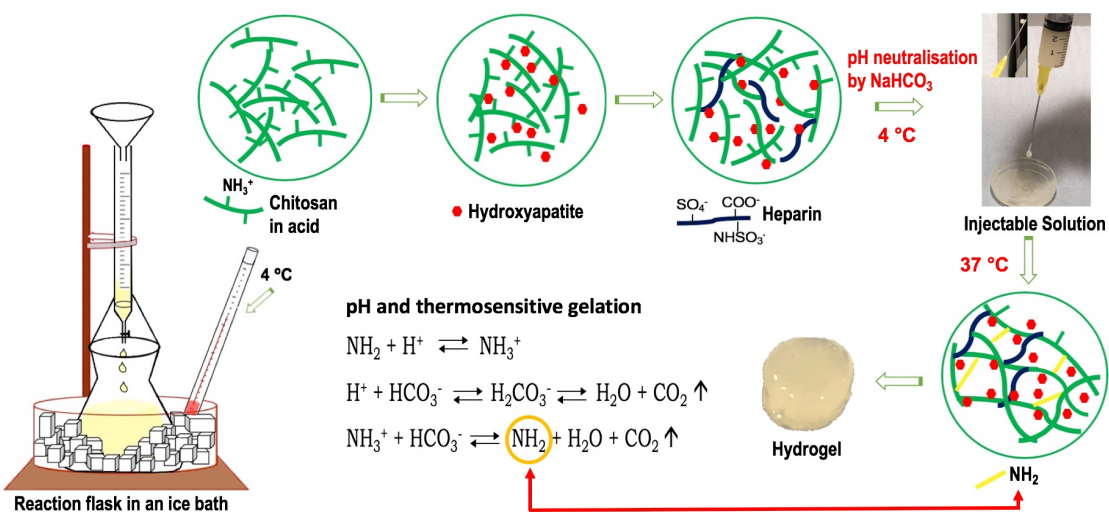


**Figure 3. 2** The illustration of synthesis steps of pH and thermosensitive CS based composite hydrogels (CS/HA/Hep) with the network structures of mixtures and the ionic crosslink mechanism stimulated by the given ionic reaction and temperature (37 °C) (This figure was reused after modification from our earlier published paper (Kocak et al., 2020) licensed under CC BY 4.0.

After synthesis of homogeneous hydrogel solutions, ionically crosslinked pH and temperature stimulated gelation occurred upon incubation of solutions at 37 °C. For some characterisations, such as in the test tube invert method for determination of initial gelation time, and in mechanical tests, 2 mL of solutions were taken into glass tubes with a push polythene plug cap ( $\varnothing$ : 18 x 75 mm, Camlab Ltd., Cambridge, UK). These were incubated for 48 h in order to obtain stable hydrogels. For other characterisations, homogeneous stable gels were obtained gradually by 48 h incubation of 40-45 mL of solution in glass dishes with lids ( $\varnothing$ : 100 x 15 mm, Steriplan®, Duran® DWK Life Sciences GmbH, Mainz, Germany).

### 3.4 Characterisation of Injectable Hydrogels

#### 3.4.1 Injectability

The injectability capacity of hydrogel solutions was evaluated through both qualitative and quantitative analyses. Qualitative assessment of injectability of hydrogels involved rating of the flow capacity of solutions tested through varying sized needles coupled with a syringe. On the other hand, quantitative injectability analyses were performed in a Universal Testing Machine (UTM). This covered the measurement of required force

response while expelling solutions through a syringe which was either needleless or coupled with a 19 Gauge (G) or 21 G needle.

#### 3.4.1.1 Qualitative Injectability Analyses

The injection properties of the homogeneous solutions were determined immediately after synthesis by comparing their flow properties. Flow performance of the solutions were manually tested by using a 5 mL syringe coupled with different sized BD needles (BD, Luer-Lok™, Becton, Dickinson U.K. Ltd, Wokingham, UK) ranging from 18 G to 25 G with decreasing needle thicknesses and lengths (Figure 3.3).



**Figure 3. 3** The images of different sized BD needles used in qualitative injectability assessments shown at left image and the corresponding sizes of needles given at right across.

Qualitative injection capacity was evaluated for each solution formulation by rating their flow consistency and convenience with different needle sizes. The results were demonstrated by using star symbols; between six-stars (\*\*\*\*\*) symbolising perfect flow and one-star (\*) indicating no-flow.

#### 3.4.1.2 Quantitative Injectability Analyses

Quantitative injectability measurements were conducted by using a UTM instrument (Instron® 3345, Norwood, MA, USA) in compression mode. The experimental design was adapted from the literature (Cilurzo et al., 2011; Shavandi et al., 2016; Yasmeen et al., 2014). Briefly, 5 mL of hydrogel solution was slowly filled into a 10 mL syringe to avoid air entering into the syringe. Tests were conducted with a needleless syringe and with the syringe coupled with a needle (19 G or 21 G). A syringe rig was employed to fix the syringe, placed between compression plates, in place. Experiments were carried

out by lowering the loading cell on the syringe plunger until they had contact. Then, 0.5 mm/s of crosshead speed was applied to expel 5 mL of solution for 30 mm of displacement. An image of the experimental set up is shown in Figure 3.4. The force changes during displacement of the syringe plunger were recorded by Bluehill® Universal Software (Version 4.06, Norwood, MA, USA).



**Figure 3. 4** The injectability test measurements set up carried out by using a UTM instrument (Instron® 3345, Norwood, MA, USA) in compression mode. The injection forces were measured during displacement of the syringe plunger at a certain speed until all 5 mL of hydrogel solution, in a 10 mL syringe fixed into a syringe ring, was expelled .

The variable forces counted were: *initial glide force (IGF)*: the force required to initiate syringe plunger motion; *dynamic glide force (DGF)*: the force required to maintain the plunger movement; and *the maximum force (Fmax)*: the maximum force exerted during the displacement of the plunger (Cilurzo et al., 2011; Moreira et al., 2018). The results were expressed as mean $\pm$ SD (n=6) and plotted in GraphPad Prism (Version 7.0, San Diego, CA, USA) software.

### 3.4.2 Test Tube Invert Method for Incipient Gelation Time

The initial gelation time of hydrogel solutions were determined by using the test-tube invert method which is a simple/common method for the determination of sol-gel transition points of hydrogels. Briefly, 2 mL of hydrogel solution was put into a close-lid glass test tube with a push polythene plug cap ( $\varnothing$ : 18 x 75 mm, Camlab Ltd., Cambridge, UK) and placed in a beaker filled with silicone oil bath on a hot plate at 37 °C. Then, the test tube was tilted horizontally after every minute to check the flow. The time that the solution showed no flow against gravity for around 20 seconds was recorded as the incipient gelation time ( $t_{i.g.}$ ) (Li et al., 2014; Wu et al., 2016). The sol-gel transition points of hydrogel solutions were analysed further via temperature sweep tests using Rheology measurements.

### 3.4.3 Rheology Measurements

The viscoelastic behaviours and sol-gel transition points of hydrogel solutions were analysed by rheology tests performed with a Rheometer (TA Instruments®, TA-AR 2000, Newcastle, DE, USA) by using a cone geometry ( $\varnothing = 40$  mm, 2°) (Figure 3.5). The small chamber on the upper site of the geometry was filled with water and sealed to provide humidified experiment conditions.



**Figure 3. 5** A rotational TA-AR 2000 Rheometer (TA Instruments®, Newcastle, DE, USA) instrument during rheology analysis of a hydrogel specimen, performed by using a cone geometry ( $\varnothing = 40$  mm, 2°) which is covered by a metal chamber.

Frequency sweep tests were performed in a viscoelastic region at a constant strain of 1% and frequency range of 0.1-10 Hz at constant temperatures; 25 °C, 15 °C and 37 °C. In addition, the oscillatory measurements were carried out at a constant frequency (1 Hz) in which the storage/elastic ( $G'$ ) and loss/viscous modulus ( $G''$ ) were measured during heating between 15 °C and 37 °C and in the same range while cooling. The sol-gel transition points of the formulations were determined via the intersection point of the elastic ( $G'$ ) and viscous ( $G''$ ) ( $\tan \delta = G''/G' = 1$ ) when a material starts to exhibit more elastic properties than liquid (Laity & Holland, 2016; Rafipoor et al., 2014). Furthermore, in another experiment, during frequency sweeps the solution temperature was held at 37 °C for 30 min to observe viscoelasticity changes at 37 °C over time. The data acquisition was provided using TA Rheology Advantage™ software (TA Instruments, V7.20, New Castle, DE, USA). The rheological data was graphed via GraphPad Prism (Version 7.0, San Diego, CA, USA) software.

#### 3.4.4 Morphological Analyses by Scanning Electron Microscopy (SEM)

The microstructure images of both initial and modified hydrogels were produced upon lyophilisation of the hydrogel specimens in a freeze drier (SciQuip Epsilon 1-4 LSC, Shropshire, UK). To freeze-dry the initial hydrogel formulations, the liquid hydrogels (~800  $\mu$ L), immediately after synthesis, were poured into the wells of a 48 well plate. Subsequently, they were frozen at -30 °C for 24 h and dried at -20 °C for 48 h. On the other hand, modified hydrogels were freeze-dried in different conditions due to the involvement of glycerol, causing alterations of freezing temperature. Hydrogels were freeze-dried, either in liquid form or hydrogel form, after gelation at 37 °C. They were frozen at -80 °C for 24 h and dried in two stages including main drying at -20 °C for 24 h and final drying at -15 °C for 24 h.

Prior to SEM imaging, freeze-dried hydrogels were gold coated at a thickness of 5 nm. Subsequently, images were taken in 7 kV accelerating voltage by using an SEM device (FEI Quanta™ 650 3D FEG/FIB ESEM™, Hillsboro, Oregon, USA). All images of modified hydrogels were obtained by FE-SEM instrument that worked at 5 kV accelerating voltage after a change in institution (university) (Schottky FE-SEM

instrument, JEOL JSM-7800F, Tokyo, Japan). The image analyses were performed by ImageJ® software (Version 1.52k, National Institutes of Health, Bethesda, MD, USA). In order to assess porosity, a series of pores were measured and counted as the mean, minimum and maximum lengths of individual and interconnected pores.

#### 3.4.5 Thermal Analyses by Simultaneous TGA & DSC

Thermal analyses of hydrogels and reagent materials used for the synthesis of hydrogels including; synthetic commercial CS, HA, and Hep was carried out by use of a simultaneous thermal analyser (NETZSCH STA 449 F3 Jupiter®, NETZSCH-Gerätebau GmbH, Selb Germany). The approximately 20 mg of powder samples were weighed and analysed in alumina crucibles. The specimens were heated from 25 °C to 700 °C at a heating rate of 10 °C/min in Nitrogen atmosphere. The data was both obtained and analysed by NETZSCH Proteus® software.

#### 3.4.6 Mechanical Analyses by Compression Tests

The mechanical testing of hydrogels involved stress/strain measurements of hydrogels exposed to compression force. The compression tests were performed by using a Universal Testing Machine (Instron® 3345, Norwood, MA, USA), equipped with a 0.5 kN load cell, in compression mode. The compression tests were performed on the modified hydrogels. The hydrogel specimens ( $\varnothing$ : 16 mm x 8 mm) were prepared for mechanical tests by gelation of 2 mL of solution in glass tubes with push polythene plugs, and incubated at 37 °C for 48 h. Experiments were performed at 1 mm/min of crosshead speed up to a certain strain point as reported in the literature (Frydrych et al., 2015). The modified hydrogels obtained with lower pH in solution state (6.2-6.4), were compressed to 40 % elongation, while the higher pH (6.4-6.5) hydrogels were compressed until 75% of elongation. A demonstration of a compression test applied to a modified hydrogel specimen placed between compression plates is shown in Figure 3.6.



**Figure 3. 6** An image taken prior to compression testing of a modified hydrogel specimen placed onto a lower compression plate in an Instron® UTM instrument (Instron® 3345, Norwood, MA, USA).

The stress versus strain curves were obtained as kPa and % units, respectively using Bluehill® Universal Software (Version 4.06, Norwood, MA, USA). In addition, the Young's Modulus, and the force and energy at break point were automatically measured and counted by the software according to the measured sample sizes ( $\varnothing$ : 16 mm x 8 mm thickness). Three samples were tested per specimen group of hydrogel composition ( $n=3$ ). The resultant graphs were plotted using GraphPad Prism (Version 7.0, San Diego, CA, USA) software.

#### 3.4.7 Fourier Transform Infrared–Attenuated Total Reflectance (FTIR-ATR) Spectroscopy

FTIR-ATR analyses were performed by using Thermo Nicolet™ iS50 FTIR spectrophotometer (Thermo Fisher Scientific Inc, Madison, WI, USA) in Attenuated Total Reflectance (ATR) mode. The data was collected in the mid-infrared region (4000 to 400  $\text{cm}^{-1}$ ) by using an aperture of 150 with a resolution of 16  $\text{cm}^{-1}$ . 128 scans were done using Detector DTGS ATR and Beam splitter, KBr. The background

spectrum measured prior to the experiments and renewed every 2 h. The spectral data collection and analyses were undertaken and obtained after automatic baseline corrections in OMNIC™ software (Version 9.5.9, Thermo Fisher Scientific Inc, Madison, WI, USA).

#### 3.4.8 Fourier Transform-Raman (FT-Raman) Spectroscopy

FT-Raman analyses of hydrogels were carried out by using a FT-Raman spectrophotometer sampling accessory fitted into Thermo Nicolet™ iS50 FTIR (Thermo Fisher Scientific Inc, Madison, WI, USA) which utilizes a near-IR, Nd:YVO<sub>4</sub> excitation laser operating at 1064 nm. The measurements were carried out by using Detector InGaAs and Beam splitter CaF<sub>2</sub>. Spectral data were obtained at 16 cm<sup>-1</sup> resolution, accumulating 64 scans over the wavenumber range of 4000–400 cm<sup>-1</sup>. The spectra were gathered through a square area mapping, confining nine equally distanced points on a square, and the resultant spectra were obtained as averages and demonstrated after automatic baseline corrections in OMNIC™ software (Version 9.5.9, Thermo Fisher Scientific Inc, Madison, WI, USA).

#### 3.4.9 X-Ray Diffraction (XRD) Analyses

X-Ray diffraction (XRD) analyses were performed in an XRD instrument (SmartLab 9kW, Rigaku Corporation, Tokyo, Japan) equipped with a DteX 250 Ultra detector, parallel beam optics (Gobbel mirror), Ge(220)x2 monochromator working with CuK  $\alpha_1$  radiation ( $\lambda=1.54060$  Å) and 5° soller slits. Fine powder specimens were prepared and analysed on a glass slide sample holder (15 mm x 15 mm). Freeze-dried hydrogel specimens were directly analysed upon placement onto another suitable holder. Diffraction patterns were obtained over a 2θ angle range of 5-80° with an increment of 0.02°. XRD patterns were obtained via integrated powder X-Ray analysis software PDXL (Version 2.1.1., Rigaku Corporation, Tokyo, Japan). For crystallographic analyses, high quality ranked standards acquired from the ICSD® Fiz database, were compared with the XRD patterns of the specimens.

### 3.5 Results

#### 3.5.1 Synthesis of Injectable Hydrogel Solutions

To synthesise initial hydrogels, experiments were conducted to compare the different concentrations of CS solutions in acetic acid (4, 5, 6, 7 and 8%(w/v)), so as to obtain homogeneous liquid hydrogels that allow for facile injectability and desired gelation features. The primary assessment of some solutions included; qualitative injectability by a 19 G needle, rheology analyses and incipient gelation time determined by the test tube inversion method.

The results showed that a 4 % (w/v) of initial CS solution, which is below 2 % (w/v) in a neutral solution, was not able to transform to a gel phase upon incubation at 37 °C. This was associated with the critical concentration ( $C^*$ ) required for gelation, which correlates inversely with the intrinsic viscosity of the polymer (Boucard et al., 2005). On the other hand, CS solutions with initial concentrations of 7-8 %(w/v) have led to quite viscous, already gel-like solutions after neutralisation. These solutions have compromised the injection capacity since quite a high pressure is required to expel these solutions during injection via a 19 G needle coupled syringe.

According to all results, a 5%(w/v) CS solution, which accounts for ~ 2.4 %(w/v) CS in final neutral solutions was chosen as the optimal concentration. This solution exhibited evenness and consistent flow during injection through a 19 G needle, incipient gelation starting in 8-10 min at 37 °C and preferred viscoelastic behaviour and a sol-gel transition point of nearly 37 °C in rheology measurements. Therefore, for synthesis of further composite hydrogels, this initial 5%(w/v) CS concentration was utilised. Figure 3.7.a. shows the appearance of a transparent bright yellow coloured CI (CS) solution obtained after neutralisation. In addition, composite CS/HA formulations were obtained by dispersion of HA powder into a CS solution with the same initial concentration of 5%(w/v) with the weight ratio of HA to CS being 1/10. This liquid hydrogel composition CII (CS.0.1HA) results in a slightly opaque homogeneous solution after neutralisation (Figure 3.7.b.).

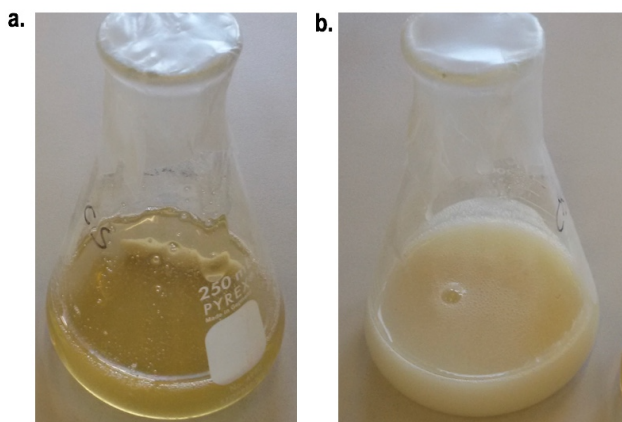


**Figure 3. 7** The images of liquid hydrogels obtained after gradual neutralisation by  $\text{NaHCO}_3$  **a.** CI: sole CS solution (with initial concentration of 5 % (w/v)) having transparent yellow colour **b.** whiter and slightly opaque composite solution CII: CS/HA(10:1).

For CS/HA/Hep composite solutions, initially Hep was added in powder form at room temperature. However, the direct powder mixing method of Hep led to formation of large precipitates during neutralisation, as shown in the Figure 3.8. This heterogeneity of solution was associated with strong electrostatic interactions of cationic CS and counter charged Hep, and is assumed particularly, to be due to their direct and sudden contact during mixing with the powder form of Hep (He et al., 2010). Therefore, a gradual inclusion method of Hep involving dropwise addition of Hep as a water solution into the CS/HA mixture was executed. This has provided acquisition of homogeneous solutions after pH neutralisation, shown in Figure 3.9.

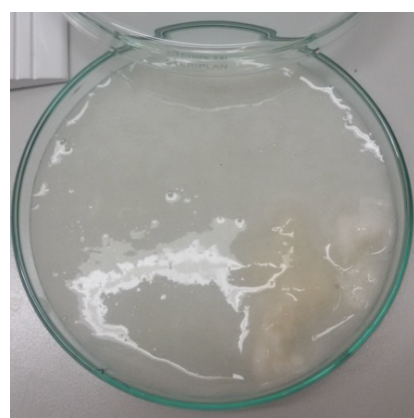


**Figure 3. 8** The composite SI (CS.0.1HA.0.005Hep) solution obtained via powder mixing method of Hep (0.12 mg/mL) into a CS/HA solution causing large precipitates after the neutralisation process which results in a heterogeneous solution.

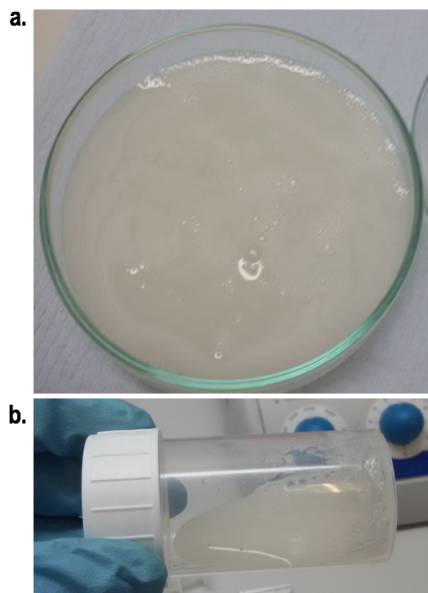


**Figure 3.9** The homogenous neutral solution of SI (CS.0.1HA.0.005Hep), achieved by dropwise and gradual addition of Hep in water solution form, is acquired without any precipitates in **a.** a glass petri-dish and **b.** a tilted plastic container in which the solution exhibits easy flow.

In initial hydrogels, CS powder was used without sterilisation while pre-sterile modified hydrogels were prepared from sterilised CS powders by steam autoclaving in dispersion form of CS in water-glycerol media. Initially, CS was directly autoclaved in powder form that caused a slight darkening of the powder that might be associated with some degradation of polymer chains. In addition, utilisation of autoclaved CS powder in dry form for hydrogel synthesis has led to the formation of a heterogeneous, viscous solution with small, localised white precipitates, after neutralisation.

The autoclaving effects on the chemical properties of CS powder were investigated by using FT-IR (ATR) and TGA analyses. The results showed that the chemical functional groups of CS slightly decreased upon autoclaving, although less than 10% of weight loss occurred at autoclaving temperature. Therefore, in further studies, in order to mitigate the detrimental effect of heat on CS, it was sterilised in water dispersion form with a glycerol additive as a heat protective agent, as is reported in the literature (Jarry et al., 2002; Yen & Sou, 1998). This technique led to almost no colour change in CS dispersion in water-glycerol media after 10 min of steam autoclaving. Homogeneous solutions were obtained upon dissolving CS in acid prior to neutralization. These modified solutions have also triggered the quicker gelation of thermosensitive solutions starting in as quickly as 2-3 min. The modified homogeneous solutions after

neutralisation were obtained via a total sterile technique and glycerol addition, demonstrated in Figure 3.10.

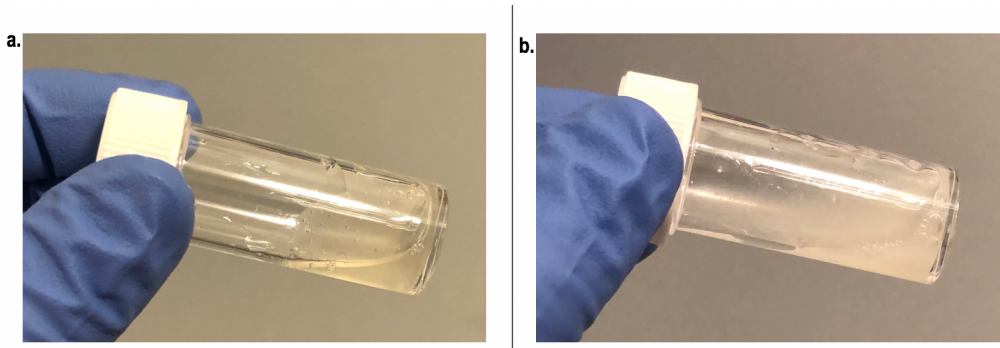


**Figure 3. 10** Photographs of sterile hydrogel solutions (2 mL) taken into test tubes upon neutralisation: **a.** CI: sole CS and **b.** composite SI (CS.0.1HA.0.005Hep) solution.

### 3.5.2 Solution pH, Homogeneity, Stability and Gelation Features

In initial hydrogels, the highest pH achieved to obtain homogeneous solution without any precipitation was at pH 6.2-6.3 at 4 °C which accounted for the slightly higher pH at room temperature. The pH values between 6.5-7.1 were obtained upon gelation at 37 °C. The pH measurements of reagent solutions during synthesis of solutions and initial hydrogels are summarized in Table 3.2.

**Table 3. 2** The pH values measured in all steps of synthesis of initial hydrogels including pH of reagent solutions and their mixtures, final solution after neutralization, and after gelation, which were given with measured temperature during pH measurements. (pH values of stock acetic acid (0.5 M) and NaHCO<sub>3</sub> (0.48 M) solutions were 2.24 and 8.50, respectively while pH of Deionised water (Dw) was 6.58. The pH values of Hep solutions in Dw for SI, SII and SIII compositions were measured as 6.58, 6.56 and 6.61, respectively.)

Sample Names and codes:	CS		CS+HA		CS+(HA)+ (Dw/Hep)		Final solution pH neutralized by NaHCO <sub>3</sub>		pH after gelation at 37°C	
	pH	Temp (°C)	pH	Temp (°C)	pH	Temp (°C)	pH	Temp (°C)	pH	Temp (°C)
<b>CI: CS</b>	4.19	16.4	-	-	4.30	14.7	<b>6.20</b>	6.5	<b>6.50</b>	27.5
<b>CII: CS+HA</b>	4.13	20.7	4.21	21.1	4.30	6.0	<b>6.24</b>	7.7	<b>6.51</b>	25.0
<b>SI: CS.0.1HA.0.005Hep</b>	4.28	18.8	4.29	20.1	4.33	10.7	<b>6.21</b>	5.0	<b>6.53</b>	24.9
<b>SII: CS.0.1HA.0.015Hep</b>	4.14	18.9	4.16	15.8	4.33	7.8	<b>6.22</b>	7.5	<b>6.72</b>	25.3
<b>SIII: CS.0.1HA.0.025Hep</b>	4.23	17.7	4.28	14.5	4.29	8.5	<b>6.24</b>	7.5	<b>7.01</b>	22.0

Regarding modified sterile hydrogel solutions, the final pH could be raised up to 6.7-6.8 at 4 °C without any resultant precipitate formation. However, after a short time, phase separation was inferred from the presence of cloudy white precipitates in the

liquid that compromised both solution homogeneity and injectability. The maximum pH achieved for homogeneous solutions with no phase separation was pH 6.40-6.45 at 4 °C. The solutions possessing slightly higher pH than 6.4 (e.g 6.46) was stable at 4 °C for 4 days. After 4 days, phase separation leading to the formation of white cloudy precipitates occurred. The pH of the sole CS hydrogel solution was pH 6.4 at 4 °C reached 6.8 at 20 °C. Composite solutions possessed higher pH, above 7, which are at the center of the physiological pH range (Chenite et al., 2000). Upon gelation at 37 °C, obtained hydrogels possessed slightly higher pH values than 7. The pH values of sterile modified hydrogel compositions at different temperatures are summarised in Table 3.3.

**Table 3. 3** The pH values of solutions at 4 °C and 20 °C for modified injectable hydrogel formulations in different compositions.

Sample names and codes	pH of Modified Formulations	
	Sol	
	(4 °C)	(20 °C)
CI: CS	6.43	6.78
CII: CS-0.1HA	6.42	7.00
S0: CS-0.1HA-0.0015Hep	6.54	7.16
SI: CS-0.1HA-0.005Hep	6.46	7.00

All liquid hydrogel formulations were stored in tightly closed universal tubes in a refrigerator at 4 °C and stability of liquid forms were checked during their storage. From initial liquid hydrogel formulations, CI and CII solutions without heparin that were still flowing well once their test tubes were tilted, were stable in this regard, up to 6-months at 4 °C. Hydrogel solutions containing Hep showed a skin like layer formation on their surface after 3-weeks of storage at 4 °C. Although they became more viscous, the underneath of the surface layer protected its liquid form for almost 2-months. The solution stability of modified hydrogels were decreased in comparison to initial formulations. Almost all compositions became more viscous after a 24 h of storage at 4 °C, and an elastic consistent flow of solutions was observed. The changes in injectability properties of all hydrogels were investigated and details are provided in the injectability analyses section of this chapter.

Stability of modified hydrogel solutions was observed upon storing at a lower temperature. The aliquots of hydrogel solutions in vials (7 mL) were stored in a freezer

at -20 °C. After 10 months of storage, these specimens were defrosted gradually at room temperature and their solution stability and flow properties were checked. Although there was a thin skin layer formation on the surface of the specimens, this layer served to protect the bulk solution below, which was still an easily injectable liquid, from air contact. It is considered that more protection of the liquid phase might be dependent on minimizing carbon dioxide evaporation using very tightly closed narrow vials with relatively less surface area. The injectable solutions CI and CII were still capable of forming crosslinked hydrogels upon incubation at 37 °C. However, the SI solution containing Hep (0.120 mg/mL) (obtained at pH 6.46) which had been exposed to phase separation, lead to a weak white precipitate agglomeration at the bottom and liquid on top. Therefore, the lyophilization method was found suitable for CI and CII control samples but not for the composite hydrogels including Hep.

### 3.5.3 Sol-gel Transition and Gelation Features

In CS-NaHCO<sub>3</sub> systems, gelation depends on pH and temperature (See Chapter 1). Since gelation is driven by carbon dioxide release during an ionic reaction, it initiates at the surface in 3-10 min and progress towards the bulk over time. Hence, more time (3-48 h) is required for complete gelation of all of the solution. The incipient gelation speed of different liquid hydrogel compositions were tested by using a common practical test for hydrogels, called the ‘test tube inversion method’ was used.

As described in Section 3.5.2., the incipient gelation time ( $t_{i.g.}$ ) of hydrogel solutions in the average human body temperature (37 °C) were determined by using a test tube inversion method. The hydrogel solution (2 mL) was placed into a glass tube sealed by a push polythene plug lid ( $\varnothing$ : 18 x 75 mm) and placed in a silicone oil bath at 37 °C. The tube was tilted every minute to detect gelation behaviour. Figure 3.11. shows a representative test-tube inversion method for testing for the sol-gel transition point, or  $t_{i.g.}$ , for a liquid hydrogel specimen (SI) (at left) and gel formation initiated in 7 min at 37 °C which is seen in the reversed test tube (at right). In addition, Table 3.4 summarizes  $t_{i.g.}$  values for all initial liquid hydrogel formulations.

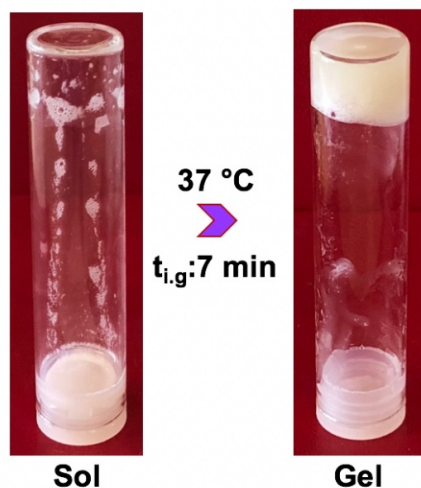


**Figure 3. 11** Demonstration of sol-gel transition using the test tube invert method. Liquid composite hydrogel solution (SI, non-modified) in a test tube which flows easily when the tube is reversed (left), and gelation started from the surface of the solution in 7 min after placing the tube in an oil bath at 37 °C (right).

**Table 3. 4** The incipient gelation time of initial hydrogel compositions was determined by the test tube inversion method at 37 °C immediately after the synthesis of the liquids at 4 °C.

Sample Names and codes	Incipient gelation time ( $t_{i.g}$ ) (min)
Cl: CS	8
CII: CS+HA	7
SI: CS.0.1HA.0.005Hep	5
SII: CS.0.1HA.0.015Hep	10
SIII: CS.0.1HA.0.025Hep	7

Modification of hydrogel formulations by exposure to the additional heat sterilisation of CS dispersion with glycerol additive has led to a decrease in the incipient gelation time, of 2-3 min. The incipient gelation times determined for all modified hydrogel compositions are given in Table 3.5. Addition of HA into CS hydrogels (CII) has led to a decrease of the gelation speed. Hep had a further contribution to gelation in composite hydrogels in that the composite SI hydrogel sample (CS.0.1HA.0.005Hep), had a  $t_{i.g}$  of 3 min and obtained a compact and stable hydrogel after 24 h incubation at 37 °C (See Figure 3.12).

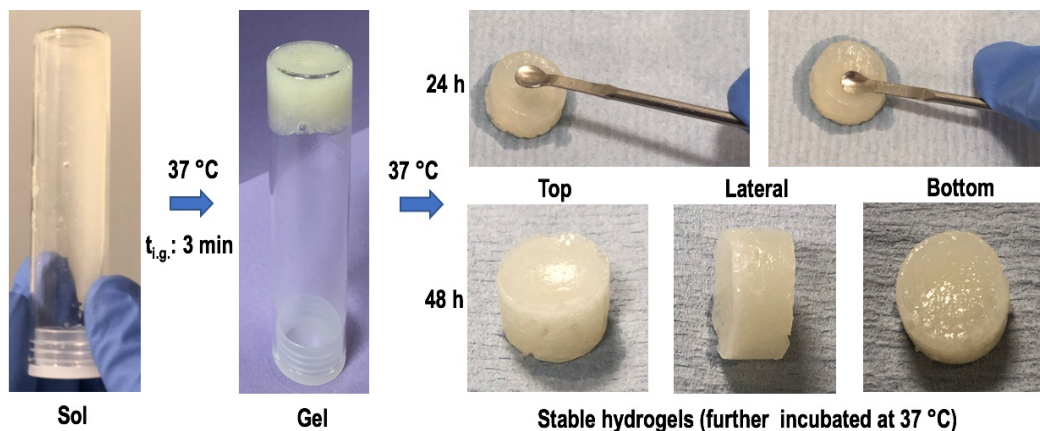


**Figure 3.12** A diagram of the sol-gel transition in a modified composite hydrogel (SI: CS.0.1HA.0.005Hep) obtained from a solution having a final pH above 6.4. Incipient gelation occurred at 3 min in a test tube placed in an oil bath at 37 °C is shown at left. The photographs of stable and elastic hydrogels acquired after further incubation at 37 °C for 24 h and 48 h are shown at the **Top** and **Bottom** images at the right side of the diagram. A hydrogel showing flexible behaviour when pressed on by a spatula, is demonstrated at the top right corner (for a 24 h sample).

**Table 3.5** The incipient gelation time for all modified hydrogel compositions was measured by test tube inversion method at 37 °C immediately after synthesis of liquids at 4 °C.

Sample names and codes	Incipient gelation time ( $t_{i,g.}$ ), (min)
Cl: CS	5
CII: CS-0.1HA	4
S0: CS-0.1HA-0.0015Hep	3
SI: CS.0.1HA.0.005Hep	3

The gelation was initiated at the surface in a few minutes while the entire hydrogel formation in bulk took more time. The gelation speed was found to be dependent on several factors, including the extent of air contact, surface area, and the amount and thickness of the solution. Once hydrogels in a 37 °C fan-oven were allowed direct air contact, the gelation reaction was visually observable, showing the formation of small bubbles on the surface; due to carbon dioxide release. Therefore showing the inevitability of direct contact to air speeding up the gelation process. In order to ensure the gradual formation of stable and uniform hydrogels, direct air contact of the solutions was avoided by obtaining hydrogels in tightly closed containers with lids (test tubes or petri dishes). The solutions in test tubes were sealed with push caps, providing loosening was left at level one to allow slow release of carbon dioxide for gradual gelation. Along with air contact and open surface area, gelation is also found to be dependent on the solution's thickness. As reported by Boucard et al., (2005), For CS

solutions in hydroalcoholic solvents, the gelation speed increases as the thickness of the solution decreases and becomes irrelevant after a certain thickness due to the formation of a skin layer on top which slows down water diffusion at a certain rate. Similar circumstance occurred in the present gelation system in which initially, a skin like gel formed on the top surface and becomes harder over time and reduces the reaction speed for its bulk.

Complete stable hydrogels were obtained faster ( $\leq 24$  h) in plastic petri dishes (90 mm x 16 mm) than those of in thicker glass petri dishes (100 mm x 15 mm) ( $\leq 48$  h) with heavier lids leading to slower carbon dioxide emission. In addition, the gelation of solutions (2 mL) in test tubes ( $\varnothing$ : 18 x 75 mm) having approximately 10 mm of solution thickness, took place slower than in those of the petri dishes (~5 mm thickness of solution) due to lower surface area and higher thickness of the solution. However, 48 h incubation at 37 °C was enough to form stable hydrogels either in glass petri-dishes or test tubes. The faster reaction and liquid removal occurred in the plastic petri dishes and stable hydrogels were acquired between 3 h to a maximum of 24 h at 37 °C. Further incubation of up to 48 h led to the formation of solid films rather than hydrogels. For storage reasons, glass dishes or test tubes were generally preferred for obtaining hydrogels within.

Employing glycerol in modified hydrogels, has served the aims of heat protection of CS and improving the elasticity and mechanical properties of hydrogels. The results showed that the sterile technique including involvement of glycerol has contributed to increase, at a final solution pH of between 6.40 and 6.45 by preserving solution homogeneity. Solutions having pH below 6.4 were still weaker during handling, as initial hydrogels. However, much more stable and elastic hydrogels were obtained when solution pH was slightly exceeded beyond pH 6.4. The significant enhancement of mechanical properties in modified hydrogels obtained with a solution of pH 6.40-6.45 was confirmed by compression strength tests (discussed at Section 3.5.8). These results were attributed to the combined effect of pH and glycerol leading to further strengthening of hydrogels, due to the formation of more hydrogen bonds leading to further crosslinking between CS and NaHCO<sub>3</sub> salts. Furthermore, the interlocking network structures of these hydrogels were also revealed by SEM analyses. Therefore,

as discussed in Section 3.5.2, in addition to the effects of solution homogeneity, gelation speed and stability was significantly affected by the pH of the last neutralised solutions. Figure 3.13 shows the of physical strength and stability of modified hydrogels which were obtained from solutions having different pH values and those were incubated at 37 °C for 24 h.

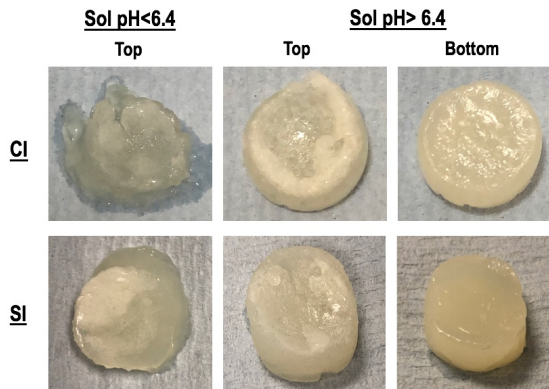


**Figure 3. 13** Demonstration of the effect of last solution pH on the physical strength and stability of modified hydrogels including CI (CS) and SI (CS.0.1HA.0.0005Hep) solutions. These specimens were obtained with a lower and higher final solution pH of 6.21 and 6.43; and 6.25 and 6.46, respectively, upon their incubation at 37 °C for 24 h. The weaker hydrogels obtained below pH 6.4 are shown at the left side of the image (only top surfaces) while the more stable hydrogels obtained from solutions having pH above 6.4 are seen at the images in the middle and right side showing their top and bottom surfaces respectively.

As shown in Figure 3.14, incubation of hydrogel solutions for 48 h at 37 °C of has led to acquisition of stronger elastic hydrogels from different compositions. While sole CS hydrogel (CI) was transparent, composite hydrogels were more opaque and whiter in colour.

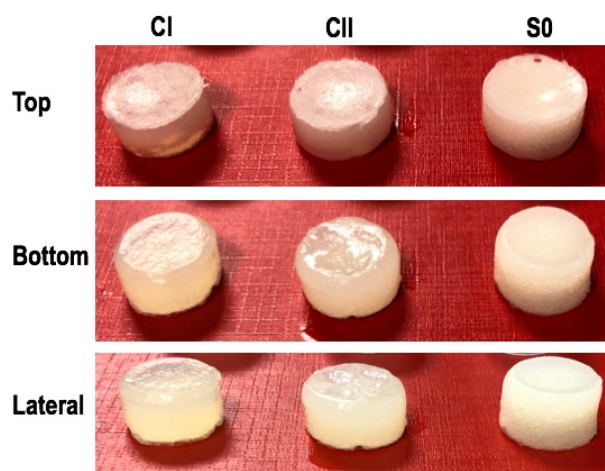


**Figure 3. 14** The photographs of physically and mechanically stable modified hydrogels taken from different angles for hydrogels with different compositions: CI (CS), CII (CS.0.1HA) and S0 (CS.0.1HA.0.0015Hep) synthesised with the last pH of 6.40-6.45 in final solution and acquired upon 48 h of incubation at 37 °C.

### 3.5.4 Injectability Measurements

#### 3.5.4.1 Qualitative Injectability Analyses

The injectability of the initial hydrogel solutions were assessed by flow features immediately after their synthesis. Each hydrogel solution specimen was manually tested by evaluating the ease of injectability against air and, assessed by the felt pressure required to expel the hydrogel solutions through a range of needles coupled with a syringe. The qualitative injectability results for each hydrogel solutions were tested by using different sized needles and are summarised in Table 3.6.

**Table 3. 6** Qualitative injectability assessment by rating the flow of different hydrogel compositions through manual injection via a range of needle sizes (1).

<b>Samples:</b>	<b>Needle Gauge (G) Sizes</b>						
	<b>18</b>	<b>19</b>	<b>20</b>	<b>21</b>	<b>22</b>	<b>23</b>	<b>25</b>
<b>C1</b>	*****	*****	*****	****	***	**	
<b>CII</b>	*****	*****	*****	****	***	**	
<b>SI</b>	*****	*****	*****	****	***	**	
<b>SII</b>	*****	*****	*****	****	***	**	
<b>SIII</b>	*****	*****	*****	****	***	**	

(1) \*\*\*\*\* *perfect flow*  
\*\*\*\*\* *good drop flow*  
\*\*\*\* *drop flow with slight pressure*  
\*\*\* *drop flow with high pressure*  
\*\* *drop flow with very high pressure*  
\* *no flow*

All liquid hydrogel formulations had steady and fast, perfect flow from 18-20 G needles; these were rated with six-stars. Fast and steady drop flow was observed in all compositions from 21 G needles. All compositions except SIII, had steady drop flow at slight pressure when a 22 G needle was used. The SIII specimen, having the highest concentration of Hep, exhibited a slightly more viscous behaviour in comparison to that of other liquid formulations. The additive impact of Hep on viscosity and elastic modulus has also been encountered in Rheology measurements, which will be discussed in Section 3.5.5. The applied (felt) injection force to expel hydrogel solutions were increased for injections through 23 and 25 G needles. However, all solutions had a steady dropwise flow with applied high pressure even with 25 G needle. Overall, a needle size of 21 G was found to be the optimal minimum needle thickness for the efficient injection of all the liquid hydrogel compositions.

Heparin-free samples may preserve their injectability capacity for a long term since they showed long term liquid flow stability during storage of up to 6 months refrigerated at 4 °C. This storage stability can be increased by keeping solutions in tightly closed test tubes. Hydrogel solutions containing Hep formed a skin-like layer on surface of solutions in tubes after 3 weeks of refrigeration. Therefore, the longer-term storage of the composite solutions may affect their injectability performance.

Regarding the modified hydrogel formulations prepared by autoclaving CS dispersion in water-glycerol media; these solutions showed a similar flow trend to that of initial hydrogel solutions in the first day of the synthesis. The flow of modified sterile hydrogel solutions captured from the videos recorded during injection testing through a range of needles, immediately after synthesis, are presented in Figure 3.15. The optimal minimal needle thickness for the injection of all compositions was also found to be 21 G. However, the viscosity of all modified liquid hydrogels increased after 24 h of refrigeration at (4 °C). Injectability of all hydrogel solutions becomes harder when using thinner needles. The injection test after 10 days of storage showed that there was still flow from the thickest needle size used (18 G) using moderate pressure. A constant elastic flow was observed by injection through the 5 mL syringe without a needle.

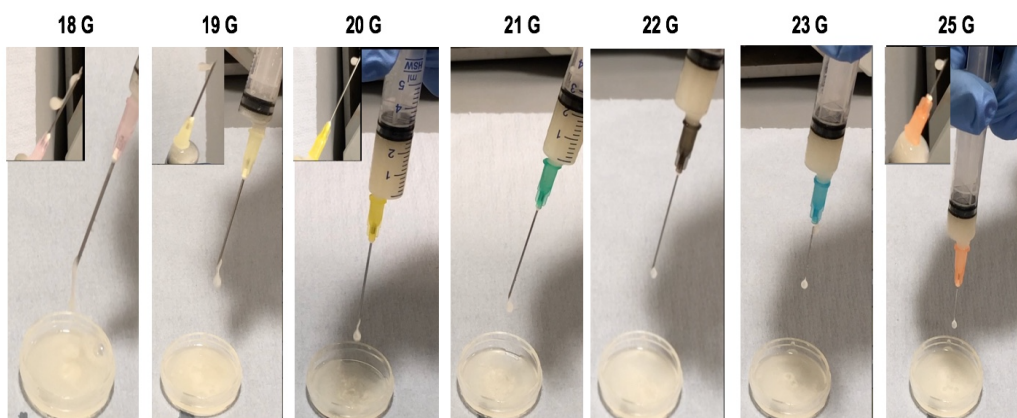


**Figure 3. 15** Photographs captured from the videos taken during from injectability tests. The steady or drop flow features of a sterile modified composite hydrogel formulation (SI) was tested immediately after synthesis, through a range of needles with increasing Gauge sizes.

The more elastic and adhesive solution properties that were observed in these modified hydrogel solutions, might be attributed to the impact of glycerol on sol-gel rheology and elasticity. The decrease in injection capacity from/after storage might be associated with the slight break down of polymer CS due to heat applied during autoclaving (132 °C). The stronger electrostatic interactions, causing an increase in the speed of

hydrophobic effects with neutralising agents and additionally, with Hep in composite solutions might cause increase in viscosity and cause early gelation of the solution. Therefore, the slight decrease of the autoclaving temperature to around 121 °C would be beneficial except that it could not be applied due to absence of temperature control in the available automatic autoclave.

### 3.5.4.2 Quantitative Injectability Analyses

Injectability tests, which involved measurements of the force applied against the constant displacement (30 mm) of a syringe plunger over 1 min to expel 5 mL of solution were performed in two different modes; the injection tests through a needleless 10 mL syringe, and tests through the syringe in conjunction with a needle (19 G or 21 G). The force versus displacement or time curves has shown similar patterns with those reported in the literature (Cilurzo et al., 2011). As an instance, in Figure 3.16.a, the first sharp peak seen with coloured dots for each sample represents the initial glide force (IGF) required for syringe plunger movement; the second part of the graph, with stable lines, indicate the dynamic glide force (DGF), which is referred to as the constant force required to maintain movement of the syringe plunger, and a sharp peak seen at the end of the graph occurs when the plunger makes contact with the end of the syringe. The IGF was detected as the maximum force point in the early part of the experiments (<5 sec) and the maximum force measured during the whole test was referred to as  $F_{max}$ . The mean IGF and  $F_{max}$  forces were calculated from the mean force values and standard deviations in repeated tests. The DGF, which is the combination of many data points into lines, was calculated as the mean of the forces on the common straight lines found at the region of 5-55 seconds for all samples. The DGF calculations also included the mean of repeated trials of each formulation ( $n=6$ ) and are presented with their standard deviations.

For initial hydrogel solutions, injectability features were tested/measured on their synthesis day (Day 0) in needleless and 19 G needle coupled syringe modes. These solutions were also tested after 3 days after their synthesis (Day 3) at needleless and 21 G needle coupled syringe modes. The force versus time graphs during the injection tests obtained in Day 0 and Day 3 are given at Figure 3.16 and Figure 3.17, respectively and

the mean IGF, DGF and  $F_{max}$  forces are summarised in Table 3.7. and Table 3.8., respectively for Day 0 and Day 3.

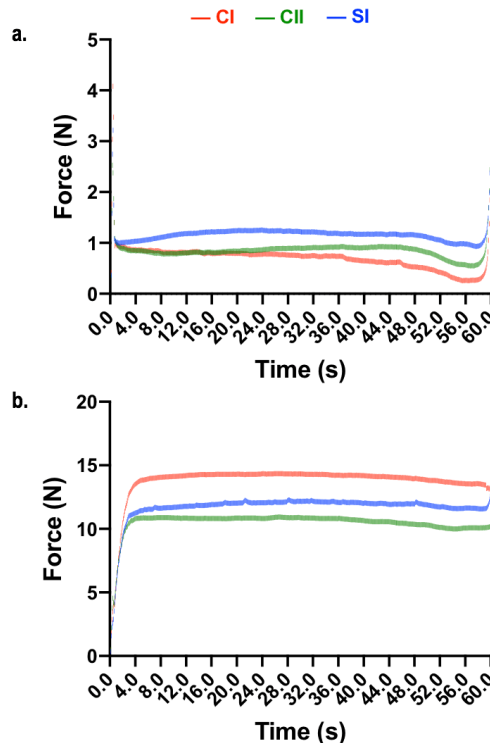


**Figure 3. 16** Quantitative injectability test results of non-modified initial hydrogel solutions with different compositions including CI, CII and SI on the same day of their synthesis (Day 0). The force measurements during injection through a 10 mL syringe **a.** without a needle (needleless) and **b.** coupled with a 19 G needle.

Day 0 injectability test results showed that all samples had approximately 1.4 N of IGF in needleless mode and up to  $\sim$ 5 N through a 19 G needle. It was seen that the DGF increased respectively for the samples: CI, CII and SI. The composite SI sample combining CS, HA and Hep required the biggest injectability force in needleless tests. However, this trend changed when injection took place with a 19 G needle wherein the maximum Day 0 DGF force ( $13.6 \pm 0.4$  N) belonged to the sole CS (CI) sample. The minimum Day 0 force ( $10.7 \pm 0.3$ ) was obtained with the CII sample. This might be associated with the contribution of HA to reducing shear stress, making flow easier. The Hep involved SI sample, however, possessed a slightly higher mean DGF force ( $11.9 \pm 0.2$ ) than CII. This may be caused by the impact of Hep slightly increasing the viscosity of the solution. This result was confirmed as well by Rheology measurements. A similar trend was observed with the  $F_{max}$  forces obtained in tests with a 19 G needle, where the highest value ( $14.3 \pm 1.7$  N) was for the CI, sole CS sample .

**Table 3. 7** The quantitative injectability results by measurements of forces in different stages of injection for diverse non-modified initials hydrogel solution compositions: CI, CII and SI obtained in the same day of synthesis (Day 0). Experiments were performed using both a needleless and 19 G needle-coupled syringe. The results were expressed as mean  $\pm$  standard deviations (SD) (n=6) (SD for experimental replicates).

Needleless			19 G needle			
	CI	CII	SI	CI	CII	
IGF (N)	4.3 $\pm$ 0.7	3.0 $\pm$ 1.1	3.3 $\pm$ 0.7	4.9 $\pm$ 2.5	5.0 $\pm$ 1.0	3.1 $\pm$ 1.6
DGF (N)	0.7 $\pm$ 0.1	0.9 $\pm$ 0.1	1.2 $\pm$ 0.1	13.6 $\pm$ 0.4	10.7 $\pm$ 0.3	11.9 $\pm$ 0.2
F <sub>max</sub> (N)	4.6 $\pm$ 0.3	4.5 $\pm$ 0.3	4.0 $\pm$ 0.2	14.3 $\pm$ 1.7	11.1 $\pm$ 1.1	13.6 $\pm$ 1.4

\*IGF: initial glide force; DGF: dynamic glide force; F<sub>max</sub>: maximum force expressed as Newton (N)

The injectability of initial hydrogel solutions tested after 3 days (Day 3) in needleless and 21 G needle are shown in Figure 3.17 and Table 3.8. In needleless flow tests, all liquid hydrogel specimens have shown very similar DGF forces ranging between 1.1-1.5 $\pm$ 0.1 N. The highest F<sub>max</sub> of 5.3 $\pm$ 0.3 N, was seen with the CI sample. In addition, needleless injectability results were almost same on Day 0 as on Day 3. The experiments did not show any significant change as a result of storage. In regards to injectability tests via a 21 G needle in Day 3, all forces were higher than those of Day 0 injectability tests done with 19 G needles and ranged between 25 and 30 N, which is comparable with reported manual injection forces (Burckbuchler et al., 2010). The increase in injectability force was due to needle size difference.

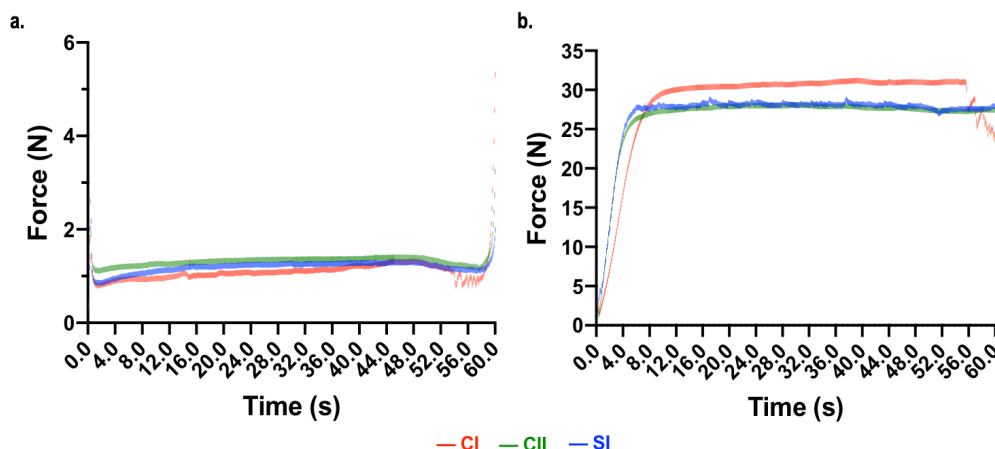


**Figure 3. 17** Injectability of non-modified initial hydrogel solutions with different compositions including CI, CII and SI, 3-days after their synthesis. The force measurements during injection through a 10 mL syringe **a.** without a needle (needleless) and **b.** coupled with a 21 G needle.

The Day 3 injectability results with 21 G needle tests have shown similar differences between the specimens as in Day 0. Similarly, the CI sample had the highest DGF and

$F_{max}$  measurements, which are  $30.3 \pm 1.5$  N and  $31.5 \pm 6.2$  N, respectively. The least injection force required belonged to the CII sample (DGF:  $27.6 \pm 0.4$  N) and  $F_{max}$   $28.2 \pm 4.3$  N). This result may be related to the beneficiary effect of HA making flow easier due to a reported shear stress reduction effect (Knowles et al., 2000; Raii et al., 2012). The mean forces acquired for the SI formulation were akin to those of CII values. However, tiny local force peaks were observed in the SI specimen which can be attributed to higher solution viscosity.

**Table 3. 8** The quantitative injectability force measurements during injection of non-modified initial hydrogel solutions: CI, CII and SI obtained after 3 days of synthesis (Day 3). Experiments were performed by both a needleless and 21 G needle coupled syringe. The results were expressed as mean  $\pm$  SD (n=6) (SD for experimental replicates).

	Needleless			21 G needle		
	CI	CII	SI	CI	CII	SI
<b>IGF (N)</b>	$1.9 \pm 0.4$	$2.6 \pm 0.5$	$2.3 \pm 0.2$	$2.6 \pm 0.8$	$1.9 \pm 0.1$	$5.5 \pm 2.0$
<b>DGF (N)</b>	$1.1 \pm 0.1$	$1.3 \pm 0.1$	$1.2 \pm 0.1$	$30.3 \pm 1.5$	$27.6 \pm 0.4$	$28.0 \pm 0.5$
<b>F Max (N)</b>	$5.3 \pm 0.3$	$3.7 \pm 0.2$	$2.3 \pm 0.2$	$31.5 \pm 6.2$	$28.2 \pm 4.3$	$29.9 \pm 4.3$

\*IGF: initial glide force; DGF: dynamic glide force;  $F_{max}$ : maximum force expressed as Newton (N)

Although during the tests, solutions in tubes were kept cold in an ice bath, the opening of the solution in test tubes leading to the evaporation of some carbon dioxide, might also have partially caused the viscosity increase in the remaining solutions that were used in tests at Day 3.

Regarding injectability tests of modified hydrogel solutions, they were tested on their synthesis day (D0) and one day after (D1) in both needleless and 19 G needle coupled syringe modes. The force measurement graphs for each of the modified hydrogel formulations are shown in Figure 3.18 and the mean IGF, DGF and  $F_{max}$  forces with their standard deviations are given in Table 3.9 for both test days.

In Day 0 tests, the sole CS solution (CS) has shown the highest DGF values of  $2.8 \pm 0.2$  N and  $18 \pm 0.8$  N for needleless and 19 G needle test modes, respectively. The fluctuations in the graph line of the CI sample might be due to local force changes during plunger displacement indicating the highest solution viscosity of all compositions. The injection forces during needleless flow tests were below 5 N for both days. However, more fluctuations, reducing the evenness of flow, at the force lines of

Hep composite hydrogels (S0 and S1) were observed. From D0 to D1, the least change in solution injectability was observed with an increase of approximately 5 N. The highest increase at DGF was belong to S0 sample with an about 20 N increase reaching almost up to 35 N.

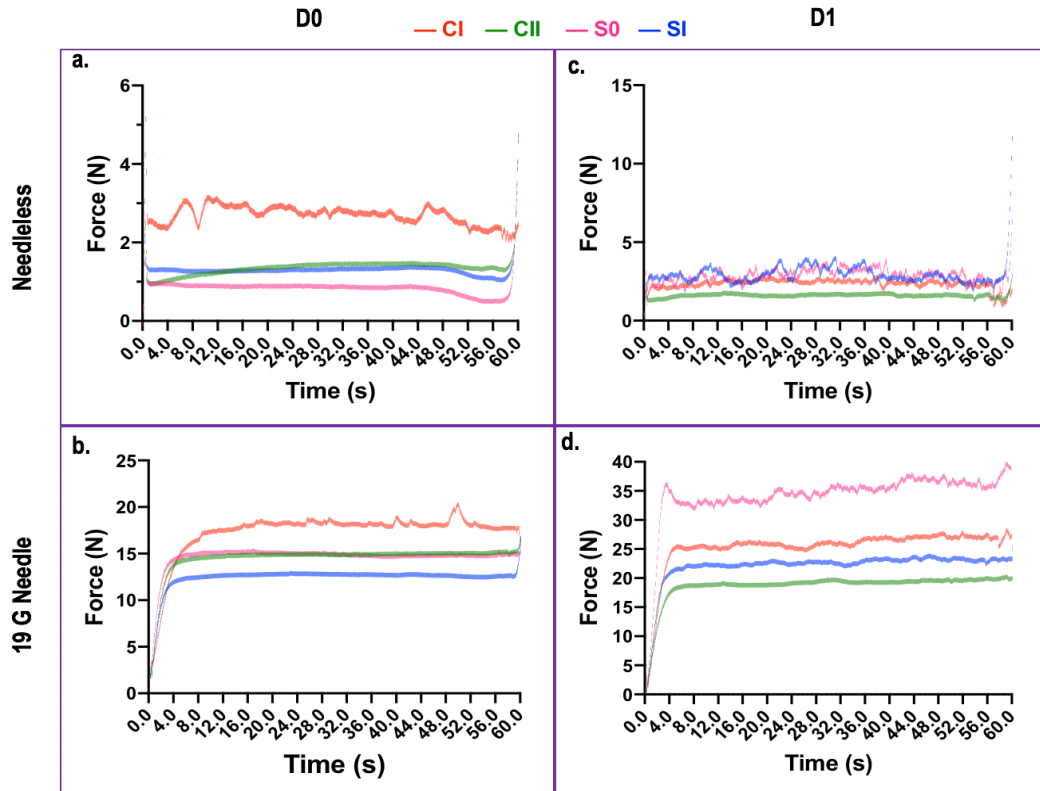


**Figure 3.18** Injectability of Modified sterile hydrogel solutions with different compositions including CI, CII, S0 and SI at Day 0 and Day 1 of the synthesis represented as D0 (at left) and D1 (at right). The force measurements versus time obtained during injection through a 10 mL syringe for D0 and D1 were given for the cases of needleless (a. and c.), and 19 G needle (b. and d.).

In Hep containing samples, the increase in viscosity after storage was expected, due to ionic interactions of counter charged Hep and CS at the molecular level. The limitations due to storage time of the solution by the addition of Hep is also covered in Section 3.5.2. Unexpectedly, a lower mean injection force ( $F_{\max}$ : 24 N) was obtained for the SI sample that had a higher amount of Hep than S0. This may be due to the degree of homogeneity of the mixture during the tests or the synthesis. The homogeneity of the solution is highly affected by the speed of the addition of the neutralizing agent. Its amount and mixing speed during synthesis could directly affect the solution viscosity and thus injectability. Therefore, more attention might be required to ensure optimal solution homogeneity both during both the synthesis and prior to the injection tests by sufficient mixing.

**Table 3. 9** The quantitative injectability results of Modified sterile hydrogel solutions for the compositions of CI, CII, S0 and SI. Experiments were performed using both a needleless and a 19 G needle coupled syringe. The results obtained on the synthesis day (Day 0) of the solutions, and 1 day after synthesis (Day 1) are represented as D0 and D1 respectively. The results were expressed as a mean  $\pm$  SD (n=6) (SD for experimental replicates).

Needleless				19 G Needle					
	CI	CII	S0	SI	CI	CII	S0	SI	
D0	IGF (N)	5.2	2.7 $\pm$ 0.3	3.0 $\pm$ 1.1	2.3 $\pm$ 0.6	3.5 $\pm$ 0.2	2.7 $\pm$ 1.2	3.1 $\pm$ 1.5	2.9 $\pm$ 0.6
	DGF (N)	2.8 $\pm$ 0.2	1.4 $\pm$ 0.1	0.9 $\pm$ 0.1	1.3 $\pm$ 0.1	18 $\pm$ 0.8	14.9 $\pm$ 0.2	14.9 $\pm$ 0.2	12.7 $\pm$ 0.2
	F <sub>max</sub> (N)	5.2 $\pm$ 0.3	5.0 $\pm$ 0.3	5.7 $\pm$ 0.4	5.0 $\pm$ 0.3	21.4 $\pm$ 2.9	16.6 $\pm$ 1.9	15.9 $\pm$ 1.7	16.9 $\pm$ 1.6
D1	IGF (N)	3.0 $\pm$ 0.5	2.7 $\pm$ 0.2	2.4 $\pm$ 0.7	Not detected	3.2 $\pm$ 1.4	3.1 $\pm$ 0.6	2.7 $\pm$ 0.2	2.2
	DGF (N)	2.4 $\pm$ 0.2	1.6 $\pm$ 0.2	3.0 $\pm$ 0.5	2.9 $\pm$ 0.6	26.1 $\pm$ 1.0	19.2 $\pm$ 0.5	34.9 $\pm$ 1.6	22.7 $\pm$ 0.7
	F <sub>max</sub> (N)	3.5 $\pm$ 0.4	3.8 $\pm$ 0.3	6.6 $\pm$ 0.7	11.6 $\pm$ 1.0	29.0 $\pm$ 4.1	20.3 $\pm$ 2.7	42.8 $\pm$ 5.2	24.4 $\pm$ 3.2

\*IGF: initial glide force; DGF: dynamic glide force; F<sub>max</sub>: maximum force expressed as Newton (N)

Overall, these injectability results show that initial hydrogel solutions showed better evenness flow and injectability performance in comparison to modified hydrogels. It was explicit from all results that the CS+HA sample (CII) showed the best injectability performance of all samples, having overall, the smallest DGF and F<sub>max</sub> among all samples. On the other hand, the results showed that addition of Hep into CS+HA systems increased viscosity, especially during storage. This was attributed to ionic interactions of oppositely charged CS and Hep promoting gelation. This has been also confirmed by Rheology analyses since composite hydrogels obtained with highest Hep concentration possessed a higher elastic modulus and decreased gelation temperature. The degree of the viscosity of the solution might also depend on Hep concentration and solution homogeneity, which is affected by neutralisation reaction conditions during the synthesis and success of mixing, prior to injection. In addition, storage time and conditions, such as air contact or storage temperature of the solution are also found to be significant parameters.

### 3.5.5 Rheology Analyses

In rheology measurements, during the temperature sweep tests, there was a slight decrease in both viscous (G'') and elastic modulus (G') occurring between 15 °C to nearly 30 °C, which was then altered by the gradual increase of G' suppressing the G''. The point where both curves crossover was determined as the incipient gelation point

( $t_{i.g.}$ ) indicating that the behaviour of solution elasticity has started to become dominant over its viscous behaviour. A key rheology graph at Figure 3.19 showing a temperature sweep test (15-60 °C and 60-15 °C) of the sole neutral CS solution with an initial CS concentration of 6% (w/v) demonstrates main sol-gel transition characteristics of CS based hydrogels neutralised by NaHCO<sub>3</sub>. As can be seen in this graph, the  $t_{i.g.}$  was determined as 35.9 °C for this solution.

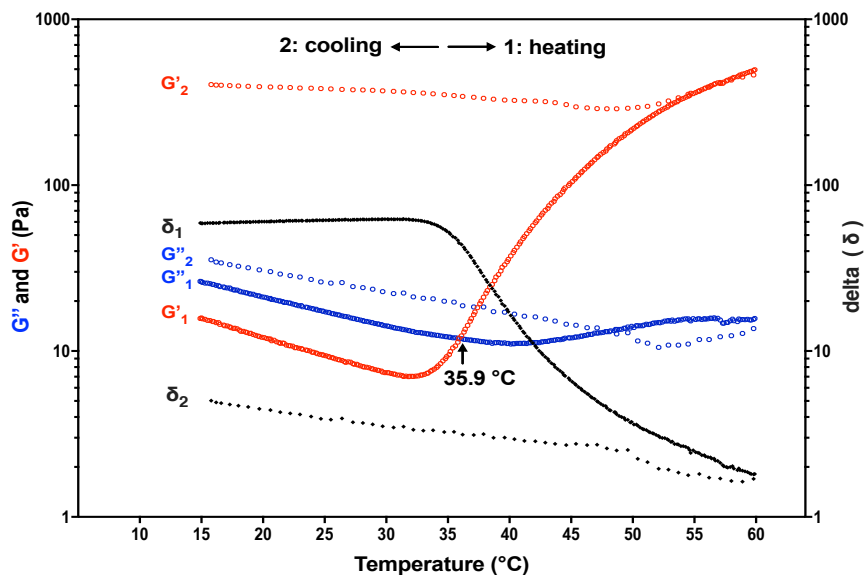


**Figure 3. 19** The viscous ( $G''$ ) and elastic modulus ( $G'$ ) changes for the sole CS solution (6% w/v initial concentration neutralised by NaHCO<sub>3</sub>) during the temperature sweeps by heating step (1) from 15 to 60 °C, with sol-gel transition starting at 35.9 °C and cooling step (2) where temperature was lowered back to 15 °C.

Between ~33 °C to 60 °C, the elastic modulus ( $G'$ ) of the solution increased up to ~500 Pa. Then, during the cooling step (2) from 60 °C to 15 °C, after a slight decrease,  $G'$  increased slightly and stayed constant at almost the same mechanical strength acquired during heating. This has indicated the irreversible thermosensitive gelation of CS based pH and thermosensitive injectable hydrogels neutralised by NaHCO<sub>3</sub>.

In Figure 3.20, elastic and viscos modulus changes in the all liquid initial hydrogel formulations during temperature sweeps from 15 to 37 °C are given. The results have shown that the CII sample, composed of CS and HA, possessed a lower incipient gelation point than the sole CS solution; from 36.6 °C to 30.9 °C. A further contribution to decreasing the gelation temperature was made by the addition of Hep in composite (CS/HA/Hep) hydrogels. The increasing Hep concentration led to quicker gelation in composite hydrogels, starting at 13 min, at 28 °C for SI (0.12 mg/mL), and at about 6

min and 21 °C for the SIII (0.60 mg/mL) samples. The exceptional SII composition showed slower gelation that started at about 31 °C. This might be associated with the distribution of Hep in samples due to the insufficient mixing of solutions prior to experiments. However, it is explicit that the SIII sample with the highest Hep concentration has exhibited a significant increase at the elastic modulus as temperature increased from about 5 Pa to 130 Pa as well as showing a lowered incipient gelation point. The high viscosity of the SIII solution was also physically observed during qualitative injection rating. Since this SIII solution with the highest Hep concentration (0.60 mg/mL) can limit injectability due to its increasing viscosity during storage, this composition was not used in further experiments despite its better mechanical strength. The composite SI solution with the lowest concentration of Hep (0.12 mg/mL), has been used instead (representing the maximum concentration of Hep) in further studies.

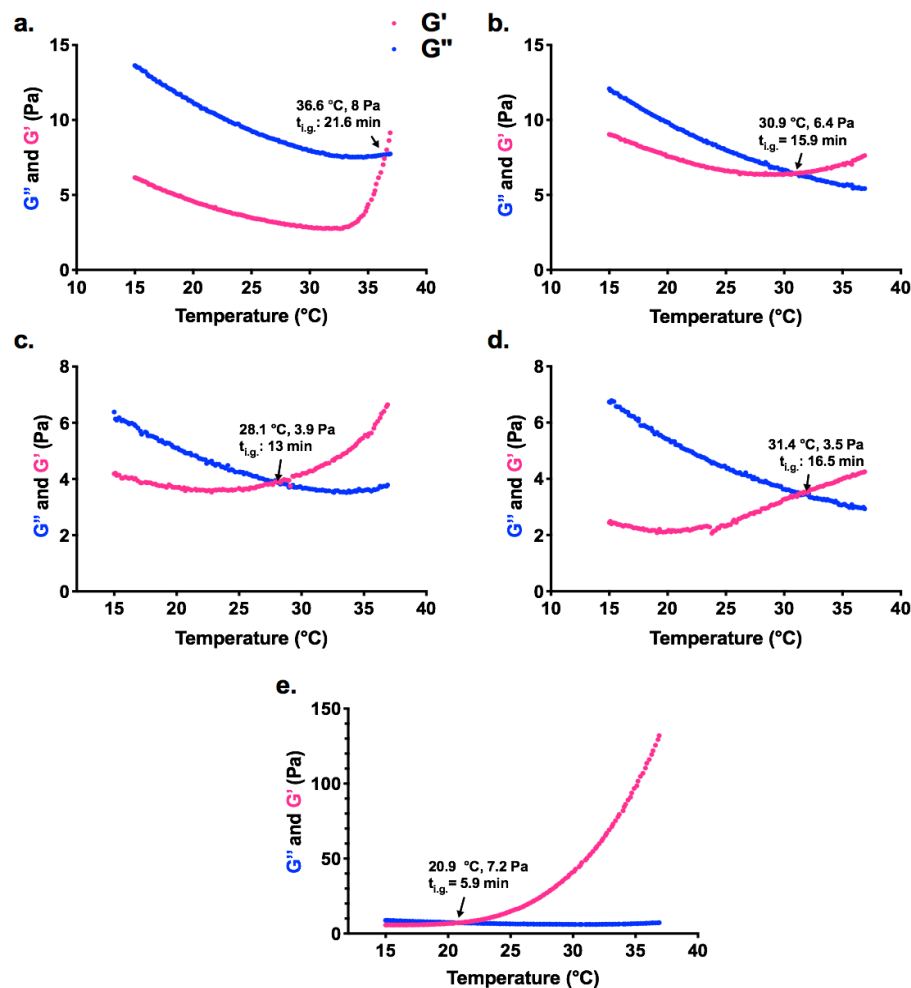


**Figure 3.20** Temperature dependent elastic and viscous modulus changes during oscillation tests carried out at a 1 Hz constant frequency and with heating from 15 to 37 °C at the speed of 1 °C/min for all initial liquid hydrogel formulations: **a.** CI (CS) **b.** CII (CS.0.1HA) **c.** SI (CS-0.1HA.0.005Hep) **d.** SII (CS.0.1HA.0.015Hep) **e.** SIII (CS.0.1HA.0.025Hep).

In addition, liquid hydrogel solutions were exposed to a time sweep at a constant average body temperature of 37 °C, to investigate time dependent viscoelastic alterations of the hydrogels. A representative rheology test result, which involve a temperature sweep from 15 to 37 °C followed by holding temperature at 37 °C for 30 min and then cooling temperature back to 15 °C, is demonstrated at Figure 3.21. During heating (15-37 °C) the  $G'$  rose from about 5 Pa to 25 Pa. Following this, during the 30 min time sweep, by holding temperature at 37 °C, the elastic modulus of the formed hydrogel increased from approximately 40 Pa to 260 Pa. This is shown as a vertical pink line in the graph at Figure 3.21.a. These results indicate that these CS based hydrogel formulations that start gelation within minutes, upon injection at tissue defects, have a great potential for time dependent strengthening and settling at body temperature. When the reversal temperature sweep (cooling) was applied, the elastic modulus gained during heating was maintained and stayed relatively constant with a slight increase, showing once again the irreversible gelation behaviour of these hydrogels.

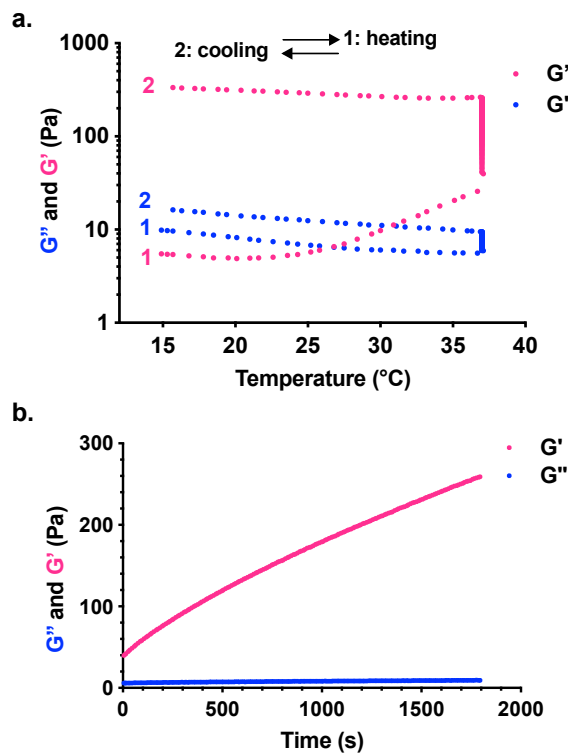


**Figure 3. 21** The elastic and viscous modulus changes for the CII (CS.0.1HA) liquid hydrogel formulation during a temperature sweep by heating (1) from 15 to 37 °C followed by a time sweep involving holding the temperature at 37 °C and then cooling the temperature back to 15 °C: **a.** whole test including temperature and time sweeps **b.** a time sweep only while holding the temperature at 37 °C.

### 3.5.6 Morphological Analyses by SEM

The initial hydrogels after freeze-drying possessed an interconnected and porous morphology. The folding polymer structure on the top surface of the hydrogels is considered due to the vacuum during freeze-drying. The measured minimum, maximum and mean pore diameters in hydrogels were 19.5  $\mu\text{m}$ , 158  $\mu\text{m}$  and, 73.4  $\mu\text{m}$  respectively. Figure 3.22 demonstrates the SEM morphological images of sole CS and composite CS/HA hydrogels, comparatively. The sole chitosan hydrogels possessed a semi crystalline polymer matrix with rough surface features. It is considered that this surface roughness has been contributed to by the evaporation of carbon dioxide from surface and the deposition of small crystals due to dissolved or precipitated sodium salts from the neutralizing agent and possibly from side products of Na acetate and  $\text{Na}_2\text{CO}_3$  (Liu et al., 2011; Rogina et al., 2017). The presence of salt crystals in hydrogels, were discussed in the section on XRD analyses. The rough surface morphology contributed to by  $\text{NaHCO}_3$  is expected to induce cell attachment on the surface as has been reported (Deligianni et al., 2000; Deng et al., 2017). Furthermore, a more crystalline rough surface microstructure was observed in composite CS/HA hydrogels. The smaller rough spherical HA particles seemed to attach on and cover crystalline salts that could be the indication of ionic binding between HA and sodium salt crystals.

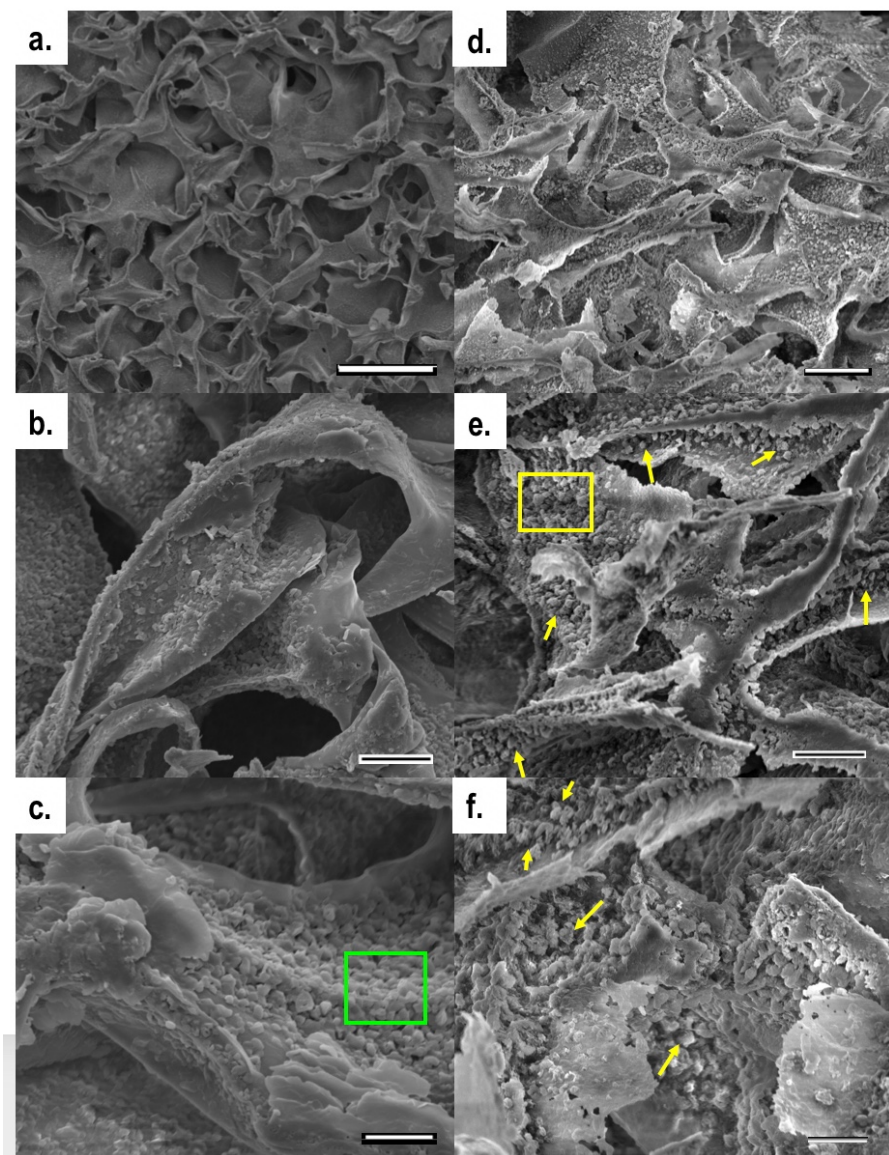


**Figure 3.22** SEM microstructure images of freeze-dried hydrogels at different magnifications: (a-c). CI (CS): sole CS hydrogel obtained after neutralisation by  $\text{NaHCO}_3$  given, and (d-f). CII (CS.0.1HA) hydrogel with HA particles deposited on a CS matrix. Yellow arrows and green squares respectively identify HA crystals and sodium salt crystals, originating possibly from the used neutralizing agent. (Scale bars correspond to a. 100  $\mu\text{m}$ , d. 20  $\mu\text{m}$ , (b and e). 10  $\mu\text{m}$ , (c and f). 5  $\mu\text{m}$ .)

The same samples were analysed by SEM after 8-months of storage in a desiccator with silica gel. The results have shown that sole CS polymer matrix hydrogel showed a relatively smoother surface when analysed, as well as a deficiency of salt crystals leaving some cracks behind. This might be associated with salt induced hygroscopic structure leading to moisture transportation and the further dissolution and evaporation of crystals by the induction of surface tension (Koniorczyk & Gawin, 2008). In addition, pores become more open by the removal of salts. This interconnected and porous

morphology can be seen more explicitly in Figure 3.23 (b-g). Hydroxyapatite crystals seem also to have deteriorated through time.

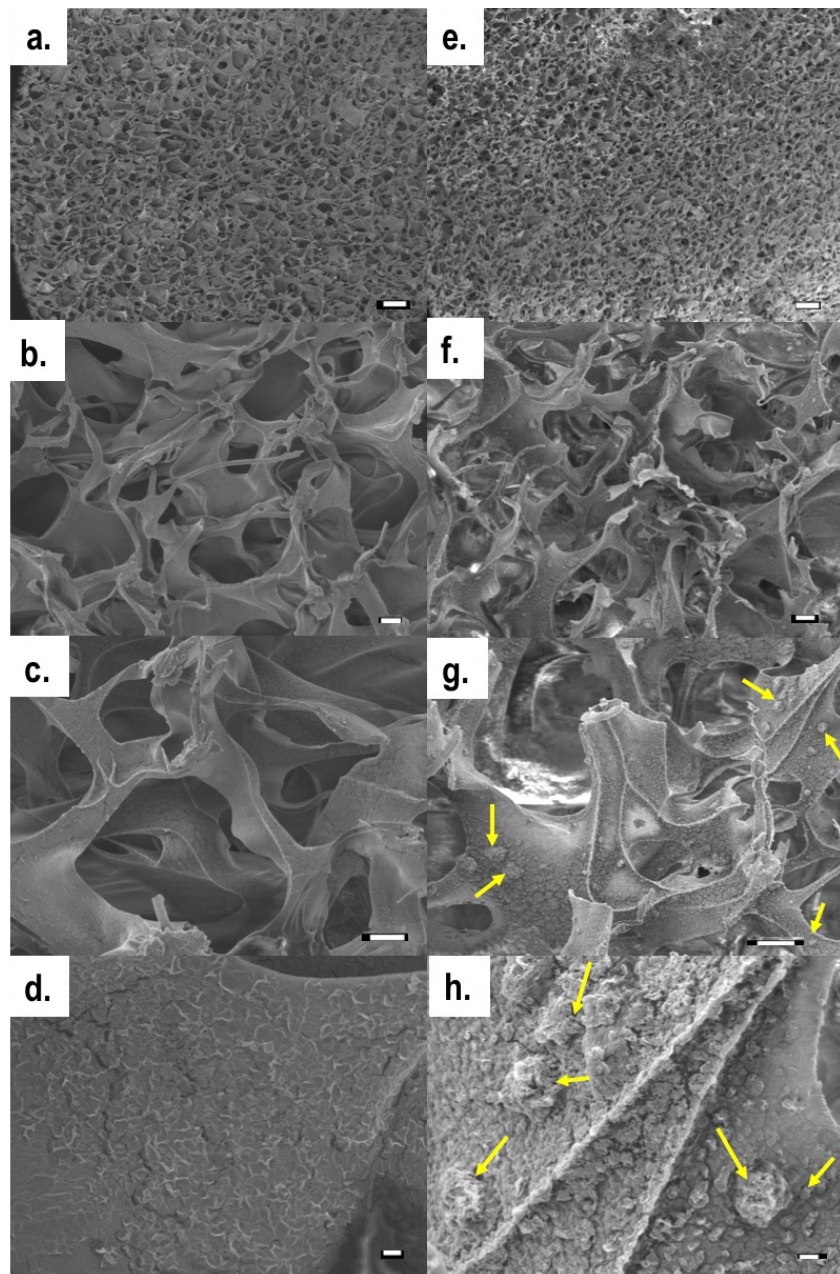


**Figure 3. 23** SEM micrographs of freeze-dried hydrogels taken after 8 months of storage given at different magnifications (a-d). CI (CS): from sole CS, and (e-h). CII (CS.0.1HA) yellow arrows indicate HA particles. (Scale bars correspond to: (a and e). 100  $\mu\text{m}$ , (b, c, f and g). 10  $\mu\text{m}$ , (d and h). 1  $\mu\text{m}$ .)

The composite hydrogels containing Hep (CS/HA/Hep) exhibited smooth surface morphology by the coating effect of Hep that covers all crystalline salts and HA particles which then seem to be embedded underneath. However, rough HA particles could be still seen at some locations. As the Hep concentration increased this coating

impact could be seen more explicitly. In Figure 3.24, the SIII composition, having the highest amount of Hep (0.60 mg/mL), showed the smoothest morphology. The HA crystals were located as agglomerates of small spherical particles dispersed in different parts of the polymer matrix surface. The bigger prismatic shaped crystalline structures were attributed to Na salts deposited on a semi crystalline polymer structure.

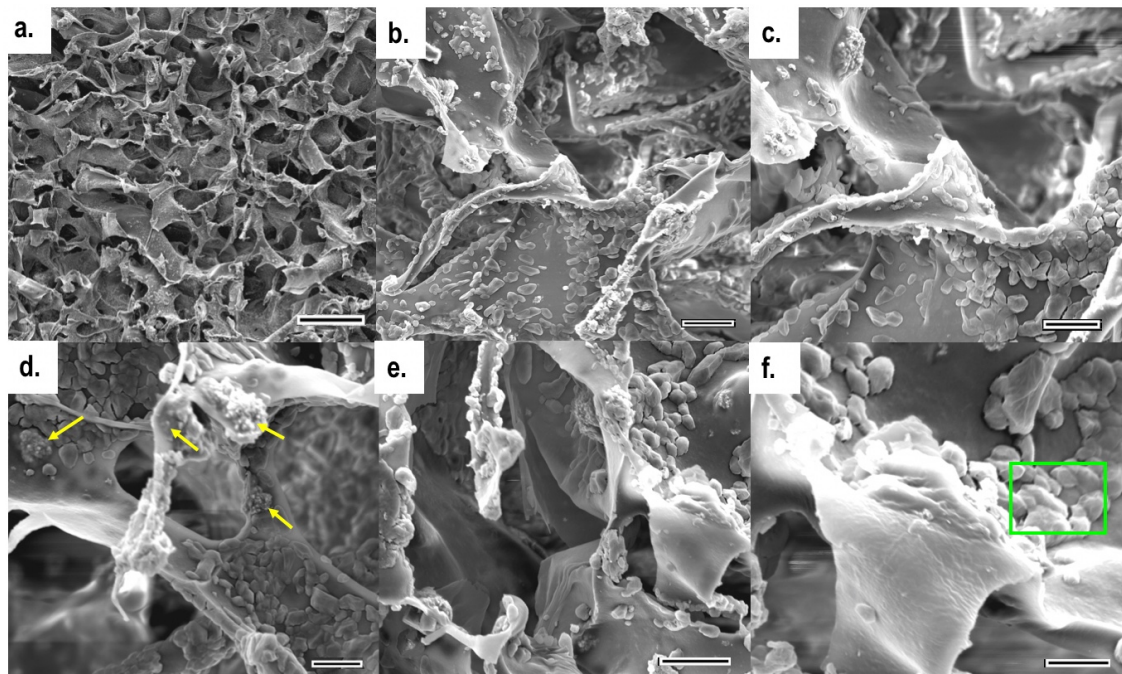


**Figure 3. 24** SEM images of freeze-dried composite hydrogel, SIII (CS.0.1HA.0.025Hep) which has the max Hep concentration (0.60 mg/mL). Yellow arrows show HA particles, while salt crystals deposited due to  $\text{NaHCO}_3$  salt are demonstrated in a green square. (Scale bars correspond to: a. 100  $\mu\text{m}$ , b. 10  $\mu\text{m}$ , (c-d). 5  $\mu\text{m}$ , e. 6  $\mu\text{m}$  f. 3  $\mu\text{m}$ .)

In the SI sample (0.12 mg/mL Hep), some bubbles appear that might be attributed to the release of  $\text{CO}_2$  during gelation. If the quick gelation occurred due to air contact with the solution, this could have caused the forming of bubbles from burst release of  $\text{CO}_2$ , (Figure 3.25).

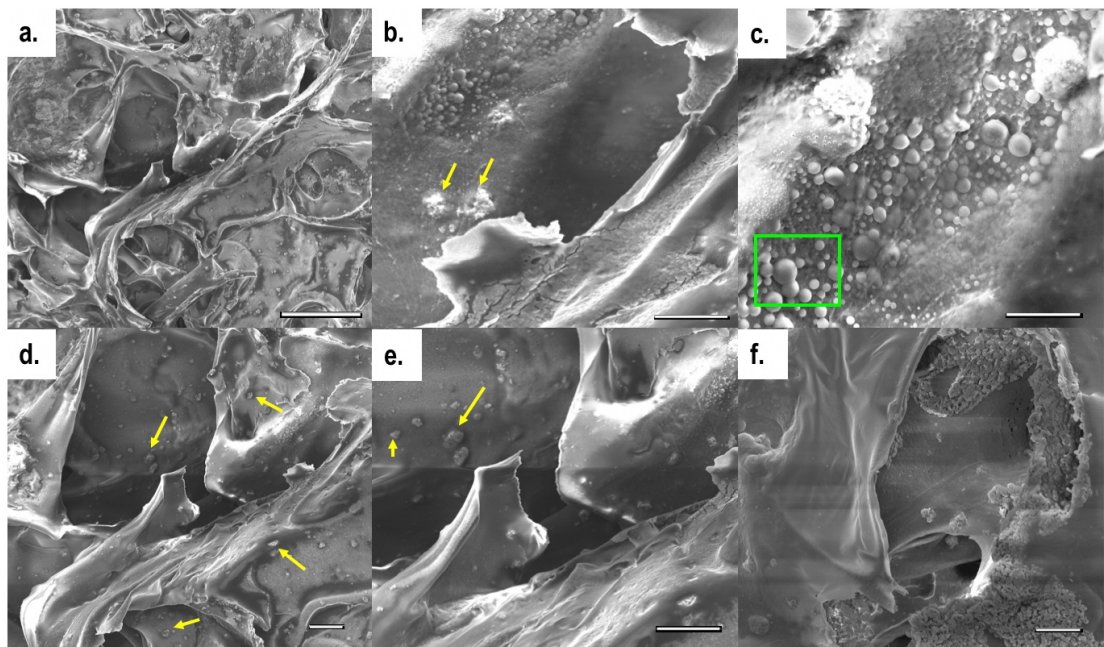


**Figure 3.25** SEM images of freeze-dried composite hydrogel SI (CS.0.1HA.0.005Hep) with 0.12 mg/mL Hep, taken at different magnifications. Yellow arrows show HA particles while the green square demonstrates the bubbles formed on the surface of the hydrogel due to CO<sub>2</sub> release during gel formation. (Scale bars correspond to **a.** 100  $\mu$ m, **b.** 10  $\mu$ m, **c.** 5  $\mu$ m, **(d-e).** 20  $\mu$ m **f.** 10  $\mu$ m.)

The modified hydrogels obtained via the CS sterilisation step, exhibited a morphology, totally different from that of the initial hydrogels. Furthermore, modified hydrogels acquired with a pH of between 6.4 and 6.5 in final solution, differed from hydrogels which were produced with lower pH (6.2-6.4). The hydrogels produced from solutions having a pH above 6.4 showed a flat bone like morphology, having a hierarchical porous structure between two flat surfaces. Figure 3.26 shows the sole CS hydrogels obtained after the gelation and freeze-drying processes. The porosity at the cross-section of hydrogels involved a hierarchical porous structure possessing very big pores (~500  $\mu$ m) which were separated by thick and denser walls composed of tiny micropores (~5  $\mu$ m) (Figure 3.26 e and f). Having a thinner and rougher morphology than the bottom surface (Figure 3.26 a), the top surface of the hydrogels (Figure 3.26 b) had some closed or open bubbling formations, considered to be formed due to CO<sub>2</sub> evaporating during gelation.

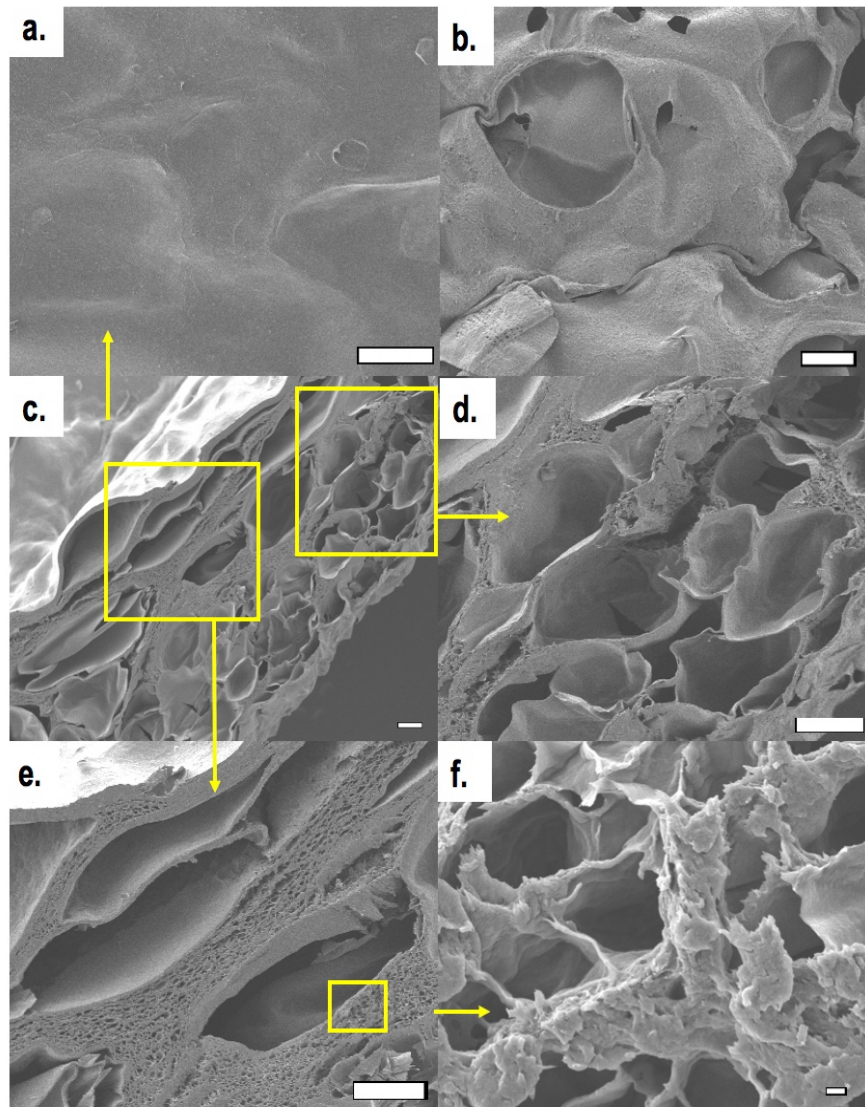


**Figure 3.26** SEM images of modified hydrogel, CI obtained from sole CS after neutralization by  $\text{NaHCO}_3$  to a pH slightly higher than 6.4. Images were taken from **a.** bottom **b.** top and **c.** cross-section and **(d-f).** the magnified versions of square areas in image c. All images have a 100  $\mu\text{m}$  scale bar except **f.** with a 1  $\mu\text{m}$  scale bar

As for CS/HA composite hydrogels possessing a pH of above 6.4 (Figure 3.27.), the decrease of pore sizes hierarchically from the outer to inner layers of the hydrogel structure is easily seen in Figure 3.27.c and Figure 3.27.d. The majority of HA crystals were located at the porous regions in the cross-section of the hydrogels, while bottom surfaces possessed only bigger HA particles due to gravity. The spherical flower like porous HA crystals covered the macropores thoroughly and dispersed on the nearby thin micropore surfaces. The porous and rough surface topology of HA (study's own synthesis, HA-5 specimen) crystals seem quite promising for bioresorption and bioactivity performance. This was later confirmed by the SBF bioactivity studies elaborated in Chapter 4.

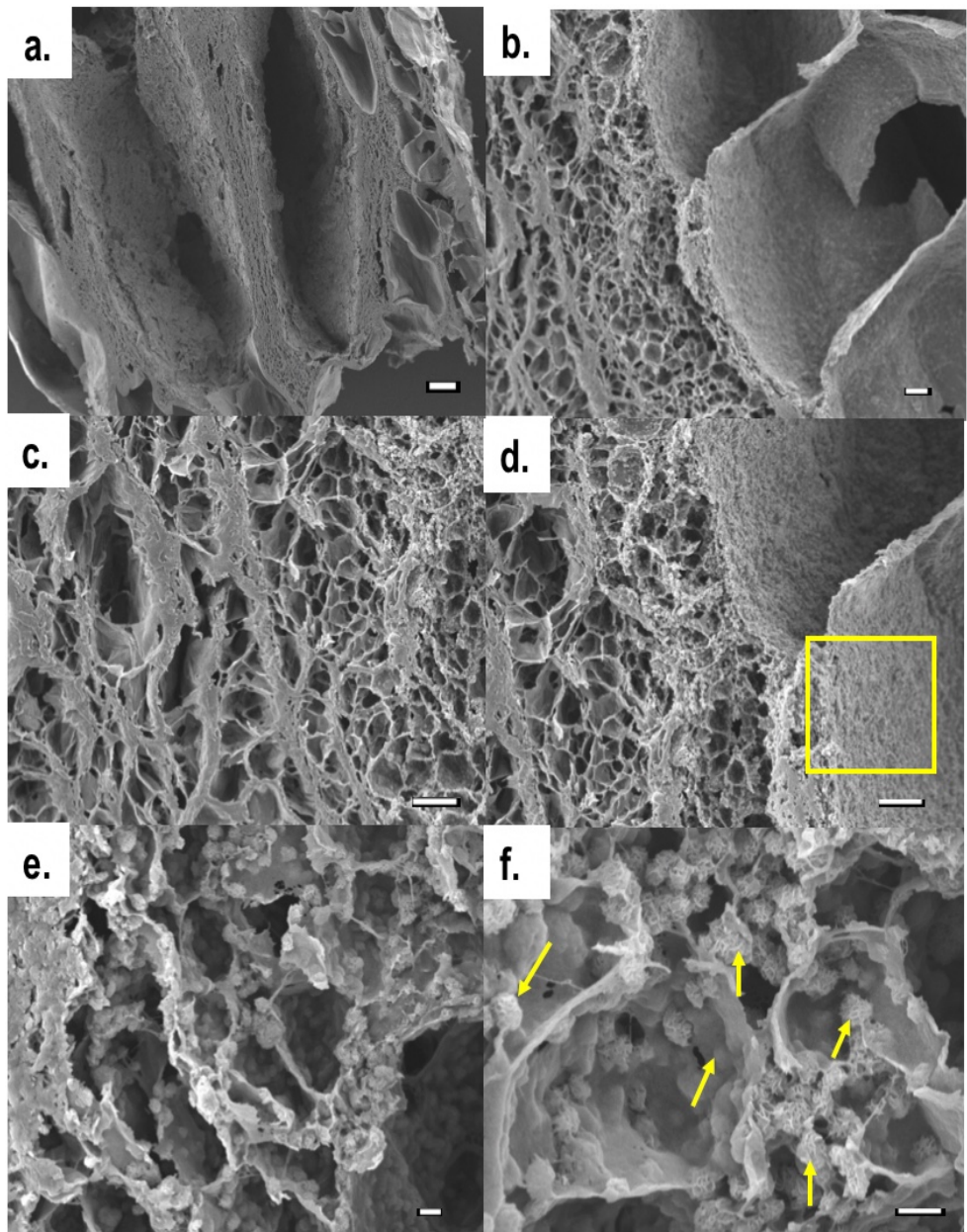


**Figure 3. 27** SEM images of modified hydrogel composite CII (CS.0.1HA) having a pH above 6.4. The cross-section images were taken at different magnifications. Yellow arrows and square show porous HA crystals covering on polymer matrix. (Scale bars correspond to **a.** 100  $\mu\text{m}$ , **(b-d).** 10  $\mu\text{m}$ , **(e-f).** 1  $\mu\text{m}$ .)

Regarding composite hydrogels involving Hep (CS/HA/Hep), these possessed a similar morphology to CS/HA hydrogels. However, the coating effect of Hep covering the surfaces of rough HA and salt crystals was observed in modified hydrogels as well (Figure 3.28).

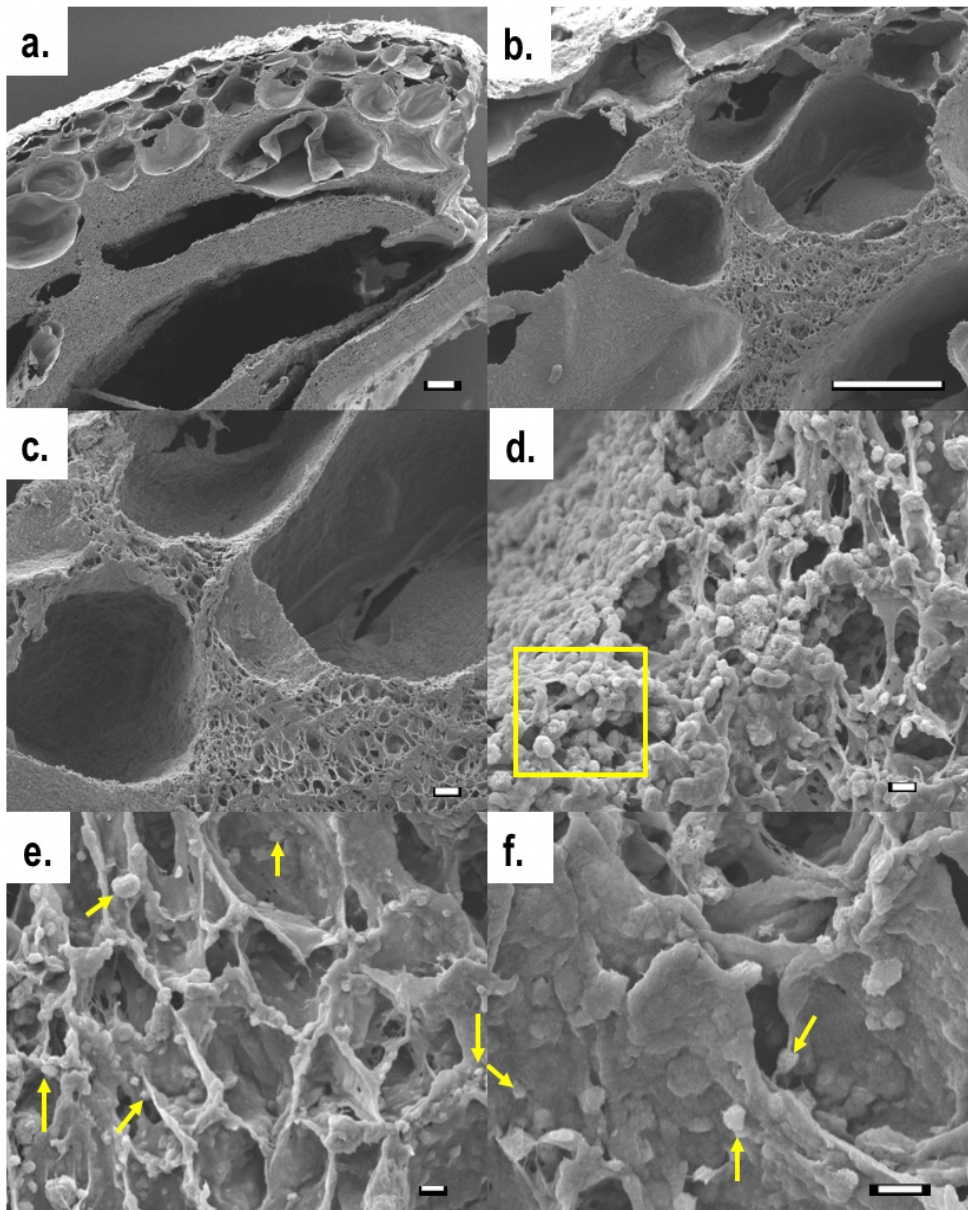


**Figure 3.28** SEM images of modified composite hydrogel, SI (0.12 mg/mL of Hep) (CS.0.1HA.0.005Hep) obtained with a pH above 6.4 in final solution. The cross-section images were taken at different magnifications. Yellow arrows and square show spherical HA crystals seemingly coated by Hep. (Scale bars correspond to: (a-b). 100  $\mu$ m, c. 10  $\mu$ m, (d-f). 1  $\mu$ m.)

Modified hydrogels obtained with lower pH than 6.4 (6.2-6.4) possessed a different morphology filled with only tiny micropores approximately 5  $\mu$ m diameter. There was a more compact layer next to the top surface, and a more porous structure underneath. The micropores exhibited a geometrical, honeycomb like morphology, as can be seen in Figure 3.29. These hydrogels have been used to evaluate their bioactivity performance and their morphology, during incubation in SBF. Their contribution to biomimetic mineralisation will be assessed in Chapter 4.

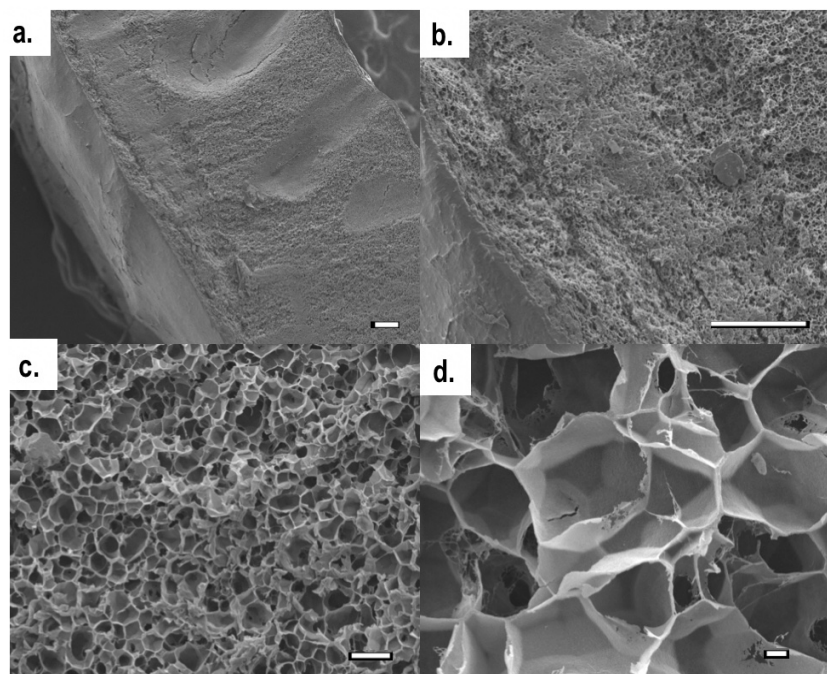


**Figure 3.29** SEM micrographs of a sole CS hydrogel obtained with a pH between 6.2-6.4 in final solution after gelation and freeze drying, at different magnifications. (Scale bars correspond to: **a-b**. 100  $\mu$ m, **c.** 10  $\mu$ m, **d.** 1  $\mu$ m.)

Overall, SEM analyses showed that the hydrogels exhibited diverse morphological properties as a result of different synthesis conditions. The initial hydrogel formulations that were not exposed to the heat sterilization of CS, showed an interconnected and porous morphology that was respectively more uniform than the microstructure of modified hydrogels whose final pH at solution state was above 6.4. The commercial HA that had been used in initial hydrogels, showed small rough spherical particle properties which were dispersed over the CS matrix. The study's own synthesis HA (HA-5) used in modified formulations also possessed a spherical and rough morphology exhibiting flower like and highly porous active surface features. In both initial and modified hydrogels, the inclusion of Hep has led to a coating effect covering the surface of particles and making it smoother.

It has been seen that morphology of the modified hydrogels strongly depends on the final pH of the hydrogel solutions after their neutralisation. As aforementioned, hydrogels obtained from a final solution having a pH below 6.4 (6.2-6.4) exhibited a more uniform structure filled with very tiny pores ( $\sim 5 \mu$ m). On the other hand, hydrogel solutions whose pH values slightly exceed 6.4 were provided a hierarchical anisotropic morphology having large pores ( $\sim 500 \mu$ m) divided by dense small micropore walls.

These interlocking pore walls in these hydrogels, having pH above 6.4, enhanced mechanical stability by having a significantly higher compression strength. This is discussed in detail in the following section.

### 3.5.7 Mechanical Analyses by Compression Tests

The mechanical durability of hydrogels under compression stress were measured up to a certain percentage of strain, which were 40% and 75% for sample groups which have a solution pH of 6.2-6.4 and 6.4-6.5, respectively. Figure 3.30 shows a demonstration of compression testing steps of a modified stable hydrogel S0 (solution pH: 6.4-6.5) tested by a UTM in compression mode.

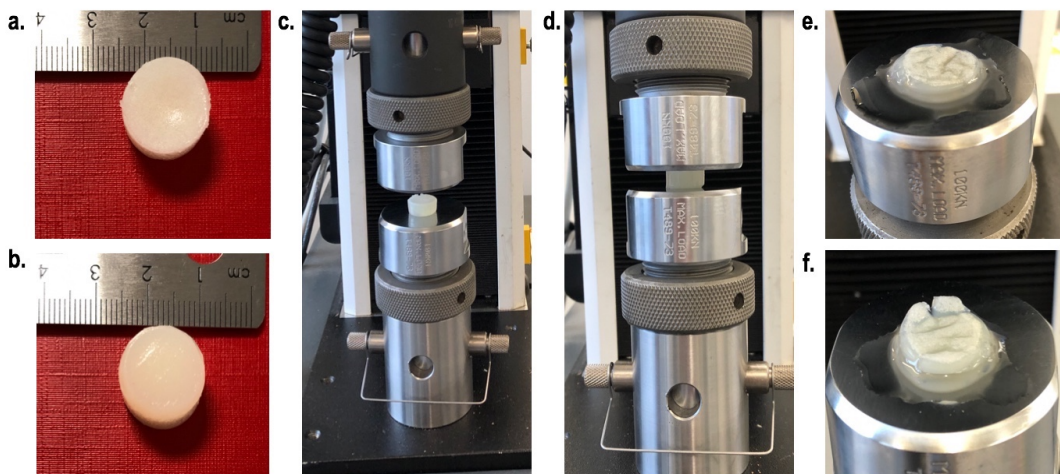


**Figure 3.30** The compression test steps applied on a composite modified hydrogel specimen, S0 (CS.0.1HA.0.0015Hep) **a.** top and **b.** bottom images of sample, and **c.** sample placed between compression plates **d.** the loading cell is lowered until it has just a contact with the sample and for **e.** and **f.**, the sample's appearance after an applied compression of up to 75% strain.

The compression stress-strain curves for hydrogels with lower pH (6.2-6.4) and higher pH (6.4-6.5) are given in Figure 3.31 and Figure 3.32, respectively. For hydrogels with lower pH (6.2-6.4), the results showed that strength range were between 1.5 kPa to 14 kPa at the 40% strain point. In comparison with the mean values of CI (CS), the CII (CS.0.1HA) sample showed a higher strength, reaching  $\sim$ 7 kPa. On the other hand, the SI sample with Hep (0.120 mg/mL) possessed the lowest mechanical strength reaching approximately 6 kPa stress. The mean elastic modulus of initial hydrogel samples was between 0.04 and 0.06 MPa.

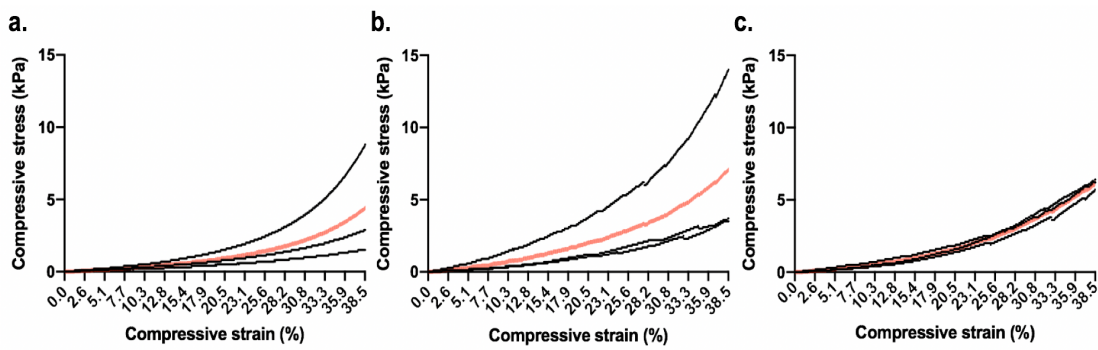


**Figure 3. 31** The compression stress-strain curves performed up to a 40% strain in modified hydrogel samples. These hydrogels were obtained at pH ranges of 6.2-6.4 in final solution in different compositions: **a.** CI (CS) **b.** CII (CS.0.1HA) and **c.** SI (CS.0.1HA.0.005Hep). Black dotted curves belong to three replicates of the same experiment whereas red curves indicate the mean values of these repetitions.

Modified hydrogels obtained from the solutions having a pH above 6.4 exhibited a significant increase in compression strength and elastic modulus in comparison to its lower pH counterparts. The elastic moduli of the composite hydrogels, except for the CII sample, were slightly higher than those of articular cartilage tissues reported to be in the range of 0.45 and 0.8 MPa (Athanasios et al., 1991; Mredha et al., 2017). The mean Young's modulus counted by software for CI, CII, S0 and SI modified hydrogels were 1.45, 0.33, 1.51 and 0.88 MPa respectively. The mean stress at the 75% strain point were in increasing order of 85, 177, 245 and 310 kPa for CII, SI, CI, and S0 samples, respectively.

A gradual deformation (creep) of the hydrogels under compression occurred during testing. There was a trend of gradual deformation showing an uprising curve of stress followed by a sudden slight decrease, and this pattern was repeated by one or two more deformation stages up to the 75% strain level at the experiment's end. The lowest first deformation point was seen in sole CS sample (CI) starting at near 56% strain, which was followed by two more deformation stages at 62% and 71% strain. This behaviour of hydrogels under strain could be associated with their hierarchical interpenetrating, latticed physical network that may be delaying the breakage of the modified hydrogels; due primarily to the elasticity and in part, the stability imparted by their structures. The occurrence of the first deformation was seen for all hydrogel compositions in the order of CI<CII<S0<SI, with the highest retardancy of the first deformation seen in a composite SI (CS.0.1HA.0.005Hep) specimen starting at 69% strain.

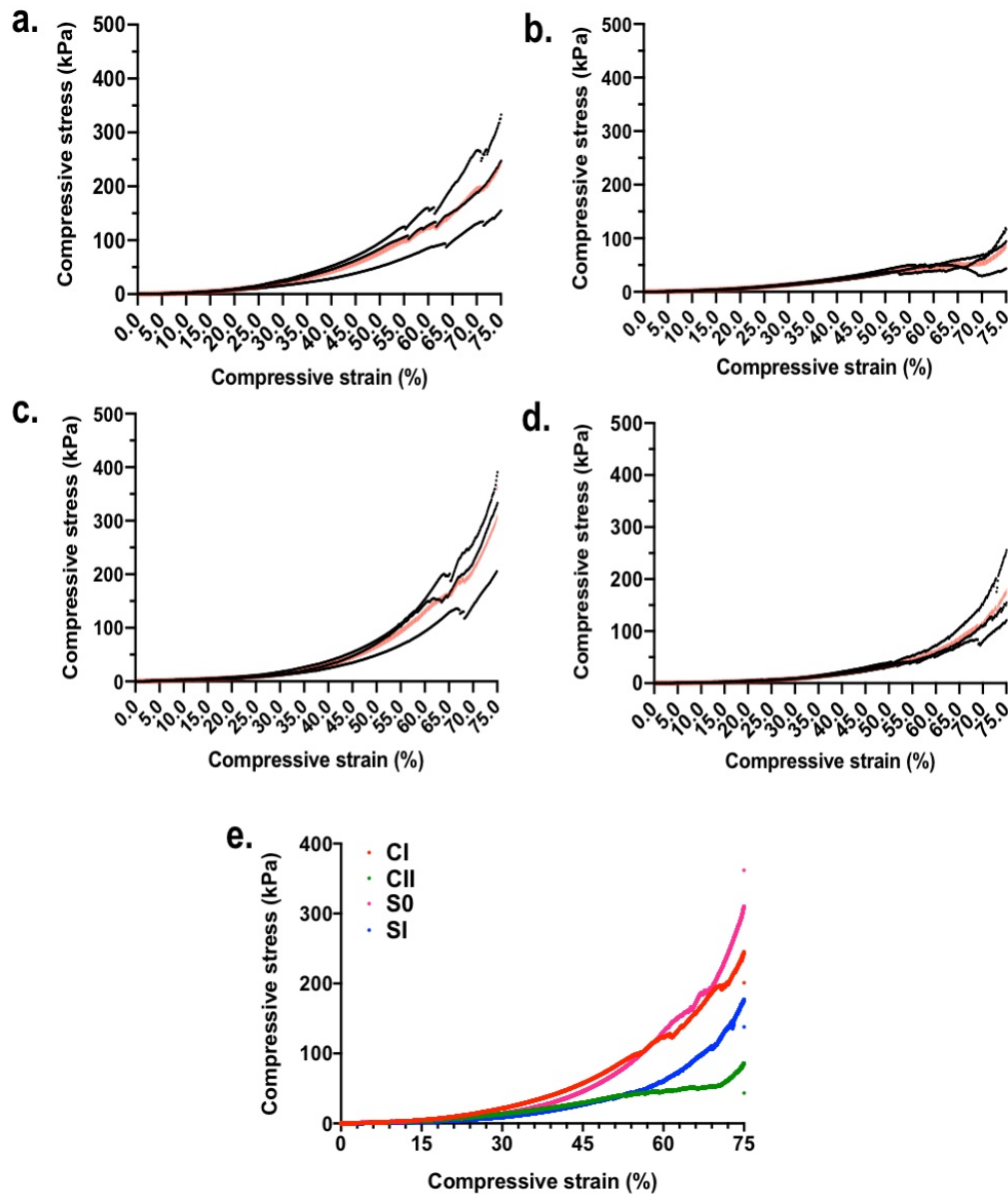


**Figure 3.32** The compression stress-strain curves performed up to a 75% strain in the samples. These modified hydrogels were obtained at a pH slightly above 6.4 in final solution in different compositions: **a.** CI (CS) **b.** CII (CS.0.1HA), **c.** S0 (CS.0.1HA.0.0015Hep), and **d.** SI (CS.0.1HA.0.0050Hep) (Black dotted curves belong to three replicates of the same experiment whereas red curves indicate the mean values of these repetitions), and **e.** the comparison of the means of all sample groups.

### 3.5.8 Chemical Analyses

The chemical structure of the hydrogels and all raw materials were analysed by Infrared and Raman vibrational spectroscopy techniques, and crystalline phases were detected by X-Ray diffraction analyses.

### 3.5.8.1 FT-IR-(ATR) Analyses

The ATR spectra of the reagent materials including CS, Hep, HA, NaHCO<sub>3</sub>, and composite initial hydrogel (SI), are given in stacked plot form in Figure 3.33. In the CS powder spectrum (Figure 3.33.a), the broad peak located between 3200 and 3500 cm<sup>-1</sup> was attributed to overlapping stretching vibrations of O–H and N–H bonds (Shahzad et al., 2015). The shoulder peak to this broad peak is attributed to C–H stretching vibrations seen at 2874 cm<sup>-1</sup>, the peaks at 1652 cm<sup>-1</sup> and 1593 cm<sup>-1</sup> to amide-I band or C=O and amide-II band or N–H deformation, respectively (Yar et al., 2017). The peaks at 1419 cm<sup>-1</sup> and 1377 cm<sup>-1</sup> were due to CH<sub>2</sub> bending and an amide III bond takes place at 1323 cm<sup>-1</sup> (Shahzad et al., 2016). The C–N stretching bonds are designated at 1260 cm<sup>-1</sup> while the peak at 1150 cm<sup>-1</sup> is attributed to C–O stretching vibrations (Yar et al., 2017). The peaks at 1060 cm<sup>-1</sup> and 1025 cm<sup>-1</sup> are attributed to C–O cyclic stretching frequencies (Moreira et al., 2016; Rokhade et al., 2007). The shoulder peak manifested at 896 cm<sup>-1</sup> is attributed to C–O–C stretching in saccharide rings of CS (Deng et al., 2017; Yar et al., 2017).

The ATR spectra of Hep (Figure 3.33.b) showed that the broad peak region of an O–H bond was seen at 3413 cm<sup>-1</sup>, whereas a small shoulder peak due to C–H vibration was detected at 2945 cm<sup>-1</sup> (Sun et al., 2011). The symmetric and antisymmetric COO<sup>-</sup> group vibrations in Hep are seen at 1610 cm<sup>-1</sup> and 1419 cm<sup>-1</sup> (Mainreck et al., 2011). The peaks at 1149 cm<sup>-1</sup> and 1221 cm<sup>-1</sup> are attributed to asymmetric S=O stretching from N-sulphate and O-sulphate groups in Hep, respectively (Cabassi et al., 1978; Yar, Gigliobianco, et al., 2016). Other sulphate group vibrations were seen at 989 cm<sup>-1</sup> and 1021 cm<sup>-1</sup> (Mainreck et al., 2011). The wavenumber region of 750-950 cm<sup>-1</sup> is attributed to sulphate half esters, and in the spectra of Hep the absorption peaks at 817 cm<sup>-1</sup> and at 891 cm<sup>-1</sup> were assigned to O-sulphate group vibrations due to C–O–S stretching; and overlapping C–O–S and C–O–C rings, respectively (Grant et al., 1991; Sun et al., 2009).

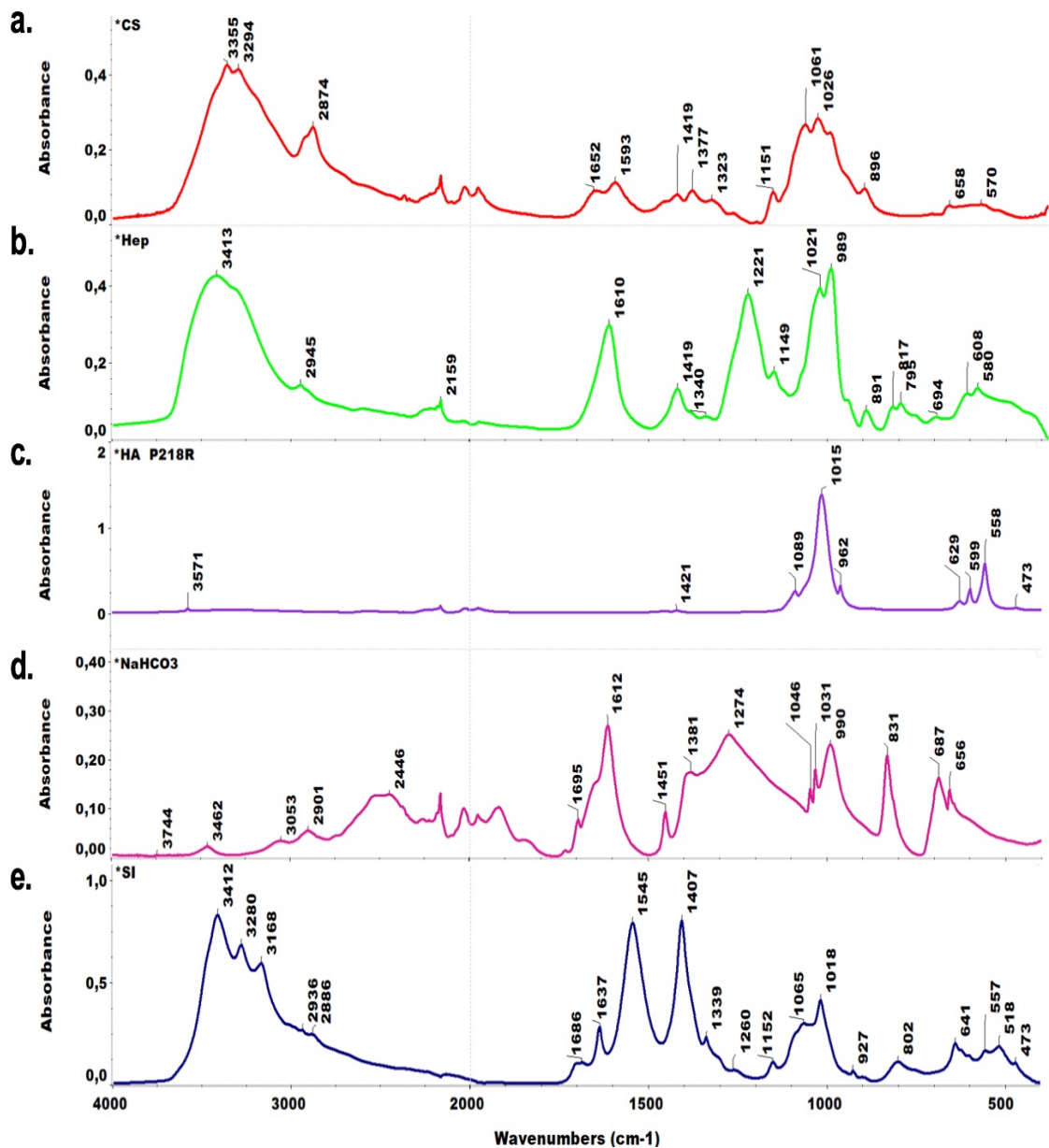


**Figure 3.33** The comparative ATR spectra of reagent powders used in synthesis of composite hydrogels including **a.** CS, **b.** Hep **c.** HA, **d.** NaHCO<sub>3</sub> and **e.** initial composite hydrogel specimen SI (CS.0.1HA.0.005Hep).

In the ATR spectra of commercial HA powder (P218 R) (Figure 3.33.c) used in the initial hydrogel formulations, hydroxyl stretching vibrations are observed at 3571 cm<sup>-1</sup>. The symmetric stretching frequency of PO<sub>4</sub><sup>-3</sup> v<sub>1</sub> groups appear at 961 cm<sup>-1</sup> (Rehman & Bonfield, 1997). The v<sub>3</sub> asymmetric stretching of phosphate bonds locate at 1015 cm<sup>-1</sup> and 1089 cm<sup>-1</sup>, and the PO<sub>4</sub><sup>-3</sup> v<sub>2</sub> bond is present at 473 cm<sup>-1</sup> (Rehman & Bonfield, 1997; Rogina et al., 2017). The all absorption peaks over the wavenumber range of 550-650 cm<sup>-1</sup> were attributed to the asymmetric bending (v<sub>4</sub>) of phosphate groups (Rehman & Bonfield, 1997).

The ATR spectra of sodium bicarbonate ( $\text{NaHCO}_3$ ) (Figure 3.33.d) possess the peaks at  $1451\text{ cm}^{-1}$  and  $687\text{ cm}^{-1}$  which are attributed to doubly degenerate  $\nu_3$  asymmetric stretching and  $\nu_4$  plane bending frequencies of  $\text{CO}_3^{2-}$  (Joshi et al., 2013). The peaks at  $1046\text{ cm}^{-1}$  was assigned to  $\nu_1$  vibrational modes of  $\text{CO}_3^{2-}$  bond (Oliver & Davis, 1973). The peak at  $831\text{ cm}^{-1}$  was attributed to out of plane deformation of carbonate ( $\nu_8$ ) from  $\text{HCO}_3^-$  ion. Other bicarbonate absorption peaks were observed at  $990\text{ cm}^{-1}$  and  $1031\text{ cm}^{-1}$  due to  $\nu_5$  C-OH stretching and  $\nu_4$  COH bending frequencies, respectively. The peak at  $1381\text{ cm}^{-1}$  and  $1612\text{ cm}^{-1}$  was assigned to symmetric and asymmetric stretching of CO, respectively. The absorption bonds at  $1381\text{ cm}^{-1}$  and  $1274\text{ cm}^{-1}$  are reported as due to  $\text{CO}_2$  in  $\text{H}_2\text{O}$  (Swayze & Clark, 1990). The bonds at  $2446\text{ cm}^{-1}$  and  $3460\text{ cm}^{-1}$  are attributed to stretching vibrations of hydrogen and hydroxyl bonds, respectively (Swayze & Clark, 1990). The wavenumber region of  $2150\text{-}2750\text{ cm}^{-1}$  is reported to assign OH stretching bond from surface water absorptions (Ozdemir et al., 2007).

Regarding the ATR spectra of composite hydrogel (SI), shown in Figure 3.33.e, the broad peak between  $3100\text{-}3500\text{ cm}^{-1}$  was due to overlapping of O-H and N-H stretching vibrations and also masked the weak C-H vibration peaks at around  $2800\text{-}2900\text{ cm}^{-1}$ . Another major alteration in peaks of the hydrogel spectrum in comparison to pristine CS spectra was observed in the wavelength region of  $1300\text{-}1700\text{ cm}^{-1}$  that hosts mainly amide bonds.

The comparative ATR spectra of all initial hydrogel compositions are given in Figure 3.34. In addition, peak assignments from chemical functional groups are summarized in Table 3.10. The overlapping of O-H and N-H stretching vibrations in the broad spectral region at right is split into three adjacent peaks on its summit, located near  $3410\text{ cm}^{-1}$ ,  $3280\text{ cm}^{-1}$  and  $3170\text{ cm}^{-1}$  wavenumbers. The peak intensities in this region were lower in the spectra of the SIII sample that has the highest Hep concentration. This might be due to the stronger interaction of O-H groups in Hep with N-H vibrations in CS. The most explicit C-H stretching bond appeared near  $2935\text{ cm}^{-1}$  in all compositions with some accompanying weaker frequencies around  $3000\text{ cm}^{-1}$  (Shahzad et al., 2015).

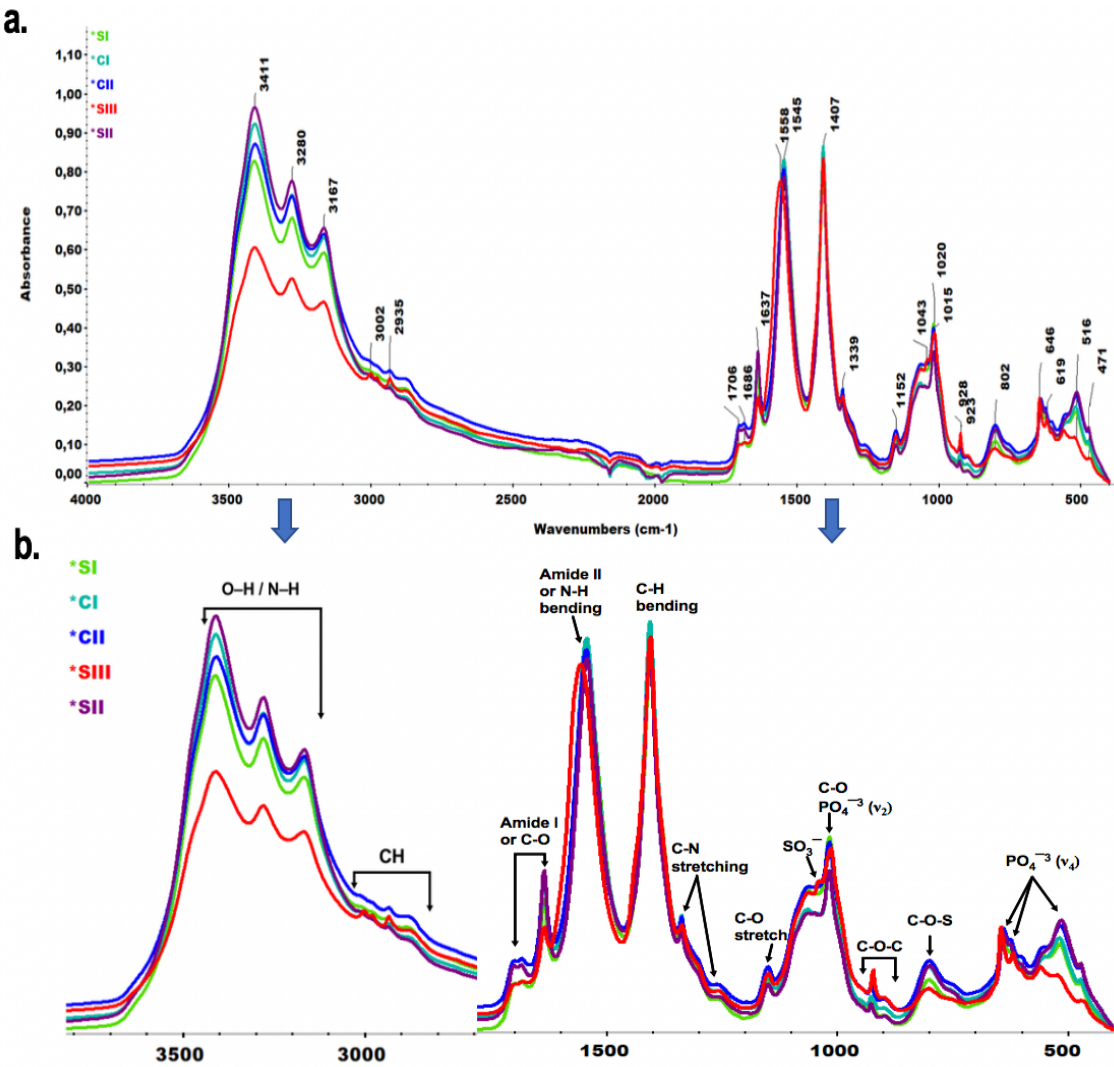


**Figure 3.34** The overlay of ATR spectra for all initial hydrogels with different compositions including CI: CS, CII: CS.0.1HA, SI: CS.0.1HA.0.005Hep, SII: CS.0.1HA.0.015Hep, and SIII: CS.0.1HA.0.025Hep are presented with **a.** peak numbers and **b.** peak assignments of chemical functional groups.

The amide I or C=O vibration peaks in the hydrogel spectra were observed at 1637 cm<sup>-1</sup> and 1686 cm<sup>-1</sup>. Amide II or N-H bending bonds were appeared at 1544-1546 cm<sup>-1</sup> except for the SIII sample spectra, with its corresponding peak upshifted to 1558 cm<sup>-1</sup> (Yar, Farooq, et al., 2016; Shahzad et al., 2015). The peaks locating at around 1545 cm<sup>-1</sup> were specifically attributed to symmetric deformation of NH<sub>3</sub><sup>+</sup> cation due to protonated amino groups of CS in acid, and the vibration at 1407 cm<sup>-1</sup> wavenumber was associated with the presence of carboxylic acid linkages (Mansur et al., 2009). The upshift of NH<sub>3</sub><sup>+</sup> bond from 1545 cm<sup>-1</sup> to 1558 cm<sup>-1</sup> in the SIII sample spectra, having the highest Hep amount, might indicate the interaction between symmetric stretching of COO<sup>-</sup> ions in Hep, and NH<sub>3</sub><sup>+</sup> groups of CS (Mainreck et al., 2011).

**Table 3. 10** The peak assignments of chemical functional groups from ATR spectra of hydrogels.

Wavenumber (cm <sup>-1</sup> )	Peak assignments with Vibrational modes	Reference
3410, 3411	O–H and N–H stretching	(Shahzad et al., 2015)
3279-3281		
2935, 2936	C–H stretching	
1685-1687	Amide I or C=O	(Yar, Farooq, et al., 2016; Shahzad et al., 2015)
1635	Amide I or C=O	(Shahzad et al., 2015)
	COO <sup>-</sup> in Hep	(Bueno et al., 2015)
1544-1546, 1558	Amide II or N–H bending Symmetric deformation of NH <sub>3</sub> <sup>+</sup>	(Mansur et al., 2009; Yar et al., 2017)
1407, 1408	C–H bending or carboxylic acid presence	
	CO <sub>3</sub> <sup>-2</sup> stretching $\nu_3$ vibration	(Koutsopoulos, 2002)
1338, 1339	C–N stretching	(Shahzad et al., 2015)
1300-1650	CO <sub>3</sub> <sup>-2</sup> $\nu_3$ bond from NaHCO <sub>3</sub>	(Rehman and Bonfield, 1997)
1259-1261	C–N stretching in CS	(Yar et al., 2017)
	S=O stretching in Hep	(Yar, Gigliobianco, et al., 2016)
1151	C–O stretching	(Shahzad et al., 2015)
1063-1066	C–O stretching in CS ring	(Mansur et al., 2009; Moreira et al., 2016)
1049-1052	asymmetric stretching of PO <sub>4</sub> <sup>-3</sup> ( $\nu_3$ ) bond in HA	(Rehman and Bonfield, 1997)
1042, 1044	S–O symmetric stretching of SO <sub>3</sub> <sup>-</sup> in Hep	(Harada et al., 2005; Sun, Pang and Zhitomirsky, 2009)
1015-1019	C–O stretching	(Rokhade, Patil and Aminabhavi, 2007)
	PO <sub>4</sub> <sup>-3</sup> $\nu_3$ asymmetric stretching in HA	(Rogina et al., 2017)
	CO <sub>3</sub> <sup>-2</sup> in non-stoichiometric apatites	(Koutsopoulos, 2002)
962	PO <sub>4</sub> <sup>-3</sup> $\nu_1$ symmetric stretching in HA	(Rehman and Bonfield, 1997)
923, 927, 928	Glycosidic bond (C–O–C) vibration	(Cabassi, Casu and Perlin, 1978)
898-901	C–O–C stretching in saccharide rings of CS	(Deng et al., 2017; Yar et al., 2017)
801-804	Axial deformation of C–O–S	(Bueno et al., 2015)
557, 560	PO <sub>4</sub> <sup>-3</sup> $\nu_4$ asymmetric bending in HA	(Rehman and Bonfield, 1997)
473, 474	PO <sub>4</sub> <sup>-3</sup> $\nu_2$ asymmetric stretching in HA	

In comparison to sole CS hydrogel (CI), composite hydrogels including HA exhibited higher intensity peaks at the region of 1020-1065 cm<sup>-1</sup> due to asymmetric stretching of PO<sub>4</sub><sup>-3</sup> groups (Rehman & Bonfield, 1997; Rogina et al., 2017). An additional peak

raised at  $1043\text{ cm}^{-1}$  which appeared only in the SIII sample spectra that had the highest Hep concentration, was attributed to symmetric S–O stretching vibrations from  $\text{SO}_3^-$  (Sun et al., 2011). On the other hand, the crystallinity, due to phosphate ( $\nu_4$ ) asymmetric bending bands at around  $550\text{--}650\text{ cm}^{-1}$ , decreased with increasing Hep concentration. This might be related to the coating effect of Hep on HA crystals making a smoother surface with less crystallinity.

For the modification of hydrogels, to perform a total pre-sterile technique, CS sterilization by autoclaving and utilisation of own synthesis HA (HA5-D) was carried out. The autoclaving effect in terms of the chemical structure of CS was investigated using ATR spectroscopy. The comparative spectra of autoclaved and non-autoclaved CS powders are given in Figure 3.35. The results showed that the main decrease in intensities of peaks was seen at the region of  $1300\text{--}1700\text{ cm}^{-1}$ , which covers the amide bonds including amide I, amide II and amide III. In addition, there was slight decrease in the intensities of peaks at  $1151\text{ cm}^{-1}$  and  $895\text{ cm}^{-1}$  which were assigned to C–O stretching and CS ring stretching vibrations, respectively (Yar et al., 2017). On the other hand, autoclaved CS possessed slightly more intense peaks raised from O–H and N–H bonds between  $3200$  and  $3500\text{ cm}^{-1}$  and C–H stretching linkages in between  $2800\text{--}3000\text{ cm}^{-1}$ . In addition, the peaks at  $1064\text{ cm}^{-1}$  and  $1027\text{ cm}^{-1}$  correspond to cyclic C–O stretching vibrations that also possess slightly higher intensity (Moreira et al., 2016; Rokhade et al., 2007). The results showed that autoclaving has not significantly affected the chemical bonds of CS with medium molecular weight ( $\text{MM}_w$ ). However, in order to minimize the heat effect, instead of direct powder sterilization, CS was sterilized in a hydroalcoholic media by dispersing CS into a water-glycerol solution. As has been shown in the literature, the additive of polyols, like glycerol, significantly enhance the reduction of heat effects and protect polymers from degradation (Jarry et al., 2002; Yen & Sou, 1998).

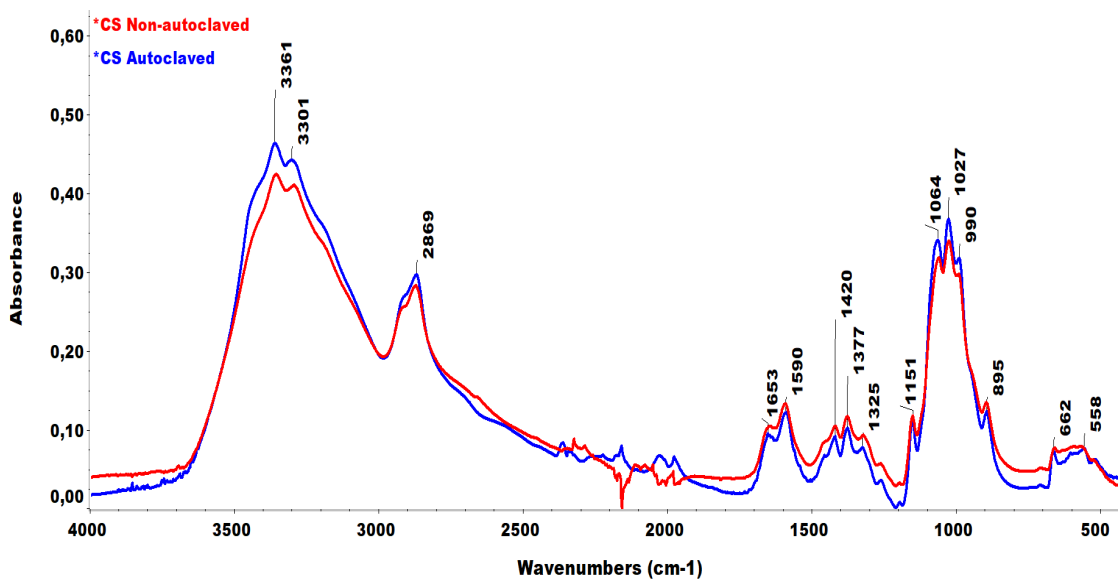


Figure 3.35 The comparative ATR spectra for autoclaved and non-autoclaved CS powders.

In comparison to initial hydrogels, own synthesis HA powders (HA5-D) were utilized in modified hydrogel formulations instead of commercial HA (P218R). The HA powders were tailored by sol-gel synthesis by optimizing the synthesis parameters e.g. high initial pH (10.5) and low calcination temperature (200°C) followed by steam sterilization (132 °C) for desired particle size, morphology and a composition with small carbonate substitutions, to provide desired bioresorbability and bioactivity. The comparison of commercial HA and own synthesis HA (HA5-D) is given in Figure 3.36. All peak positions in HA-5D spectra overlapped with those of the commercial non-sintered HA.

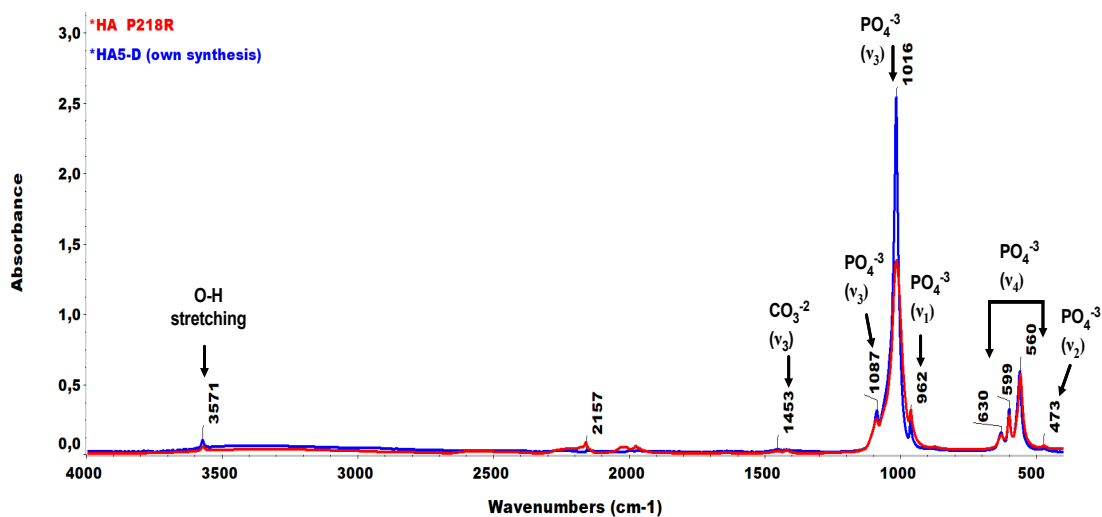


Figure 3.36 The comparison of ATR spectra for commercial HA (P218 R) powder used in the synthesis of initial hydrogels versus the own synthesis HA5-D powder which was utilised in the synthesis of modified hydrogels.

Except for the symmetric stretching of the  $\text{PO}_4^{3-}$  ( $\nu_1$ ) bonds at  $961\text{ cm}^{-1}$  and the phosphate  $\nu_2$  bond at  $473\text{ cm}^{-1}$ , all other functional group peaks in the HA-5D sample spectra possessed higher peak intensities than those of their commercial counterparts. A particular difference was observed in the peak intensities at  $1016\text{ cm}^{-1}$ , in the asymmetric stretching of  $\text{PO}_4^{3-}$  ( $\nu_3$ ) bands (Rogina et al., 2017). This indicates the respectively more crystalline structure of HA-5D which can contribute to enhancement of the mechanical properties of HA (Pazarlioglu & Salman, 2017; Witek et al., 2013). On the other hand, superimposition of  $\text{PO}_4^{3-}$  ( $\nu_3$ ) bands that increase the phosphate/carbonate ratio in HA-5D, might show a decrease in the amount of carbonate ions; which might be due to a higher drying temperature in comparison to commercial synthetic HA. However, weak carbonate bonds are still detected in both samples at around  $1420\text{ cm}^{-1}$  and  $1453\text{ cm}^{-1}$  that correspond to the  $\nu_3\text{ CO}_3^{2-}$  ions, and  $\nu_2$  carbonate vibration peak at  $876\text{ cm}^{-1}$  (Rehman & Bonfield, 1997).

A comparative graph showing the ATR spectra of initial and modified hydrogels possessing the same composition (SI) is given in Figure 3.37. In the spectra of modified hydrogels at the region of  $2500\text{-}3500\text{ cm}^{-1}$  right shifts of the peaks and broadening were very explicit. In contrast to initial hydrogels that have a broad peak region splitting into three different peaks corresponding to O-H and N-H bonds, the spectra of modified hydrogels possessed only a single peak raised at around  $3285\text{ cm}^{-1}$  in all compositions. This broadened single peak at this region was associated with the effect of glycerol, leading to hydrogel bonding between oxygen in the OH group of glycerol, and nitrogen in the  $\text{NH}_2$  groups of CS, with the peaks merging in this region towards the glycerol position at  $3280\text{ cm}^{-1}$  (Yusof, 2017).

On the other hand, the intensities of C-H bonds in modified hydrogels, located at  $2932\text{ cm}^{-1}$  and  $2879\text{ cm}^{-1}$ , were quite stronger than those of its initial counterparts (Shahzad et al., 2015). In the amide bond region, there was a decrease in the peak intensities which might be a result of the autoclaving of CS. Particularly, the amide I bond is very weak in intensity and shifts from  $1637\text{ cm}^{-1}$  to  $1641\text{ cm}^{-1}$ . This upshift of the peak numbers were observed in the whole amide region located between  $1300\text{ cm}^{-1}$  and  $1700\text{ cm}^{-1}$  due to the higher wavelength positions of glycerol that indicates an interaction of glycerol with amide bonds. There was significant decrease of peak intensities at upshifted  $\text{NH}_3^+$  symmetric deformation bands from  $1545\text{ cm}^{-1}$  to  $1565\text{ cm}^{-1}$ . Also,

HCOO<sup>-</sup> linkages shifted from 1407 cm<sup>-1</sup> to 1409 cm<sup>-1</sup>. This could be associated with the more neutralised and crosslinked structure of modified hydrogels in comparison to that of the initial hydrogels (Mansur et al., 2009).

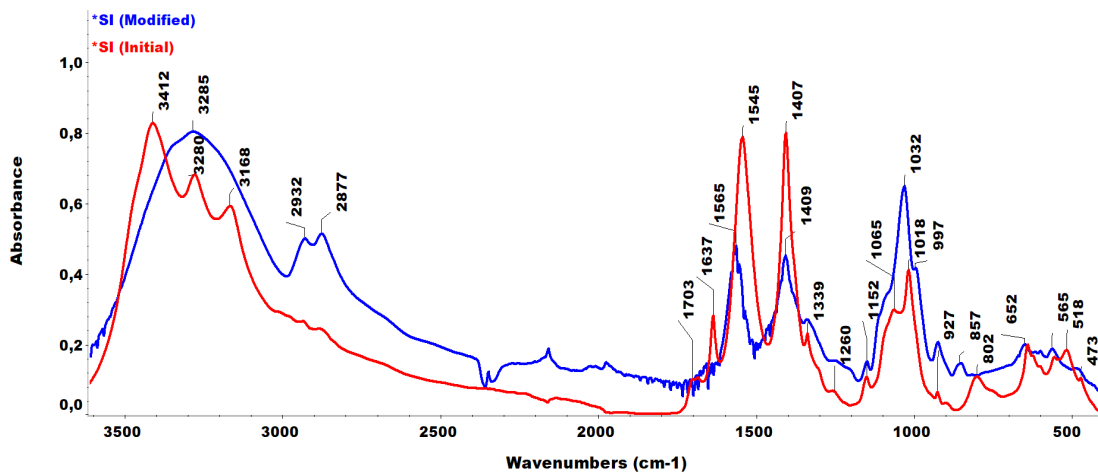


**Figure 3.37** The comparative ATR spectra of initial and modified forms of hydrogel composition SI: CS.0.1HA.0.005Hep.

One of the most explicit differences in the modified hydrogel was seen in the wavelength region of 800-1000 cm<sup>-1</sup>. The peak at 1065 cm<sup>-1</sup> (C-O) almost disappears, while the peak at 1018 cm<sup>-1</sup>, due to a C-O cyclic stretching bond, upshifts to 1032 cm<sup>-1</sup>. This shows the interaction with glycerol that has been reported to possess a peak at around 1029 cm<sup>-1</sup> (Yusof, 2017). In addition, the significant increase at peak intensity 1032 cm<sup>-1</sup> might be associated with stronger PO<sub>4</sub><sup>-3</sup> asymmetric stretching (v<sub>3</sub>) vibrations in (own synthesis) HA (HA5-D) used in the modified hydrogels in comparison to commercial HA used in the initial hydrogels. The asymmetric bending (v<sub>4</sub>) of phosphate groups is also seen at 652 cm<sup>-1</sup> and 565 cm<sup>-1</sup> (Rehman & Bonfield, 1997). An additional peak appears at 997 cm<sup>-1</sup> for modified hydrogels; which may be due to the bicarbonate ions that might appear, due to the dissociative impact of glycerol on this ion, from NaHCO<sub>3</sub> corresponding to a C-OH stretching vibration. In addition, the COO<sup>-</sup> symmetric stretching vibration at 927 cm<sup>-1</sup> (Mikhailov et al., 2014) becomes stronger in modified hydrogels. Furthermore, the modified hydrogel showed a peak at 857 cm<sup>-1</sup> which has been attributed to O-C-O out of plane bending vibrations (v<sub>2</sub>) from CO<sub>3</sub><sup>-2</sup> (Swayze & Clark, 1990). Overall, glycerol used in modified hydrogels caused significant alterations in chemical structure that cause separation of ions, leading to further association of polymers and salts, and its own interaction with them leading to hydrogen bonding (Yusof, 2017).

Top and bottom surfaces of modified hydrogels analysed upon normal drying at 37 °C exhibited very similar peak intensities for each composition indicating homogeneous distribution of reagents in the hydrogel networks. However, except for the CI sample, spectral peak intensities of functional groups were slightly higher at the top surfaces than in their bottom surfaces. The ATR spectra of modified hydrogels, including top and bottom and top surface analyses, are given comparatively for different compositions in Figure 3.38. In top surface analyses, the peak intensities of CI, (sole CS gel) sample spectra were the lowest; whereas the SI composite hydrogel containing HA and Hep possessed the highest peak intensities over the whole spectral range. The broad O-H/N-H peak and its shoulder peak which is assigned to C-H stretching bonds, were observed around 3285 cm<sup>-1</sup>; and 2878 cm<sup>-1</sup> and 2932 cm<sup>-1</sup> wavenumbers, respectively. The C-H bonds in CII and SI composite hydrogel spectra had higher intensities than CI sample on their top surface, but bottom surface spectra were identical. Weak amide I or C=O vibrations were observed at 1641 cm<sup>-1</sup> and 1658 cm<sup>-1</sup>, while symmetric deformations of NH<sub>3</sub><sup>+</sup> ions and carboxylic acid linkages were seen near 1565 cm<sup>-1</sup> and 1408 cm<sup>-1</sup>, respectively. These last two bonds had a slight downward shift in the bottom surface spectra to 1564 cm<sup>-1</sup> and 1405 cm<sup>-1</sup>, respectively (Mansur et al., 2009).

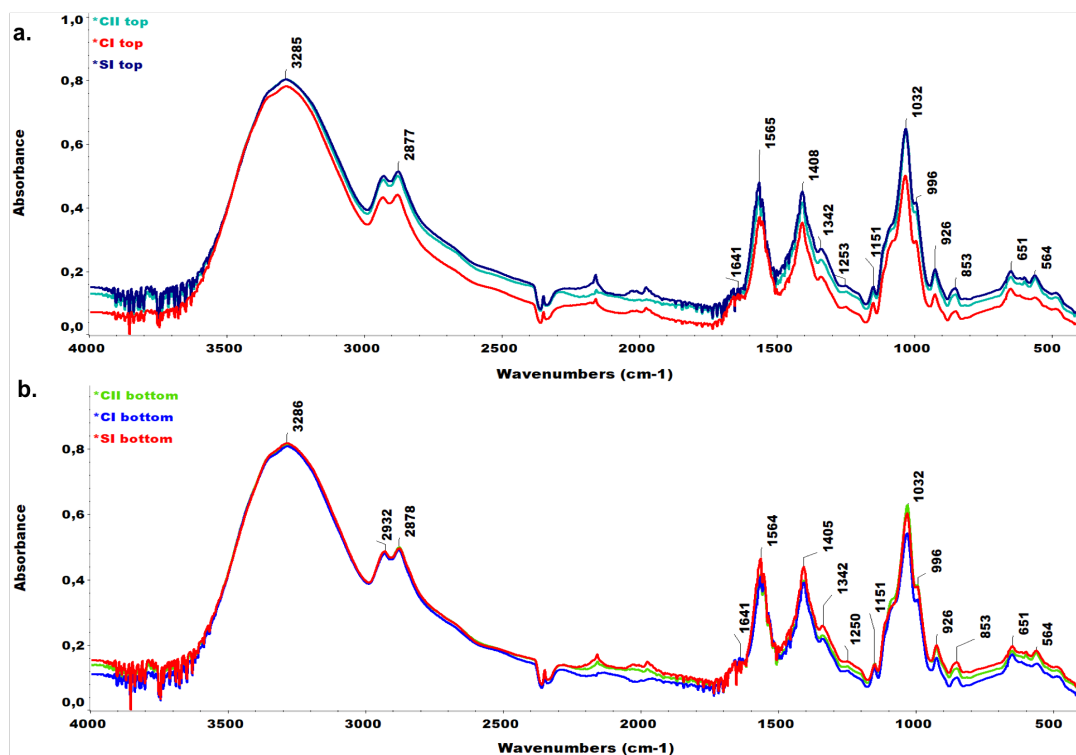


**Figure 3. 38** The comparison of ATR spectrums of modified hydrogels obtained in different compositions (CI: CS, CII: CS.0.1HA, and SI: CS.0.1HA.0.005Hep) analysed from **a.** top **b.** and bottom surface.

C-O stretching vibrations were seen at  $1151\text{ cm}^{-1}$  in all hydrogel compositions (Yar et al., 2017). The composite hydrogels containing HA possessed stronger peaks at  $1032\text{ cm}^{-1}$  due to asymmetric stretching of  $\text{PO}_4^{3-}$  ( $\nu_3$ ) vibrations (Chaudhry et al., 2006). In addition, asymmetric bending ( $\nu_4$ ) of phosphate groups were detected at  $651\text{ cm}^{-1}$  and  $564\text{ cm}^{-1}$  wavenumbers, in composite samples (Rehman & Bonfield, 1997). The shoulder peak at  $997\text{ cm}^{-1}$  might be attributed to C-OH stretching vibration peaks due to the interactions of bicarbonate ions and glycerol moieties (Swayze & Clark, 1990; Yusof, 2017). The relatively higher intensity of this peak at  $997\text{ cm}^{-1}$  in composite hydrogels might be contributed to by shifted  $\nu_1$  stretching of P-O bonds in HA located at  $961\text{ cm}^{-1}$  as well as to sulphate group vibrations from Hep at around  $989\text{ cm}^{-1}$  (Rehman and Bonfield, 1997; Mainreck *et al.*, 2011). In addition, The peak symmetric stretching  $\text{COO}^-$  in acetate ions was designated at  $926\text{ cm}^{-1}$  in all modified hydrogel compositions (Mikhailov et al., 2014).

### 3.5.8.2 FT-Raman Analyses

FT-Raman analyses by area mapping of a nine-point square obtained with a resultant average spectrum is demonstrated in Figure 3.39. The FT-Raman analyses of raw materials are given in Figure 3.40. In the CS powder spectrum, the peak detected at  $3372\text{ cm}^{-1}$  is assigned to asymmetric vibrations of  $\text{NH}_2$  frequencies whereas the peak at position  $3310\text{ cm}^{-1}$  is attributed to symmetric stretching of  $\text{CH}_2$  bonds, and these bonds are also assigned to overlapping OH bonds making hydrogen bonds. The high intensity peak at  $2889\text{ cm}^{-1}$  with its shoulder peak at  $2749\text{ cm}^{-1}$  are attributed to C-H stretching vibrations (Mikhailov et al., 2014; Zajac et al., 2015). The peaks at  $1375\text{ cm}^{-1}$  are associated with  $\text{CH}_2$  deformation. In addition, a transitional C-H bond was seen at  $1459\text{ cm}^{-1}$ . The peaks located at  $1115$  and  $1090\text{ cm}^{-1}$  are attributed to ether group frequencies from C-O-C bonds whereas CS ring stretching vibrations are assigned at  $897\text{ cm}^{-1}$  (Mikhailov et al., 2014).

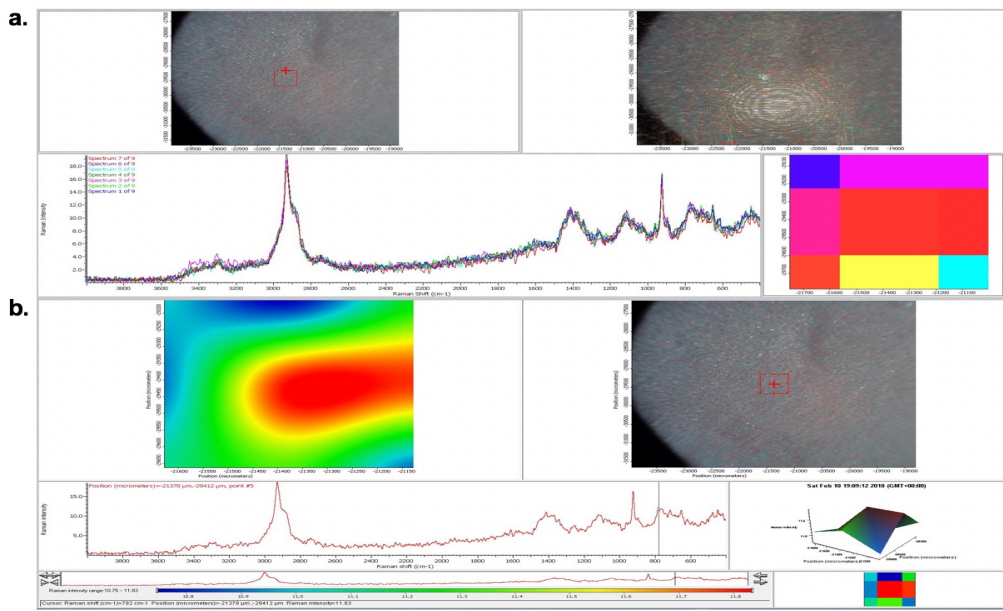


**Figure 3.39** The demonstration of the FT-Raman square area mapping analyses of an initial hydrogel sample SI (CS.0.1HA.0.005Hep). **a.** during data collection: the sample at top left with a red framed square area covering the analyses points, and the collected spectra are given at the bottom, and a heat map at the left bottom corner showing the analyses regions. **b.** after data collection is complete: the sample at right corner, heat map at left corner and the average spectra is given at the bottom.

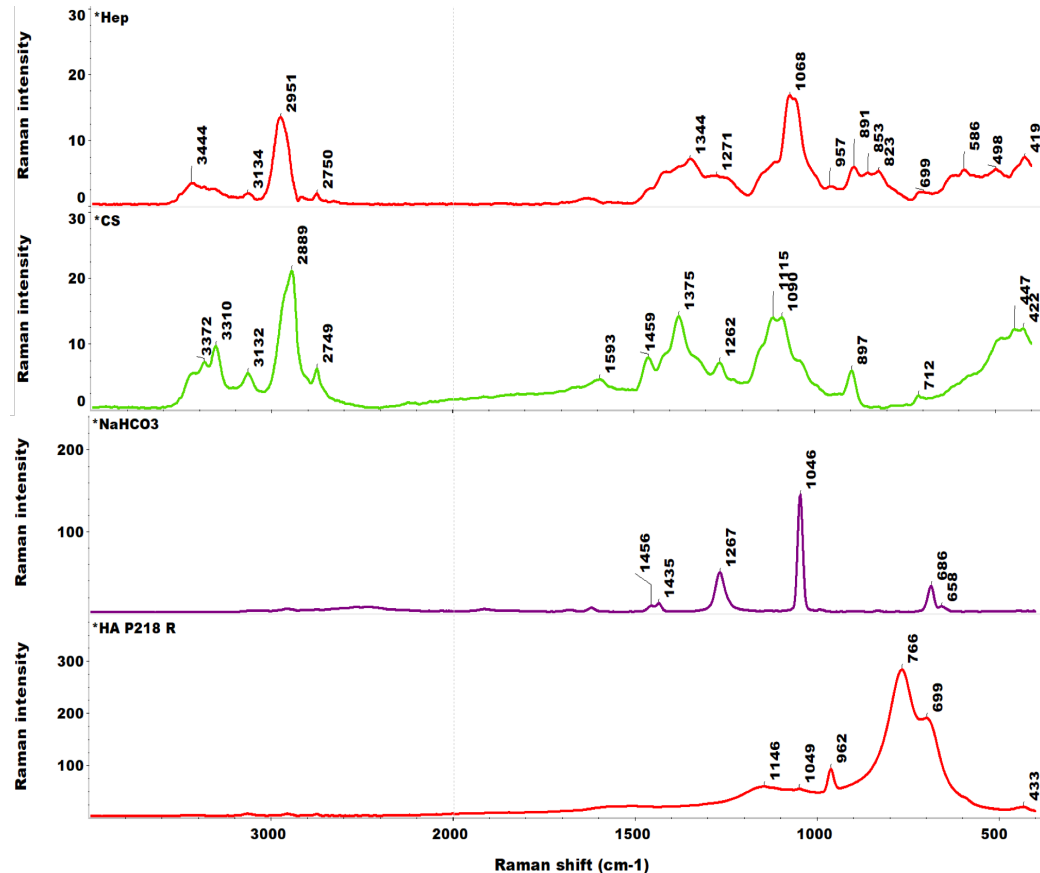


**Figure 3.40** The comparison of FT-Raman spectra of reagent powders, which were used in the synthesis of hydrogels **a.** Hep, **b.** CS, **c.** NaHCO<sub>3</sub> and **d.** the commercial HA (P218 R).

Regarding the Raman spectrum of Hep powder, the wavenumbers detected at 1626  $\text{cm}^{-1}$  and 1411  $\text{cm}^{-1}$  are assigned to antisymmetric and symmetric stretching of  $\text{COO}^-$  vibrations (Mainreck et al., 2011). The shoulder peaks around 1271  $\text{cm}^{-1}$  were attributed to S=O asymmetric stretching from O-sulphate groups (Cabassi et al., 1978). The strongest Raman active peak of Hep was present at 1068  $\text{cm}^{-1}$  due to symmetric stretching of S-O bonds due to 2-O- $\text{SO}_3$  bonds (Atha et al., 1996).

The fingerprint region that differentiates Hep from other glycosaminoglycans is located at lower frequencies; between 600  $\text{cm}^{-1}$  and 1015  $\text{cm}^{-1}$  (Mainreck et al., 2011). The peaks at the region of 800-950, hosts the asymmetric stretching vibrations of C-O-S linkages (Cabassi et al., 1978). The peaks located at 823  $\text{cm}^{-1}$  and 853  $\text{cm}^{-1}$  are attributed to equatorial and axial  $\text{OSO}_3^-$  frequencies in residual galactosamines, respectively (Mainreck et al., 2011). These peaks as well as the peak at 891  $\text{cm}^{-1}$  might be due to C-H deformation or antisymmetric stretching of C-O-C vibrations (Atha et al., 1996; Cabassi et al., 1978).

Raman spectra of sodium bicarbonate peaks include the strongest sharp peak at 1046  $\text{cm}^{-1}$  and is attributed to carbonate ions. The  $\nu_3$  vibration of  $\text{CO}_3^{2-}$  peaks are located at 1435  $\text{cm}^{-1}$  and 1456  $\text{cm}^{-1}$  whereas the locations 686  $\text{cm}^{-1}$  and 658  $\text{cm}^{-1}$  are attributed to  $\nu_4$  frequency modes of carbonate (Davis & Oliver, 1972; Koura et al., 1996). The peak at 1267  $\text{cm}^{-1}$  is attributed to dissolved  $\text{CO}_2$  (Davis & Oliver, 1972).

The phosphate vibrations in the FT-Raman spectrum of HA were seen at 1146, 1049, 962, and 433  $\text{cm}^{-1}$ . The peak at 962  $\text{cm}^{-1}$  was attributed to  $\nu_1$  P=O symmetric stretching of phosphate bonds. The broad and most intense peak located at 766  $\text{cm}^{-1}$  and its shoulder at 699  $\text{cm}^{-1}$  were assigned to asymmetric stretching of P-O bonds. The  $\text{PO}_4^{3-}$  bending vibrations were assigned at 433  $\text{cm}^{-1}$  and the peak at 1049  $\text{cm}^{-1}$  was attributed to the  $\text{CO}_3^{2-}$  bending frequency (Rehman et al., 1995; Smith & Rehman, 1994). The peak at 1146  $\text{cm}^{-1}$  was designated as asymmetric stretching of P-O vibrations ( $\nu_3$ ) (Ulian et al., 2013).

The comparison of FT-Raman analyses of all different compositions of initial hydrogels are given in Figure 3.41. The small but sharp peak locating at around 3511  $\text{cm}^{-1}$  was

assigned to  $\text{OH}^-$  ions (Antonakos et al., 2007). The peak at  $3372 \text{ cm}^{-1}$  was assigned to asymmetric stretching of  $\text{NH}_2$  bond vibrations (Mikhailov et al., 2014). The most intense sharp peak located at  $2934 \text{ cm}^{-1}$  and very weak shoulder at  $2896 \text{ cm}^{-1}$  and a detached peak at  $2748 \text{ cm}^{-1}$  were attributed to  $\text{CH}_3$   $\text{CH}_2$  and  $\text{CH}$  stretching vibrations, respectively. The peaks belong to amide I bonds or C-O stretching bonds in the region of  $1646 \text{ cm}^{-1}$ . Amide II or N-H vibrations near  $1551 \text{ cm}^{-1}$  and  $1599 \text{ cm}^{-1}$  that were detected in hydrogels were much weaker in FT-Raman spectra than in IR spectra (Zajac et al., 2015).

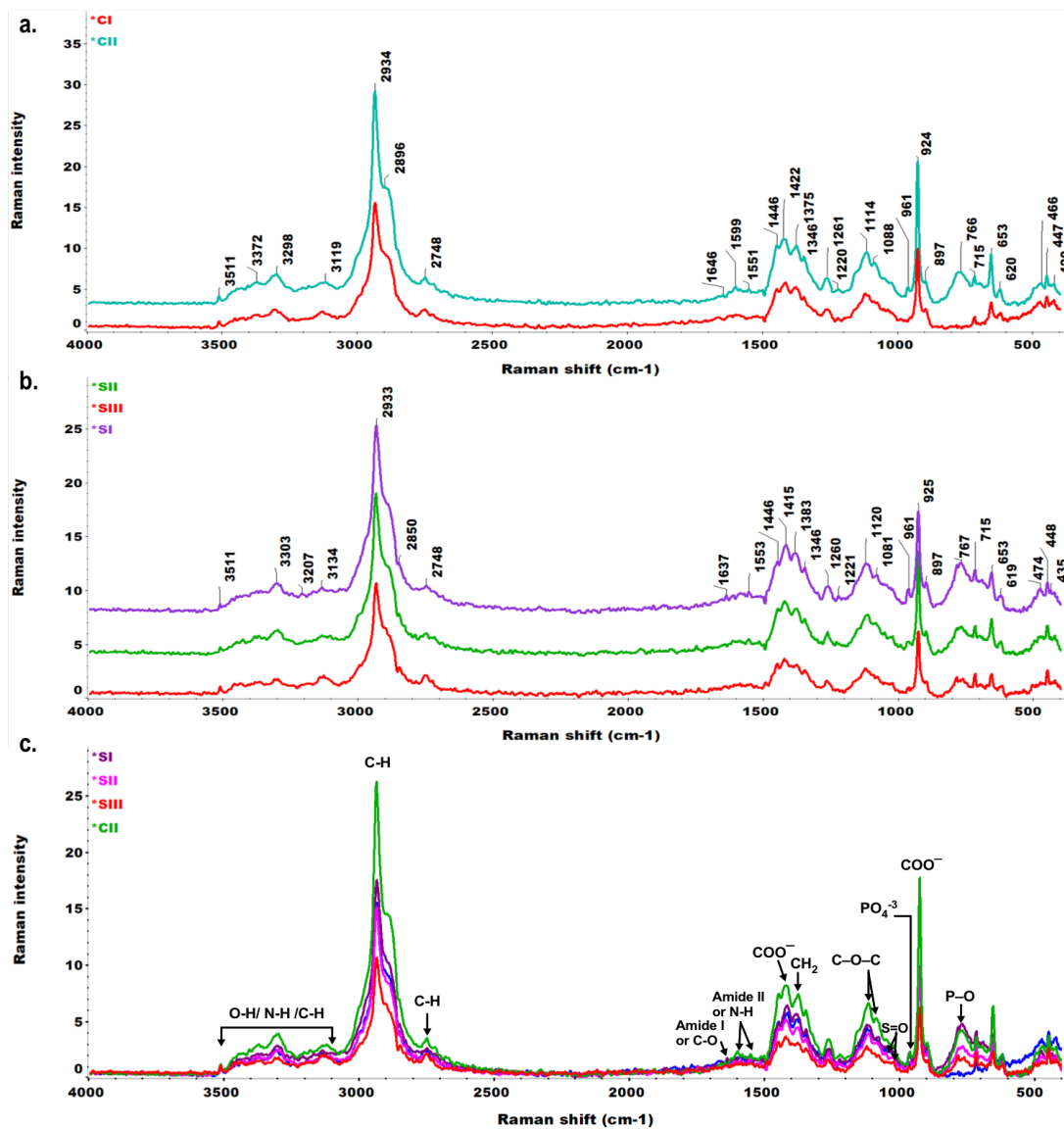


**Figure 3.41** The comparison of FT-Raman spectra of initial hydrogels obtained in different compositions: **a.** without Hep including CI: CS and CII: CS.0.1HA, and **b.** compositions with different Hep concentrations: SI: CS.0.1HA.0.005Hep (0.12 mg/mL), SII: CS.0.1HA.0.015Hep (0.36 mg/mL), and SIII: CS.0.1HA.0.025Hep (0.60 mg/mL) and **c.** the overlay spectrums of all hydrogel compositions.

The peaks located at 1114 cm<sup>-1</sup> and 1088 cm<sup>-1</sup> were attributed to C-O-C ether bonds in CI and CII samples without Hep, while the corresponding peaks have shifted to 1120 cm<sup>-1</sup> and 1081 cm<sup>-1</sup> in sample spectrums containing Hep. These can be related to the interaction of symmetric stretching of S-O bonds locating around 1068 cm<sup>-1</sup> (Atha et al., 1996).

The sharp peak around 925 cm<sup>-1</sup> was attributed to symmetric stretching of COO<sup>-</sup> vibration from acetate ions. The peak at 897 cm<sup>-1</sup> was assigned to symmetric stretching of C-C frequencies (Mikhailov et al., 2014). This peak number has slightly decreased to 896 cm<sup>-1</sup> in SIII sample possessing the highest Hep concentration. This might be contributed to by C-O-S stretching vibrations in Hep at this location (Cabassi et al., 1978). The phosphate v<sub>1</sub> stretching vibrations appearing at 961 cm<sup>-1</sup> and P-O vibrations at around 766 cm<sup>-1</sup> were observed in all composite hydrogel spectrums containing HA except for the CI hydrogel obtained from sole CS (Rehman et al., 1995; Smith & Rehman, 1994). As the concentration of Hep increases, this peak tends to decrease. This may be associated with the coating effect of Hep on HA crystals reducing the crystallinity.

The peak detected at around 653 cm<sup>-1</sup> in all hydrogels was attributed to v<sub>4</sub> frequency modes of carbonate (Davis & Oliver, 1972; Koura et al., 1996). The sharpest peak having the highest intensity at 653 cm<sup>-1</sup> was seen in the CII sample containing HA without Hep, which might indicate the interaction between HA and carbonate ions. Although it has not been confirmed, the substitution of CO<sub>3</sub><sup>-2</sup> ions in an HA crystal lattice may occur during neutralizing of CS/HA solutions with NaHCO<sub>3</sub>, which can provide further benefits in terms of bioresorbability of HA (Rogina et al., 2017). The peaks at 1446 cm<sup>-1</sup> and 1422 cm<sup>-1</sup> were attributed to C-H bond vibrations interacting with CO<sub>3</sub><sup>-2</sup> v<sub>3</sub> frequencies in this region (Koura et al., 1996; Zajac et al., 2015). The weak bands appearing at 998 cm<sup>-1</sup> and 1044 cm<sup>-1</sup> in the SI sample spectra were assigned to OSO<sub>3</sub><sup>-</sup> equatorial sulphate and C-O-C stretching vibrations in Hep. The other sulphate peaks observed in composite hydrogels containing Hep, seen at around 1037 cm<sup>-1</sup>, 1050 cm<sup>-1</sup> and 1060 cm<sup>-1</sup> were attributed to different sulphate groups including N-SO<sub>3</sub>, 6-O-SO<sub>3</sub> and 2-O-SO<sub>3</sub>, respectively (Atha et al., 1996).

### 3.5.8.3 XRD Analyses

The XRD patterns of commercial reagents including CS, HA, Hep and  $\text{NaHCO}_3$  powders used in the hydrogel synthesis and an initial freeze-dried hydrogel SII (CS.0.1HA.0.015Hep) are given in Figure 3.42. XRD patterns of CS and Hep powder revealed a similar amorphous structure, involving broad peaks near each other. The main broad peak in CS was obtained at  $20.8^\circ$  and a weaker peak around  $13.3^\circ$ , similar to those reported previously (Dessì et al., 2013; Tang et al., 2009). The XRD pattern of Hep showed a weak peak at  $13.3^\circ$  and a broad main peak at  $23.5^\circ$  which was comparable to a reported XRD pattern of Hep (Bueno et al., 2015). The commercial HA (P218 R) peaks were located at the  $2\theta$  angles of  $10.8^\circ$ ,  $16.7^\circ$ ,  $25.8^\circ$ ,  $31.7^\circ$ ,  $32.2^\circ$ ,  $43.8^\circ$ ,  $46.7^\circ$  and  $49.5^\circ$  matching with the HA standard (ICSD Fiz, code # 26204) (Sudarsanan & Young, 1969). The  $\text{NaHCO}_3$  XRD peaks, detected at  $2\theta$  angles of  $18.4^\circ$ ,  $25.6^\circ$ ,  $29.1^\circ$ ,  $30.5^\circ$ ,  $34.6^\circ$ ,  $44.6^\circ$ ,  $47.7^\circ$  and  $57^\circ$ , matched with the standard reference (ICSD Fiz, code # 18183) (Sharma, 1965). The XRD pattern of the composite hydrogel SII specimen exhibited a semi crystalline structure and possessed peak positions at  $2\theta$  angles of  $8.77^\circ$ ,  $11.3^\circ$ ,  $11.5^\circ$ ,  $17^\circ$ ,  $19.1^\circ$ ,  $22.4^\circ$ ,  $22.6^\circ$ ,  $24.9^\circ$ ,  $29.6^\circ$  and  $43.8^\circ$ .

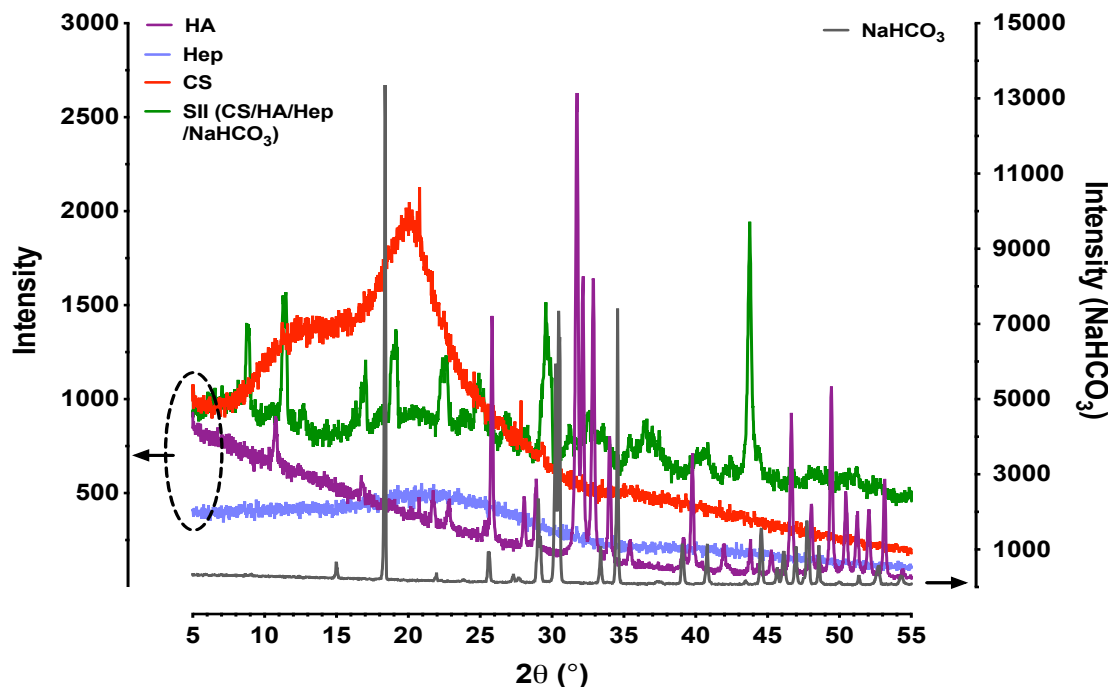


**Figure 3.42** The comparison of XRD patterns of commercial reagent powders which were used in the synthesis of hydrogels including Hep, CS,  $\text{NaHCO}_3$  and HA (P218 R) and a freeze-dried composite initial hydrogel sample SII: CS.0.1HA.0.015Hep. (The right -Y axis shows the intensity of only the  $\text{NaHCO}_3$  XRD pattern, due to its excess intensities. The intensity of all other samples are indicated by the left Y axis).

In the diffraction pattern of hydrogel samples, HA phase peaks either matched with those of HA reagent or slightly shifted:  $11.3^\circ$   $17.0^\circ$ ,  $24.9^\circ$   $29.6^\circ$  and  $43.8^\circ$ . The most prominent sharp peak raised at  $43.8^\circ$ , indicates the dominant position of (113) lattice parameters in the HA crystals present in hydrogels (ICSD Fiz, code # 26204) (Sudarsanan & Young, 1969). The peaks raised at  $2\theta$  angles of  $8.8^\circ$  and  $17.6^\circ$  correspond to sodium acetate phase peaks reported in the literature (Ruiz-Caro & Veiga-Ochoa, 2009). Although this has not been fully confirmed, by similar studies, it raises the possibility of the formation of sodium acetate ( $\text{NaCH}_3\text{COO}$ ) and  $\text{Na}_2\text{CO}_3$  as side products, when CS is dissolved in acetic acid and neutralized by  $\text{NaHCO}_3$ . This may result from the reaction between free  $\text{Na}^+$  ions from neutralizing agent  $\text{NaHCO}_3$  and  $\text{CH}_3\text{COO}^-$  in acetic acid (Liu et al., 2011; Rogina et al., 2017).

The morphology of the prismatic shaped crystals on neutralized sole CS initial hydrogels were observed in SEM analyses and possessed a morphology similar to that of sodium acetate trihydrate crystals exhibiting hexagonal plates in water media, reported by Doxsee & Stevens (1990). Although it has not been fully confirmed, there is a possibility of the presence of sodium acetate in hydrogels. In addition, the high intensity peaks at  $2\theta$  diffraction angle of  $43.8^\circ$  and  $17^\circ$  in the SII hydrogel pattern, matches with  $\text{Na}_2\text{CO}_3$  peak positions. However, the presence of this phase is not confirmed, since HA has matching or close peak positions at these diffraction angles (ICSD Fiz, code # 1852)(Wu & Brown, 1975).

### 3.5.9 Thermal Analyses by TGA & DSC

The TGA&DSC curves of reagent powders of CS and Hep, and HA and  $\text{NaHCO}_3$ , are given in Figures 3.43 and 3.44, respectively. The first weight loss stage in the CS powder occurred between  $25^\circ\text{C}$  and  $150^\circ\text{C}$ . This was considered to be due to the removal of adsorbed water, accounting for about a 10% loss. It is seen that less than 10% of weight loss occurs in the autoclaving temperature ( $132^\circ\text{C}$ ) used in CS sterilization. The second step of weight loss starts at an onset point of  $244^\circ\text{C}$  and continues until approximately  $300^\circ\text{C}$ , which indicates the evaporation of organic molecules in CS, and accounts for an approximately 30 % weight loss. A subsequently quicker degradation of CS occurred at the temperature range of  $300^\circ\text{C}$  to  $700^\circ\text{C}$ , which

was due to degradation of all the organic components of CS (Shahzadi et al., 2016). The TGA curve of Hep was similar to those reported in the literature (Cestari et al., 2014; Sun et al., 2009). Hep showed a gradual weight loss up to 150 °C, reaching a loss of approximately 15%. Subsequently weight loss was more rapid with two different inflection points observed in the Hep DSC curves at 249 °C and 480 °C, indicating sudden degradation stages. These degradation stages of Hep are bisected by an endothermic peak at 414 °C on the DSC plot. After the third stage of degradation ending at 700 °C, only about 30 % of Hep residue remained.

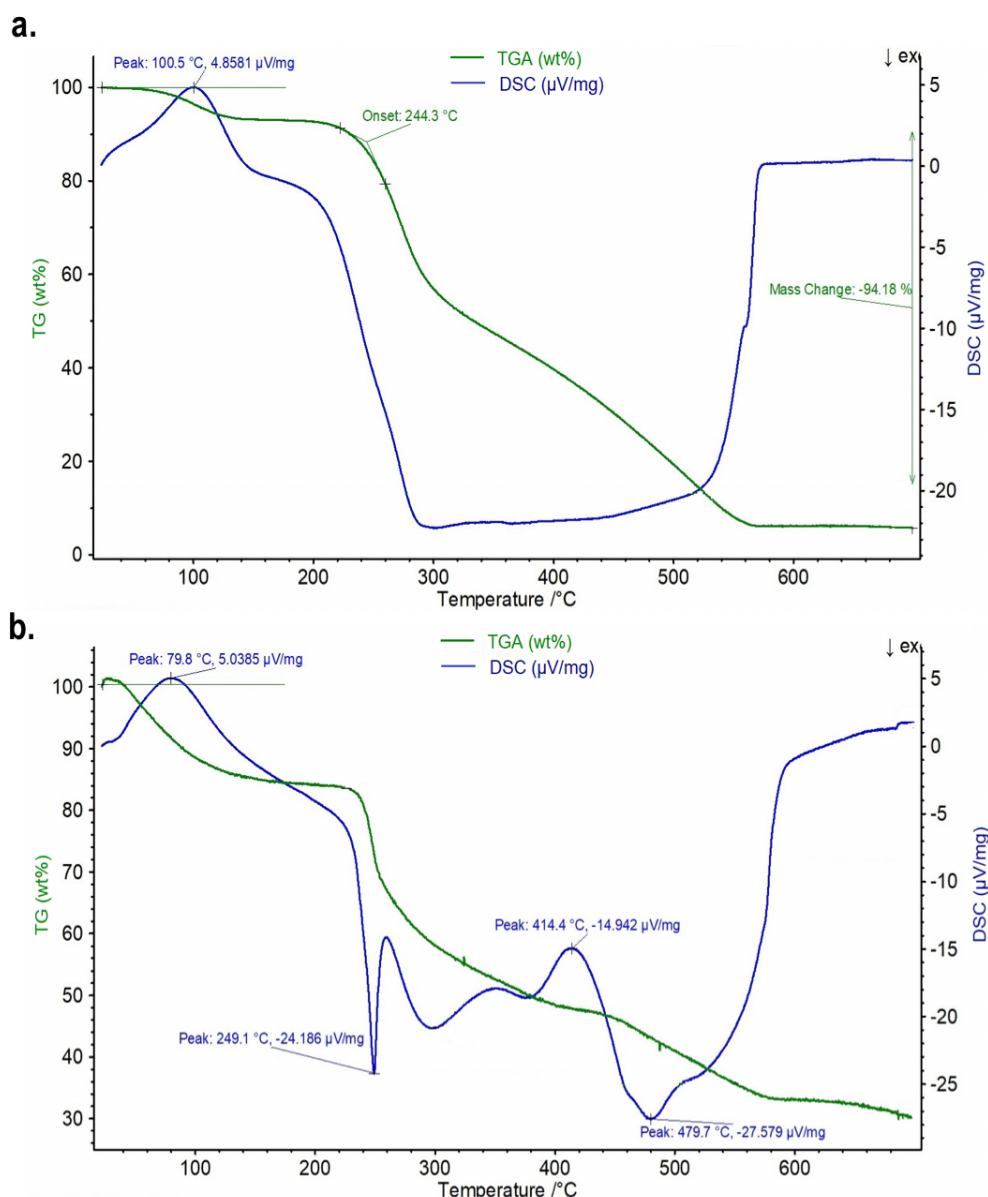


**Figure 3.43** TGA/DSC curves obtained from thermal analyses of reagent powders between 25–700 °C including **a.** CS and **b.** Hep.

Regarding HA, the first weight loss due to dehydration of adsorbed water, occurs between 37 °C and ~150 °C, accounting for a ~1% loss. A broad exothermic peak, pointing at 266 °C in the first degradation step between 150 and 380 °C is attributed to the evaporation of structural water molecules in HA. The slight weight loss at the region of 380-700 °C was attributed to the vaporization of carbonate and carbon dioxide molecules (Chaudhry et al., 2006; Pazarlioglu & Salman, 2017). A total of 2.9 % weight loss occurred in the thermal treatment of HA up to 700 °C. Regarding the TGA & DSC curves of NaHCO<sub>3</sub>, weakly bound water removal occurred in the region of ~40-120 °C. Following this, a very sharp decrease was observed in the weight of NaHCO<sub>3</sub> causing an endothermic DSC peak at 158 °C. The heating of up to approximately 240 °C led to a total weight loss of almost 40%.

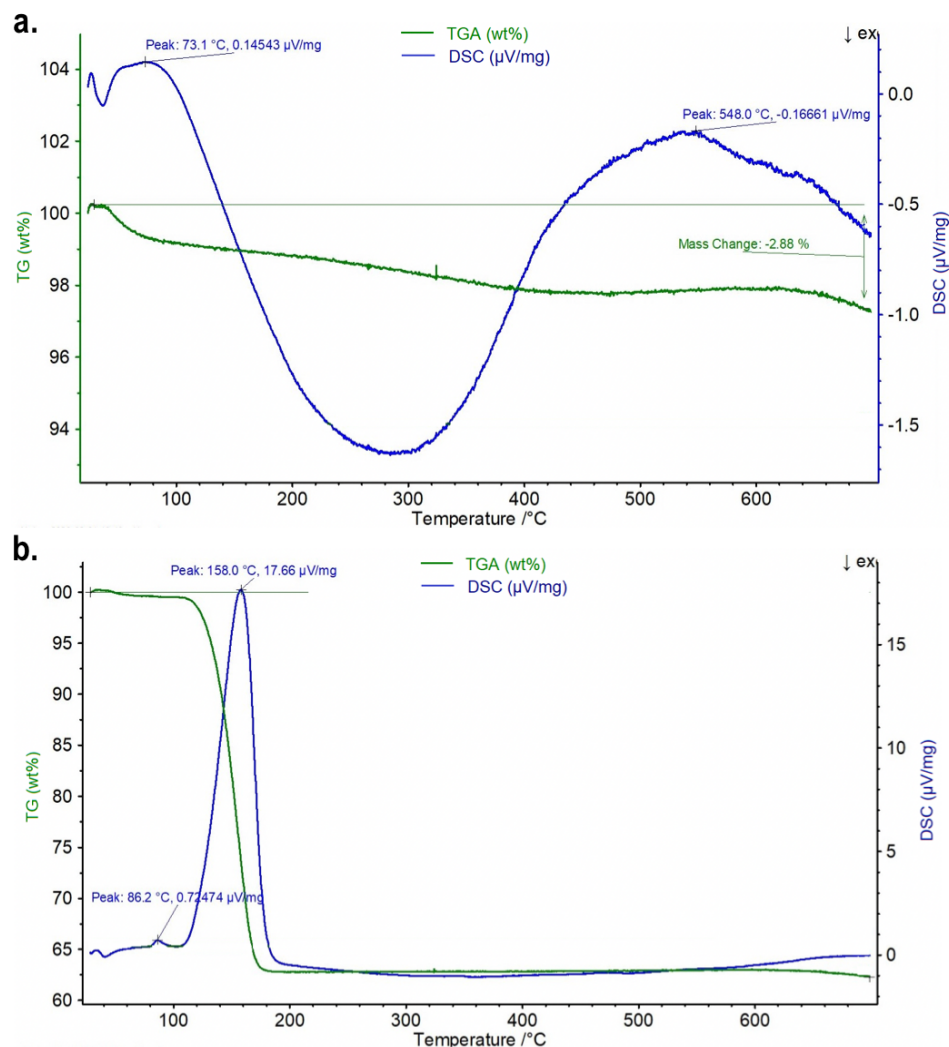


**Figure 3.44** TGA/DSC curves obtained from thermal analyses of reagent powders between 25-700 °C including **a.** HA and **b.** NaHCO<sub>3</sub>.

### 3.6 Discussion

The neutralisation of CS solutions by  $\text{NaHCO}_3$  is a relatively new method. Although CS is mostly neutralised by  $\beta$ -glycerol phosphate ( $\beta$ -GP), high amounts of  $\beta$ -GP to achieve a physiological pH level can cause cell cytotoxicity (Kim et al., 2010). Di-sodium carbonate ( $\text{Na}_2\text{CO}_3$ ) Li *et al.*, (2014), and  $\text{NaHCO}_3$  (Liu et al., 2011) was also investigated as alternatives to  $\beta$ -GP. In addition,  $\text{NaHCO}_3$  was explored as an additive to  $\beta$ -GP, and it was seen that  $\text{NaHCO}_3$  enhanced the cell viability and mechanical properties of hydrogels (Deng et al., 2017).

Composite CS/HA scaffolds or hydrogels are widely researched in bone tissue engineering to integrate the unique biodegradable, antibacterial and cationic features of CS and HA to increase mechanical and biological performance of scaffolds, due to their inherent bioactivity that leads to bonding with natural tissues. In this study, novel injectable CS/HA/Hep composite hydrogels were produced with the inclusion of highly anionic glycosaminoglycan Hep via a polymer blending method, to ensure blood compatibility, sustainable Hep release, and physiological activity to achieve vascularised bone repair and regeneration. The primary aim was to acquire pH neutralised homogeneous injectable solutions that, upon injection into targeted bone defects, allow suitable quick in-situ gelation via natural body temperature and pH stimuli. The liquid hydrogels (CS/HA/Hep), having different compositions, were obtained by neutralization with  $\text{NaHCO}_3$  at 4 °C. Ionically crosslinked hydrogels, on the other hand, were acquired by the incubation of neutral solutions at 37 °C.

Initially, the most suitable CS concentration was selected from among the different tested concentrations; from 4% (w/v) to 8 (w/v). The 5 % (w/v) initial CS concentration, which is around 2.4 %(w/v) in final neutral solution, was chosen as optimal since it provides evenness and is manually injectable. This concentration shows a sol-gel transition starting at nearly 37 °C in rheology analyses, and quick incipient gelation at 37 °C between 8 and 10 min as shown in tests using the test tube inversion method. For composite hydrogels, mixing HA particles in powdered form has resulted in homogeneous dispersions in the CS polymer matrix.

Hep involvement inside hydrogels is very important in terms of the stability of heparin and blood compatibility, as well as the homogeneity of solutions in a CS/Hep polycomplex system. Native tissues start producing platelets as a reaction against any applied external biomaterials that impair blood circulation. Also, the functions and effects of biomaterials may cause different health problems. Blood compatibility of Hep results from its anticoagulant capacity, reducing blood clotting by increasing the presence of blood cells and decreasing platelet attachment (Murugesan et al., 2008). However, it should be pointed out that for the proper utilization of the functions and biocompatibility of Hep, biomaterials should be monitored for its sustainable release. Immobilization of Hep into biomaterials chemically or ionically, provides superiority on commonly reported physical adsorption of Hep onto scaffolds, in terms of efficiency of Hep delivery. Different applications of Hep bonded bioengineered materials have been reported, such as Hep functionalized collagen stents (Lai & Kan, 2017), blood compatible CS/Hep films and scaffolds (He et al., 2010) and silk fibroin/collagen scaffolds integrated with Hep in a polymer blend, providing sustainable release of Hep and increased biocompatibility and blood compatibility (Lu et al., 2007).

In this study, instead of chemical crosslinking, the ionic binding of Hep to a polymer matrix, by blending into polymer mixtures, was preferred to avoid any cytotoxic effects which can be caused by chemical crosslinkers. As well as the suitability of this method for injectable formulations, the polymer blending method can retard the release of the bioactive agent Hep and sustains its long-term availability and efficiency. In this regard, making polycomplex systems, based on ionic bonding of counter charged polymers, seems to be quite a beneficial method. It was implemented in this project to synthesise injectable and thermosensitive CS/HA/Hep polycomplexes. As has been reported, polycomplex networks that have an impact on retarding particle diffusion, due to strength of ionic binding, show promise for sustainable drug delivery systems (Fatin-Rouge et al., 2003). However, maintaining final solution homogeneity in polycomplex systems involves some challenges, since it requires a controlled bonding of counterions in different polymers. The ensuring solution homogeneity depends on several parameters, including the mixing order of compounds, mixing speed and consistency, as well the addition of polymers in liquid or solid form (He et al., 2010). In this project, at the very first experiments, a powdered form of Hep was supplemented into a CS/HA

solution, leading to large local precipitates that are associated with strong electrostatic interactions of counter charged ions in a CS/Hep polycomplex system, when they come into direct and sudden contact. This problem was overcome by drop-by-drop inclusion of the Hep-water solution into the CS/HA mixture while maintaining constant stirring, leading to the acquisition of a homogeneous solution.

Regarding pH neutralisation, the pH of the solution mixtures was at the vicinity of 4.3 prior to neutralisation. Its pH can be raised up to a maximum of 6.2 to 6.3 at 4 °C, at which, homogeneous solutions are acquired without any precipitation. The pH of the solutions were slightly higher at room temperature, and pH values reached between 6.5 and 7.1 upon gelation at 37 °C. The rising pH of solutions above 6.4 caused a precipitation problem. This could be associated with the decrease in ionic charge when pH is above the pKa value of CS (6.2-6.5). This proportionally effects electrostatic repulsion and triggered formation of different domains of hydrogen bonding, causing precipitation (Jarry et al., 2002). It is reported that as the acetylation degree of CS decreases intrinsic pKa comes closer to pH 6.5. In addition, it is reported that the change in the pKa of CS, depends on the electrostatic interactions in the solvent media (Sorlier et al., 2001). The reason for achieving respectively lower pH after final neutralisation could be due to the chosen acid concentration in the dissolution media. A more diluted acid could provide controlled increments in pH. Recently, injectable CS/HA hydrogels created by co-synthesis of HA in CS mixtures that could help increase the final solution pH up to 6.9, was investigated (Rogina et al., 2017). However, in this study co-synthesis of HA was avoided since excessive ammonia used in HA synthesis and any other side product cannot be removed from the injectable solution. Alternatively, incrementing the amount of HA that is used in hydrogels as well as by decreasing used acetic acid concentration slightly, can be investigated in future studies to help efficient incrementation of pH.

The characteristic rheological behaviour of the sole CS hydrogel solution neutralised by NaHCO<sub>3</sub> showed a thermo-irreversible gelation behaviour with an increasing elastic modulus during heating (37-60 °C) that was preserved when the solution was reversibly cooled down. The rheology analyses showed that the hydrogel solutions obtained with a maximum Hep concentration had a significantly higher elastic modulus, enhanced by

more than 25 folds up to 130 Pa. The beneficial effect of Hep on improving mechanical properties of hydrogels has been reported by researchers (He et al., 2010; Lu et al., 2007). Rheological results showed that thermosensitive hydrogels started to form in the temperature vicinity of 37 °C in neutral sole CS solutions. This sol-gel transition point was lowered in composite solutions to around 31 °C in CS/HA, while it decreased in CS/HA/Hep solutions to 28 °C and to 21 °C for SI and SIII samples having minimum and maximum Hep concentrations of 0.12 mg/mL and 0.6 mg/mL, respectively.

Although initial hydrogels showed very promising results in terms of injectability, gelation features and interconnected porous morphology, they were physically weaker during handling, and in their synthesis, a CS sterilisation step was not implemented. Prior to biological testing of initial hydrogels, UV was used to sterilise the liquid hydrogels, while when in solid hydrogel form, ethanol or UV was used (this will be addressed in Chapter 5). However, as it has been reported, UV is efficient for surface sterilisation but cannot penetrate deeply into matter, which may render it an unsuitable method for the sterilisation of pharmaceuticals (Ghosh and Jasti, 2004, p.404). Therefore, in the synthesis of modified hydrogels, a sterile synthesis technique was used that involve the heat sterilisation of CS and HA reagents and all the tools used in the synthesis, as well as filter sterilisation of liquid reagents. Therefore, in the second step of the project it was aimed to provide a totally pre-sterile technique for the synthesis of hydrogels and to enhance the mechanical properties of the final hydrogels by the use of glycerol (See section 3.3).

The sterilisation of thermosensitive injectable hydrogels is discussed in detail in Chapter 1 (Section 1.9.4). In the light of the literature, there is still no perfect method for the sterilisation of thermosensitive injectables based on biodegradable polymers. One of the most promising, affordable approaches could be the non-thermal plasma technique which works based on a dielectric barrier discharge at room conditions, which is suitable for thermosensitive solutions and is efficient at destroying multi-drug resistant bacteria, fungus, spores and prions in a time as short as 3 minutes (Albala et al., 2015). However, this system was not available to this research. Other clinically accepted methods, such as ethylene and oxide ozone treatment involve chemical treatments that require their removal, may cause cytotoxicity and are not suitable for

direct sterilisation of injectable liquid formulations (Dai et al., 2016). The gamma sterilisation of CS is also reported to cause a significant viscosity decrease compromising gelation even when protective stabilising additives are used, and is not found suitable for thermosensitive injectables (Jarry et al., 2002). Heat sterilisation has the best overall capacity for inactivation of all pathogens including: prions, myobacteria, vegetative bacteria, enveloped and non-enveloped virus, bacteria spores and fungi (Dai et al., 2016). However, it also causes decrease in the molecular weight and viscosity loss of polymers. As reported by Jarry *et al.*, (2002), heat induced chain breakage and crosslinking can be reduced by steam sterilisation of CS in solution in the presence of some polyols including: glucose, mannitol, sorbitol and glycerol. Sterility was obtained after 10 min of steam sterilisation of CS. As reported, sugars such as glycerol, can prevent degradation of polymers by their hydroxyl moieties forming a protective layer between polymer chains, protecting them from breakage (Galante et al., 2016; Yen & Sou, 1998).

Among the discussed sterilisation techniques, a pre-sterile technique involving steam autoclaving of a CS dispersion in a glycerol-water medium was utilised. In first experiments, the dry autoclaving of CS in a powder state was investigated. However, dry heat caused a darkening in the colour of the CS powder, and a heterogeneous very viscous solution with local white precipitates were obtained upon neutralisation. Thermogravimetric analyses of CS powder showed a below 10% of weight loss of CS in the autoclaving temperature. In addition, ATR spectroscopy studies showed a decrease in the intensities of some chemical bonds including amide groups. Therefore, in further experiments, steam autoclaving of CS was used, and glycerol was used as stabilising agent mitigating detrimental heat effects and to contribute to improved final hydrogel elasticity and strength. Prior to autoclaving, CS dispersion was prepared in a water-glycerol media and subsequently dissolved by acetic acid and neutralised by NaHCO<sub>3</sub>. In contrast to the powdered form, sterilisation of CS dispersed in a hydroalcoholic water-glycerol media did not show considerable colour change. Furthermore, dissolution of CS after the autoclaving and neutralisation steps, yielded homogeneous and injectable solutions. Furthermore, this method did not impair the thermosensitive gelation behaviour of CS. These results were concordant with those reported (Jarry et al., 2002; Yen & Sou, 1998). However, while neutral solutions had

good injectability and flow potential on the synthesis day, the viscosity of these neutralised thermosensitive solutions increased after 24 h of storage at 4 °C, decreasing solution injectability. This could be due to the respectively higher autoclaving temperature and time. Ideally, as reported , autoclaving at 121 °C for 10 min would be sufficient for sterility (Jarry et al., 2002). However, due to the absence of temperature and time controls in available automatic autoclaves, these parameters could not be implemented. In addition, the slightly acidic media used for CS dissolution may cause a partial breaking down of CS, leading to some crosslinking during storage. By tailoring these parameters, solution stability and injectability could be enhanced.

Involving glycerol in hydrogel systems had a beneficial impact on further incrementing the pH up to 6.5, while maintaining solution homogeneity. The homogeneous solutions with final pH ranges of between 6.4 and 6.5 enhanced the gelation speed, and decreased the incipient gelation time from 5-10 min to 2-3 min. These results revealed the effect of the final solution pH on gelation speed that stimulates further crosslinking in polymers; an effect also confirmed by SEM. This was expected since gelation is mainly driven by pH, and its increments stimulate the reaction of CS by NaHCO<sub>3</sub> leading to the further decrease of remaining acidic NH<sub>3</sub><sup>+</sup> groups which turn into deprotonated NH<sub>2</sub>, making more junctions in the CS chain. However, this could be the evidence that pKa values of CS can be raised by the addition of glycerol by reducing the ionic interactions in CS chains in solution, via hydrophobic forces. It has been reported that change in the pKa of polymers depends on electrostatic interactions in solvent media (Sorlier et al., 2001). The ATR spectroscopy results also confirmed significant interactions and changes in chemical functional groups of hydrogels upon modification. This was associated with the effect of glycerol which causes separation of ions, making them free to lead to further associations of polymers and salts, as well as its own interactions that lead to strong hydrogen bonding (Yusof, 2017).

Furthermore, the mechanic properties of modified hydrogels improved significantly at higher pH (6.4-6.5) in comparison to lower pH (6.2-6.4) solutions. The compression modulus and compression stress at the same strain point (40%) were at around 0.05 MPa and 10 kPa; and 1.51 MPa and 19-42 kPa for hydrogels having lower and a higher pH in solutions, respectively. The maximum compression strength obtained in the

composite S0 sample (CS/HA/Hep) soared up to 310 kPa at 75 % strain. The higher pH hydrogels exhibited a gradual (creep) deformation in which the first deformation point observed a nearly 56% strain for the sole CS sample and rose up to 69% in the SI composite sample. The gradual deformation behaviour of these hydrogels could be associated with their entangled hierarchical microstructure which delays their breakage.

The enhancing of crosslinked points and mechanical properties due to the effect of pH, were well observed in SEM morphology images of higher pH specimens, revealing hierarchical interpenetrating structures, comparable to that of natural bone that were characterised by macropores reaching 500  $\mu\text{m}$  and denser interlocking thick micropore ( $\sim 5 \mu\text{m}$ ) walls separating the big pores. However, some pores were open while others seem to be closed which might reduce interconnectivity to a certain level. The hierarchically strengthened structure of the modified hydrogels obtained with a higher pH could be associated with the hydroalcoholic medium due to the recruitment of glycerol. As reported, glycerol leads to alteration of water structure covering throughout the CS chains by reducing charge density of polymer. Having hydrophobic and hydrophilic features, alcohol-water moieties interacting with CS ensure the formation of hydrophobic sites leading to intra-molecular bonding of CS (Boucard et al., 2005; Jarry et al., 2002). In addition, glycerol treatment of chitosan-gelatine crosslinked hydrogels enhancing the elasticity and flexibility of hydrogels has been reported by Badhe *et al.*, (2017). Also, enhanced chain flexibility and plasticizers that provide stress relaxation behaviour leads to a decrease in deformation and an increase in strength (Ahmad et al., 2012). Furthermore, Nam *et al.*, (2019) has reported that the stress relaxation behaviour in alginate hydrogels has increased with use of another polyol, polyethylene glycol (PEG), which provides biomimetic, more cell friendly, tuneable hydrogels that stimulate fibroblast attachment and proliferation, as well as osteogenesis through the differentiation of mesenchymal stem cells.

In regard to injectability properties, according to the manual assessment of injectability, a 21 G needle size was found suitable for the injection of all compositions of both initial and modified hydrogel solutions on their synthesis day. As reported, a 21 G needle size can facilitate most injections carried out in orthopaedic and dental applications, which are in the range of gauge sizes 10–16 G and 16–25 G, respectively (Burguera et al.,

2007). In modified formulations, shear thinning, and adhesive solution flow features were observed with an increase of solution density in comparison to initial hydrogels. This may prevent or hinder the washing out of the solution after injection but provide, possibly, better adhesion to an injury site. Regarding quantitative injectability analyses, both initial and modified formulations exhibited similar injection forces, between 1-2 N and 10-15 N for the injection tests through needless and 19 G needle coupled syringe cases, respectively, in the tests performed on the day of their synthesis (Day 0). For both types of liquid hydrogel, the CS/HA compositions generally lowered the injection force needed, in comparison to that of the sole CS specimens. This has confirmed the beneficiary impact of HA on enhancing the injection performance of CS matrix hydrogel solutions. This might be associated with the shear stress reduction feature of hydroxyapatite, leading to better flow features (Knowles et al., 2000; Raii et al., 2012). The opposite effect was observed in Hep involved liquids. This was considered to be due to the presence of counter charged ions triggering slight bonding in the solution state, leading to an increase in viscosity. Needleless injection tests of initial liquid hydrogels after 3 days of storage at 4 °C showed similar injection force requirements as in those obtained on Day 0. The injection tests that used a thinner syringe (21 G) after 3 days of storage had results still comparable with reported manual injection forces (Burckbuchler et al., 2010). Although injectability was very convenient on the synthesis day of the modified liquid hydrogels, the needed injection forces of modified formulations increased respectively, and less even flow properties were observed in injection tests after 24 h. The observed thickening of solutions after 24 h of storage at 4 °C made injection only possible with an 18 G or larger needle.

In terms of solution stability, the modified solutions having a pH of 6.4-6.5 were maintained for 4 days, and thereafter, phase separation occurred as is reported in the literature (Liu et al., 2011). However, the phase separation was not observed in solutions obtained at a pH of between 6.2 and 6.4. Initial formulations having a pH range between 6.2 and 6.4 were more stable, and their liquid forms were preserved for 6-months at 4 °C for the CS and CS/HA formulations. On the other hand, Hep involved samples formed a thin (film) layer at the top after 3 weeks while the liquid phase below could be preserved for just under 2 months.

### 3.7 Summary and Conclusions

Injectable pH and thermo-sensitive CS/HA/Hep composite hydrogels were produced by two different methods and their properties were compared by different characterisation techniques. Hydrogel compositions showed facile injectability that allows suitable manual injection by a 21 G minimum needle thickness and great gelation capacity at an average body temperature of 37 °C. Incipient gelation time for initial and modified hydrogels were 5-10 min and 2-3 min, respectively. However, in modified liquid hydrogels, injectability capacity decreased upon storage for 24 h while initial hydrogel solutions were stable for a much longer period.

Interconnected, porous homogeneous pore structures were obtained from initial hydrogels while their counterparts modified in higher pH solutions (up to 6.5), possessed hierarchical and interpenetrating micropore wall domains separating huge pores. Both porous morphologies were comparable with the pore sizes required to maintain cell activity and allow diffusion in bone tissue engineering (75-100  $\mu$ m) (Hulbert et al., 1970). In terms of surface morphology, HA incorporated modified composite hydrogels (CS/HA) possessed rough featured spherical crystals, having high surface area due to a specific flower like morphology of each crystal. This is promising for their bioactive performance, and is discussed in the following chapter. On the other hand, the comparatively smoother surface features associated with the coating effect of Hep, were seen in the CS/HA/Hep hydrogels. Despite the fact that surface smoothening decrease cell attachment, as reported by Gümüşderelioğlu, Karakeçili and Demirtaş, (2011), the active binding capacity of Hep for diverse living cells, proteins and growth factors, due to its highly anionic chemical nature, led to better cell attachment, migration and proliferation, for osteogenesis. Furthermore, in this study, the bioactivity performance of the composite samples involving Hep has led to the achievement of better mineralisation in stimulated body fluid (SBF) in comparison to that of controls (to be discussed in Chapter 4).

Mechanical properties of modified hydrogels showed tuneable mechanical enhancement when the pH in a solution state is slightly increased from 6.2-6.3 to 6.4-6.5, 0.05 MPa, and whose compression modulus and compression strain at 40% are at

the range of 0.05 MPa and 10 kPa; and 1.5 MPa and 40 kPa, respectively. The modified hydrogels, having a pH of about 6.5 in solution, showed gradual deformation behaviour. The first deformation was seen at nearly 60% for sole CS hydrogels while composite hydrogels sustained up to around a 70 % strain. None of them were broken at the 75% strain upon which the experiment ended. The achieved highest mean compression strength at 75% strain and the compression modulus in composite hydrogels were 310 kPa and 1.51 MPa, respectively. These results were comparable with the tough hierarchical double networked hydrogels; poly(2-acrylamido-2-Methylpropanesulfonic acid)/poly(N,N0-dimethylacrylamide) (PAMPS/PDMAAm) (Mredha et al., 2017) Furthermore, these hydrogels possess 250 and 10 folds higher stiffness and compression modulus respectively than reported UV crosslinked methacrylated gelatine (GelMA) / methacrylated hyaluronic acid (HAMA) hydrogels (Eke et al., 2017). The compression stress at first fracture points ranged between 51 and 172 kPa, which were more than the sufficient stiffness values required, reported for osteogenic stem cell differentiation (45-49 kPa) (Jiang et al., 2015; Zouani et al., 2013).

To conclude, novel pH and thermosensitive injectable CS/HA/Hep hydrogels have been produced by two different methods. This contributed to acquiring significant knowledge about their versatile chemical, structural and mechanical properties. The combinational effects of pH and the modification process involving CS sterilisation in dispersion media by glycerol addition, provided a desired interpenetrating morphology via further crosslinking; due to additional hydrogen bonding and better mechanical performance. However, negative heat effects during sterilisation could not be totally avoided since the solution's stability and injectability decreased upon storage, whereas injectability was very convenient on the synthesis day. It is believed that by utilising lower autoclaving time and temperature, decreasing acid concentration slightly, and increasing the amount of HA, could lead to achieving better stability, increment of final solution pH and mechanical properties. Bioactivity, *in-vitro* degradation and *in-vivo* angiogenesis studies by CAM assay were investigated and are described in the following chapters. These novel pH and thermosensitive injectable CS/HA/Hep hydrogels neutralised by NaHCO<sub>3</sub> could be considered for potential clinical use, as advanced pro-angiogenic bone tissue engineering materials.

## 4 BIOACTIVITY, BIODEGRADATION AND DRUG RELEASE STUDIES FOR SYNTHESIZED HYDROGELS

### 4.1 Introduction

This chapter describes the biochemical characteristics of injectable modified hydrogels in diverse aspects, including swelling, in-vitro degradation, bioactivity, and drug (Hep) determination and release. The bioactivity of hydrogels, in terms of their capacity to form mineralised apatite layer on their surfaces was analysed by use of Simulated Body Fluid (SBF) immersion tests at 37 °C. *In-vitro* degradation studies were performed by the immersion of hydrogels (at 37 °C) in a Phosphate Buffer Saline (PBS), in the presence or absence of lysozyme enzymes. The various associated common analyses for these tests included weight and pH measurements, chemical analyses by FTIR-ATR, elemental analyses by EDS, and morphological analyses by SEM, which were performed at certain intervals of sample incubation. Similarly, the swelling capacity of hydrogels were determined by weight and pH analyses during the incubation of hydrogels in PBS. The Hep in modified hydrogel networks was detected by Toluidine Blue (TB) staining and imaging. In addition, Hep stability in initial freeze-dried hydrogels after 2-years of storage were tested by TB staining. The drug release profile of Hep was quantitatively determined by a colorimetric TB assay based on chemical complexation of Hep with TB leading to a colour change from blue to purple. Results showed the homogeneous distribution of Hep on the top surface, indicating surface functionalised CS/HA/Hep hydrogels. The release of Hep from hydrogel networks in water media was in a prolonged manner of up to 7-days. This would be compared to the modified higher pH solutions (6.4-6.5) that lead to a more stable and interpenetrating hydrogel morphology, as well decreased swelling behaviour (55%); factors presumed to enhance the sustainable release of Hep. Biominerilization was not only triggered by HA but also by Hep in CS/HA/Hep hydrogels. This led to the significant promotion of carbonated apatite mineral layer formation. The gradual weight loss of hydrogels was obtained for both PBS and lysozyme media. They displayed surface cracks from day-

14 which propagated towards the bulk of the hydrogels at day-42, showing 60% and 70% degradation in the PBS, and lysozyme media, respectively.

## 4.2 Materials and Methods

### **Materials**

For preparation of the SBF solution, the following reagents were supplied: NaCl, NaHCO<sub>3</sub>, KCl, K<sub>2</sub>HPO<sub>4</sub>.2H<sub>2</sub>O, MgCl<sub>2</sub>.6H<sub>2</sub>O, CaCl<sub>2</sub> and Na<sub>2</sub>SO<sub>4</sub>, (Sigma-Aldrich®, Dorset, UK), 1 N HCl and (CH<sub>2</sub>OH)<sub>3</sub>CNH<sub>2</sub> (Tris) (Thermo Fisher Scientific™, ACROS Organics™, Geel, Belgium). For degradation studies, Phosphate Buffer Saline tablets (PBS-Dulbecco A, Thermo Scientific™, Oxoid™, Basingstoke, UK) and Lysozyme from chicken egg white ( $\leq$  20.000 U/mg, Thermo Fisher Scientific™, MP Medical™, Loughborough, UK) were purchased. For Hep determination and drug release studies, Toluidine Blue (TB), n-hexane (95+%), 1N HCl (Thermo Fisher Scientific™, ACROS Organics™, Geel, Belgium) and NaCl (Sigma-Aldrich®, Dorset, UK) were supplied. In all experiments, de-ionised ultrapure (Type-I) water (Veolia Water Technologies, PURELAB® Chorus, 18.2 MΩ.cm, Wycombe, UK) was utilised.

## 4.3 Swelling (Liquid Absorption) Tests

The liquid absorption capacity (swelling) of hydrogels is a significant parameter determining drug delivery performance and needs to be quantified by testing. This absorption capacity can be modulated by electrostatic charge density, degree of acidity or basicity, the surrounding pH, the rate of entanglement, and the degree of hydrophilicity (Rizwan et al., 2017).

### 4.3.1 Preparation of Test Samples and Phosphate Buffer Saline (PBS) Media

PBS solutions were prepared by dissolving one PBS tablet (PBS-Dulbecco A, pH 7.3 $\pm$ 0.2 at 25 °C Thermo Scientific™, Oxoid™, Basingstoke, UK) in 100 mL de-ionised water and autoclaved at 132 °C in an automatic autoclave for 20 min including heating and ventilation times of 5 min. each (LMS, Jencons Scientific Ltd., Leighton Buzzard, Bedfordshire, UK). PBS solutions were stored in a refrigerator at 10 °C until needed for swelling and *in-vitro* degradation studies.

Hydrogel samples were prepared from 48 mL of hydrogel solution poured into glass dishes with lids ( $\varnothing$ : 100 x 15 mm, Steriplan®, Duran® DWK Life Sciences GmbH, Mainz, Germany) and were incubated at 37 °C for 48 h. Then specimens were cut by using a cork borer (5/16 inch), subsequently weighted to  $0.07 \pm 0.01$  g and recorded as  $W_i$ . Three sample replicas were prepared for each sample group and experiments were repeated in triplicate. The specimens were immersed into 3 mL of prepared PBS media in a vial (7 mL), and incubated in an oven adjusted at 37 °C.

#### 4.3.2 pH Analyses

Samples in vials were swirled gently at each time intervals of 0.5, 1, 2, 4, 6, 15, 24, 48 and 72 hours and pH values of the PBS media were measured by using a pH-meter (Mettler-Toledo GmbH, Analytical, FiveEasy Plus™, Greifensee, Switzerland) by keeping samples on a hot-stirrer adjusted to 37 °C.

#### 4.3.3 Weight Analyses

At designed time intervals (0.5, 1, 2, 4, 6, 15, 24, 48 and 72 hours), the samples were taken out and weighted accurately ( $W_s$ ) after removing their surface water. The swelling percentage was calculated by the formula given at Equation (4.1) where  $W_i$  and  $W_s$  represent the initial and swollen sample weights, respectively.

$$\text{Swelling ratio (\%)} = \frac{(W_s - W_i)}{W_i} * 100 \quad (4.1)$$

### 4.4 In-vitro Degradation Tests

Biodegradation behaviours of hydrogels have crucial impact on drug delivery and tissue regeneration efficiencies. The ideal tissue scaffolds should be mechanically stable when they support the regeneration of damaged tissues by releasing the active agents in their structure. Once the native tissue has started regenerating itself, ideally, hydrogel scaffolds should be degradable. Accordingly, this parameter must be tested for.

#### 4.4.1 Preparation of Test Samples and Degradation Media

Degradation studies were performed in two different media, PBS and lysozyme (prepared in PBS media). The PBS media was prepared as described in Section 4.3.1. The lysozyme solution (5 mg/mL) was prepared by dissolving an amount of lysozyme from hen egg white ( $\leq 20.000$  U/mg, Thermo Fisher Scientific<sup>TM</sup>, MP Medical<sup>TM</sup>, Loughborough, UK) in the PBS media and stored at 10 °C.

Hydrogels were obtained as described in Section 4.3.1. The cylindrical shaped hydrogels were prepared for degradation tests by cutting via a cork borer (5/16 inch). Four sample replicates from each sample group were prepared, and experiments were repeated three times. The samples were prepared in the same condition for both PBS and lysozyme media test groups. Each hydrogel sample was weighted to a similar mass of  $0.1 \pm 0.05$  g and recorded as  $W_i$ . Then, photographs of a first sample from each group was taken with a ruler, and this was repeated in each time intervals.

The hydrogel specimens, including 3 mL of media solutions (PBS or lysozyme), were placed into 7 mL vials and incubated at 37 °C for the tests at different time intervals: 1, 3, 7, 14, 21, 28, 35 and 42 days. The sample tubes were manually swirled two-times a day. The sample media were renewed every 3-days and these samples were stored at 10 °C for further drug release studies.

For chemical analyses by ATR and microstructure changes by SEM, hydrogel samples were prepared separately. Samples for each group were prepared in triplicate, and were immersed into 3 mL of media, including PBS and lysozyme specimens incubated at 37 °C, over certain periods. At certain time points (14, 28 and 42 days) the samples were taken from the media and washed with de-ionized water and subsequently freeze dried (freezing at -80 °C for 24 h & drying at -20 for 24 h) prior to ATR and SEM analyses.

#### 4.4.2 pH Analyses

During degradation tests, pH alteration in media was determined by measuring the pH of the solutions via a pH-meter, at each designed time intervals (1, 3, 7, 14, 21, 28, 35 and 42 days). This was performed on sample tubes placed on a hot stirrer adjusted to 37 °C.

#### 4.4.3 Weight Analyses

After pH measurements, samples were placed into the wells of a 24 well-plate and washed with 1 mL of de-ionized water thrice to remove any ions adsorbed on the surface. Then, all samples were placed into new vials with slightly loosened lids and incubated at 37 °C for 24 h for the removal of surface water while still maintaining their gel form rather than as dried film. After 24 h incubation, hydrogels were weighted which were recorded as ( $W_t$ ). The weight loss was expressed as the dry weight remaining ratio or weight loss percentage at Equation (4.2) and (4.3), respectively.

$$\text{Dry weight remaining ratio (\%)} = W_t/W_i * 100 \quad (4.2)$$

$$\text{Weight loss (\%)} = (W_t - W_i)/W_i * 100 \quad (4.3)$$

After weighing, the images of certain samples were taken in each time intervals for physical observations of degradation.

#### 4.4.4 Morphological Analyses by SEM

The morphological analyses of hydrogels, before and after incubation in a media (PBS/Lysozyme) for 14, 28 and 42 days were analysed in freeze-dried form by SEM. The top, bottom and a cross-section of each sample was prepared on one metal stub. Subsequently samples were gold coated (5 nm) and imaged by applying 5.0 kV of an accelerating voltage using a Schottky FE-SEM (JEOL JSM-7800F, Tokyo, Japan) instrument equipped with EDS (50 mm<sup>2</sup> area) with a Silicon Drift Detector (SDD) (Oxford Instruments, UK).

#### 4.4.5 Chemical Analyses by FTIR-ATR

*In-vitro* degradation samples were analysed for their chemical structure changes at time intervals of 0, 14, 28 and 42 days. A Thermo Nicolet<sup>TM</sup> iS50 FTIR spectrophotometer instrument (Thermo Fisher Scientific Inc., Madison, WI, USA) in Attenuated Total Reflectance (ATR) mode, was utilised for chemical analyses. Spectra were acquired in the mid-infrared region (4000 to 400 cm<sup>-1</sup>) by using a DTGS ATR detector and a KBr infrared beam splitter. The analyses were performed by using an aperture of 150 with a resolution of 16 cm<sup>-1</sup> accumulating 128 scans. The background spectrum was acquired prior to the experiments and renewed after 120 min. The spectral data were acquired and analysed in Thermo Nicolet OMNIC<sup>TM</sup> (Version 9.5.9, Thermo Fisher Scientific Inc, Madison, WI, USA) software in which spectra were overlaid after automatic baseline correction of each spectrum.

### 4.5 Bioactivity Tests by Simulated Body Fluid (SBF)

The mineralised carbonated apatite layer formation capacity of biomaterials facilitate bioactive surface features that provide binding between natural tissues and biomaterials. Bioactivity evaluation in an SBF is based on a chemical reaction between the biomaterial surface and ions from salts in the SBF, facilitating formation of an hydroxy carbonate apatite layer (Ohtsuki et al., 2009). SBF is an ionic solution that mimics the composition of blood plasma and has been first developed by Kokubo (1991).

#### 4.5.1 Preparation of Test Samples and SBF Media

In the current study, conventional SBF (c-SBF) with a refined recipe was prepared as per the protocol reported by Kokubo and Takadama, (2006). Briefly, 1 L of SBF was prepared in a smooth graduated plastic beaker free from any scratches (Thermo Fisher Scientific<sup>TM</sup>, Nalgene<sup>TM</sup> PMP, Loughborough, UK). The amounts of various salts were dissolved one-by-one in de-ionised water, kept at 36.5±1.5 °C in the following sequence,: NaCl (8.035 g), NaHCO<sub>3</sub> (0.355 g), KCl (0.225 g), K<sub>2</sub>HPO<sub>4</sub>.2H<sub>2</sub>O (0.231 g), MgCl<sub>2</sub>.6H<sub>2</sub>O (0.311 g), 1 M HCl (39 mL), CaCl<sub>2</sub> (0.292 g), Na<sub>2</sub>SO<sub>4</sub> (0.072 g) and with pH adjustment by the gradual addition of (CH<sub>2</sub>OH)<sub>3</sub>CNH<sub>2</sub> (Tris) (6.118 g) and 1

M HCl (0–5 mL). The final SBF solution was produced at a pH of 7.4 at 36.5 °C and stored in a tightly closed plastic bottle kept at 10 °C up to a month to avoid any possible crystal nucleation compromising solution stability and efficiency.

Hydrogels were obtained as described in Section 4.3.1, and they were cut into small circular specimens by using a cork borer (1/4 inch) for bioactivity tests. Following that, each sample was weighted to similar masses (0.03±0.003 g) and recorded. Three replicates of samples were prepared, and these experiments were repeated in triplicate for each time intervals of 7, 14, and 21 days. Specimens were placed into individual universal test tubes and 10 mL of prepared SBF solution (pH 7.4) was warmed to 37 °C and added onto samples for their complete immersion. The required minimum media amount in the SBF protocol was calculated from the given Equation (4.4), which was symbolised with a V and S represents the surface area of the specimen (Kokubo & Takadama, 2006). The SBF media was refreshed after 7-days. The media taken in each stored at 10 °C before use for drug release studies.

$$V = \frac{S}{10} \quad (4.4)$$

#### 4.5.2 pH Analyses

The pH of SBF incubation media samples at each time intervals (7, 14, and 21 days) were measured on a hot stirrer at 37 °C.

#### 4.5.3 Weight Analyses

After pH measurements, samples were put into 24 well-plates, washed thrice with de-ionised water, and weighted following removal of surface water. This weight was recorded as  $W_i$ . Subsequently, samples were freeze-dried (freezing at -80 °C for 24 h; main drying at -20 °C for 24 h) and weighted, which were recorded as  $W_{fd}$ . Dry mass percentage of samples were calculated (see equation 4.5 below) and compared between time intervals as a measurement of mineralisation. The freeze-dried samples were stored in a desiccator for further analyses including, SEM, EDS and FTIR-ATR.

$$Dry\ Weight\ Ratio\ (\%) = W_i/W_{fd} * 100 \quad (4.5)$$

#### 4.5.4 Chemical Analyses by FTIR-ATR

The mineralised hydrogel samples after incubation in SBF for different intervals of 0, 7, 14, and 21 days were characterised by FTIR-ATR spectroscopic analyses. The ATR spectroscopic data collection was performed by using the same parameters used for chemical analyses of degradation samples as described in Section 4.4.5. The data was presented as an overlay of spectra after automatic baseline correction in Thermo Nicolet OMNIC<sup>TM</sup> (Version 9.5.9, Thermo Fisher Scientific Inc., Madison, WI, USA) software.

#### 4.5.5 Morphological Analyses by SEM

The microstructures of the mineralised hydrogels after 7, 14 and 21 days of incubation in SBF were analysed in freeze-dried form. The top, bottom and cross-section images of gold coated (5 nm) specimens were acquired via a Schottky FE-SEM instrument (JEOL JSM-7800F, Tokyo, Japan) by applying a 5.0 kV of accelerating voltage and a 9 to 12 mm working distance.

#### 4.5.6 Elemental Analyses by EDS

Mineralised apatite layer formation capacity on hydrogels was investigated via EDS elemental analyses. A Schottky Field Emission Scanning Electron Microscope (FESEM) (JEOL JSM-7800F, Tokyo, JAPAN) in conjunction with an X-ray Energy Dispersive Spectrometer (EDS) with a large area (50 mm<sup>2</sup>) equipped with a Silicon Drift Detector (SDD) (Oxford Instruments, UK) was utilised. The analyses were performed by mapping of elements and their mean weight percentage in the compositions.

### 4.6 Drug (Hep) Delivery Analyses by Toluidine Blue (TB) Assay

Toluidine Blue (TB) is a cationic metachromatic stain that serves as a complex making agent with anionic glycosaminoglycans including Hep due to the content of sulphuric acid esters. The formation of chemical TB/Hep complex alter the solution colour from blue to purple. By adding an immiscible organic compound, TB/Hep complex could be

separated by surface adsorption. The optical density measurements of the remaining unreacted TB solution in the mixture is extracted and its optical density measurements are used to count the concentration of Hep (Gattás-Asfura et al., 2006; MacIntosh, 1941).

In this study, TB staining was used to determine the distribution of Hep inside hydrogel networks. In addition, the amount of Hep released in a media at different time intervals was quantified by TB assay in which TB/Hep complexes were made in the presence of a hexane compound, and absorption measurements of an un-complexed dye solution was performed as reported in the literature (Sun et al., 2011).

#### 4.6.1 Toluidine Blue (TB) Solution Preparation

0.005 % (w/v) of Toluidine Blue (TB) solution was prepared in 0.01 N HCl solution containing 0.2 w % of NaCl, as reported (MacIntosh, 1941). The TB solution was freshly prepared every week and stored in a glass bottle covered with aluminium foil and kept at room temperature.

#### 4.6.2 Local Hep Determination

The hydrogel samples were cut into circular shapes by using a cork borer ( $\varnothing$ : 3/8 inch) and immersed into 2 mL of TB solution in vials and left for 30 min. The stained samples were washed three times with de-ionised water to remove unbounded TB stains. The images of samples were taken by phone camera and under an optical microscope (EVOS<sup>TM</sup> XL Core Configured Microscope, Invitrogen<sup>TM</sup>, Thermo Fisher Scientific Inc, Madison, WI, USA).

#### 4.6.3 Drug (Hep) Release Studies

The TB assay protocol was used to determine drug (Hep) release from hydrogel networks based on optical density measurements of unreacted TB solution extracts underneath the formed TB/Hep complexes, which are then correlated with Hep concentrations via an obtained standard curve.

TB-Hep complexes were obtained by using a TB protocol adapted from the literature (Kim et al., 2000; Lu et al., 2007). For this, 1.5 mL of prepared TB solution was poured into vials. Then, 1 mL of the standard Hep solution in known concentration was added and mixed with TB. After swirling, the mixtures in vials, they were rested at room temperature for 30 min. Following that, 1.5 mL of hexane was poured into the mixtures and swirled vigorously for at least 30 sec to provide a complex layer formation on top of the solutions. The formation of a TB-Hep complex in the presence of hexane could be visually verified, especially at higher concentrations of Hep due to the colour change in the solution, having a purple complex layer on top separated by unreacted blue TB solution below. The unreacted TB solution located at the bottom of the vials were carefully extracted; avoiding taking hexane solution or any precipitate from the complex. 100  $\mu$ L aliquots of the media were placed into 96 well-plates with 10 replicates per sample. Then, absorbance measurements of the solutions were performed with a micro-plate reader instrument (800TS, BioTek<sup>®</sup> Instruments GmbH, Bad Friedrichshall, Germany) using 630 nm wavelength of the light. The acquired data was analysed, and the mean of the absorbance values were plotted against TB concentrations in GraphPad Prism (Version 7.0, San Diego, CA, USA) software.

For the correlations of the Hep concentrations in the TB/Hep mixtures, a standard curve was obtained via absorbance measurements of noncomplex TB solution aliquots that were prepared for the Hep standard solutions in increasing concentrations. Hep standard solutions were individually prepared in a media (water or SBF) at different concentrations of: 0, 20, 40, 60, 80, 100, 120, 140  $\mu$ g/mL that include the range of the Hep concentrations of approximately 30 and 120  $\mu$ g/mL in the modified hydrogel samples: S0 and SI respectively. The required standard solution concentrations were prepared as 10 mL aliquots diluted from the prepared stock solution (200  $\mu$ g/mL Hep).

To investigate the drug release profile of hydrogel samples in D.H<sub>2</sub>O, hydrogels were prepared from solutions (approx. 45 mL) that were cast into glass dishes with lids ( $\varnothing$ : 100 x 15 mm, Steriplan<sup>®</sup>, Duran<sup>®</sup> DWK Life Sciences GmbH, Mainz, Germany) and incubated at 37 °C for 48 h. Then, the hydrogels were cut into small circular specimens by using a cork borer (5/16 inch). Following that, each sample was weighted to similar masses (0.1±0.05 g), recorded and incubated in 10 mL of D.H<sub>2</sub>O in universal test tubes.

At different time intervals (4 h, 1, 3, and 7 days), 1 mL of Hep release media was taken and replaced with 1 mL of fresh D.H<sub>2</sub>O. The Hep release media (1 mL) was then added into 1.5 mL of TB solution, and the steps for making TB/Hep complex were carried out as previously described. The acquired absorbance measurements were correlated with the concentration of Hep by using a standard curve equation. Furthermore, the drug (Hep) release in SBF media was undertaken in the same way, but by using supernatant SBF as a Hep release media, taken during bioactivity studies at 7, 14 and 21 days of experiment intervals, and refreshed in every 7-days.

#### 4.7 Statistical Analyses

Statistical analyses on data were performed in GraphPad Prism (Version 7.0, San Diego, CA, USA) software. 2-way ANOVA analyses were performed by using TUKEY multiple comparison method. A correlation of  $p \leq 0.05$  was considered as significant.

#### 4.8 Results

##### 4.8.1 Swelling Analyses by Weight and pH Change

The swelling capacities of modified hydrogels were tested by incubation in PBS for different time intervals of up to 72 hours (h). Figure 4.1.a shows the percentage swelling of different hydrogel compositions. The sole CS hydrogel (CI) possessed the highest swelling ratios during all experiment periods whereas the minimum swelling ratios were seen with the composite CS/HA/Hep (SI) sample, which could be more efficient for prolonged drug release applications. The swelling equilibriums reached in 6 h for CI, CII and SI samples were 68%, 61% and 55%, respectively. The swelling pattern of all compositions showed the similar trends that the most swelling occurred in first 30 min and increased gradually up to 6 h in which the maximum swelling occurred. After 15 h, hydrogels showed a tendency to slightly loose the absorbed liquid for up to 72 h possibly due to the starting of degradation.

The pH profile of the supernatant media of hydrogels incubated in PBS are given for the same incubation periods in Figure 4.1.b. In contrast to their swelling ratio, the highest pH values belonged to SI composite sample while the sole CS hydrogel CI,

possessed the lowest solution pH. This could be associated with the final pH of the composite hydrogels having respectively higher pH in comparison to sole CS hydrogels. In addition, the absorption of anions from salts in PBS are attracted by cationic sites of CS that decrease the pH of the media. In the same way, due to less liquid absorption in composite hydrogels, CII and SI possessed respectively higher pH in the supernatant media.

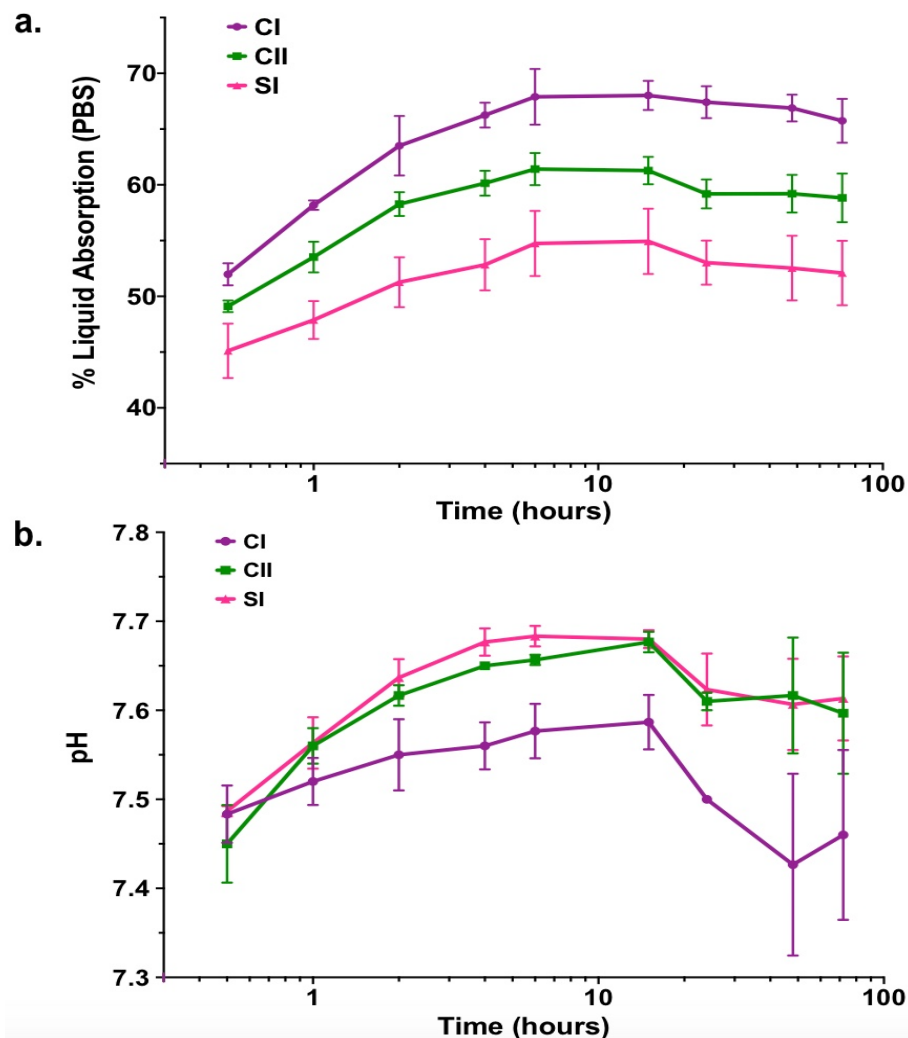


**Figure 4.1** The swelling analyses results of different modified hydrogel compositions: CI (CS), CII (CS.0.1HA) and SI (CS.0.1HA.0.005Hep) with standard error bars (n=3) **a.** % liquid absorption ratio, and **b.** pH change in supernatant PBS media in which hydrogels were incubated at different time points of swelling tests up to 72 hours.

It was seen that pH of the media increased for up to 15 h, which was parallel to the rising swelling ratio pattern. In the first 15 h, the pH of CII and SI rose to approximately 7.70, while the pH of CI increased to around 7.55. Between 15 and 24 h, there was a sudden decrease in the pH of all solutions that was parallel with the deswelling of the

hydrogels, as losing some water decreases pH. The deswelling continued until 48 h in CI and SI samples that both showed a decrease in pH to around 7.4 and 7.6, respectively, and subsequently, rising slightly at the 72 h interval.

#### 4.8.2 *In-vitro* Degradation Analyses

##### 4.8.2.1 Weight and pH Analyses During Degradation

The *in-vitro* degradation based on weight decrease of the samples and pH alteration in media during the incubation of samples in both the presence and absence of the lysozyme enzyme (5mg/mL) in PBS over 6-weeks, were studied for different time intervals (the resultant plots are shown in Figure 4.2). During the first day of incubation in both media, hydrogels lost almost 20% of their weight. This high weight loss ratio at the beginning could be associated with water lost due to further gelation at 37 °C during drying for 24 h. The degradation speed of hydrogels incubated in the presence of lysozyme was faster in comparison to sole PBS media specimens.

In lysozyme specimens, a nearly 50% degradation was seen at day-14, following by a gradual degradation reaching the vicinity of 70% at day-42. On the other hand, PBS specimens showed gradual but slower degradation reaching around 35% of weight loss in the first two-weeks, following by a total 60% degradation after 42-days. In PBS specimens, the CII sample showed the least degradation although it had the highest standard deviation; while the degradation rate of SI samples was the fastest. However, for both PBS and lysozyme specimens, the in degradation were not statistically significant ( $p: 0.0959$ ). However, a significant difference ( $p<0.0001$ ) occurred between the time intervals of the degradation tests.

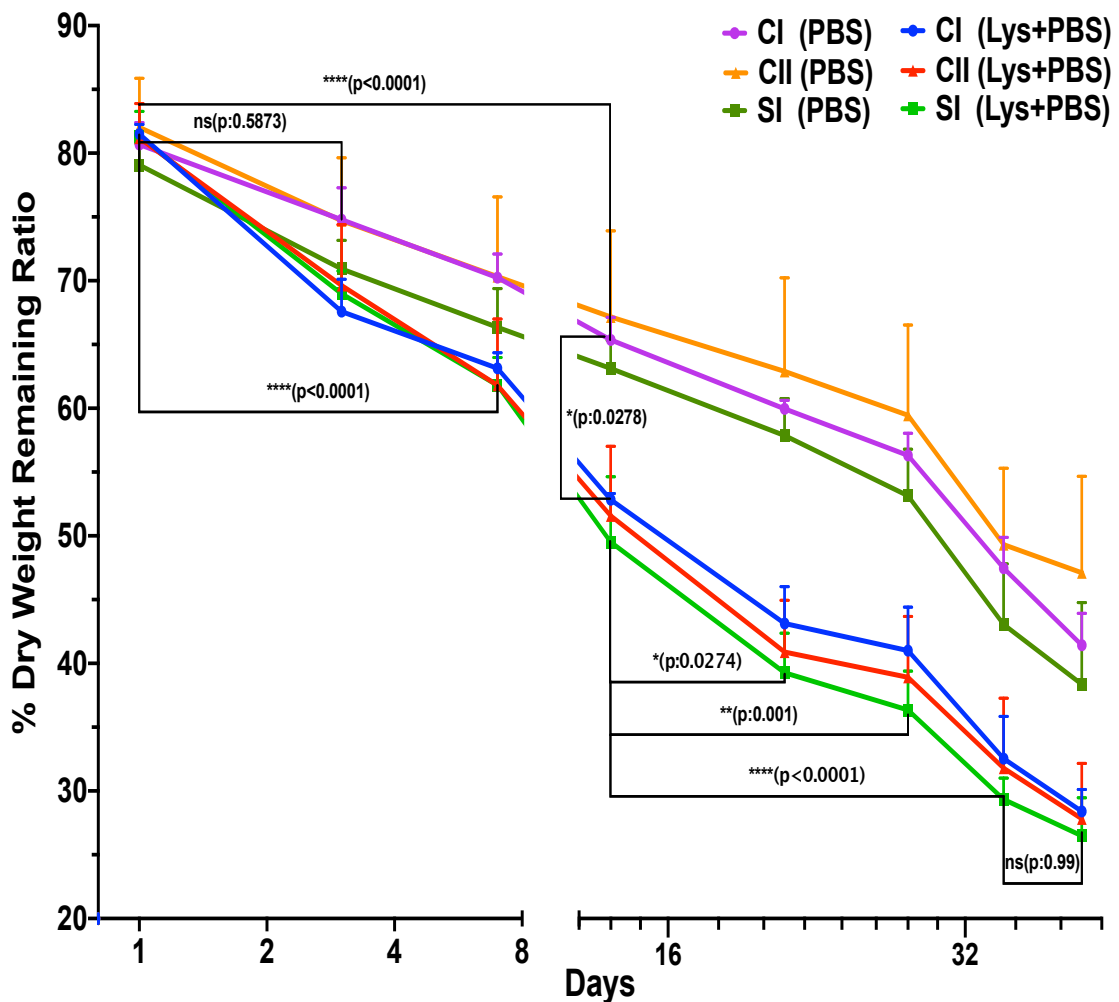


**Figure 4.2** The comparative in-vitro degradation weight analyses plotted as the percentage of dry weight remaining ratios of the modified hydrogels: CI (CS), CII (CS.0.1HA) and SI (CS.0.1HA.0.005Hep) in different time intervals up to 42 days, during incubation in PBS and Lysozyme (5 mg/mL) in PBS solution with standard deviation (n=4). Statistical analyses performed by 2-way ANOVA; Tukey multiple comparison tests were performed with  $\alpha$ : 0.05. The adjusted p-values above show differences of the degradation profile of the CI sample in PBS media (purple line) while below p-values belong to comparison of the SI sample in Lysozyme + PBS media (bright green line). The p-value connected with a vertical line demonstrates the significant difference between the CI sample in PBS and Lysozyme + PBS media at day 14.

The comparative pH alteration plots of the degradation of samples in both PBS and lysozyme media specimens are given in Figure 4.3. The pH range over the whole degradation period was lower in Lysozyme media specimens (~6.9-7.5) while sole PBS media specimens were higher (~7.2-7.7). During the first 3 days, the pH of the hydrogel supernatants in both media showed an increase that could be associated with swelling of the hydrogels. A sudden decrease in the pH was observed between day-3 and day-7, which indicates the start of deswelling and weight loss.

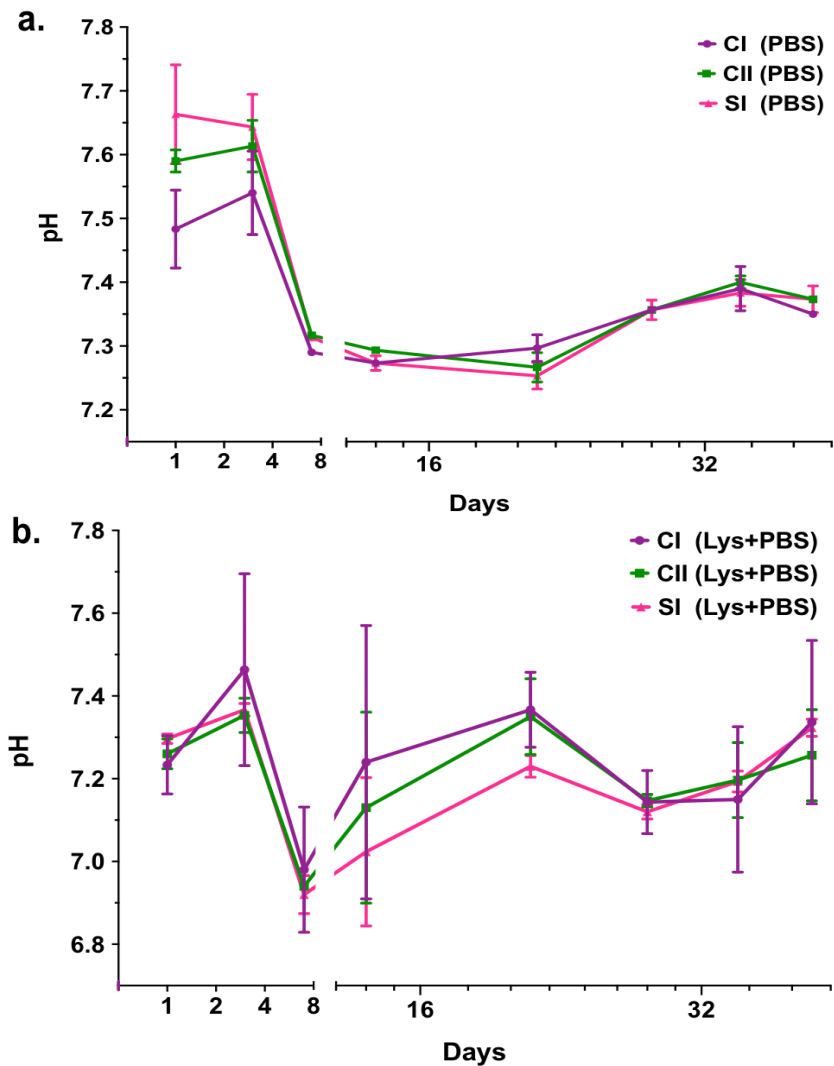


**Figure 4.3** The pH alteration of supernatant media taken at different time intervals of up to 42 days in the in-vitro degradation tests of modified hydrogels in **a.** PBS and **b.** Lysozyme (5 mg/mL) solution in PBS. The involved hydrogel specimens are CI (CS), CII (CS.0.1HA) and SI (CS.0.1HA.0.005Hep).

Between 7 and 21 days, pH became almost stable at around 7.3 for the sole PBS media specimens, while lysozyme specimens showed an increase in pH level of up to 7.4 followed by a decrease until day-28 and an increase until day-42 returning to around 7.4, equalising with the pH of the PBS media specimens.

The physical indications of degradation in hydrogel specimens were also compared by taking photographs of the same specimens from each sample group in every time intervals (See Figure 4.4). There was decrease in the sample thicknesses and other dimensions, and some cracks appear in the samples over the degradation period.

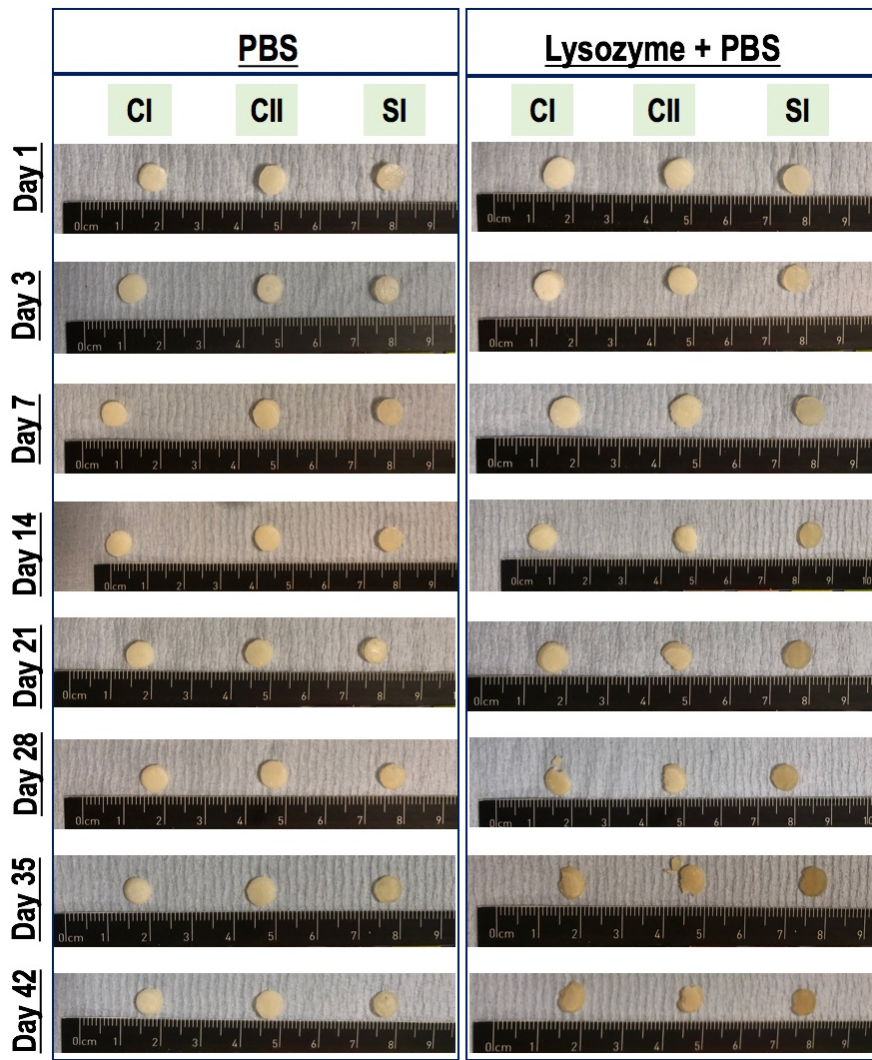


**Figure 4.4** The appearance of modified hydrogels during *in-vitro* degradation tests: the same specimens were photographed in each time intervals up to 42 days which were incubated in PBS and lysozyme (5 mg/mL) media are given in the left and right column, respectively. Test specimens, labelled at the top of the columns belong to CI (CS), CII (CS.0.1HA) and SI (CS.0.1HA.0.005Hep) specimens.

During incubation with lysozyme media, there was darkening in the sample colour from beige to brown. The breakdown of some samples into small pieces were seen. In one sample of sole CS in lysozyme, the media became a dark brown hard film having only the polymer skeleton after 42 days. (See Figure 4.5). In addition, a sample incubated in PBS became very fragile and totally broke down into small pieces when it was taken out the media at day-42.

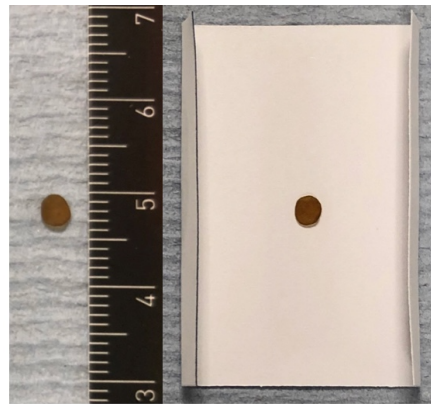


**Figure 4. 5** The appearance of a modified hydrogel, CI (CS) becoming a hard, brown thin film after 42 days of incubation in Lysozyme (5 mg/mL) media in PBS during in-vitro degradation test. (The image of the sample with a ruler on a tissue at left and on a white paper at right).

#### 4.8.2.2 Morphological Analyses by SEM

The morphological degradation of hydrogels was investigated by SEM analyses of freeze-dried hydrogels taken at 14-, 28- and 42- days of incubation in both PBS and lysozyme sample groups. The microstructure images of the samples were also compared with prepared hydrogels before incubation in any media, after freeze drying. These were nominated as Day-0 samples. Figure 4.6 shows the comparison of microstructural images of the sole CS hydrogel (CI) specimen PBS and lysozyme media groups, at different time intervals, taken from top, bottom and cross-section. As can be seen in the images, the hydrogel specimens possessed cracks after 14-days of incubation in both PBS or Lysozyme media. Progressive degradation was seen in the samples having large cracks with deterioration and final break down of the bulk of the hydrogels at day-42 (Figure 4.6.j-l). Hydrogels initially having a flat surface were broken and degraded, leading to an appearance of porous microstructure in the bulk (See Figure 4.6.l).

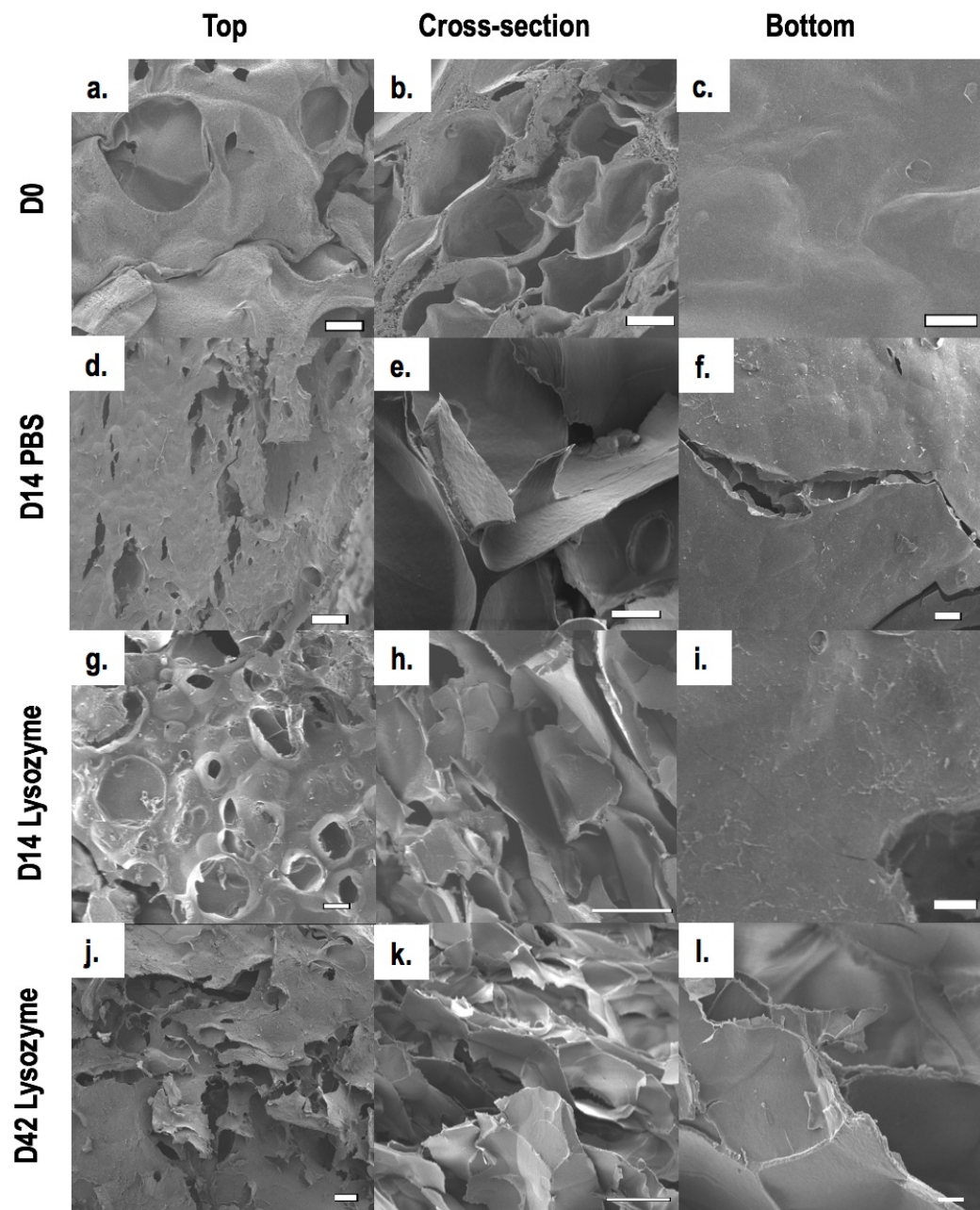


**Figure 4.6** The SEM micrographs of modified hydrogel CI (CS) during degradation in PBS and Lysozyme (5mg/mL Lysozyme in PBS) media. The images at the three columns from left to right show top, cross-section and bottom sites while the vertical labels given at left represent the following: D0: hydrogels before incubation in media (a-c); D14 PBS : after 14 day incubation in PBS (d-f); D14 Lysozyme: after 14 day incubation in Lysozyme (g-i), D42 Lysozyme: after 42 day incubation in Lysozyme media (j-l). (The scale bars at the images are respectively (a-d, f-g and i-j). 100  $\mu$ m, (e and l). 10  $\mu$ m, and (h and k). 100  $\mu$ m.)

The SEM images of composite the modified hydrogel, SI (CS.0.1HA.0.005Hep) specimen during different time points of the degradation tests in PBS and lysozyme media are given at different positions in Figure 4.7. It has been seen that surface cracks appeared in 14-day specimens, whereas the signs of breakdown in the bulk of the

hydrogels can easily be noticed in Day-28 samples that belong to PBS test group (Figure 4.7.d-e). A large crack in the cross-section region (Figure 4.7.h) and degradation at the bottom surface in a high magnification image (Figure 4.7.i), were clearly seen.

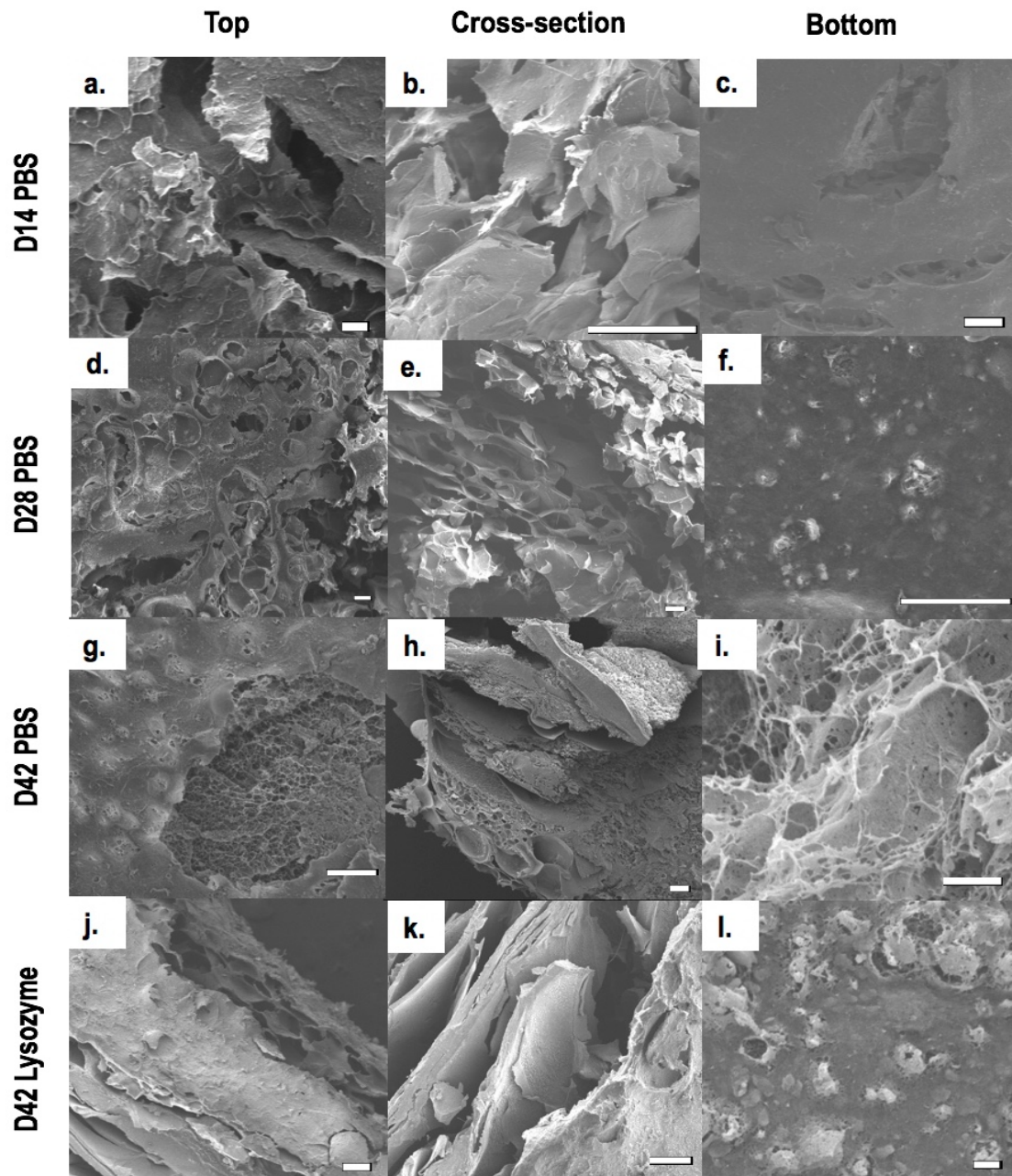


**Figure 4. 7** The SEM micrographs of modified composite hydrogel SI (CS.0.1HA.0.005Hep) during degradation in both PBS and Lysozyme (5mg/mL Lysozyme in PBS) media. The images in the three columns from left to right show top, cross-section and bottom sites while the vertical labels given at left represent the following: D14 PBS : 14-days of degradation sample in PBS (a-c); D28 PBS : 28-days of degradation sample in PBS (d-f); D42 PBS: 42-days of degradation sample in PBS (g-i), D42 Lysozyme: 42-days of degradation sample in Lysozyme media (j-l). (The scale bars at the images are respectively (a and f-g). 10  $\mu$ m, (b-e, h and j-k). 100  $\mu$ m, (i and l). 1  $\mu$ m.)

The day-42 degradation sample in lysozyme media show a large cavity in the middle of the top surface progressing towards the bulk of the specimen (Figure 4.7.j), big cracked regions at the cross-section (Figure 4.7.k), and deterioration at the bottom surface (Figure 4.7.l).

The appearance of HA crystals in composite CII (CS.0.1HA) and SI (CS.0.1HA.0.005Hep) hydrogels during degradation tests are shown in Figure 4.8. As can be seen in the images, needle-like spherical crystals forming flower shapes are dispersed over the polymer matrix (Figure 4.8.a). In the SI (CS.0.1HA.0.005Hep) composite sample, the effect of the Hep coating on the surface was to slightly smoothen the crystal surfaces as has been mentioned in the previous chapter (Figure 4.8.b).

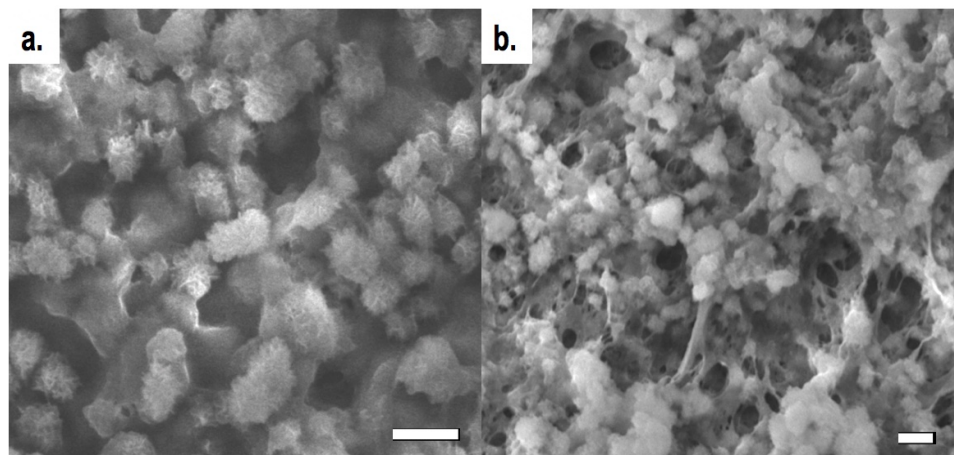


**Figure 4.8** The HA crystals present in SEM micrographs of modified composite hydrogels during degradation tests in PBS **a.** CII (CS.0.1HA) after 14 days of incubation (10  $\mu\text{m}$  scale bar); and **b.** SI (CS.0.1HA.0.005Hep) after 28 days of incubation (1  $\mu\text{m}$  scale bar).

#### 4.8.2.3 Chemical Analyses by ATR

The chemical changes in hydrogels during incubation in PBS and lysozyme (5mg/mL in PBS) were analysed at different time intervals of the in-vitro degradation tests, including Day-0 (hydrogels prior to incubation in any media), Day 14, Day 28 and Day 42, from both top and bottom surfaces. The spectral graphs obtained from top surfaces of PBS and lysozyme specimens are presented, for each sample group: CI (CS), CII (CS.0.1HA), and SI (CS.0.1HA.0.005Hep), in Figure 4.9, Figure 4.10, and Figure 4.11, respectively. Gradual decreases were seen at most peak intensities of the chemical groups during the degradation periods of all samples. The biggest change was observed

at the peak region belonging to O-H and N-H groups locating between 3200-3500  $\text{cm}^{-1}$ , and C-H stretching bonds between 2800-3000  $\text{cm}^{-1}$  (Shahzad et al., 2015).

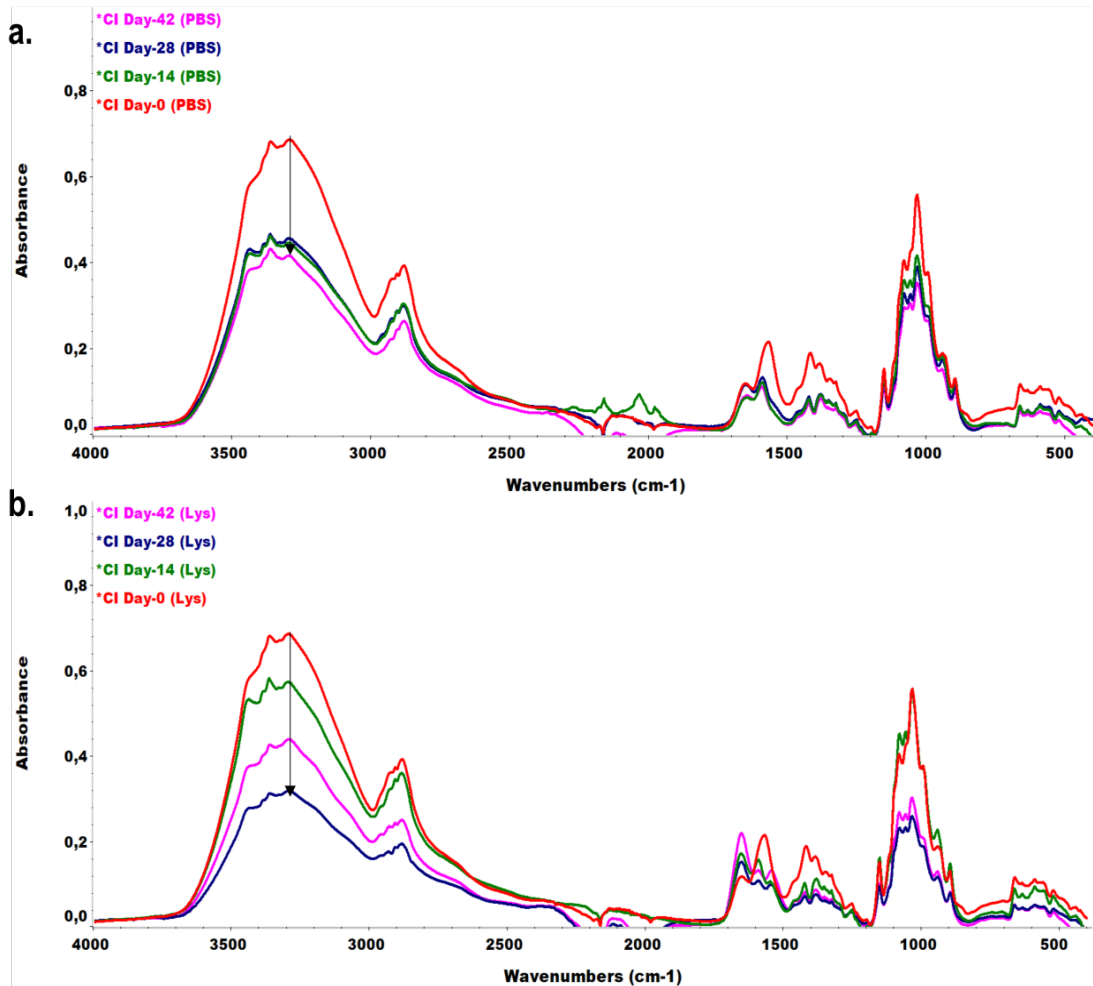


**Figure 4.9** The comparative ATR spectra of degradation samples, CI (CS) modified hydrogels at different time intervals over 42 days of incubation in **a.** PBS and **b.** Lysozyme in PBS solution (5mg/mL).

In addition, the peaks at 1078  $\text{cm}^{-1}$  corresponds to cyclic C-O stretching vibrations (Rokhade et al., 2007), and the peaks at 993  $\text{cm}^{-1}$  and 1031  $\text{cm}^{-1}$  are due to  $\nu_5$  C-OH stretching and  $\nu_4$  COH bending frequencies, respectively (Swayze & Clark, 1990). The samples in lysozyme display much less intensity at day-21 and at day-42 in comparison to the Day-0 counterpart specimen. Furthermore, the decrease in the intensities of peaks at 1151  $\text{cm}^{-1}$  and 895  $\text{cm}^{-1}$ , which were assigned to C-O stretching and CS ring stretching vibrations, also indicated degradation (Yar et al., 2017).

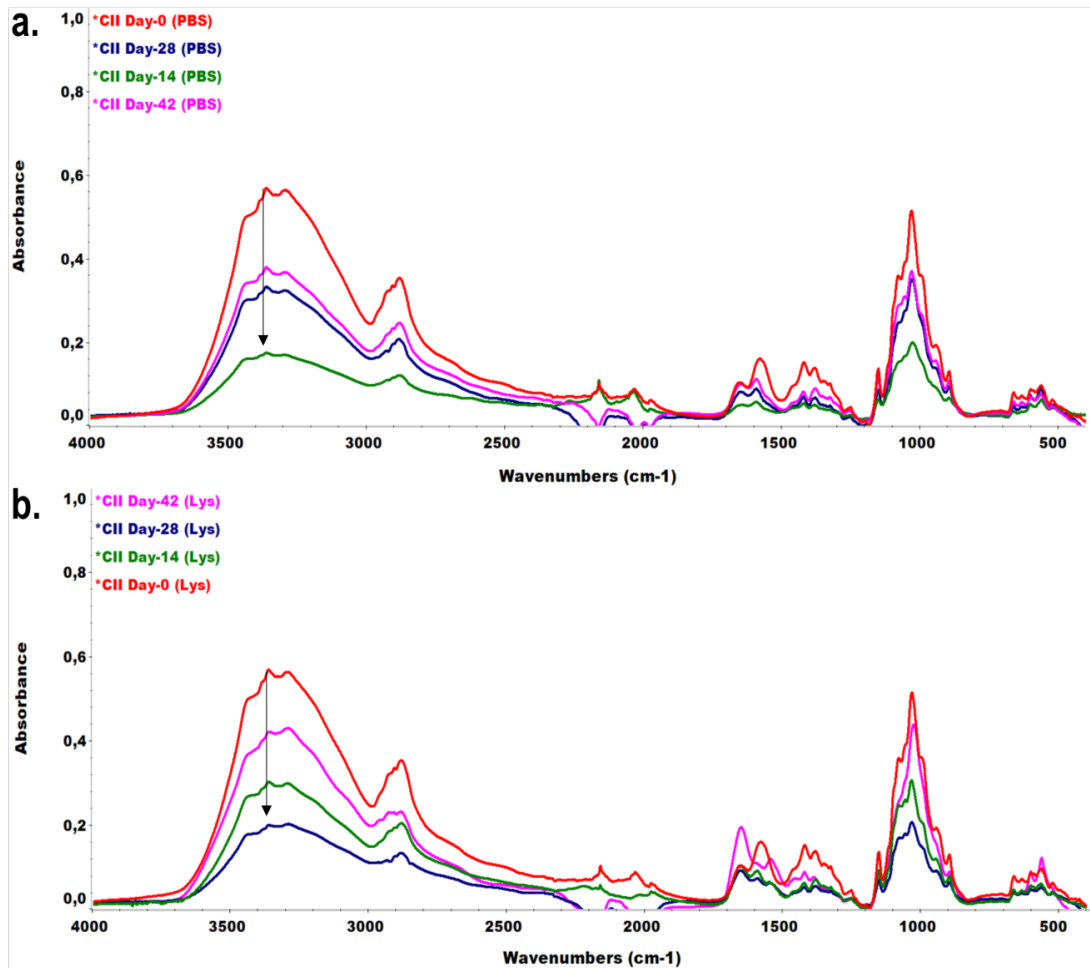


**Figure 4.10** The comparative ATR spectra of degradation samples, CII (CS.0.1HA) modified hydrogels at different time intervals over 42 days of incubation in **a.** PBS and **b.** Lysozyme solution in PBS (5mg/mL).

The single peak at  $1567\text{ cm}^{-1}$ , due to N-H bending linkages (Shahzad et al., 2015) in PBS samples, was split into two peaks in lysozyme specimens, at around  $1553\text{ cm}^{-1}$  and  $1618\text{ cm}^{-1}$  and are attributed to asymmetric stretching of  $\text{COO}^-$ . In addition, the presence of lysozyme caused an increase of the amide-I bond at  $1649\text{ cm}^{-1}$  confirming the chemical interaction of lysozyme with CS (Mizuguchi et al., 1997) which did not occur in the PBS specimen spectrums. Moreover, the intensity of peaks at  $1416\text{ cm}^{-1}$  and  $1383\text{ cm}^{-1}$  resulting from  $\text{CH}_2$  bending vibrations (Shahzad et al., 2015) showed an explicit decrease in all samples.

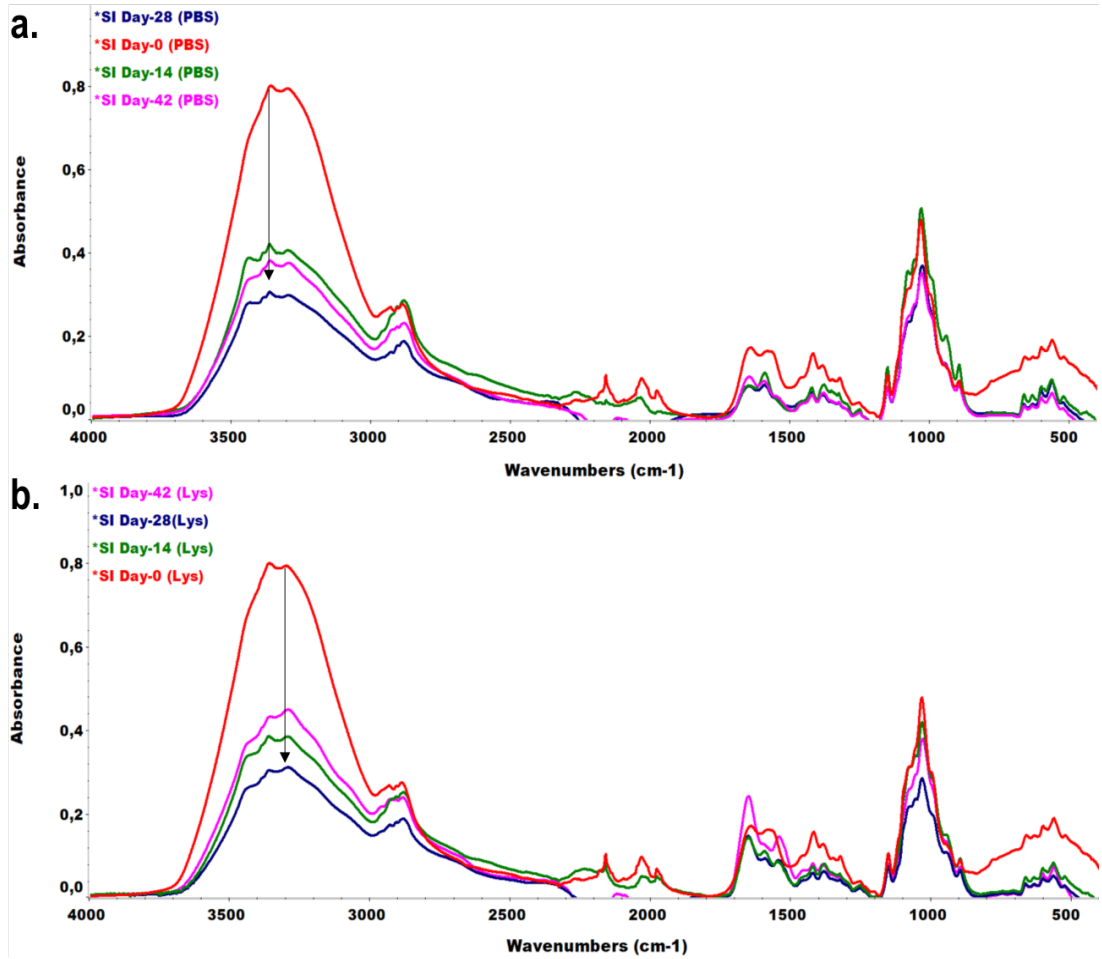


**Figure 4.11** The comparative ATR spectra of degradation samples, SI (CS.0.1HA.0.005Hep) modified hydrogels in different time intervals over 42 days of incubation in **a.** PBS and **b.** Lysozyme solution in PBS (5mg/mL).

#### 4.8.3 Bioactivity Analyses by SBF

##### 4.8.3.1 Weight and pH Tests

The bioactivity of the hydrogels in terms of carbonated apatite mineral deposition on their surface during incubation in SBF were measured by comparing by their % dry weight ratio determined at different time intervals up to 21 days. At day 7, the CII (CS.0.1HA) samples showed a significantly higher percentage of dry weight ratio than the CI (CS) sample ( $p: 0.0091$ ) which was associated with the additive effect of HA on mineralisation. However, no-significant difference was observed between CII (CS.0.1HA) and SI (CS.0.1HA.0.005Hep) specimens ( $p: 0.5453$ ) at day-7. During all incubation periods, the CI, sole CS sample showed much less of an increase in its weight, accounting for only 0.7 % from day-7 to day-21. Between the 7 and 14-day

intervals, there was an increase in the dry weight ratio of both CII and SI samples which were 1.4 % and 2.5 %, respectively, whereas the weight change between 14 and 21 days was negligible in both samples. At day-21, there was a significant difference not only between CI and CII, but also CII and SI. The weight ratio of SI was significantly higher than the CII specimen ( $p=0.0183$ ), indicating that the final composite hydrogel possessing Hep also contributed to in-vitro biomineralisation in SBF; which can be associated with the highly anionic nature of Hep attracting ions in SBF promoting apatite formation.

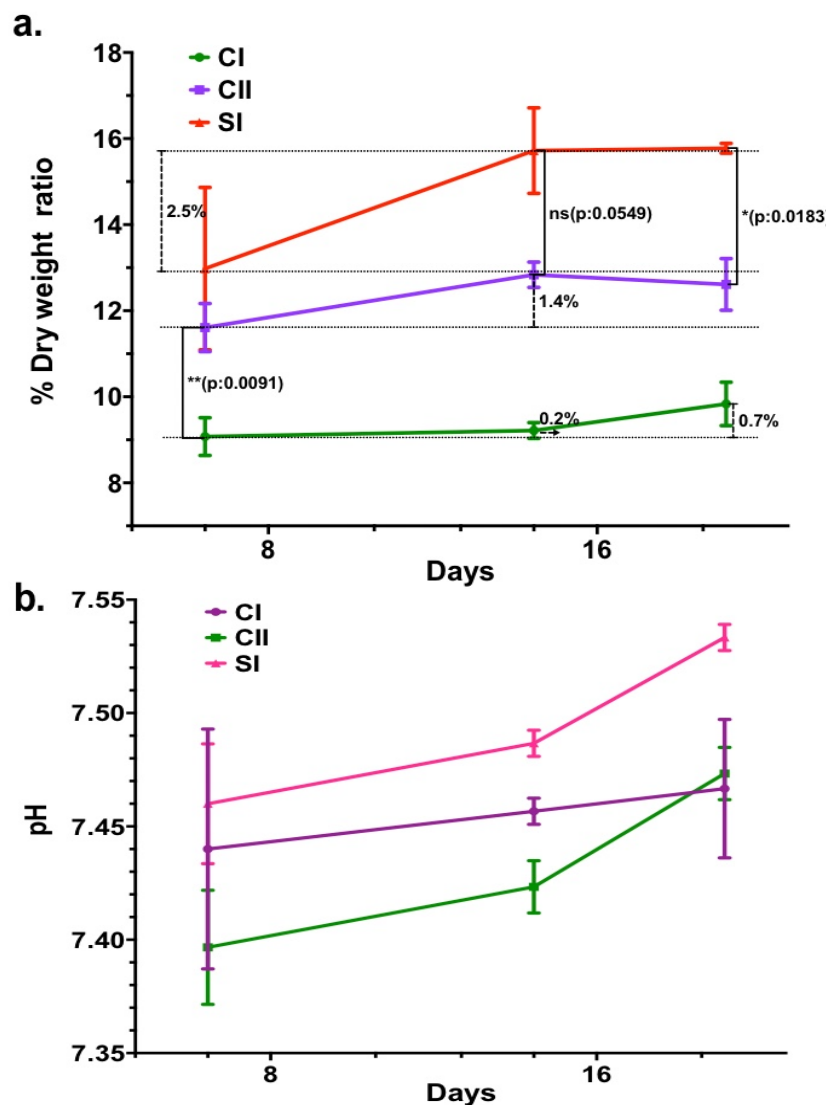


**Figure 4.12** The bioactivity test results performed by incubation of modified hydrogels (CI (CS), CII (CS.0.1HA) and SI (CS.0.1HA.0.005Hep)) in SBF media in different intervals up to 21 days to investigate biomineralization by **a.** the comparison of % of the dry weight ratio of hydrogels and **b.** the pH changes in different time intervals of the bioactivity tests. Results were expressed as a mean  $\pm$  SD ( $N=3$ ). Statistical analyses were performed by 2-way ANOVA; Tukey multiple comparison tests were performed with  $\alpha$ : 0.05. Weight increase percentage values between time intervals for the same sample group were demonstrated with loosely dashed lines, and the statistical difference between samples were shown with solid line with adjusted  $p$  values.

Regarding pH alteration, the highest pH was possessed by SBF supernatant media that belonged to the SI sample, while the CII sample had the second highest pH at most intervals of the bioactivity test. All media specimens showed an increase at the pH up to 21-days. A faster pH increase between time points was observed with a parallel trend for CII and SI composite samples in which the mean pH change was 7.46-7.53 and 7.40-7.47, respectively.

The physical indication of mineralisation on the top surface of hydrogels were observed by taking comparative photographs of each specimen composition from their top and bottom surfaces in their wet and freeze-dried forms. The representative sample photographs are given in Figure 4.13. As can be seen in the images, day-0 hydrogels possess from a beige to cream colour.

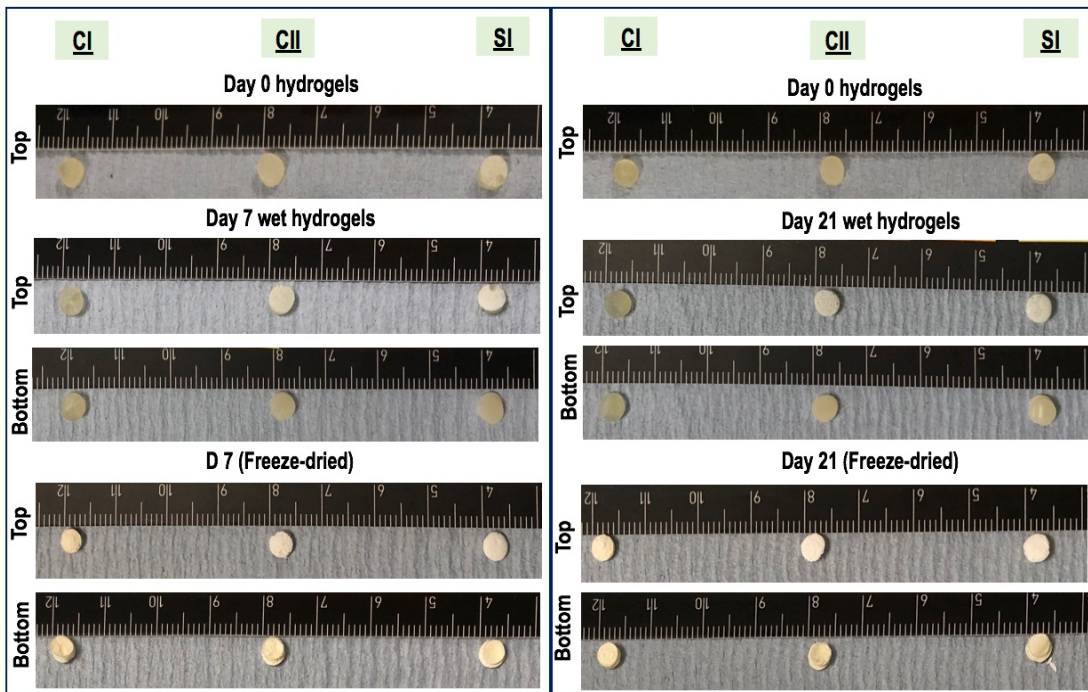


**Figure 4. 13** The physical indication of biominerisation during bioactivity studies of modified hydrogels incubated in SBF media up to 21 days. The images of Day-7 and Day-21 samples are shown at left and right column, respectively. From top to below image labels 'Day-0 hydrogel' indicates the specimens before incubation in SBF, 'Day-7 wet hydrogels' represents the samples incubated 7 days in SBF and imaged after washing, and 'Day-7 (freeze-dried)' demonstrates the samples freeze-dried after washing. The test specimens are labelled on top of the columns belong to CI (CS), CII (CS.0.1HA) and SI (CS.0.1HA.0.005Hep).

After 7 days of incubation in SBF, the composite hydrogels including CII and SI hydrogels had a white layer formation on their top surfaces becoming harder and whiter

upon freeze-drying, while there was not a change in their bottom surfaces. Furthermore, CII and SI samples possessed much whiter and harder mineral layer after 21 days of incubation in SBF. On the other hand, there was not a noticeable colour change of sole CS sample (CI) on its neither top nor bottom surface after incubation in SBF even after 21 days.

#### 4.8.3.2 Morphological Analyses by SEM

The microstructure images of freeze-dried hydrogels taken in different intervals (7, 14 and 21 days) of the bioactivity studies were studied comparatively by SEM. Figure 4.14 shows the SEM images of sole CS (CI) hydrogel after incubation in SBF for 7 and 21 days. There was not any indication of crystalline mineral formation in microstructure images of the CI sample at different orientations after SBF incubation up to 21 days. In terms of morphology, modified CI hydrogel, which was obtained from a solution having pH between 6.2-6.4 showed dense, tiny micropores at its cross-section and an almost flat, top and bottom surface morphology. After 21-days of incubation in SBF media, the little holes formed on the top surface might be associated with some degradation of the sample surface. The honeycomb-like microporosity is seen at the cross-section images of hydrogels in Figures 4.14.(c and f) while big micropores can be seen underneath the top surface of the hydrogels in Figure 4.14.e.

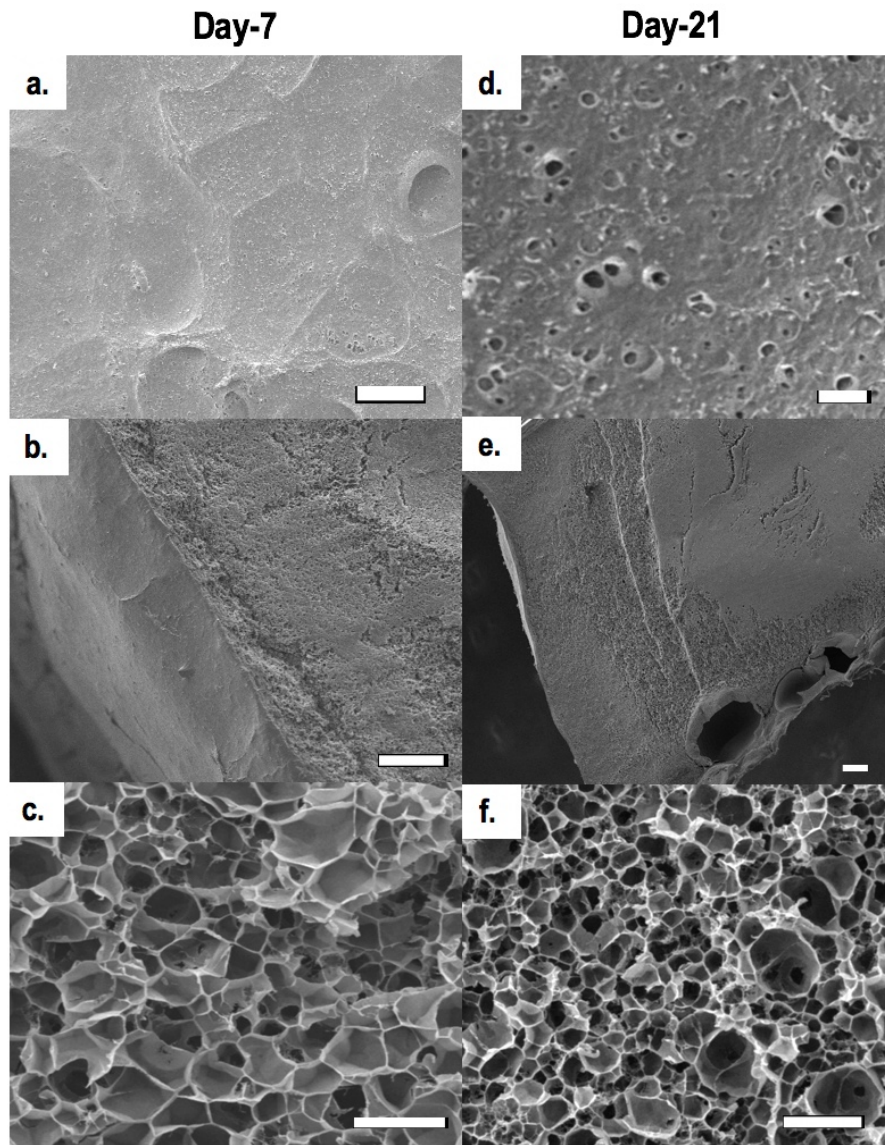


**Figure 4. 14** The SEM micrographs of modified hydrogel CI (CS) during bioactivity studies in SBF. The left and right column belong to the samples exposed to 7-days and 21-days of incubation in SBF media, respectively. The images **a** and **d** belong to top surface of samples while **b, c, e, and f** are cross-section images. (The scale bars at the images are as follows: **(a-b and e)**. 100  $\mu$ m, **(c-d and f)**. 10  $\mu$ m)

CII (CS.0.1HA) involving HA, possessed a rough mineralised layer covering the whole top surface of the specimen analysed after incubation in SBF for 7 up to 21 days (Figure 4.15). Seen explicitly in a high magnification image at Figure 4.15.h, the carbonated apatite crystals possessed single flower like crystals formed with a needle like surface morphology showing the biggest crystal size at around 1  $\mu$ m dispersed throughout top surface of the specimens. This surface topography is indicative of highly bioactive surface features which may provide very efficient bonding with natural bone tissues. Formation of some cracks at the top surface, seen

in 21-day SBF specimens, was attributed to some degradation in the sample.

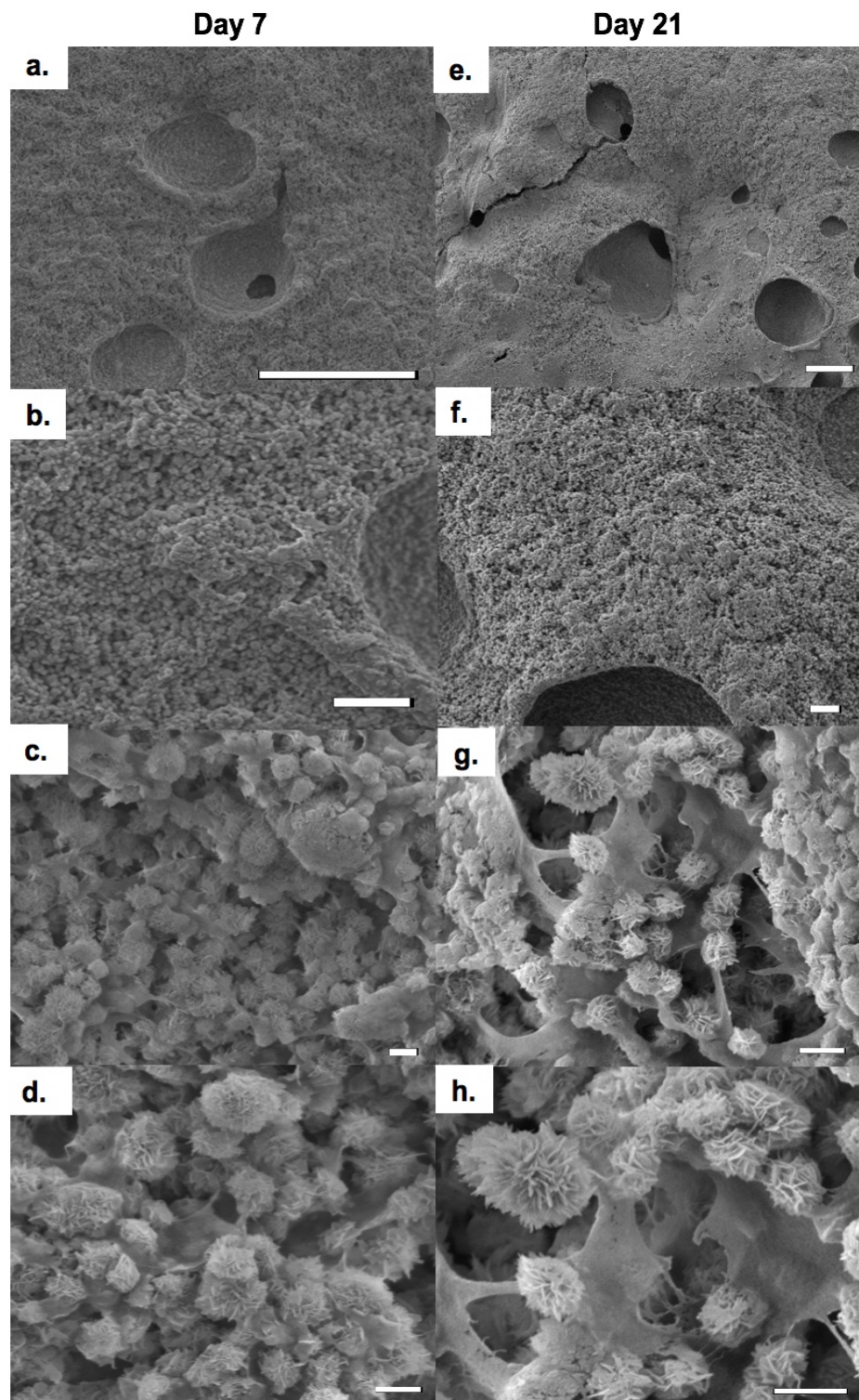


**Figure 4. 15** The SEM micrographs of the top surfaces of modified composite hydrogel CII (CS.0.1HA) samples after incubation in SBF media for 7 days and 21 days at left and right column, respectively. (The scale bars at the images are (a and e). 100  $\mu$ m, (b and f). 10  $\mu$ m, and (c-d. and g-h). 1  $\mu$ m)

The morphology of a composite hydrogel specimen containing also Hep, SI (CS.0.1HA.0.005Hep) after 7 and 14 days of incubation in SBF are shown comparatively in Figure 4.16. The flat top surface with some bubble holes (Figure 4.16.a) and smooth bottom surface (not shown), and small micropores in the cross-section images (Figure 4.16.f) with less and more dense layered areas (Figure 4.16.i-l) and some big pores at certain locations (Figure 4.16.e) were observed.

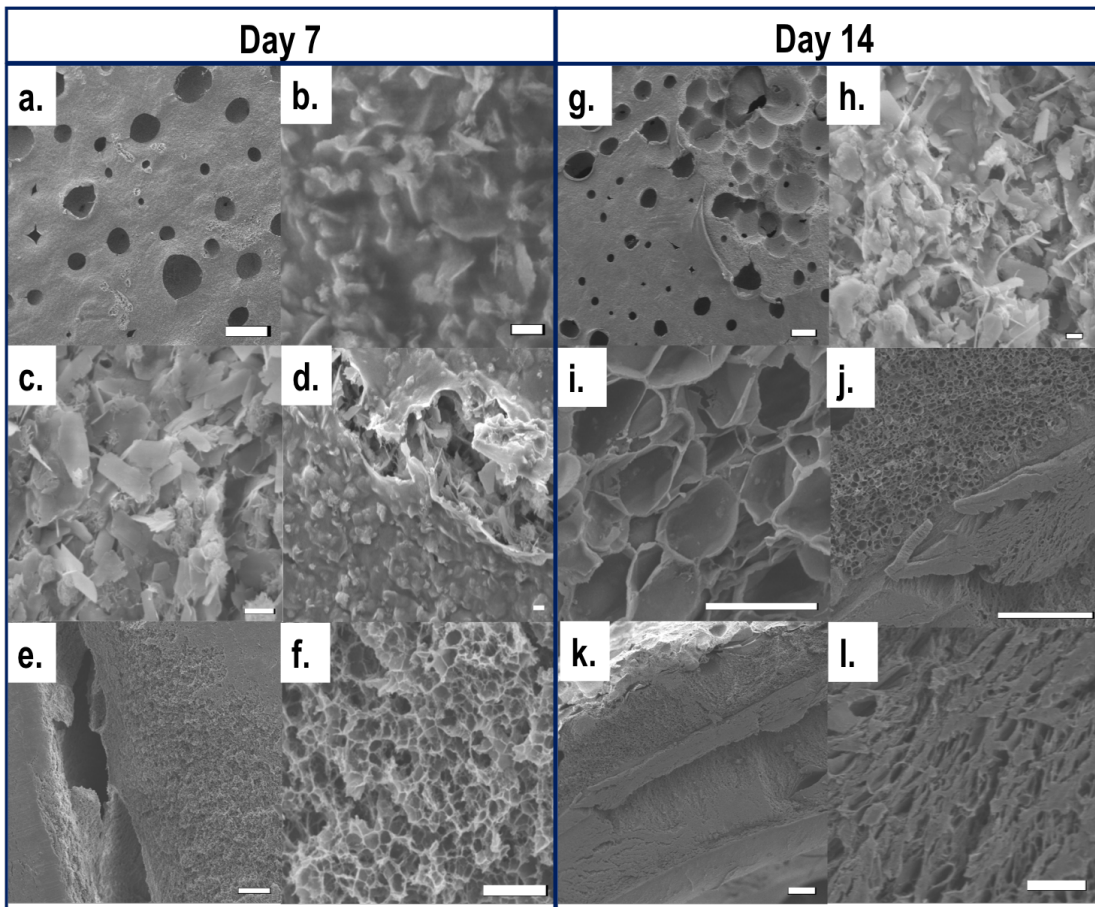


**Figure 4. 16** SEM micrographs of a modified composite hydrogel SI (CS.0.1HA.0.005Hep) in SBF. Starting at left, the first and second column pairs belong to the sample after 7 and 14 days incubation in SBF media, respectively. The images a-d and e-f are top and cross-section images, respectively for 7-day samples while g-h and i-l images are top and cross-section images, respectively for 14-day samples. (The scale bars at the images are as following: (a, e, g and j-k). 100  $\mu$ m, (b-d and h). 1  $\mu$ m, (f, i and l). 10  $\mu$ m)

In terms of crystalline structure, a highly mineralised layer with rough crystals was hidden under the polymer matrix due to the coating effect of Hep on the top surface. This is explicit in Figure 4.16.b. This crystalline morphology is uncovered by observing the sample regions possessing some cracks in the top surface, as seen in Figure 4.16.d and in its magnified image in Figure 4.16.c. Similarly, seen in Figure 4.16.g, there is a

rolled polymer layer on the top surface of the specimen and on the uncovered area possessing a lighter colour. When this region is magnified in Figure 4.16.h, spherical apatite crystals accompanied by flake like morphology are seen.

#### 4.8.3.3 Elemental Analyses by EDS

The *in-vitro* biomineralization in the hydrogel samples was also assessed by performing elemental analyses via EDS following SEM imaging. The EDS analyses of the hydrogel specimens from each group were analysed at different time intervals. The compositional analyses for freeze-dried CI, CII and SI hydrogels obtained after 7 days of incubation in SBF are given in Figure-4.17, Figure-4.18, and Figure-4.19, respectively.

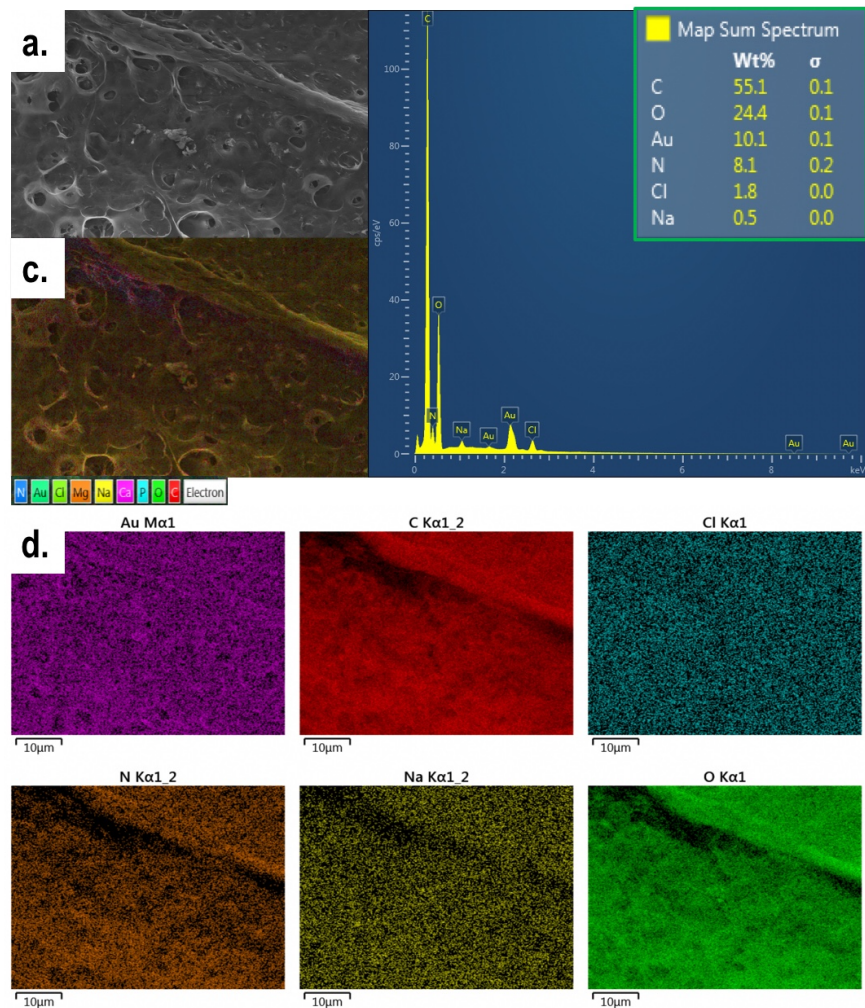


**Figure 4.17** The EDS analyses determining elemental composition of modified hydrogel CI (CS) after 7 days incubation in SBF media and freeze-drying **a.** SEM micrographs from top surfaces of the specimen **b.** elemental composition, **c.** the colour mapping of elements distributed on the sample and **d.** colour distribution density for each individual element on the specimen region.

For CI (CS) as can be seen in Figure 4.17, calcium and phosphorous were not detected as solely polymer matrix components such as, C, O, N, and Na. In addition, Au is found due to coating and Cl, present in trace amounts, might be due to an impurity in the reagents. On the other hand, the elemental composition of CII (CS.0.1HA) is indicated by the high intensity peaks of Ca, P and O, elements which comprise calcium phosphate-apatite mineral deposits (Figure 4.18).

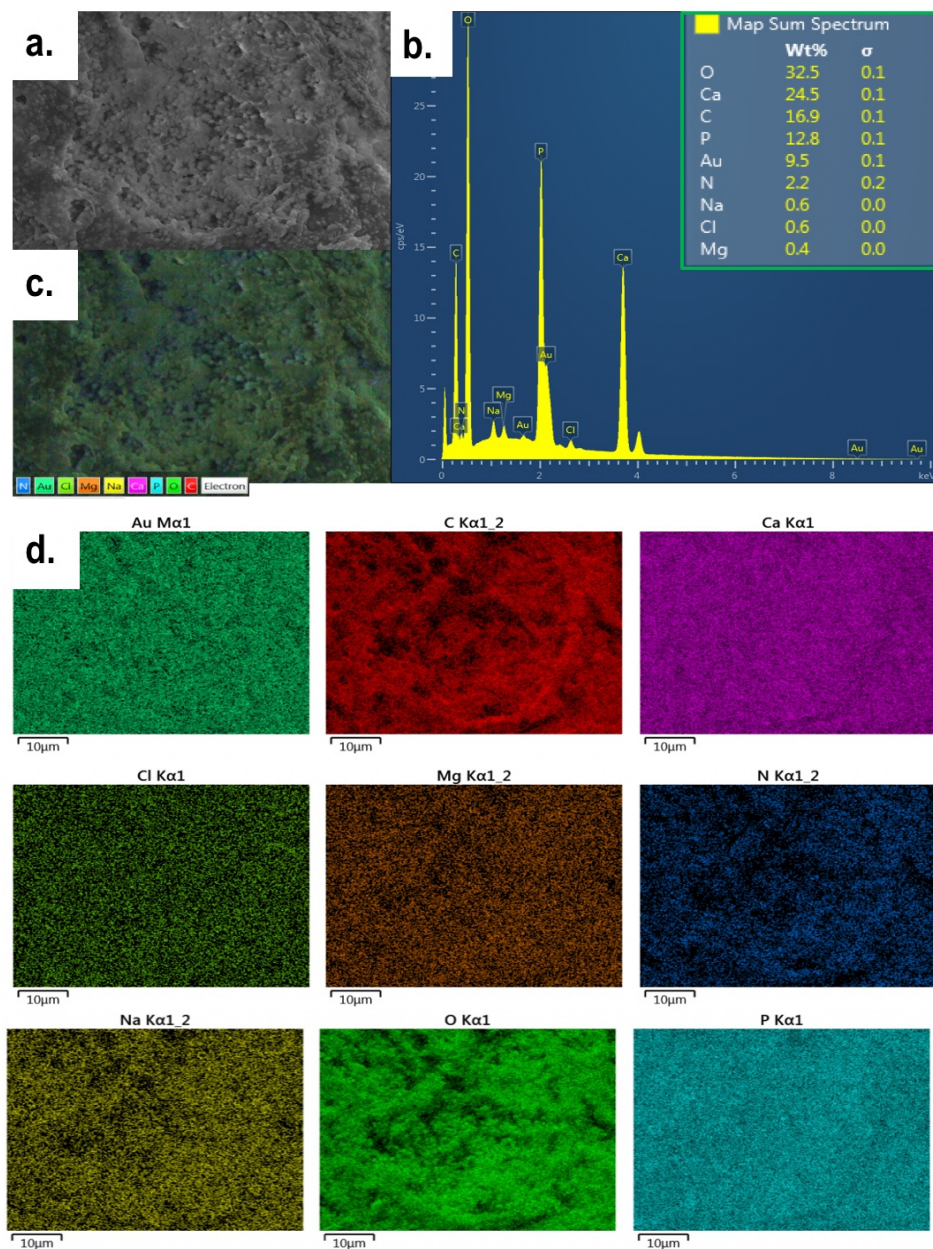


**Figure 4. 18** The EDS analyses determining elemental composition of modified composite hydrogel CII (CS.0.1HA) after 7 days incubation in SBF media and freeze-drying **a.** SEM micrographs from top surfaces of the specimen **b.** elemental composition, **c.** the colour mapping of elements distributed on sample and **d.** colour distribution density for each individual element on specimen region.

In the CII sample, the Ca/P ratio was 1.9, which is slightly higher than that of stoichiometric HA (1.67). This high ratio could be related to phosphate deficient HA due to CO<sub>3</sub>-2 B-type substitution with the PO<sub>4</sub>-3 site of HA, as is reported in the literature (Landi et al., 2003). The carbonate source might have been contributed by both NaHCO<sub>3</sub>, used for neutralising the hydrogels, and the non-sintered HA involved in the synthesis, having little carbonate substitution. B-type CO<sub>3</sub>-2 is favourable to reducing stability of HA by enhancing its bioresorption that increases the bioactivity and efficiency of HA.

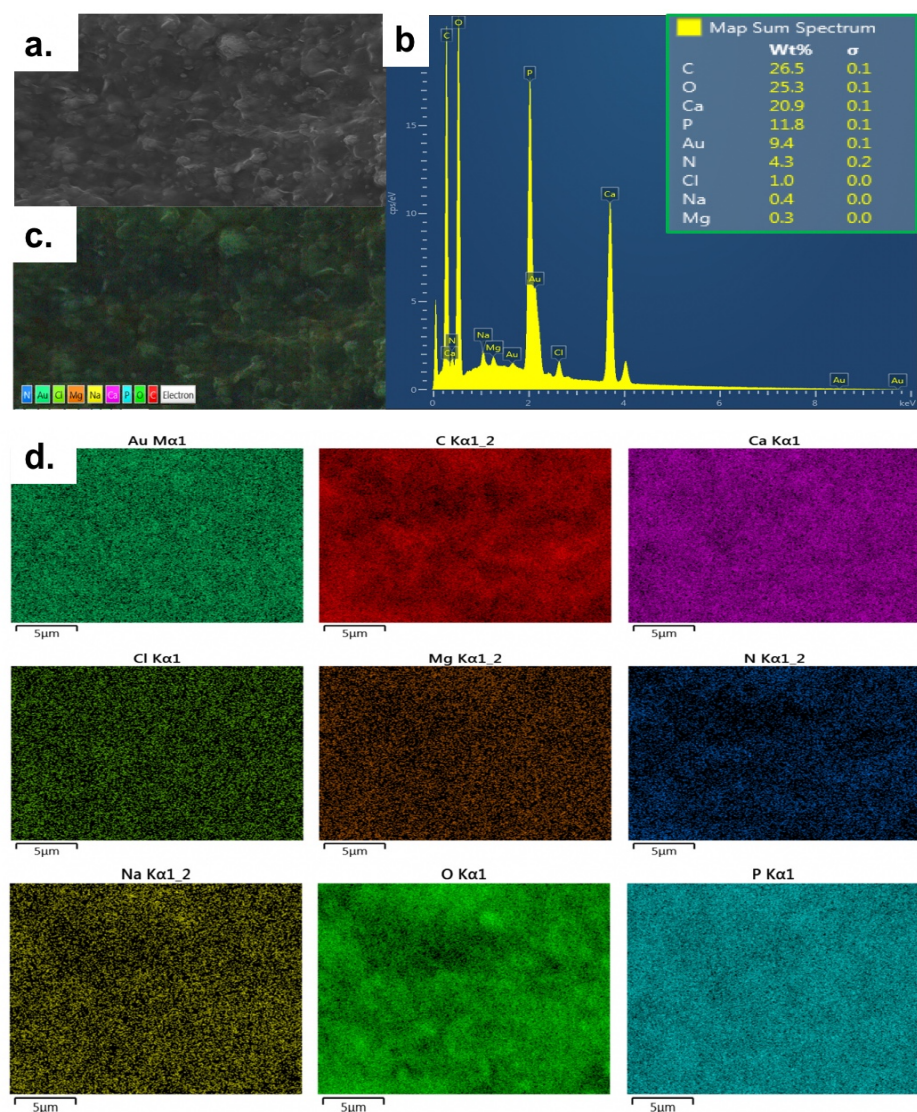


**Figure 4.19** The EDS analyses determining elemental composition of modified composite hydrogel SI (CS.0.1HA.0.005Hep) after 7 days incubation in SBF media and freeze-drying **a.** SEM micrographs from top surfaces of the specimen **b.** elemental composition, **c.** the colour mapping of elements distributed on sample and **d.** colour distribution density for each individual element on specimen region.

In addition, in the hydrogel composition with Hep (SI: CS.0.1HA.0.005Hep), the EDS analyses also showed the presence of Calcium phosphate at high intensity with a Ca/P ratio of 1.77. This could also be evidence for B-type carbonate substitution in HA.

#### 4.8.3.4 Chemical Functional Group Analyses by ATR

The freeze-dried modified hydrogel specimens before incubation in SBF (Day 0) and after immersion in SBF at different intervals of 7, 14 and 21 days were chemically analysed by FTIR-ATR spectroscopy.

The comparative spectra of the CI (CS) sample without HA is given in Figure 4.20. The CI sample spectra possessed higher intensities in O-H and N-H bonds between 3000-3500 cm<sup>-1</sup> and in C-H groups (2800-3000 cm<sup>-1</sup>). In the amide bond region, detected peaks were for: amide-I or C=O bond at 1649 cm<sup>-1</sup>, amide-II or N-H deformation at 1567 cm<sup>-1</sup>, and amide III vibrations at 1324 cm<sup>-1</sup>. The peaks at 1416 cm<sup>-1</sup> and 1383 cm<sup>-1</sup> are attributed to CH<sub>2</sub> bending (Shahzad et al., 2015; Yar et al., 2017).

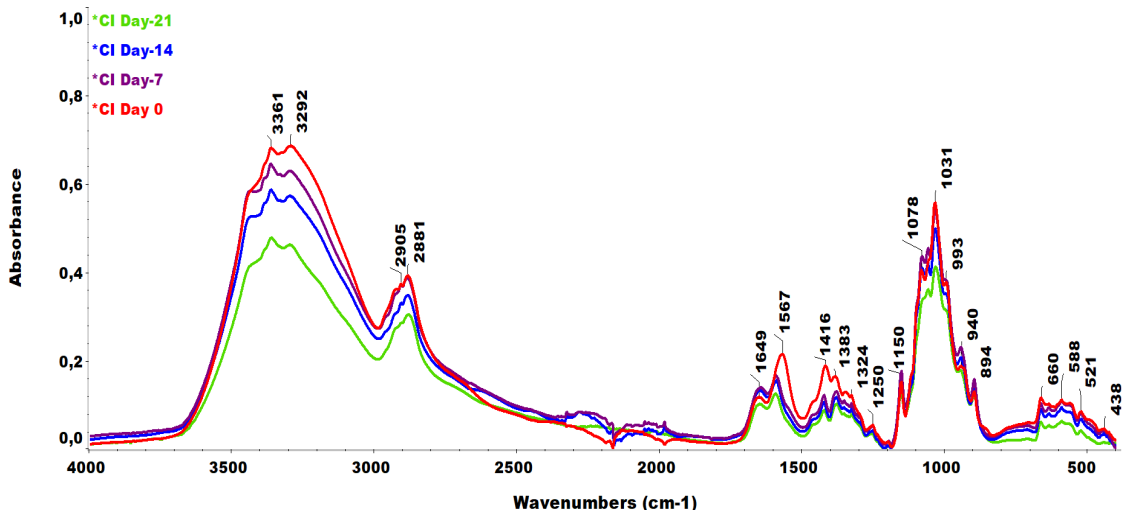


**Figure 4. 20** The comparative ATR spectra of bioactivity test specimens of modified CI (CS) hydrogels (top surfaces) in different experiment intervals up to 21 days.

The C-N stretching bond was detected at 1250 cm<sup>-1</sup> while the peak at 1150 cm<sup>-1</sup> is attributed to C-O stretching vibrations (Yar et al., 2017). The peaks at 1078 cm<sup>-1</sup> and 1031 cm<sup>-1</sup> are due to C-O ring stretching frequencies (Moreira et al., 2016; Rokhade et al., 2007). The shoulder peak manifested at 894 cm<sup>-1</sup> is attributed to C-O-C stretching in saccharide rings of CS (Deng et al., 2017; Yar et al., 2017). However, phosphate bonds were absent in the CI spectra after all incubation durations in SBF. In addition,

there was a gradual decrease in the peak intensities of most functional groups, especially O-H and N-H bonds, which indicate a gradual degradation of samples over time.

The ATR analyses of all hydrogels before incubation in SBF (Day 0) in Figure 4.21.a, and the comparative spectra of composite samples after 7, 14 and 21-days of incubation in SBF are given in Figure 4.21.b, and Figure 4.21.c. for the CII (CS.0.1HA) and SI (CS.0.1HA.0.005Hep) samples, respectively.

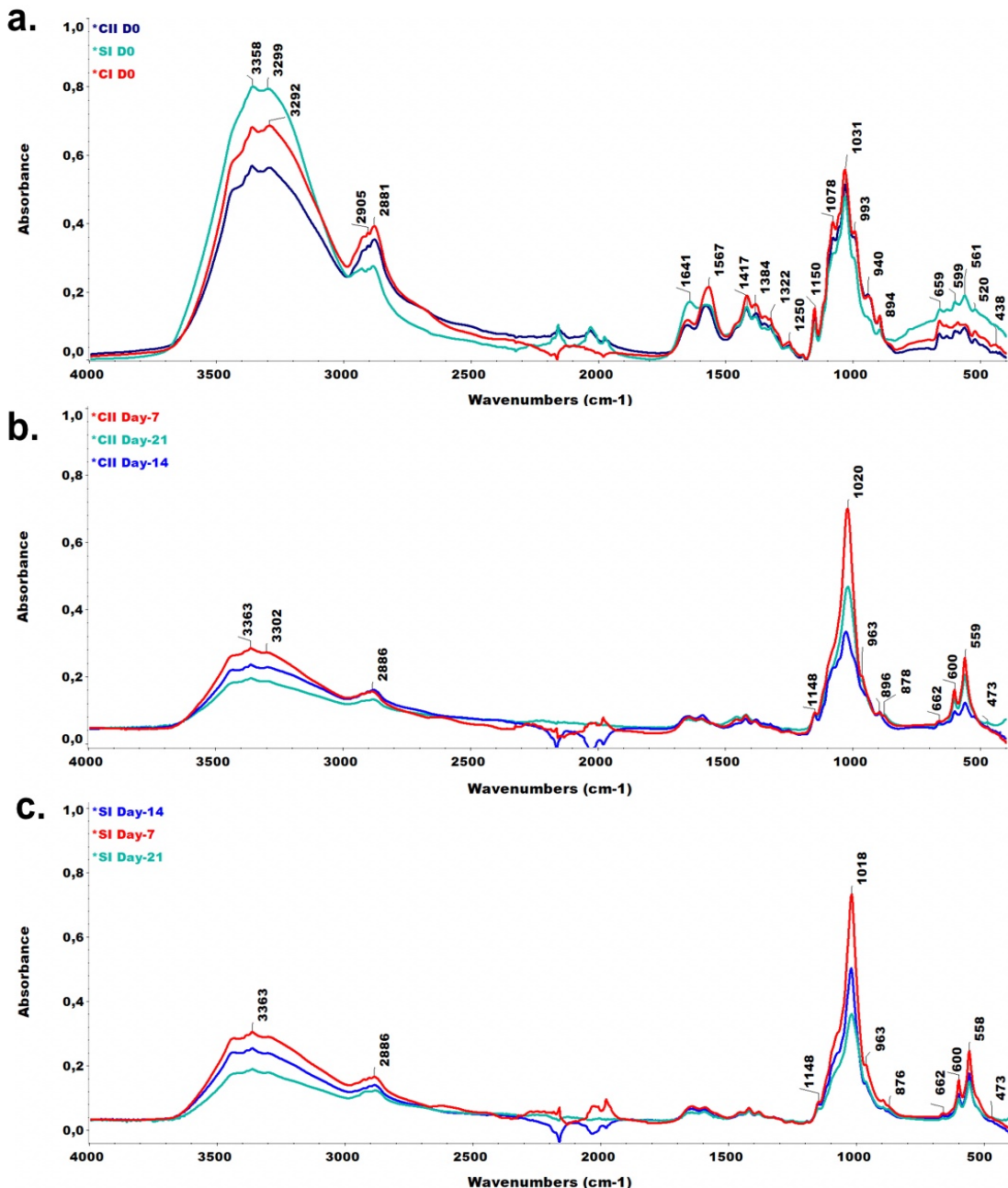


**Figure 4. 21** The comparative ATR spectra of modified hydrogels (top surfaces) **a.** before incubation in SBF (Day-0) including CI(CS), and the comparative spectra of **b.** CII (CS.0.1HA) and **c.** (CS.0.1HA.0.005Hep) after incubation in SBF for different periods (7, 14, and 21-days).

The composite CII (CS.0.1HA) and SI (CS.0.1HA.0.005Hep) hydrogels showed intense crystalline phosphate peaks locating in the region of 450-1100  $\text{cm}^{-1}$  dominating the other frequencies including, O-H/N-H (3000-3500  $\text{cm}^{-1}$ ), C-H (2800-3000  $\text{cm}^{-1}$ ), and amide groups (1200-1700  $\text{cm}^{-1}$ ) starting from Day-7. The sharpest peaks of the spectra were found at 1018-1020  $\text{cm}^{-1}$  due to the  $\nu_3$  asymmetric stretching of vibrations of phosphate bonds. The more Raman active  $\nu_1$  symmetric stretching of  $\text{PO}_4^{3-}$  bonds were detected as a weak shoulder peak at 963  $\text{cm}^{-1}$  or 964  $\text{cm}^{-1}$  at Day-7 and onward. Upon incubation in SBF, the spectra of specimens showed sharp peaks at 559  $\text{cm}^{-1}$  and 601  $\text{cm}^{-1}$ ; elevated due to  $\nu_4$  asymmetric bending of  $\text{PO}_4^{3-}$  vibrations. The weak shoulder peak at 473  $\text{cm}^{-1}$  manifested due to the  $\nu_2$  phosphate bending mode (Antonakos et al., 2007; Rehman & Bonfield, 1997). The peaks raised at 875  $\text{cm}^{-1}$  or 876  $\text{cm}^{-1}$  in CII and at around 878  $\text{cm}^{-1}$  in SI specimens, were attributed to  $\nu_2$   $\text{CO}_3^{2-}$  bonds (Gibson & Bonfield, 2002; Rehman & Bonfield, 1997).

There was a progressive decrease at the peak intensities throughout the spectra from day-7 onwards. This could indicate possible degradation of the hydrogels, and a slight decrease in crystallinity due to the resorption of crystals during incubation. These results, supported also by EDS analyses, provide chemical confirmation of carbonated apatite layer formation on hydrogel surfaces. In addition, the promotion of *in-vitro* bio-mineralisation by the composite hydrogels CII (CS.0.1HA) and SI: (CS.0.1HA.0.005Hep), was confirmed by weight, pH and morphology analyses and could be potential candidates for the promotion of *in-vivo* bioactivity.

#### 4.8.4 Heparin Determination and Drug (Heparin) Release Studies

##### 4.8.4.1 Local Heparin Determination by Toluidine Blue (TB) Assay

Identifying Hep locations inside a hydrogel network was achieved by complexation of Hep with a colorimetric stain, toluidine blue (TB). The purple stained regions on hydrogels after TB staining indicated the presence of Hep. Figure 4.22 gives the comparative photographs of two hydrogel specimens; a control (CII: CS.0.1HA) specimen without Hep and S0: CS.0.1HA.0.0015, a Hep sample comprising the minimum Hep concentration (33  $\mu\text{g}/\text{mL}$ ). The purple colour formed only at the top

surface as a thin layer of the S0 sample whereas bottom surfaces were blue indicating the absence of Hep (Figure 4.22.d). The control samples (CII) possessed blue colour in their all sites (Figure 4.21.b).

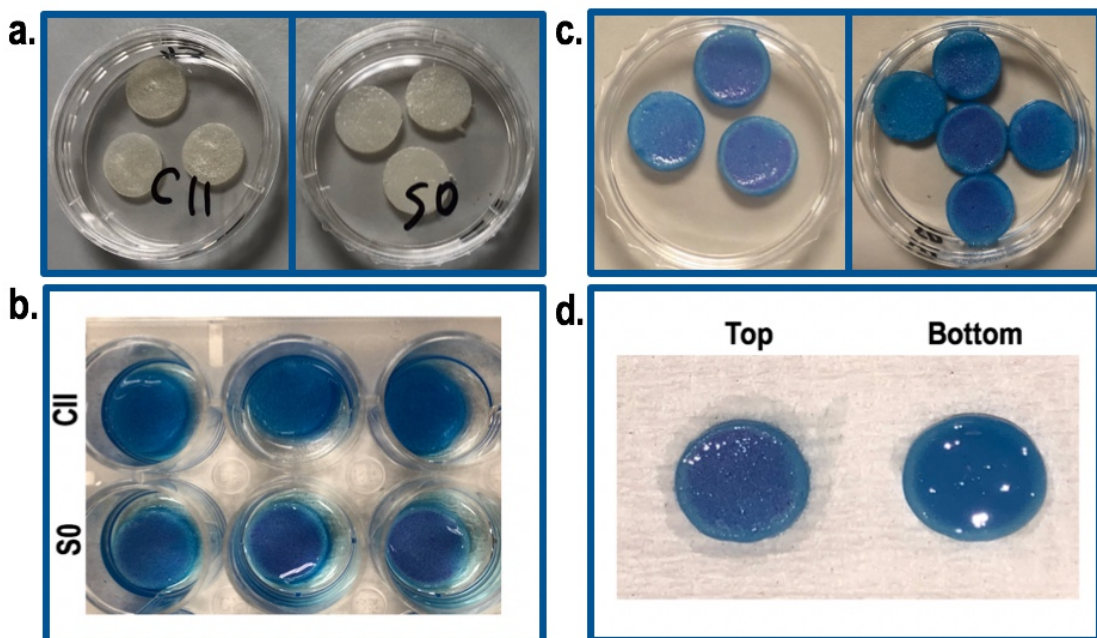


**Figure 4. 22** The photographs of Toluidine Blue (TB) stained hydrogels (30 min) for local determination of Hep via purple colour formation in TB/Hep complexes. The images belong to the composite modified hydrogels having a pH of 6.4-6.5 in solution, including the CII (CS.0.1HA) control sample without Hep and the S0 (CS.0.1HA.0.0015Hep) sample containing the minimum Hep concentration (33  $\mu$ g/mL). CII and S0 hydrogels **a.** before TB staining and **b.** after TB staining, **c.** S0 hydrogel specimens in two different plastic petri dishes from their top surfaces, and **d.** the comparison of top and bottom surfaces of an S0 hydrogel specimen.

Furthermore, local distribution of Hep in hydrogels were imaged under an optical microscope. In Figure 4.23, the optical microscope images of CII: CS.0.1HA and S0: CS.0.1HA.0.0015Hep samples are demonstrated from their top and bottom surfaces comparatively. This method also enabled observation of the microstructure of samples in hydrogel forms. The images, observed from their top surfaces, showed that hydrogels comprise many bubbles in their networks. These bubbles might occur during  $\text{CO}_2$  release during gelation, and due as well to their abundant water content. In bottom surface, the beige coloured particles were attributed to respectively bigger HA particles that formed as sediment due to the effect of gravity.

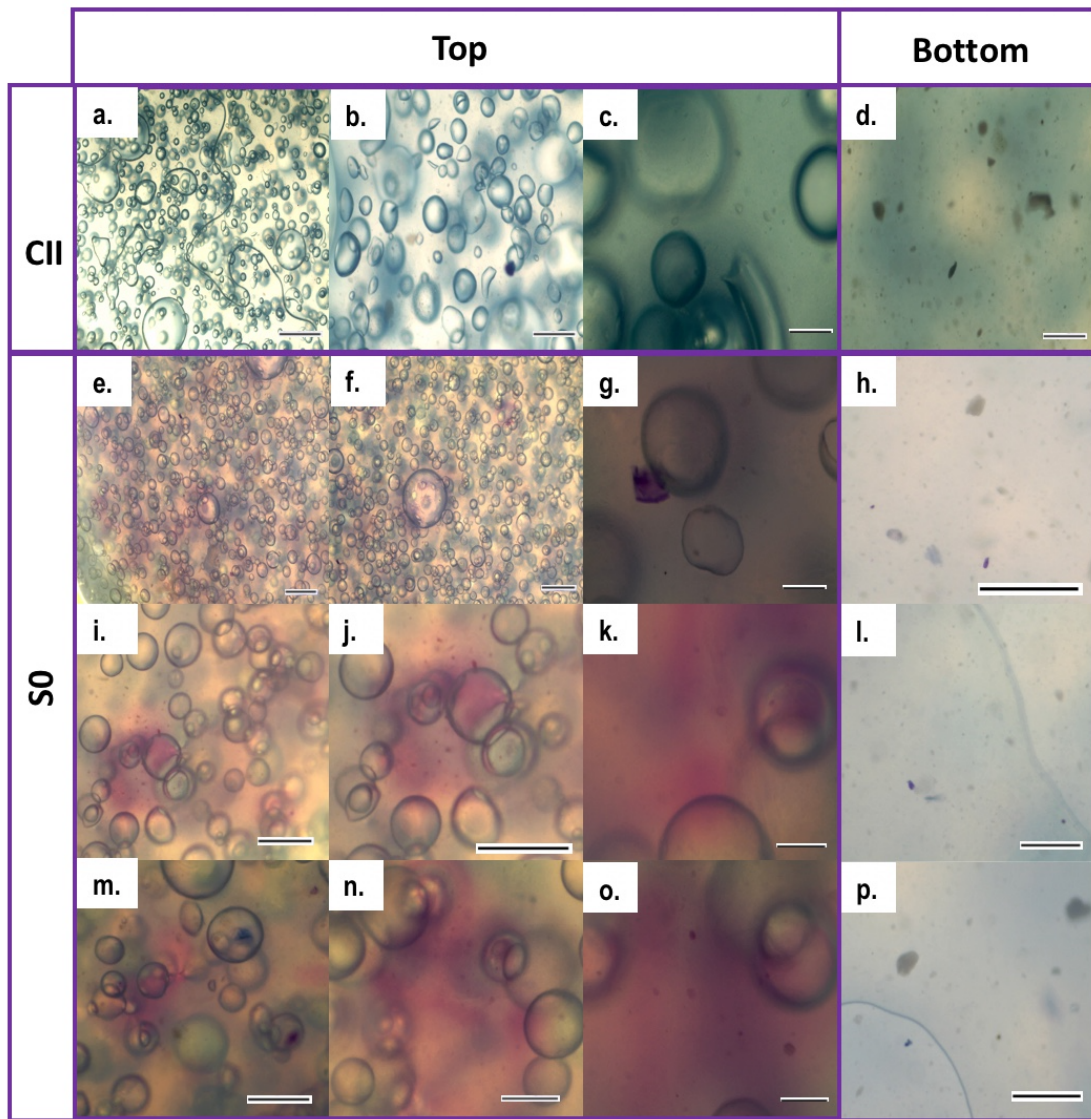


**Figure 4. 23** The optical microscope images of Toluidine Blue (TB) stained hydrogels (30 min) for local determination of Hep, indicating a TB/Hep complex by purple colour: The comparison is of (a-d). CII (CS.0.1HA) control sample without Hep and (e-p). S0 (CS.0.1HA.0.0015Hep) with 33  $\mu$ g/mL Hep. These composite modified hydrogel specimens were prepared with a pH range of 6.2-6.4 in solution. The purple to pink colours indicates Hep locations distributed on the samples. The yellow particles at the bottom surfaces belong to HA particles. (Scale bars correspond to the following: (e-f). 0.4 mm, (c, g, k, o). 0.05 mm, (d, n and p). 0.1 mm and other images (a-b, h-j, l-m). 0.2 mm)

The control hydrogel, CII, possessed more greenish colour and, they did not exhibit purple coloured locations. On the other hand, the S0 specimen with Hep shows a purple colour distributed evenly on its top surface. In higher magnifications, the purple to pink colour becomes more explicit. At the bottom surface of S0 there were a few particles stained in blue or purple colour, but it was negligible in comparison to the top surface. These results have shown that the hydrogels possessed a Hep functionalised top surface

feature. The presence of Hep on the top surface having a coating effect with smoother surface features covering the polymer matrix and HA crystals was confirmed earlier by SEM analyses.

The local presence of Hep was confirmed at higher concentrations in modified hydrogels in the more stable forms produced with a solution pH above 6.4 (6.4-6.5). The images of a TB stained SI hydrogel (CS.0.1HA.0.005Hep) having 120  $\mu\text{g}/\text{mL}$  Hep is shown in Figure 4.24. This sample showed a dense and thick purple complex layer on only the top surface, providing a functionalised surface, while Hep was absent at other locations.

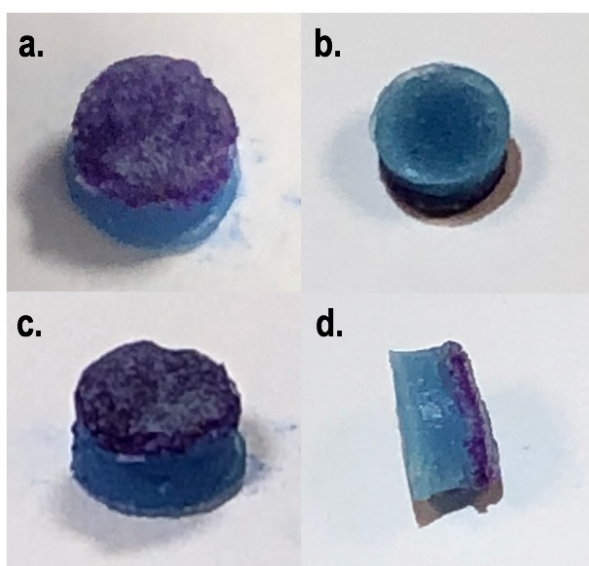


**Figure 4. 24** The photographs of a Toluidine Blue (TB) stained composite modified hydrogel, SI (CS.0.1HA.0.005Hep) with 120  $\mu\text{g}/\text{mL}$  Hep, which was obtained with a pH 6.4-6.5 (stable hydrogel) indicating the presence of Hep with dense purple colour. The appearance of SI sample from different angles given as **a.** top, **b.** bottom, **c.** top to lateral, and **d.** lateral images.

Furthermore, the stability and presence of Hep at initial hydrogel compositions were investigated by TB staining and optical microscope imaging after 2-years of storage in their freeze-dried forms. Figure 4.25 shows the optical microscope images of different initial hydrogel compositions including a control sample CII (CS.0.1HA.), and hydrogels with different concentrations of Hep including SI (120  $\mu\text{g}/\text{mL}$  Hep) SII (360  $\mu\text{g}/\text{mL}$  Hep) and SIII (600  $\mu\text{g}/\text{mL}$  Hep).

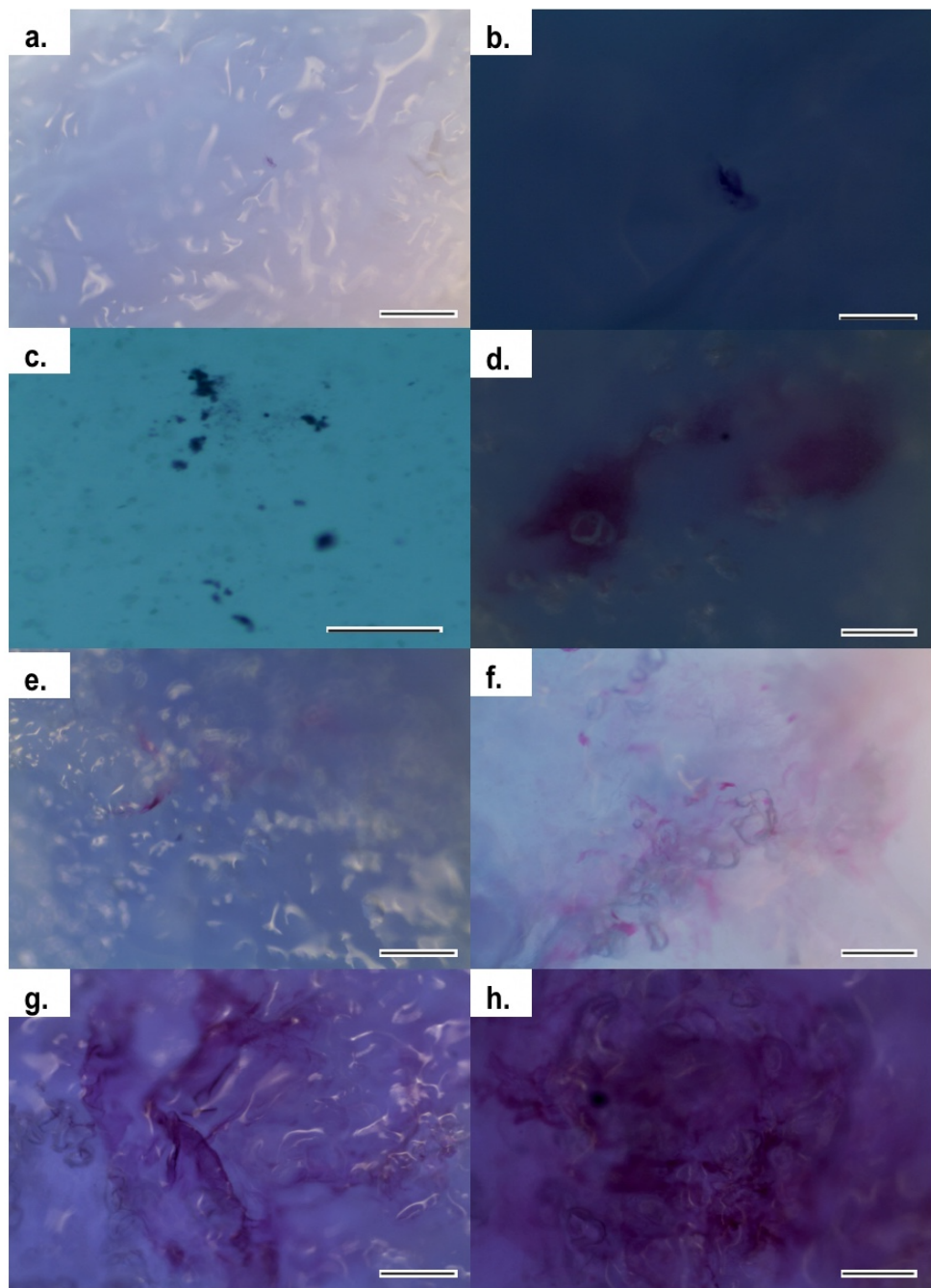


**Figure 4. 25** Toluidine blue stained freeze-dried initial hydrogels to indicate local Hep after 2-years of storage to investigate their stability **a-b.** CII (CS.0.1HA) as control, **c.** SI (CS.0.1HA.0.005Hep)-120 µg/mL Hep **d-f.** SII (CS.0.1HA.0.015Hep)-360 µg/mL Hep and **g-h.** SIII (CS.0.1HA.0.025Hep)-600 µg/mL Hep (Scale bars : **(a and d-h).** 0.2 mm and **(b-c).** 0.05 mm)

The results revealed that the hydrogel compositions having higher Hep concentrations were still well possessed of Hep bound in their hydrogel networks. This is seen by the dark purple colour on the hydrogel surface, particularly in SIII. The SI sample was blue and some dark areas were present but almost no clear purple colour was detected indicating that little or no Hep remained. In the CII control sample, the hydrogel matrix

seemed respectively bright and there was one point that had a purple stained particle. Although this sample does not contain Hep, this staining might result from contamination by contact with other samples comprising Hep. Alternatively, the possible sulphate impurities in chitosan can make a complex with TB, since it has been reported that the presence of sulphuric acid esters in polymers can lead complexation with any metachromatic stain (MacIntosh, 1941).

#### 4.8.4.2 Heparin Release Studies

Drug release studies were performed using the TB assay protocol for the quantitative analyses of Hep released from hydrogels incubated in a media for specific periods. In this study, drug release was performed either by using the release media of hydrogels incubated in de-ionised water (D.H<sub>2</sub>O), or the SBF media supernatants which were allocated while refreshing the solutions at certain time points of the bioactivity tests (7, 14 and 21 days).

Firstly, standard Hep solutions were prepared in D.H<sub>2</sub>O or SBF which were in the range of Hep concentration in the samples. By considering the lower concentrations in modified hydrogels including the maximum Hep concentration, 120 µg/mL of Hep in the SI sample and the minimum 33 µg/mL of Hep in the S0 sample. Standard solutions were prepared in the following concentrations: 0, 20, 40, 60, 80, 100, 120, and 140 µg/mL of Hep.

As described earlier, to make complex solutions 1.5 mL of TB solution was mixed with 1 mL of standard solution in a plastic vial, and let stand. 30 min. Then, 1.5 mL of hexane was added forming a complex purple coloured layer at the top. The TB/Hep/hexane (1.5/1/1.5) complex was obtained upon vigorous shaking while the non-reacted aqueous TB solution was acquired from underneath the jelly complex. The absorbance of aliquots non-complexed solutions were measured at 630 nm wavelength in a microplate reader. The purple TB/Hep complex solutions and noncomplexed solutions in blue tones illustrated in Figure 4.26.

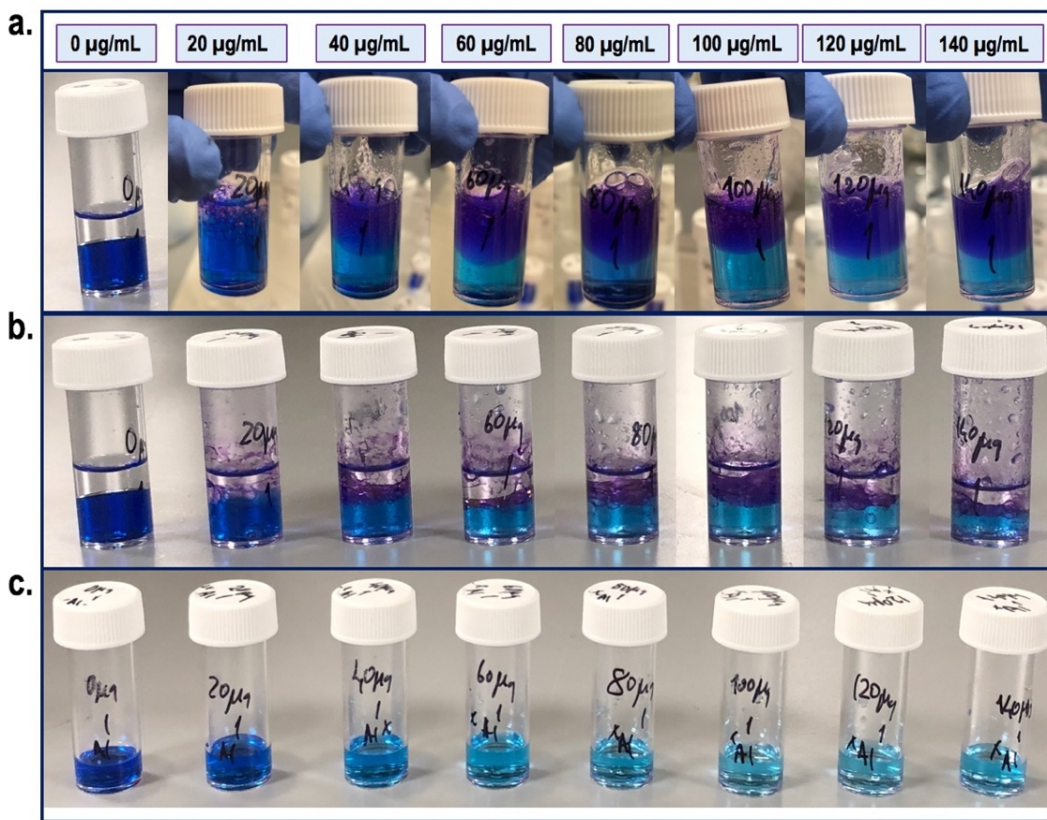


**Figure 4.26** Heparin (Hep) standard solutions prepared in gradually increasing concentrations from 0 to 140 µL in vials and made complex with toluidine blue (TB) by using hexane (Hex) while the ratio of TB: Hep: Hex was 1.5:1:1.5 **a.** the TB/Hep complex formed after vigorous shaken on the top of the tubes on purple colour, **b.** after extraction of some of the unreacted TB solution and the solutions were settled, and **c.** the extracted unreacted TB solutions which were used in absorbance measurements to obtain a standard curve for different concentrations of Hep.

All absorbance measurements for gradually increasing Hep concentrations were plotted in Microsoft Excel to form a linear standard curve obtained with a line equation and  $R^2$  value. In the Hep concentrations, for those with above 60 µg/mL of Hep solution, the unreacted solution colour was very clear and they had very low optical density approaching zero (approx. 0.13) that were not proportional to Hep concentrations. Therefore, in the experiments, it was decided to use only the workable range of concentrations up to 60 µg/mL of Hep. Figure 4.27 shows the noncomplexed TB solution extract aliquots prepared in a well-plate with increasing Hep concentrations of up to 60 µg/mL for absorbance measurements, the resultant standard curve plot with a linear average in the range up to 60 µg/mL of Hep concentration and the following non-linear region of the rest, where absorbance bottoms out at approximately 0.13..

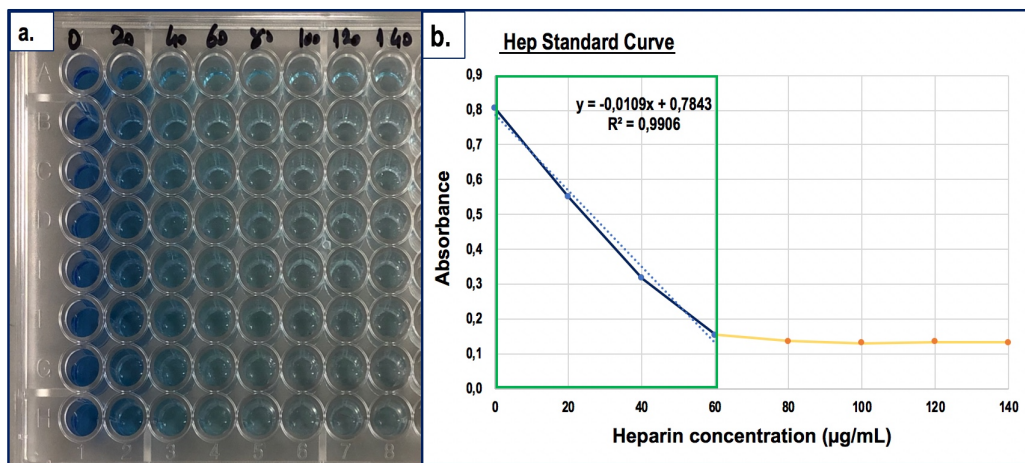


**Figure 4. 27** Absorbance measurement for Hep standard solutions in D.H<sub>2</sub>O to obtain a standard curve for different concentrations of Hep: **a.** The colour difference at unreacted liquid extracts were placed as 100 µL aliquots with 8 replicates into columns at increasing concentrations, and **b.** Hep standard curve obtained with absorbance measurements of specimens at 630 nm wavelength of the light. The linear region from 0 to 60 µg/mL Hep concentrations (shown by green rectangular frame) by dark-blue straight line used as standard curve having the line equation and R<sup>2</sup> value on top while nonlinear portion of rest of the curve is given in yellow colour.

Hep release studies were performed on the Hep release media of hydrogels which were immersed into 10 mL of D.H<sub>2</sub>O and incubated at 37 ° C. At different intervals over a week, TB assays were carried out by using 1 mL of Hep release media instead of the Hep standard solution, to obtain the TB/Hep/hexane (1.5/1/1.5) complex, and measure the optical densities of the extracted noncomplexed liquids. The absorbance measurements at time intervals and the cumulative drug release profile of the S0 sample (33 µg/mL Hep) were plotted along with the standard deviation (n=3) (given in Figure 4.28). In these results, unexpectedly, the absorbance values of the 4-hours (Day-0) and Day-3 intervals, for CII control sample without Hep, were almost identical to each other. This might be caused by a transparent hexane compound mixed into the liquid extracts, decreasing the colour intensity in CII samples, if in the initial experiments, protocol was not performed properly. In addition, S0 possesses a very small amount of Hep (33 µg/mL) leading to having closer absorbance values to those of the CII specimen. The percentage of cumulative drug (Hep) release calculated from the standard curve was 22.6 ± 0.9 % after the first 4 h (day-0), and reached 36.9 ± 0.05 % after 24 h (day-1). The greatest increase of drug release occurred between day-1 and day-3 where cumulative release went from approximately 36% to slightly over 70 %. After a week, only 8% of the drug remained in the samples. Although a progressive release was observed the speed of Hep release could be considered still too fast. This could be

associated with the used, less crosslinked hydrogels, obtained below a pH of 6.4 in the modified formulation solution. It would be very beneficial to perform drug release experiments with higher pH counterparts (6.4-6.5), assumed to lead to more sustainable drug release, due to their more crosslinked and stable hydrogel forms. However, these experiments could not be performed due to time limitations in the project and a covid 19 lock-down period where facilities were unavailable.

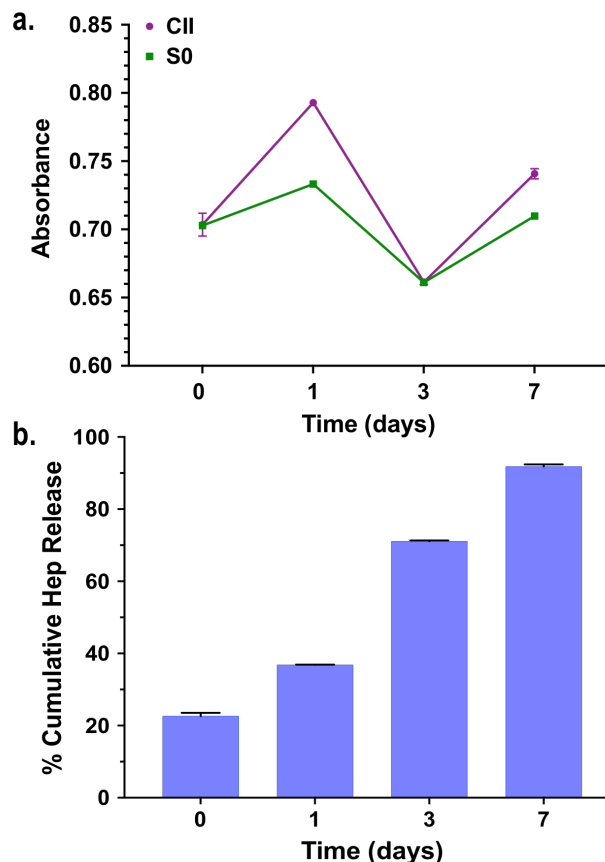


**Figure 4. 28** The drug (Hep) release study performed with the D.H<sub>2</sub>O immersion media of hydrogels incubated at 37 °C, in different time periods of 4 hours (Day 0), Day 1, 3 and 7. **a.** the change of the absorbance values of TB extract solutions were performed by using Hep release media for modified hydrogel specimens obtained with a pH 6.2-6.3 in solution, including CII (CS.0.1HA) as a control and S0 (CS.0.1HA.0.0015Hep) with 33 µg/mL Hep **b.** the cumulative Hep release of Hep from S0 (CS.0.1HA.0.0015Hep) calculated from the standard curve.

A further drug release study was performed by using the SBF supernatant media that were allocated from the 7, 14 and 21-day intervals of the bioactivity studies. The Hep standard solutions were prepared in SBF in different concentrations of up to 60 µg/mL and the standard curve was obtained via absorbance measurements of non-complexed aqueous TB solutions (the line equation is  $y = -0.0096x + 0.7254$  and  $R^2 = 0.9694$ ). Figure 4.29 gives the comparative absorbance measurements of the sole TB solution, and

noncomplexed TB solutions taken from the release media of CII and SI samples incubated in SBF which were taken at 7, 14 and 21 days of the bioactivity study. The TB solution had high absorbance values ranging between 1 and 1.1 over the whole period. Having a high standard error, the mean absorbance value of the SI sample was  $0.65 \pm 0.14\%$  and slightly increased to  $0.68 \pm 0.02\%$ . On the other hand, CII control samples had respectively higher absorbance values between 0.72 and 0.76 which was almost the same as the absorbance value for the SI sample at day-21. The counted drug release amount during first two weeks was quite low, at around 14 % and 17%, respectively with a high standard deviation. However, the Hep concentration measured at day 21 was negative. Therefore, these experiments performed in SBF release media need to be repeated for confirmation of the results. However, the drug release experiments could not be repeated due to covid 19 lock down.

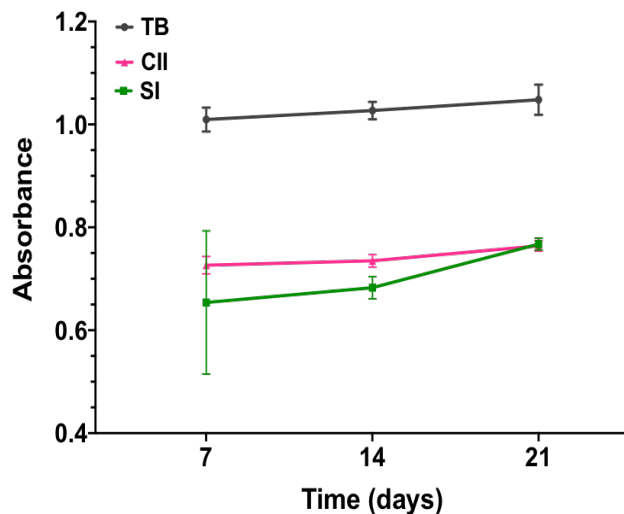


**Figure 4. 29** The drug (Hep) release profile in SBF performed by using the supernatant media taken during bioactivity studies at different time interval over 21 days. The absorbance measurements are of the sole TB solution and the TB extract solutions of modified hydrogel samples after complexation with hexane including CII (CS.0.1HA) both used as controls and SI (CS.0.1HA.0.005Hep) with 120  $\mu\text{g}/\text{mL}$  Hep. (The decrease of absorbance indicates an increase of Hep concentration).

#### 4.9 Discussion

The hydrogel compositions did not show a very high swelling ratio in PBS media (pH 7.4). It was in the range of 55-68 % of the equilibrium point after 6 hours. The swelling ratio of the hydrogels in this study were more than the swelling ratio of reported CS/HA/PVA hydrogels reaching to the equilibrium in about 20 min with 17% of swelling (Tang et al., 2009). On the other hand, the swelling ratio of hydrogels in the

current study was much lower than from reported CS/HA/TCP hydrogel compositions having swelling ratios ranging between 1000-2000% (Shavandi et al., 2016). The relatively smaller swelling ratio of hydrogels in this study could be associated with the well ionically crosslinked interpenetrating structure of the tested modified hydrogel specimens, having a slightly higher pH in solutions (6.4-6.5) in comparison to the weaker modified hydrogels obtained at below 6.4 pH (6.2-6.3) which were discussed in the previous chapter. In addition, the smallest swelling ratio of the composite hydrogels (CS/HA/Hep) might be related to a counter charged CS and Hep polycomplex system that strengthens the gel network due to stronger electrostatic bonding. Less swelling could be beneficial for sustainable drug release applications. The mitigated burst release and sustainable release of basic fibroblast growth factor (bFGF) was reported to be achieved by Hep functionalisation of CS-alginate polycomplexes (Ho et al., 2009). In addition, Hep integrated CS/hyaluronic acid conjugates produced by an ionotropic gelation technique was reported, and these gels showed successful prolonged release of Hep to the lungs for asthma treatment (Oyarzun-Ampuero et al., 2009). At lower pH media, CS is expected to have a much higher swelling ratio since its cationic structure, causing a strong cationic charge in acidic media, leads to repulsion forces and subsequent swelling (Rizwan et al., 2017). Additionally, it was reported that Hep based hydrogels had less swelling in PBS in comparison to water media, due to the involvement of salts in PBS that are attracted by anionic Hep rather than by occurrence of electrostatic repulsion (Tae et al., 2007).

Regarding *in-vitro* degradation of modified hydrogels, they exhibited gradual degradation in both PBS and lysozyme media. The lysozymes slightly accelerated the gradual degradation speed in comparison to sole PBS media. Total degradation in lysozyme and PBS media reached up to 60% and 70 %, respectively after 6-weeks. These results were mostly concordant with the reported degradation studies of TEOF crosslinked hydrogels and CS/PVA hydrogels loaded with Hep, which showed degradation between 30% and 50% in 10-days, but acceleration of degradation by lysozyme was negligible (Shahzadi et al., 2016). In this study, around a 10% more degradation difference contributed by lysozyme is considered due to the chosen higher concentration of lysozyme used. In another study reported by Qasim *et al.*, (2015) the used lysozyme concentration in PBS was the same as in the current study; CS/HA

scaffolds showed a similar degradation rate, nearly above 40% of weight loss at day-7 reaching 60% after 28 days.

The degradation difference between the different hydrogel compositions were not found to be significant, but the degradation between time intervals were statistically significant for each sample. The crack formations on the hydrogel surfaces started from day-14 and continued to propagate leading to break down of the bulk of the polymer network. Very large cracks and severe deterioration of the samples after 42-days were observed in SEM images that confirmed the morphological degradation. Furthermore, chemical analyses of the hydrogels by FTIR-ATR spectroscopy showed the gradual decrease of the peak intensities of most chemical functional groups. In particular, the O-H/N-H region  $3100\text{-}3500\text{ cm}^{-1}$  and the adjacent shoulder peak of C-H bonds in the region of  $2800\text{-}3000\text{ cm}^{-1}$ , and C-O ring stretching and bending vibrations at around  $900\text{-}1200\text{ cm}^{-1}$ , showed an explicit progressive decrease in the peak intensities. In addition, an increment of amide-I bond at around  $1650\text{ cm}^{-1}$  and the changing peak shape around  $1550\text{-}1620\text{ cm}^{-1}$  due to  $\text{COO}^-$  stretching vibrations, showed the chemical interaction of lysozyme with CS. As reported, degradation rate can be modulated by the degree of acetylation (DA) of CS; as the DA of CS increases the degradation rate increases (Nordtveit et al., 1996; Ren et al., 2005). In this study, the used CS had medium molecular weight and a highly deacetylated form.

Bioactivity studies performed by SBF showed the promising *in-vitro* biominerilization potential of the composite hydrogels; (CS-HA) and (CS-HA-Hep) supported by various characterisations. On the other hand, sole chitosan hydrogels showed almost no mineralisation *in-vitro*. The gradual increase of the dry mass percentage of hydrogels were attained and the dense white mineralised layer formation on the top surfaces were easily noticed. The needle like carbonated hydroxyapatite layer deposition on the surface of the composite hydrogels were confirmed through microstructural imaging by SEM. The elemental analyses of composite hydrogels by EDS showed the high intensity Ca, P, O, and H peaks as well as C, having a respectively higher Ca/P ratio of approximately 2 % which might be associated with possible B-site carbonate substituted apatite formation. The prominent phosphate bonds including  $\nu_3$  asymmetric stretching ( $\sim 1020\text{ cm}^{-1}$ ),  $\nu_1$  symmetric stretching ( $963\text{ cm}^{-1}$ ) and  $\nu_2$  phosphate bending ( $473\text{ cm}^{-1}$ )

and  $\nu_4$  asymmetric  $\text{PO}_4^{3-}$  bending vibrations at  $559\text{ cm}^{-1}$  and  $601\text{ cm}^{-1}$  with an increment at peak intensities and sharpness were detected from prominent phosphate peaks in hydroxyapatite. In addition, the presence of carbonate ( $\nu_2$ ) substitutions were confirmed by the peaks raised around  $875\text{ cm}^{-1}$ .

The positive effect of HA in bioactivity in terms of mineralisation is very well known for serving as crystal nuclei for further apatite formation, as is reported in the literature for CS/HA scaffolds (Kong et al., 2006). Furthermore, in this study, it was seen in longer term (at day-21) that the CS/HA/Hep hydrogels showed significantly higher mineralisation than CS/HA hydrogels, indicating that Hep also induced the biomineratisation process in CS/HA/Hep hydrogels. In terms of the effect of Hep on mineralisation, the Hep conjugated fibrinogen injectable gels are reported to induced alkaline phosphatase activity leading to mineralisation (Yang et al., 2010). Furthermore, Hep functionalised poly(caprolactone) (PCL) membranes showed osteogenic differentiation via alkaline phosphatase activity with induced osteocalcin production, and osteoblast-like cell proliferation (Gümüşderelioğlu et al., 2011).

The local presence of Hep was confirmed by TB staining, marking purple coloured homogeneous distributions of Hep locations as a functional layers on the top surface of composite hydrogels. The smooth surface feature caused by the coating effect of Hep on the top surface of hydrogels was also confirmed by SEM analyses. This surface functionalisation by Hep might be very beneficial to attract living entities, such as cell, proteins and growth factor which are bound by Hep due to its highly anionic nature. Thus, the functional composites produced by cooperative bioactive properties of both HA and Hep are considered to promote a strong interaction and bonding with natural bone tissue. The stability of Hep in hydrogel networks was investigated via initial hydrogel formulation after 2 years of storage in freeze-dried form. Hydrogels with higher Hep concentrations of above  $0.36\text{ mg/mL}$  were still stained in purple colour by TB, and dense homogenous purple colour distribution was seen with the SIII sample having the maximum Hep concentration ( $0.60\text{ mg/mL}$ ) indicating that it still possessed a significant amount of Hep. Drug release in water media showed the gradual release of Hep in 7 days for the S0 hydrogel composition (solution pH 6.2-6.3) that had the lowest Hep concentration ( $0.033\text{ mg/mL}$ ). The results showed a more sustainable release of Hep than reported shape memory hydrogels (Guo et al., 2018) and polyurethane-silk

membrane composites (Yang et al., 2011). In addition, N,N-Dimethyl CS/Hep polycomplex tested in Simulated Intestinal Fluid (SIF) at pH 6.8 showed around 60% of Hep release in the first 24 h and was stable up to the 48 h when the test was ended. However, in Simulated Gastric Fluid (SGF) at pH 1.2, more sustainable release of Hep was seen around 5% which was related to the initial low pH of this polycomplex (3.0) which has led to bonding of anionic Hep due to cationic sites of CS (Bueno et al., 2015). In this study, the used solution pH to obtain gels were between 6.2 and 6.3 which then rose to around 6.8-7.2 upon gelation. The hydrogels obtained upon further solution neutralisation of up to pH 6.4-6.5 led to better mechanical strength and stability, as has been discussed in Chapter 3. Therefore, the more electrostatically crosslinked, stable hydrogels are presumed to lead to the more prolonged release of Hep. The Hep release experiments performed by using SBF release media taken from bioactivity studies showed non-conclusive results. However, these experiments could not be repeated due to the remaining short time of the project and the covid lock down period.

#### 4.10 Summary and Conclusions

The swelling capacity of modified hydrogels (CS/HA/Hep) obtained with a solution pH slightly above 6.4 was low (55%) enough that they could be desired for sustainable Hep or other targeted drug release applications. The tested modified hydrogels that were produced with a lower solution pH (6.2-6.3) possessed gradual release of Hep up to 7 days. However, to enhance its bioavailability and function for binding angiogenic growth factors, cells and proteins, a more sustainable release is preferred. Therefore, the experiments with modified hydrogels obtained from higher pH solutions (6.4-6.5), due to their reduced swelling results and mechanical stability, are expected to lead to the more prolonged release of Hep. In terms of bioactivity, the CS/HA/Hep hydrogels tested in SBF highly induced biomineralized carbonated apatite layer deposition on hydrogels, not only due to HA, but also further promoted significantly by Hep. The gradual degradation of all hydrogels in PBS and slightly better degradation in lysozyme media were obtained regardless of the hydrogel compositions. Overall, Hep surface functionalised CS/HA/Hep injectable hydrogel compositions were obtained that are good candidates for use as bioactive and biodegradable sustainable delivery tools for Hep or other targeted drugs or active agents for vascularised bone regeneration.

## 5 BIOCOMPATIBILITY AND ANGIOGENESIS OF SYNTHESIZED HYDROGELS

### 5.1 Introduction

In this chapter, the biological analyses of hydrogels in terms of biocompatibility and angiogenesis performance are included. The cell cytocompatibility, cell adhesion proliferation, and cell differentiation in term of ECM deposition capacities of hydrogels were investigated by utilising MG-63 osteoblast-like cell lines. The cell cytotoxicity and proliferation were evaluated by employing cell friendly repeatable Alamar Blue (AB) assay, and cell adhesion was observed under optical microscopy. The promotion of hydrogels to produce ECM components; calcium and collagen, were investigated by colorimetric Alizarin Red (AR) and Sirius Red (SR) assays, respectively. Angiogenesis was investigated with different hydrogel compositions having varying concentrations of Hep and without Hep for initial and modified hydrogel formulations individually. An *ex-ovo (shell-less)* Chick Chorioallantoic Membrane (CAM) assay was recruited by thermosensitive liquid injection on CAM tissue of chick embryos that form hydrogel upon incubation at 37.5 °C. The micro vascularisation on CAM in contact with samples was imaged, and the vascular index was counted to compare angiogenesis in different specimens. In addition, histology studies using Haematoxylin-Eosin (H&E) staining was performed on retrieved CAM-hydrogel tissue sections to assess angiogenesis and tissue-sample reactions morphologically.

### 5.2 Materials and Methods

#### 5.2.1 Materials

For cell culture studies, MG-63-Human osteosarcoma cell lines, preserved in Liquid N<sub>2</sub> at The University of Sheffield, from passage number-63 were used. The following chemicals were supplied: Dulbecco's Modified Eagles' Medium (DMEM) (Biosera,

Sussex, UK), Fetal Calf Serum (FCS), L-glutamine, Penicillin & Streptomycin, Amphotericin-B, Trypsin-EDTA, Formaldehyde and Resazurin sodium salt (Sigma-Aldrich®, Dorset, UK), Phosphate Buffer Saline (PBS) (Dulbecco A, Thermo Scientific™, Oxoid™, Basingstoke, UK), Ethanol ( $\geq 99.8\%$ , AnalaR NORMAPUR®, VWR-Prolabo Chemicals, France), Dimethyl Sulphoxide (DMSO) (Fisher Scientific, Thermo Scientific™, Loughborough, UK). For ECM deposition assays: Alizarin Red, Direct Red-80 (Sirius Red) and Saturated Picric Acid (Sigma-Aldrich®, Dorset, UK); Perchloric acid 70% (ACROS Organics™, Thermo Fisher Scientific, Geel, Belgium); Sodium Hydroxide and Methanol (Thermo Scientific™, Oxoid™, Basingstoke, UK) were purchased from suppliers.

For CAM assays, fertilised chicken eggs were supplied on the date they were laid. (Henry Stewart & Co. Ltd, Louth, UK). For histology staining and sectioning, Haematoxylin (Harris modified) & Eosin-Y (H & E) stains (Sigma-Aldrich®, Dorset, UK); Industrial Methylated Spirit (IMS) and Xylene (Fisher Scientific, Thermo Scientific™, Loughborough, UK); Tissue freezing media (Leica, Germany); and DPX mounting solution (Merck Chemical Ltd., Germany) were supplied.

### 5.3 Cell Culture Studies

The biocompatibility of hydrogels was assessed by cell cytocompatibility, cell proliferation and cell attachment tests with cultured osteosarcoma cells (MG-63). In addition, ECM deposition capability on hydrogels was investigated, after cell culturing, by using colorimetric assays for measurement of calcium and collagen.

#### ***Cell Growth, Sample Preparation and Cell Seeding***

To investigate cell cytotoxicity and proliferation, osteoblast-like MG-63 cell lines which were grown in a DMEM culture media supplemented with 10 % of FCS, L-glutamine (2mM), penicillin (100U/mL)/streptomycin(1.2 $\mu$ g/mL) and amphotericin - B (0.0625  $\mu$  g/mL), were utilised . The cells were incubated in a humidified incubator (37 °C, %5 CO<sub>2</sub>). The adherent MG-63 cell-lines were detached, by using trypsin-EDTA when they reached 80-90% confluence and passaged. The utilised cell-line passage numbers in the experiments were between 65 and 71.

For cell culture studies, hydrogel samples were freeze-dried from solutions (500  $\mu$ L) in the wells of a 48 well-plate. Foam like porous cylindrical hydrogels were obtained and prepared with four sample replicates from each of the sample groups. In addition, some experiments were performed, using hydrogels obtained by incubation at 37 °C. Samples were sterilised by immersing them into 70 % ethanol for 30 min, and then evaporating the ethanol for 1 h in a Biological Safety Cabinet (Type-II) (BSC). Sterile samples were then washed with PBS thrice with incubation between washes for 15 min to remove ethanol residue.

Three individual cell-culture experiments were performed. In the first experiment freeze-dried hydrogels were seeded with a low cell number ( $2 \times 10^3$ ) in metal rings placed in 12 well-plates. Following removal of the metal rings after 24 h, this culture was grown in the same well plates up to 28 days in 2 mL of growth media. The second method, performed with freeze dried hydrogels, is explained in detail in the following paragraph. In the third method, hydrogel samples, obtained from liquid hydrogels upon incubation at 37 °C, were used after cutting them into circular shapes ( $\sim \varnothing$ : 8 mm). Hydrogels, cultured in 1 mL of growth media in a 24-well plate without using metal rings, were seeded with  $5 \times 10^4$  cells per sample.

The second method with the optimal cell seeding density is explained in this section. Freeze-dried hydrogel foams ( $\sim \varnothing$ : 8 mm) were placed inside sterile stainless-steel rings ( $\varnothing$ : 10 mm) in the wells of 12-well plates. Prior to cell seeding, samples were conditioned with 200  $\mu$ L of serum containing DMEM for 1 hour. Then, a MG-63 cell suspension with a concentration of  $2 \times 10^5$  cell/mL was seeded onto each hydrogel specimen, by 100  $\mu$ L drops to achieve the final concentration of  $2 \times 10^4$  cell/mL per sample and then incubated in 1 mL of growth media. The cells, using the same concentration, were also seeded into empty wells of Tissue Culture Plastic (TCP) as a control. After cell seeding, the well plates were incubated overnight at 37.5 °C for cell attachment. The next day, the metal rings surrounding samples were carefully removed by using a sterile tweezer. Samples were then transferred into a new 24-well plate. The Alamar Blue (AB) assay was performed after 24 h to test for cell attachment and cytotoxicity. In the rest of the experiments, samples with attached cells were grown in the same 24-well plate in 1 mL of cell growth media. The cell proliferation was

maintained up to 28-days of the culture and measured by AB assay in different time intervals, including 1, 4, 7, 14, 21 and 28 days.

### 5.3.1 Alamar Blue (Resazurin) Assay

Resazurin (alamarBlue®) is a blue coloured non-fluorescent stain that is reduced to a fluorescent resorufin compound inside the cells as a result of oxygen consumption and the enzymatic activities of cells. This reduction leads to a pink colour that can be detected by optical density or fluorescence measurements and is an indication of the cell's viability or cytotoxicity. Since resazurin is non-toxic to the cells, the experiments can be carried out on the same cells for repeated measurement. Hence, the Alamar Blue assay saves the cells and samples, and reduces cost, time and energy (Brien et al., 2000).

### 5.3.2 Preparation of Resazurin Solution

First, a 0.251 g/L of resazurin stock solution was prepared by dissolving 0.125 g of resazurin in 500 mL of de-ionised water. This solution was sterilised by pouring it through a 0.22 µm polyethersulfone (PES) filter into a sterile glass bottle, covering it with aluminium foil to prevent light contact and storing it at 10 °C . Resazurin solution (1 mM) for cell culture experiments was freshly prepared for use in each experiment day by dilution of a stock resazurin solution in sole serum-free DMEM (ratio 1:10).

### 5.3.3 Alamar Blue Assay

*In-vitro* cell viability and proliferation assays were performed by using a standard Alamar Blue (AB) assay protocol. Briefly, at three determined culture intervals, cultured samples were washed with 1 mL of PBS. Then, samples were immersed into 1 mL of resazurin solution in the wells of a 24 well-plate, which was covered with aluminium foil to prevent light contact, and incubated for 4 hours. After 4 h, the reduced resazurin media (resorufin), which transforms from blue towards pink tones, were taken in triplicate from each well as 200 µL aliquots, and poured into the wells of a 96 well-plate with a zigzag pattern to prevent fluorescent interference of adjacent wells. The

fluorescence values of the aliquot solutions were measured in a microplate reader (Bio-TEK, North Star Scientific Ltd. Leeds, UK) by using excitation and emission light wavelengths of 540/35 and 635/32 nm, respectively.

### 5.3.4 Cell Attachment Observation by Optical Microscopy

During cell culture studies at different time intervals, the closed cell-culture plates were observed under optical microscopy, photographed quickly and returned for incubation at 37 °C. Care was taken to avoid any contamination of the culture.

### 5.3.5 Extracellular Matrix Production Assays

The effects of cell-seeded hydrogels on  $\text{Ca}^{+2}$  ion release as an indication of mineralisation, and the formation of collagen as an organic matrix were investigated by using colorimetric Alizarin Red (AR) and Sirius Red (SR) assays, respectively.

#### 5.3.5.1 Calcium Deposition Analyses by Alizarin Red Assay

The Alizarin Red (AR) solution (1% (w/v)) was prepared by dissolving AR stain in de-ionised water and sterilising it by filtration (0.22  $\mu\text{m}$ , PES membrane filter). The cell seeded hydrogels were cultured for 28 days, and subsequently fixed with 3.7% of formaldehyde and stored in PBS at 10 °C until utilised for AR assay.

The cell seeded hydrogels in 24 well-plates were washed thrice with de-ionised water. Then, samples were submerged into a certain volume of AR solution and rested for 30 min. Subsequently, the supernatant AR solution was removed and washed while under orbital shaking for 5 min. This process was repeated until the release media became clear. Following this, AR stains bound to samples were released by immersion into 5% (v/v) of perchloric acid for destaining with the help of gentle orbital shaking for 15 min. Then, aliquots (150  $\mu\text{L}$ ) of the released media containing AR were placed into a 96 well-plate in triplicate, and absorbance values were measured at the 405 nm wavelength of light. The optical density measurements were then converted to AR concentration in the samples by correlation with a previously obtained standard curve. To obtain the AR

standard curve, the solutions with different concentrations of AR in perchloric acid (5%) were prepared (0, 5, 10, 25, 50, 100, 250, 500 and 1000 µg/mL), and the absorbance measurements of 150 µL of aliquot solutions were performed at the 405 nm light wavelength. After subtracting the absorbance value for 0 µg/mL AR (sole perchloric acid) from the mean absorbance values of each sample group, the remaining mean values were plotted against the corresponding AR concentrations using a line equation and  $R^2$  value.

### 5.3.5.2 Collagen Deposition Analyses by Sirius Red Assay

After performing the AR assay on fixed cell culture samples (28-days), the Sirius Red (SR) assay was applied to the same specimens to determine their collagen deposition capacities. The SR solution (1% (w/v)), was prepared by dissolving SR dye in saturated picric acid and was filter sterilised (0.22 µm, PES membrane filter). The specimens retrieved from the AR assay were washed thrice in de-ionised water and immersed into a set volume of SR solution by leaving it in an orbital shaker for 18 h at 100 rpm. Then, supernatant solutions were taken out, and the samples were washed in water for 5 min intervals under gentle orbital shaking to remove unbound stains.. Then, the samples were immersed in 0.2 M NaOH: Methanol (MeOH) (1:1) solution under orbital shaking at 100 rpm for 20 min to release any SR stain bound to the samples. Following this, the aliquots of the stain released media (150 µL) were put into a 96 well-plate in triplicate for absorbance measurements at 405 nm. The collagen concentration in the samples were detected by correlation from the previously obtained standard SR curve. The standard curve was obtained for the following concentrations of standard SR solutions: 0, 1, 2.5, 5, 10, 25, 50, 100 µg/mL, prepared by diluting stock SR solution with 0.2M NaOH: MeOH (1:1) and their absorbance readings performed at 405 nm. After subtraction of the control values for 0 µg/mL SR solution, the mean absorbance values were plotted against the different concentrations. Using a line equation, a trendline with  $R^2$  value were obtained. The SR concentration in the samples were calculated by using this standard line equation.

## 5.4 Angiogenesis Evaluation by Ex-ovo Chick Chorioallantoic Membrane (CAM) Assay

The effects of different hydrogels on angiogenesis were investigated by using a chick embryo model. An *ex-ovo (shell-less)* Chick Chorioallantoic Membrane (CAM) assay technique was applied in sterile clean room conditions. This technique was applied as reported by Mangir *et al.*, (2019) with some differences to apply thermosensitive injectable hydrogels on CAM. Same day laid fertilised hen eggs were supplied (Henry Stewart & Co.Ltd, Louth, UK) and stored at (10±1 °C) until the experiments started in one to a few days. Prior to incubation, eggs were purified from any dirt and dust by using rough tissues sprayed with 20% IMS sterilizing spray. The egg incubators (RCOM King SURO, P&T Poultry, Powys, Wales) were sterilised by 70% alcohol. The eggs were transferred into an egg incubator placed inside a Biological Safety Cabinet (BSC), and incubated for 3 days in horizontal humidified (60-80%) rotating egg incubators at 37.5 °C.

After 3 days of incubation, the eggs were cracked by using a sterile *ex-ovo* technique. Standard weighing boats were prepared prior to egg cracking by cutting their edges and sterilisation with 70% alcohol. The boats were left in the BSC until all the alcohol was evaporated. The rotational parts of the egg incubators were stopped at least 15 min before egg cracking to ensure a static position of embryos on top which were then marked by a drawn horizontal line. Four eggs were carefully transferred into the BSC for cracking at each time, keeping the drawn lines on top. Eggs were cracked by hitting them onto the sharp edge of a beaker twice or thrice allowing the leakage of some egg white into the beaker. Then, the egg was carefully transferred into a sterile weighing boat containing 2 mL of a sterile 1% (v/v) Penicillin (100U/mL)/Streptomycin (1.2µg/mL) solution in PBS. To crack an egg, a special finger positioning of two hands was applied by holding the egg horizontally with index fingers and thumbs on the top and bottom, respectively. Then, a gentle downward pressure was made with the thumbs and ring fingers below by providing a vacuum effect by contact of the egg white with the solution in the weighing boat. Then, egg content was slowly released out of shell while maintaining the embryo's position on the top and in the middle of the egg yolk. The accurate practice of this technique prevents any damage to the egg yolk and

embryo. The live, heart beating and blood circulating embryos in the weighing boats on petri-dishes were closed with lids and labelled, then gently transferred onto a hot-plate set at 37 °C. After 4 eggs were cracked, they were gently transferred into a static incubator at 37.5 °C with % 60 humidity. The embryos were checked daily, and their development and survival status were recorded.

The sample implantation took place at day-7 when chick embryos develop circulatory vessels and the shiny CAM border becomes explicit. In this study, to mimic *in-vivo* injection of hydrogels, the liquid hydrogel solutions were directly applied on the CAM as a liquid, which then formed hydrogels upon incubation at 37.5 °C. Prior to implantation, pre-sterile hydrogel solutions were terminally sterilised by UV to prevent any airborne contamination. For this, the liquid test specimens in vials were placed into an ice box to prevent gelation in room temperature and sterilised under UV light for 1 h. To maintain body temperature, each embryo was kept on a hot stirrer adjusted to 37 °C during the hydrogel injection. Then, sterile hydrogel solution in a micro-syringe was applied as a 100 µL drop between two major arteries of the embryo and at the midway of the embryo's formation and the shiny CAM border. Upon gelation from the surface of the hydrogel solution from a few minutes on the hot stirrer at 37 °C, the chick embryos were gently transferred back to the incubator at 37.5 °C. The steps in *ex-ovo* CAM assay for thermosensitive injectable hydrogels are demonstrated in Figure 5.1.

At day-10 and day-14 intervals, newly formed blood vessels surrounding the samples were photographed alongside a scale by using a digital USB microscope (Maplin, x400) supported with white lightening from below and sides. At day 14, the images of the embryos were also taken after the injection of a white cream solution underneath the sample for imaging contrast, by using a 20 mL syringe coupled with a 20 G needle (BD, Becton, Dickinson UK Ltd., Wokingham, UK). After the imaging of each sample, the hydrogel samples with attached CAM tissue were retrieved, and the embryos sacrificed by cutting the major artery, using a dissection kit, to minimizing pain to the embryo. Hydrogel samples retrieved with adjacent vascular CAM tissue were washed and fixed in 4 mL of formaldehyde (3.7%) in vials for 24 h. Then, tissue-samples were washed with PBS twice and preserved in 70% ethanol at 10 °C until needed for further histology

analyses. The embryonic waste in the firmly closed plastic bottles were frozen at -20 °C to be later discarded according to regulations for animal waste.

For initial hydrogels, the tested hydrogel compositions were the CII(CS.0.1HA) sample without Hep; and the SI(CS.0.1HA.0.005Hep), SII(CS.0.1HA.0.015Hep) and SIII(CS.0.1HA.0.025Hep) samples having 0.12, 0.36, and 0.60 mg/mL of Hep, respectively. The test specimens for modified hydrogels involved CI(CS), CII(CS.0.1HA) samples without Hep and the SI and S0 (CS.0.1HA.0.0015Hep) samples having 0.12 and 0.03 mg/mL of Hep respectively. In addition, filter paper (F.p.) was used as a control.

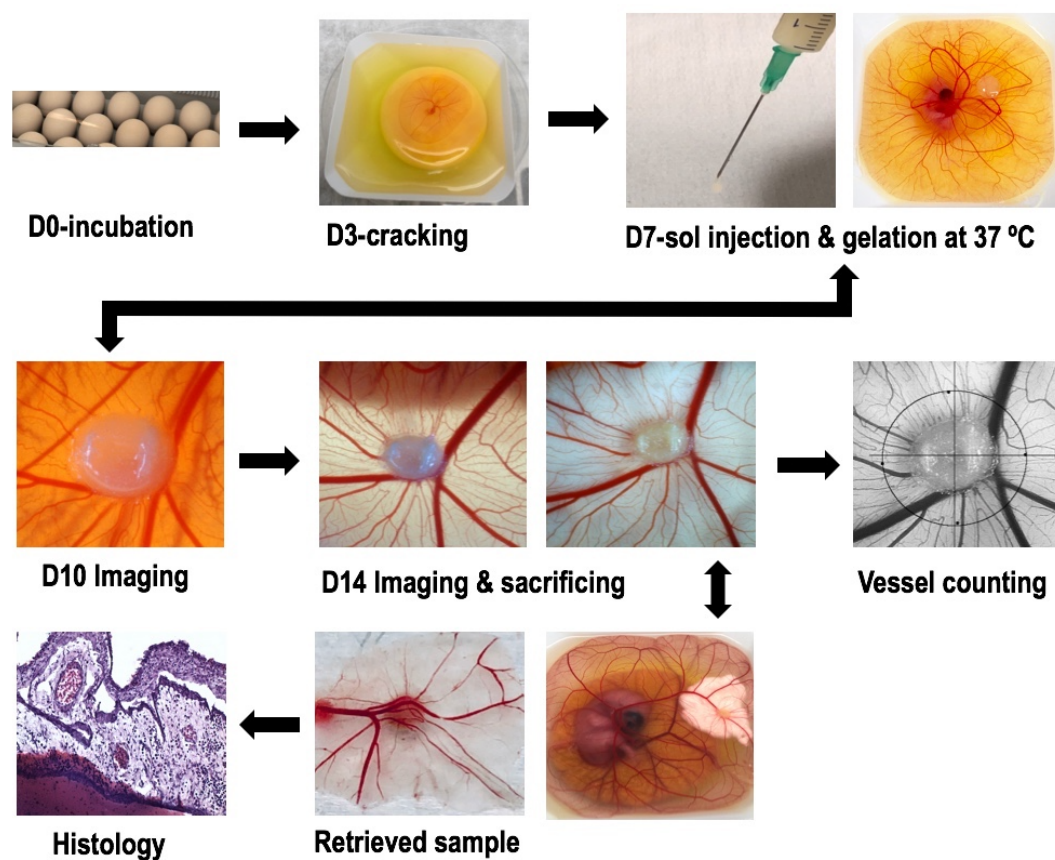


**Figure 5.1** Demonstration of an *ex-ovo* CAM assay steps for in-situ forming injectable thermosensitive hydrogels (CS/HA/Hep): 1. the incubation of fertilized hen eggs in day-0 (D0), 2. cracking at day-3 (D3), 3. the solution injection into CAM tissue and in-situ gelation at average body temperature (37.5 °C) at day-7 (D7), 4. the imaging of micro-vessel formations at day-10 (D10) and day-14 (D14) which is also the sacrificing day of embryos (5), 6. quantifying blood vessels from CAM images via the vascular index method and 7. histological assessment of CAM-tissue sections. (This diagram was reused from our published paper (Kocak et al., 2020) licensed under CC BY 4.0.).

#### 5.4.1 Quantification of Angiogenesis by Vascular Index Method

Angiogenesis was quantified from CAM images taken at day 14 through a ‘vascular index’ method reported by Barnhill and Ryan, (1983) by using ImageJ® Software (Version 1.52 k, National Institutes of Health, Bethesda, MD, USA). Briefly, newly formed micro vessels attaching to a hydrogel sample were counted if a blood vessel locates within an imaginary circle drawn with 1 mm annulus, if the angle between the vessel and a virtual central line is equal or less than 45°. A vessel branching inside the imaginary circle was counted 1 whereas a diverging vessel outside the circle was quantified as 2. The vascular index was counted from at least 6 sample images per sample group along with the standard deviation (SD) for initial hydrogels. In the following analyses, with modified hydrogels, from 9 up to 11 sample images were involved per sample group for counting the vascular index and the calculation of the mean and SD.

#### 5.4.2 Histology

The fixed and preserved CAM tissue-samples were histologically analysed to observe angiogenesis, morphology of blood vessels and biomaterial-tissue interactions. For tissue sectioning, hydrogel-tissue specimens were prepared by moulding with tissue freezing media in circular or square sample moulds and snap frozen in liquid N<sub>2</sub>. Frozen samples were then adhered onto metal stubs and sectioned at 10 µm thickness in both horizontal and vertical angles in a cryostat (Leica Biosystems, CM1860 UV, Nussloch, Germany). Tissue sections were collected on Polysine adhesion slides (25 x 75 x 1.0 mm, Thermo Fisher Scientific™, Germany) and dried at room temperature prior to the Haematoxylin and Eosin (H&E) staining.

For H&E staining of hydrogel-CAM tissue sections, a standard protocol was applied including staining by H&E and washing between stains; dehydration by graded alcohol (IMS): 70% and 100% and Xylene treatment. The stained histology sections were left to dry at room temperature. Then, the sections were treated with DPX mounting solution and covered with protective coverlids. The H&E stained histology slides were imaged at different magnifications by using a Motic (Barcelona, Spain) optical microscope, or

an EVOS™ XL Core Configured Microscope (Invitrogen™, Thermo Fisher Scientific Inc, Madison, WI, USA) to image some of the slides.

## 5.5 Statistical Analysis

The results were expressed as a mean with standard deviations (SD) for repetitions. The statistical analyses were performed in GraphPad Prism (Version 7.0, San Diego, CA, USA) software by using TUKEY multiple comparison tests when  $p \leq 0.05$ , by using Two-way ANOVA for cell culture studies and by One-way ANOVA for CAM (angiogenesis) analyses.

## 5.6 Results

### 5.6.1 Cell Viability and Proliferation

The cell cytocompatibility of hydrogels was investigated by three main experiments on 4-week cultures with varying cell concentrations. Figure 5.2. shows the measurements of cell metabolic activities as indicators of cell viability via Alamar Blue assay by fluorescent reading at regular time intervals. The results of two different experiments are shown in Figure 5.2.a and Figure 5.2.b that were performed by seeding cells on freeze-dried hydrogels in different cell densities. In the first experiment (Figure 5.2.a), 2,000 cells were seeded per sample and were grown in 2 mL of media in a 12 well-plate. In the second experiment, the cell concentration was 20,000 cells/sample incubated with 1 mL of media in a 24 well-plate (Figure 5.2.b). Cell compatibility was also analysed in the hydrogel forms of samples which were obtained upon gelation of solutions at 37 °C. These hydrogels were seeded by 50,000 cells/sample and the cell viability results for this culture is given in Figure 5.2.c.

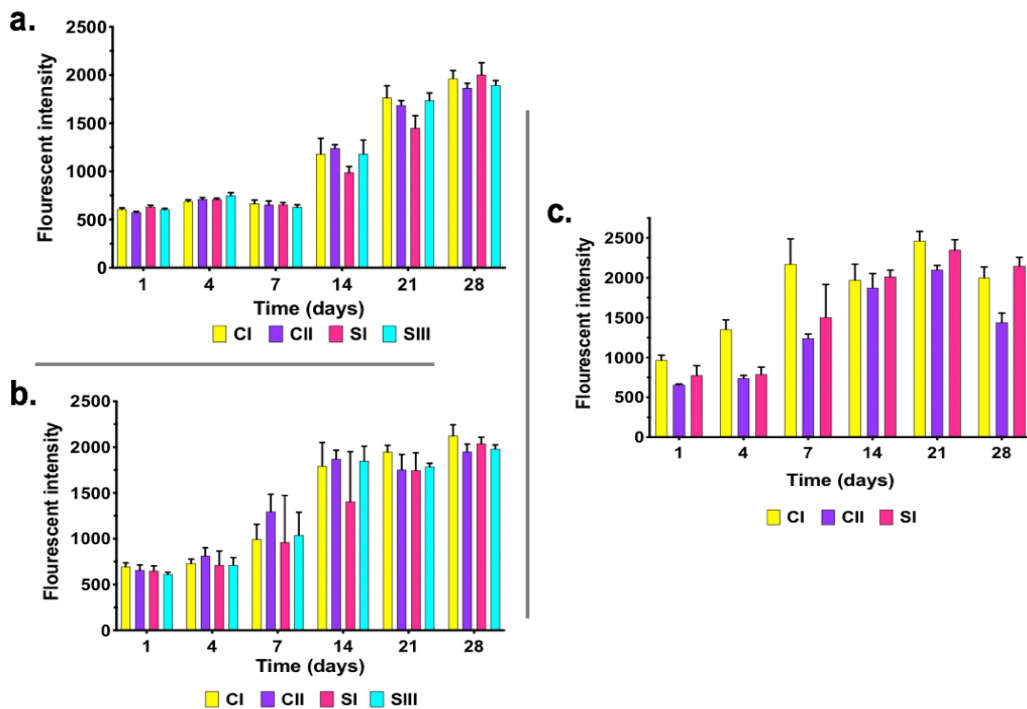


**Figure 5.2** The cell viability and proliferation analyses by fluorescent measurements up to 4-weeks of cultures in three individual experiments: **a.** freeze-dried hydrogels (solid foam) seeded with 20,000 cells/sample grown in 1 mL media in 24 well-plate, **b.** freeze-dried hydrogels (solid foam) seeded with 2,000 cells/ sample grown in 2 mL of media in 12 well-plate, **c.** oven-dried hydrogels (obtained in gel form at 37 °C) seeded with 50,000 cells per hydrogel which were grown in 1 mL media in 24 well-plate (Hydrogel specimens used in experiments shown in graphs **a.** and **b.** are CI(CS), CII(CS/HA), SI(CS.HA.0.005Hep) and SIII(CS.HA.0.005Hep), and CI, CII and SI samples in the experiment are shown in plot **c.** (The experiments were performed with 4 sample replicates and results are expressed as the mean±SD).

In the first experiment group (in Figure 5.2.a.), the fluorescent intensities of samples were in the vicinity of 500 in day 1 and showed a slight increase during the first week of culture. The slow growth can be associated with the low cell seeding density per sample in this experiment that has slowed down the speed of transition from the lag phase to the log phase of cell growth. The delayed log phase occurred between 7 and 14 days at which exponential cell growth occurred showed by a sudden doubling increase in cell metabolic activities. Then, gradual cell growth was observed in the cultures for the rest of the culturing period up to day 28, reaching in the vicinity of 2,000 in fluorescent intensities. The cell metabolic activities with all sample groups were very similar. At the second experiment (Figure 5.2.b.), the higher cell seeding concentration (20,000 cells/sample) led to shortening the lag phase, and higher cell viability was seen at the initial stage, reaching around 1200 fluorescent intensities at day-7, which was comparable with the day-14 results of the first experiment with lower cell

concentrations. The highest cell viability was obtained with the composite CII (CS.0.1HA) sample at day-4, day-7, and day 14 which was very similar to that of the SIII (CS.HA.0.025Hep) composite sample with Hep. During day-21 and day-28 a slightly higher fluorescent intensity was observed with the CI sole CS sample. Between week 2 and week 4, slower but gradual cell proliferation was observed in all samples as was expected.

The cell viability results in the hydrogel form of the samples in the third experiment are given in Figure 5.2.c. The first day viability results showed better cell attachment in the CI sole CS sample, initially. The transfer of the samples with attached cells into a new well plate in day-1 led to a much higher difference in cell metabolic activities between the CI and composite hydrogels for up to 7-days. This was due to the initial cell attachments from the higher initial cell concentration (50,000 cells/sample) in comparison to the other sample groups. Although much fewer cells remained in the composite hydrogels after plate transfer in day 1, they reached the fluorescent level of the CI sample in time. In day-14 and day-28, the highest cell viability was observed in the composite SI (CS.HA.0.005Hep) sample. The cells were gradually proliferated during the experiments with a slight decrease was seen in fluorescent intensities at day 28.

Overall, the hydrogels did not lead to cell cytotoxicity, and gradual cell proliferation was observed in all culture experiments. The cell seeding at density (2,000 cell/mL) on hydrogel samples ( $\varnothing$ : 8 mm) was found to be very low, retarding the log phase cell growth, although it reached similar viability values with the second experiment after almost three weeks. Since MG-63 cell lines grow very fast, rather than 50,000 cells per sample, the seeding density of 20,000 cells per hydrogel ( $\varnothing$ : 8 mm, 2-3 mm thickness) was found to be optimal. The best initial cell attachment mostly belonged to the sole CS hydrogel cultures. Although the transfer of samples to different plates after cell attachment had a lower number of remaining cells, the composite hydrogels reached the same or higher levels of cell viability as the others, over the culture days. Although researchers apply different cell culture protocols, as a result of experience gained in this work, it would be more beneficial to carry out cell attachment and cell proliferation assays separately. Sample transfer into another plate after 24 h of cell attachment can lead to a big difference in the remaining cell number on samples, which then may not

be completely comparable with different samples in terms of their cell-proliferation attributes. In addition, it would be more useful and accurate to compare the same cell density in both hydrogels obtained at 37 °C and in freeze-dried hydrogel form in the same conditions. to make a better comparison. It was planned to repeat these experiments with the desired optimal conditions, with shorter term of proliferation assays, with three experiment replicates in the same conditions. However, this was not possible due to the shortening of the project time, and the additional lockdown situations.

### 5.6.2 Cell Attachment/Morphology Observation by Optical Microscopy

The cell morphologies during cell growth and proliferation, and the cell attachments at the edges of the hydrogel samples were observed by optical microscopy imaging at different time intervals during cell culture studies. The images of cultured cells with freeze-dried hydrogels seeded with a density of 20,000 cells/sample, which were taken at day-16 and day-28 of the culture, are given in Figure 5.3. These comparative images of culture plates show the cells and the adjacent samples that seem darker in colour due to the opaqueness of the samples. On day 16 of cell culture imaging, proliferated and spreading cells were observed. Cell culture plates seem much more confluent, with cells spreading across the wells in the well-plate at the 28<sup>th</sup> day of the culture.

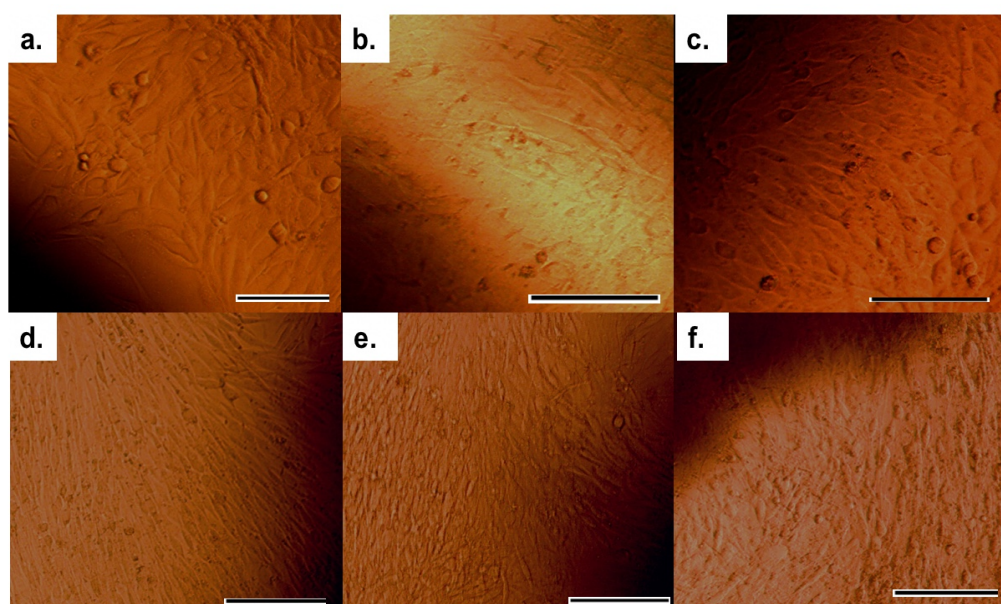


**Figure 5. 3** The cell morphological images by optical microscopy: 28-days of cell culture study performed via seeding 20,000 cell per sample on freeze-dried hydrogels at different intervals: at day-16 (a., b., and c. for CI (CS), CII (CS.0.1HA), SI (CS.0.1HA.0.005Hep) samples, respectively); and day-28 (d., e and f. for CI, CII, SI, respectively). (Scale bars are 0.2 mm)

The imaging of control samples which were incubated in sole growth media without cells gave the opportunity to observe the hydrogel morphologies under optical microscopy. Figure 5.4 demonstrates the comparative images of sample groups in the freeze-dried forms of hydrogels. The long chain polymer matrix of CS making a porous network was observed. The shiny HA crystal particles attached onto the polymer matrix were noticeable in the image of the SIII (CS.0.1HA.0.025Hep) composite sample in Figure 5.4.f. Since the samples were incubated in media for 28 days, some degradation was observed, which could be seen at the edges of the samples as in Figure 5.4.c.

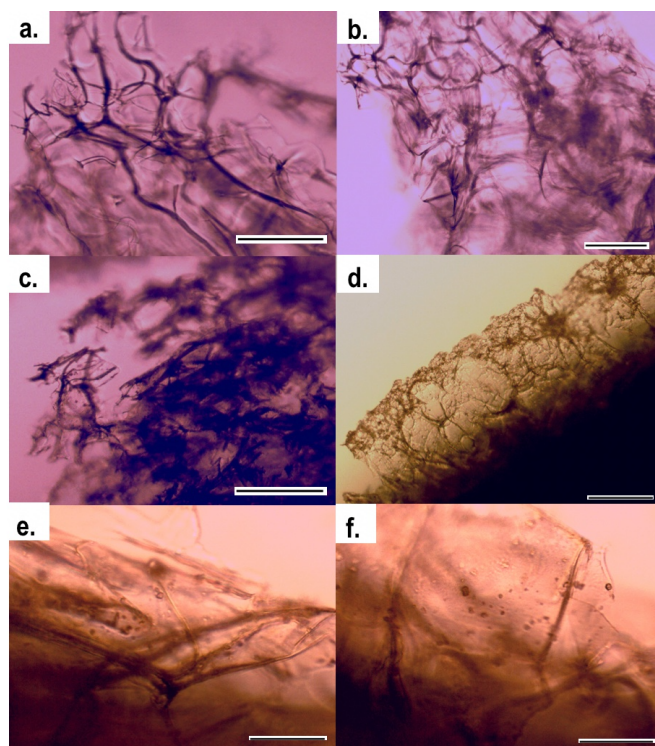


**Figure 5.4** The appearance of freeze-dried hydrogel samples incubated in media without cells for 28-days **a-b.**, and **c-d** show CI (CS) and CII (CS.0.1HA) samples, respectively and **e-f** SIII (CS.0.1HA.0.025Hep) samples. (Scale bars: **(a-d)**. 0.2 mm, and **(e-f)**. 0.05 mm)

Due to the transparency of the sole CS sample (CI), it allowed imaging of cell attachments on the hydrogel samples. The images of hydrogels that were obtained upon incubation at 37 °C and seeded with 50,000 cells/sample at different culture days are given at different magnifications in Figure 5.5. A low magnification image (x4) shows dispersion of cells on the sample, which is shown on Figure 5.5.a. The cell attachment on samples and the proliferating and spreading of cells across the sample can be seen more explicitly in Figure 5.5.b and Figure 5.5.c. In other images (e-h), the darker fields hosting the samples and the good cell attachments on the hydrogels can be easily observed, especially in Figure 5.5.e.

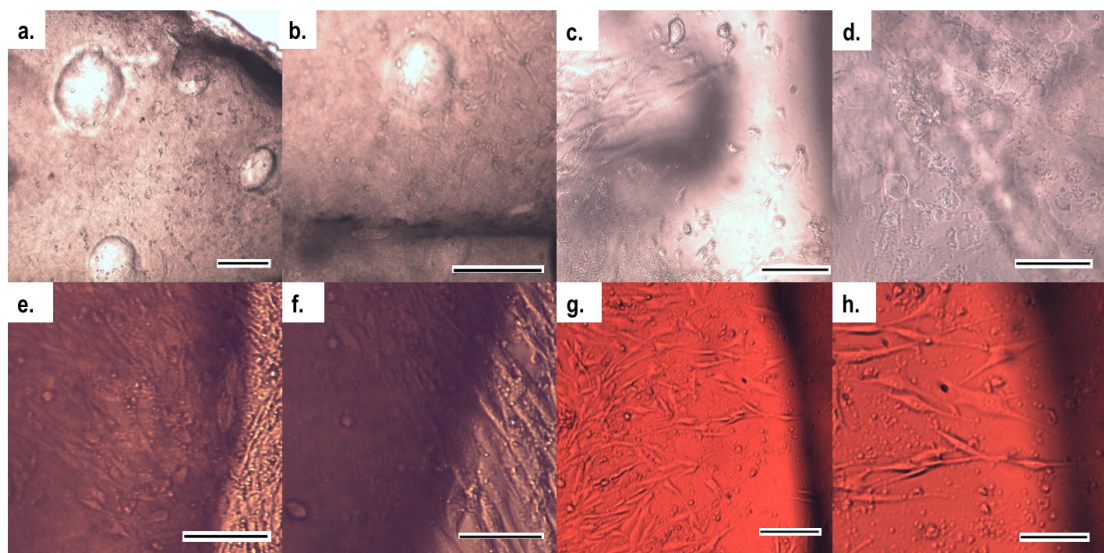


**Figure 5.5** Cellular morphology images by optical microscopy during cell culture studies. The images belong to CI, sole CS sample in hydrogel form obtained upon incubation at 37 °C and seeded by 50,000 cell per specimen. The images **a-d** show sample surfaces with attached cells in transparent CS hydrogels at Day-28 of culture after cell fixation. The other images taken at **e-f**. Day 15 and **g-h** Day 21 show the cell attachments on the circular sample edges or adjacent to the samples. (Scale bars: **a**. 0.4 mm, **b, e, and g**. 0.2 mm, **c-d and h**. 0.1 mm and **f**. 0.05 mm)

In addition, the cell attachment to composite hydrogel specimens CII (CS.0.1HA) is given in Figure 5.6. The spherical cell nuclei were seen in cell-cultures with the CII sample at day 10 in Figure 5.6.a., and the good spreading of long cell morphologies were observed in other images at different time intervals.

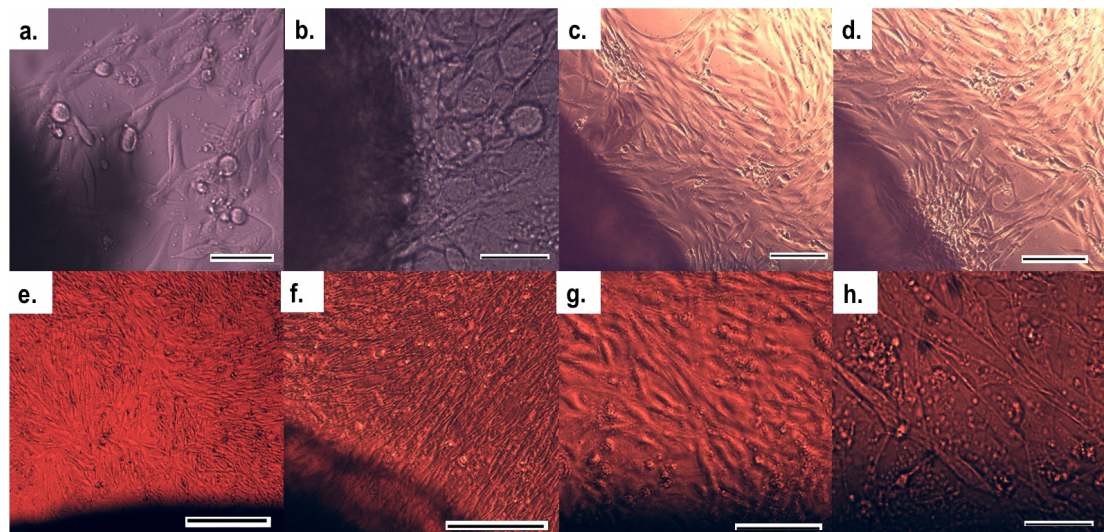


**Figure 5.6** Cellular morphology images by optical microscopy in cell culture studies performed with samples in hydrogel form obtained upon incubation at 37 °C: 28 days of cell culture study performed via seeding of 50,000 cells per hydrogel specimen of the CII (CS/HA) sample at different intervals: **a-b**. Day-10, **c-d**. Day-15 and **e-h**. Day-21 (The darker areas at the corners of images belong to samples and the brighter areas with attached adjacent cells are in the wells of the well-plate). (Scale bars: **(a and g)**. 0.1 mm, **(b and h)**. 0.05 mm, **(c-d and f)**. 0.2 mm and **e**. 0.4 mm)

The images of the composite SI (CS.HA.0.005Hep) sample during cell culture are compared in Figure 5.7. The edge of a shiny control sample (SI) incubated in media without cells is shown in Figure 5.7.e. A big cell cluster attached at the edge of the sample and adjacent attached individual cells are seen in Figure 5.7.a and Figure 5.7.b. In addition, at the edge of a sample, a weak hydrogel piece is surrounded with cells inside the sample as well, are seen in Figure 5.7.c. In addition, at the edge of a sample, a weak hydrogel piece is surrounded with cells inside the sample as well, are seen in Figure 5.7.c.

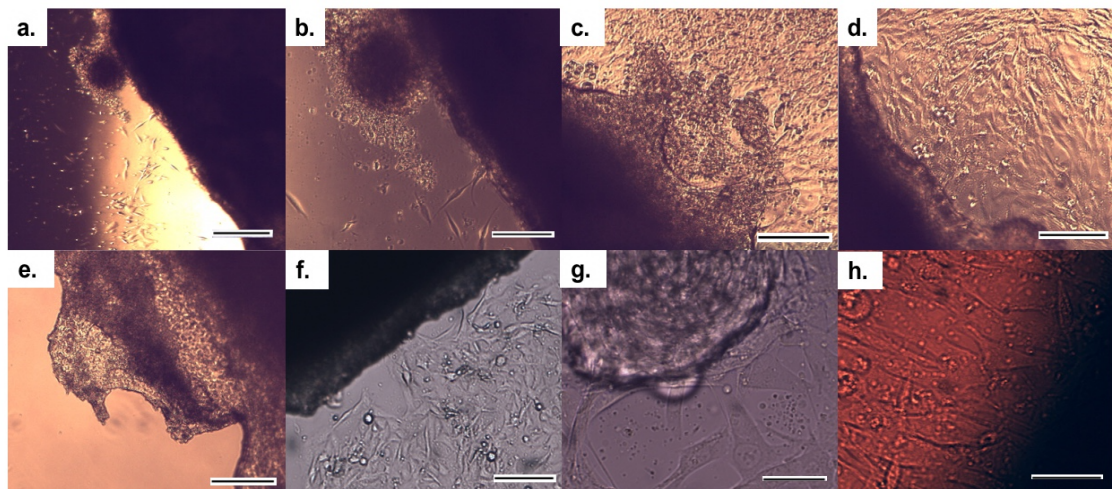


**Figure 5. 7** Cellular morphology images during the cell culture study by optical microscopy for the hydrogel form of the SI (CS.HA.0.005Hep) sample seeded by 50,000 cells/hydrogel and imaged at different intervals: **a-e.** Day-15, **f-h.** Day-21 (The image **e** belongs to the sole SI sample incubated in media without cells while other images belong to the cell seeded samples in the wells of a well-plate). (Scale bars: **a.** 0.4 mm, **(b-f).** 0.2 mm, **(g-h).** 0.05 mm)

### 5.6.3 Calcium and Collagen Deposition during Cell Culture

#### 5.6.3.1 Calcium Deposition Evaluation via Alizarin Red Assay

The calcium and collagen deposition in cell-seeded hydrogels were measured by consecutive AR and SR experiments, following cell fixation at the end of the cell-proliferation experiments in day 28. The standard curve obtained by plotting absorbance measurements of AR standard solutions against their corresponding concentrations at increasing values is given in Figure 5.8.a. The optical density of concentrated solutions (500  $\mu$ g/mL and 1000  $\mu$ g/mL of AR) could not be detected at 405 nm of wavelength, and therefore, were not involved in the standard curve. The AR stain concentration in samples were calculated by correlations from the standard curve equation and shown in Figure 5.8.b. The mean highest amount of AR concentration, which was  $140.5 \pm 27$   $\mu$ g/mL, was found in the CII composite sample (CS.0.1HA). Calcium was already

present in CII and SI samples due to presence of hydroxyapatite. However, it was surprising to see that the sole CS sample (CI) and the SI (CS.HA.0.005Hep) composite hydrogels showed very close values in their AR concentrations.

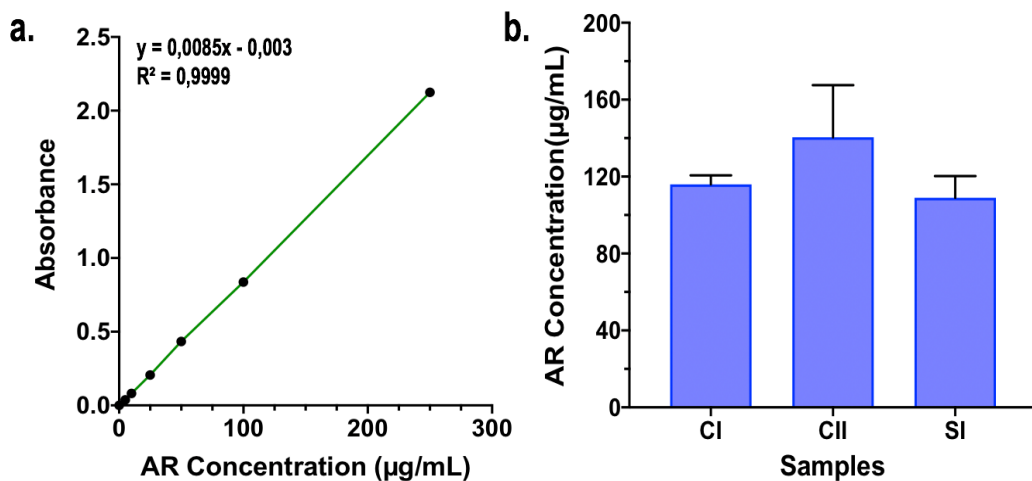


**Figure 5.8** The results of Alizarin Red (AR) assay for calcium deposition in hydrogel specimens: CI (CS), CII (CS/HA), SI (CS.HA.0.005Hep) which were tested after 28-days of cell culture (50,000/hydrogel) **a.** The AR standard curve obtained with plotting absorbance measurements of AR solutions in different concentrations (0, 5, 10, 25, 50, 100 and 250  $\mu\text{g}/\text{mL}$ ) in perchloric acid (5%(w/v)) and **b.** AR concentrations in samples obtained via correlating the absorbance measurements of AR destained solutions (sample immersion media containing AR dye released from samples after staining) with the standard curve equation, which indicates calcium deposition capacities.

As discussed in the previous chapter, the SI sample showed a slightly lower calcium content than the CII sample in EDS analyses, during bioactivity tests in SBF. However, the weight analyses showed that the best mineralization was obtained on the SI sample in weight-based analyses.

The images of hydrogel samples after staining by AR and destaining by perchloric acid are shown in Figure 5.9. After performing AR staining, and absorbance measurements of aliquots of destained solutions, the remaining acid in the well plates caused further swelling of the hydrogels leading to their dissolution, as shown in Figure 5.10. The degradation made them very difficult to handle preventing further SR analyses.

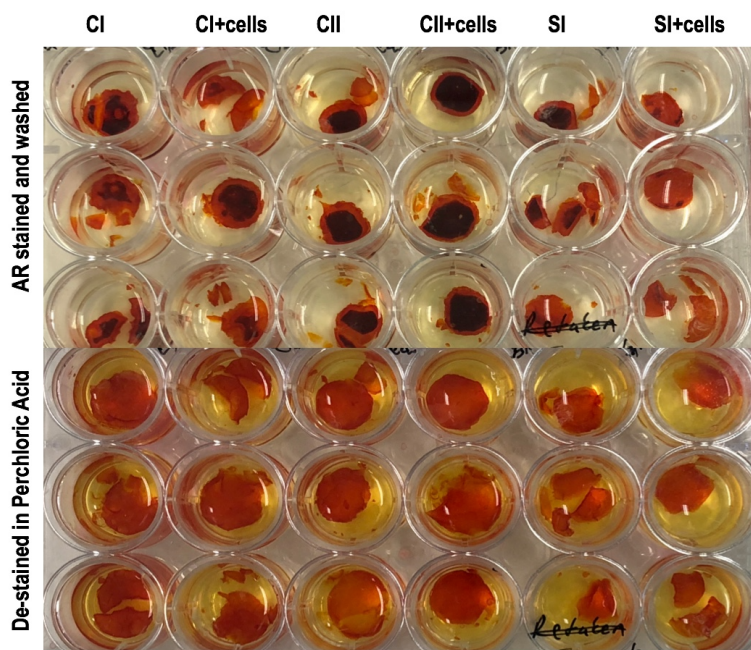


**Figure 5.9** The images during AR staining for calcium measurements of hydrogel specimens (obtained upon gelation at 37 °C): CI (CS), CII (CS/HA), SI (CS.HA.0.005Hep) without cells as control and the same hydrogel groups seeded with cells (50,000 cells per hydrogel) fixed after 28-days of cell culture. The above image was taken after samples were stained by AR and washed to remove unbounded AR stains whereas the image below shows samples destained by perchloric acid which provided dissolution of bound AR in samples to a liquid phase. The swelling occurred in hydrogels due to acidic media.

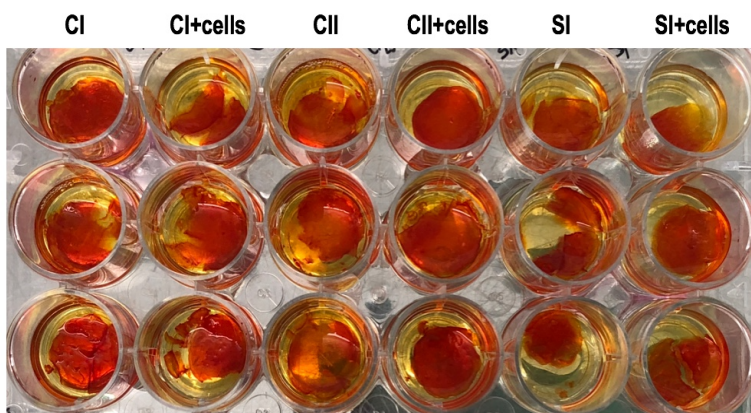


**Figure 5.10** The images of swollen hydrogels after destaining and waiting in acid for long time showing a high amount of swelling leading to weakening and dissolution of these hydrogels in acidic low pH (Test specimens: CI (CS), CII (CS/HA), SI(CS.HA.0.005Hep)). Therefore, these samples could not be used for further SR analyses for collagen determination.

Another individual cell culture experiment was performed with freeze-dried composite SI (CS.HA.0.005Hep) hydrogel with increasing cell concentrations (40,000-85,000). The results of the AR assay performed with this SI sample, with varying cell concentrations, are given in Figure 5.11.

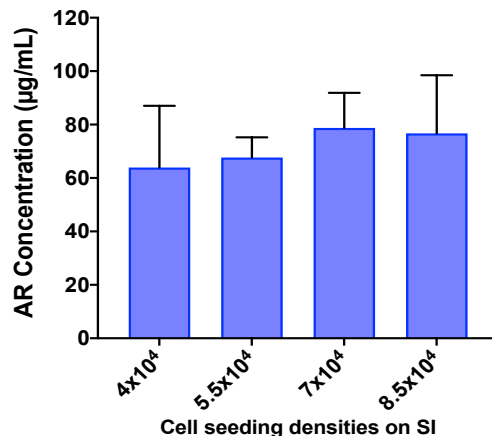


**Figure 5. 11** The correlated AR concentrations in freeze-dried SI (CS.HA.0.005Hep) hydrogels with increasing cell concentrations (40,000-85,000) as an indication of calcium deposition, which were tested after 28-days of culture and cell fixation.

The counted calcium concentrations mostly increased by increasing cell concentration which range between  $63 \pm 23$  and  $77 \pm 22$   $\mu\text{g}/\text{mL}$  for the concentration of 40,000-85,000 cells/sample. However, the calcium concentration slightly decreased in the sample having 85,000 cells/hydrogel concentration, and a negative mean value was obtained for the samples seeded with 100,000 cells that was not plotted. The images of freeze-dried hydrogels taken after staining by AR solution and destaining by perchloric acid are shown in Figure 5.12.

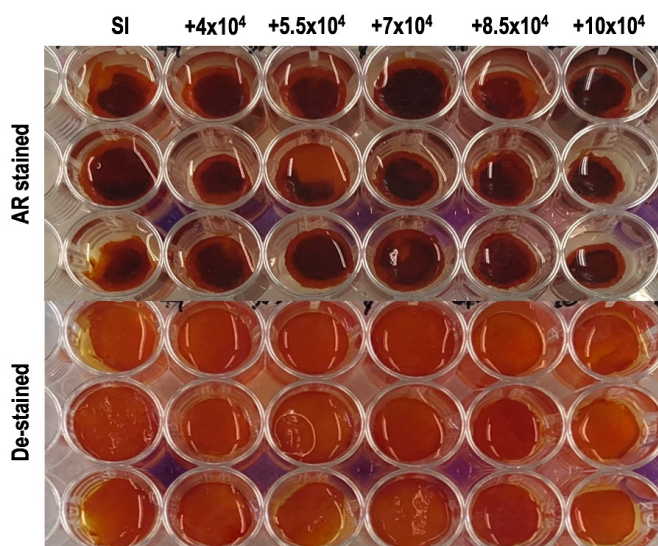


**Figure 5. 12** The images during AR staining for calcium measurements with a composite hydrogel SI (CS.HA.0.005Hep) in freeze-dried form. The SI sample without cells is shown as a control. Increasing cell concentrations (40,000-100,000) were tested by AR assay after 28-days of culture and cell fixation in a 48 well-plate. The AR stained and the samples destained by perchloric acid leading to swelling of the hydrogels are at the top and bottom halves of the image, respectively.

### 5.6.3.2 The Collagen Deposition Evaluation by Sirius Red Assay

The standard curve obtained from the absorbance measurements of standard SR solutions at varying concentrations is shown in Figure 5.13.a. The SR concentration in freeze-dried SI hydrogel seeded with cells at gradually increasing concentrations (40,000-85,000 cells/sample) are counted by correlation with the standard curve equation and plotted in Figure 5.13.b. In addition, the samples during the SR assay steps are demonstrated in Figure 5.14. Some absorbance readings were out of range or gave negative values during the measurements of destained solution of samples. The results given in Figure 5.13.b were obtained from the means of only the obtained positive absorbance values with their standard deviations. Therefore, these results may not indicate the real mean values, but they might show approximate values. The obtained negative values of SR concentrations can result from an insufficient destaining step to remove all bound SR stain in samples since most samples seemed still dark in colour after treated with the destaining solution (0.2M (NaOH:MeOH)). The images of samples during SR assay are presented with all the different steps in Figure 5.14. The quantitative results for collagen deposition in hydrogel samples may not be very conclusive and need repetition. However, this could not be performed due to time constraints on the project completion time and the unforeseen lockdown period.

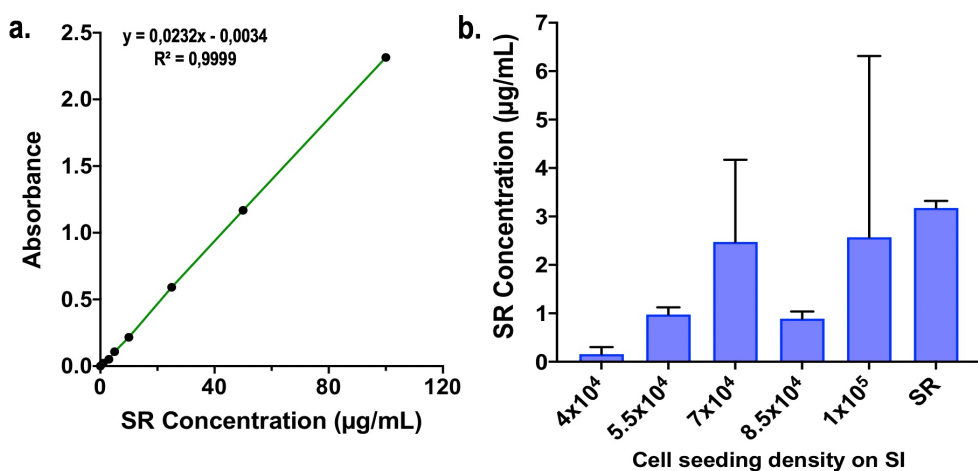


**Figure 5. 13** The results of the Sirius Red (SR) assay for collagen deposition in freeze-dried hydrogel, of the composite SI specimen (CS/HA.0.005Hep) with increasing cell concentrations (40,000-100,000) tested after 28-days of cell culture, and cell fixation. **a.** The SR standard curve obtained by plotting absorbance measurements of SR solutions with different concentrations (0, 1, 2.5, 5, 10, 25, 50, and 100  $\mu\text{g/mL}$  in picric acid (1 %(w/v))) **b.** The correlated SR concentrations in freeze-dried hydrogels as an indication of calcium deposition and the concentrated SR solution as a control.

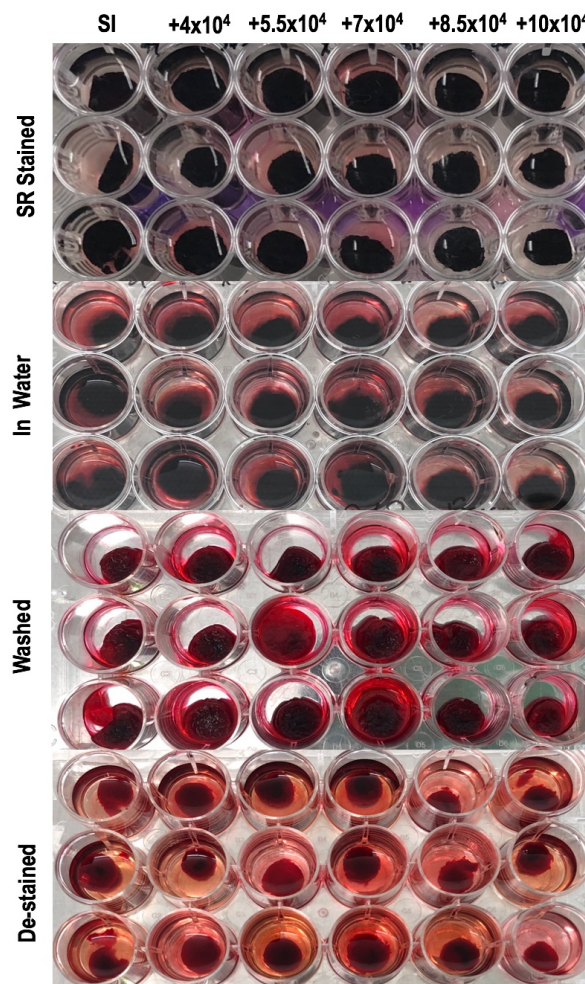


**Figure 5. 14** The images during SR staining for collagen deposition assay with a composite hydrogel SI (CS.HA.0.005Hep) in freeze-dried form. SI sample without cells shown as control and with increasing cell concentrations (40,000-100,000) were stained by SR assay after 28-days of culture and cell fixation. The SR staining, washing and destaining step of samples by a basic 0.2M (NaOH:MeOH) solution leading to shrinkage of hydrogels (the bottom image) are demonstrated.

#### 5.6.4 The Angiogenesis Studies by CAM Assay

The effects of injectable hydrogels on formation of new micro vessels (angiogenesis) were investigated by Chorioallantoic Membrane (CAM) assay on chick embryos. The effect of different hydrogel compositions in the absence or with varying concentrations of Hep were investigated. The initial and modified hydrogels were tested separately.

The angiogenesis results of initial hydrogels counted by the vascular index method was plotted for different sample groups including CII (CS.HA), SI (CS.HA.0.005Hep) and SIII (CS.HA.0.025Hep) in Figure 5.15. The SII (CS.HA.0.025Hep) sample with the

middle concentration of Hep was not involved in vascular index counting due to the very limited sample images obtained being insufficient for the comparison.

According to results with the initial hydrogels, the SI (CS.HA.0.005Hep) sample, having the lowest Hep concentration (0.120mg/mL), was found to be the best in pro-angiogenic response; slightly better than the CII (CS.HA) sample without Hep. In statistical analyses using an un-paired t-test, the difference between CII and SI was not significant ( $p: 0.3482$ ) while that of SI and SIII was significant in difference ( $p: 0.0408$ ). However, One-way ANOVA showed no significant difference between all samples and adjusted  $p$  values for CII&SI, CII&SIII, and SI&SIII, which were 0.5918, 0.4035 and 0.0837, respectively.

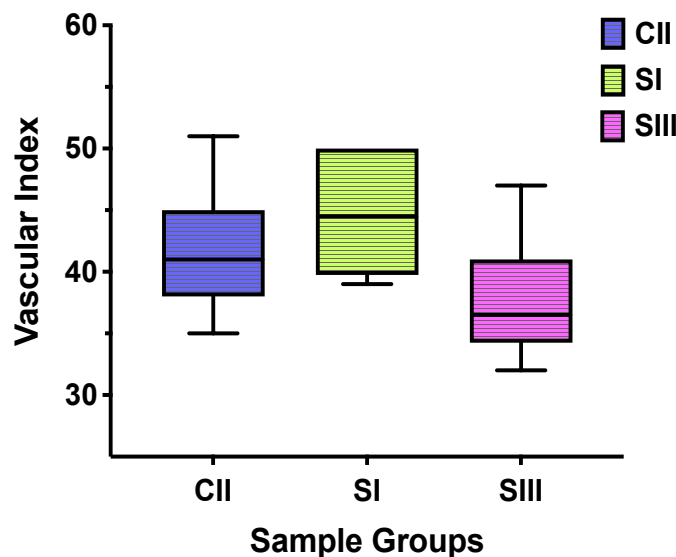


**Figure 5. 15** The vascular index counted from CAM images taken at Day-14 of chick embryos' incubation (which is also the sacrificing day) for each sample group as the Mean  $\pm$  SD for 6 specimens with tested initial hydrogels: CII (CS.HA) without Hep, SI (CS.HA.0.005Hep) (0.12  $\mu$ g/mL Hep in hydrogel solution), and SIII (CS.HA.0.025Hep) (0.60  $\mu$ g/mL Hep).

The comparison of CII (CS.HA) without Hep and SI (CS.HA.0.005Hep)-(0.120 mg/mL Hep) samples are shown by representative images demonstrated in three different versions for two representative samples in a group are shown in Figure 5.16.a and Figure 5.16.b, respectively.

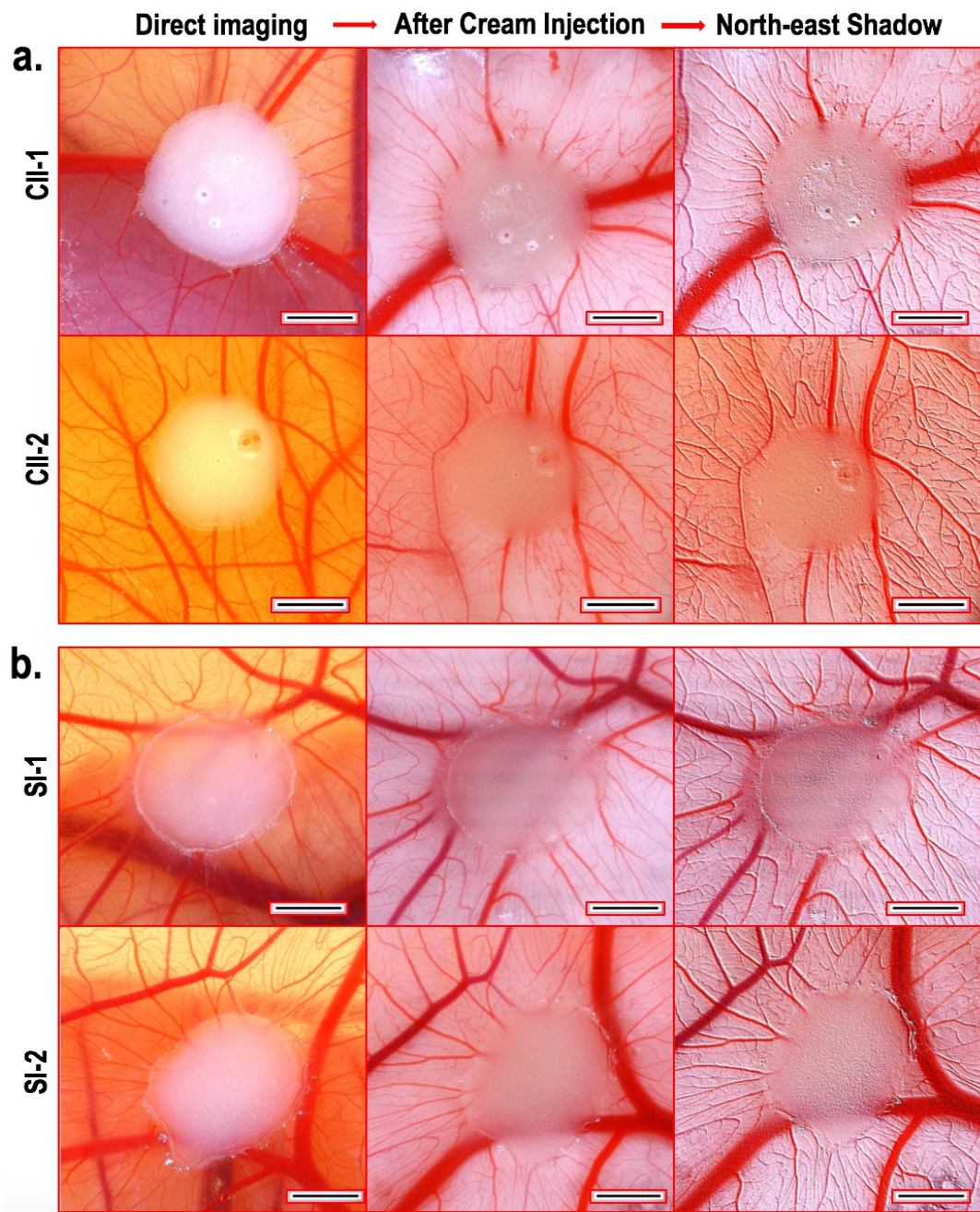


**Figure 5.16** The comparative CAM images taken at Day-14 (the sacrificing day of chick embryos) with tested initial hydrogels: two representative sample images from **a.** CII (CS.HA) and **b.** SI (CS.HA.0.005Hep) sample groups. The three images in rows from left to right show, respectively: direct imaging of CAM, after white cream injection underneath the CAM as a contrast for red blood vessels, and the processed versions of the middle images by North-east shadow in ImageJ Software (All scale bars are 2 mm).

The day 14 images show newly forming blood vessels shaping and growing towards and branching out of the circular hydrogel samples were very explicit in both groups, which was slightly better in the SI sample group. The comparisons of other compositions with higher Hep concentrations: SII (CS.HA.0.015Hep) - (0.36 mg/mL)

and SIII (CS.HA.0.025Hep) - (0.60 mg/mL) are given in Figure 5.17.a and Figure 5.17.b, respectively. Although the samples with higher concentrations also indicated angiogenesis to some extent, this varied from sample to sample, which can be seen in the images.

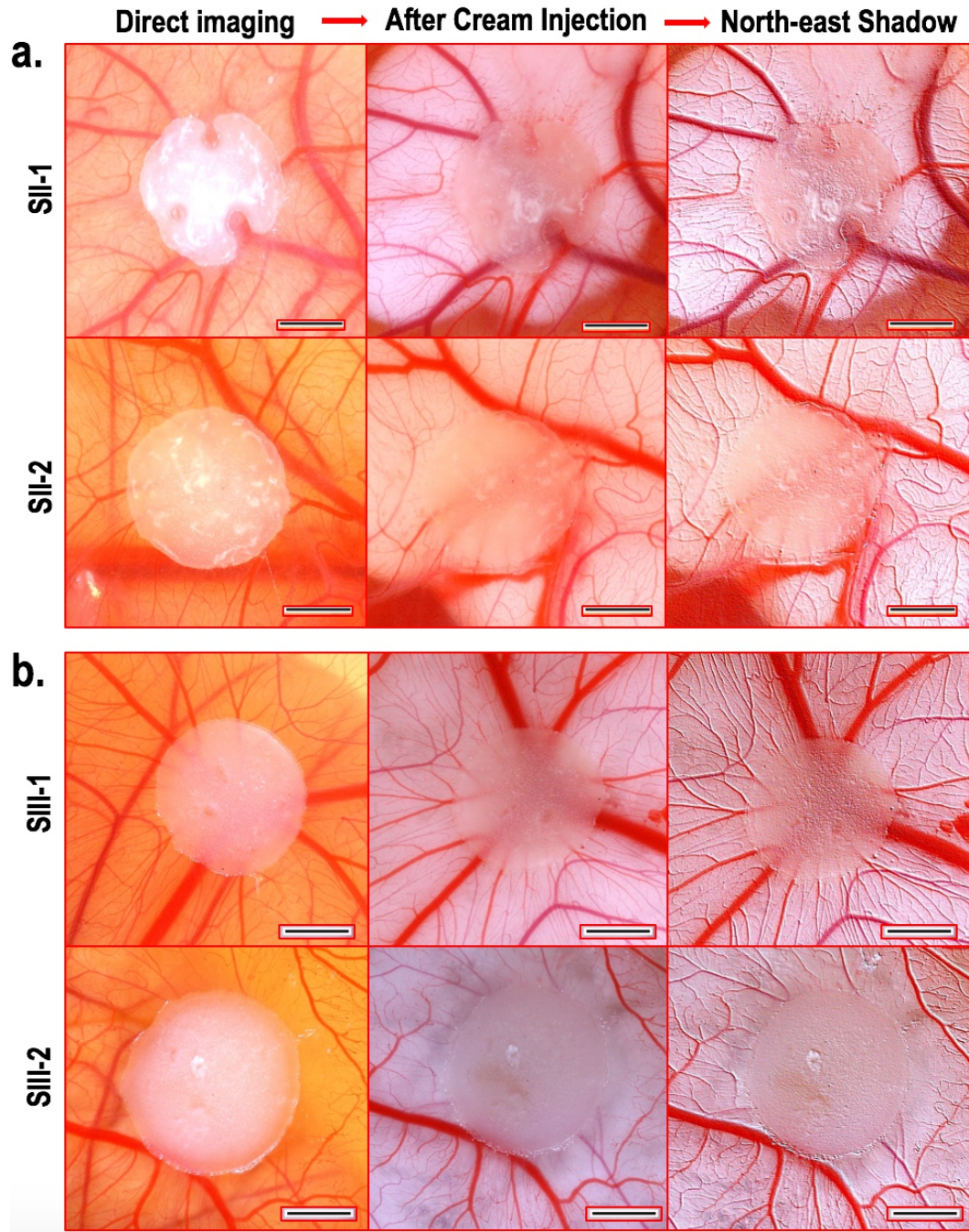


**Figure 5. 17** The comparative CAM images taken at Day 14 (the sacrificing day of chick embryos) with tested initial hydrogels: two representative sample images from **a.** SII (CS.HA.0.015Hep) and **b.** SIII (CS.HA.0.025Hep) sample groups. The three images at rows from left to right show, respectively: direct imaging of CAM, after white cream injection underneath the CAM as a contrast for red blood vessels, and the processed versions of the middle images by North-east shadow in ImageJ Software (All scale bars are 2 mm).

A proangiogenic response was seen in even the control samples without Hep. It was presumed that this could be contributed to by HA since the effects of bioceramics on angiogenesis was also reported (Zhai et al., 2012, 2013; Malhotra & Habibovic, 2016). Therefore, in the following experiments it was decided to involve the sole CS sample as a control and simple filter paper as another control. In addition, since the SI sample performed better in angiogenic response than SIII, in the subsequent experiments, only the SI sample and the additional lower Hep concentration (0.03 mg/mL) S0 (CS.HA.0.0015Hep) sample have been involved in CAM analyses of modified hydrogels.

The investigation of angiogenesis with modified hydrogels involved the CI, CII, SI and S0 hydrogel samples as well as filter paper as another control. The comparative vascular index count is given in Figure 5.18. The highest vascular index of  $45.7 \pm 4.7$  belongs to the composite S0 specimen with 0.03 mg/mL Hep. This was significantly higher than those counted for CI sole CS (p:0.0298) sample and filter paper (F.p.) (p:0.0026). Having higher variation between samples, CII and SI samples showed closer mean values with S0, and the difference between S0 and SI was not found statistically significant (p:0.2902).

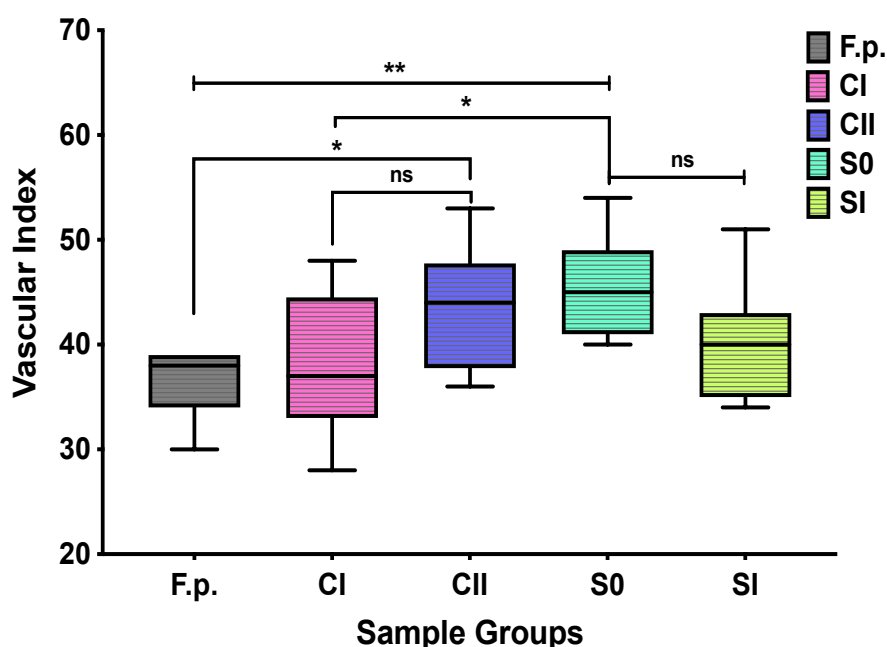


**Figure 5. 18** The vascular index counted from CAM images taken at Day-14 as the Mean  $\pm$  SD from 7-11 specimens for each tested modified hydrogel group: CI (CS) and CII (CS.HA) without Hep; and S0 (CS.HA.0.0015Hep) (0.03  $\mu$ g/mL Hep) and SI (CS.HA.0.005Hep) (0.12  $\mu$ g/mL Hep) as well as Filter Paper (F.p.). The adjusted p-values counted by one-way ANOVA method are CI&S0(\*): 0.0298, F.p.&CII(\*):0.0287, F.p.&S0 (\*\*): 0.0026, S0&SI(ns):0.2902.

Although some proangiogenic response was observed with the CI sample, it was not statistically significant with that of filter paper in vascular index ( $p: 0.9449$ ). However, the mean vascular index with the CII sample was significantly higher than filter paper ( $p: 0.0287$ ).

The experiments with filter paper also showed a response on CAM that to some extent could also be attributed to the PBS used to wet samples before implantation. It would be better to use filter papers without any treatments. The representative images of CAM experiments with filter paper implants are shown in Figure 5.19.

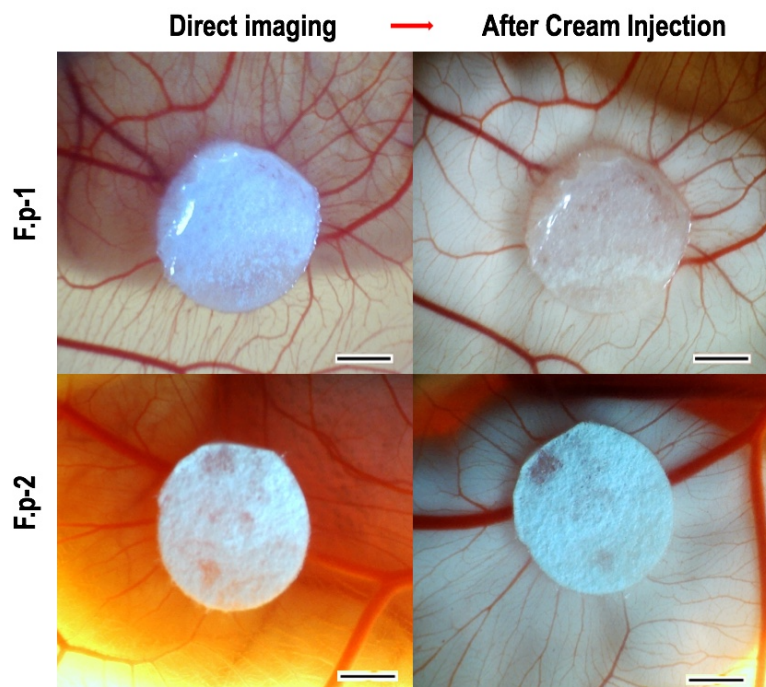


**Figure 5. 19** The CAM images taken at Day-14 of filter paper (F.p.) implants ( $\varnothing: 5.5$  mm) applied in Day-7 after being wet by PBS, which was used as negative control in comparison to hydrogels. The images of two representative samples are given in two rows including direct imaging of CAM (at left) and after white cream injection underneath the CAM as contrast to blood vessels (at right), (All scale bars are 2 mm).

The CAM images with the sole CS sample (CI) and CII with HA (CS.0.1HA) which are modified hydrogels, are compared in Figure 5.20.a and Figure 5.20.b, respectively. Although some proangiogenic response was seen with the sole CS hydrogel (CI), it was less in comparison to the CII sample with HA.

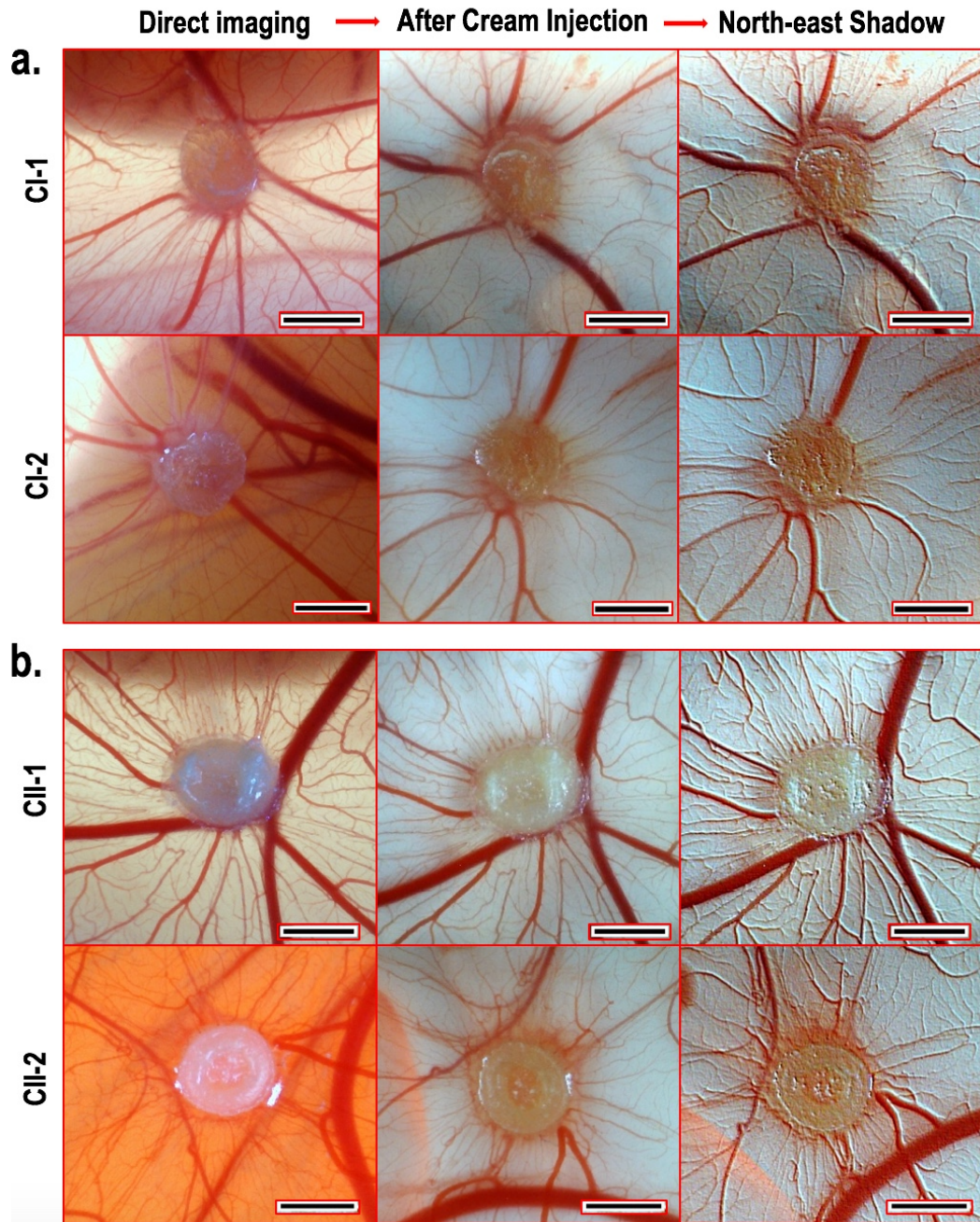


**Figure 5.20** The comparative CAM images taken at Day-14 (the sacrificing day of chick embryos) with tested modified hydrogels: two representative sample images from **a.** CI (CS) and **b.** CII (CS.HA) sample groups. The three images at rows from left to right showing, respectively: direct imaging of CAM, after white cream injection underneath the CAM as a contrast for red blood vessels, and the processed versions of the middle images by North-east shadow in ImageJ Software (All scale bars are 2 mm).

The comparative CAM images of composite hydrogels (CS/HA/Hep): SI and S0 samples having 0.12 and 0.03 mg/mL Hep, respectively are seen in Figure 5.21a, and Figure 5.21.b, respectively. Both samples seem to have good proangiogenic response contributing to the formation of a good number of new vessels on CAM. In addition,

particularly in the S0 sample, the maturation of blood vessels, as well as the presence of a good number of micro-vessels, was seen in most sample images. Therefore, the S0 (CS.HA.0.0015Hep) hydrogel composition comprising a small amount of Hep (0.03 mg/mL) showing the best proangiogenic response and leading in blood vessel maturation was chosen as the optimal composition among all the samples.

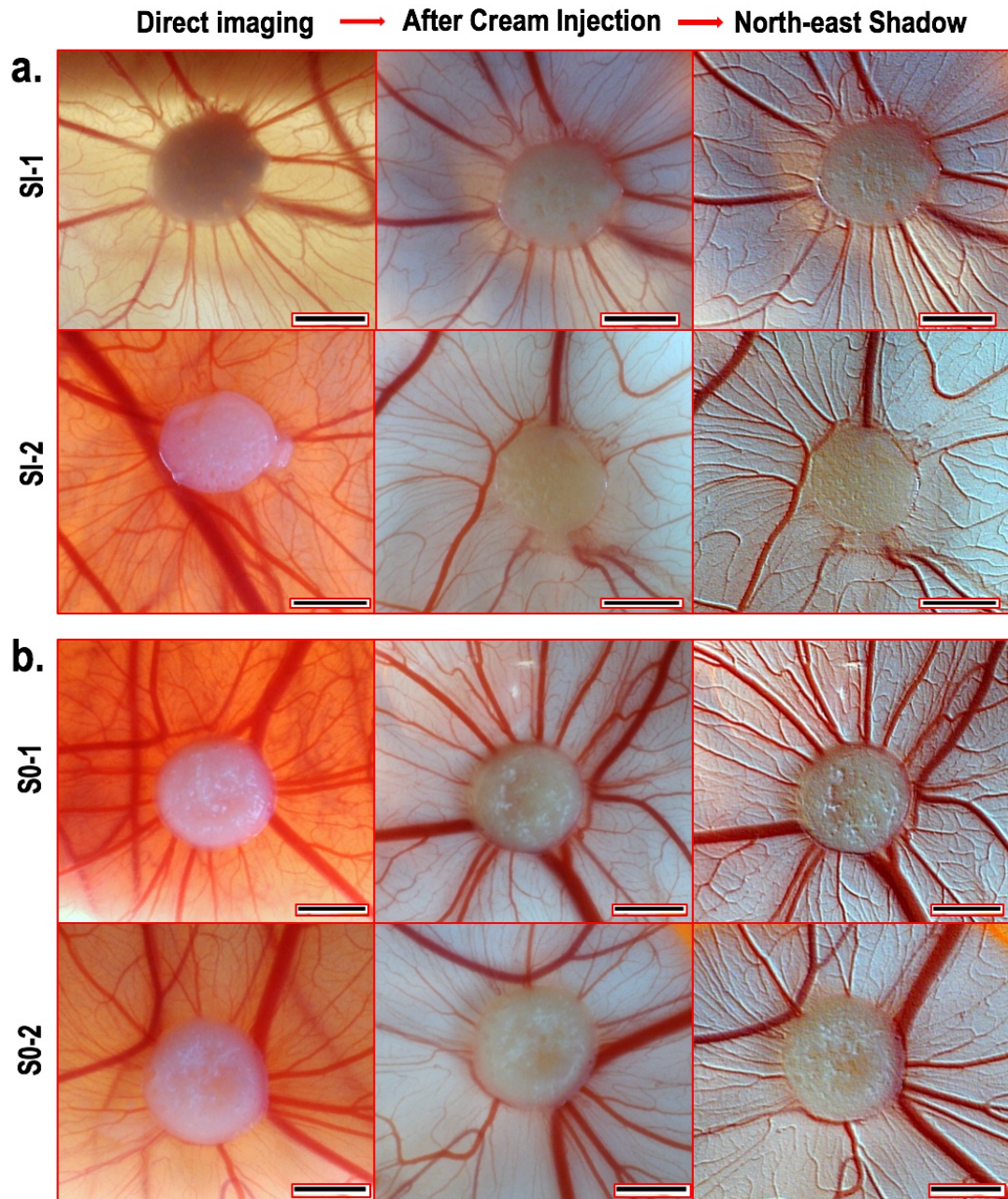


**Figure 5.21** The comparative CAM images taken at Day-14 (the sacrificing day of chick embryos) with tested modified hydrogels: two representative sample images from **a.** SI (CS.HA.0.005Hep) and **b.** S0 (CS.HA.0.0015Hep) sample groups. The three images at rows from left to right show, respectively: direct imaging of CAM, after white cream injection underneath the CAM as a contrast for red blood vessels, and the processed versions of the middle images by North-east shadow in ImageJ Software (All scale bars are 2 mm).

#### 5.6.4.1 Histology Analyses of Hydrogels Tested in CAM Assay

The observation of CAM tissue-hydrogel interactions, density and morphology of blood vessels during CAM development were investigated by histology analyses, which were performed with the initial hydrogels. Hydrogels become very fragile upon snap freezing by liquid N<sub>2</sub>, leading to breakage of the samples during sectioning. Therefore, it was hard to obtain whole section images. However, histology images still provided information regarding the structure of growing blood vessels in some regions and tissue-sample interactions. Figure 5.22 shows horizontal tissue sections of CAM with the CII hydrogel sample.

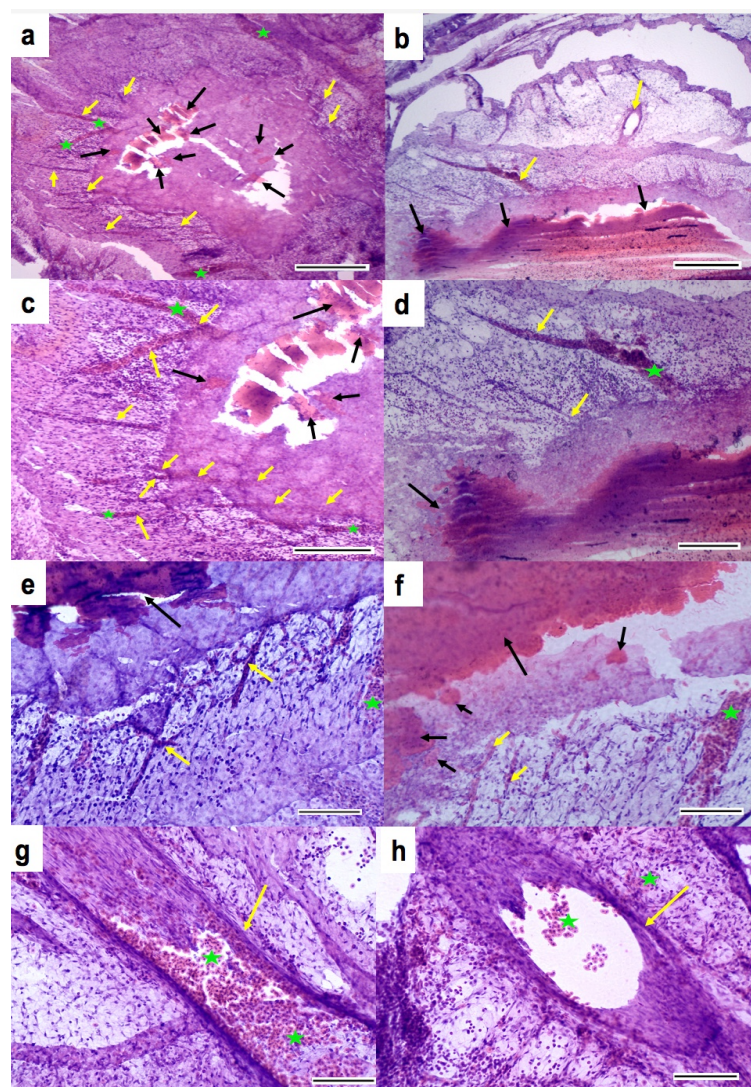


**Figure 5. 22** The histology images of Hydrogel- CAM tissue sections (horizontal) after H&E staining, obtained via optical microscope imaging. The images belong to one initial hydrogel specimen CII (CS.0.1HA). (Scale bars: (a- b). 0.4 mm; (c-d). 0.2 mm, (e-f). 0.1 mm, respectively. Green stars indicate blood cells while yellow and black arrows show the blood vessels, and hydrogel samples, respectively).

The circular hydrogels which were integrated with CAM tissue and growing blood vessels at the edges are seen in these images. Tissues growing into sample sites showed good interaction of hydrogels with CAM tissues. In addition, the vertical sections of one CII sample with attached CAM tissue is demonstrated in Figure 5.23. This sample showed good attachment with adjacent CAM tissue, which contained big round blood vessels filled with many red blood cells.

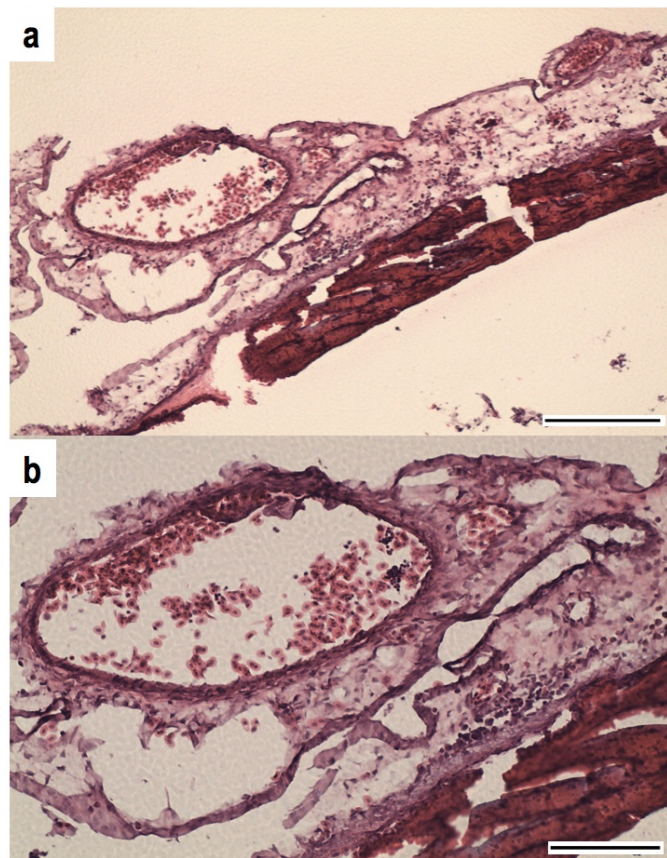


**Figure 5. 23** The histology image of CAM sample sectioned in vertical direction after H&E staining for an initial hydrogel specimen CII (CS.0.1HA). (Scale bars: **a.** 0.2 mm and **b.** 0.1 mm)

The histology images belonging to an SI (CS.HA.0.005Hep) composite sample containing 0.12 mg/mL Hep are shown in Figure 5.24. Although this sample was exposed to breakage during freezing process, the obtained images still show excellent tissue-hydrogel interactions in which samples were totally integrated with tissue possessing many blood vessels with blood cells.

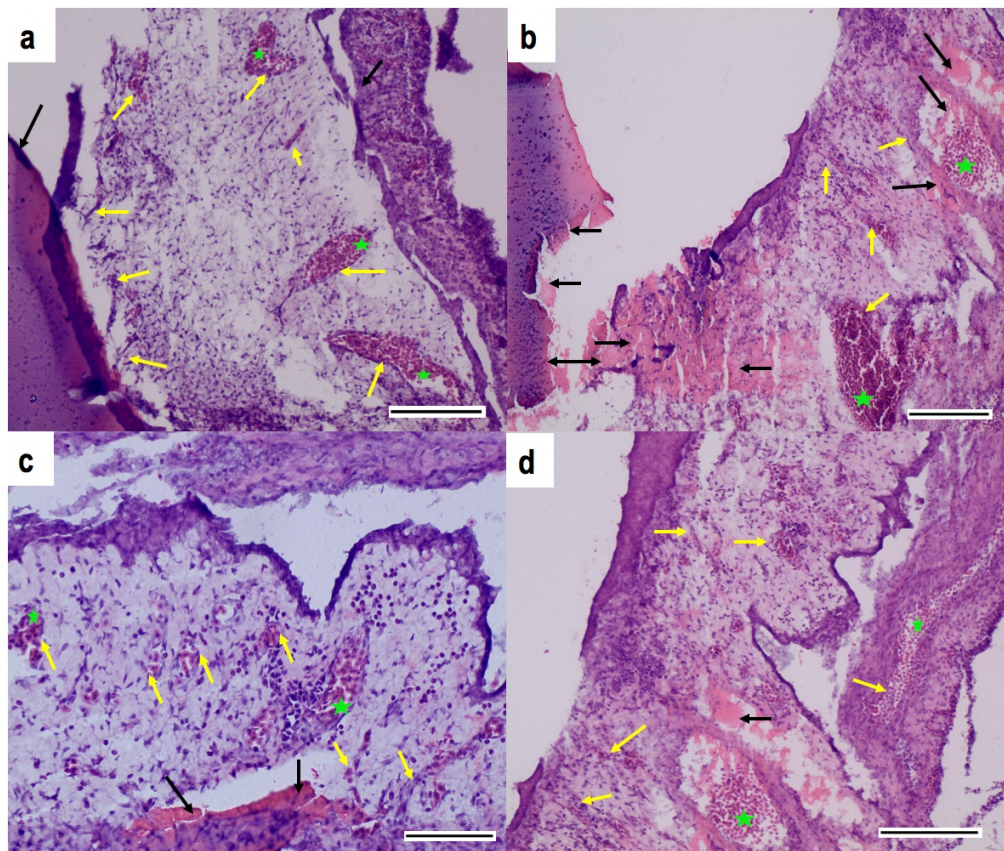


**Figure 5. 24** The histology image of the composite initial hydrogel specimen, SI (CS.HA.0.005Hep)-(0.12 mg/mL Hep) retrieved from CAM. (Scale bars: (a-b and d). 0.2 mm and c. 0.1 mm, respectively. The green stars indicate blood cells while yellow and black arrows show the blood vessels, and hydrogel samples, respectively).

In addition, histology images of an SIII (CS.HA.0.025Hep) composite hydrogel with 0.6 mg/mL Hep is given in Figure 5.25. Some micro vessels in darker purple colour at tissue adjacent to the sample growing in from different directions, and a sample piece surrounded by the tissue, can be seen in Figure 5.25.c. Blood vessels with different shapes and filled with blood cells are seen, especially in Figure 5.25.a and Figure 5.25.b.

The histology sectioning images of another sample; SIII are presented in Figure 5.26. The difference in the lighting of these images was due to using a different optical microscope (EVOS<sup>TM</sup> XL, Thermo Fisher Scientific Inc, Madison, WI, USA) after a university change. The well-integrated CAM tissue at the sample edges (Figure 5.26 (a and b)) and the bulk of the sample totally interacting with CAM tissue with long thin blood vessels at certain vicinities are seen in Figure 5.26 (c and d).

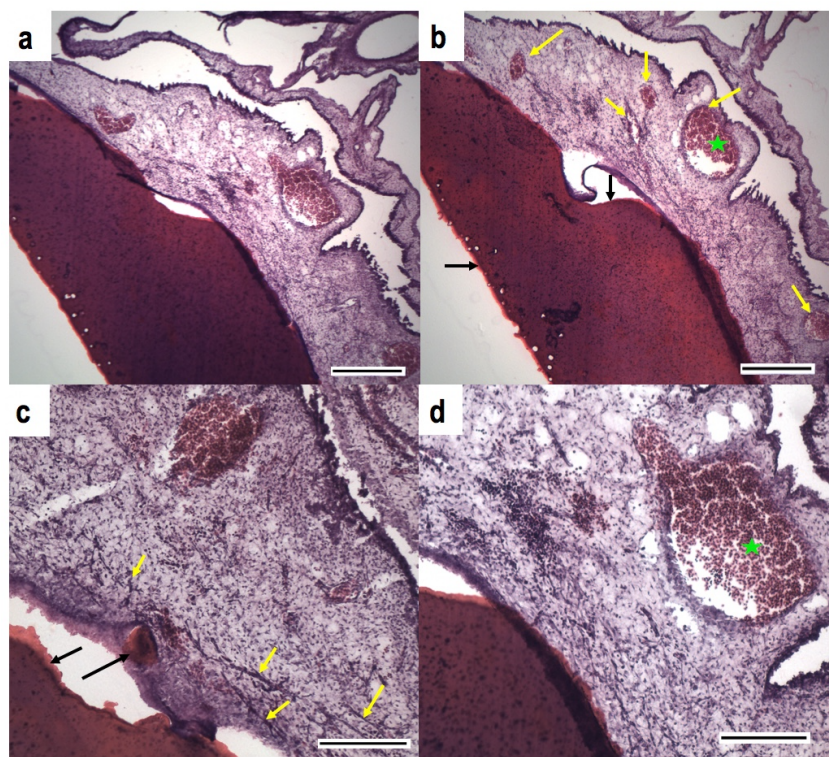


**Figure 5. 25** The histology image of the composite initial hydrogel specimen, SIII (CS.HA.0.025Hep)-(0.60 mg/mL Hep) retrieved from CAM. (Scale bars: (a-b). 0.4 mm and (c-d). 0.2 mm. The green stars indicate blood cells while yellow and black arrows show the blood vessels, and hydrogel samples, respectively).

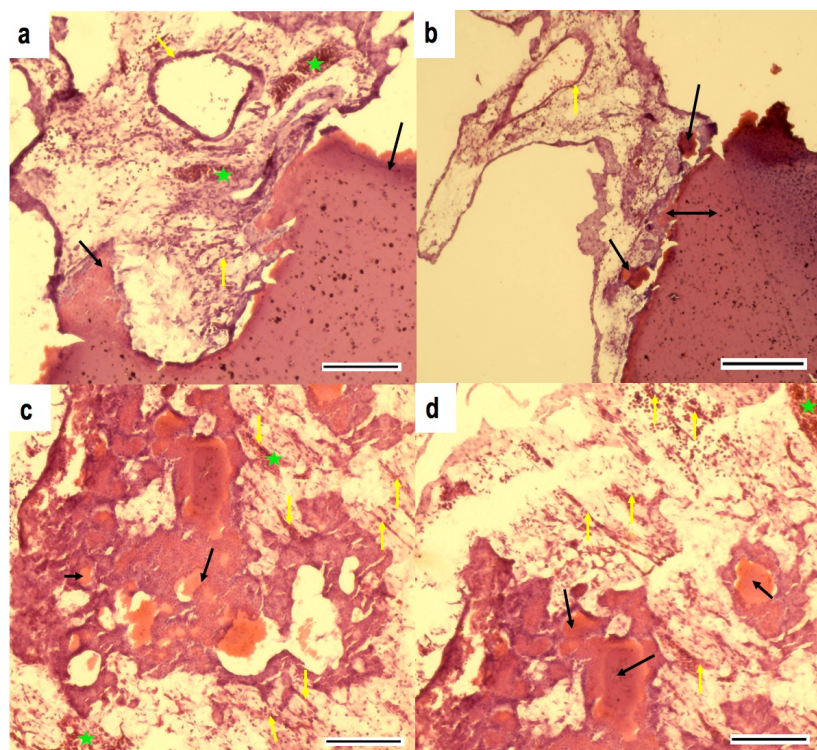


**Figure 5. 26** The histology images of the composite initial hydrogel specimen, SIII (CS.HA.0.025Hep)-(0.60 µg/mL Hep) retrieved from CAM, given with 0.2 mm scale bars (the green stars indicate blood cells while yellow and black arrows show the blood vessels, and hydrogel samples, respectively).

## 5.7 Discussion

In cell culture studies, hydrogel compositions did not show any cytotoxicity effect on the cells, and cells gradually proliferated during the culturing of up to 28 days. The measured fluorescent values for cell proliferation were similar to those reported for a short-term biocompatibility study of CS-HA based freeze-gelated scaffolds with MG-63 cell lines (Qasim et al., 2015). In the first experiment group, slower initial cell growth was observed in culture due to the lower cell (MG-63) seeding density (2000 cell/sample in 2 ml media). The cell seeding density of 20,000 cells per hydrogel ( $\varnothing:8$  mm x 3 mm) cultured in 24-well plate by using 1 mL growth media was found to be the optimal seeding condition as was found in the second experiment. In this experiment, the initial cell attachment after 24 h was very similar in samples, and composite hydrogels showed better cell viability than the sole CS sample (CI) in progressing cultures up to 14-days. In third experiment, performed with hydrogels produced via gelation at 37 °C and seeded with a comparatively higher cell count (50,000 cell/hydrogel), the highest initial cell attachment after 24 h was with the sole CS (CI) sample which can be associated with more open pores in the sole polymer matrix leading to better attachment of cells at high seeding density. Although with initial low cell attachment and with less remaining cells after 24 h, the composite hydrogels including SI (CS.0.1HA.0.005Hep)-(0.12 mg/mL- Hep) showed very regular cell proliferation and showed the best cell viability values at day-14 and day-28 of the culture. The beneficial effect of HA and Hep at increasing cell compatibility is reported by different studies. The effect of HA in contributing to absorption of serum proteins including fibronectins and vitronectins leading to the attachment of integrins and hence providing attachment of osteoblast precursor cells has been reported (Kilpadi et al., 2001). In addition, better adhesion and proliferation of osteoblast cells with increasing HA concentration in injectable CS-HA and in sodium tripolyphosphate (TPP) scaffolds was reported (Uswatta et al., 2016). Also, the addition of Hep in silk fibroin/collagen scaffolds has been reported to enhance cell viability (Lu et al., 2007). The Hep coated alginate/polyacrylamide hydrogels used as artificial veins promoted adhesion of Human Umbilical Vein Endothelial Cells (HUVECs), which was due to the fibronectin binding capacity of Hep which attracted the endothelial cells (Deng et al., 2017). In this study, the cell viability of samples varied between test intervals, and the cell proliferation performance with all compositions were similar. This can be due to the low

concentrations of HA and Hep used, which could not show profound effects. The highest ratio of calcium deposition with hydrogels after 4 weeks of cell culture was in the CII sample (CS.0.1HA) while respectively lower and similar concentration values were obtained for CI (CS) and SI (CS.0.1HA.0.005Hep) specimens. The collagen deposition assays were not conclusive.

The angiogenesis studies with CAM assay showed that composite hydrogels (CS/HA/Hep) with the low Hep concentration S0 (0.03 mg/mL) showed the best proangiogenic response which was significantly higher than sole CS (CI) sample and filter paper as controls. This composition (S0) has led to not only formation of new micro vessels but also showed an impact on maturation of blood vessel that could be very promising in bone tissue engineering to promote angiogenesis. The injectable hydrogels from CII composition (CS-HA) which was better than that of the sole CS (CI) sample (although not statistically higher) also showed good pro-angiogenic response in CAM experiments. The role of bioceramics on angiogenesis, including calcium silicate ceramics (Zhai et al., 2012, 2013) and calcium phosphates (Malhotra & Habibovic, 2016) were investigated. It has been reported that the co-culture of osteoblast and endothelial based cells on HA and TCP ceramics has led to the formation of micro-capillary vessel like structures which could be useful in pre-vascularised scaffolds systems (Unger et al., 2007).

The pre-vascular scaffold systems involve some limitations in terms of discrepancy of cells due to their origin and difficulty in connecting pre-formed vessel structures with present vessels in the body (Malhotra & Habibovic, 2016). Although the strategies for rapid vascularisation by utilising angiogenic growths factors, such as VEGF and bFGF, their safety due to stability issues and high cost, limit their usage alone. To provide their sustainable release, angiogenic growth factors are bound with Hep or HPSG in a scaffold which monitors proliferation and migration of endothelial cells forming blood vessels (Chiodelli et al., 2015; Oliviero et al., 2012). Due to high cost and stability issues in the utilisation of external growth factors, promoting *in-vivo* attraction of growth factors led by a guided scaffold regenerative system by itself is another promising strategy. The researchers have reported Hep loaded chemically crosslinked CS-PVA hydrogels (Shahzadi et al., 2016) and chitosan-PVA-PCL hydrogels (Yar, Gigliobianco, et al., 2016) showed significant increase in newly forming blood vessels in an *in-vivo* CAM model (tested by opening square hole on the egg shell and sample implantation

on CAM). In addition, Hep functionalised deproteinated bone matrix coated with CS-Hep scaffolds, led to blood perfusion and formation of new micro vessels in rabbits 3 days after the implantation, with significant tissue infiltration into the scaffolds (Sun et al., 2011).

Novel CS/HA/Hep injectable compositions designed in this project for bone regeneration, provided integration of bioactive HA and Hep in a CS polymer matrix, showed excellent pro-angiogenic response and significantly enhanced newly forming blood vessels and their maturation in comparison to sole CS hydrogels. The *ex-ovo* CAM technique was optimised for in-situ gelling on thermosensitive injectable hydrogels in chick embryo CAM tissue. Histology analyses showed good tissue interactions, infiltration of hydrogels into tissues and formation of abundant micro blood vessels. In terms of the mean vessel counts and obtained CAM images, these hydrogels show better pro-angiogenic response than reported sole or deoxy-ribose added poly-3-hydroxybutyrate-co-3-hydroxyvalerate (PHBV) based biomaterials, and were comparable with their VEGF loaded counterparts as positive controls and as pro-angiogenic wound healing materials (Dikici et al., 2020). Therefore, in optimal compositions, injectable CS/HA/Hep hydrogels, by having a functional Hep layer on top, could eliminate the utilisation of any external growth factors. Instead, they would bind indigenous angiogenic growth factors and proteins, which regulate endothelial cells, and guide the formation of endothelial tubules. It would be very useful to investigate in the future, the effect of Hep comprised hydrogels on the proliferation and migration of endothelial cells, their efficiency in binding proteins such as fibronectins and to investigate their role in guidance of endothelial cells.

## 5.8 Summary and Conclusions

In-situ formed novel injectable CS/HA/Hep hydrogels showed biocompatible features that allowed good proliferation of osteoblast like cells. Significantly increased microvascularity and rapid maturation of newly formed blood vessels was achieved by using composite hydrogels at optimal compositions with low Hep amounts (0.03 and 0.12 mg/mL). These bioactive and pro-angiogenic thermosensitive injectable hydrogels could be very efficient in the provision of strong anchorage with native bones at defect sites through rapid vascularisation leading to bone regeneration.

## 6 SUMMARY, CONCLUSIONS AND FUTURE WORKS

### 6.1 Summary

In this study, *in-situ* formed novel injectable CS/HA/Hep hydrogel compositions were designed and developed, as bioactive and proangiogenic, degradable functional biomaterials, for bone repair and regeneration. Two types of hydrogels were developed, initial and modified hydrogels, which were characterised separately and compared in certain aspects, which are mainly dealt with in Chapter 3. First, the initial injectable hydrogels were synthesised and optimised for certain properties. This set of hydrogels, produced with different compositions, mainly after dissolving optimised amount of CS in acetic acid (5% (w/v) at initial solution) and mixing it with commercial HA at a ratio of 1/10. The Hep solutions were gradually added to the CS/HA mixtures by a polymer blending method which provided the acquisition of homogeneous solutions in a counterion polycomplex system. Solution neutralisation, using a weak base,  $\text{NaHCO}_3$  at 4 °C, was then performed using a sol-gel method for thermosensitive solutions to adjust the pH of the acidic CS solution. Subsequently, crosslinked hydrogels were formed upon incubation at 37 °C. Initial hydrogels were evaluated according to different aspects involving, solution homogeneity, final pH, injectability, rheology, solution storage capacity, and gelation performance at 37 °C. Biological analyses focused on cell: cytocompatibility, attachment, proliferation, and ability to differentiate into ECM compounds such as calcium and collagen; which were tested for. In addition, accompanied by histological analyses, angiogenesis studies were conducted by using an *ex-ovo* (shell-les) CAM assay on chick embryos by *in-situ* formation of hydrogels from the solutions at 37.5 °C (See Chapter 5).

As elaborated on in Chapter 3, to improve the mechanical properties of initial hydrogels and provide a totally pre-sterile system involving CS sterilisation, hydrogel synthesis was modified in the second part of the study. In the new synthesis technique, CS was sterilised by heat by water-glycerol hydroalcoholic media in dispersion form, in which glycerol was used as a heat protective and mechanical strengthening agent. In addition,

the HA powders that were produced, following investigation of certain parameters and optimisation using small carbonate substitutions in non-sintered form, used after autoclaving in modified hydrogels to achieve the project goals of better bioresorption and mineralisation of HA. These modified hydrogels were tested mainly by the same methods used for testing initial hydrogels excluding cell compatibility, rheology and histology studies. Angiogenesis evaluation was carried out by CAM assay (See Chapter 5). Modified hydrogels were also analysed in terms of their compressive strength measurements (See Chapter 3), swelling, bioactivity, biodegradation and drug release properties (See Chapter 4).

## 6.2 Conclusions

- HA powders were synthesised by the sol-gel method and optimised by comparing different synthesis parameters, including pH and heat treatment (See Chapter 2). The initial pH of reagent solutions had a significant impact on HA phase purity at high sintering temperatures. The solutions with initial pH of 10.5 results in pure HA with small carbonate substitutions in their dried form; obtained at a 86% yield that was stable at 1100 °C but less crystalline TCP phase formed at 1300 °C, according to Raman spectroscopy analyses. However, biphasic HA was acquired with a 78% yield from the reactions of lower initial pH solutions (8) that led to formation of a  $\beta$ -TCP phase at lower temperature (950 °C). The HA powder synthesised with a higher initial pH (10.5) with small carbonate content in non-sintered form, resulting in rough porous surface features, was chosen as optimal due to an expected better bioresorption and mineralisation capacity. Therefore, this optimal HA (HA-5D) powder was used in the modified hydrogel compositions, and has led to very good mineralisation capacity in the hydrogels; as confirmed by bioactivity studies in SBF.
- Initial hydrogel solutions were obtained with a final, maximum pH of 6.3 for homogeneous formulations that reached a pH of 6.5-7 upon gelation at 37 °C. The composite hydrogels with Hep were stable for at least three weeks in liquid form at 4 °C, while formulations without Hep maintained their fluid form for up to 6 months when kept sealed in test tubes at 4 °C. These solutions showed an even flow in injectability tests using different sized needles attached to a syringe. The optimal

needle size chosen, enabling a steady dropwise flow of all solutions, was 21 G, which makes possible most orthopaedic (10–16 G) and dental (16–25 G) injections (Burguera et al., 2007). The pH of a final solution could be raised further, in modified hydrogels of up to pH 6.4-6.5, by maintaining solution homogeneity, to a pH of between 6.8 and 7.2 at 20 °C. This could be attributed as due to the raised solution pKa value by the addition of glycerol, which reduces the ionic interactions in the solution via hydrophobic forces. Also, the pKa change phenomenon as being due to electrostatic interactions, is reported for solvent media (Sorlier et al., 2001). Injectability results of modified hydrogels were comparable with that of the initial hydrogels at the synthesis day, with maximum injectability required forces at around 15 and 21 N for initial and modified hydrogel solutions, respectively. However, after 24 hours of storage at 4 °C, the solution viscosity of the modified solutions were respectively higher with increased, required injectability force and adhesive properties with less flow evenness. The increase of solution viscosity can be associated with the effect of heat during sterilisation, leading to a slight degradation of CS and to the entanglement of some polymer chains. By minimising the autoclaving temperature and time, if or when available, the detrimental effects of heat can be minimised.

- The rheology studies of initial hydrogel solutions showed thermo-irreversible sol-gel transitions, starting in the vicinity of the average human body temperature of 37 °C. This was decreased to 31 °C by the addition of HA and by 21-31 °C with the addition of Hep. The highest Hep concentration (0.60 mg/mL) in these compositions led to a significant increase of the elastic modulus of resultant hydrogels, from 5 Pa to 130 Pa. The elastic modulus of hydrogels at 37 °C maintained for 30 min, from the same Hep concentration of 0.60, increased to 250 Pa.,
- Freeze-dried initial hydrogels possessed an interconnected and porous morphology. The measured minimum, maximum and mean pore diameters were 19.5 µm, 158 µm and, 73.4 µm respectively. Slight pH increments in the modified hydrogels from 6.2-6.3 to 6.4-6.5 led to significant alterations in hydrogel formation, morphology and mechanical strength. The weaker hydrogels with a more homogeneous microporous morphology was acquired from lower pH solutions. On the other hand, when pH

slightly exceeded 6.4, functional hydrogels were obtained with a morphology looking like flat bones in which an interpenetrating hybrid porous structure, located between two flat surfaces, consisted of huge macropores ( $\sim 500 \mu\text{m}$ ) and porous walls between them composed of dense small pores ( $\sim 5 \mu\text{m}$ ) (See figure 3.26). These hydrogel solutions were apparently triggered their gelation by the significant effect of pH, since incipient gelation time was diminished to as fast as 2 to 3 min. This hierarchical and interpenetrating network structure, from higher pH solutions has led to major enhancements in the compressive strength and elasticity of functional hydrogels compared to that of lower pH solutions.

- The compressive strength measurements confirmed the excellent boosting of mechanical properties. As pH increased, the compressive modulus and compressive stress has increased 3 and 4 fold respectively, at the same strain point (40%). The composite S0 (CS.0.1HA.0.0015Hep) hydrogel specimen showed the highest elastic modulus and compression strength 1.51 MPa and 310 kN (at 75% strain), respectively. Hydrogels showed gradual deformation behaviour in which the initial deformation, seen with sole CS hydrogels at around 60% strain, rose to around 70% with composite (CS/HA/Hep) hydrogels. None of the hydrogels were totally broken at the final 75% strain point. These were good achievements in improving the mechanical properties of physically crosslinked CS based hydrogels. The compression stress at first fracture points ranged between 51 and 172 kPa in compositions; these were more than the reported sufficient stiffness values required for osteogenic stem cell differentiations of 45-49 kPa (Jiang et al., 2015; Zouani et al., 2013).
- Overall, pH had a major effect on the fine tuning of hydrogel properties, including injectability, gelation, morphology, and strength etc. This was expected since gelation is mainly driven by pH leading to the reaction of CS and  $\text{NaHCO}_3$  that decrease acidic  $\text{NH}_3^+$  groups and turn into deprotonated  $\text{NH}_2$  that forms more junctions between CS chains. The highly strengthened structure of the modified hydrogels obtained from a slightly higher pH (6.4-6.5) could also be associated with the contribution of hydroalcoholic media with glycerol present. As reported, glycerol leads to an alteration of the water structure covering CS chains, by reducing the

charge densities of polymers. Having hydrophobic and hydrophilic features, alcohol-water moieties interacting with CS, ensure the formation of hydrophobic sites, leading to the intra-molecular bonding of CS (Boucard et al., 2005; Jarry et al., 2002). In addition, it has been reported that glycerol treated chitosan-gelatine crosslinked hydrogels enhance hydrogel elasticity and flexibility (Badhe et al., 2017). Due to improved chain flexibility, plasticizers provides stress relaxation behaviour decreasing deformation and increasing strength (Ahmad et al., 2012). Furthermore, Nam *et al.*, (2019) have reported that the stress relaxation behaviour in alginate hydrogels has increased with use of another polyol, polyethylene glycol (PEG), which provides biomimetic, more cell friendly, tuneable hydrogels that stimulate fibroblast attachment and proliferation as well as osteogenesis through the differentiation of mesenchymal stem cells. It would be very interesting to investigate stress relaxation behaviour as well as cell response of these hydrogels in the future.

- The swelling capacity of modified high pH hydrogels, which reached equilibrium in 6 h, ranged between 68% and 55% for sole CS hydrogels CI and SI (CS.01HA.0.025Hep) composite hydrogels. The pH plot patterns show a tendency to increase for 15 h, followed by a decrease, becoming more stable at up to 72 h. The comparatively smaller swelling ratio among these hydrogels indicates a strong hydrogel network structure which could be beneficial for gradual drug release studies.
- Drug release studies of present Hep, and local Hep determination were undertaken using colorimetric toluidine blue (TB) assay based on its chemical complexation with Hep leading to a colour change from blue to purple. Hep in lower pH modified hydrogels, showed in tests, a sustained release profile of over one week, which is presumed to be even more extended with higher pH hydrogels. Hep in hydrogel structures were detected by TB staining. Results showed a well distributed functional Hep coating layer on the top surface of the hydrogels, stained with purple colour. This could be very beneficial for guided tissue regeneration by attracting physiological proteins, growth factors and endothelial cells to the ECM mimic heparinised surface, triggering angiogenesis and osteogenesis.

- The biomineralisation capacity of modified lower pH composite hydrogels facilitated the formation of a white, densely carbonated apatite layer on the top surface and inside the pores of the hydrogels during incubation in SBF. Flower like crystals with a needle like, rough surface morphology formed. This was indicative of highly bioactive surface features, which could provide very efficient bonding with natural bone tissue. Mineralisation with sole CS hydrogels (CI) were negligible during the weight tests in SBF, whereas composite CII and SI samples showed a significantly higher dry weight ratio than CI without HA. At day 21, SI samples with Hep (0.12 mg/mL) also showed a significant difference with the CII sample, showing that Hep, as confirmed by testing in, also promotes bioactivity. EDS analyses after 7 days of incubation in SBF showed C, O, N, Na elements in the sole CS (CI) sample, as high intensity peaks of Ca, P and O; elements that form calcium phosphate-apatite minerals. The Ca/P ratio in CII (CS.0.1HA) and (SI: CS.0.1HA.0.005Hep) samples were 1.9 and 1.77, respectively, which are slightly above that of stoichiometric HA. This might be attributed the possible formation of  $\text{CO}_3^{2-}$  B-type substitution with  $\text{PO}_4^{3-}$  at the site of HA, as has been reported in the literature (Landi et al., 2003). Having little carbonate substitution, the carbonate source, might have been contributed to, by both the  $\text{NaHCO}_3$  used for neutralising the hydrogels and the non-sintered HA used in the synthesis. B-type  $\text{CO}_3^{2-}$  is favourable to the reduction of the stability of HA by enhancing its bioresorption, which increases the bioactivity and efficiency of HA.
- The gradual weight decrease that occurred for modified, higher pH hydrogels in PBS, in both the presence and absence of the enzyme lysozyme, were 60% and 70%, respectively after 6-week *in-vitro* degradation tests. For both PBS and lysozyme specimens, degradation rates among samples were not significantly different ( $p: 0.0959$ ) but a significant difference ( $p<0.0001$ ) occurred between time intervals during degradation. SEM images showed evidence of degradation with propagation of surface cracks seen at day-14, eventually leading to breakage of the bulk (up to day-42) of the polymer network during the progressing degradation test. Furthermore, chemical analyses by FTIR-ATR spectroscopy confirmed the degradation by showing a gradual decrease in the peak intensities of most chemical functional groups; particularly for O-H/N-H in the region of  $3100\text{-}3500\text{ cm}^{-1}$ , C-H

bonds in the region of 2800-3000 cm<sup>-1</sup>, and C-O ring stretching and bending vibrations around wavenumbers 900-1200 cm<sup>-1</sup>.

- Biocompatibility studies of initial hydrogels in their gel or freeze-dried forms showed good cell attachment and proliferation of osteoblast like cells (MG-63), with non-significant differences between sample groups. The amount of calcium deposited in cell-cultured samples were highest in the CII sample composed of CS and HA.
- Angiogenesis studies with the initial hydrogels showed comparable results between sample groups. The highest number of blood vessels were counted in the composite SI sample, with 0.12 mg/mL Hep showing a very good pro-angiogenic response, but not significantly different to the CII sample (CS.0.1HA) without Hep. Histology analyses of CAM tissue sections confirmed the presence of micro vessels growing towards or branching out of circular hydrogel samples, indicating effective sample-tissue integration and infiltration. In further angiogenesis studies of modified hydrogels, as well as composite CII(CS.0.1HA), simple filter paper and the sole CS sample (CI) without Hep were also used as control; and hydrogel samples with Hep were involved: SI (0.12 mg/mL Hep) and S0 (0.03 mg/mL Hep). The results of statistical analyses by one-way ANOVA showed that the S0 sample with the lowest amount of Hep showed the best pro-angiogenic response; significantly higher than of those counted for, the CI sole CS (p:0.0298) sample and for filter paper (F.p.) (p:0.0026). The vascular index counted for the CII sample was significantly higher than that of filter paper (p: 0.0287) but not from that of CI (p:0.1998). The S0 composition with an optimal Hep concentration led to the formation of a significant amount of new blood vessels (vascular index: 45.7±4.7) as well as the promotion of vessel maturation. This composition (S0:CS.0.1HA.0.0015Hep) showed comparable results to that of investigated VEGF bonded polymers as pro-angiogenic wound healing materials (Dikici et al., 2020). Although angiogenic growth factors such as VEGF can enhance angiogenesis significantly, growth factor delivery involves many challenges including instability issues, the risk of toxicity and malformation of bones, and the risk of inflammatory and malignant tissue formation; as is reported in the literature (Carragee et al., 2011; Raftery et al., 2017). Therefore, in the current

strategy, the attraction of natural physiological growth factors and proteins by use of functional heparinised bioactive composite CS/HA/Hep hydrogels of optimal composition should provide a natural pathway for the efficient formation of endothelial blood vessels.

- Injectable and pro-angiogenic novel CS/HA/Hep based hydrogels with enhanced flexibility and strength were successfully produced and modified for sterile formulations. By their functional bioactive, biodegradable and proangiogenic properties, it is believed that CS/HA/Hep based hydrogels offer good regenerative potential for repair and regeneration of non-load bearing bones. These injectable solutions, which may also be mixed with additional drugs and delivered into targeted defects, that start forming gel *in-situ* within minutes upon injection and set and strengthen with time, could be particularly efficient for filling complex shaped bone defects. These hydrogels can serve as bioactive materials that stimulate bonding with tissues, not only from their surface but also through vascularised network bridging and tissue infiltration that triggers eventual natural bone tissue regeneration by their gradual degradation.

### 6.3 Future Works

- It would be very beneficial to harness increasing HA concentrations in hydrogel compositions to enhance elastic modulus and toughness since respectively low amounts of HA were used in the formulations (HA/CS: 1/10). In addition, one of the project goals was to involve different ionic substitutions during HA synthesis, especially co-substituted silicate and carbonate ions. However, due to the requirement of comprehensive characterisations for ionic substitutions which would exceed the project time limitations, no external ionic substitutions were involved in HA. Instead, dried synthesised or commercial HA containing a small amount of carbonate substitutions were used in the experiments.
- It would be useful to investigate Heparin release profiles with the higher pH solution-hydrogels since their more crosslinked strengthened polymer network might contribute to the slower release of Hep.

- It would be interesting to investigate the biocompatibility of Hep composite hydrogels by using Human Umbilical Vein Endothelial Cells (HUVEC), or other endothelial cells representing vascularization. In addition, by further training and by gaining more expertise in this area, the attachment of proteins such as fibronectin and integrin as well as angiogenic growth factors, could be measured to assess endothelialization and angiogenesis.
- Although cell differentiation was investigated via calcium and collagen deposition assay, the results were inconclusive and would have been useful to repeat. Additionally, osteogenic cell differentiation could be investigated by alkaline phosphatase assay.
- The observation of hydrogel structures with cryo-SEM might be a better indicator of water abundant, porous hydrogel morphologies, depending on availability of this system. However, it could also be performed with a chemical drying method along with HMDS for the preparation of wet samples/tissues. This would be a useful study to be conducted in the future in order to observe cell-adhesion on hydrogels under SEM.
- Solution density and adhesion are also important parameters that affect whether an injectable solution is stable in position or quickly washes out. It would be useful to compare initial and modified hydrogels in terms of solution adhesiveness capacity on bone samples by performing compression test using a UTM. In addition, the stress relaxation behaviour of hydrogel specimens should also be determined via cyclic stress experiments in compressive mode.
- Performing sterility tests and blood compatibility tests on modified hydrogels in the future would also be very useful.
- Although performing *in-vivo* experiments in big animal models were aimed for initially, due to the long processing time for the acquisition of ethical approval, it was not possible. However, it is intended that these be done in the future.

## APPENDIXES

### APPENDIX A. Comparison of Bovine and Porcine Heparin

Heparin is one of the most significant antithrombotic drugs. Its main supply depends mainly on porcine sources which suffer from shortage and recently raised contamination and diarrheal virus epidemiological issues. Though United States and European countries only use Hep from porcine intestinal mucosa, South America countries such as Brazil, Argentina, and Middle Eastern countries use bovine lung and intestinal sourced Hep, while ovine sourced and porcine lung Hep is used in Asia (Jasper et al., 2015; Xie et al., 2018). Recently, many researchers have been investigating alternative non-porcine originated Hep. As reported, bovine and ovine sourced Hep are the alternatives that most resemble porcine Hep. The results have shown that bovine Hep has a slightly lower activity than porcine Hep but can be obtained at higher activities by special production (Xie et al., 2018).

In this study, initially porcine Hep had been used, and upon supply of purified injectable grade sodium bovine Hep having respectively high activity (156 IU/mg) as kind gift by Extrasul (Ext. An. Veg. LTDA, Sao Paulo, Brazil), it has been used in all experiments. The initial chemical analyses result from FTIR-ATR and FT-Raman spectroscopy comparing porcine and bovine Hep were shown in Figure A.1-A.2, and Figure A-3, respectively. The obtained hydrogels were also comparable in terms of their chemical structures. The studies with sodium bovine Hep showed substantial contribution to angiogenesis at very low optimal concentrations in CS/HA/Hep injectable hydrogel system.

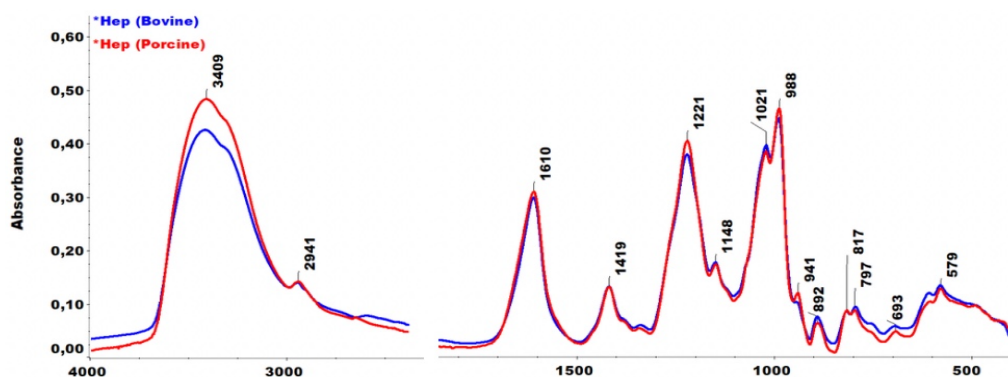
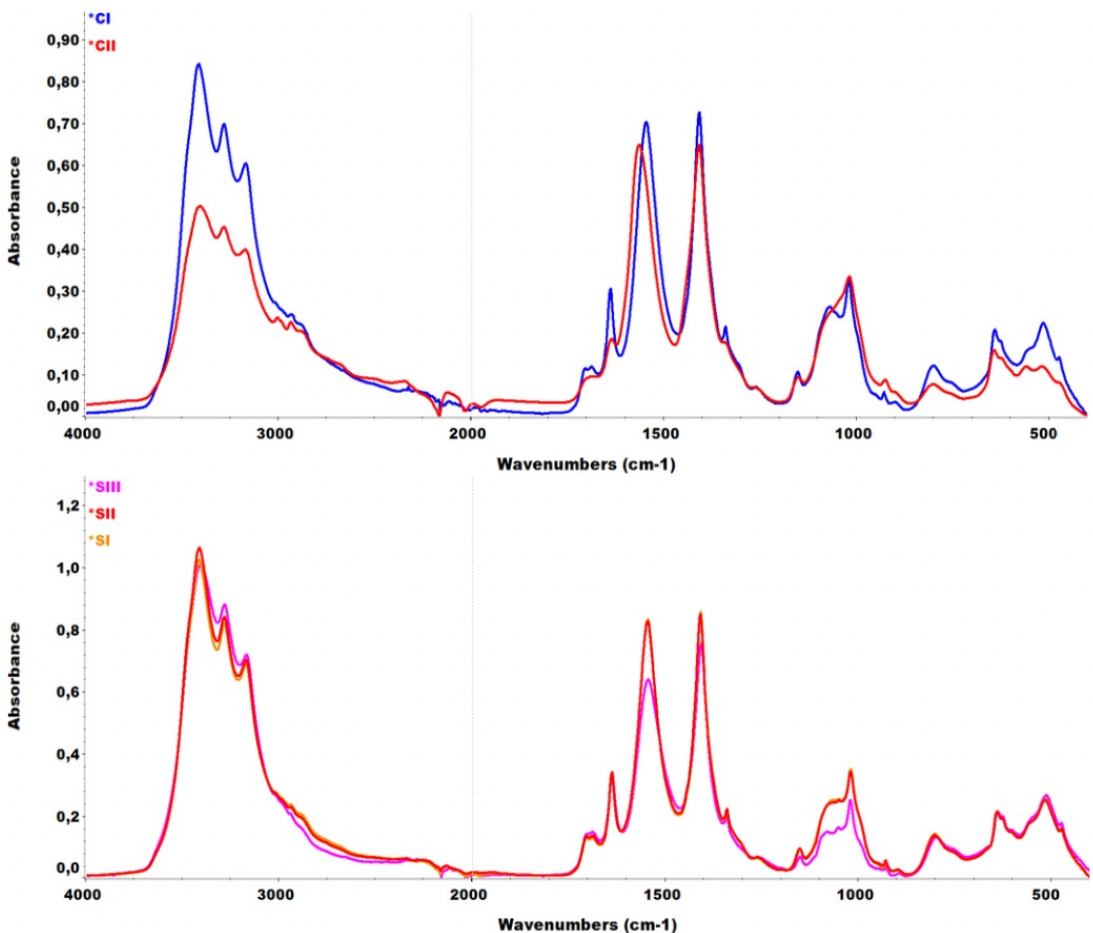
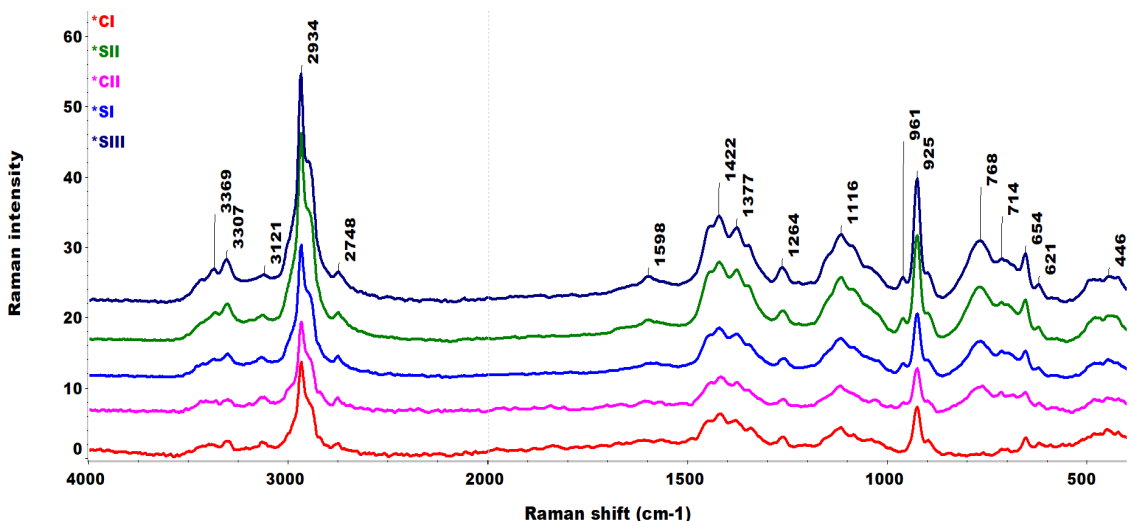


Figure A. 1 Comparison of chemical structure of bovine and porcine originated sodium Heparin.



**Figure A. 2** ATR spectra of Hydrogels obtained with porcine Hep for different hydrogel compositions CI (CS) and CII (CS.0.1HA) (at above), and samples with Hep at different concentrations: SI (CS.0.1HA.0.005Hep)-0.12 mg/mL, SII (CS.0.1HA.0.015Hep)-0.36 mg/mL and SI (CS.0.1HA.0.025Hep)-0.60 mg/mL(at below graph).



**Figure A. 3** FT-Raman spectra of hydrogels obtained with porcine Hep for different hydrogel compositions including CI (CS) and CII (CS.0.1HA) and samples with Hep at different concentrations: SI (CS.0.1HA.0.005Hep)-0.12 mg/mL, SII (CS.0.1HA.0.015Hep)-0.36 mg/mL and SI (CS.0.1HA.0.025Hep)-0.60 mg/mL

## APPENDIX B. Use of Carboxymethyl-cellulose in Hydrogels

In a part of study, the utilisation of carboxymethyl cellulose (CMC) in hydrogels as stabilisation agent and for enhancing mechanical properties were involved in a few experiment trials. However, especially at high concentration of Hep, huge precipitation problem was faced which is attributed to anionic charged structure of CMC which was competing with Hep at interaction with CS. Therefore, another method by involving glycerol, desired mechanical enhancement and stabilisation were ensured in further studies which reduced the precipitation even enhancing the solution pKa leading further pH neutralisation without any precipitates.

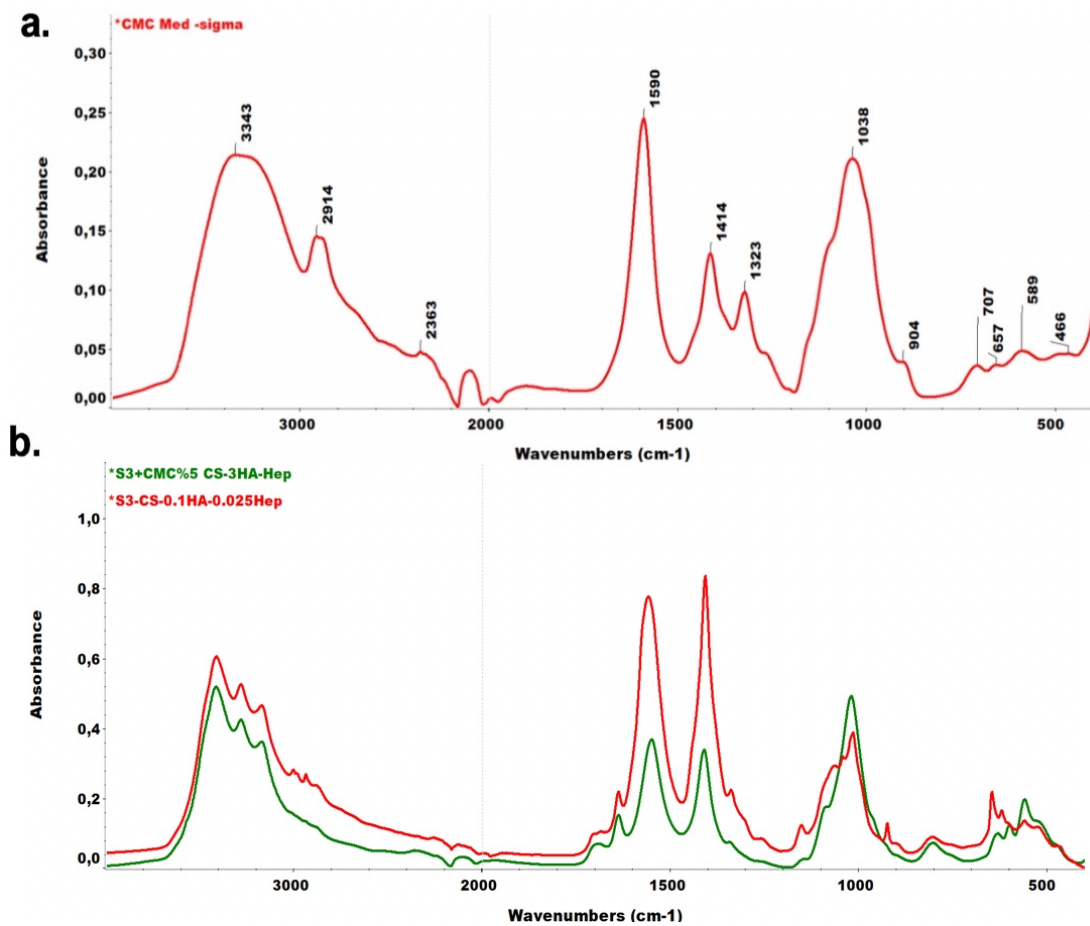


**Figure B. 1** FTIR-ATR chemical analyses **a.** CMC and **b.** composite hydrogel with 0.6 mg/mL Hep, HA/CS:0.3 with or without CMC.

## APPENDIX C. Interesting Images Obtained During Research

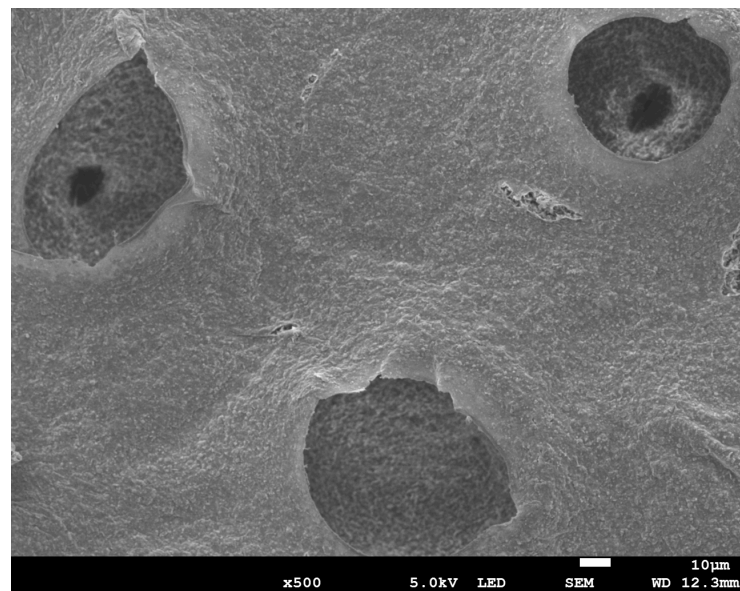


**Figure C. 1** SEM image of top surface of a modified composite hydrogel specimen looking like a face.

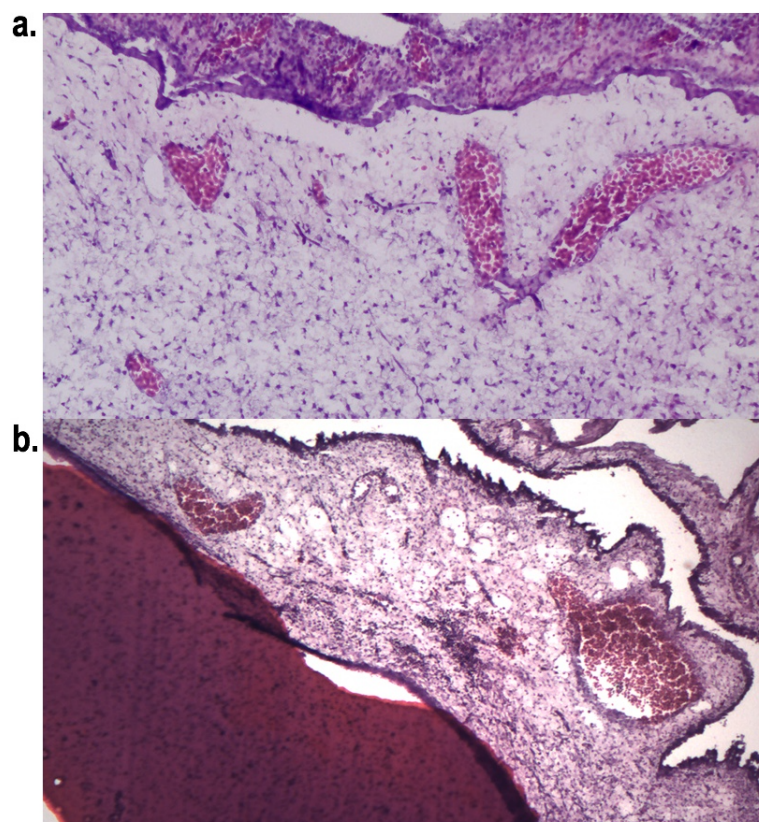


**Figure C. 2** Histology images of CAM tissues having blood vessels at different shapes with composite hydrogel sample **a.** SI, **b.** SIII

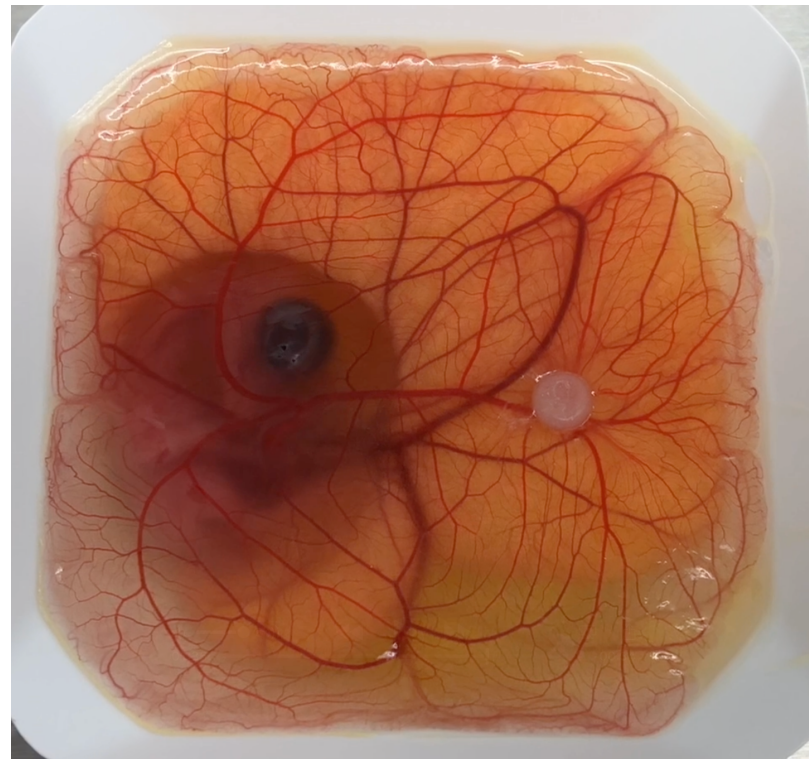


**Figure C. 3** A chick embryo image during its development day of 10 during CAM assay, which formed a good vascular network (after injection of thermosensitive solution on CAM and *in-situ* formed hydrogel upon incubation at 37.5 °C, at day 7).

## APPENDIX D. Abstract of Published Research Article

 International Journal of  
**Molecular Sciences**

[Submit to this Journal](#)  
[Review for this Journal](#)  
[Edit a Special Issue](#)

**Article Menu**

**Article Overview** ^

- [Abstract](#)
- [Open Access and Permissions](#)
- [Share and Cite](#)
- [Article Metrics](#)
- [Related Articles](#)
- [Order Article Reprints](#)

---

**Article Versions** ^

**Export Article** ^

**Related Info Links** ^

---

**Views** 732

---

**Downloads** 934

---

 **ICA 2021**

**The First International Conference on Antioxidants**  
**Sources, Methods, Health Benefits and Industrial Applications**

Open Access Article

### In-Situ Forming pH and Thermosensitive Injectable Hydrogels to Stimulate Angiogenesis: Potential Candidates for Fast Bone Regeneration Applications

by  Fatma Z. Kocak<sup>1</sup>   Abdullah C.S. Talari<sup>1</sup>   Muhammad Yar<sup>2</sup>  and  Ihtesham U. Rehman<sup>1,†</sup> 

<sup>1</sup> Engineering Department, Lancaster University, Lancaster LA1 4YW, UK

<sup>2</sup> Interdisciplinary Research Centre in Biomedical Materials (IRCBM), COMSATS University Islamabad, Lahore Campus, Punjab 54000, Pakistan

\* Author to whom correspondence should be addressed.

† Current address: Engineering Department, Faculty of Science and Technology, Lancaster University, Gillow Avenue, Lancaster, LA1 4YW, UK.

*Int. J. Mol. Sci.* **2020**, *21*(5), 1633; <https://doi.org/10.3390/ijms21051633>

Received: 17 December 2019 / Revised: 15 February 2020 / Accepted: 24 February 2020 / Published: 27 February 2020

(This article belongs to the Special Issue Recent Advances in Dental Materials and Biomaterials)

[View Full-Text](#)

[Download PDF](#)

[Browse Figures](#)

[Review Reports](#)

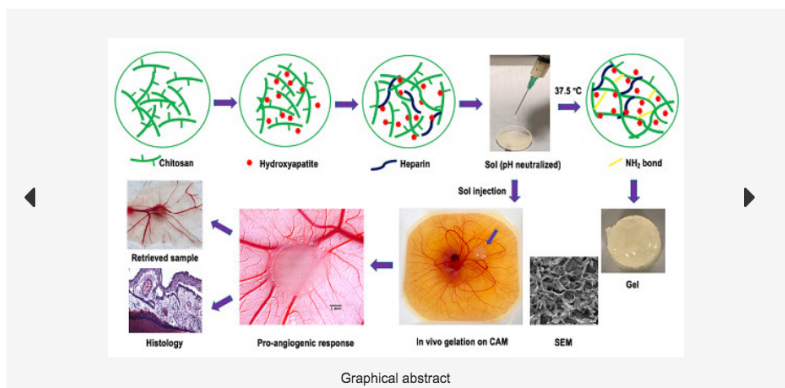
[Cite This Paper](#)

#### Abstract

Biomaterials that promote angiogenesis are required for repair and regeneration of bone. In-situ formed injectable hydrogels functionalised with bioactive agents, facilitating angiogenesis have high demand for bone regeneration. In this study, pH and thermosensitive hydrogels based on chitosan (CS) and hydroxyapatite (HA) composite materials loaded with heparin (Hep) were investigated for their pro-angiogenic potential. Hydrogel formulations with varying Hep concentrations were prepared by sol-gel technique for these homogeneous solutions were neutralised with sodium bicarbonate ( $\text{NaHCO}_3$ ) at 4 °C. Solutions (CS/HA/Hep) constituted hydrogels setting at 37 °C which was initiated from surface in 5–10 minutes. Hydrogels were characterised by performing injectability, gelation, rheology, morphology, chemical and biological analyses. Hydrogel solutions facilitated manual dropwise injection from 21 Gauge which is highly used for orthopaedic and dental administrations, and the maximum injection force measured through 19 G needle ( $17.191 \pm 2.296 \text{ N}$ ) was convenient for manual injections. Angiogenesis tests were performed by an ex-ovo chick chorioallantoic membrane (CAM) assay by applying injectable solutions on CAM, which produced in situ hydrogels. Hydrogels induced microvascularity in CAM assay this was confirmed by histology analyses. Hydrogels with lower concentration of Hep showed more efficiency in pro-angiogenic response. Thereof, novel injectable hydrogels inducing angiogenesis (CS/HA/Hep) are potential candidates for bone regeneration and drug delivery applications. [View Full-Text](#)

**Keywords:** thermosensitive injectable hydrogels; injectability; angiogenesis; ex-ovo chick chorioallantoic membrane (CAM) assay; chitosan; hydroxyapatite; heparin

[▼ Show Figures](#)



## REFERENCES

Ahmad, Z., Ansell, M., Smedley, D. & Tahir, P. M. (2012). Creep behavior of epoxy-based adhesive reinforced with nanoparticles for bonded-in timber connection. *Journal of Materials in Civil Engineering*, 24(7), 825–831. [https://doi.org/10.1061/\(ASCE\)MT.1943-5533.0000453](https://doi.org/10.1061/(ASCE)MT.1943-5533.0000453)

Albala, L., Ercan, U. K., Joshi, S. G., Eisenbrey, J. R., Teraphongphom, N. & Wheatley, M. A. (2015). Preservation of imaging capability in sensitive ultrasound contrast agents after indirect plasma sterilization. *International Journal of Pharmaceutics*, 494(1), 146–151. <https://doi.org/10.1016/j.ijpharm.2015.07.064>

Albrektsson, T. & Johansson, C. (2001). *Osteoinduction, osteoconduction and osseointegration*. *Eur Spine*, 96–101.

Aleem, A. R., Shahzadi, L., Alvi, F., Khan, A. F., Chaudhry, A. A., ur Rehman, I. & Yar, M. (2017). Thyroxin releasing chitosan/collagen based smart hydrogels to stimulate neovascularization. *Materials and Design*, 133, 416–425. <https://doi.org/10.1016/j.matdes.2017.07.053>

Alves, H. L. R., Dos Santos, L. A. & Bergmann, C. P. (2008). Injectability evaluation of tricalcium phosphate bone cement. *Journal of Materials Science: Materials in Medicine*, 19(5), 2241–2246. <https://doi.org/10.1007/s10856-007-3329-6>

Amini, A. a & Nair, L. S. (2012). Injectable hydrogels for bone and cartilage repair. *Biomedical Materials*, 7(2), 024105. <https://doi.org/10.1088/1748-6041/7/2/024105>

Antonakos, A., Liarokapis, E. & Leventouri, T. (2007). Micro-Raman and FTIR studies of synthetic and natural apatites. *Biomaterials*, 28(19), 3043–3054. <https://doi.org/10.1016/j.biomaterials.2007.02.028>

Apkarian, R. P., Caran, K. L. & Robinson, K. A. (1999). Topographic imaging of chromium-coated frozen-hydrated cell and macromolecular complexes by in-lens field emission scanning electron microscopy. *Microscopy and Microanalysis*, 5(3), 197–207. <https://doi.org/10.1017/S1431927699000148>

Apkarian, R. P., Wright, E. R., Seredyuk, V. A., Eustis, S., Lyon, L. A., Conticello, V. P. & Menger, F. M. (2003). In-lens cryo-high resolution scanning electron

microscopy: Methodologies for molecular imaging of self-assembled organic hydrogels. *Microscopy and Microanalysis*, 9(4), 286–295. <https://doi.org/10.1017/S1431927603030551>

Arun Kumar, R., Sivashanmugam, A., Deepthi, S., Iseki, S., Chennazhi, K. P., Nair, S. V. & Jayakumar, R. (2015). Injectable chitin-poly(??-caprolactone)/nanohydroxyapatite composite microgels prepared by simple regeneration technique for bone tissue engineering. *ACS Applied Materials and Interfaces*, 7(18), 9399–9409. <https://doi.org/10.1021/acsami.5b02685>

Atha, D. H., Gaigalas, A. K. & Reipa, V. (1996). Structural Analysis of Heparin by Raman Spectroscopy. *Journal of Pharmaceutical Sciences*, 85(1), 52–56. <https://doi.org/10.1021/jf950216c>

Athanasiou, K. A., Rosenwasser, M. P., Buckwalter, J. A., Malinin, T. I. & Mow, V. C. (1991). Interspecies comparisons of in situ intrinsic mechanical properties of distal femoral cartilage. *Journal of Orthopaedic Research*, 9(3), 330–340. <https://doi.org/10.1002/jor.1100090304>

Auerbach, R., Lewis, R., Shinners, B., Kubai, L. & Akhtar, N. (2003). Angiogenesis assays: A critical overview. *Clinical Chemistry*, 49(1), 32–40. <https://doi.org/10.1373/49.1.32>

Ba'rtolo, P. & Bidanda, B. (2008). *Bio-Materials and Prototyping Applications in Medicine*. Springer.

Babensee, J. E., Anderson, J. M., McIntire, L. V. & Mikos, A. G. (1998). Host response to tissue engineered devices. *Advanced Drug Delivery Reviews*, 33(1–2), 111–139. [https://doi.org/10.1016/S0169-409X\(98\)00023-4](https://doi.org/10.1016/S0169-409X(98)00023-4)

Badhe, R. V., Bijukumar, D., Chejara, D. R., Mabrouk, M., Choonara, Y. E., Kumar, P., du Toit, L. C., Kondiah, P. P. D. & Pillay, V. (2017). A composite chitosan-gelatin bi-layered, biomimetic macroporous scaffold for blood vessel tissue engineering. *Carbohydrate Polymers*, 157, 1215–1225. <https://doi.org/10.1016/j.carbpol.2016.09.095>

Baker, M. J., Gazi, E., Brown, M. D., Shanks, J. H., Gardner, P. & Clarke, N. W. (2008). FTIR-based spectroscopic analysis in the identification of clinically aggressive prostate cancer. *British Journal of Cancer*, 99(11), 1859–1866. <https://doi.org/10.1038/sj.bjc.6604753>

Baker, Matthew J., Hughes, C. S. & Hollywood, K. A. (2016). Biophotonics:

Vibrational spectroscopic diagnostics. In *Biophotonics: Vibrational Spectroscopic Diagnostics*. A Morgan & Claypool publication as part of IOP Concise Physics. <https://doi.org/10.1088/978-1-6817-4071-3>

Balcerzak, M., Hamade, E., Zhang, L., Pikula, S., Azzar, G., Radisson, J., Bandorowicz-Pikula, J. & Buchet, R. (2003). The roles of annexins and alkaline phosphatase in mineralization process Circled white star. *Acta Biochimica Polonica*, 50(4), 1019–1038. <https://doi.org/0350041019>

Bang, L. T., Long, B. D. & Othman, R. (2014). Carbonate hydroxyapatite and silicon-substituted carbonate hydroxyapatite: Synthesis, mechanical properties, and solubility evaluations. *The Scientific World Journal*, 2014. <https://doi.org/10.1155/2014/969876>

Barnhill, R. L. & Ryan, T. J. (1983). Biochemical modulation of angiogenesis in the chorioallantoic membrane of the chick embryo. *Journal of Investigative Dermatology*, 81(6), 485–488. <https://doi.org/10.1111/1523-1747.ep12522728>

Berzina-Cimdina, L. & Borodajenko, N. (2012). Research of Calcium Phosphates Using Fourier Transform Infrared Spectroscopy. In *Infrared Spectroscopy – Materials Science, Engineering and Technology*. <https://doi.org/10.5772/36942>

Bessa, P. C., Machado, R., Nürnberg, S., Dopler, D., Banerjee, A., Cunha, A. M., Rodríguez-Cabello, J. C., Redl, H., van Griensven, M., Reis, R. L. & Casal, M. (2010). Thermoresponsive self-assembled elastin-based nanoparticles for delivery of BMPs. *Journal of Controlled Release*, 142(3), 312–318. <https://doi.org/10.1016/j.jconrel.2009.11.003>

Bhattarai, N., Gunn, J. & Zhang, M. (2010). Chitosan-based hydrogels for controlled, localized drug delivery. *Advanced Drug Delivery Reviews*, 62(1), 83–99. <https://doi.org/10.1016/j.addr.2009.07.019>

Bienert, M. (2018). Angiogenesis in Bone Tissue Engineering. *Journal of Stem Cell Research and Medicine*, 3(1), 1–2. <https://doi.org/10.15761/JSCRM.1000129>

Biga, L. M., Dawson, S., Harwell, A., Hopkins, R., Kaufmann, J., LeMaster, M., Matern, P., Morrison-Graham, K., Quick, D. & Runyeon, J. (n.d.). *6.5 Fractures: Bone Repair – Anatomy & Physiology*. OpenStax/Oregon State University. Retrieved 2 February 2021, from <https://open.oregonstate.education/aandp/chapter/6-5-fractures-bone-repair/>

Bigi, A., Foresti, E., Gandolfi, M., Gazzano, M. & Roveri, N. (1997). Isomorphous

substitutions in  $\beta$ -tricalcium phosphate: The different effects of zinc and strontium. *Journal of Inorganic Biochemistry*, 66(4), 259–265. [https://doi.org/10.1016/S0162-0134\(96\)00219-X](https://doi.org/10.1016/S0162-0134(96)00219-X)

Borkowski, L., Sroka-Barwicka, A., Draczkowski, P., Ptak, A., Zięba, E., Łosarczyk, A. & Ginalski, G. (2016). The comparison study of bioactivity between composites containing synthetic non-substituted and carbonate-substituted hydroxyapatite. *Materials Science and Engineering C*, 62, 260–267. <https://doi.org/10.1016/j.msec.2016.01.056>

Boucard, N., Viton, C. & Domard, A. (2005). New aspects of the formation of physical hydrogels of chitosan in a hydroalcoholic medium. *Biomacromolecules*, 6(6), 3227–3237. <https://doi.org/10.1021/bm050653d>

Boyer, L., Carpena, J. & Lacout, J. L. (1997). Synthesis of phosphate-silicate apatites at atmospheric pressure. *Solid State Ionics*, 95(1–2), 121–129. [https://doi.org/10.1016/s0167-2738\(96\)00571-1](https://doi.org/10.1016/s0167-2738(96)00571-1)

Braet, F., De Zanger, R. & Wisse, E. (1997). Drying cells for SEM, AFM and TEM by hexamethyldisilazane: A study on hepatic endothelial cells. *Journal of Microscopy*, 186(1), 84–87. <https://doi.org/10.1046/j.1365-2818.1997.1940755.x>

Brien, J. O., Wilson, I., Orton, T. & Pognan, F. (2000). Investigation of the Alamar Blue (resazurin) fluorescent dye for the assessment of mammalian cell cytotoxicity. *Eur. J. Biochem*, 267, 5421–5426.

Bueno, P. V. A., Souza, P. R., Follmann, H. D. M., Pereira, A. G. B., Martins, A. F., Rubira, A. F. & Muniz, E. C. (2015). N,N-Dimethyl chitosan/heparin polyelectrolyte complex vehicle for efficient heparin delivery. *International Journal of Biological Macromolecules*, 75, 186–191. <https://doi.org/10.1016/j.ijbiomac.2015.01.030>

Burckbuchler, V., Mekhloufi, G., Giteau, A. P., Grossiord, J. L., Huille, S. & Agnely, F. (2010). Rheological and syringeability properties of highly concentrated human polyclonal immunoglobulin solutions. *European Journal of Pharmaceutics and Biopharmaceutics*, 76(3), 351–356. <https://doi.org/10.1016/j.ejpb.2010.08.002>

Burguera, E. F., K., H. H. & Xu, L. S. (2007). Injectable Calcium Phosphate Cement: Effects of Powder-to-Liquid Ratio and Needle Size Elena. *Journal of Biomedical Materials Research Part B: Applied Biomaterials*, 493–502, 340–344. <https://doi.org/10.1002/jbmb>

Burton, J. D. (2005). The MTT Assay to Evaluate Chemosensitivity. In *Methods in Molecular Medicine, Chemosensitivity* (pp. 69–79). Blumenthal © Humana Press Inc.

Cabassi, F., Casu, B. & Perlin, A. S. (1978). Infrared absorption and raman scattering of sulfate groups of heparin and related glycosaminoglycans in aqueous solution. *Carbohydrate Research*, 63(C), 1–11. [https://doi.org/10.1016/S0008-6215\(00\)80924-6](https://doi.org/10.1016/S0008-6215(00)80924-6)

Camarero-Espinosa, S., Rothen-Rutishauser, B., Foster, E. J. & Weder, C. (2016). Articular cartilage: from formation to tissue engineering. *Biomaterials Science*, 4(5), 734–767. <https://doi.org/10.1039/C6BM00068A>

Cao, W. & Hench, L. L. (1996). Bioactive materials. *Ceramics International*, 22(6), 493–507. [https://doi.org/10.1016/0272-8842\(95\)00126-3](https://doi.org/10.1016/0272-8842(95)00126-3)

Carragee, E. J., Hurwitz, E. L. & Weiner, B. K. (2011). A critical review of recombinant human bone morphogenetic protein-2 trials in spinal surgery: Emerging safety concerns and lessons learned. *Spine Journal*, 11(6), 471–491. <https://doi.org/10.1016/j.spinee.2011.04.023>

Cestari, M., Muller, V., Henrique, J., Nakamura, C. V., Rubira, A. F. & Muniz, E. C. (2014). Preparing Silk Fibroin Nano fibers through Electrospinning: Further Heparin Immobilization toward Hemocompatibility Improvement. *Biomacromolecules*, 1762–1767. <https://doi.org/10.1021/bm500132g>

Chang, S. H., Lin, H. T. V., Wu, G. J. & Tsai, G. J. (2015). pH Effects on solubility, zeta potential, and correlation between antibacterial activity and molecular weight of chitosan. *Carbohydrate Polymers*, 134, 74–81. <https://doi.org/10.1016/j.carbpol.2015.07.072>

Chaudhry, A. A., Haque, S., Kellici, S., Boldrin, P., Rehman, I., Khalid, F. A. & Darr, J. A. (2006). Instant nano-hydroxyapatite: a continuous and rapid hydrothermal synthesis. *Chemical Communications*, 21, 2286. <https://doi.org/10.1039/b518102j>

Chaudhry, A. A., Knowles, J. C., Rehman, I. & Darr, J. A. (2013). Rapid hydrothermal flow synthesis and characterisation of carbonate- and silicate-substituted calcium phosphates. *Journal of Biomaterials Applications*, 28(3), 448–461. <https://doi.org/10.1177/0885328212460289>

Chen, H. & Fan, M. (2008). Novel Thermally Sensitive pH-dependent Chitosan/Carboxymethyl Cellulose Hydrogels. *Journal of Bioactive and Compatible Polymers*, 23(1), 1–10. <https://doi.org/10.1177/0885328207310201>

*Polymers*, 23(1), 38–48. <https://doi.org/10.1177/0883911507085070>

Chen, S. C., Wu, Y. C., Mi, F. L., Lin, Y. H., Yu, L. C. & Sung, H. W. (2004). A novel pH-sensitive hydrogel composed of N,O-carboxymethyl chitosan and alginate cross-linked by genipin for protein drug delivery. *Journal of Controlled Release*, 96(2), 285–300. <https://doi.org/10.1016/j.jconrel.2004.02.002>

Chen, T., Embree, H. D., Wu, L. Q. & Payne, G. F. (2002). In vitro protein-polysaccharide conjugation: Tyrosinase-catalyzed conjugation of gelatin and chitosan. *Biopolymers*, 64(6), 292–302. <https://doi.org/10.1002/bip.10196>

Chen, Y. C., Lin, R. Z., Qi, H., Yang, Y., Bae, H., Melero-Martin, J. M. & Khademhosseini, A. (2012). Functional human vascular network generated in photocrosslinkable gelatin methacrylate hydrogels. *Advanced Functional Materials*, 22(10), 2027–2039. <https://doi.org/10.1002/adfm.201101662>

Chen, Z., Zhang, X., Kang, L., Xu, F., Wang, Z., Cui, F. Z. & Guo, Z. (2015). Recent progress in injectable bone repair materials research. *Frontiers of Materials Science*, 9(4), 332–345. <https://doi.org/10.1007/s11706-015-0310-z>

Chenite, A., Chaput, C., Wang, D., Combes, C., Buschmann, M. ., Hoemann, C. ., Leroux, J. ., Atkinson, B. ., Binette, F. & Selmani, A. (2000). Novel injectable neutral solutions of chitosan form biodegradable gels in situ. *Biomaterials*, 21(21), 2155–2161. [https://doi.org/10.1016/S0142-9612\(00\)00116-2](https://doi.org/10.1016/S0142-9612(00)00116-2)

Chiodelli, P., Bugatti, A., Urbinati, C. & Rusnati, M. (2015). Heparin/heparan sulfate proteoglycans glycomic interactome in angiogenesis: Biological implications and therapeutic use. *Molecules*, 20(4), 6342–6388. <https://doi.org/10.3390/molecules20046342>

Choi, H. W., Lee, H. J., Kim, K. J., Kim, H. M. & Lee, S. C. (2006). Surface modification of hydroxyapatite nanocrystals by grafting polymers containing phosphonic acid groups. *Journal of Colloid and Interface Science*, 304(1), 277–281. <https://doi.org/10.1016/j.jcis.2006.05.069>

Cilurzo, F., Selmin, F., Minghetti, P., Adami, M., Bertoni, E., Lauria, S. & Montanari, L. (2011). Injectability evaluation: An open issue. *AAPS PharmSciTech*, 12(2), 604–609. <https://doi.org/10.1208/s12249-011-9625-y>

Cui, G., Li, J., Lei, W., Bi, L., Tang, P., Liang, Y., Tao, S. & Wang, Y. (2010). The mechanical and biological properties of an injectable calcium phosphate cement-fibrin glue composite for bone regeneration. *Journal of Biomedical Materials*

*Research - Part B Applied Biomaterials*, 92(2), 377–385.  
<https://doi.org/10.1002/jbm.b.31525>

Currey, J. D. (2012). The structure and mechanics of bone. *Journal of Materials Science*, 47(1), 41–54. <https://doi.org/10.1007/s10853-011-5914-9>

Cuscó, R., Guitián, F., de Aza, S. & Artús, L. (1998). Differentiation between hydroxyapatite and  $\beta$ -tricalcium phosphate by means of  $\mu$ -Raman spectroscopy. *Journal of the European Ceramic Society*, 18(9), 1301–1305. [https://doi.org/10.1016/S0955-2219\(98\)00057-0](https://doi.org/10.1016/S0955-2219(98)00057-0)

Dai, Z., Ronholm, J., Tian, Y., Sethi, B. & Cao, X. (2016). Sterilization techniques for biodegradable scaffolds in tissue engineering applications. *Journal of Tissue Engineering*, 7, 204173141664881. <https://doi.org/10.1177/2041731416648810>

Dardouri, M., Borges, J. P. & Omrani, A. D. (2017). Tailoring the morphology of hydroxyapatite particles using a simple solvothermal route. *Ceramics International*, 43(4), 3784–3791. <https://doi.org/10.1016/j.ceramint.2016.12.022>

Darr, J. a, Guo, Z. X., Raman, V., Bououdina, M. & Rehman, I. U. (2004). Metal organic chemical vapour deposition (MOCVD) of bone mineral like carbonated hydroxyapatite coatings. *Chemical Communications (Cambridge, England)*, 6, 696–697. <https://doi.org/10.1039/b312855p>

Dau, M., Ganz, C., Zaage, F., Staedt, H., Goetze, E., Gerber, T. & Kämmerer, P. W. (2020). In vivo comparison of a granular and putty form of a sintered and a non-sintered silica-enhanced hydroxyapatite bone substitute material. *Journal of Biomaterials Applications*, 34(6), 864–874. <https://doi.org/10.1177/0885328219877584>

Davis, A. R. & Oliver, B. G. (1972). A vibrational-spectroscopic study of the species present in the  $\text{CO}_2\text{?H}_2\text{O}$  system. *Journal of Solution Chemistry*, 1(4), 329–339. <https://doi.org/10.1007/BF00715991>

De Carvalho, B., Rompen, E., Lecloux, G., Schupbach, P., Dory, E., Art, J. F. & Lambert, F. (2019). Effect of sintering on in vivo biological performance of chemically deproteinized bovine hydroxyapatite. *Materials*, 12(23). <https://doi.org/10.3390/ma122333946>

Deligianni, D. D., Katsala, N. D., Koutsoukos, P. G. & Missirlis, Y. F. (2000). Effect of surface roughness of hydroxyapatite on human bone marrow cell adhesion, proliferation, differentiation and detachment strength. *Biomaterials*, 22(1), 87–96.

[https://doi.org/10.1016/S0142-9612\(00\)00174-5](https://doi.org/10.1016/S0142-9612(00)00174-5)

Deng, A., Kang, X., Zhang, J., Yang, Y. & Yang, S. (2017). Enhanced gelation of chitosan/β-sodium glycerophosphate thermosensitive hydrogel with sodium bicarbonate and biocompatibility evaluated. *Materials Science and Engineering: C*, 78, 1147–1154. <https://doi.org/10.1016/j.msec.2017.04.109>

Deng, J., Cheng, C., Teng, Y., Nie, C. & Zhao, C. (2017). Mussel-inspired post-heparinization of a stretchable hollow hydrogel tube and its potential application as an artificial blood vessel. *Polymer Chemistry*, 8(14), 2266–2275. <https://doi.org/10.1039/c7py00071e>

Dessì, M., Borzacchiello, A., Mohamed, T. H. A., Abdel-Fattah, W. I. & Ambrosio, L. (2013). Novel biomimetic thermosensitive β-tricalcium phosphate/chitosan-based hydrogels for bone tissue engineering. *Journal of Biomedical Materials Research Part A*, 101(10), 2984–2993. <https://doi.org/10.1002/jbm.a.34592>

Dikici, S., Claeysens, F. & MacNeil, S. (2020). Bioengineering Vascular Networks to Study Angiogenesis and Vascularization of Physiologically Relevant Tissue Models in Vitro. *ACS Biomaterials Science and Engineering*, 6(6), 3513–3528. <https://doi.org/10.1021/acsbiomaterials.0c00191>

Dillon, J. P., Waring-Green, V. J., Taylor, A. M., Wilson, P. J. M., Birch, M., Gartland, A. & Gallagher, J. A. (2012). Primary Human Osteoblast Cultures. In M. H. Helfrich & S. H. Ralston (Eds.), *Methods in Molecular Biology* (Vol. 816, pp. 3–19). [https://doi.org/10.1007/978-1-61779-415-5\\_26](https://doi.org/10.1007/978-1-61779-415-5_26)

Dorozhkin, S. V. (2016). Calcium orthophosphates (CaPO<sub>4</sub>): occurrence and properties. *Progress in Biomaterials*, 5(1), 9–70. <https://doi.org/10.1007/s40204-015-0045-z>

Doxsee, K. M. & Stevens, R. C. (1990). Complexation-mediated crystallization. Crystallization of sodium acetate trihydrate needles from cyclohexane solution. *Journal of Inclusion Phenomena and Molecular Recognition in Chemistry*, 9(4), 327–336. <https://doi.org/10.1007/BF01033312>

Drug, U. S. D. of H. and H. S. F. and & (ORA) Administration, C. for D. E. and R. (CDER) C. for B. E. and R. (CBER) O. of R. A. (2006). Guidance for industry: patient-reported outcome measures: use in medical product development to support labeling claims: draft guidance. *Health and Quality of Life Outcomes*, 4(August), 79. <https://doi.org/10.1186/1477-7525-4-79>

Edgar, L., McNamara, K., Wong, T., Tamburrini, R., Katari, R. & Orlando, G. (2016). Heterogeneity of scaffold biomaterials in tissue engineering. *Materials*, 9(5). <https://doi.org/10.3390/ma9050332>

Eke, G., Mangir, N., Hasirci, N., MacNeil, S. & Hasirci, V. (2017). Development of a UV crosslinked biodegradable hydrogel containing adipose derived stem cells to promote vascularization for skin wounds and tissue engineering. *Biomaterials*, 129, 188–198. <https://doi.org/10.1016/j.biomaterials.2017.03.021>

Elliott, J. C. (1994). *Structure and chemistry of the apatites and other calcium orthophosphates* (J. C. Elliott (ed.); 1st ed.). Elsevier. <https://doi.org/10.1016/B978-0-444-88534-0.50001-1>

Fathi, M. H., Hanifi, A. & Mortazavi, V. (2008). Preparation and bioactivity evaluation of bone-like hydroxyapatite nanopowder. *Journal of Materials Processing Technology*, 202(1–3), 536–542. <https://doi.org/10.1016/j.jmatprotec.2007.10.004>

Fatin-Rouge, N., Milon, A., Buffle, J., Goulet, R. R. & Tessier, A. (2003). Diffusion and Partitioning of Solutes in Agarose Hydrogels: The Relative Influence of Electrostatic and Specific Interactions. *The Journal of Physical Chemistry B*, 107(44), 12126–12137. <https://doi.org/10.1021/jp0303164>

Feng, Y., Li, Q., Wu, D., Niu, Y., Yang, C., Dong, L. & Wang, C. (2017). A macrophage-activating, injectable hydrogel to sequester endogenous growth factors for in situ angiogenesis. *Biomaterials*, 134, 128–142. <https://doi.org/10.1016/j.biomaterials.2017.04.042>

Fernandez-Tarrio, M., Yañez, F., Immesoete, K., Alvarez-Lorenzo, C. & Concheiro, A. (2008). Pluronic and tetronic copolymers with polyglycolized oils as self-emulsifying drug delivery systems. *AAPS PharmSciTech*, 9(2), 471–479. <https://doi.org/10.1208/s12249-008-9070-8>

Forrest, C. R. (2005). *What 's New in Plastic and Maxillofacial Surgery*. 399–408. <https://doi.org/10.1016/j.jamcollsurg.2004.11.016>

Fricain, J. C., Granja, P. L., Barbosa, M. A., De J ! E Eso, B., Barthe, N. & Baquey, C. (2002). Cellulose phosphates as biomaterials. In vivo biocompatibility studies. *Biomaterials*, 23(4), 971–980. [https://doi.org/10.1016/s0142-9612\(01\)00152-1](https://doi.org/10.1016/s0142-9612(01)00152-1)

Frydrych, M., Román, S., Green, N. H., MacNeil, S. & Chen, B. (2015). Thermoresponsive, stretchable, biodegradable and biocompatible poly(glycerol sebacate)-based polyurethane hydrogels. *Polymer Chemistry*, 6(46), 7974–7987.

<https://doi.org/10.1039/c5py01136a>

Fujita, M., Ishihara, M., Simizu, M., Obara, K., Ishizuka, T., Saito, Y., Yura, H., Morimoto, Y., Takase, B., Matsui, T., Kikuchi, M. & Maehara, T. (2004). Vascularization in vivo caused by the controlled release of fibroblast growth factor-2 from an injectable chitosan/non-anticoagulant heparin hydrogel. *Biomaterials*, 25(4), 699–706. [https://doi.org/10.1016/S0142-9612\(03\)00557-X](https://doi.org/10.1016/S0142-9612(03)00557-X)

Galante, R., Rediguieri, C. F., Kikuchi, I. S., Vasquez, P. A. S., Colaço, R., Serro, A. P. & Pinto, T. J. A. (2016). About the sterilization of chitosan hydrogel nanoparticles. *PLoS ONE*, 11(12). <https://doi.org/10.1371/journal.pone.0168862>

Gallart-Mateu, D., Armenta, S. & De La Guardia, M. (2014). Implementing the contamination prevention programs in the pesticide industry by infrared spectroscopy. *Talanta*, 119, 312–319. <https://doi.org/10.1016/j.talanta.2013.10.062>

Gattás-Asfura, K. M., Naistat, D. M. & Leblanc, R. M. (2006). Color change of toluidine blue induced by polyanionic quantum dots. *Colloids and Surfaces A: Physicochemical and Engineering Aspects*, 282–283, 471–474. <https://doi.org/10.1016/j.colsurfa.2005.10.068>

Gerber, H. P., Vu, T. H., Ryan, A. M., Kowalski, J., Werb, Z. & Ferrara, N. (1999). VEGF couples hypertrophic cartilage remodeling, ossification and angiogenesis during endochondral bone formation. *Nature Medicine*, 5(6), 623–628. <https://doi.org/10.1038/9467>

Ghosh, T. K. & Jasti, B. R. (2004). Theory and Practice of Contemporary Pharmaceutics. In *Theory and Practice of Contemporary Pharmaceutics*. <https://doi.org/10.1201/9780203644478>

Gibson, I. R. & Bonfield, W. (2002). Novel synthesis and characterization of an AB-type carbonate-substituted hydroxyapatite. *Journal of Biomedical Materials Research*, 59(4), 697–708. <https://doi.org/10.1002/jbm.10044>

Göpferich, A. (1996). Mechanisms of polymer degradation and erosion. *Biomaterials*, 17(2), 101–114. <https://doi.org/10.1016/B978-008045154-1.50016-2>

Götz, H. E., Müller, M., Emmel, A., Holzwarth, U., Erben, R. G. & Stangl, R. (2004). Effect of surface finish on the osseointegration of laser-treated titanium alloy implants. *Biomaterials*, 25(18), 4057–4064. <https://doi.org/10.1016/j.biomaterials.2003.11.002>

Grant, D., Long, W. F., Moffat, C. F. & Williamson, F. B. (1991). Infrared spectroscopy of heparins suggests that the region 750-950 cm<sup>-1</sup> is sensitive to changes in iduronate residue ring conformation. *Biochemical Journal*, 275(1), 193–197. <https://doi.org/10.1042/bj2750193>

Gregory, C. A., Gunn, W. G., Peister, A. & Prockop, D. J. (2004). An Alizarin red-based assay of mineralization by adherent cells in culture: Comparison with cetylpyridinium chloride extraction. *Analytical Biochemistry*, 329(1), 77–84. <https://doi.org/10.1016/j.ab.2004.02.002>

Grosso, A., Burger, M. G., Lunger, A. & Schaefer, D. J. (2017). *It Takes Two to Tango: Coupling of Angiogenesis and Osteogenesis for Bone Regeneration*. 5(November), 1–7. <https://doi.org/10.3389/fbioe.2017.00068>

Gümüşderelioğlu, M., Karakeçili, A. & Demirtaş, T. T. (2011). Osteogenic activities of MC3T3-E1 cells on heparin-immobilized poly(caprolactone) membranes. *Journal of Bioactive and Compatible Polymers*, 26(3), 257–269. <https://doi.org/10.1177/0883911511406329>

Guo, H., Dai, W., Miao, Y., Wang, Y., Ma, D. & Xue, W. (2018). Sustained heparin release actuator achieved from thermal and water activated shape memory hydrogels containing main-chain LC units. *Chemical Engineering Journal*, 339(February), 459–467. <https://doi.org/10.1016/j.cej.2018.02.009>

Gupta, K. C. & Jabrail, F. H. (2008). Effect of molecular weight and degree of deacetylation on controlled release of isoniazid from chitosan microspheres. *Polym. Adv. Technol.*, 19(December), 432–441. <https://doi.org/10.1002/pat1035>

Gupta, P., Vermani, K. & Garg, S. (2002). Hydrogels: From controlled release to pH-responsive drug delivery. *Drug Discovery Today*, 7(10), 569–579. [https://doi.org/10.1016/S1359-6446\(02\)02255-9](https://doi.org/10.1016/S1359-6446(02)02255-9)

Gurcan, M. N., Boucheron, L. E., Can, A., Madabhushi, A., Rajpoot, N. M. & Yener, B. (2009). Histopathological Image Analysis: A Review. *IEEE Reviews in Biomedical Engineering*, 2, 147–171. <https://doi.org/10.1109/RBME.2009.2034865>

Hankenson, K. D., Dishowitz, M., Gray, C., Schenker, M. & Manuscript, A. (2011). Angiogenesis in bone regeneration. *Injury*, 42(6), 556–561. <https://doi.org/10.1016/j.injury.2011.03.035>

Hanna, H., Mir, L. M. & Andre, F. M. (2018). In vitro osteoblastic differentiation of

mesenchymal stem cells generates cell layers with distinct properties. *Stem Cell Research and Therapy*, 9(1), 1–11. <https://doi.org/10.1186/s13287-018-0942-x>

Hattori, H., Amano, Y., Nogami, Y., Kawakami, M., Yura, H. & Ishihara, M. (2013). Development of a Novel Emergency Hemostatic Kit for Severe Hemorrhage. *Artificial Organs*, 37(5), 475–481. <https://doi.org/10.1111/aor.12004>

Hattori, T., Iwadate, Y., Inai, H., Sato, K. & Imai, Y. (1987). Preparation of Hydroxyapatite Powder Using a Freeze-Drying Method. *Journal of the Ceramic Association, Japan*, 95(1104), 825–827. [https://doi.org/10.2109/jcersj1950.95.1104\\_825](https://doi.org/10.2109/jcersj1950.95.1104_825)

Hawkins, D. M., Ellis, E. A., Stevenson, D., Holzenburg, A. & Reddy, S. M. (2007). Novel critical point drying (CPD) based preparation and transmission electron microscopy (TEM) imaging of protein specific molecularly imprinted polymers (HydroMIPs). *Journal of Materials Science*, 42(22), 9465–9468. <https://doi.org/10.1007/s10853-007-1806-4>

He, Q., Ao, Q., Gong, K., Zhang, L., Hu, M., Gong, Y. & Zhang, X. (2010). Preparation and characterization of chitosan–heparin composite matrices for blood contacting tissue engineering. *Biomedical Materials*, 5(5), 055001. <https://doi.org/10.1088/1748-6041/5/5/055001>

He, X., Dziak, R., Mao, K., Genco, R., Swihart, M., Li, C. & Yang, S. (2013). Integration of a Novel Injectable Nano Calcium Sulfate/Alginate Scaffold and BMP2 Gene-Modified Mesenchymal Stem Cells for Bone Regeneration. *Tissue Engineering Part A*, 19(3–4), 508–518. <https://doi.org/10.1089/ten.tea.2012.0244>

Hench, L. L. & Polak, J. M. (2002). Third-Generation Biomedical Materials. *Science*, 295(5557), 1014–1017. <https://doi.org/10.1126/science.1067404>

Hench, L. L., Splinter, R. J., Allen, W. C. & Greenlee, T. K. (1971). Bonding mechanisms at the interface of ceramic prosthetic materials. *Journal of Biomedical Materials Research*, 5(6), 117–141. <https://doi.org/10.1002/jbm.820050611>

Hench, Larry L. (1988). Bioactive ceramics. *Bioactive Ceramics Part II*, 523, 54–71. <https://doi.org/10.1111/j.1749-6632.1988.tb38500.x>

Hench, Larry L. (1991). Bioceramics: From Concept to Clinic. *Journal of the American Ceramic Society*, 74(7), 1487–1510. <https://doi.org/10.1111/j.1151-2916.1991.tb07132.x>

Herradi, S., Bouhazma, S., Khaldi, M., El Hachadi, A., El Bali, B. & Lachkar, M.

(2018). The effect of microwave and conventional heating on a modified sol-gel derived biphasic calcium phosphate. *Journal of Physics: Conference Series*, 984(1), 012016. <https://doi.org/10.1088/1742-6596/984/1/012016>

Herradi, S., El Bali, B., Khaldi, M. & Lachkar, M. (2017). Thermal stability of a modified sol-gel derived hydroxyapatite nanopowders. *IOP Conference Series: Materials Science and Engineering*, 186(1), 012023. <https://doi.org/10.1088/1757-899X/186/1/012023>

Higashi, S., Yamamuro, T., Nakamura, T., Ikada, Y., Hyon, S. H. & Jamshidi, K. (1986). Polymer-hydroxyapatite composites for biodegradable bone fillers. *Biomaterials*, 7(3), 183–187. [https://doi.org/10.1016/0142-9612\(86\)90099-2](https://doi.org/10.1016/0142-9612(86)90099-2)

Hing, K. A., Annaz, B., Saeed, S., Revell, P. A. & Buckland, T. (2005). Microporosity enhances bioactivity of synthetic bone graft substitutes. *Journal of Materials Science: Materials in Medicine*, 16(5), 467–475. <https://doi.org/10.1007/s10856-005-6988-1>

Hing, K. A., Saeed, S., Annaz, B., Buckland, T. & Revell, P. A. (2003). Microporosity Affects Bioactivity of Macroporous Hydroxyapatite Bone Graft Substitutes. *Key Engineering Materials*, 254–256(May), 273–276. <https://doi.org/10.4028/www.scientific.net/KEM.254-256.273>

Ho, Y.-C., Mi, F.-L., Sung, H.-W. & Kuo, P.-L. (2009). Heparin-functionalized chitosan–alginate scaffolds for controlled release of growth factor. *International Journal of Pharmaceutics*, 376(1–2), 69–75. <https://doi.org/10.1016/j.ijpharm.2009.04.048>

Hochberg, R. & Litvaitis, M. K. (2000). Hexamethyldisilazane for scanning electron microscopy of Gastrotricha. *Biotechnic and Histochemistry*, 75(1), 41–44. <https://doi.org/10.3109/10520290009047984>

Hoemann, C. D., Sun, J., Légaré, A., McKee, M. D. & Buschmann, M. D. (2005). Tissue engineering of cartilage using an injectable and adhesive chitosan-based cell-delivery vehicle. *Osteoarthritis and Cartilage*, 13(4), 318–329. <https://doi.org/10.1016/j.joca.2004.12.001>

Holzwarth, J. M. & Ma, P. X. (2011). Biomimetic nanofibrous scaffolds for bone tissue engineering. *Biomaterials*, 32(36), 9622–9629. <https://doi.org/10.1016/j.biomaterials.2011.09.009>

Hu, Y., Rawal, A. & Schmidt-Rohr, K. (2010). Strongly bound citrate stabilizes the

apatite nanocrystals in bone. *Proceedings of the National Academy of Sciences of the United States of America*, 107, 22425–22429. <https://doi.org/10.1073/pnas.1009219107>

Huang, T., Fan, C., Zhu, M., Zhu, Y., Zhang, W. & Li, L. (2019). 3D-printed scaffolds of biominerIALIZED hydroxyapatite nanocomposite on silk fibroin for improving bone regeneration. *Applied Surface Science*, 467–468(October 2018), 345–353. <https://doi.org/10.1016/j.apsusc.2018.10.166>

Huang, Z., McWilliams, A., Lui, H., McLean, D. I., Lam, S. & Zeng, H. (2003). Near-infrared Raman spectroscopy for optical diagnosis of lung cancer. *International Journal of Cancer*, 107(6), 1047–1052. <https://doi.org/10.1002/ijc.11500>

Hulbert, S. F., Young, F. A., Mathews, R. S., Klawitter, J. J., Talbert, C. D. & Stelling, F. H. (1970). Potential of ceramic materials as permanently implantable skeletal prostheses. *Journal of Biomedical Materials Research*, 4(3), 433–456. <https://doi.org/10.1002/jbm.820040309>

Hustedt, J. W. & Blizzard, D. J. (2014). The controversy surrounding bone morphogenetic proteins in the spine: a review of current research. *The Yale Journal of Biology and Medicine*, 87(4), 549–561. <http://www.ncbi.nlm.nih.gov/pubmed/25506287>

Hutmacher, D. W. (2000). Scaffolds in tissue engineering bone and cartilage. *Biomaterials*, 21(24), 2529–2543. [https://doi.org/10.1016/S0142-9612\(00\)00121-6](https://doi.org/10.1016/S0142-9612(00)00121-6)

Ishihara, M., Obara, K., Ishizuka, T., Fujita, M., Sato, M., Masuoka, K., Saito, Y., Yura, H., Matsui, T., Hattori, H., Kikuchi, M. & Kurita, A. (2003). Controlled release of fibroblast growth factors and heparin from photocrosslinked chitosan hydrogels and subsequent effect on in vivo vascularization. *Journal of Biomedical Materials Research*, 64A(3), 551–559. <https://doi.org/10.1002/jbm.a.10427>

Ito, A., Maekawa, K., Tsutsumi, S., Ikazaki, F. & Tateishi, T. (1997). Solubility product of OH-carbonated hydroxyapatite. *Journal of Biomedical Materials Research*, 36(4), 522–528. [https://doi.org/10.1002/\(SICI\)1097-4636\(19970915\)36:4<522::AID-JBM10>3.0.CO;2-C](https://doi.org/10.1002/(SICI)1097-4636(19970915)36:4<522::AID-JBM10>3.0.CO;2-C)

Jain, K. K. (2008). Drug Delivery Systems. In K. K. Jain (Ed.), *Methods in molecular biology (Clifton, N.J.)* (Vol. 437). Humana Press. <https://doi.org/10.1007/978-1-59745-210-6>

Jain, R. K., Au, P., Tam, J., Duda, D. G. & Fukumura, D. (2005). *Engineering vascularized tissue*. 23(7), 821–823.

Jarry, C., Chaput, C., Chenite, A., Renaud, M.-A., Buschmann, M. & Leroux, J.-C. (2001). Effects of steam sterilization on thermogelling chitosan-based gels. *Journal of Biomedical Materials Research*, 58(1), 127–135. [https://doi.org/10.1002/1097-4636\(2001\)58:1<127::AID-JBM190>3.0.CO;2-G](https://doi.org/10.1002/1097-4636(2001)58:1<127::AID-JBM190>3.0.CO;2-G)

Jarry, C., Leroux, J.-C., Haeck, J. & Chaput, C. (2002). Irradiating or Autoclaving Chitosan/Polyol Solutions: Effect on Thermogelling Chitosan- $\beta$ -glycerophosphate Systems. *Chemical & Pharmaceutical Bulletin*, 50(10), 1335–1340. <https://doi.org/10.1248/cpb.50.1335>

Jasper, J. P., Zhang, F., Poe, R. B. & Linhardt, R. J. (2015). Stable isotopic analysis of porcine, bovine, and ovine heparins. *Journal of Pharmaceutical Sciences*, 104(2), 457–463. <https://doi.org/10.1002/jps.24134>

Jayakumar, R., Prabaharan, M. & Muzzarelli, R. A. A. (2012). *Synthetic Biodegradable Polymers* (B. Rieger, A. Kunkel, G. W. Coates, R. Reichardt, E. Dinjus, & T. A. Zevaco (eds.); Vol. 245). Springer Berlin Heidelberg. <https://doi.org/10.1007/978-3-642-27154-0>

Jazayeri, H. E., Fahmy, M. D., Razavi, M., Stein, B. E., Nowman, A., Masri, R. M. & Tayebi, L. (2016). Dental Applications of Natural-Origin Polymers in Hard and Soft Tissue Engineering. *Journal of Prosthodontics*, 25(6), 510–517. <https://doi.org/10.1111/jopr.12465>

Jelvehgari, M., Zakeri-Milani, P., Siahi-Shadbad, M. R., Loveymi, B. D., Nokhodchi, A., Azari, Z. & Valizadeh, H. (2010). Development of pH-sensitive Insulin Nanoparticles using Eudragit L100-55 and Chitosan with Different Molecular Weights. *AAPS PharmSciTech*, 11(3), 1237–1242. <https://doi.org/10.1208/s12249-010-9488-7>

Jennings, J. A. (2017). Controlling chitosan degradation properties in vitro and in vivo. In *Chitosan Based Biomaterials* (Vol. 1, pp. 159–182). <https://doi.org/10.1016/B978-0-08-100230-8.00007-8>

Jha, L. J., Best, S. M., Knowles, J. C., Rehman, I., Santos, J. D. & Bonfield, W. (1997). Preparation and characterization of fluoride-substituted apatites. *Journal of Materials Science: Materials in Medicine*, 8(4), 185–191. <https://doi.org/10.1023/A:1018531505484>

Jiang, P., Mao, Z. & Gao, C. (2015). Combinational effect of matrix elasticity and alendronate density on differentiation of rat mesenchymal stem cells. *Acta Biomaterialia*, 19, 76–84. <https://doi.org/10.1016/j.actbio.2015.03.018>

Jin, R., Moreira Teixeira, L. S., Dijkstra, P. J., Karperien, M., van Blitterswijk, C. A., Zhong, Z. Y. & Feijen, J. (2009). Injectable chitosan-based hydrogels for cartilage tissue engineering. *Biomaterials*, 30(13), 2544–2551. <https://doi.org/10.1016/j.biomaterials.2009.01.020>

Jin, Rong, Hiemstra, C., Zhong, Z. & Feijen, J. (2007). Enzyme-mediated fast in situ formation of hydrogels from dextran-tyramine conjugates. *Biomaterials*, 28(18), 2791–2800. <https://doi.org/10.1016/j.biomaterials.2007.02.032>

Joshi, S., Kalyanasundaram, S. & Balasubramanian, V. (2013). Quantitative analysis of sodium carbonate and sodium bicarbonate in solid mixtures using Fourier Transform Infrared Spectroscopy (FT-IR). *Applied Spectroscopy*, 67(8), 841–845. <https://doi.org/10.1366/12-06915>

Juhasz, J. A. & Best, S. M. (2012). Bioactive ceramics: processing, structures and properties. *Journal of Materials Science*, 47(2), 610–624. <https://doi.org/10.1007/s10853-011-6063-x>

Kami, M., Kuberski, S., Komorowski, P. & Modrzejewska, Z. (2017). Thermosensitive chitosan gels containing calcium glycerophosphate for bone cell culture. <https://doi.org/10.1177/0883911516671150>

Kannan, S., Goetz-Neunhoeffer, F., Neubauer, J. & Ferreira, J. M. F. (2008). Ionic substitutions in biphasic hydroxyapatite and  $\beta$ -tricalcium phosphate mixtures: Structural analysis by rietveld refinement. *Journal of the American Ceramic Society*, 91(1), 1–12. <https://doi.org/10.1111/j.1551-2916.2007.02117.x>

Karageorgiou, V. & Kaplan, D. (2005). Porosity of 3D biomaterial scaffolds and osteogenesis. *Biomaterials*, 26(27), 5474–5491. <https://doi.org/10.1016/j.biomaterials.2005.02.002>

Katsimbri, P. (2017). The biology of normal bone remodelling. *European Journal of Cancer Care*, 26(6), 1–5. <https://doi.org/10.1111/ecc.12740>

Khan, A. F., Awais, M., Khan, A. S., Tabassum, S., Chaudhry, A. A. & Rehman, I. U. (2013). Raman Spectroscopy of Natural Bone and Synthetic Apatites. *Applied Spectroscopy Reviews*, 48(4), 329–355. <https://doi.org/10.1080/05704928.2012.721107>

Kilpadi, K. L., Chang, P. L. & Bellis, S. L. (2001). Hydroxylapatite binds more serum proteins, purified integrins, and osteoblast precursor cells than titanium or steel. *Journal of Biomedical Materials Research*, 57(2), 258–267. [https://doi.org/10.1002/1097-4636\(200111\)57:2<258::AID-JBM1166>3.0.CO;2-R](https://doi.org/10.1002/1097-4636(200111)57:2<258::AID-JBM1166>3.0.CO;2-R)

Kim, S.-K. (2014). *Chitin and Chitosan Derivates Advances in Drug Discovery and Developments* (pp. 1–492). [https://books.google.co.uk/books?id=V2DOBQAAQBAJ&dq=properties+of+chitosan&source=gbs\\_navlinks\\_s](https://books.google.co.uk/books?id=V2DOBQAAQBAJ&dq=properties+of+chitosan&source=gbs_navlinks_s)

Kim, S., Nishimoto, S. K., Bumgardner, J. D., Haggard, W. O., Gaber, M. W. & Yang, Y. (2010). A chitosan/β-glycerophosphate thermo-sensitive gel for the delivery of ellagic acid for the treatment of brain cancer. *Biomaterials*, 31(14), 4157–4166. <https://doi.org/10.1016/j.biomaterials.2010.01.139>

Kim, Y. J., Kang, I. K., Huh, M. W. & Yoon, S. C. (2000). Surface characterization and in vitro blood compatibility of poly(ethylene terephthalate) immobilized with insulin and/or heparin using plasma glow discharge. *Biomaterials*, 21(2), 121–130. [https://doi.org/10.1016/S0142-9612\(99\)00137-4](https://doi.org/10.1016/S0142-9612(99)00137-4)

King, A. G. (2002). 11. Ceramic Property Measurements. In *Ceramic Technology and Processing* (pp. 378–499). <https://doi.org/10.1016/b978-081551443-5.50014-7>

Klouda, L. (2015). Thermoresponsive hydrogels in biomedical applications A seven-year update. *European Journal of Pharmaceutics and Biopharmaceutics*, 97, 338–349. <https://doi.org/10.1016/j.ejpb.2015.05.017>

Knowles, J. C., Callcut, S. & Georgiou, G. (2000). Characterisation of the rheological properties and zeta potential of a range of hydroxyapatite powders. *Biomaterials*, 21(13), 1387–1392. [https://doi.org/10.1016/S0142-9612\(00\)00032-6](https://doi.org/10.1016/S0142-9612(00)00032-6)

Kocak, F. Z., Talari, A. C. S., Yar, M. & Rehman, I. U. (2020). In - Situ Forming pH and Thermosensitive Injectable Hydrogels to Stimulate Angiogenesis : Potential Candidates for Fast Bone Regeneration Applications. *International Journal of Molecular Sciences*, 21(5), 1–26. <https://doi.org/10.3390/ijms21051633>

Kokubo, T. (1990). Surface chemistry of bioactive glass-ceramics. *Journal of Non-Crystalline Solids*, 120(1–3), 138–151. [https://doi.org/10.1016/0022-3093\(90\)90199-V](https://doi.org/10.1016/0022-3093(90)90199-V)

Kokubo, T. (1991). Bioactive glass ceramics: properties and applications. *Biomaterials*.

https://doi.org/10.1016/0142-9612(91)90194-F

Kokubo, T. & Takadama, H. (2006). How useful is SBF in predicting in vivo bone bioactivity? *Biomaterials*, 27(15), 2907–2915. <https://doi.org/10.1016/j.biomaterials.2006.01.017>

Kondiah, P. J., Choonara, Y. E., Kondiah, P. P. D., Marimuthu, T., Kumar, P., Du Toit, L. C. & Pillay, V. (2016). A review of injectable polymeric hydrogel systems for application in bone tissue engineering. *Molecules*, 21(11). <https://doi.org/10.3390/molecules21111580>

Kong, L., Gao, Y., Lu, G., Gong, Y., Zhao, N. & Zhang, X. (2006). A study on the bioactivity of chitosan/nano-hydroxyapatite composite scaffolds for bone tissue engineering. *European Polymer Journal*, 42(12), 3171–3179. <https://doi.org/10.1016/j.eurpolymj.2006.08.009>

Koniorczyk, M. & Gawin, D. (2008). Heat and Moisture Transport in Porous Building Materials Containing Salt. *Journal of Building Physics*, 31(4), 279–300. <https://doi.org/10.1177/1744259107088003>

Koura, N., Kohara, S., Takeuchi, K., Takahashi, S., Curtiss, L. A., M, G. & Saboungi, M.-L. (1996). Alkali carbonates: Raman spectroscopy, ab initio calculations, and structure. *Journal of Molecular Structure* 382, 382, 163–169.

Koutsopoulos, S. (2002). Synthesis and characterization of hydroxyapatite crystals: A review study on the analytical methods. *Journal of Biomedical Materials Research*, 62(4), 600–612. <https://doi.org/10.1002/jbm.10280>

Kuriakose, T. A., Kalkura, S. N., Palanichamy, M., Arivuoli, D., Dierks, K., Bocelli, G. & Betzel, C. (2004). Synthesis of stoichiometric nano crystalline hydroxyapatite by ethanol-based sol–gel technique at low temperature. *Journal of Crystal Growth*, 263(1–4), 517–523. <https://doi.org/10.1016/j.jcrysGro.2003.11.057>

Kwon, S. H., Jun, Y. K., Hong, S. H. & Kim, H. E. (2003). Synthesis and dissolution behavior of  $\beta$ -TCP and HA/ $\beta$ -TCP composite powders. *Journal of the European Ceramic Society*, 23(7), 1039–1045. [https://doi.org/10.1016/S0955-2219\(02\)00263-7](https://doi.org/10.1016/S0955-2219(02)00263-7)

Lafon, J. P., Champion, E. & Bernache-Assollant, D. (2008). Processing of AB-type carbonated hydroxyapatite  $\text{Ca}_{10-x}(\text{PO}_4)_{6-x}(\text{CO}_3)_x(\text{OH})_{2-x-2y}(\text{CO}_3)_y$  ceramics with controlled composition. *Journal of the European Ceramic Society*, 28(1), 139–147. <https://doi.org/10.1016/j.jeurceramsoc.2007.06.009>

Lafon, J. P., Champion, E., Gibert, R. & Danna, A. M. (2003). Thermal Decomposition of Carbonated Calcium Phosphate Apatites. *Journal of Thermal Analysis and Calorimetry*, 72, 1127–1134. <https://doi.org/10.1023/A:1025036214044>

Lai, Y.-P. & Kan, C.-D. (2017). Improve blood compatibility of bioresorbable magnesium stents coated with functionalized anti-CD34 antibody and heparin-collagen multiplayers. *2017 39th Annual International Conference of the IEEE Engineering in Medicine and Biology Society (EMBC)*, 2068–2071. <https://doi.org/10.1109/EMBC.2017.8037260>

Laity, P. R. & Holland, C. (2016). The Rheology behind Stress-Induced Solidification in Native Silk Feedstocks. *International Journal of Molecular Sciences*, 17(11). <https://doi.org/10.3390/ijms17111812>

Landi, E., Celotti, G., Logroscino, G. & Tampieri, A. (2003). Carbonated hydroxyapatite as bone substitute. *Journal of the European Ceramic Society*, 23(15), 2931–2937. [https://doi.org/10.1016/S0955-2219\(03\)00304-2](https://doi.org/10.1016/S0955-2219(03)00304-2)

Landi, Elena, Tampieri, A., Mattioli-Belmonte, M., Celotti, G., Sandri, M., Gigante, A., Fava, P. & Biagini, G. (2006). Biomimetic Mg- and Mg<sub>2</sub>CO<sub>3</sub>-substituted hydroxyapatites: synthesis characterization and in vitro behaviour. *Journal of the European Ceramic Society*, 26(13), 2593–2601. <https://doi.org/10.1016/j.jeurceramsoc.2005.06.040>

Laurencin, D., Almora-Barrios, N., de Leeuw, N. H., Gervais, C., Bonhomme, C., Mauri, F., Chrzanowski, W., Knowles, J. C., Newport, R. J., Wong, A., Gan, Z. & Smith, M. E. (2011). Magnesium incorporation into hydroxyapatite. *Biomaterials*, 32(7), 1826–1837. <https://doi.org/10.1016/j.biomaterials.2010.11.017>

Lee, F., Chung, J. E. & Kurisawa, M. (2009). An injectable hyaluronic acid-tyramine hydrogel system for protein delivery. *Journal of Controlled Release*, 134(3), 186–193. <https://doi.org/10.1016/j.jconrel.2008.11.028>

Lee, J. I., Kim, H. S. & Yoo, H. S. (2009). DNA nanogels composed of chitosan and Pluronic with thermo-sensitive and photo-crosslinking properties. *International Journal of Pharmaceutics*, 373(1–2), 93–99. <https://doi.org/10.1016/j.ijpharm.2009.01.016>

Lee, K. Y. & Mooney, D. J. (2001). Hydrogels for tissue engineering. *Chemical Reviews*, 101(7), 1869–1879. <https://doi.org/10.1021/cr000108x>

Lee, K. Y. & Mooney, D. J. (2012). Alginate: Properties and biomedical applications.

*Progress in Polymer Science*, 37(1), 106–126.  
<https://doi.org/10.1016/j.progpolymsci.2011.06.003>

Lee, Y., Hahm, Y. M., Lee, D. H., Matsuya, S., Nakagawa, M. & Ishikawa, K. (2008). Preparation and characterization of macroporous carbonate-substituted hydroxyapatite scaffold. *Industrial and Engineering Chemistry Research*, 47(8), 2618–2622. <https://doi.org/10.1021/ie071474a>

LeGeros, R. Z. & Ben-nissan, B. (2014). Introduction to Synthetic and Biologic Apatites. In *Advances in Calcium Phosphate Biomaterials* (pp. 1–19).

Li, F., Liu, Y., Ding, Y. & Xie, Q. (2014). A new injectable in situ forming hydroxyapatite and thermosensitive chitosan gel promoted by Na<sub>2</sub>CO<sub>3</sub>. *Soft Matter*, 10(13), 2292–2303. <https://doi.org/10.1039/C3SM52508B>

Li, P. & De Groot, K. (1994). Better bioactive ceramics through sol-gel process - Code: G2. *Journal of Sol-Gel Science and Technology*, 2(1–3), 797–801. <https://doi.org/10.1007/BF00486353>

Li, Y., Rodrigues, J. & Tomás, H. (2012). Injectable and biodegradable hydrogels: gelation, biodegradation and biomedical applications. *Chemical Society Reviews*, 41(6), 2193–2221. <https://doi.org/10.1039/c1cs15203c>

Li, Z., Fan, Z., Xu, Y., Niu, H., Xie, X., Liu, Z. & Guan, J. (2016). Thermosensitive and Highly Flexible Hydrogels Capable of Stimulating Cardiac Differentiation of Cardiosphere-Derived Cells under Static and Dynamic Mechanical Training Conditions. *ACS Applied Materials and Interfaces*, 8(25), 15948–15957. <https://doi.org/10.1021/acsami.6b04932>

Lin, C. C. & Metters, A. T. (2006). Hydrogels in controlled release formulations: Network design and mathematical modeling. *Advanced Drug Delivery Reviews*, 58(12–13), 1379–1408. <https://doi.org/10.1016/j.addr.2006.09.004>

Lin, K. & Chang, J. (2015). Structure and properties of hydroxyapatite for biomedical applications. In M. Mucalo (Ed.), *Hydroxyapatite (HAp) for Biomedical Applications* (pp. 3–21). Woodhead Publishing is an imprint of Elsevier.

Lin, Kaili, Chen, L. & Chang, J. (2012). Fabrication of Dense Hydroxyapatite Nanobioceramics with Enhanced Mechanical Properties via Two-Step Sintering Process. *International Journal of Applied Ceramic Technology*, 9(3), 479–485. <https://doi.org/10.1111/j.1744-7402.2011.02654.x>

Lin, Kaili, Liu, P., Wei, L., Zou, Z., Zhang, W., Qian, Y., Shen, Y. & Chang, J. (2013).

Strontium substituted hydroxyapatite porous microspheres: Surfactant-free hydrothermal synthesis, enhanced biological response and sustained drug release. *Chemical Engineering Journal*, 222, 49–59. <https://doi.org/10.1016/j.cej.2013.02.037>

Lin, Y. S., Meyers, M. A. & Olevsky, E. A. (2012). Microchannelled hydroxyapatite components by sequential freeze drying and free pressureless spark plasma sintering. *Advances in Applied Ceramics*, 111(5–6), 269–274. <https://doi.org/10.1179/1743676111Y.0000000067>

Lisková, J., Bačáková, L., Skwarczyńska, A., Musial, O., Bliznuk, V., De Schampelaere, K., Modrzejewska, Z. & Douglas, T. (2015). Development of Thermosensitive Hydrogels of Chitosan, Sodium and Magnesium Glycerophosphate for Bone Regeneration Applications. *Journal of Functional Biomaterials*, 6(2), 192–203. <https://doi.org/10.3390/jfb6020192>

Liu, L., Gao, Q., Lu, X. & Zhou, H. (2016). In situ forming hydrogels based on chitosan for drug delivery and tissue regeneration. *Asian Journal of Pharmaceutical Sciences*, 11(6), 673–683. <https://doi.org/10.1016/j.ajps.2016.07.001>

Liu, L., Tang, X., Wang, Y. & Guo, S. (2011). Smart gelation of chitosan solution in the presence of NaHCO<sub>3</sub> for injectable drug delivery system. *International Journal of Pharmaceutics*, 414(1–2), 6–15. <https://doi.org/10.1016/j.ijpharm.2011.04.052>

Liu, Q., Huang, S., Matinlinna, J. P., Chen, Z. & Pan, H. (2013). Insight into biological apatite: Physiochemical properties and preparation approaches. *BioMed Research International*, 2013. <https://doi.org/10.1155/2013/929748>

Liu, X., Chen, Y., Huang, Q., He, W., Feng, Q. & Yu, B. (2014). A novel thermo-sensitive hydrogel based on thiolated chitosan/hydroxyapatite/beta-glycerophosphate. *Carbohydrate Polymers*, 110, 62–69. <https://doi.org/10.1016/j.carbpol.2014.03.065>

Liu, Y., Luo, D. & Wang, T. (2016). Hierarchical Structures of Bone and Bioinspired Bone Tissue Engineering. In *Small (Weinheim an der Bergstrasse, Germany)* (Vol. 12, Issue 34, pp. 4611–4632). <https://doi.org/10.1002/smll.201600626>

Lu, H., Qu, Z. & Zhou, Y. (1998). Preparation and mechanical properties of dense polycrystalline hydroxyapatite through freeze-drying. *Journal of Materials Science: Materials in Medicine*, 9(10), 583–587.

https://doi.org/10.1023/A:1008913609857

Lu, Q., Zhang, S., Hu, K., Feng, Q., Cao, C. & Cui, F. (2007). Cytocompatibility and blood compatibility of multifunctional fibroin/collagen/heparin scaffolds. *Biomaterials*, 28(14), 2306–2313.  
https://doi.org/10.1016/j.biomaterials.2007.01.031

Luger, P. (2014). 2. Fundamental results of diffraction theory, X-radiation. In *Modern X-Ray Analysis on Single Crystals* (A Practica, pp. 14–41).  
https://doi.org/10.1515/9783110308280.14

Luo, Z. (2016). *A Practical Guide to Transmission Electron Microscopy* (A practica). (222 East 46th Street, New York, NY 10017): Momentum Press.

MacIntosh, F. C. (1941). A colorimetric method for the standardization of heparin preparations. *Biochemical Journal*, 35(7), 776–782.  
https://doi.org/10.1042/bj0350776

Mahadevan-Jansen, A. & Richards-Kortum, R. (1997). Raman spectroscopy for cancer detection: a review. *Annual International Conference of the IEEE Engineering in Medicine and Biology - Proceedings*, 6(C), 2722–2728.  
https://doi.org/10.1109/tembs.1997.756895

Mainreck, N., Brézillon, S., Sockalingum, G. D., Maquart, F.-X., Manfait, M. & Wegrowski, Y. (2011). Rapid Characterization of Glycosaminoglycans Using a Combined Approach by Infrared and Raman Microspectroscopies. *Journal of Pharmaceutical Sciences*, 100(2), 441–450. https://doi.org/10.1002/jps.22288

Malhotra, A. & Habibovic, P. (2016). Calcium Phosphates and Angiogenesis: Implications and Advances for Bone Regeneration. In *Trends in Biotechnology* (Vol. 34, Issue 12, pp. 983–992). Elsevier Ltd.  
https://doi.org/10.1016/j.tibtech.2016.07.005

Mangir, N., Dikici, S., ClaeysSENS, F. & Macneil, S. (2019). Using ex Ovo Chick Chorioallantoic Membrane (CAM) Assay to Evaluate the Biocompatibility and Angiogenic Response to Biomaterials. *ACS Biomaterials Science and Engineering*, 5, 3190–3200. https://doi.org/10.1021/acsbiomaterials.9b00172

Mansfield, E., Kar, A. & Hooker, S. A. (2010). Applications of TGA in quality control of SWCNTs. *Analytical and Bioanalytical Chemistry*, 396(3), 1071–1077.  
https://doi.org/10.1007/s00216-009-3319-2

Mansur, H. S., de S. Costa Jr., E., Mansur, A. A. P. & Barbosa-Stancioli, E. F. (2009).

Cytocompatibility evaluation in cell-culture systems of chemically crosslinked chitosan/PVA hydrogels. *Materials Science and Engineering C*, 29(5), 1574–1583. <https://doi.org/10.1016/j.msec.2008.12.012>

Marković, S., Veselinović, L., Lukić, M. J., Karanović, L., Bračko, I., Ignjatović, N. & Uskoković, D. (2011). Synthetical bone-like and biological hydroxyapatites: a comparative study of crystal structure and morphology. *Biomedical Materials*, 6(4), 045005. <https://doi.org/10.1088/1748-6041/6/4/045005>

Marks, S. C. & Odgren, P. R. (2002). *Structure and development of the skeleton* (J. P. Bilezikian, L. G. Raisz, & G. A. Rodan (eds.); Academic P). <https://www.elsevier.com/books/principles-of-bone-biology/bilezikian/978-0-12-098652-1>

Marreco, P. R., Da Luz Moreira, P., Genari, S. C. & Moraes, Â. M. (2004). Effects of different sterilization methods on the morphology, mechanical properties, and cytotoxicity of chitosan membranes used as wound dressings. *Journal of Biomedical Materials Research - Part B Applied Biomaterials*, 71(2), 268–277. <https://doi.org/10.1002/jbm.b.30081>

Martino, M. M., Briquez, P. S., Maruyama, K. & Hubbell, J. A. (2015). Extracellular matrix-inspired growth factor delivery systems for bone regeneration. *Advanced Drug Delivery Reviews*, 94, 41–52. <https://doi.org/10.1016/j.addr.2015.04.007>

Matsumoto, A., Chen, J., Collette, A. L., Kim, U. J., Altman, G. H., Cebe, P. & Kaplan, D. L. (2006). Mechanisms of silk fibroin sol-gel transitions. *Journal of Physical Chemistry B*, 110(43), 21630–21638. <https://doi.org/10.1021/jp056350v>

Matsumoto, T., Okazaki, M., Inoue, M., Yamaguchi, S., Kusunose, T., Toyonaga, T., Hamada, Y. & Takahashi, J. (2004). Hydroxyapatite particles as a controlled release carrier of protein. *Biomaterials*, 25(17), 3807–3812. <https://doi.org/10.1016/j.biomaterials.2003.10.081>

Matzelle, T. R., Ivanov, D. A., Landwehr, D., Heinrich, L. A., Herkt-Brunn, C., Reichelt, R. & Kruse, N. (2002). Micromechanical properties of ‘smart’ gels: Studies by scanning force and scanning electron microscopy of PNIPAAm. *Journal of Physical Chemistry B*, 106(11), 2861–2866. <https://doi.org/10.1021/jp0128426>

McCusker, L. B., Von Dreele, R. B., Cox, D. E., Louër, D. & Scardi, P. (1999). Rietveld refinement guidelines. *Journal of Applied Crystallography*, 32(1), 36–50.

<https://doi.org/10.1107/S0021889898009856>

Meijering, E. (2010). Neuron Tracing in Perspective. *Journal of International Society for Advancement of Cytometry: Cytometry Part A*, 77A, 693–704. <https://doi.org/10.1002/cyto.a.20895>

Méthot, S., Changoor, A., Tran-Khanh, N., Hoemann, C. D., Stanish, W. D., Restrepo, A., Shive, M. S. & Buschmann, M. D. (2016). Osteochondral Biopsy Analysis Demonstrates That BST-CarGel Treatment Improves Structural and Cellular Characteristics of Cartilage Repair Tissue Compared With Microfracture. *Cartilage*, 7(1), 16–28. <https://doi.org/10.1177/1947603515595837>

Michio, I. & Feiyu, K. (2016). Scanning Electron Microscopy 5. In *Materials Science and Engineering of Carbon - Characterization* (pp. 71–93). Elsevier.

Mikhailov, G. P., Tuchkov, S. V., Lazarev, V. V. & Kulish, E. I. (2014). Complexation of chitosan with acetic acid according to Fourier transform Raman spectroscopy data. *Russian Journal of Physical Chemistry A*, 88(6), 936–941. <https://doi.org/10.1134/S0036024414060181>

Mischnick, P. & Momcilovic, D. (2010). Chemical Structure Analysis of Starch and Cellulose Derivatives. In *Advances in Carbohydrate Chemistry and Biochemistry* (Vol. 64, Issue C). [https://doi.org/10.1016/S0065-2318\(10\)64004-8](https://doi.org/10.1016/S0065-2318(10)64004-8)

Mizuguchi, M., Nara, M., Ke, Y., Kawano, K., Hiraoki, T. & Nitta, K. (1997). Fourier-transform infrared spectroscopic studies on the coordination of the side-chain COO- groups to Ca<sup>2+</sup> in equine lysozyme. *European Journal of Biochemistry*, 250(1), 72–76. <https://doi.org/10.1111/j.1432-1033.1997.00072.x>

Moreira, C. D. F., Carvalho, S. M., Mansur, H. S. & Pereira, M. M. (2016). Thermogelling chitosan-collagen-bioactive glass nanoparticle hybrids as potential injectable systems for tissue engineering. *Materials Science and Engineering C*, 58, 1207–1216. <https://doi.org/10.1016/j.msec.2015.09.075>

Moreira, C. D. F., Carvalho, S. M., Sousa, R. G., Mansur, H. S. & Pereira, M. M. (2018). Nanostructured chitosan/gelatin/bioactive glass in situ forming hydrogel composites as a potential injectable matrix for bone tissue engineering. *Materials Chemistry and Physics*, 218(April), 304–316. <https://doi.org/10.1016/j.matchemphys.2018.07.039>

Moreira Teixeira, L. S., Feijen, J., van Blitterswijk, C. A., Dijkstra, P. J. & Karperien, M. (2012). Enzyme-catalyzed crosslinkable hydrogels: Emerging strategies for

tissue engineering. *Biomaterials*, 33(5), 1281–1290. <https://doi.org/10.1016/j.biomaterials.2011.10.067>

Mredha, M. T. I., Kitamura, N., Nonoyama, T., Wada, S., Goto, K., Zhang, X., Nakajima, T., Kurokawa, T., Takagi, Y., Yasuda, K. & Gong, J. P. (2017). Anisotropic tough double network hydrogel from fish collagen and its spontaneous in vivo bonding to bone. *Biomaterials*, 132, 85–95. <https://doi.org/10.1016/j.biomaterials.2017.04.005>

Munarin, F., Bozzini, S., Visai, L., Tanzi, M. C. & Petrini, P. (2013). Sterilization treatments on polysaccharides: Effects and side effects on pectin. *Food Hydrocolloids*, 31(1), 74–84. <https://doi.org/10.1016/j.foodhyd.2012.09.017>

Murugesan, S., Xie, J. & Linhardt, R. J. (2008). Immobilization of Heparin: Approaches and Applications. *October*, 8(2), 80–100. <https://doi.org/10.1016/j.surg.2006.10.010>

Naahidi, S., Jafari, M., Logan, M., Wang, Y., Yuan, Y., Bae, H., Dixon, B. & Chen, P. (2017). Biocompatibility of hydrogel-based scaffolds for tissue engineering applications. *Biotechnology Advances*, 35(5), 530–544. <https://doi.org/10.1016/j.biotechadv.2017.05.006>

Najeeb, S., Khurshid, Z., Zafar, M. S., Khan, A. S., Zohaib, S., Mart??, J. M. N., Sauro, S., Matinlinna, J. P. & Rehman, I. U. (2016). Modifications in glass ionomer cements: Nano-sized fillers and bioactive nanoceramics. *International Journal of Molecular Sciences*, 17(7). <https://doi.org/10.3390/ijms17071134>

Nam, S., Stowers, R., Lou, J., Xia, Y. & Chaudhuri, O. (2019). Varying PEG density to control stress relaxation in alginate-PEG hydrogels for 3D cell culture studies. *Biomaterials*, 200(January), 15–24. <https://doi.org/10.1016/j.biomaterials.2019.02.004>

Nguyen, M. K. & Lee, D. S. (2010). Injectable biodegradable hydrogels. *Macromolecular Bioscience*, 10(6), 563–579. <https://doi.org/10.1002/mabi.200900402>

Nicholson, J. W. (2020). *The Chemistry of Medical and Dental Materials - John W Nicholson - Google Books*. Royal Society of Chemistry, - Technology & Engineering. <https://books.google.com.tr/books?id=HP3oDwAAQBAJ&pg=PA61&dq=osteoinductive+vs+osteoprotective&hl=en&sa=X&ved=2ahUKEwjI8OqTqXuAhVykosKHVTkCGAQ6AEwAnoECAUQAg#v=onepage&q=osteoinductive+vs+osteoprotective&f=false>

Nicosia, R. F. (2009). The aortic ring model of angiogenesis: A quarter century of search and discovery. *Journal of Cellular and Molecular Medicine*, 13(10), 4113–4136. <https://doi.org/10.1111/j.1582-4934.2009.00891.x>

Nikpour, M. R., Tavakol, S., Rabiee, S. M., Jahanshahi, M. & Amani, A. (2011). Syntheses, characterization and comparative study of bone regeneration on nano hydroxyapatite and hydroxyapatite/chitosan nanocomposite in rat. *2011 18th Iranian Conference of Biomedical Engineering, ICBME 2011, December*, 146–151. <https://doi.org/10.1109/ICBME.2011.6168543>

Nordtveit, R. J., Vårum, K. M. & Smidsrød, O. (1996). Degradation of partially N-acetylated chitosans with hen egg white and human lysozyme. *Carbohydrate Polymers*, 29(2), 163–167. [https://doi.org/10.1016/0144-8617\(96\)00003-3](https://doi.org/10.1016/0144-8617(96)00003-3)

Norton, J., Malik, K. R., Darr, J. A. & Rehman, I. (2006). Recent developments in processing and surface modification of hydroxyapatite. *Advances in Applied Ceramics*, 105(3), 113–139. <https://doi.org/10.1179/174367606X102278>

Nyman, J. S., Makowski, A. J., Patil, C. A., Masui, T. P., O’Quinn, E. C., Bi, X., Guelcher, S. A., Nicollala, D. P. & Mahadevan-Jansen, A. (2011). Measuring differences in compositional properties of bone tissue by confocal raman spectroscopy. *Calcified Tissue International*, 89(2), 111–122. <https://doi.org/10.1007/s00223-011-9497-x>

O’Brien, F. J. (2011). Biomaterials & scaffolds for tissue engineering. *Materials Today*, 14(3), 88–95. [https://doi.org/10.1016/S1369-7021\(11\)70058-X](https://doi.org/10.1016/S1369-7021(11)70058-X)

Ohtsuki, C., Kamitakahara, M. & Miyazaki, T. (2009). Bioactive ceramic-based materials with designed reactivity for bone tissue regeneration. *Journal of the Royal Society Interface*, 6(SUPPL. 3). <https://doi.org/10.1098/rsif.2008.0419.focus>

Okada, M. & Furuzono, T. (2012). Hydroxylapatite nanoparticles: fabrication methods and medical applications. *Science and Technology of Advanced Materials*, 13(6), 064103. <https://doi.org/10.1088/1468-6996/13/6/064103>

Oliver, B. G. & Davis, A. R. (1973). Vibrational Spectroscopic Studies of Aqueous Alkali Metal Bicarbonate and Carbonate Solutions. *Canadian Journal of Chemistry*, 51(5), 698–702. <https://doi.org/10.1139/v73-106>

Oliviero, O., Ventre, M. & Netti, P. A. (2012). Functional porous hydrogels to study angiogenesis under the effect of controlled release of vascular endothelial growth

factor. *Acta Biomaterialia*, 8(9), 3294–3301. <https://doi.org/10.1016/j.actbio.2012.05.019>

Olszta, M. J., Cheng, X., Jee, S. S., Kumar, R., Kim, Y. Y., Kaufman, M. J., Douglas, E. P. & Gower, L. B. (2007). Bone structure and formation: A new perspective. *Materials Science and Engineering R: Reports*, 58(3–5), 77–116. <https://doi.org/10.1016/j.mser.2007.05.001>

Ong, S. R., Trabbic-Carlson, K. A., Nettles, D. L., Lim, D. W., Chilkoti, A. & Setton, L. A. (2006). Epitope tagging for tracking elastin-like polypeptides. *Biomaterials*, 27(9), 1930–1935. <https://doi.org/10.1016/j.biomaterials.2005.10.018>

Ooi, C. Y., Hamdi, M. & Ramesh, S. (2007). Properties of hydroxyapatite produced by annealing of bovine bone. *Ceramics International*, 33(7), 1171–1177. <https://doi.org/10.1016/j.ceramint.2006.04.001>

Orriss, I. R., Utting, J. C., Brandao-Burch, A., Colston, K., Grubb, B. R., Burnstock, G. & Arnett, T. R. (2007). Extracellular nucleotides block bone mineralization in vitro: Evidence for dual inhibitory mechanisms involving both P2Y2 receptors and pyrophosphate. *Endocrinology*, 148(9), 4208–4216. <https://doi.org/10.1210/en.2007-0066>

Oyarzun-Ampuero, F. A., Brea, J., Loza, M. I., Torres, D. & Alonso, M. J. (2009). Chitosan-hyaluronic acid nanoparticles loaded with heparin for the treatment of asthma. *International Journal of Pharmaceutics*, 381(2), 122–129. <https://doi.org/10.1016/j.ijpharm.2009.04.009>

Ozdemir, O., Çelik, M. S., Nickolov, Z. S. & Miller, J. D. (2007). Water structure and its influence on the flotation of carbonate and bicarbonate salts. *Journal of Colloid and Interface Science*, 314(2), 545–551. <https://doi.org/10.1016/j.jcis.2007.05.086>

Patan, S. (2000). Vasculogenesis and angiogenesis as mechanisms of vascular network formation, growth and remodeling. In *Journal of Neuro-Oncology* (Vol. 50, Issues 1–2, pp. 1–15). <https://doi.org/10.1023/A:1006493130855>

Pazarlioglu, S. & Salman, S. (2017). Sintering effect on the microstructural, mechanical, and in vitro bioactivity properties of a commercially synthetic hydroxyapatite. *Journal of the Australian Ceramic Society*, 53(2), 391–401. <https://doi.org/10.1007/s41779-017-0048-4>

Penel, G., Leroy, G., Rey, C. & Bres, E. (1998). MicroRaman Spectral Study of the PO<sub>4</sub> and CO<sub>3</sub> Vibrational Modes in Synthetic and Biological Apatites. *Calcified*

*Tissue International*, 63(6), 475–481. <https://doi.org/10.1007/s002239900561>

Percival, M. (1999). Bone Health & Osteoporosis. *Nutritional, Applied Reports, Science*, 5(4), 1–6.

Pietak, A. M., Reid, J. W., Stott, M. J. & Sayer, M. (2007). Silicon substitution in the calcium phosphate bioceramics. *Biomaterials*, 28(28), 4023–4032. <https://doi.org/10.1016/j.biomaterials.2007.05.003>

Popko, J., Fernandes, A., Brites, D. & Lanier, L. M. (2009). Automated Analysis of NeuronJ Tracing Data. *Journal of International Society for Advancement of Cytometry: Cytometry Part A*, 75(4), 371–376. <https://doi.org/10.1002/cyto.a.20660>

Potta, T., Chun, C. J. & Song, S. C. (2009). Chemically crosslinkable thermosensitive polyphosphazene gels as injectable materials for biomedical applications. *Biomaterials*, 30(31), 6178–6192. <https://doi.org/10.1016/j.biomaterials.2009.08.015>

Prabaharan, M. (2012). 2. Sources of chitosan. In *Chitosan and Its Derivatives as Promising Drug Delivery Carriers* (p. 13). American Society Of Mechanical Engineers (ASME). <https://doi.org/10.1115/1.860052>

Puchtler, H., Meloan, S. N. & Terry, M. S. (1969). On the history and mechanism of alizarin red S stains for calcium. *The Journal of Histochemistry and Cytochemistry*, 17(2), 110–124.

Qasim, S. Bin. (2015). *Development of a Novel Bioactive Functionally Guided Tissue Graded Membrane for Periodontal Lesions* [The University of Sheffield]. <https://doi.org/10.15445/01012014.07>

Qasim, S. B., Delaine-Smith, R. M., Fey, T., Rawlinson, A. & Rehman, I. U. (2015). Freeze gelated porous membranes for periodontal tissue regeneration. *Acta Biomaterialia*, 23, 317–328. <https://doi.org/10.1016/j.actbio.2015.05.001>

Qasim, S. B., Husain, S., Huang, Y., Pogorielov, M., Deineka, V., Lyndin, M., Rawlinson, A. & Rehman, I. U. (2017). In-vitro and in-vivo degradation studies of freeze gelated porous chitosan composite scaffolds for tissue engineering applications. *Polymer Degradation and Stability*, 136, 31–38. <https://doi.org/10.1016/j.polymdegradstab.2016.11.018>

Radivojša Matanović, M., Grabnar, I., Gosenca, M. & Ahlin Grabnar, P. (2015). Prolonged subcutaneous delivery of low molecular weight heparin based on

thermoreponsive hydrogels with chitosan nanocomplexes: Design, in vitro evaluation, and cytotoxicity studies. *International Journal of Pharmaceutics*, 488(1-2), 127–135. <https://doi.org/10.1016/j.ijpharm.2015.04.063>

Rafipoor, M., Sefti, M. V., Salimi, F., Jarrahian, K. & Ghorashi, S. S. (2014). Investigation of Rheological Properties of Polyacrylamide/Chromium Triacetate Hydrogels Performed for Water Shutoff Treatment in Oil Reservoirs. *Journal of Dispersion Science and Technology*, 35(1), 56–63. <https://doi.org/10.1080/01932691.2013.773446>

Raftery, R. M., Castano, I. M., Chen, G., Cavanagh, B., Quinn, B., Curtin, C. M., Cryan, S. A. & O'Brien, F. J. (2017). Translating the role of osteogenic-angiogenic coupling in bone formation : Highly efficient chitosan-pDNA activated scaffolds can accelerate bone regeneration in critical-sized bone defects. *Biomaterials*, 149, 116–127. <https://doi.org/10.1016/j.biomaterials.2017.09.036>

Raii, M., Escudero Sanz, F. J. & Nzihou, A. (2012). Rheological behavior of gypsum, plaster, and hydroxyapatite gel blends. *Industrial and Engineering Chemistry Research*, 51(34), 11163–11169. <https://doi.org/10.1021/ie301154d>

Rehman, I. & Bonfield, W. (1997). Characterization of hydroxyapatite and carbonated apatite by photo acoustic FTIR spectroscopy. *Journal of Materials Science: Materials in Medicine*, 8(1), 1–4. <https://doi.org/10.1023/A:1018570213546>

Rehman, I., Smith, R., Hench, L. L. & Bonfield, W. (1995). Structural evaluation of human and sheep bone and comparison with synthetic hydroxyapatite by FT-Raman spectroscopy. *Journal of Biomedical Materials Research*, 29(10), 1287–1294. <https://doi.org/10.1002/jbm.820291016>

Rehman, I. U., Movasaghi, Z. & Rehman, S. (2012). Vibrational spectroscopy for tissue analysis. In *Vibrational Spectroscopy for Tissue Analysis* (Vol. 20124820). <https://doi.org/10.1201/b12949>

Ren, D., Yi, H., Wang, W. & Ma, X. (2005). The enzymatic degradation and swelling properties of chitosan matrices with different degrees of N-acetylation. *Carbohydrate Research*, 340(15), 2403–2410. <https://doi.org/10.1016/j.carres.2005.07.022>

Ren, Z., Wang, Y., Ma, S., Duan, S., Yang, X., Gao, P., Zhang, X. & Cai, Q. (2015). Effective Bone Regeneration Using Thermosensitive Poly(N-Isopropylacrylamide) Grafted Gelatin as Injectable Carrier for Bone Mesenchymal

Stem Cells. *ACS Applied Materials and Interfaces*, 7(34), 19006–19015. <https://doi.org/10.1021/acsami.5b02821>

Ribatti, D., Vacca, A., Roncali, L. & Dammacco, F. (1996). *The chick embryo chorioallantoic membrane as a model for in vivo research on angiogenesis*. 1197, 1189–1197.

Ringe, J. D. (2004). Fluoride and Bone Health. In Holick M. F. and Dawson-Hughes B. (Ed.), *Nutrition and Bone Health* (pp. 345–362). Humana Press. [https://doi.org/10.1007/978-1-59259-740-6\\_21](https://doi.org/10.1007/978-1-59259-740-6_21)

Risau, W. (1997). Mechanisms of angiogenesis. *Nature*, 386(April), 671–674.

Rizwan, M., Yahya, R., Hassan, A., Yar, M., Azzahari, A. D., Selvanathan, V., Sonsudin, F. & Abouloula, C. N. (2017). pH sensitive hydrogels in drug delivery: Brief history, properties, swelling, and release mechanism, material selection and applications. *Polymers*, 9(4). <https://doi.org/10.3390/polym9040137>

Rockwood, D. N., Gil, E. S., Park, S. H., Kluge, J. A., Grayson, W., Bhumiratana, S., Rajkhowa, R., Wang, X., Kim, S. J., Vunjak-Novakovic, G. & Kaplan, D. L. (2011). Ingrowth of human mesenchymal stem cells into porous silk particle reinforced silk composite scaffolds: An in vitro study. *Acta Biomaterialia*, 7(1), 144–151. <https://doi.org/10.1016/j.actbio.2010.07.020>

Rogers, K. D. & Ziopoulos, P. (1999). Bone tissue of the rostrum of a *Mesoplodon densirostris* whale: A mammalian biomineral demonstrating extreme texture. *Journal of Materials Science Letters*, 18(8), 651–654. <https://doi.org/10.1023/A:1006615422214>

Rogina, A., Ressler, A., Matić, I., Gallego Ferrer, G., Marijanović, I., Ivanković, M. & Ivanković, H. (2017). Cellular hydrogels based on pH-responsive chitosan-hydroxyapatite system. *Carbohydrate Polymers*, 166, 173–182. <https://doi.org/10.1016/j.carbpol.2017.02.105>

Rokhade, A. P., Patil, S. A. & Aminabhavi, T. M. (2007). Synthesis and characterization of semi-interpenetrating polymer network microspheres of acrylamide grafted dextran and chitosan for controlled release of acyclovir. *Carbohydrate Polymers*, 67(4), 605–613. <https://doi.org/10.1016/j.carbpol.2006.07.001>

Ruiz-Caro, R. & Veiga-Ochoa, M. D. (2009). Characterization and dissolution study of chitosan freeze-dried systems for drug controlled Release. *Molecules*, 14(11), 4370–4386. <https://doi.org/10.3390/molecules14114370>

Rutkovskiy, A., Stensløkken, K.-O. & Vaage, I. J. (2016). Osteoblast Differentiation at a Glance. *Medical Science Monitor Basic Research*, 95–106. <https://doi.org/10.12659/MSMBR.901142>

Sa, Y., Wang, M., Deng, H., Wang, Y. & Jiang, T. (2015). Beneficial effects of biomimetic nano-sized hydroxyapatite/antibiotic gentamicin enriched chitosan–glycerophosphate hydrogel on the performance of injectable polymethylmethacrylate. *RSC Advances*, 5(110), 91082–91092. <https://doi.org/10.1039/C5RA15915F>

Sadat-Shojaei, M., Khorasani, M. T., Dinpanah-Khoshdargi, E. & Jamshidi, A. (2013). Synthesis methods for nanosized hydroxyapatite with diverse structures. *Acta Biomaterialia*, 9(8), 7591–7621. <https://doi.org/10.1016/j.actbio.2013.04.012>

Schick, C. (2009). Differential scanning calorimetry (DSC) of semicrystalline polymers. *Analytical and Bioanalytical Chemistry*, 395(6), 1589–1611. <https://doi.org/10.1007/s00216-009-3169-y>

Schindeler, A., McDonald, M. M., Bokko, P. & Little, D. G. (2008). Bone remodeling during fracture repair: The cellular picture. *Seminars in Cell & Developmental Biology*, 19(5), 459–466. <https://doi.org/10.1016/j.semcd.2008.07.004>

Schneiders, W., Reinstorf, A., Pompe, W., Grass, R., Biewener, A., Holch, M., Zwipp, H. & Rammelt, S. (2007). Effect of modification of hydroxyapatite/collagen composites with sodium citrate, phosphoserine, phosphoserine/RGD-peptide and calcium carbonate on bone remodelling. *Bone*, 40(4), 1048–1059. <https://doi.org/10.1016/j.bone.2006.11.019>

Scholz, M.-S., Blanchfield, J. P., Bloom, L. D., Coburn, B. H., Elkington, M., Fuller, J. D., Gilbert, M. E., Muflahi, S. A., Pernice, M. F., Rae, S. I., Trevarthen, J. A., White, S. C., Weaver, P. M. & Bond, I. P. (2011). The use of composite materials in modern orthopaedic medicine and prosthetic devices: A review. *Composites Science and Technology*, 71(16), 1791–1803. <https://doi.org/10.1016/j.compscitech.2011.08.017>

Schwarz, K. (1973). A Bound Form of Silicon in Glycosaminoglycans and Polyuronides. *Proceedings of the National Academy of Sciences of the United States of America*, 70(5), 1608–1612.

Shafer-Peltier, K. E., Haka, A. S., Fitzmaurice, M., Crowe, J., Myles, J., Dasari, R. R. & Feld, M. S. (2002). Raman microspectroscopic model of human breast tissue:

Implications for breast cancer diagnosis in vivo. *Journal of Raman Spectroscopy*, 33(7), 552–563. <https://doi.org/10.1002/jrs.877>

Shahzad, S., Shahzadi, L., Mahmood, N., Siddiqi, S. A., Rauf, A., Manzoor, F., Chaudhry, A. A., Rehman, I. U. & Yar, M. (2016). A new synthetic methodology for the preparation of biocompatible and organo-soluble barbituric- and thiobarbituric acid based chitosan derivatives for biomedical applications. *Materials Science and Engineering C*, 66, 156–163. <https://doi.org/10.1016/j.msec.2016.04.056>

Shahzad, S., Yar, M., Siddiqi, S. A. nwar, Mahmood, N., Rauf, A., Qureshi, Z. ul A., Anwar, M. S. abieh & Afzaal, S. (2015). Chitosan-based electrospun nanofibrous mats, hydrogels and cast films: novel anti-bacterial wound dressing matrices. *Journal of Materials Science. Materials in Medicine*, 26(3), 136. <https://doi.org/10.1007/s10856-015-5462-y>

Shahzadi, L., Yar, M., Jamal, A., Siddiqi, S. A., Chaudhry, A. A., Zahid, S., Tariq, M., Rehman, I. u. U. & MacNeil, S. (2016). Triethyl orthoformate covalently cross-linked chitosan-(poly vinyl) alcohol based biodegradable scaffolds with heparin-binding ability for promoting neovascularisation. *Journal of Biomaterials Applications*, 0(0), 1–12. <https://doi.org/10.1177/0885328216650125>

Shalaby, S. W. & Salz, U. (2007). *Polymers for dental and orthopedic applications*. CRC Press Taylor & Francis Group. <http://www.crcpress.com>

Sharma, B. D. (1965). Sodium bicarbonate and its hydrogen atom. *Acta Crystallographica*, 18(4), 818–819. <https://doi.org/10.1107/S0365110X65001895>

Sharma, R., Bisen, D. P., Shukla, U. & Sharma, B. G. (2012). X-ray diffraction: a powerful method of characterizing nanomaterials. *Recent Research in Science and Technology*, 4(8), 77–79. <http://recent-science.com/>

Shavandi, A., Bekhit, A. E. D. A. D. A., Sun, Z. & Ali, M. A. (2016). Injectable gel from squid pen chitosan for bone tissue engineering applications. *Journal of Sol-Gel Science and Technology*, 77(3), 675–687. <https://doi.org/10.1007/s10971-015-3899-6>

Sheikh, Z., Hamdan, N., Ikeda, Y., Grynpas, M., Ganss, B. & Glogauer, M. (2017). Natural graft tissues and synthetic biomaterials for periodontal and alveolar bone reconstructive applications: A review. *Biomaterials Research*, 21(1), 1–20. <https://doi.org/10.1186/s40824-017-0095-5>

Shive, M. S., Hoemann, C. D., Restrepo, A., Hurtig, M. B., Duval, N., Ranger, P., Stanish, W. & Buschmann, M. D. (2006). BST-CarGel: In Situ ChondroInduction for Cartilage Repair. *Operative Techniques in Orthopaedics*, 16(4), 271–278. <https://doi.org/10.1053/j.oto.2006.08.001>

Shive, M. S., Stanish, W. D., McCormack, R., Forriol, F., Mohtadi, N., Pelet, S., Desnoyers, J., Méthot, S., Vehik, K. & Restrepo, A. (2015). BST-CarGel® Treatment Maintains Cartilage Repair Superiority over Microfracture at 5 Years in a Multicenter Randomized Controlled Trial. *Cartilage*, 6(2), 62–72. <https://doi.org/10.1177/1947603514562064>

Shively, S. & Miller, W. R. (2009). The use of HMDS ( hexamethyldisilazane ) to replace Critical Point Drying ( CPD ) in the preparation of tardigrade for SEM ( Scanning Electron Microscope ) imaging Author ( s ): Shawn Shively and William R . Miller Source : Transactions of the Kansas Acad. *Transactions of The Kansas Academy of Science (1903)*, 112(3), 198–200. [www.jstor.org/stable/40588242](http://www.jstor.org/stable/40588242)

Shriky, B., Kelly, A., Isreb, M., Babenko, M., Mahmoudi, N., Rogers, S., Shebanova, O., Snow, T. & Gough, T. (2020). Pluronic F127 thermosensitive injectable smart hydrogels for controlled drug delivery system development. *Journal of Colloid and Interface Science*, 565, 119–130. <https://doi.org/10.1016/j.jcis.2019.12.096>

Smith, R. & Rehman, I. (1994). Fourier transform Raman spectroscopic studies of human bone. *Journal of Materials Science: Materials in Medicine*, 5(9–10), 775–778. <https://doi.org/10.1007/BF00120375>

Sorlier, P., Denuzière, A., Viton, C. & Domard, A. (2001). Relation between the degree of acetylation and the electrostatic properties of chitin and chitosan. *Biomacromolecules*, 2(3), 765–772. <https://doi.org/10.1021/bm015531+>

Stegen, S., Gastel, N. Van & Carmeliet, G. (2015). Bringing new life to damaged bone : The importance of angiogenesis in bone repair and regeneration ☆. *Bone*, 70, 19–27. <https://doi.org/10.1016/j.bone.2014.09.017>

Stenzel, K. H., Miyata, T. & Rubin, A. L. (1974). Collagen as a biomaterial. *Annual Review of Biophysics and Bioengineering*, 3(0), 231–253. <https://doi.org/10.1146/annurev.bb.03.060174.001311>

Stevens, B., Yang, Y., Mohandas, A., Stucker, B. & Nguyen, K. T. (2008). A review of materials, fabrication methods, and strategies used to enhance bone regeneration in engineered bone tissues. *Journal of Biomedical Materials Research - Part B*

*Applied Biomaterials*, 85(2), 573–582. <https://doi.org/10.1002/jbm.b.30962>

Stone, N., Kendall, C., Shepherd, N., Crow, P. & Barr, H. (2002). Near-infrared Raman spectroscopy for the classification of epithelial pre-cancers and cancers. *Journal of Raman Spectroscopy*, 33(7), 564–573. <https://doi.org/10.1002/jrs.882>

Sudarsanan, K. & Young, R. A. (1969). Significant precision in crystal structural details. Holly Springs hydroxyapatite. *Acta Crystallographica Section B Structural Crystallography and Crystal Chemistry*, 25(8), 1534–1543. <https://doi.org/10.1107/S0567740869004298>

Sun, F., Pang, X. & Zhitomirsky, I. (2009). Electrophoretic deposition of composite hydroxyapatite-chitosan-heparin coatings. *Journal of Materials Processing Technology*, 209(3), 1597–1606. <https://doi.org/10.1016/j.jmatprotec.2008.04.007>

Sun, X., Peng, W., Yang, Z., Ren, M., Zhang, S., Zhang, W., Zhang, L., Xiao, K., Wang, Z., Zhang, B. & Wang, J. (2011). Heparin-Chitosan-Coated Acellular Bone Matrix Enhances Tissue Engineering Scaffolds. *Tissue Engineering Part A*, 17. <https://doi.org/10.1089/ten.tea.2011.0027>

Sutter, B., Dalton, J. B., Amundson, R., Ewing, S. A. & McKay, C. P. (2005). Infrared spectroscopic analyses of sulfate, nitrate, and carbonate-bearing Atacama desert soils: analogs for the interpretation of infrared spectra from the martian surface. *Lunar and Planetary Science*. <https://doi.org/20050175994>

Swarbrick, B. (2014). The current state of near infrared spectroscopy application in the pharmaceutical industry. *Journal of Near Infrared Spectroscopy*, 22(3), 153–156. <https://doi.org/10.1255/jnirs.1122>

Swayze, G. A. & Clark, R. N. (1990). Infrared Spectra and Crystal Chemistry of Scapolites' Implications for Martian Mineralogy. *Journal of Geophysical Research*, 95, 14881–14495.

Swetha, M., Sahithi, K., Moorthi, A., Srinivasan, N., Ramasamy, K. & Selvamurugan, N. (2010). Biocomposites containing natural polymers and hydroxyapatite for bone tissue engineering. *International Journal of Biological Macromolecules*, 47(1), 1–4. <https://doi.org/10.1016/j.ijbiomac.2010.03.015>

Synowiecki, J. & Al-Khateeb, N. A. (2003). Production, properties, and some new applications of chitin and its derivatives. *Critical Reviews in Food Science and Nutrition*, 43(2), 145–171. <https://doi.org/10.1080/10408690390826473>

Tabata, Y. & Ikada, Y. (1998). Protein release from gelatin matrices. *Advanced Drug*

*Delivery Reviews*, 31(3), 287–301. [https://doi.org/10.1016/S0169-409X\(97\)00125-7](https://doi.org/10.1016/S0169-409X(97)00125-7)

Tae, G., Kim, Y. J., Choi, W. Il, Kim, M., Stayton, P. S. & Hoffman, A. S. (2007). Formation of a novel heparin-based hydrogel in the presence of heparin-binding biomolecules. *Biomacromolecules*, 8(6), 1979–1986. <https://doi.org/10.1021/bm0701189>

Takahashi, C., Ueno, K., Aoyama, J., Adachi, M. & Yamamoto, H. (2017). Imaging of intracellular behavior of polymeric nanoparticles in *Staphylococcus epidermidis* biofilms by slit-scanning confocal Raman microscopy and scanning electron microscopy with energy-dispersive X-ray spectroscopy. *Materials Science and Engineering C*, 76, 1066–1074. <https://doi.org/10.1016/j.msec.2017.03.132>

Talavera-Adame, D., Xiong, Y., Zhao, T., Arias, A. E., Sierra-honigmann, M. R. & Farkas, D. L. (2008). Quantitative and morphometric evaluation of the angiogenic effects of leptin. *Journal of Biomedical Optics*, 13(December 2008), 1–7. <https://doi.org/10.1117/1.3028010>

Tamimi, F. M., Torres, J., Tresguerres, I., Clemente, C., López-Cabarcos, E. & Blanco, L. J. (2006). Bone augmentation in rabbit calvariae: Comparative study between Bio-Oss® and a novel  $\beta$ -TCP/DCPD granulate. *Journal of Clinical Periodontology*, 33(12), 922–928. <https://doi.org/10.1111/j.1600-051X.2006.01004.x>

Tan, H., Ramirez, C. M., Miljkovic, N., Li, H., Rubin, J. P. & Marra, K. G. (2009). Thermosensitive injectable hyaluronic acid hydrogel for adipose tissue engineering. *Biomaterials*, 30(36), 6844–6853. <https://doi.org/10.1016/j.biomaterials.2009.08.058>

Tang, Y., Du, Y., Li, Y., Wang, X. & Hu, X. (2009). A thermosensitive chitosan/poly(vinyl alcohol) hydrogel containing hydroxyapatite for protein delivery. *Journal of Biomedical Materials Research - Part A*, 91(4), 953–963. <https://doi.org/10.1002/jbm.a.32240>

Terentis, A. C., Fox, S. A., Friedman, S. J. & Spencer, E. S. (2013). Confocal Raman microspectroscopy discriminates live human metastatic melanoma and skin fibroblast cells. *Journal of Raman Spectroscopy*, 44(9), 1205–1216. <https://doi.org/10.1002/jrs.4363>

Tetteh, G. A. J. (2016). *Polyurethane-based Scaffolds for Bone Tissue Engineering The Role of Hydroxyapatite Particles, Solvent Combinations, Electrospun Fibre*

*Orientations, In Vivo & In Vitro Characterisation, and Particulate Leached Foams for creating 3-D Bone Models.* [The University of Sheffield]. [http://etheses.whiterose.ac.uk/16015/1/G\\_Tetteh\\_Final Thesis Resized.pdf](http://etheses.whiterose.ac.uk/16015/1/G_Tetteh_Final Thesis Resized.pdf)

Thakral, N. K., Zanon, R. L., Kelly, R. C. & Thakral, S. (2018). Applications of Powder X-Ray Diffraction in Small Molecule Pharmaceuticals: Achievements and Aspirations. *Journal of Pharmaceutical Sciences*, 107(12), 2969–2982. <https://doi.org/10.1016/j.xphs.2018.08.010>

U.S. Department of Health and Human Services Food and Drug Administration Center. (2004). *Guidance for Industry Sterile Drug Products Produced by aseptic Processing- Current Good Manufacturing Practice* (Issue September). <https://doi.org/10.1186/1477-7525-4-79>

Ulian, G., Valdré, G., Corno, M. & Ugliengo, P. (2013). The vibrational features of hydroxylapatite and type A carbonated apatite: A first principle contribution. *American Mineralogist*, 98(4), 752–759. <https://doi.org/10.2138/am.2013.4315>

Ullah, F., Othman, M. B. H., Javed, F., Ahmad, Z. & Akil, H. M. (2015). Classification, processing and application of hydrogels: A review. *Materials Science and Engineering C*, 57, 414–433. <https://doi.org/10.1016/j.msec.2015.07.053>

Unger, R. E., Sartoris, A., Peters, K., Motta, A., Migliaresi, C., Kunkel, M., Bulnheim, U., Rychly, J. & James Kirkpatrick, C. (2007). Tissue-like self-assembly in cocultures of endothelial cells and osteoblasts and the formation of microcapillary-like structures on three-dimensional porous biomaterials. *Biomaterials*, 28(27), 3965–3976. <https://doi.org/10.1016/j.biomaterials.2007.05.032>

Urist, M. R. (1965). Bone : Formation by Autoinduction. *American Association for the Advancement of Science*, 150(3698), 893–899. <https://www.jstor.org/stable/1717499>

Urist, M. R., Mikulski, A. & Lietze, A. (1979). Solubilized and insolubilized bone morphogenetic protein. *Cell Biology*, 76(4), 1828–1832.

US Department of Health and Human Services. (2004). Bone health and osteoporosis: a report of the Surgeon General. In *US Health and Human Services*. <https://doi.org/10.2165/00002018-200932030-00004>

Uswatta, S. P., Okeke, I. U. & Jayasuriya, A. C. (2016). Injectable porous nano-hydroxyapatite/chitosan/tripolyphosphate scaffolds with improved compressive strength for bone regeneration. *Materials Science and Engineering C*, 69, 505–

512. <https://doi.org/10.1016/j.msec.2016.06.089>

Vallet-Regí, M. & González-Calbet, J. M. (2004). Calcium phosphates as substitution of bone tissues. In *Progress in Solid State Chemistry* (Vol. 32, Issues 1–2, pp. 1–31). <https://doi.org/10.1016/j.progsolidstchem.2004.07.001>

Vo, T. N., Kasper, F. K. & Mikos, A. G. (2012). Strategies for controlled delivery of growth factors and cells for bone regeneration. *Advanced Drug Delivery Reviews*, 64(12), 1292–1309. <https://doi.org/10.1016/j.addr.2012.01.016>

Wang, P., Li, C., Gong, H., Jiang, X., Wang, H. & Li, K. (2010). Effects of synthesis conditions on the morphology of hydroxyapatite nanoparticles produced by wet chemical process. *Powder Technology*, 203(2), 315–321. <https://doi.org/10.1016/j.powtec.2010.05.023>

Wang, X., Nyman, J. S., Dong, X., Leng, H. & Reyes, M. (2010). Fundamental Biomechanics in Bone Tissue Engineering. In *Synthesis Lectures on Tissue Engineering* (Vol. 2, Issue 1). <https://doi.org/10.2200/S00246ED1V01Y200912TIS004>

Wang, Yihu, Ma, M., Wang, J., Zhang, W., Lu, W., Gao, Y., Zhang, B. & Guo, Y. (2018). Development of a photo-crosslinking, biodegradable GelMA/PEGDA hydrogel for guided bone regeneration materials. *Materials*, 11(8), 6–8. <https://doi.org/10.3390/ma11081345>

Wang, Yongsheng, Zhang, S., Zeng, X., Ma, L. L., Weng, W., Yan, W. & Qian, M. (2007). Osteoblastic cell response on fluoridated hydroxyapatite coatings. *Acta Biomaterialia*, 3(2), 191–197. <https://doi.org/10.1016/j.actbio.2006.10.002>

Weatherell, A. J. (1966). Fluoride and the Skeletal and Dental Tissues. In *Handbook of Experimental Pharmacology* (Vol. 20, pp. 141–143).

Wegst, U. G. K., Bai, H., Saiz, E., Tomsia, A. P. & Ritchie, R. O. (2015). Bioinspired structural materials. *Nature Materials*, 14(1), 23–36. <https://doi.org/10.1038/nmat4089>

Williams, D. F. (2008). On the mechanisms of biocompatibility. *Biomaterials*, 29(20), 2941–2953. <https://doi.org/10.1016/j.biomaterials.2008.04.023>

Witek, L., Smay, J., Silva, N. R. F. A., Guda, T., Ong, J. L. & Coelho, P. G. (2013). Sintering effects on chemical and physical properties of bioactive ceramics. *Journal of Advanced Ceramics*, 2(3), 274–284. <https://doi.org/10.1007/s40145-013-0072-y>

Wu, J., Liu, J., Shi, Y. & Wan, Y. (2016). Rheological, mechanical and degradable properties of injectable chitosan/silk fibroin/hydroxyapatite/glycerophosphate hydrogels. *Journal of the Mechanical Behavior of Biomedical Materials*, 64, 161–172. <https://doi.org/10.1016/j.jmbbm.2016.07.007>

Wu, K. K. & Brown, I. D. (1975). A neutron diffraction study of Na<sub>2</sub>CO<sub>3</sub>.H<sub>2</sub>O. *Acta Crystallographica Section B Structural Crystallography and Crystal Chemistry*, 31(3), 890–892. <https://doi.org/10.1107/S0567740875004001>

Xia, L., Lin, K., Jiang, X., Xu, Y., Zhang, M., Chang, J. & Zhang, Z. (2013). Enhanced osteogenesis through nano-structured surface design of macroporous hydroxyapatite bioceramic scaffolds via activation of ERK and p38 MAPK signaling pathways. *Journal of Materials Chemistry B*, 1(40), 5403–5416. <https://doi.org/10.1039/c3tb20945h>

Xie, S., Guan, Y., Zhu, P., Li, F., Yu, M., Linhardt, R. J., Chi, L. & Jin, L. (2018). Preparation of low molecular weight heparins from bovine and ovine heparins using nitrous acid degradation. *Carbohydrate Polymers*, 197(April), 83–91. <https://doi.org/10.1016/j.carbpol.2018.05.070>

Yang, H. S., La, W. G., Bhang, S. H., Jeon, J. Y., Lee, J. H. & Kim, B. S. (2010). Heparin-conjugated fibrin as an injectable system for sustained delivery of bone morphogenetic protein-2. *Tissue Engineering - Part A*, 16(4), 1225–1233. <https://doi.org/10.1089/ten.tea.2009.0390>

Yang, H., Xu, H., Liu, H., Ouyang, C. & Xu, W. (2011). A novel heparin release system based on blends of biomedical polyurethane and native silk fibroin powder. *Journal of Controlled Release : Official Journal of the Controlled Release Society*, 152 Suppl, e106–e108. <https://doi.org/10.1016/j.jconrel.2011.08.155>

Yar, M., Farooq, A., Shahzadi, L., Khan, A. S., Mahmood, N., Rauf, A., Chaudhry, A. A. & Rehman, I. U. (2016). Novel meloxicam releasing electrospun polymer/ceramic reinforced biodegradable membranes for periodontal regeneration applications. *Materials Science and Engineering C*, 64, 148–156. <https://doi.org/10.1016/j.msec.2016.03.072>

Yar, M., Gigliobianco, G., Shahzadi, L., Dew, L., Siddiqi, S. A., Khan, A. F., Chaudhry, A. A., Rehman, I. ur & MacNeil, S. (2016). Production of chitosan PVA PCL hydrogels to bind heparin and induce angiogenesis. *International Journal of Polymeric Materials and Polymeric Biomaterials*, 65(9), 466–476.

<https://doi.org/10.1080/00914037.2015.1129959>

Yar, M., Shahzad, S., Shahzadi, L., Shahzad, S. A., Mahmood, N., Chaudhry, A. A., Rehman, I. ur & MacNeil, S. (2017). Heparin binding chitosan derivatives for production of pro-angiogenic hydrogels for promoting tissue healing. *Materials Science and Engineering: C*, 74, 347–356.

<https://doi.org/10.1016/j.msec.2016.12.021>

Yasmeen, S., Lo, M. K., Bajracharya, S. & Roldo, M. (2014). Injectable Scaffolds for Bone Regeneration. *Langmuir*, 30(43), 12977–12985.

<https://doi.org/10.1021/la503057w>

Yen, S.-F. & Sou, M. (1998). *Process for preparing stabilized chitin derivative compounds* (Patent No. 5,773,608). United States Patent (19).

Yusof, Y. M. (2017). *Characteristics of Corn Starch / Chitosan Blend Green Polymer Electrolytes Complexed With Ammonium Iodide and Its Application in Energy Devices*. Institute of Graduate Studies University of Malaya.

Zajac, A., Hanuza, J., Wandas, M. & Dymińska, L. (2015). Determination of N-acetylation degree in chitosan using Raman spectroscopy. *Spectrochimica Acta - Part A: Molecular and Biomolecular Spectroscopy*, 134, 114–120.

<https://doi.org/10.1016/j.saa.2014.06.071>

Zakaria, S. M., Sharif Zein, S. H., Othman, M. R., Yang, F. & Jansen, J. A. (2013). Nanophase Hydroxyapatite as a Biomaterial in Advanced Hard Tissue Engineering: A Review. *Tissue Engineering Part B: Reviews*, 19(5), 431–441.

<https://doi.org/10.1089/ten.teb.2012.0624>

Zeller-Plumhoff, B., Malich, C., Krüger, D., Campbell, G., Wiese, B., Galli, S., Wennerberg, A., Willumeit-Römer, R. & Wieland, D. C. F. (2019). Analysis of the bone ultrastructure around biodegradable Mg–xGd implants using small angle X-ray scattering and X-ray diffraction. *Acta Biomaterialia*, 101, 637–645.

<https://doi.org/10.1016/j.actbio.2019.11.030>

Zhai, W., Lu, H., Chen, L., Lin, X., Huang, Y., Dai, K., Naoki, K., Chen, G. & Chang, J. (2012). Silicate bioceramics induce angiogenesis during bone regeneration. *Acta Biomaterialia*, 8(1), 341–349. <https://doi.org/10.1016/j.actbio.2011.09.008>

Zhai, W., Lu, H., Wu, C., Chen, L., Lin, X., Naoki, K., Chen, G. & Chang, J. (2013). Stimulatory effects of the ionic products from Ca-Mg-Si bioceramics on both osteogenesis and angiogenesis in vitro. *Acta Biomaterialia*, 9(8), 8004–8014.

<https://doi.org/10.1016/j.actbio.2013.04.024>

Zhang, J. & Peppas, N. A. (2002). Morphology of poly(methacrylic acid)/poly(N-isopropyl acrylamide) interpenetrating polymeric networks. *Journal of Biomaterials Science, Polymer Edition*, 13(5), 511–525. <https://doi.org/10.1163/15685620260178373>

Zhang, Q., Fassihi, M. A. & Fassihi, R. (2018). Delivery Considerations of Highly Viscous Polymeric Fluids Mimicking Concentrated Biopharmaceuticals: Assessment of Injectability via Measurement of Total Work Done “W T”. *AAPS PharmSciTech*, 19(4), 1520–1528. <https://doi.org/10.1208/s12249-018-0963-x>

Zhang, W., Wang, W., Chen, Q. Y., Lin, Z. Q., Cheng, S. W., Kou, D. Q., Ying, X. Z., Shen, Y., Cheng, X. J., Nie, P. F., Li, X. C., Rompis, F. A., Huang, H., Zhang, H., Mu, Z. L. & Peng, L. (2012). Effect of calcium citrate on bone integration in a rabbit femur defect model. *Asian Pacific Journal of Tropical Medicine*, 5(4), 310–314. [https://doi.org/10.1016/S1995-7645\(12\)60045-5](https://doi.org/10.1016/S1995-7645(12)60045-5)

Zhang, X. & Williams, D. (2019). Biocompatibility and immune responses to biomaterials. In X. Zhang & D. Williams (Eds.), *Definitions of Biomaterials for the Twenty-First Century* (pp. 55–101). Elsevier. <https://doi.org/10.1016/c2018-0-02529-3>

Zhang, Y., Venugopal, J. R., El-Turki, A., Ramakrishna, S., Su, B. & Lim, C. T. (2008). Electrospun biomimetic nanocomposite nanofibers of hydroxyapatite/chitosan for bone tissue engineering. *Biomaterials*, 29(32), 4314–4322. <https://doi.org/10.1016/j.biomaterials.2008.07.038>

Zhao, X. (2010). *Injectable Degradable Composite Materials for Bone Repair and Drug Delivery*. University College London.

Zheng, H., Tang, C. & Yin, C. (2015). Oral delivery of shRNA based on amino acid modified chitosan for improved antitumor efficacy. *Biomaterials*, 70, 126–137. <https://doi.org/10.1016/j.biomaterials.2015.08.024>

Zheng, K., Zhang, J. & Cheng, J. (2016). Miscibility, morphology, structure, and properties of porous cellulose-soy protein isolate hybrid hydrogels. *Journal of Applied Polymer Science*, 133(36), 1–7. <https://doi.org/10.1002/app.43853>

Zouani, O. F., Kalisky, J., Ibarboure, E. & Durrieu, M. C. (2013). Effect of BMP-2 from matrices of different stiffnesses for the modulation of stem cell fate. *Biomaterials*, 34(9), 2157–2166. <https://doi.org/10.1016/j.biomaterials.2012.12.007>